Investigations of Initiation and Evolution of Transient Phenomena in Solar Atmosphere

A thesis submitted to GUJARAT UNIVERSITY *for the degree of*

Doctor of Philosophy

by

Prabir Kumar Mitra

(Registration No. 8632; date of registration: 12 January 2019)

Under the guidance of

Dr. Bhuwan Joshi

Associate Professor

Udaipur Solar Observatory

Physical Research Laboratory, Udaipur, India

DEPARTMENT OF PHYSICS

GUJARAT UNIVERSITY

NAVRANGPURA, AHMEDABAD, INDIA

FEBRUARY, 2022

to

my family, teachers

&

the solar physics community

Declaration

I declare that the thesis entitled **"Investigations of Initiation and Evolution of Transient Phenomena in Solar Atmosphere"** has been prepared by me under the guidance of **Dr. Bhuwan Joshi, Associate Professor, Udaipur Solar Observatory, Physical Research Laboratory**. The thesis represents my ideas in my own words and where others' ideas or words have been included, I have adequately cited and referenced the original sources. I also declare that I have adhered to all principles of academic honesty and integrity and have not misrepresented or fabricated or falsified any idea/data/fact/source in my submission. I understand that any violation of the above will be cause for disciplinary action by the university and can also evoke penal action from the sources which have thus not been properly cited or from whom proper permission has not been taken when needed. No part of the thesis has formed the basis for the award of any degree or fellowship previously.

Prabir Kumar Mitra
19/09/2022

(Signature)

(Name: Prabir Kumar Mitra)

(Registration No: 8632)

(Registration date: 12 January 2019)

CERTIFICATE

It is certified that the work contained in the thesis titled **"Investigations of Initiation and Evolution of Transient Phenomena in Solar Atmosphere"** by **Prabir Kumar Mitra** (Registration no: 8632), is a record of original research work done by him during the period of study under my supervision and that the thesis has not previously formed the basis for the award to the candidate of any Degree, Diploma or other similar titles and that the thesis represents independent research work on the part of the scholar.

I have read this dissertation and in my opinion, it is fully adequate in scope and quality as a dissertation for the degree of Doctor of Philosophy.

Bhuwan Joshi
19/09/2022

Dr. Bhuwan Joshi

(Thesis Supervisor)

डॉ. भुवन जोशी / Dr. Bhuwan Joshi
एसोसिएट प्रोफेसर / Associate Professor
उदयपुर सौर वेधशाला
Udaipur Solar Observetory
भौतिक अनुसंधान प्रयोगशाला
Physical Research Laboratory
अंतरिक्ष विभाग, भारत सरकार
Dept. of Space, Govt. of India
उदयपुर / Udaipur-313001

Acknowledgements

This thesis would not have come to reality without the help, support and guidance of a number of people. I would like to take this opportunity to express my sincere gratitude towards all of them.

First and foremost, I am utmost indebted to my Ph.D. supervisor, Dr. Bhuwan Joshi, for all his continuous motivation, intellectual and spiritual support, and help in uncountable aspects. I received his continuous guidance throughout my Ph.D. tenure that includes identifying research problems, learning data analysis and image processing techniques, scientific writing, presentation skills, etc. It was a great experience to work under his supervision. His continuous aspiration and encouragement enabled me to develop as an independent researcher.

I am also grateful to Prof. Astrid M. Veronig for her constructive comments, suggestions and other academic supports which helped me improve the quality of my Ph.D. work. She provided me multiple opportunities to visit her lab and work in collaboration which enriched my Ph.D. experience in more than one aspects.

I take this opportunity to express my sincere thanks to my Doctoral Studies Committee (DSC) members, Prof. Varun Sheel, Dr. Ramitendranath Bhattacharyya, and Dr. Amitava Guharay for continuous evaluation of my work and useful suggestions throughout the duration of my Ph.D. Their invaluable comments helped me improve the scientific outcomes. Also I am grateful to them for examining the thesis.

I express my gratitude to Prof. Anil Bhardwaj, Director, Physical Research Laboratory (PRL) for providing the necessary facilities to carry out my research work. I thank the PRL academic committee members for reviewing my research progress and providing important instructions and valuable suggestions toward improving the thesis content. I am specially thankful to Dr. Bhushit Vaishnav for his enormous involvement during my Ph.D. registration at Gujarat University and various types of help since my joining at PRL.

I am grateful to Gujarat University for my Ph.D. registration.

I would like to express my deepest appreciation to the entire family of PRL, USO/PRL, and all the members of USO residency.

I thank all the team members of SDO, RHESSI, GOES, LASCO, HiRAS, GONG for providing data which I utilized in this thesis. I also thank Dr. Thomas Wiegelmann for providing the NLFFF extrapolation code which has been an integral part of my thesis work.

I am deeply indebted to all my friends, seniors and juniors, without the joyful company and constant support of whom it would not have been possible to pass the Ph.D. days. I convey my sincere thanks to my beloved seniors Sajal da, Avijeet da, Alok da, Sanjay bhaiya, Rahul bhaiya, Supriya di, Sowmya di, Sangeetha di, Navin bhaiya, Syed Ibrahim, Ranadeep da for always motivating and supporting me during the highs and lows of my Ph.D. years. I express my love and best wishes to my friends and juniors, especially to Kamlesh, Binal, Satyam, Priyank, Suraj, Sushree, Abdur, Ayan, Harish, Sandeep, Surendra, Nisha, Deepika, Sana, Sovan.

Finally, I would like to thank my family members, specially my mother and brother; and my best friends Soumyajeet and Sushovan for all their unconditional love and lifelong support. I thank all my friends in Kolkata, Ahmedabad, Udaipur and all over the world. I feel immense pleasure to dedicate this thesis to them. They have always been by my side all the time. I also thank all my B.Sc and M.Sc teachers and batch mates. Lastly, I convey my thanks to those with whom I have lost contact during my Ph.D. tenure but considered important once.

Prabir Kumar Mitra

Abstract

Solar transient phenomena correspond to various explosive activities observed in the solar atmosphere on a wide spatial, temporal, and spectral scales. The most spectacular manifestations of solar transients include energetic outbursts in the form of solar flares, prominence eruptions, coronal mass ejections (CMEs) etc. These events are observed to occur over a time-scale from few minutes to few hours. It is globally accepted that localized, explosive energy release in solar atmosphere is powered by previously stored magnetic energy by the magnetic reconnection process. Naturally, they mostly originate from the solar active regions which consist of complex configurations of strong magnetic field extending from the sub-photospheric levels, crossing through the photosphere to the coronal layers. Emission signatures during these events spread across the entire electro-magnetic spectrum, being associated with an array of activities taking place at different layers of the Sun. Thus, multi-wavelength analysis is crucial to diagnose the different underlying processes associated with the solar transient activities. Eruption of plasma and magnetic field associated with eruptive flares and ejection of highly energetic particles accelerated during the reconnection process are known to produce extreme space weather and hazardous effects at the near-Earth environment. Therefore, the investigations of solar transient phenomena are considered as one of the important topics in contemporary solar physics.

With a combined multi-wavelength observational and modeling approaches, in this thesis, I have explored key aspects related to the onset and evolution of solar transient phenomena, at a wide range of spatial, temporal, and spectral scales. We have extensively used high resolution and high cadence imaging observations in extreme ultraviolet (EUV) and ultraviolet (UV) channels from the Atmospheric Imaging Assembly (AIA) and photospheric magnetic field observations from the Helioseismic and Magnetic Imager (HMI) on board the Solar Dynamics Observatory (SDO). X-ray imaging and spectroscopic data from the Reuven Ramaty High Energy Solar Spectroscopic Imager (RHESSI) have been used to investigate the thermal and non-thermal energy release processes associated the transient activities. Kinematic details of the CMEs in the corona and near-Sun region, was provided by the Large Angle and Spectrometric Coronagraph (LASCO). Tem-

poral information of solar flares was obtained by the disk-integrated soft X-ray lightcurves in the 1–8 Å and 0.5–4 Å bands of the Geostationary Operational Environmental Satellite (GOES) system. Depending upon the specific science objectives, we have also included optical and radio observations from the Global Oscillation Network Group (GONG) and Hirasio Radio Spectrograph (HiRAS), respectively. Complementary to the observational analysis, in order to probe the precise coronal magnetic configuration associated with the flaring events, we have extensively used coronal magnetic field reconstruction techniques using the potential and Non-linear Force Free Field (NLFFF) models. We extended our numerical analysis by computing magnetic decay index (n), degree of squashing factor (Q) and twist numbers (T_w) using the reconstructed coronal magnetic field.

With an objective to investigate the triggering mechanisms of large-scale solar eruptions, we carried out thorough analysis of two spectacular eruptive flares: a dual-peak M-class flare from the active region NOAA 12371 on 21 June 2015 and an X-class flare from the active region NOAA 11875 on 28 October 2013. These case studies especially focused on the exploration of the pre-flare phases. Both the eruptive events were associated with multiple episodes of small-scale energy release prior to the onset of the main flares, i.e., pre-flare activities, originating within or in the vicinity of the main flaring site. Prior to the onset of the M-class flare, NOAA 12371 exhibited an extended phase of striking display of photopsheric activities including motions of small magnetic patches as well as sunspot rotations. Prolonged phase of flux enhancement followed by a relatively shorter period of flux cancellation along the polarity inversion line (PIL) led to the build up and activation of a flux rope. Pre-flare activity from a location characterized by strong photospheric currents of opposite polarities, most likely induced a slipping reconnection towards the northern leg of the activated flux rope which resulted in its complete destabilization during the M-class flare. The X-class flare from NOAA 11875 initiated with the eruption of a pre-existing coronal hot channel. The hot channel underwent an activation phase during which we observed localized and prolonged pre-flare events occurring adjacent to one of its footpoints. The eruption of the hot channel was characterized by a distinct precursor phase when the hot channel underwent a slow rise, which transitioned to eruptive motion with the onset of the impulsive phase of the X-class flare. The results of our investigations suggest that continuous small-scale reconnection activities close to a flux rope can result in the slow activation and eruption of it by adding flux content to the flux rope as well as reducing the strapping magnetic field confining the flux rope. Further, we have gathered different multi-wavelength observational signatures of the standard flare which can be explained as manifestations of magnetic reconnection in two-dimension (2D).

We extended our observational investigations of magnetic reconnection to three-dimension (3D) by carrying out thorough multi-wavelength and modeling analysis of circular ribbon flares. Particularly, we present in-depth study of the origin and magnetic field evolution during quasi-circular ribbon eruptive flares from NOAA 11977 on 16 February 2014. The unique photospheric configuration governing the homologous flares was characterized by dispersed negative polarity regions surrounded by positive polarity regions in a shape analogous to the geological 'atoll' structures. A filament channel resided along the PIL at the northern edge of the magnetic atoll region. Repetitive formation and activation of flux ropes from the filament channel led to the onset of four flares within an interval of ≈11 hours. NLFFF coronal modeling complemented by the computation of Q revealed a fan-spine-like configuration associated with the magnetic atoll region. However, instead of the coronal null point, the fan-spine-like configuration involved a hyperbolic flux tube (HFT). With the course of the flares, the apparent length of the HFT gradually decreased and the overall fan-spine-like configuration reduced to a null-point-like configuration before the fourth flare. Prior to the eruption of the filaments, we observed localized brightening from the location of the filament as well as flux cancellation at the PIL, which are supportive of the tether-cutting model for flux rope activation. Interaction of the erupting filament with the quasi-separatrix layer (QSL) associated with the fan-like configuration gave rise to the quasi-circular ribbons along the boundary of the magnetic atoll region.

In order to closely examine the conditions responsible for the failed eruption of magnetic flux ropes during intense flares, we carried out comprehensive analysis of a confined M-class flare originating from quadrupolar magnetic configuration of NOAA 11302 on 26 September 2011. Notably, quadrupolar configurations are frequently observed to produce large eruptive flares. NLFFF-reconstructed coronal configuration revealed the presence of a coronal null point in association with the quadrupolar configuration. Over an extended phase prior to the onset of the M-class flare, we observed multiple periods of small-scale flux enhancements in the soft X-ray observations of GOES and RHESSI, which were associated with small-scale reconnections from the location of the null point. Such pre-flare configuration and evolution are consistent with the breakout model of solar eruptions. EUV images prior to the onset of the M-class flare clearly revealed the presence of two spatially well-separated filaments at the flaring location. Onset of the flare was characterized by the activation of a filament which underwent a brief phase of eruption during the impulsive phase of the flare. However, the eruption soon halted and we observed the formation of an intertwined double-decker system involving the two filaments during the gradual phase of the flare. Analysis of magnetic decay index revealed a saddle-type profile above the axis of the flux rope, where the values of decay index initially increased reaching to the conditions of torus instability within much lower heights. However, following the initial increase, magnetic decay index values decreased rapidly reaching to negative values before steadily increasing again. Based on this important observation, we propose that the negative value of the magnetic decay index not only decelerated the eruption of the flux rope but also repelled it back downward resulting in the failed eruption.

In the year 2017, when the solar cycle 24 was progressing in the decline phase, an exceptionally eruptive active region NOAA 12673 emerged during the period 28 August – 10 September. We undertook a comprehensive study of the evolution, build up of magnetic complexity, and eruptivity of this historical active region which produced 4 X-class and 27 M-class flares besides numerous C-class events. Notably, it was NOAA 12673 which set off the largest flare of solar cycle 24, the X9.3 flare on 6 September 2017. Our analysis suggests that continuous flux emergence and photospheric activities including shearing and rotational motions were responsible for the quick evolution of the active region from a simple α-type to the most complex $\beta\gamma\delta$-type. As a consequence of the photospheric motions, strong horizontal currents of both polarities built up on the photosphere along with the developments of complex 3D features in the corona, including magnetic flux ropes,

coronal null points, etc. In addition to the analysis of the long term evolution of the AR, we carried out case studies of the X-class flares on 6 September 2017 and highly impulsive homologous M-class flares on 7 September 2017. Importantly, the M-class flares originated from a highly localized coronal sigmoid situated at the northern edge of the central sunspot region of NOAA 12673. In view of the much smaller length scale, the localized sigmoid can be justifiably termed as a minisigmoid. NLFFF extrapolation results suggested the presence of two intertwined flux ropes in a double-decker configuration within the minisigmoidal region. Our study suggests that the magnetic complexity of active regions is strongly linked with the flare productivity rather than the area or strength of the corresponding magnetic flux region.

In summary, by combining high resolution high cadence observational data and latest numerical techniques, this thesis has explored a few ill-understood and less studied aspects of the solar transient phenomena. The thesis presents thorough investigations of complex magnetic configurations, initiation processes and evolutionary aspects of solar flares, considering events of a wide spatial, temporal and morphological varieties.

Keywords: Solar active regions, Solar magnetic fields, Solar flares, Solar filaments/prominences, Magnetic flux ropes, Solar coronal mass ejections

List of Publications

1. **Mitra, P. K.** & Joshi, B., 2019, *"Preflare Processes, Flux Rope Activation, Large-scale Eruption, and Associated X-class Flare from the Active Region NOAA 11875"*, **Astrophysical Journal**, 884, 1.

2. **Mitra, P. K.**, Joshi, B. & Prasad, A., 2020, *"Identification of Pre-flare Processes and Their Possible Role in Driving a Large-scale Flux Rope Eruption with Complex M-class Flare in the Active Region NOAA 12371"*, **Solar Physics**, 295, 29.

3. **Mitra, P. K.**, Joshi, B., Veronig, A. M., Chandra, R., Dissauer, K. & Wiegelmann, T., 2020, *"Eruptive-Impulsive Homologous M-class Flares Associated with Double-decker Flux Rope Configuration in Minisigmoid of NOAA 12673"*, **Astrophysical Journal**, 900, 23.

4. **Mitra, P. K.**, Joshi, B., 2021, *"Successive occurrences of quasi-circular ribbon flares in a fan-spine-like configuration involving hyperbolic flux tube"*, **Monthly Notices of the Royal Astronomical Society**, 503, 1017.

5. **Mitra, P. K.**, Joshi, B., Veronig, A. M., & Wiegelmann, T., 2022, *"Multi-wavelength Signatures of Episodic Null Point Reconnection in a Quadrupolar Magnetic Configuration and the Cause of Failed Flux Rope Eruption"*, **Astrophysical Journal**, 926, 143.

Contents

List of Figures

List of Tables

Chapter 1

Introduction

Human interest on the Sun was, perhaps, developed from the inception of the human capability of thinking. Among all the objects they could see in the sky, undoubtedly the Sun was the most interesting object as it alone creates the difference between days and nights. As the source of light and warmth, the Sun was naturally placed at the top positions among the Gods and all the scientifically curious minds have always been intrigued by the sheer elegance and complexity of the Sun. Naturally, with the advancements of human civilization, our understanding on the Sun has increased steadily. However, beyond the capability of our normal vision, there lies a quite dark side of the Sun which have only become apparent in the last few years. Therefore, in modern science, the Sun is widely studied and a lot of research facilities are dedicated for solar studies. In particular, the eruptive phenomena occurring on the Sun have maintained its importance in the contemporary solar studies in view of their intrinsic relation with the space weather phenomena (Schwenn, 2006).

1.1 Solar transient phenomena

Solar transient phenomena correspond to various explosive activities observed in the solar atmosphere on a wide spatial, temporal, and spectral scales. The most spectacular manifestations of solar transients include energetic outbursts in the form of solar flares, prominence eruptions, coronal mass ejections (CMEs) etc. These events are observed to occur over a time-scale from few minutes to few hours. Solar flares and CMEs provide observational constraints and physical insight into magnetically-driven impulsive phenomena on the Sun and also similar phenomena in stars and other astrophysical objects. Solar transients are key components in the Sun-Earth connection, shaping the heliospheric environment by releasing enhanced electromagnetic radiation and energetic particles which create a range of geomagnetic activity classified as space weather. These space weather events produce energetic photon and particle radiation that can adversely affect human life, ground-based electrical systems, and space-assets, such as communications satellites (Forsyth et al., 2006; Webb & Howard, 2012). Therefore, the investigations of solar transient phenomena are considered as one of the important topics in contemporary solar physics.

1.2 Prominence or filament

Prominences are structures composed of relatively cool, dense plasma commonly observed to levitate in the solar atmosphere over the limb (Figure 1.1). They are commonly observed in the Hα emission line as well as other chromospheric images (see reviews by Parenti, 2014; Gibson, 2018). When these structures are viewed on the disk of the Sun, they appear in the absorption lines (Zirin, 1988); these dark, thread like structures are called filaments (Figure 1.2). Filaments or prominences are believed to be supported in the corona against gravity by sheared magnetic field with a dip (Antiochos et al., 1994) or helically twisted field lines (Amari et al., 2003).

Structure and physical properties

Based on their location, filaments are commonly classified in three categories– active region filament, quiescent filament, and intermediate filament (Tandberg-Hanssen, 1995). However, the basic structures of filaments are similar, regardless of their location on the solar disk. The main upper body of the filament, usually called the spine, stretches through the corona above the boundary between two opposite-polarity regions on the photosphere called a polarity inversion line (PIL). A filament can be several tens of thousands kilometers high and hundreds of thou-

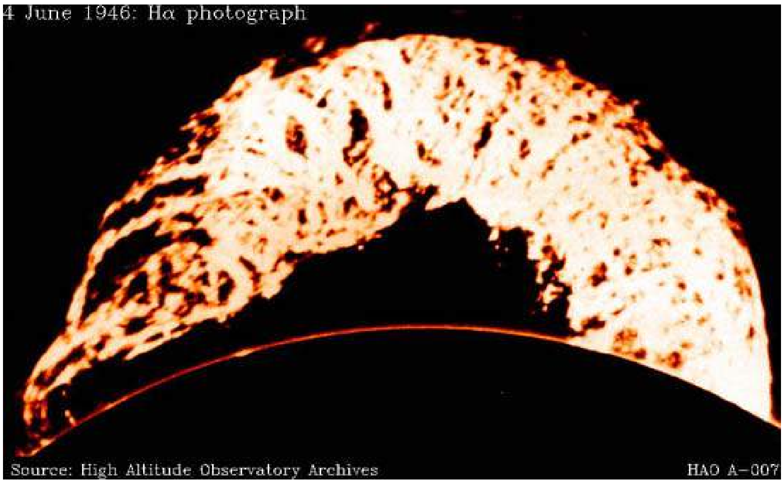

Figure 1.1: A historical prominence, nicknamed as 'grand daddy prominence' observed in Hα images on 4 June 1946 that extended $\sim$200 Mm above the solar surface. The figure is adopted from https://www2.hao.ucar.edu/Education/Sun/grand-daddy-prominence.

sands kilometers long, yet only a few thousands of kilometers wide. The ends of the spine, called legs, terminate in the photosphere in opposite polarity regions. On many occasions, one can see filamentary pieces sticking out of the spine which are called barbs (Martin, 1998).

Temperature of filaments can vary between 5000–8000 K while their particle density ranges between 10^{12}–10^{15} m^{-3}. It is important to note that, the temperature of filaments are $\sim$3 orders lesser than the temperature of the ambient corona while its density is $\sim$3 orders higher than that of the corona. The mechanism which enables filaments to sustain their low temperature and high density in the hot and tenuous corona is still a point of discussion among the solar physicists (Parenti, 2014).

Active region filaments are low-lying, rapidly evolving structures which are formed in the newly emerged magnetic fields of an active region (AR). Quiescent filaments, on the other hand, are relatively large structures, formed in the quiet regions of the Sun or in the decayed ARs, which levitate high in the corona. Intermediate filaments are formed in the mid latitudes of the Sun with one leg terminating in ARs while the other leg terminating in a quiet region. When these structures erupt, both prominence material and magnetic fields are expelled together, leading to radiative signatures at multi-wavelengths in the source region (in the form of flares) and a CME beyond the solar atmosphere.

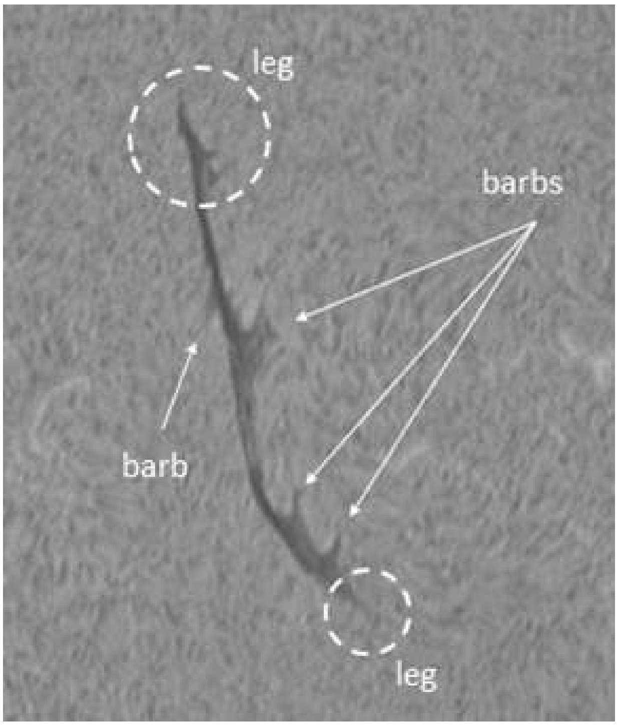

Figure 1.2: A filament with spine and barbs. The figure is adopted from http://sidc.be/news/219/welcome.html

1.3 Flare

Solar flares are the most powerful explosions in the solar system. In tens of minutes, they can release in excess of 10^{32} erg of energy. Depending on the size and released energy, solar flares exhibit a wide variety of morphological evolution and characteristics. During a flare, huge amount of magnetic energy is released in the form of thermal and non-thermal energies, radiating across the entire electromagnetic spectrum, i.e., from γ-rays to radio waves. Thermal signatures of flares include optical, ultra-violet (UV), extreme ultra-violet (EUV), and soft X-ray (SXR) emissions from post-reconnection loop arcades and flare ribbons (see review by, Fletcher et al., 2011). Non-thermal signatures of flares include hard X-ray (HXR), microwave (MW), and radio bursts which individually carries evidences of different physical mechanisms of particle acceleration during a flare (Krucker et al., 2008; White et al., 2011). Careful observation and appropriate analysis of flare HXR sources can be used to constraint the location of magnetic reconnection and particle acceleration (Masuda et al., 1994; Benz, 2017) whereas type III and type II radio bursts can indirectly provide information on the restructuring of coronal field and early phases of CME propagation (Cairns et al., 2003; Reid & Ratcliffe, 2014).

Flare classification

- **Hα classification:** In this category, a flare is characterized by its brightness and spatial extents as observed in the Hα spectral line (wavelength 6563 Å). A flare is considered to occur when the brightness exceeds the threshold of 150% of the background brightness and the area exceeds more than ten millionth of the area of the visible hemisphere of the Sun $\approx 1.5\times10^{12}$ km^2. In the Hα classification scheme, a flare is classified by a character (called importance class) and a letter (f, n, and b for faint, normal and bright, respectively) corresponding to a subjective estimate of the brightness (Staude, 1990). The details of Hα classification is given in Table 1.1.

- **GOES classification:** In this scheme, a flare is classified by the SXR flux emission during the peak phase of the flare as measured by the 1–8 Å channel of GOES satellites. SXR flux from the Sun in measured in the units of W m^{-2} and expressed on a logarithmic scale. Depending on the power of 10 during the peak emission, a flare is classified with a letter and a number that acts as a multiplier. The details of GOES flare classification is given in Table 1.2. For example, if the peak SXR flux of a flare is 9.3×10^{-4} W m^{-2}, then the flare will be classified as X9.3 flare.

Table 1.1: Hα classification of solar flare

Importance class	Corrected area (A)	
	In millionths of solar hemisphere	In square degrees
S	A<100	A<2.0
1	100≤A<250	2.0≤A<5.1
2	250≤A<600	5.1≤A<12.4
3	600≤A<1200	12.4≤A<24.7
4	A≥1200	A≥24.7

1.4 Coronal Mass Ejection (CME)

Coronal Mass Ejections (CMEs) are one of the most spectacular and catastrophic events in the solar system in which huge amount of plasma ($\sim10^{12}$–10^{13} kg) along

Table 1.2: GOES SXR classification of solar flare

Flare class	Peak flux in 1–8 Å (W m^{-2})
A	10^{-8} to 10^{-7}
B	10^{-7} to 10^{-6}
C	10^{-6} to 10^{-5}
M	10^{-5} to 10^{-4}
X	10^{-4} and above

with magnetic flux ($\sim 10^{21}$–10^{23} Mx) are ejected into the interplanetary space from the solar corona (Gosling et al., 1990). Often, CMEs are generated during large solar flares, confirming that flares and CMEs are different manifestations of a common underlying basic physical mechanism.

Structure and characteristics of CMEs

Although CMEs are observed in various sizes and shapes depicting many topological variations, a classical '3 part structure' of CMEs has been proposed which is followed by majority of CMEs. A CME having 3 part structure is made up of a bright leading arc followed by a dark cavity and a bright core (Figure 1.3). CMEs travel in the interplanetary space with a wide range of speed which can be as low as 30 km s^{-1} or as high as 2500 km s^{-1} with an average value of $\sim$300–500 km s^{-1} (Yashiro et al., 2004; Webb & Howard, 2012). Majority of the CMEs show constant velocity or moderate acceleration. Statistical studies have confirmed that dynamical evolution of CMEs are intrinsically related with the evolutionary phases of flares (Zhang et al., 2001, 2004; Zhang & Dere, 2006).

1.5 Location of flare origin: active region (AR)

Solar flares almost always occur from ARs (Figure 1.4) in which high magnetic non-potentiality resides in a wide variety of forms (see review by Toriumi & Wang, 2019). In the white light photospheric images, such locations appear as dark patches known as sunspot groups (see bottom left panel in Figure 1.4). Because of strong magnetic pressure in the sunspot regions, temperature decreases to $\sim$3000–4000 K which is much less compared to the quiet Sun photospheric temperature of $\approx$5770 K.

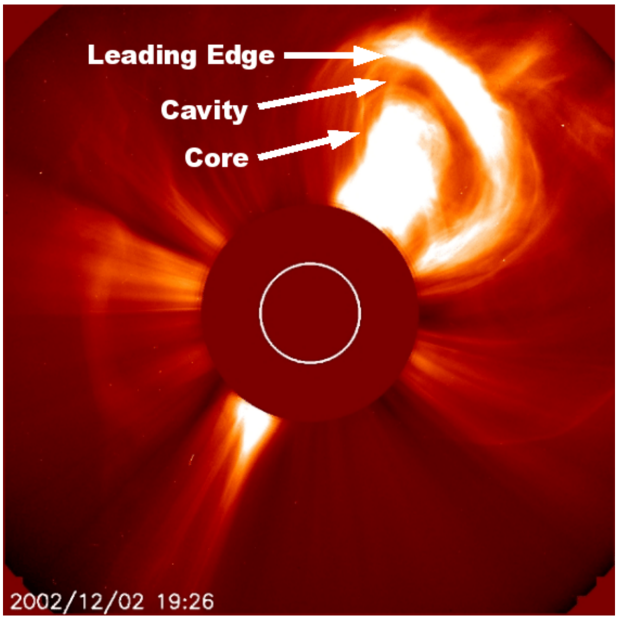

Figure 1.3: A three-part structure of CME, showing the loop like leading edge, dark cavity and bright core, as seen by LASCO C2.

Depending on the strength on magnetic strength, the structure of sunspots is divided in two parts: the umbra which is the darkest, central part, where the magnetic field is strongest ($\sim$2000–3500 G) and approximately vertical (normal to the Sun's surface) and the surrounding penumbra, which is lighter than umbra but darker than the quiet Sun, where the magnetic field is more inclined with a magnetic strength of $\sim$700–900 G (see Priest, 2014).

Magnetic classification of solar ARs

ARs appear in a wide variety in the spatial extension and magnetic complexity. Depending upon the magnetic configuration, solar ARs are classified into four primary groups: α, β, γ, and δ (Mount Wilson classification; see Figure 1.5).

α **type:** α-type ARs are the simplest types which are composed of one unipolar sunspot only.

β **type:** These are the simplest types of bipolar sunspot groups containing both positive and negative polarity regions which are separated by clear PILs.

γ **type:** γ-type ARs are complex bipolar sunspot groups in which regions of both polarities are arranged in a complex distribution that they can not be separated by one PIL.

δ **type:** These are the most complex category in the primary classification, which are

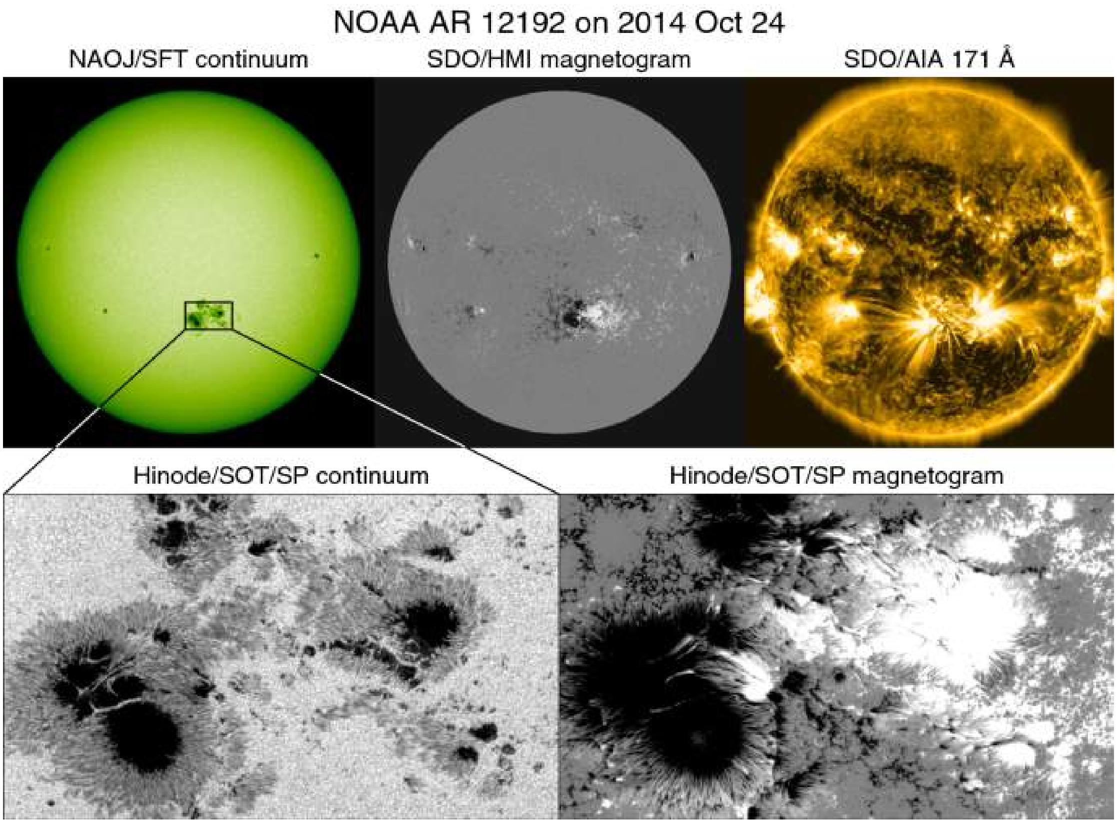

Figure 1.4: Solar Dynamics Observatory (SDO), Hinode, and Solar Flare Telescope (SFT)/NAOJ observations of a huge flare-productive active region NOAA 12192. Figure is adopted from Toriumi & Wang (2019).

characterized by fragmented umbrae of opposite polarities within a common penumbra (Künzel, 1960).

Notably, often ARs show signatures of multiple categories of the sunspot-classification and in such cases, they are classified as mixed categories e.g., $\beta\gamma$, $\gamma\delta$, $\beta\gamma\delta$ etc. On average, β-type ARs are observed to be most abundant and $\beta\gamma\delta$-type ARs are found to be most flare productive (Jaeggli & Norton, 2016; Toriumi & Wang, 2019). Table 1.3 shows statistically estimated occurrence of ARs according to their magnetic classification.

1.6 Temporal evolution of typical flares

During a flare, energy is released in the form of electromagnetic radiation in the entire electromagnetic spectrum, making it a truly multi-wavelength phenomena. Flare emissions in different electromagnetic regimes are manifestations of various physical mechanisms taking place at different layers of solar atmosphere, and

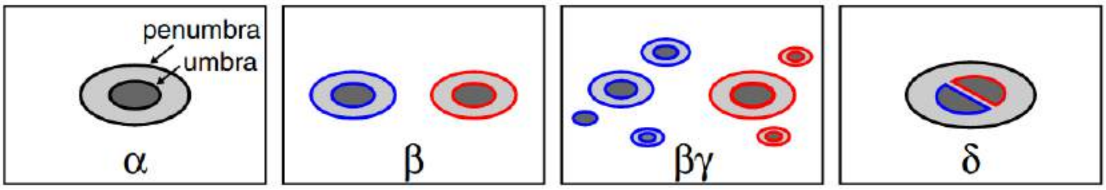

Figure 1.5: Cartoon diagrams showing different categories of solar active region according to the Mount Wilson classification scheme. Figure is adopted from Toriumi & Wang (2019).

Table 1.3: Occurrence of solar active regions according to their magnetic classification as found by Jaeggli & Norton (2016)

Configuration	Percentage of appearance
α	≈19.5
β	≈64
γ	≈0.04
$\beta\gamma$	≈11
$\beta\delta$	≈0.8
$\gamma\delta$	≈0.04
$\beta\gamma\delta$	≈4

hence, they differ in time. Therefore, it is important to study the temporal evolution in different wavelength bands during a flare to understand it in detail. In Figure 1.6, we illustrate different phases in the temporal evolution of a typical flare.

1.6.1 Pre-flare and precursor phase

Prior to main energy release phase, initial signatures of small-scale energy release can be observed during the pre-flare phase. This term covers both pre-flare activity, which refers to the very early stages of energy release, temporarily disjoint from the onset of the impulsive phase, and the flare precursor events, which are small-scale brightenings in UV to SXR wavelengths happening some tens of minutes before the flare (Fletcher et al., 2011). Here, it should be noted that the small-scale intensity enhancements observed in the spatially unresolved lightcurves might be misleading in the identification of pre-flare activities; as independent activities may occur close or away of the subsequent main flaring site. Spatially resolved observations reveal that flare precursors might occur within the core field of the AR

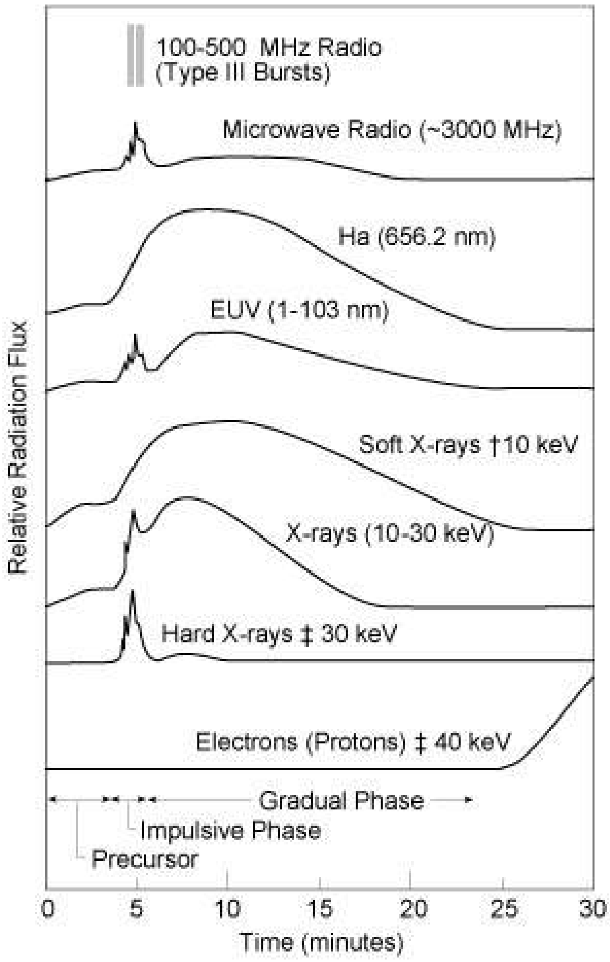

Figure 1.6: A schematic representation of different phases of a typical flare in electromagnetic wavelength bands and particle motion. Figure taken from Kane (1974).

which is involved in the main flare emission while pre-flare activity can originate from locations near and far from the core field (Fárník et al., 1996; Fárník & Savy, 1998; Fárník et al., 2003). Explorations of pre-flare activities are considered to be important in order to understand the physical conditions that lead to flares and associated eruptions (Chifor et al., 2006, 2007; Joshi et al., 2011, 2013).

1.6.2 Impulsive phase

Impulsive phase is the short-lived phase of a flare, lasting for only a few seconds to a few minutes, during which magnetic energy is rapidly released in the forms of thermal and non-thermal energies, via a fundamental process called 'magnetic reconnection' (Priest & Forbes, 2002). This primary energy release phase is characterized by sudden enhancements in the HXR, MW, type III radio bursts, UV, EUV, optical and, in some cases, γ-rays also. The release of non-thermal energy implies accelerations of electrons to the relativistic speeds, collision of which with the chromospheric materials give rise to HXR sources (shown by blue color in Fig-

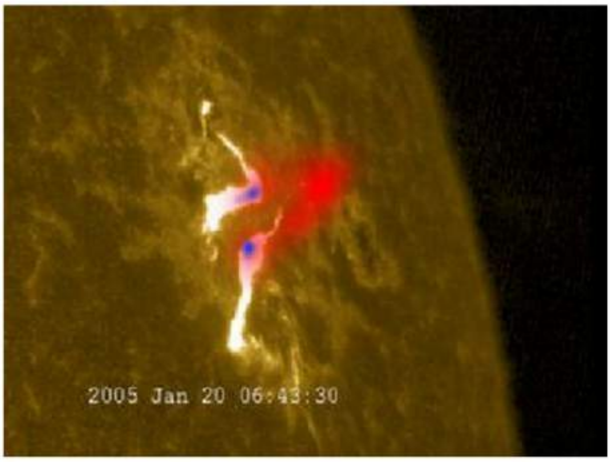

Figure 1.7: RHESSI flare observations of soft X-rays (8–12 keV; red) and hard X-rays (20–50 keV; blue) overlaid on an Hα background. The two elongated brights structures on the Hα background are called flare ribbons. Figure taken from Benz (2017).

ure 1.7) at the footpoints of the post-reconnection loops. Recent observations have also revealed that HXR sources can be found in the corona which mark the precise location of magnetic reconnection (Fletcher et al., 2011; Benz, 2017). The thermal signatures of impulsive phase is characterized by a pair of elongated brightening along the footpoints of the post-reconnection arcade known as 'flare ribbons' (see Figure 1.7). With the flare evolution, flare ribbons apparently move away from each other (see e.g., Fletcher & Hudson, 2002; Krucker et al., 2003; Veronig et al., 2006; Temmer et al., 2007; Mitra et al., 2018). Further, interaction between the accelerated electron beams with the ambient corona gives rise to type III radio signatures (Reid & Ratcliffe, 2014).

1.6.3 Gradual phase

The gradual phase is the relatively long-lived phase following the impulsive phase that may last from tens of minutes to a few hours. Magnetic reconnection usually stops during this phase or the location of magnetic reconnection moves to much coronal heights with significant reduction in the reconnection rate. Heated chromospheric plasma during the impulsive phase slowly moves upward along the post-reconnection loops, in a process called 'chromospheric evaporation' (Doschek & Warren, 2005). EUV and SXR emission from these hot plasma is identified in the form of highly structured post-reconnection arcade (left panel in Figure 1.8) which connect the chromospheric flare ribbons. With the evolution of the gradual phase, post-reconnection arcades appear to grow upwards and outwards in time in conjunction with the increasing separation of the flare ribbons (Gallagher et al.,

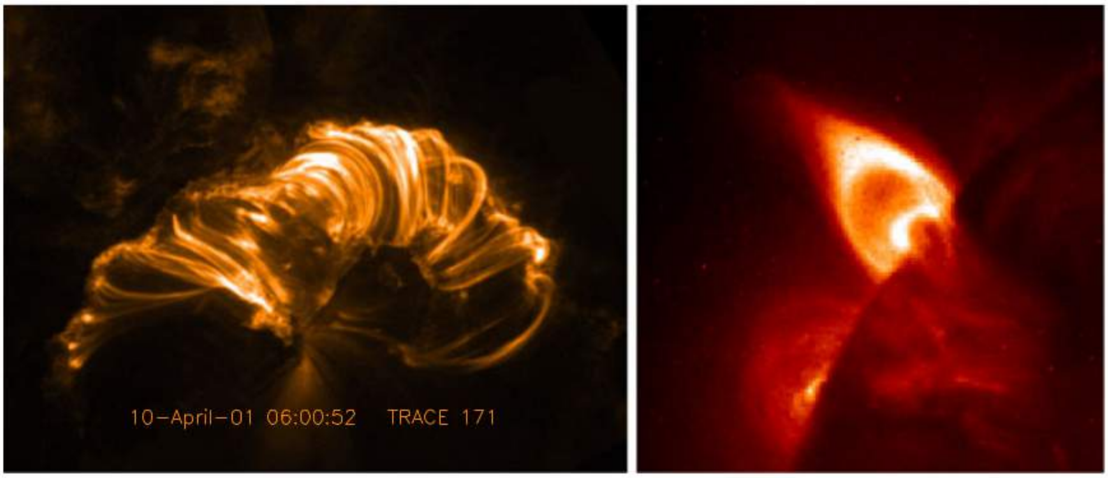

Figure 1.8: Left panel: A dense, highly structured post-reconnection flare arcade observed in the TRACE 171 Å channel. Right panel: A post-reconnection cusp structure observed by Yohkoh/SXT. Figure is adopted from Fletcher et al. (2011).

2002). When post-reconnection arcades are viewed from a side angle, they appear as 'cusp' structures which can be observed in SXR and EUV wavelengths (Tsuneta et al., 1992; Yokoyama et al., 2001; Hernandez-Perez et al., 2019a). The post-reconnection arcades generally show a temperature gradient with the outermost loops being the hotter than the inner loops (i.e., loops closer to the PIL) (Forbes & Acton, 1996). This suggests that as the magnetic reconnection region moves upwards in the solar corona, it involves successive shells of magnetic loops with footpoints rooted at the chromospheric ribbons (Shibata et al., 1996). As the flare moves into the decay phase, the hot plasma from the post-flare arcade slowly radiates its energy and cools down (Fletcher et al., 2011; Benz, 2017).

1.7 Standard flare model

Solar flares offer a wide variety of spatial and temporal evolutionary aspects. However, flares which are triggered by eruption of filaments seem to follow a few common multi-wavelength signatures, viz., a pair of ribbon-like brightening, footpoint HXR sources, development of a highly structured flare arcade, etc. (see Section 1.6). To explain these broad flare signatures, a standard flare model, also known as CSHKP model (Figure 1.9) has been developed combining the studies of Carmichael (1964); Sturrock (1968); Hirayama (1974); Kopp & Pneuman (1976).

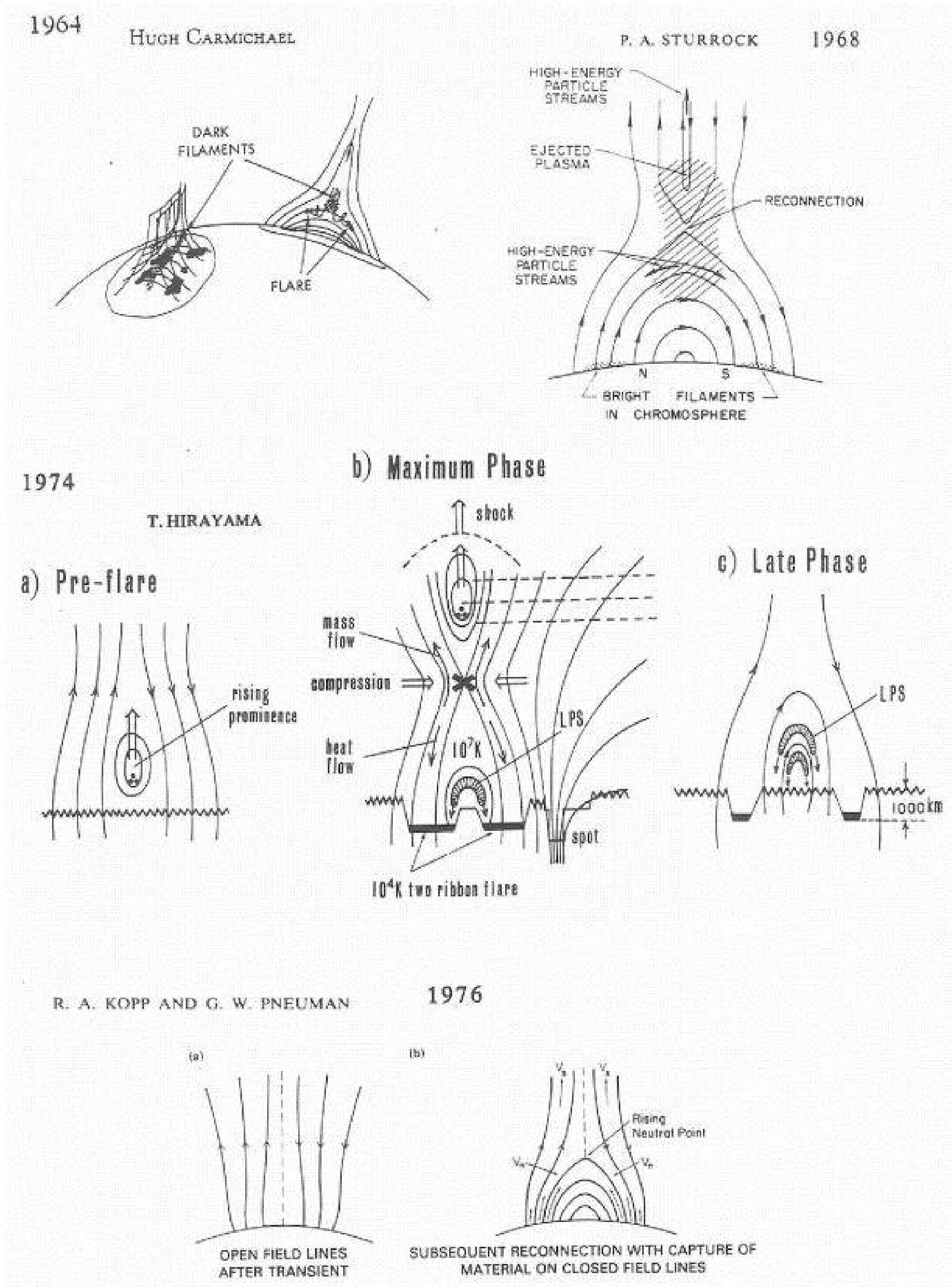

Figure 1.9: The basic coronal magnetic field configuration first proposed for eruptive flares by Carmichael (1964) (upper left), later improved by Sturrock (1968) (upper right), Hirayama (1974) (middle), and lastly by Kopp & Pneuman (1976) (bottom). Figure taken from Švestka & Cliver (1992).

Carmichael (1964) first suggested that flare ribbons and flare loops are coupled and can be interpreted as the consequences of relaxation of magnetic field which was initially stretched by the erupting plasma body. Sturrock (1968) proposed that the main energy release during a flare is manifested by magnetic reconnection caused by 'tearing-mode' instability (Tenerani et al., 2015) in the stretched magnetic field. Tearing mode instability leads to the formation of strong current sheets where magnetic reconnection takes place. Hirayama (1974) recognized three distinct phases of flares, namely, pre-flare, main, and late phases. During the pre-flare phase, a prominence or a coronal arch lying along the PIL rapidly expands vertically. Due to the expansion of the prominence, a magnetic cavity appears following the path of the eruption, which collapses from both sides leading to magnetic reconnection at the so called 'X' point. As the prominence rises further up in the corona, the 'X' point also rises and magnetic reconnection involves magnetic lines which are anchored further from the PIL, thus explaining the gradual separation of the flare ribbons. Kopp & Pneuman (1976) proposed that the post-flare loop arcades are the consequences of magnetic reconnection in magnetic field which were previously torn apart by flare outburst.

In conclusion, all these studies provide a common argument that the main energy release during flares is caused by the process of magnetic reconnetion which occurs on a vertical current sheet formed within stretched magnetic field. However, the processes responsible for the formation of the current sheet seems to differ in these studies.

Plasmoid induced reconnection model

Based on Yohkoh satellite observations that detected plasmoid ejection from compact flares, Shibata et al. (1995, 1996) proposed the plasmoid induced reconnection model (Figure 1.10) by extending the CSHKP model. According to the model, the rapid release of energy during flares are caused by fast magnetic reconnection which is triggered by the ejection of plasmoids. A plasmoid stores magnetic energy in it well before the flaring activity initiates. When the plasmoid is subjected to eruptive motion, a current sheet is developed beneath the erupting plasmoid between the inflow magnetic flux. Since, the plasma density does not change much

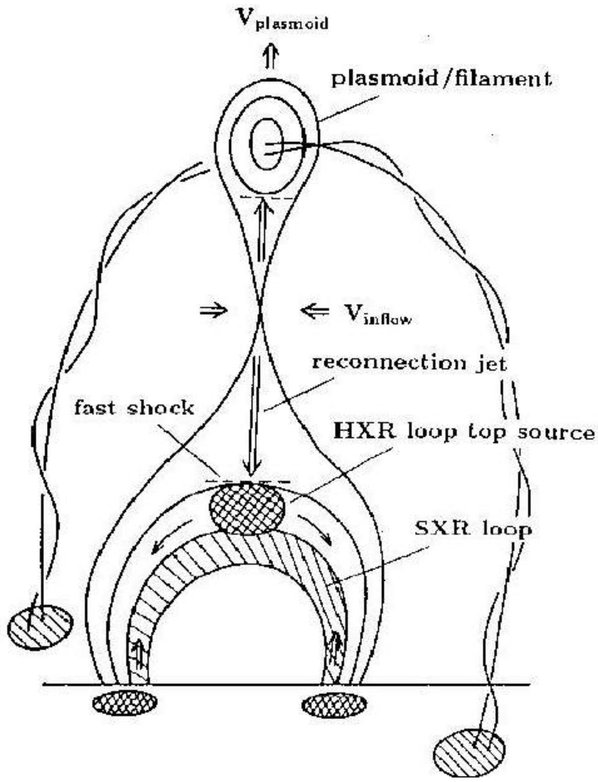

Figure 1.10: The plasmoid–induced–reconnection model proposed by Shibata et al. (1995).

during the eruption process, an 'X-type' configuration is developed by the inflow magnetic field. Rate of reconnection is determined by the inflow velocity which in turns depend on the eruption speed of the plasmoid. Shibata et al. (1996); Shibata (1997) further proposed that this model is also applicable for small flares and X-ray jets since the plasmoid formation and eruption are scale invariant processes.

In summary, presence of vertically expanding prominence/flux rope system is a pre-requisite in the standard flare model. The upward expansion of the flux rope creates a pressure suction beneath it which, in turns, leads to an inflow of plasma and magnetic field below the flux rope. The inflowing magnetic field undergoes magnetic reconnection at the 'X' point beneath the erupting flux rope. During reconnection, most of the magnetic free energy previously stored in the flaring system is rapidly released resulting into particle acceleration and impulsive HXR bursts. From the site of reconnection, the highly accelerated particles move along the magnetic field lines toward denser chromosphere with relativistic speed as synchrotron motion leading to a sudden enhancement in MW emission. As the accelerated particles collide with cool, denser material in chromosphere, 'thick target bremsstrahlung' process takes place and conjugate HXR sources are formed at the footpoints of the magnetic field lines (Brown, 1971; Hudson, 1972). In the optical and (E)UV wavelengths, footpoint emissions are observed as two elongated bright regions termed as flare ribbons, which are formed on the either sides of the PIL where the footpoints of the coronal loops are anchored in the chromosphere. A flare may result into the successful eruption of the flux rope which eventually leads to a CME (Isenberg et al., 1993; Forbes & Acton, 1996; Lin et al., 1998; Shibata & Yokoyama, 1999; Forbes, 2000; Lin & Forbes, 2000; Priest & Forbes, 2002; Hudson et al., 2006). Such flares are called eruptive flares. However, not all the flares are associated with eruption of filament and CME (known as, confined flares) and many eruptive flares do not follow morphological evolution as described in the CSHKP model (Joshi et al., 2019). Further, in a few cases, triggered flux ropes initially undergo a brief phase of eruption but subsequently fails to escape from the overlying layers of solar corona and eventually the material falls back. Flares associated with such unsuccessful eruptions are called failed-eruptive flares (Gilbert et al., 2007).

1.7.1 3D standard flare model

It is important to note that the CSHKP model explains the flare associated observational features as a consequence of coronal magnetic reconnection in two-dimension (2D). Subsequently, several 2D and 2.5D magnetohydrodynamic (MHD) simulation studies have successfully recreated and estimated the magnetic and thermal properties of the flare observables, validating the applicability of the CSHKP model (e.g., Chen & Shibata, 2000; Reeves & Forbes, 2005; Shiota et al., 2005). However, many observational signatures of solar flares exhibit true three dimensional (3D) features that include coronal sigmoids (e.g., Rust & Kumar, 1996; Manoharan et al., 1996; Sterling, 2000; Joshi et al., 2017a), motion of bright footpoint sources along 'J'-shaped flare ribbons observed in X-ray and EUV channels (e.g., Fletcher & Hudson, 2002; del Zanna et al., 2006; Chandra et al., 2009; Joshi et al., 2017a), gradual transition of magnetic shear from pre- to post-flare configurations (e.g., Chandra et al., 2009; Wang et al., 2012) etc. To implement such true 3D observational features of solar flares, the standard flare model has been extended to 3D on the basis of a series of numerical simulations (Aulanier et al., 2012, 2013; Janvier et al., 2013, 2014). The results of these studies suggest that in the highly sheared pre-flare magnetic configurations, small-scale current sheets could be generated in the regions of high magnetic gradients, i.e., quasi-separatrix layers (QSLs; Titov et al., 2002). These narrow but strong current layers are responsible for the J-shaped pattern observed during the pre-flare or early flare phases. The straight part of the 'J' corresponds to the footpoints of the cusp-shaped arcade which forms below the vertical current sheet (Aulanier et al., 2012). Magnetic reconnection at this current sheet is responsible for the development of a flux rope from sheared arcade. During the eruption of the flux rope, the inner legs of the field lines overlying the erupting flux tube straighten vertically and eventually reconnect, resulting in the formation of mostly potential post-flare arcades; which is in line with the 2D CSHKP model.

1.8 Mechanisms for flux rope formation

Presence of a flux rope in the AR is a pre-requisite in the CSHKP model as the core part of CMEs the formed by the flux rope. However, the mechanisms for the build up of the flux ropes are not explained in the standard flare model and are considered as an open question till date. Two different categories of flux rope formation models have been proposed. In the first category, a twisted flux tube emerges in the solar atmosphere through the photosphere due to magnetic buoyancy (e.g., Fan, 2001, 2009; Chatterjee & Fan, 2013; MacTaggart et al., 2021). In the second category, a flux rope is developed in the corona from sheared arcade in response to small-scale magnetic reconnection (van Ballegooijen & Martens, 1989; Amari et al., 2003). Sheared arcades in the corona are developed by shearing motions on the photosphere, as well as, if emergence of a flux rope stops when its axis hits the photosphere (Fan, 2001). Notably, the development of a flux rope from sheared arcade is also explained in the 3D standard flare model (see Section 1.7.1).

Formation of flux rope in response to photospheric magnetic flux cancellation

A mechanism for the formation of flux rope in the solar atmosphere as a result of photospheric flux cancellation was proposed by van Ballegooijen & Martens (1989) in their 'flux cancellation' model (Figure 1.11) which was subsequently supported and demonstrated by numerical simulations by Amari et al. (1999, 2003, 2010). According to this model, flux cancellation along PIL in a sheared magnetic field configuration leads to the formation of helically twisted magnetic structure (i.e., flux rope; Figure 1.12) which is capable of supporting prominence plasma. When the footpoints of the sheared arcade are pushed closer to each other due to photospheric converging flows, some of the magnetic energy of the sheared magnetic field is released via reconnection. The reconnection produces smaller loops which cross the neutral line nearly at right angles and larger loops which connect the distant footpoints. While the larger loop, lying over the PIL consequently develops the flux rope, the smaller loop submerges as a result of its small curvature radius. The helical field (forming the flux rope) cannot be submerged because magnetic buoyancy prevents it from entering the convection zone below.

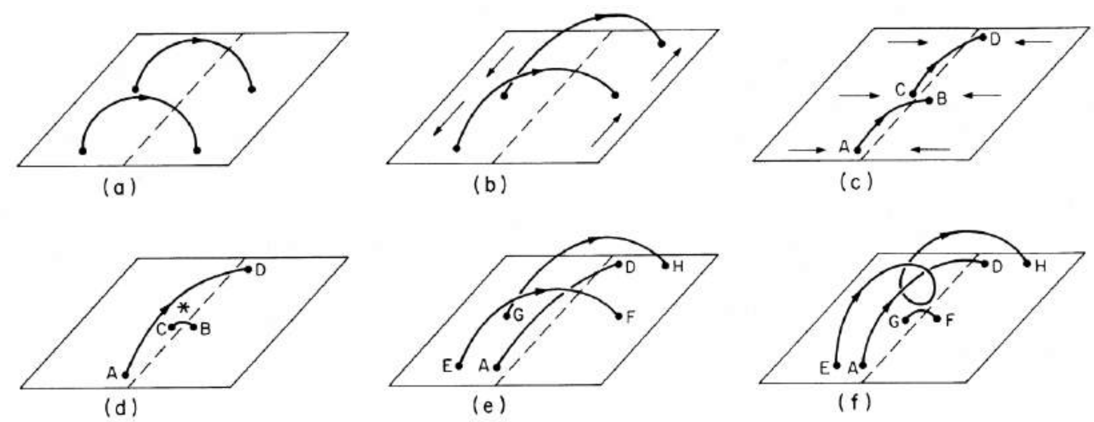

Figure 1.11: Flux cancellation in a sheared magnetic field. The rectangle represents the solar photosphere, and the dashed line is the neutral line separating two regions of opposite magnetic polarity. Panel (a): Initial potential field. Panel (b): sheared magnetic field produced by flows along the neutral line. Panel (c): magnetic shear is increased further due to flows toward the neutral line. Panel (d): reconnection produces long loop AD and a shorter loop CB which subsequently submerges. Panel (e): overlying loops EF and GH are pushed to the neutral line. Panel (f): reconnection produces the helical loop EH and a shorter loop GF which again submerges. Figure is adopted from van Ballegooijen & Martens (1989).

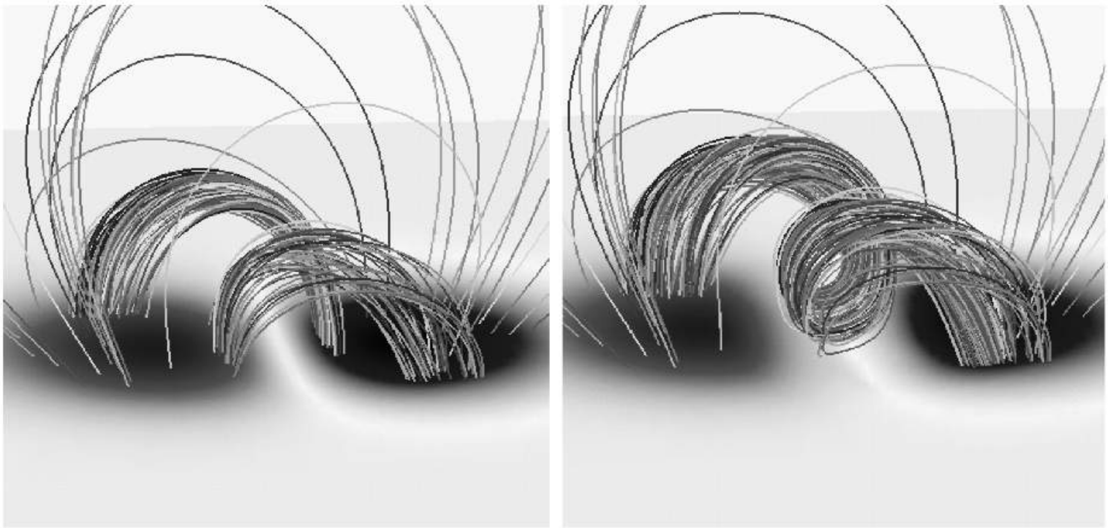

Figure 1.12: A highly sheared core magnetic field (left panel) which evolves into the formation of a helically twisted magnetic structure (flux rope; right panel) as a result of flux cancellation along the polarity inversion line. Figure is adopted from (Amari et al., 1999).

1.9 Triggering of solar eruption

Large-scale solar eruptions essentially involve eruption of a flux rope. Theoretically, it is understood that a flux rope can be set into eruptive motion in response to magnetic reconnection or as a result of ideal MHD instabilities. In this section, we discuss both reconnection based and ideal MHD instability models of solar eruptions in detail.

1.9.1 Reconnection based models

It is widely accepted that magnetic reconnection is the most fundamental process responsible for the changes in the topology of coronal magnetic fields, as well as the rapid conversion of stored magnetic energy into thermal and kinetic energy of plasma and particles during solar eruptive events (e.g., see reviews by Priest & Forbes, 2002; Fletcher et al., 2011; Wiegelmann et al., 2014). Depending upon the morphology of the AR, two basic classes of reconnection-based models for solar eruption have been developed, namely, tether-cutting model and breakout model.

Tether-cutting model

To materialize the removal of the strong stabilizing force from the overlying magnetic arcade by means of a slow magnetic reconnection in the low corona, Moore & Labonte (1980); Moore & Roumeliotis (1992); Moore et al. (2001) proposed the tether-cutting mechanism based on a single bipolar field geometry. In this model, the strongly sheared core fields are overlaid by less-sheared envelope magnetic arcades (Figure 1.13). At first, the strongly sheared core fields with opposite polarities reconnect slowly above the PIL, but beneath the filament, which leads to the formations of a large-scale twisted flux rope connecting the far ends of the core fields and small flaring loops which shrink downward. Then, due to the 'out of balance' situation between the outward magnetic pressure and the downward magnetic tension, the whole field expands outward. As the overlying envelope magnetic arcades are stretched up by the erupting filament, fast reconnection occurs with an elongated current sheet forming below the filament, which produces the flare ribbons and further speeds up the filament eruption to form the coronal mass ejection (CME).

Breakout model

The breakout model (Antiochos et al., 1999) involves a complex quadrupolar magnetic flux system with four distinct flux domains (shown by different colors in Figure 1.14 as: central arcade (blue lines), two side arcades (green lines), and overlying envelope arcade (red lines)) that include one or more pre-existing coronal null points. Shearing motion in the core field region imposes stretching of the inner field lines which are shown by the thicker blue lines in Figure 1.14. The enhanced magnetic pressure in the inner field region causes the core to expand outward which results in the development of a current sheet at the null point (denoted as breakout current sheet). As the system becomes more stressed, the thickness of the current sheet is reduced. Once the thickness of the breakout current sheet reduces sufficiently, magnetic reconnection is initiated, which rapidly converts both the blue and red lines into the green lines reducing the downward magnetic tension. As a result, the core field expands even further ensuring successful eruption of the core field (Karpen et al., 2012).

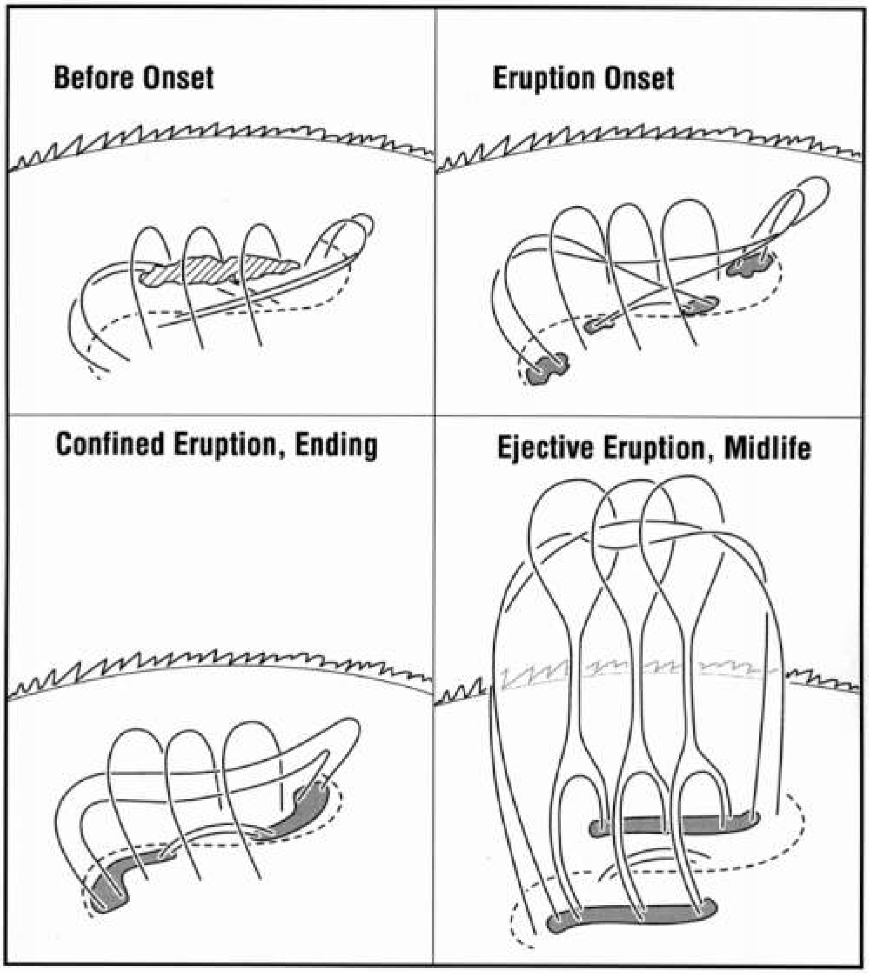

Figure 1.13: The tether-cutting reconnection model depicting the onset of flares and subsequent eruptions. Figure is adopted from Moore et al. (2001).

1.9.2 Ideal MHD instability models

Although it is universally accepted that solar eruptions are intrinsically related to magnetic reconnection, observations have revealed a number of cases of flux rope eruption from the solar atmosphere where obvious signatures of triggering reconnection (i.e., early brightening in the flaring region) were missing. Theoretical studies have revealed that a flux rope can be set to instability if some parameters reach critical values. In this section, we briefly discuss two of the ideal instability models, namely, the torus instability and kink instability.

Torus instability

According to the torus instability model, a flux rope can be subjected to eruptive motion if the downward strapping magnetic field of a flux rope, is exceeded by

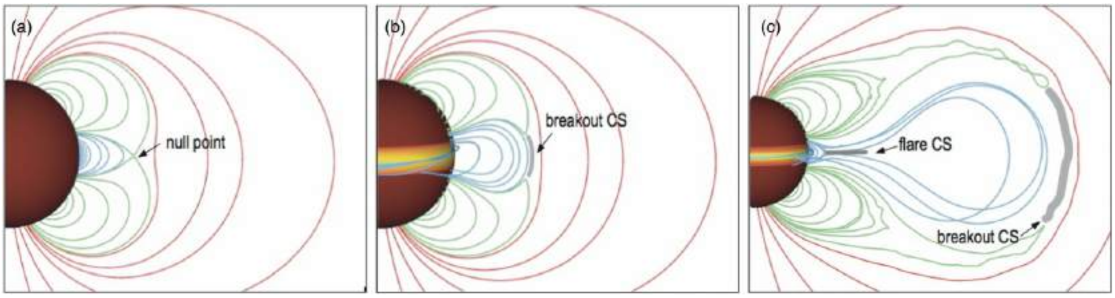

Figure 1.14: Selected magnetic field lines at three times illustrating the key structures of the breakout model including current sheets (CS). Red lines indicate overlying field, green indicates side lobe field lines, and blue indicates core field lines. All field lines are drawn from the same set of footpoints. Gray lines show the general locations of the flare and breakout CS. Figure is adopted from Karpen et al. (2012).

the corresponding outward hoop force (Figure 1.15). Therefore, any outward perturbation of the flux rope can lead to a catastrophic eruption if the poloidal (or, horizontal) magnetic field overlying the flux rope decays with height faster than a critical value. To quantify decay of magnetic field, a parameter named 'magnetic decay index' (n) is defined as

$$n = -\frac{dlog(B_h)}{dlog(H)} \tag{1.1}$$

where B_h and H are the horizontal field above the flux rope and height, respectively (Kliem & Török, 2006). Observational results have suggested that torus instability occurs at the height where $n \geq n_{crit}$ with $n_{crit} = 1.3 - 1.5$ (e.g., Zuccarello et al., 2014).

Kink instability

The theory of kink instability states that a flux rope can lose its stability if the twist of the flux rope increases beyond 3.5π. In this respect, a convenient numerical method is to calculate the 'twist number' (T_w) which is defined by number of turns of a flux rope over a given length (L), as

$$T_w = \int_L \frac{(\nabla \times \mathbf{B}) \cdot \mathbf{B}}{4\pi B^2} dl \tag{1.2}$$

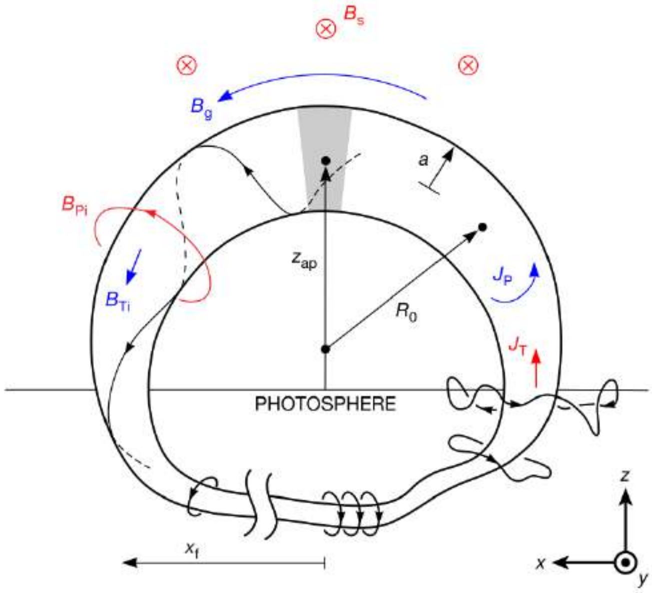

Figure 1.15: Magnetic fields and currents in a line-tied magnetic flux rope. The arched flux rope is line-tied to the dense photosphere at two footpoints separated by $2x_f$. Those fields and currents associated with the poloidal magnetic field are shown in red, while those associated with the toroidal magnetic field are shown in blue. Torus instability occurs when the upward hoop force $|\mathbf{J_T} \times \mathbf{B_{pi}}|$ exceeds the downward strapping force $|\mathbf{J_T} \times \mathbf{B_s}|$. Figure is adopted from Myers et al. (2016).

Statistically estimated critical value of T_w for kink instability has been found to be 2 i.e., a flux rope can be subjected to kink instability when $|T_w| \geq 2$ (Duan et al., 2019).

1.10 Objectives of the thesis

Despite the theoretical and observational advancements, some key questions related to the onset and evolution of solar eruptions have remained ill-understood and form topics of intense discussions in the contemporary solar physics. By employing high resolution multi-wavelength observations combined with the numerical analysis techniques, we aim to provide interpretations and explanations on crucial yet less understood aspects of solar transient phenomena which lie beyond the scope of the standard flare model. In the following, the context and objectives of the thesis work is outlined.

1.10.1 Study of observational signatures of magnetic reconnection during solar flares in 2D and 3D

Magnetic reconnection is a fundamental process that is ubiquitous in astrophysical plasmas. It is a topological restructuring of a magnetic field causing a change in connectivity of its field lines (see review by Pontin, 2012). Historically, the concepts of magnetic reconnection was put forward using a two-dimensional, steady-state model, where reconnection occurs at thin current sheets developed by the stretching of magnetic X-points (Syrovatskii, 1971). The 2D magnetic reconnection is envisaged as the main energy release mechanism in the standard flare model. Observational signatures of 2D magnetic reconnection during such solar flares include development of parallel ribbon brightening. On the other hand, in 3D, the sites of current sheet formation and, therefore, magnetic reconnection involve a variety of topological and geometrical features that include magnetic null points (Longcope, 2005), quasi-separatrix layers (QSLs; Janvier et al., 2013), hyperbolic flux tubes (Titov et al., 2002), etc. In the thesis, we have carried out extensive observational and numerical analysis to investigate the pre-reconnection magnetic configurations of solar flares in 2D and 3D and identified corresponding observational signatures.

1.10.2 Investigation of the triggering mechanisms and driver of large-scale solar eruptions

Reconnection models of solar eruptions, i.e., tether-cutting (Moore et al., 2001) and breakout (Antiochos et al., 1999) models involve different pre-flare conditions to explain the eruption of a flux rope. Tether-cutting model sketches a scenario where the earliest reconnection occurs deep in the highly sheared bipolar core fields whereas the breakout model involves a multipolar flux system in the corona having one or more pre-existing magnetic nulls. In the breakout model, eruption is initiated by reconnection well above the core region. Pre-flare brightening and earliest signatures of reconnection are observed beneath the flux rope in tether-cutting model. In contrast, the breakout model predicts simultaneous core and remote brightening prior to the eruption. In this thesis, we have put special emphasis to investigate the magnetic configurations associated with different triggering mechanisms by comparing the structure and evolution of complex coronal loop systems of ARs during the pre-flare stage with modeled coronal magnetic field structures.

1.10.3 Study of formation and activation of flux rope

In the standard flare model, existence of a flux rope is prerequisite. From theoretical point of view, a flux rope is a twisted helical magnetic structure which can be observed in the form of filament (or prominence) in solar images. Existence of flux ropes are indicated by 'Sigmoidal ARs' which are 'S' (or inverted 'S') shaped coronal structures observed in SXR and EUV channels (Rust & Kumar, 1996; Manoharan et al., 1996; Sterling, 2000; Joshi et al., 2017a). The exact process of the formation and topology of flux ropes is, however, not yet clearly understood and have remained as a topic of debate till the present time. One hypothesis is that the flux rope is created as a consequence of constant rotation and shearing motion of sunspots along the PIL (e.g., Amari et al., 2000; Aulanier et al., 2012). From theoretical considerations, magnetic flux cancellation along the PIL is strongly required to build up enough helicity in a sheared magnetic loop arcade which can develop into a flux rope (see e.g., Mackay & van Ballegooijen, 2006). In this thesis, detailed observational and theoretical investigations of photospheric and coronal magnetic fields have been carried out to study how the evolution of magnetic fields in ARs are related to the development of flux ropes in the corona.

1.10.4 Understanding the magnetic configurations of eruptive and non-eruptive flares

During solar transient phenomena, eruption of flux rope is not guaranteed (see e.g., Kushwaha et al., 2015; Sarkar & Srivastava, 2018). A statistical study conducted by Yashiro et al. (2005) revealed that flare-CME association rate increases significantly with the flare class: from 20% for C-class flares to 91% for X-class flares while the flare-CME association rate for M-class flares was found to be 49%. Strength of the overlying magnetic fields, decay of magnetic field strength with height, location of the flare with respect to the extent of the AR are believed to be few of many factors which collectively decide whether a flare will be eruptive or confined (see e.g., Amari et al., 2018). In this thesis, we have put efforts to develop a clear understanding of the factors which constrain flux ropes from eruption.

1.11 Structure of the thesis

The thesis is composed of seven chapters. In the following, brief description of each chapter is provided.

Chapter 1: ***Introduction***

This chapter provides a detailed introduction of different aspects of solar eruptive phenomena which are relevant to the work presented in this thesis, including descriptions on multi-wavelength flare emissions, flare models, and triggering mechanisms of solar eruptions. This chapter concludes with the formulation of scientific objectives of the thesis.

Chapter 2: ***Observational Data and Numerical Techniques***

In this chapter, we provide detailed descriptions of the sources of the multi-wavelength observational data used in the thesis work. We also discuss in detail the different numerical techniques applied to analyze the observational data and modeling of coronal magnetic field. The major observational data used in this thesis was provided by the Solar Dynamics Observatory (SDO), the Reuven Ramaty High Energy Solar Spectroscopic Imager (RHESSI), the Large Angle and Spectrometric Coronagraph (LASCO); whereas, the numerical analysis techniques used in this thesis include the potential and Non-linear Force Free Field (NLFFF) extrapolation techniques, computation of quasi-separatrix layers (QSL), twist number, calculation of magnetic decay index, etc.

Chapter 3: ***Pre-flare Activity and its Role in Driving Subsequent Large-scale Eruptions***

This chapter is dedicated toward understanding the effects of small-scale activities toward the development and activation of magnetic flux ropes and their subsequent large-scale eruption. For the purpose, this chapter presents two case studies of spectacular flux ropes eruptions leading to the formation of CMEs: (1) M-class flare occurring in the AR NOAA 12371 from a location near to disk center (≈N12E16) and (2) X-class flare in NOAA 11875, which was situated close to the western limb of the Sun (≈N07W66). In both the events under study, the pre-flare activity occurred adjacent to the main flaring site i.e., both the events were associated with adjacent/overlapping pre-flare events. We explored the processes governing the build up and activation of flux ropes, the triggering mechanisms, and multi-wavelength signatures of 2D magnetic reconnetion.

Chapter 4: ***Quasi Circular Ribbon Flares and Aspects of 3D Magnetic Reconnection***

In this chapter, we focus on the ARs with special magnetic configurations governing circular ribbon flares. For the purpose, we discuss multi-wavelength evolutionary aspects of circular ribbon flares and associated complex magnetic field configuration. Further, we present the results of multi-wavelength observational and numerical analysis on the homologous circular ribbon flares occurring from the selective AR NOAA 11977 on 16 February 2014. The flaring site of the AR was characterized by a unique photospheric configuration where dispersed negative polarity regions were surrounded by positive polarity regions, analogous to the geological 'atoll' shape. Using high resolution EUV data from Atmospheric Imaging Assembly (AIA) on board SDO and NLFFF extrapolation results, we study the evolution of four homologous quasi-circular ribbon flares that originated from the magnetic atoll region and thoroughly analyze the corresponding pre-flare magnetic configurations.

Chapter 5: ***Reconnection in a Quadrupolar Coronal Configuration and Magnetic Confinement of Flux Ropes***

Quadrupolar magnetic configurations often include 3D coronal null points which are potential sites for the triggering of solar eruptions. However, sometimes, flux ropes, initially triggered from such configurations, fail to successfully erupt from the solar corona. Physical understanding of such failed eruptive events is important in order to reduce 'false alarms' in the context of flare-predicting algorithms.

In this chapter, we present a detailed study of an intense yet failed-eruptive flare from NOAA 11302 on 26 September 2011, and investigate the possible reasons for the associated failed eruption.

Chapter 6: ***Magnetic Characteristics and Large-Scale Solar Eruptions in δ-sunspot region NOAA 12673***

The most flare productive AR in the solar cycle 24 was NOAA 12673 which, surprisingly, appeared during the minimum phase of the solar cycle. During its transit through the visible hemisphere of the Sun, it produced 4 X-class flares, 27 M-class flares, and numerous C-class flares. Importantly, the X9.3 flare produced in the AR on 6 September 2017 was the largest solar flare of cycle 24. This chapter focuses on the evolution of this historical, excessive flare productive AR. We especially discuss multi-wavelength observation and numerical analysis results of the X-class flares on 6 September 2017 and highly impulsive homologous eruptive flares from a very compact site of the AR on 7 September 2017.

Chapter 7: ***Conclusions and Future Prospectus***

This chapter provides a summary of the contents of this thesis and highlights the main conclusions. This chapter further outlines the scopes for research in this field.

Chapter 2

Observational Data and Numerical Techniques

2.1 Introduction

Solar transient phenomena involve sequence of activities that occur in a wide range of solar coronal heights. Since, coronal emission lines are dependent on the local ambient temperatures which vary widely with height in the corona, it is very important to study solar transient phenomena in multi-wavelengths. Therefore, the studies included in the Ph.D. thesis utilize observational data from various instruments which observe the Sun in different wavelengths from different vantage points. Combination of such multi-wavelength and multi-instrument observations is essential for a comprehensive exploration of the solar phenomena and related modeling efforts. A major objective of the thesis is to understand the exact topological structures involved in the triggering of the solar eruptive phenomena. Investigation of such atmospheric structures require modeling of coronal magnetic field, since direct observation of coronal magnetic field is not yet possible. Therefore, the results presented in this thesis were obtained by employing a combination of comprehensive observational data reduction, data modeling, and numerical techniques for coronal magnetic field reconstruction.

In particular, in this thesis, we have extensively used (E)UV observations of the Atmospheric Imaging Assembly (AIA; Lemen et al., 2012) and photospheric line of sight (LOS) and vector magnetograms from the Helioseismic and Magnetic Imager

(HMI; Schou et al., 2012) on board the Solar Dynamics Observatory (SDO; Pesnell et al., 2012). For understanding the thermal and non-thermal energy release processes associated with different evolutionary phases of solar transient activities, we have extensively performed the X-ray imaging and spectroscopic analyses using data from the Reuven Ramaty High Energy Solar Spectroscopic Imager (RHESSI; Lin et al., 2002). For observing the CMEs in the corona and near-Sun region, we used coronagraphic observations of the Large Angle and Spectrometric Coronagraph (LASCO; Brueckner et al., 1995) on board the Solar and Heliospheric Observatory (Domingo et al., 1995). Temporal informations of solar flares were obtained by the disk-integrated soft X-ray lightcurves in the 1–8 Å and 0.5–4 Å bands of the Geostationary Operational Environmental Satellite (GOES) system. For observing the optical and radio signatures associated with the activities, we used data from the Global Oscillation Network Group (GONG; Harvey et al., 1996) and Hirasio Radio Spectrograph (HiRAS; Kondo et al., 1995). Along with the observational analysis, in this thesis, we employed potential and Non-linear Force Free Field (NLFFF) models for the extrapolation of coronal magnetic field. Using the NLFFF-modeled field, we further computed degree of squashing factor (Q; Demoulin et al., 1996) and twist numbers (T_w; Berger & Prior, 2006). In this chapter, we provide a brief description of all the above-mentioned solar observing instruments and numerical techniques.

2.2 Observational data

2.2.1 Solar Dynamic Observatory (SDO)

The Solar Dynamics Observatory (SDO; Pesnell et al., 2012) was launched by National Aeronautics and Space Administration (NASA) on 11 February 2010 as a part of the 'Living with a Star' (LWS) programme. Major scientific objectives of the SDO include monitoring the evolution of the topology of magnetic field on photosphere and its associated structures in the solar corona. The continuous observational data of different layers of the full Sun, including photosphere, chromosphere and corona, have been used to understand the configurations required for storing magnetic energy in the system and its evolution during the transient phenomena. SDO has three instrument on board, namely, Atmospheric Imaging Assembly (AIA; Lemen et al., 2012), Helioseismic and Magnetic Imager (HMI; Schou et al., 2012) and Extreme Ultraviolet Variability Experiment (EVE; Woods et al., 2012). In the following, we provide a brief descriptions of AIA and HMI instruments, data of which we have extensively used in this thesis.

Atmospheric Imaging Assembly (AIA)

The objective of the Atmospheric Imaging Assembly (AIA) is to provide high resolution simultaneous multi-wavelength view of different layers of the solar atmosphere from photosphere to corona. AIA takes full disk solar images up to a height of 0.5 $R_\odot$ above the solar limb with an unprecedented spatial resolution of $1''.5$ (pixel scale of $0''.6$) and a temporal cadence of ≈12 s.

AIA consists of four generalized Cassegrain telescopes (see Table 2.1). All the four telescopes have multilayer coating enabling them to observe in two characteristic wavelengths each (see Figure 2.1). Telescopes 1, 2, and 4 are characterized for observing in two different EUV channels (131 and 335 Å; 193 and 211 Å; and 94 and 304 Å; respectively). The mirror of telescope 3 has a 171 Å band pass on one half and the other half has a broad-band UV coating which is used to provide observation in two UV channels: 1600 Å and 1700 Å. In total, AIA has 10 observing channels including one continuum channel (centered around 4500 Å; see Table 2.2), that covers a wide characteristic temperature range from $\approx 6\times10^4$ K to $\approx 2\times10^7$ K.

Table 2.1: Key characteristics of the AIA instrument (Lemen et al., 2012)

Diameter of primary mirror	20 cm
Effective focal length	4.125 m
Field of view	$41' \times 41'$ (along detector axis)
	$46' \times 46'$ (along detector diagonal)
Pixel size/Spatial resolution	$0''.6/1''.5$
Temporal cadence	10–12 s
Detector	4096×4096 pixels CCD
Typical exposure times	0.5–3 s

Helioseismic and Magnetic Imager (HMI)

The Helioseismic and Magnetic Imager (HMI) is designed to take measurements of

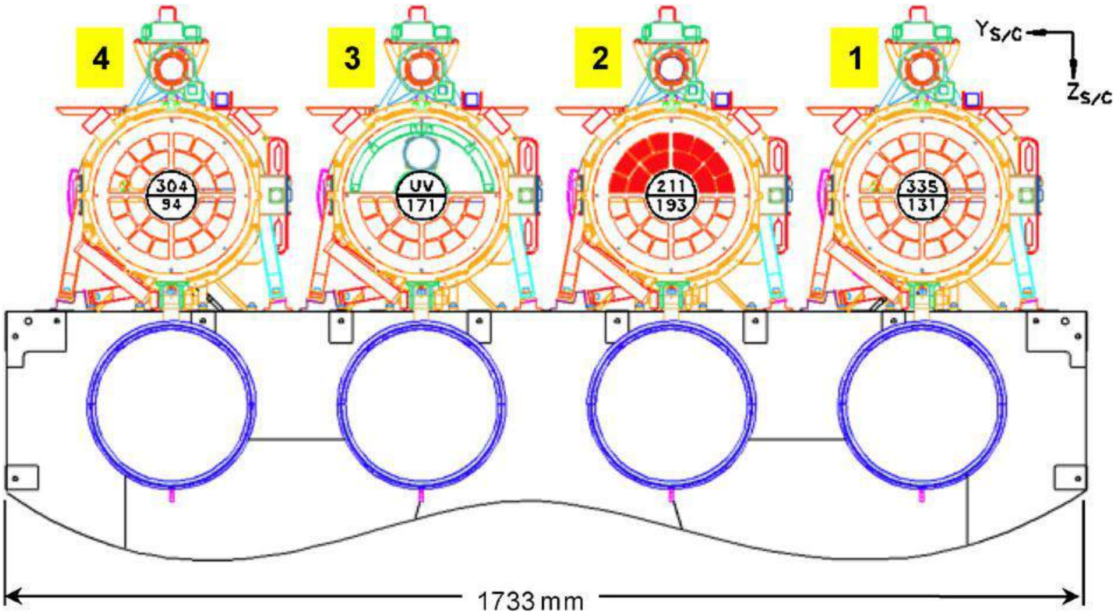

Figure 2.1: The layout of the wavelength channels or band passes in each of the four AIA telescopes. Figure is adopted from Lemen et al. (2012).

Doppler shift, intensity maps, and vector magnetic field at the solar photosphere by analyzing the Fe I 6173 Å absorption line. HMI consists of a front-window filter, a front illuminated telescope with 14 cm clear aperture giving images with a nominal diffraction limit (λ/D) of $0\farcs91$, a set of wave-plates for polarimetry, an image-stabilization system, a blocking filter, a five-stage Lyot filter with one tunable element, two wide-field tunable Michelson interferometers, a pair of 4096$\times$4096 pixel cameras with independent shutters, and associated electronics. HMI produces full disk LOS observables e.g., LOS magnetogram, dopplerogram, intensity images with a spatial resolution of $\sim1''$ (pixel scale of $0\farcs5$) and temporal cadence of $\approx$45 s, and vector magnetograms with temporal cadence of 90 s, 135 s, and 720 s depending on specific data sets[1]. A summary of the instrument specification is provided in Table 2.3.

In this thesis, we have extensively used the LOS magnetogram, intensity images and vector magnetograms from the series hmi.sharp_cea_720s[2]. In this series of vector magnetogram, data is provided for selective photospheric regions based on 'Space weather HMI Active Region Patches' (SHARP; Bobra et al., 2014) with a spatial resolution of $0\farcs5$ and a temporal cadence of 12 m. In order to construct the

[1]http://hmi.stanford.edu/
[2]http://jsoc.stanford.edu/HMI/Vector_products.html

Table 2.2: Summary of different channels of AIA (Lemen et al., 2012)

Channel	Primary ion(s)	Region of atmosphere	Char. log(T)
4500 Å	continuum	photosphere	3.7
1700 Å	continuum	photosphere	3.7
304 Å	He II	chromosphere, transition region	4.7
1600 Å	C IV + cont.	transition region, upper photosphere	5.0
171 Å	Fe IX	quiet corona, upper transition region	5.8
193 Å	Fe XII, XXIV	corona and hot flare plasma	6.2, 7.3
211 Å	Fe XIV	active-region corona	6.3
335 Å	Fe XVI	active-region corona	6.4
94 Å	Fe XVIII	flaring corona	6.8
131 Å	Fe VIII, XXI	transition region, flaring corona	5.6,7.0

vector magnetograms, the Stokes parameters (i.e., I, Q, U, and V) are measured across filterograms of six wavelengths centered at the Fe I 6173 Å spectral line and are inverted using the Very Fast Inversion of the Stokes Algorithm code (Borrero et al., 2011). The 180° ambiguity in the azimuthal field component is resolved using the minimum energy method proposed by Metcalf (1994); Leka et al. (2009). Finally, a coordinate transformation is carried out for remapping the vector fields onto the Lambert Cylindrical Equal Area (CEA) projection and the vector fields are transformed into heliocentric spherical coordinates (Gary & Hagyard, 1990).

2.2.2 Reuven Ramaty High Energy Solar Spectroscopic Imager (RHESSI)

The Reuven Ramaty High Energy Solar Spectroscopic Imager (RHESSI; Lin et al., 2002) was launched by NASA on 5 February 2002 as a part of the Small Explorer (SMEX) Mission. With a prime objective of exploring the basic physics of particle acceleration and explosive energy release processes during solar flares, RHESSI provided full Sun observations with high spatial and spectral resolutions for imaging and spectroscopic analysis. After more than 16 years of successful operation, RHESSI was finally decommissioned on 16 August 2018[3]. A summary of the instrumental characteristics of RHESSI is provided in Table 2.4.

RHESSI imager

[3] https://hesperia.gsfc.nasa.gov/rhessi3/

Table 2.3: Instrument specification of HMI (Schou et al., 2012)

Telescope aperture	14 cm
Optical resolution (λ/D)	$0''.91$
Target wavelength	6173 ± 0.1 Å (Fe I line)
Filter FWHM	76 mÅ
Detector	Two 4096×4096 CCD detectors
Pixel scale/Spatial resolution	$0''.505/\approx 1''$
Camera image cadence	3.75 s
LOS products cadence	45 s

Table 2.4: Instrument characteristics of RHESSI (Lin et al., 2002)

Energy range	3 keV – 17 MeV
Energy resolution (FWHM)	$\approx$1 keV up to 100 keV
	3 keV up to 1 MeV
	5 keV up to 17 MeV
Angular resolution	$2''.3$ up to 100 keV
	$7''$ up to 400 keV
	$36''$ up to 1 MeV
Temporal resolution	2 s (for final image)
Field of view	Full Sun ($\sim 1^\circ$)

RHESSI is equipped for producing images of solar HXR and γ-ray emission over a large energy range of 3 keV – 17 MeV with an extremely high energy resolution of $\sim$1 keV, time resolution of $\sim$2 s or better and spatial resolution as high as $\approx 2''.3$. Achieving such high angular and energy resolution in this large energy range requires indirect imaging techniques (Hurford & Curtis, 2002). RHESSI imaging is therefore achieved on the basis of a Fourier Transform technique using a set of nine Rotational Modulation Collimators (RMCs) which are mounted on the rotating spacecraft (Hurford et al., 2002). Each of the nine RMCs is equipped with a set of two widely-spaced, fine-scale linear grids which are able to temporally modulate the photon signals (Figure 2.2). The grids are essentially planar arrays of equally-spaced, X-ray opaque slats separated by transparent slits (Figure 2.3) where the slits are parallel to each other having identical pitches. In this way, the transmission through the grid pair depends only on the direction of the incident X-rays. Germanium detectors placed behind the RMCs are used for measuring the modulations.

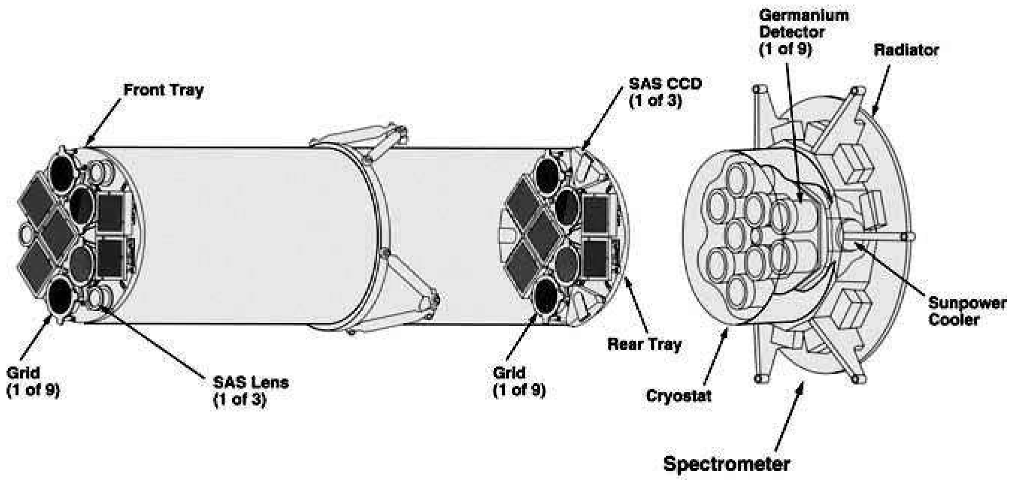

Figure 2.2: Perspective of the RHESSI imager. The key imager components are two identical sets of nine grids mounted on front and rear grid trays. A corresponding set of nine cooled germanium detectors is mounted behind the rear grids. The solar aspect system (SAS) consists of three lenses mounted on the front grid tray which focus optical images onto SAS CCDs on the rear grid tray. Figure is adopted from Hurford et al. (2002).

Image reconstruction

Several algorithms are developed for reconstructing images of the X-ray sources of the solar disk by modeling the spatial distribution of photons by employing the observed modulated time profiles and using information about the spacecraft's roll position as well as pointing. These image reconstruction algorithms are available in the RHESSI software package[4]. Details on all the image reconstructions techniques are provided in Hurford et al. (2002). In the following, we briefly discuss a few image reconstruction algorithms.

BACK PROJECTION (Mertz et al., 1986), the most straightforward and basic method of image reconstruction, is a linear process where each detected photon is projected back from the detector through the slits of the grid pairs to all possible locations on the Sun using Fourier transform method. In this way, a probability map is created which is made up of parallel ridges aligned with the slit orientation at a given time; the spacing between the ridges being twice the the FWHM resolution of the sub-collimator. This process is repeated for each detected photon and all the resulting probability maps are summed up to form the so called 'dirty map'. One major characteristic drawback of the images reconstructed by

[4] https://hesperia.gsfc.nasa.gov/rhessi3/software/imaging-software/imaging-software/index.html

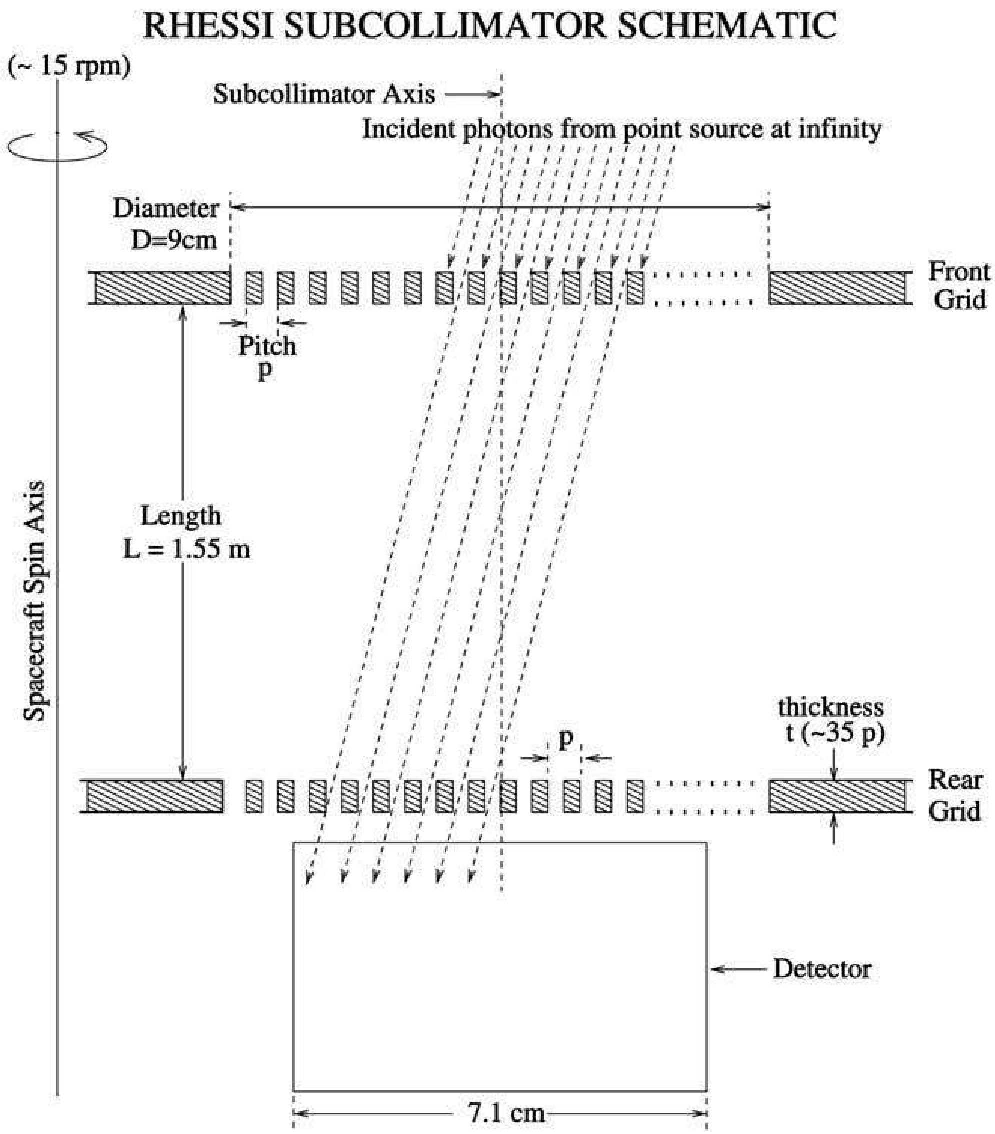

Figure 2.3: Schematic geometry of the RHESSI subcollimators, showing representative incident photons with respect to the collimator axis. Figure is adopted from Hurford et al. (2002).

the BACK PROJECTION method is the ringed patterned artifacts surrounding the real X-ray sources which is caused by incomplete sampling of the Fourier plane (see Figure 2.4). This algorithm is widely used as the basis of other complex image reconstruction techniques e.g., CLEAN, PIXON etc.

CLEAN, developed by (Högbom, 1974), is an iterative algorithm which postulates that the observed 'dirty' map produced by the BACK PROJECTION algorithm is a convolution of a set of point sources with the instrument Point Spread Function (PSF). PSF is the dirty map created by a point source at a given pixel location, i.e., the imager's response to a delta function source. The Clean

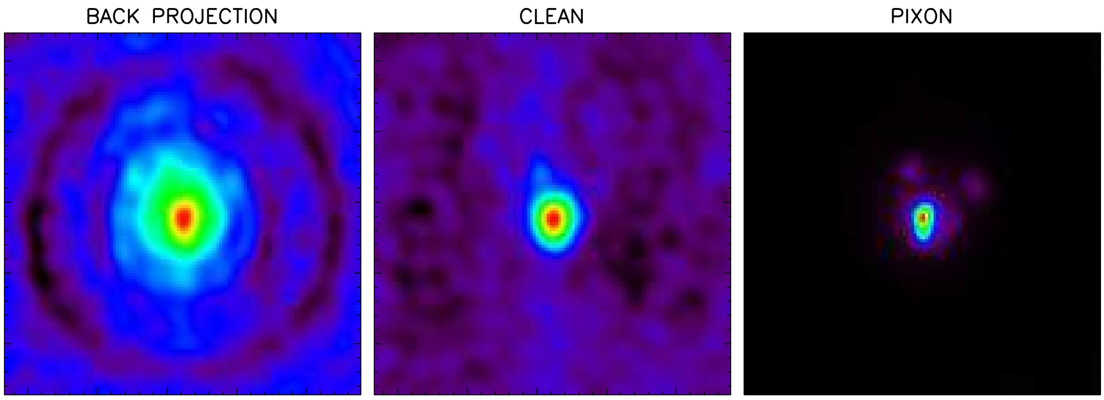

Figure 2.4: Comparison of RHESSI images reconstructed by BACK PROJECTION, CLEAN and PIXON algorithms.

algorithm first locates the pixel with the highest flux in the dirty map and assigns a point source with a fixed fraction (known as the 'loop gain') of that flux at that pixel location in a new 'CLEAN map'. It then subtracts that same fractional flux from the dirty map but spread out according to the PSF centered on that pixel to generate the so-called 'residual map'. This iteration is continued for a specified predefined number or until the peak absolute flux in the residual map is negative. CLEAN is a relatively fast process and generates images with commendable accuracy. Therefore, it is among the most preferred RHESSI image reconstruction algorithms.

Similar to the CLEAN algorithm, PIXON (Metcalf et al., 1996) also produces images without sidelobe patterns or circular artifacts which was the characteristic of the images produced by the BACK PROJECTION technique. Unlike CLEAN which relies on PSFs, PIXON uses superposition of circular sources or pixons of different sizes and parabolic profiles that best reproduces the measured modulations from the different detectors. The goal of this algorithm is to construct the simplest model for the image with the fewest degrees of freedom (i.e., pixons) that is consistent with the data (i.e., having an acceptable χ^2 fit). Being the simplest model, the derived image is expected to be artifact free with no spurious sources. PIXON algorithm is thought to produce images with superior photometric and positional accuracy (see Figure 2.4); however, this algorithm is extremely slow (approximately 2 orders of magnitude slower than the CLEAN algorithm).

RHESSI Spectrometer

RHESSI spectrometer (Smith et al., 2002) is composed of nine cryogenically cooled coaxial germanium detectors (GeD). The purpose of using ultra-pure germanium in cryogenic temperatures is to prevent natural formation of electron-hole pairs in the conduction band. In this way, electron-hole pairs in the germanium detectors of RHESSI are only produced when HXR or γ-ray photons interact with the crystal, releasing one or more energetic electrons. In the presence of high electric field ($\sim$1000 V cm^{-1}) across the crystal, the electrons and holes are pulled toward each electrode, creating a current pulse which is then amplified and digitized by suitable electronics.

RHESSI spectroscopy is performed through the Object Spectral Executive (OSPEX; Tolbert & Schwartz, 2020) software package which creates an object-oriented interface for spectral analysis of solar X-ray data. OSPEX allows the user to read and display the input data, select and subtract background, define the time intervals of interest, determine a combination of photon flux model components to fit different components to the spectrum. During the fitting process, the response matrix is used to convert the photon counts to the model counts to compare with the input count data. The resulting time-ordered fit parameters can be saved in the form of a script and the fit results stored in the form of a FITS file.

2.2.3 Large Angle and Spectrometric Coronagraph (LASCO)

The Large Angle Spectrometric Coronagraph (LASCO; Brueckner et al., 1995) is one of the twelve instruments on board the Solar and Heliospheric Observatory (SOHO; Domingo et al., 1995) mission, a joint project of European Space Agency (ESA) and NASA. LASCO consists of three coronagraph instruments, namely, C1, C2 and C3, which together can image the solar corona from 1.1 to 30 $R_\odot$ (C1: 1.1–3 $R_\odot$, C2: 1.5–6 $R_\odot$, and C3: 3.7–30 $R_\odot$; see Table 2.5). The C1 coronagraph is a classical internally occulted Lyot coronagraph which observes the solar corona in emission lines of Fe XIV and Fe X, while the C2 and C3 are externally occulted instruments which image the solar corona in white light. The C1 instrument became nonoperational following the SOHO interruption in 1998 after a successful observations for a period of two and a half year from January 1996 to June 1998.

C2 and C3 coronagraphs are still functional and providing regular observations of white light corona. In this thesis, we have used data from the C2 and C3 coronagraphs for the observation of CMEs in the near-Sun interplanetary space.

Notably, a catalog has been developed that contains all CMEs manually identified since 1996 from LASCO observations. The catalog provides most of the information assembled from manual measurements and online data bases, that include date and time of the first appearance of a CME in LASCO field of view, the central position angle of the CME propagation, angular width, linear speed, acceleration etc. This 'SOHO LASCO CME catalog' is open to all users and available at https://cdaw.gsfc.nasa.gov/CME_list/.

2.2.4 Geostationary Operational Environmental Satellite (GOES)

The Geostationary Operational Environmental Satellite Program (GOES[5]) is a joint effort of NASA and the National Oceanic and Atmospheric Administration (NOAA). The GOES system consists of a series of spacecrafts, first launched in 1975 (GOES-1). Presently GOES-15, GOES-16 and GOES-17 are operational whereas all the previous missions of GOES series have been decommissioned.

Two X-ray Sensors (XRS) on board the GOES satellites provide simultaneous, uninterrupted measurement of disk integrated solar SXR flux in 1–8 Å and 0.5–4 Å bands, with a time resolution of ≈2 s. GOES-12 and subsequent satellites of the GOES series also carry X-ray imaging telescopes called 'Solar X-ray Imager' (SXI[6]) designed to record coronal images in continuous sequence at 1 minute intervals at multiple wavelengths ranging from 6 to 60 Å. Notably, GOES SXI on board GOES-12 satellite was the first instrument to take a full-disk image of the Sun in X-rays.

2.2.5 Global Oscillation Network Group (GONG)

The Global Oscillation Network Group (GONG; Harvey et al., 1996) is a worldwide network of identical telescopes strategically situated at six different locations

[5]https://www.nasa.gov/content/goes-overview/index.html
[6]https://solarscience.msfc.nasa.gov/SXI.shtml

Table 2.5: System parameters for C1, C2 and C3 (Brueckner et al., 1995)

	Field-of-view ($R_\odot$)	Occulter Type	Spectral Bandpass	Objective Element	Pixel Size	Brightness Range $B_\odot$
C1	1.1–3.0	Internal	Fabry-Perot	Mirror	5″.6	2×10^{-5} to 2×10^{-8}
C2	1.5–6.0	External	Broadband	Lens	11″.4	2×10^{-7} to 5×10^{-10}
C3	3.7–30	External	Broadband	Lens	56″.0	3×10^{-9} to 1×10^{-11}

all over the world with the aim to have continuous observations of the Sun. The six locations[7] are the Big Bear Solar Observatory (California, USA), the High Altitude Observatory at Mauna Loa (Hawaii, USA), the Learmonth Solar Observatory (Western Australia), the Udaipur Solar Observatory (India), the Observatorio del Tiede (Canary Islands, Spain), and the Cerro Tololo Inter-American Observatory (Chile). Together, these six stations enable the GONG network to have continuous observation of the Sun, typically ≈91% of the time. The scientific objectives of the GONG telescopes include taking observations for helioseismology, which is a tool to understand the solar interior by analyzing the sound waves that are trapped in it. The original, 'GONG classic' system was upgraded to 'GONG+' in 2001 and further to 'GONG++' in 2010. In addition to full-disk intensity maps, magnetograms, and dopplerograms at a pixel scale of $\sim2''$ and a temporal cadence of 1 min, the GONG++ (Harvey et al., 2011) program started full-disk imaging of the Sun in the Hα (6563 Å) spectral line with a pixel scale of $\sim1''$ and temporal cadence of 1 min. In the thesis, we have used full-disk Hα images of the Sun provided by the GONG network.

2.2.6 Hiraiso Radio Spectrograph (HiRAS)

The Hiraiso Radio Spectrograph (HiRAS[8]; Kondo et al., 1995) began regular solar observations late in May 1993 in a fully automated mode, i.e., the antennas automatically tracked the sun from sunrise to sunset, and the data acquired by the spectrograph were processed by a workstation to produce a composite dynamic

[7]https://gong.nso.edu/sites/
[8]https://sunbase.nict.go.jp/solar/denpa/hiras/doc.html

spectrogram. Special software packages were developed to remove the contamination of artificial signals such as radio and TV broadcasts, especially at frequencies lower than 1 GHz from the raw data.

The HiRAS consisted of three antennas, namely, HiRAS-1, HiRAS-2, and HiRAS-3, which observed within the frequency ranges of 25–70 MHz, 70–500 MHz and 500–2500 MHz, respectively. Both right- and left-handed circular polarization signals received by the antennas were amplified with low-noise pre-amplifiers and fed to spectrum analyzers. HiRAS was decommissioned on 30 September 2016.

2.2.7 Solar data analysis using IDL and SolarSoft (SSW)

The solar observations from multiple instruments operating in space and ground, have been analyzed using the Interactive Data Language (IDL[9]). IDL is a high-level language for data analysis and visualization. IDL has strong signal and image processing capabilities and extensive mathematical and statistical functions. There is extensive web support with hundreds of freely available applications from a large userbase. SolarSoftWare (SSW[10]) is a set of integrated software libraries, databases, and system utilities which provide a common programming and data analysis environment for solar physics. It is primarily an IDL-based system, although some instrument teams integrate executables written in other languages.

2.3 Coronal magnetic field modeling and numerical techniques

Magnetic field arguably plays the most important role in the solar transient phenomena. Presently, direct observation of magnetic field is only possible on the photospheric layer. Therefore, in order to understand the magnetic configuration in the corona, we need to rely on different magnetic field extrapolation techniques which can reconstruct magnetic field at a given height by extrapolating photospheric magnetic field via some theoretically well defined models. In the following, we discuss the potential and NLFFF extrapolation methods which have been ex-

[9]https://www.harrisgeospatial.com/Software-Technology/IDL
[10]http://www.lmsal.com/solarsoft/

tensively utilized in our works. We also describe relevant numerical techniques which have been used to explore different topological features of coronal magnetic fields.

2.3.1 Potential Field Extrapolation

The characteristics of potential magnetic field is the current density ($\vec{J}$) being zero, i.e.,

$$\vec{J} = \frac{1}{\mu}\vec{\nabla} \times \vec{B} = 0 \ . \tag{2.1}$$

This enables $\vec{B}$ to be expressed as the gradient of a scalar potential ψ, i.e.,

$$\vec{B} = -\vec{\nabla}\psi \tag{2.2}$$

In addition to Equation 2.1, $\vec{B}$ must also satisfy Gauss law i.e.,

$$\vec{\nabla} \cdot \vec{B} = 0 \tag{2.3}$$

Combining Equations 2.2 and 2.3, one gets

$$\vec{\nabla}^2\psi = 0 \tag{2.4}$$

In the potential magnetic field extrapolation technique, Equations 2.3 and 2.4 are solved within a given 3D volume. As the boundary condition, photospheric vector magnetograms are used. There are several methods available for solving the above mentioned equations. The works included in the thesis utilized the Fourier Transform (Wiegelmann, 2004) as well as the Potential Field Source Surface (PFSS[11]) techniques for the potential field extrapolation.

2.3.2 Non-linear Force Free Field Extrapolation

In order to investigate the non-potential topological features in the solar corona e.g., flux rope, sheared coronal arcade etc., we employed the Non-Linear Force Free Field (NLFFF) extrapolation method. In the general force free field model,

[11] https://ccmc.gsfc.nasa.gov/models/modelinfo.php?model=PFSS

magnetic field ($\vec{B}$) follows the following relation:

$$\vec{J} \times \vec{B} = 0 \tag{2.5}$$

For non-zero $\vec{J}$, Equation 2.5 leads to the condition

$$\vec{J} \parallel \vec{B} \Rightarrow \vec{J} = \frac{1}{\mu}\vec{\nabla} \times \vec{B} = \alpha\vec{B} \tag{2.6}$$

Here, α is the mathematical representation of physical twist. In the NLFFF model, α is considered to be a variable of the position, i.e., $\alpha = \alpha(\vec{r})$ implying α is different in different locations of the AR. In this thesis, for finding the NLFFF solutions, we used a numerical code developed on the basis of an optimization technique (Wheatland et al., 2000; Wiegelmann, 2004). In this approach, a functional L is minimized (Wiegelmann, T. & Inhester, B., 2010), where

$$L = \int_V \left(\omega_f \frac{\mid (\vec{\nabla} \times \vec{B}) \times \vec{B} \mid^2}{B^2} + \omega_d \mid \vec{\nabla} \cdot \vec{B} \mid^2\right) dv + \nu \int_S (\vec{B} - \vec{B}_{obs}) \cdot \mathbf{W} \cdot (\vec{B} - \vec{B}_{obs}) d\vec{S} \tag{2.7}$$

where, ω_f, ω_d, and ν are weighting functions while $\mathbf{W}$ is a diagonal error matrix with the elements w_{los}, w_{trans}, and w_{trans}; 'los' and '$trans$' being the line-of-sight and transverse components, respectively. The numerical code developed for finding the NLFFF solutions, used in this thesis, calculates ω_f, ω_d (in the code, ω_f and ω_d are chosen to be identical i.e., ω_f=ω_d) and allows ν, w_{los}, and w_{trans} as free parameters (i.e., these parameters can be explicitly defined upon calling of the preprocessing/optimization; see Mitra et al., 2020b). Since the photosphere is not force-free, the photospheric mangetograms used as the input boundary conditions, need to be pre-processed (Wiegelmann et al., 2006). In Equation 2.7, $\vec{B_{obs}}$ denotes the preprocessed magnetic field. For the purpose of preprocessing, a second functional $\mathscr{L}$ is defined as

$$\mathscr{L} = \mu_1\mathscr{L}_1 + \mu_2\mathscr{L}_2 + \mu_3\mathscr{L}_3 + \mu_4\mathscr{L}_4 \tag{2.8}$$

where

$$\mathscr{L}_1 = \left(\sum B_x B_z\right)^2 + \left(\sum B_y B_z\right)^2 + \left(\sum B_z^2 - B_x^2 - B_y^2\right)^2$$
$$\mathscr{L}_2 = \left(\sum x(B_z^2 - B_x^2 - B_y^2)\right)^2 + \left(\sum y(B_z^2 - B_x^2 - B_y^2)\right)^2 + \left(\sum yB_xB_z - xB_yB_z\right)^2$$
$$\mathscr{L}_3 = \sum (B_x - B_{x,obs})^2 + \sum (B_y - B_{y,obs})^2 + \sum (B_z - B_{z,obs})^2$$
$$\mathscr{L}_4 = \sum \left((\Delta B_x)^2 + (\Delta B_y)^2 + (\Delta B_z)^2\right)$$

Here, the summations are done over all the grid nodes of the bottom boundary. The values of μ_1, μ_2, μ_3, and μ_4 are free parameters and therefore, user defined.

According to the theory of the NLFFF model (see e.g., Wiegelmann & Sakurai, 2021), the angle between current ($\vec{J}$) and magnetic field ($\vec{B}$) should be 0. However, since the NLFFF-code uses real measurements of magnetic field, small but non-zero values of $|\vec{J} \times \vec{B}|$ are expected from the reconstructed magnetic field (Thalmann et al., 2019). Therefore, to assess the quality of the coronal magnetic field reconstruction, the average value of fractional flux ratio ($< |f_i| >=< |(\vec{\nabla} \cdot \vec{B})_i|/(6|\vec{B}|_i/\triangle x) >$), weighted angle ($\theta_J$) between $\vec{J}$ and $\vec{B}$ can be considered (see, DeRosa et al., 2015). In general, NLFFF solutions are considered as good solutions if they return the values of the residual errors: $< |f_i| > \lesssim 2 \times 10^{-3}$, $\theta_J \lesssim 10^\circ$ (see e.g., DeRosa et al., 2015; Thalmann et al., 2019).

2.3.3 Computation of Degree of Squashing Factors (Q)

Magnetic field lines in the solar corona usually connect opposite polarity regions on the solar photosphere. Therefore, considering the footpoint locations of a field line on the photosphere being (u^1, u^2) and (w^1, w^2) (see Figure 2.5), the connectivity can be represented by the mapping $\Pi : (u^1, u^2) \mapsto (w^1, w^2)$ which can be determined by some vector function $(W^1(u^1, u^2), W^2(u^1, u^2))$ (Titov et al., 2009). The local properties of this mapping are described by the Jacobian matrix

$$D = \begin{pmatrix} \frac{\partial W^1}{\partial u^1} & \frac{\partial W^1}{\partial u^2} \\ \frac{\partial W^2}{\partial u^1} & \frac{\partial W^2}{\partial u^2} \end{pmatrix} \equiv \begin{pmatrix} a & b \\ c & d \end{pmatrix} \tag{2.9}$$

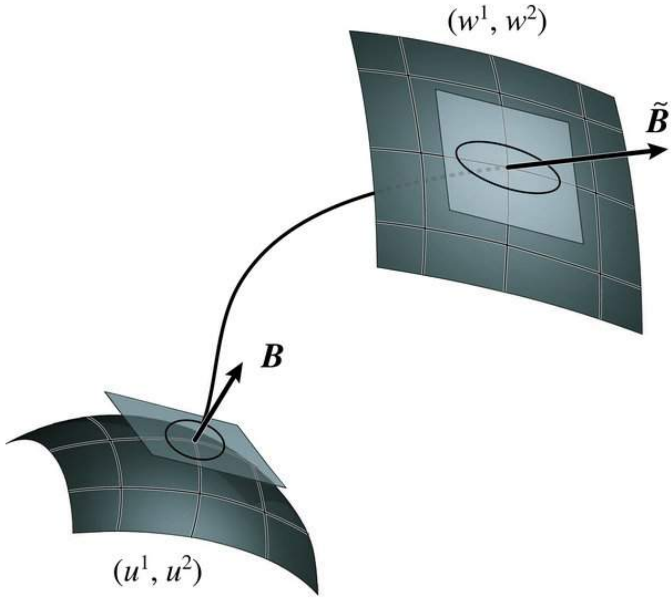

Figure 2.5: A schematic for the concept of field line connectivity. A circle is mapped into an ellipse by a linearized field-line mapping acting between the tangent planes of the launch and target boundaries, where two different curvilinear coordinates (u^1, u^2) and (w^1, w^2), respectively, exist. The aspect ratio of the ellipse, when it is large, coincides with a high value of the squashing factor Q. Figure is adopted from Titov et al. (2009).

The determinant ($\triangle$) and norm (N) of the matrix is given by

$$\triangle = ad - bc \tag{2.10}$$

$$N = [a^2 + b^2 + c^2 + d^2]^{\frac{1}{2}} \tag{2.11}$$

The degree of squashing factor (Q) is defined as

$$Q = \frac{N^2}{\triangle} = \frac{a^2 + b^2 + c^2 + d^2}{ad - bc} \tag{2.12}$$

In this thesis, we computed the Q-maps using the NLFFF extrapolation results by employing the IDL-based code developed by Liu et al. (2016b).

2.3.4 Calculation of Twist Number (T_w)

Twist number T_w of a flux rope (Equation 1.2) is used as a quantification of the number of turns between two infinitesimally close field lines of the flux rope (Berger & Prior, 2006).

Combining Equation 2.6 with Equation 1.2, one gets

$$T_w = \int_L \alpha dl \tag{2.13}$$

In this thesis, we calculated twist number using NLFFF extrapolation results by employing the IDL-based code developed by Liu et al. (2016b).

2.3.5 Determination of coronal null points

Coronal null points are defined as locations in the solar corona, where the strengths of all the three components of magnetic field become locally zero (see review by Longcope, 2005). In order to locate 3D null-points within the extrapolation volumes, we used the trilinear method as suggested by Haynes & Parnell (2007). According to the technique, the whole AR volume are divided into several grid cells of same dimension. In our works, we used grids of dimension 2×2×2 pixels. The first step of the trilinear method is to quickly scan through every grid cell by examining the signs of each component of magnetic field at all the eight corners of the grid cells. If any of the three components have same sign at all the eight corners, a null-point cannot reside within the grid cell and therefore, the corresponding cell is excluded from further analysis. Each of the remaining other cells are then further divided into subgrid cells of dimensions that is defined by the user and 3D Newton-Raphson method[12] can be used to locate the null point. In our studies, we divided each of the cells that can possibly house the null point by 100×100×100 subgrid cells and used the threshold $\triangle x \leq 2$ subgrid cell width for locating null-points.

[12]http://fourier.eng.hmc.edu/e176/lectures/NM/node21.html

Chapter 3

Pre-flare Activity and its Role in Driving Subsequent Large-scale Eruptions

3.1 Introduction

Eruptive flares are mostly associated with large-scale eruptions of plasma and magnetic field into the interplanetary space i.e., CMEs (Yashiro et al., 2006; Toriumi & Takasao, 2017; Kawabata et al., 2018). As explained in the standard CSHKP model of solar flares (Shibata et al., 1996, see Section 1.7), the process initiates with the eruptive expansion with a magnetic flux rope (observationally identified in the form of solar filaments/prominences, coronal hot channels etc.). Despite the general success of the CSHKP model in explaining the observable signatures of eruptive flares, the mechanisms involved in the build up and activation of the flux ropes along with triggering of their eruption are not clearly understood and remain out of the scope of the standard model. Therefore, observational and theoretical studies on the triggering mechanisms of solar eruptions have been the topic of numerous investigations over the years and still form one of the major areas of research in the contemporary solar physics (see e.g., Chifor et al., 2006, 2007; Liu et al., 2009; Joshi et al., 2011, 2013; Sterling et al., 2011; Kushwaha et al., 2015).

Prior to the onset of intense flaring emission, events of small-scale energy release are often observed, which are referred to as 'pre-flare' activities (Fárník et al., 1996). Statistical studies on the spatial relation between pre-flare activities and the subsequent main flares conducted by Fárník & Savy (1998) revealed that ≈25% of all the pre-flare activities occur within the core field i.e., co-spatial to the main flaring site. The tether-cutting model (Moore & Roumeliotis, 1992; Moore et al., 2001) suggests development and eventual eruption of flux ropes in response to small-scale magnetic reconnections within the highly sheared core magnetic field; thus, providing an explanation to the causal connections between the co-spatial and main flare emissions. However, the majority of the pre-flare activities (≈69%) are observed to originate within the larger extent of the AR while core of the pre-flare brightening touches or lays over only a part of the main flaring site ('adjacent/overlapping' pre-flare activity; Fárník & Savy, 1998). The exact influence of such pre-flare activities toward the triggering of the subsequent main flares is still not well understood. Catastrophic stabilization of flux ropes often temporarily follow a 'slow rise' phase in SXR/EUV emissions during which the filament gradually ascends (see e.g., Veronig et al., 2002). Such 'precursor' phases are mostly associated with a gradual activation of the flux ropes, complete destabilization of which precisely matches the onset of impulsive phase of flares (Zhang et al., 2001; Zhang & Dere, 2006).

Investigations of pre-flare and precursor activities provide important clues to understand the activation of flux ropes and the triggering mechanism for their catastrophic eruption. In this chapter, we carry out thorough analysis of two eruptive flares, both associated with multiple pre-flare events and precursor phase, by employing multi-wavelength imaging, spectroscopic, and numerical techniques including coronal magnetic field reconstruction. The locations of the pre-flare activities associated with both the events were spatially detached from the core region that included flux ropes. However, they originated from locations within the extent of the AR implying that the pre-flare activities can be considered in the adjacent/overlapping category. A summary of the two events are provided in Table 3.1.

Table 3.1: Summary of the two eruptive flares studied in this chapter

Sr. No.	Date	Active region	Flare class	Duration	Location
1	21 Jun 2015	NOAA 12371	M2.6	≈01:20–03:20 UT	≈N12E16
2	28 Oct 2013	NOAA 11875	X1.0	≈01:41–02:12 UT	≈N07W66

3.2 Triggeing and evolution of eruptive M-class flaring activity in NOAA 12371

3.2.1 Evolution of AR and build up of magnetic complexity

NOAA 12371 appeared on the visible hemisphere of the Sun over its eastern limb on 15 June 2015. Although the magnetic morphology of the AR was initially a moderately complex β-type, it gradually evolved into more complex $\beta\gamma$-type on 18 June and further into $\beta\gamma\delta$-type on 19 June. NOAA 12371 produced a total of 40 C-class and 6 M-class flares. Interestingly, despite producing such high number of C-class and moderate number of M-class flares, NOAA 12371 did not produce any X-class flare. It produced the largest flare (of GOES class M7.9) on 25 June 2015 when it was into its declining phase. However, in terms of the objectives of this thesis, the most interesting flare from the AR occurred on 21 June 2015. This dual-peak M-class eruptive flare was preceded by multiple episodes of distinct pre-flare SXR flux enhancements. Notably, this flare followed the characteristics of a long duration flare with peak GOES flux reaching a level of M2.6 and a fast CME with linear speed of 1366 km s^{-1} which gave rise to one of the strongest space weather manifestations of the solar cycle 24 (Joshi et al., 2018).

The location of the AR on 21 June 2015 near the disk center (≈N12E16) gave us a unique opportunity to carry out comprehensive investigations of the photospheric magnetic activities during the prolonged phase prior to the onset of the dual-peak M2.6 flare, in order to understand the effects of energy build up and photospheric magnetic changes towards the triggering of subsequent flaring activity. The observations revealed that, on 21 June 2015, the AR was consisted of two major sunspot groups (Figure 3.1(a)). A comparison of the white light image of the AR with a co-temporal magnetogram (cf. Figures 3.1(a)–(b)) unveiled

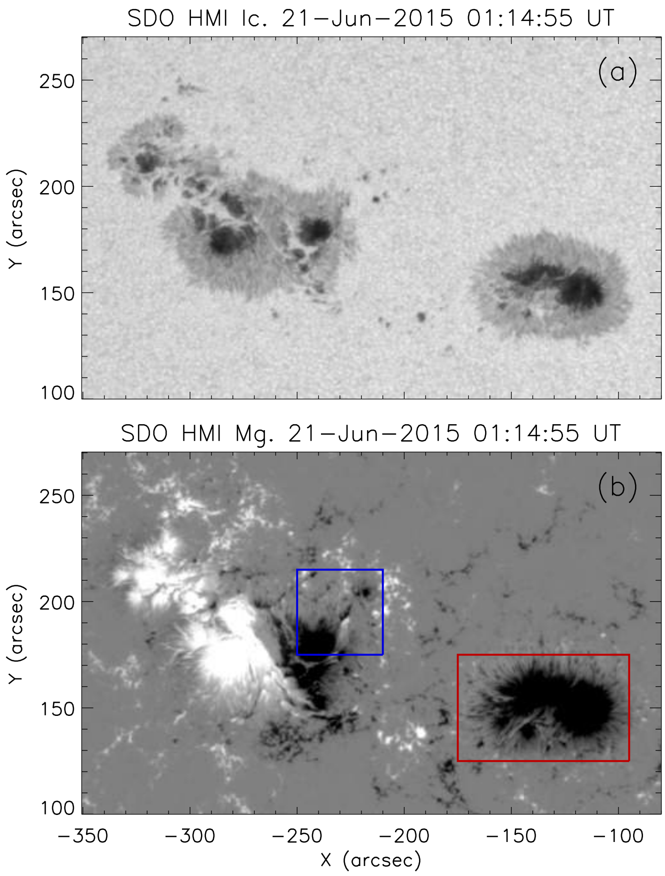

Figure 3.1: Panel (a): A white light image of the AR during the pre-flare phase of the M-class flare on 21 June 2015. Panel (b): A co-temporal LOS magnetogram. The blue and red boxes indicate two regions that showed striking photospheric changes.

that almost all of the leading sunspot group of the AR was consisted of negative polarity while the trailing sunspot group was of mixed polarities that formed a δ-type configuration, making the overall photospheric magnetic configuration of the AR on 21 June 2015 to be a $\beta\gamma\delta$ sunspot region. Notably, the flaring activities on 21 June 2015 occurred from the trailing part of the AR.

The evolution of LOS magnetic flux through the AR was interesting (Figure 3.2). Since, the M-class flare originated from the trailing part of the AR, we have specified the region by a black box in Figure 3.2(a) and showed the evolution of the LOS magnetic flux through the whole AR as well as only from the trailing sunspot region from 20 June 2015 12:00 UT to 21 June 2015 05:00 UT in Figure 3.2(c)–(d). Notably, the trailing sunspot group was highly dynamic which can be inferred by comparing Figures 3.2(b1) and (b2) where the area marked by dashed circles was associated with rapidly evolving magnetic elements and moving magnetic features (MMFs; discussed in detail in Section 3.2.2). As it is evident from Figure 3.2(c), photospheric flux of both polarities from the AR initially increased during ≈13:30 UT–23:00 UT on 20 June 2015 (we denote this period as 'phase 1') and thereafter

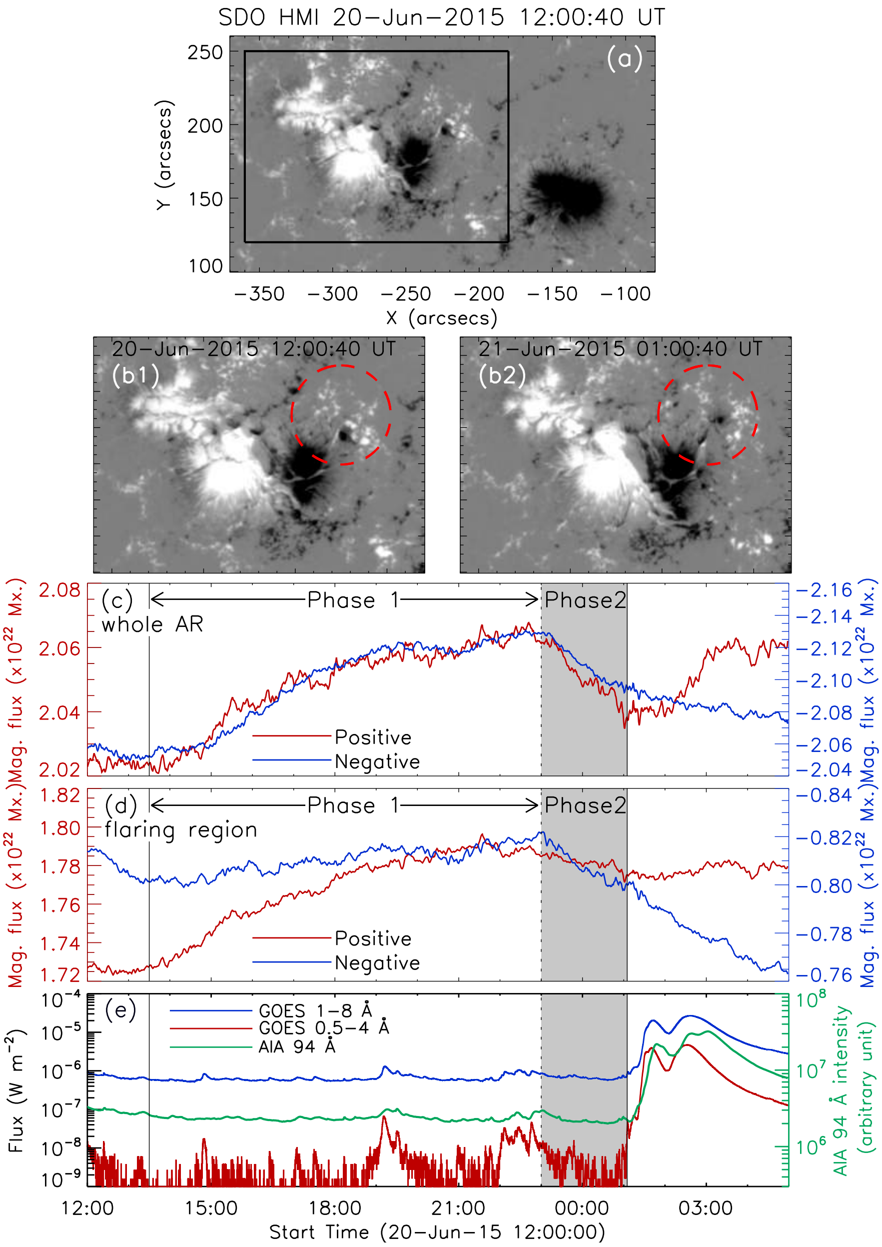

Figure 3.2: Panel (a): HMI LOS magnetogram of NOAA 12371. We outline the flaring region in the AR by the black box. Panels (b1) and (b2): The flaring region as indicated by the black box in panel (a), at two different times with a time-gap of ≈23 hours. The red dashed circles in these two panels mark the region with striking moving magnetic features (MMFs). Panel (c): Evolution of magnetic flux in the whole AR from 20 June 2015 12:00 UT to 21 June 2015 05:00 UT. Panel (d): Evolution of magnetic flux in the flaring region (within the box in panel 9a)). In panel (e), we plot GOES SXR lightcurves in both the channels as well as the AIA 94 Å intensity profile. In panels(c)–(e), the interval marked as 'phase 1' depicts flux emergence of both polarities in the AR as well as flaring region. The 'phase 1' was followed by a period of flux cancellation of both polarities ('phase 2'; the shaded region) which lasts up to the initiation of the M-class flare on 21 June 2015.

decreased till the onset of the flare at ≈01:05 UT on 21 June 2015 (we denote this period as ‘phase 2’). Magnetic flux from the trailing sunspot group, (i.e., the flaring region) underwent a similar evolution as the entire AR (Figure 3.2(d)). During phase 1, flux of both polarities increased; however, increase of negative flux was less prominent than positive flux. Flux of both polarities decayed at similar rate during phase 2. In order to have an understanding of flaring activity within this time period from the AR, we have also plotted the variation of GOES SXR flux along with AIA 94 Å intensity in Figure 3.2(e). We find that, during the selected interval, there was no appreciable enhancement of SXR and EUV fluxes prior to the onset of the M-class flare on 21 June 2015.

3.2.2 Sunspot rotation and moving magnetic features

NOAA 12371 was highly dynamic as it underwent significant morphological changes which include MMFs, emerging/canceling flux elements, and sunspot rotation throughout its lifetime. To highlight these features, we identified two sub-regions in the AR that showed most prominent photospheric changes: the leading negative polarity sunspot group and a region with dispersed mixed polarity flux (marked by the red and blue colored boxes in Figure 3.1(b), respectively). The leading sunspot group of the AR (inside the red box in Figure 3.3(b)) was associated with a very interesting display of morphological evolution during which the extension of the leading sunspot group along the east-west direction increased from ≈55″ at 20 June 2015 12:00 UT to ≈65″ prior to the onset of the flare. During the same time, the north-south extension of the leading sunspot group decreased from ≈40″ to ≈35″ (cf. Figures 3.3(a) and (f)). Further, we identified a small circular element of negative polarity (indicated by the blue arrows in Figure 3.3) which exhibited continuous motion along the southern boundary of the leading sunspot group. The diagonal expansion of the region alongside the motions of the small patch resembled a ‘clockwise rotation’ of the overall leading sunspot group. We also identified a distinct patch of small magnetic region (indicated by the red arrows in Figure 3.3) which, after initially exhibiting constant converging motion toward the major sunspot, merged with it during the final hours of 20 June 2015 (Figure 3.3(e)).

The photospheric activities within the region inside the blue box (Figure 3.1(b))

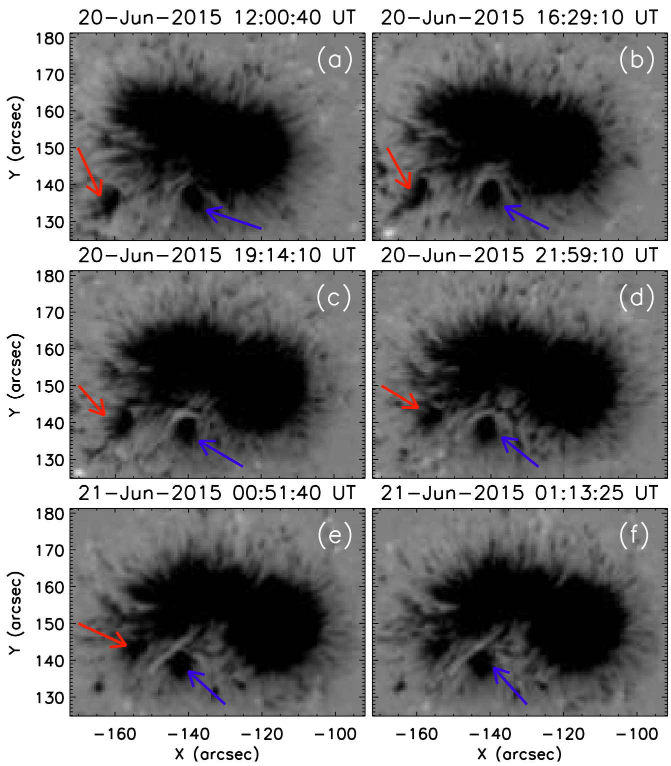

Figure 3.3: Series of LOS magnetograms showing the evolution of the leading sunspot group of the AR (shown within the red box in Figure 3.1(b)). We have identified a small, nearly circular patch that exhibited significant clockwise rotation (indicated by the blue arrows) and another small magnetic patch displayed converging motion towards the sunspot (indicated by the red arrows).

is shown in Figure 3.4, where we have indicated two particular features by red and green arrows. The red arrows indicate a striking MMF element of negative polarity which also shows significant morphological changes. The green arrows mark persistent cancellation of a positive flux element as the negative MMF moves toward north-west direction.

3.2.3 Temporal evolution: SXR and (E)UV lightcurves

The temporal evolution of the M-class flare on 21 June 2015 is depicted by the SXR flux variation in the GOES 1–8 Å and 0.5–4 Å channels which are plotted between 21 June 2015 00:00 UT and 05:00 UT in Figure 3.5(a). The GOES 1–8 Å channel time profile suggests that the event started at ≈01:20 UT while the peaks of the two subsequent episodes of energy release were recorded at ≈01:42 and ≈02:36 UT during which the SXR flux rose to the levels of M2.1 and M2.6, respectively. Further, the flare was associated with two brief pre-flare flux enhancements at ≈01:05 and ≈01:14 UT (indicated by the dashed and dotted lines, respectively, in Figure 3.5). Profile of GOES 0.5–4 Å channel clearly reveals that, while the flux enhancement during the first pre-flare peak was quite impulsive and short-lived, it was relatively gradual during the second pre-flare peak. We attribute

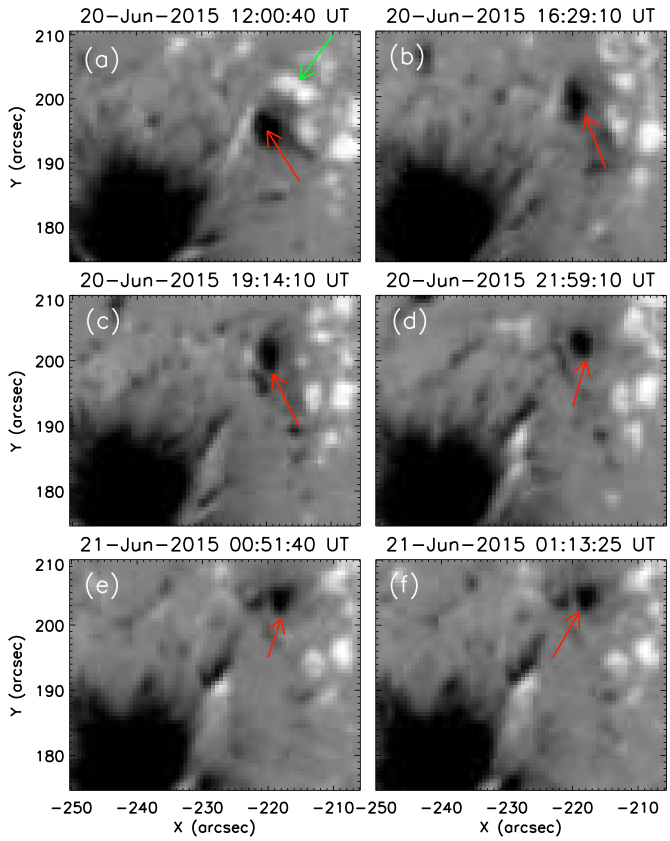

Figure 3.4: Series of LOS magnetograms of the selected region shown within the blue box in Figure 3.1(b) showing striking and rapidly evolving MMFs along with flux emergence and cancellation. The red arrows indicate an MMF of a negative polarity. The green arrow indicates a region associated with cancellation of positive flux.

the short-lived episodes of small-scale flux enhancements prior to the onset of the main flare as the signatures of SXR pre-flare activities. The intensity variation derived from different AIA (E)UV channels on 21 June 2015 between 00:00 UT and 05:00 UT are shown in Figure 3.5(b). We readily note that none of the AIA intensity profiles exhibited enhancement during the first GOES pre-flare peak; while a subtle enhancement was observed during the second pre-flare period in the AIA 304 and 171 Å channels (cf. the dashed and dotted lines in Figure 3.5(a) and (b)). Intensity in all the AIA channels, except the hot 94 Å ($\log(T)$=6.8) channel, displayed a sharp peak at ≈01:36 UT (indicated by the solid line in Figure 3.5(b)) while the second peak in these relatively low temperature AIA channels was rather gradual. The intensity variation in the AIA 94 Å channel diverged from other AIA channels in the timing and extended duration of the peaks. Interestingly, the AIA 94 Å channel displayed three distinct peaks, first and second ones of which were consistent with the GOES M2.1 and the GOES M2.6 peaks, respectively. The highest of the three AIA 94 Å peaks occurred during the gradual phase of the M-class flare. The flare entered into the gradual phase after ≈03:00 UT in all the AIA (E)UV and GOES SXR channels.

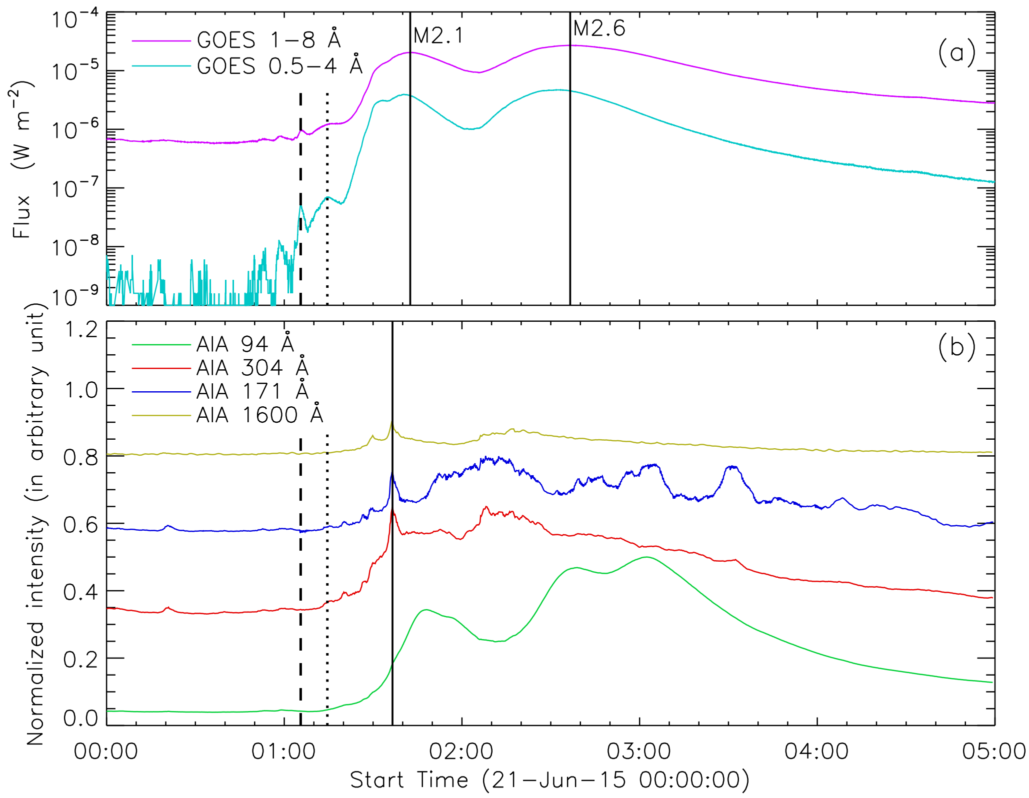

Figure 3.5: Panel (a): GOES SXR flux variation in the 1–8 Å (magenta) and 0.5–4 Å (cyan) channels showing the initiation and evolution of the dual-peak M-class flare on 21 June 2015. Panel (b): Normalized intensity variations in the 94 Å (green), 304 Å (red), 171 Å (blue), and 1600 Å (yellow) channels of AIA during the flare. For better visualization, the AIA channels are scaled by factors of 0.5, 0.65, 0.8, and 0.9, respectively. The dashed and dotted lines in both the panels indicate two precursor events identified in the GOES SXR channels prior to the initiation of the main flare. The two peaks of the main flare are indicated by the solid lines in (a) during which GOES 1–8 Å flux attained levels of M2.1 and M2.6, respectively. The solid line in panel (b) indicates an impulsive but short-lived intensity enhancement observed in the AIA 304, 171, and 1600 Å channels.

3.2.4 Two-stage energy release and flux rope eruption

Comparison of Figure 3.5(a) with Figure 3.5(b) suggests that the intensity variation in the AIA 94 Å channel, compared to the other AIA channels, was in the best agreement with the dual-peak nature of the flare. Therefore, to understand the morphological evolution of the AR during the dual-peak M-class flare, we looked into AIA 94 Å images (Figure 3.6). From the images, we readily identified the presence of a prominent hot channel at the core of the AR during the pre-flare phase (indicated by the yellow arrow in Figure 3.6(b)). Comparison of the location of the hot channel with the HMI LOS magnetogram contours in Figure 3.6(a)

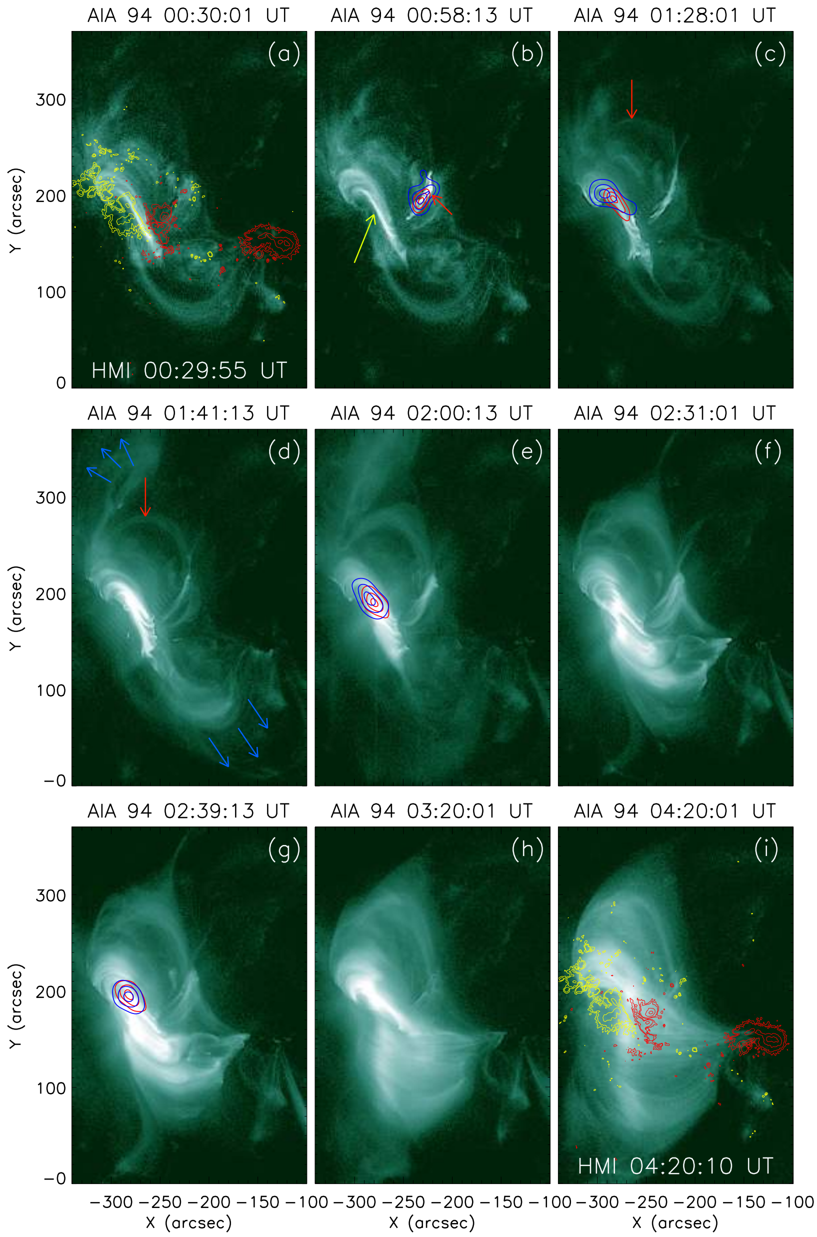

Figure 3.6: Series of AIA 94 Å images showing the evolution of the M-class flare on 21 June 2015 from NOAA 12371. A distinct hot channel was observed during the pre-flare phase over the polarity inversion line in the AR which is marked by the yellow arrow in panel (b). A remote brightening observed prior to the onset of the flare is indicated by the red arrow in panel (b). The red arrows in panels (c) and (d) indicate a moving flash connecting the remote region and the northern leg of the hot channel. The blue arrows in panel (d) indicate the direction of erupting plasma during the impulsive phase of the flare. Co-temporal HMI LOS magnetogram contours are overplotted in panels (a) and (i) at $\pm(500, 800, 1500, 2000)$ G. Red and yellow contours refer to negative and positive polarities, respectively. Co-temporal RHESSI contours in the energy bands 6–12 keV (red) and 12–25 keV (blue) are overplotted in selective panels. Contour levels are 60%, 80% and 95% of the corresponding peak flux. All the images are derotated to 21 Jun 2015 00:30 UT.

confirms that the hot channel was lying over the PIL in the trailing sunspot of the AR. After ≈00:52 UT, we observed a localized yet prominent brightening from a location near to the hot channel (indicated by the red arrow in Figure 3.6(b). Notably, this remote location of pre-flare EUV brightenings was co-spatial with hard X-ray (HXR) emission of energies up to ≈25 keV. AIA 94 Å images further suggest that the brightness of this localized region initially increased up to ≈01:05 UT and then decreased till ≈01:10 UT before increasing again. These pre-flare episodic brightenings observed in AIA 94 Å images are exactly co-temporal with the pre-flare GOES SXR flux enhancements observed at ≈01:05 UT and ≈01:14 UT (cf. Figure 3.5(a)). However, the most interesting phenomena in the context of the triggering of the flare occurred around ≈01:28 UT when we observed an anti-clockwise motion of a localized bright kernel, depicting a narrow semicircular path from the northern end of the region of precursor brightening to the northern leg of the hot channel (indicated by the red arrows in Figures 3.6(c) and (d)). This strange motion of the bright patch was immediately followed by the catastrophic eruption of the hot channel, resulting the flare to reach the first peak at ≈01:42 UT. During this time, we noted HXR emission of energies up to ≈25 keV predominantly from the northern part of the hot channel. During the impulsive phase, the activated hot channel underwent eruptive motion leading to the development of a fast halo CME (Joshi et al., 2018). The projected directions of the eruption of the hot channel are indicated by the blue arrows in Figure 3.6(d). As expected from the standard flare model, the eruption of the hot channel was followed by formation of post-reconnection arcade in the trailing sunspot (Figures 3.6(e) and (f)). We observed structured HXR emission of energies up to ≈25 keV from the dense post-reconnection arcade. Notably, a second phase of the eruption occurred between ≈01:53 UT and ≈02:05 UT which was followed by further restructuring of the AR loops at even larger scales leading to the development of a large-scale loops arcade connecting the trailing sunspot with the leading sunspot. The large post-flare arcade was associated with strong diffused emission till ≈02:40 UT (Figure 3.6(g)) when the flare reached its second peak. As the flare moved into the gradual phase, the brightness of the large post flare arcade slowly reduced and the AR did not show any significant morphological change till the end of our studied period (Figures 3.6(h), (i)). The above observations led Joshi et al. (2018) to conclude that two distinct phases of magnetic reconnection occurred successively at two separate locations and heights of the AR corona in the wake of single, large hot channel eruption. Based on the temporal and spatial proximity of the two distinct energy release phases along with spectral characteristics of emission, Lee et al. (2018) has termed the two-phases of energy release as the signature of a 'composite flare' triggered by the flux rope eruption.

To have a further clarification on the triggering of the hot channel eruption, we selected three slits and computed time-slice diagrams along them (Figure 3.7). These time-slice diagrams can be effectively used to observe the time evolution of plasma eruption and progression of the bright kernel along the selected slits. From Figure 3.7(b), we find that the motion of bright kernel (apparent signatures of slipping reconnection) from the precursor location started at ≈01:26 UT. We have highlighted the motion of the bright kernel in Figure 3.7(b) by a dotted curve. The estimated time of the arrival of the bright kernel at the T_2 point is indicated by the dashed vertical line in Figures 3.7(b)–(c). From Figures 3.7(c) and (d), it becomes evident that the eruption started immediately after the bright kernel reached the core of the AR, i.e., the eruption was triggered by the processes linked with the motion of the bright kernel.

In order to understand the evolution of the flare in the lower atmospheric layer of the Sun, we looked into AIA 304 Å images (Figure 3.8). We observed the presence of a filament (marked by the blue arrow in Figure 3.8(b)) lying along the PIL in the trailing sunspot region (cf. Figure 3.8(b) with HMI LOS contours in Figure 3.8(a)). Notably, the location of the filament was co-spatial with the location of the hot channel observed in the AIA 94 Å channel images (cf. Figures 3.8(b) and 3.6(b)). The adjacent precursor activity was also observed in the AIA 304 Å images (Figure 3.8(b) and (c)). The impulsive phase of flare was characterized by the formation of a clear set of flare ribbons in the trailing sunspot region (indicated by the arrows in Figure 3.8(d)). As expected from the standard flare scenario, the separation between the two ribbons increased with time, albeit rather slowly, which was followed by the development of a dense post flare arcade connecting the two ribbons (Figures 3.8(d)–(h)).

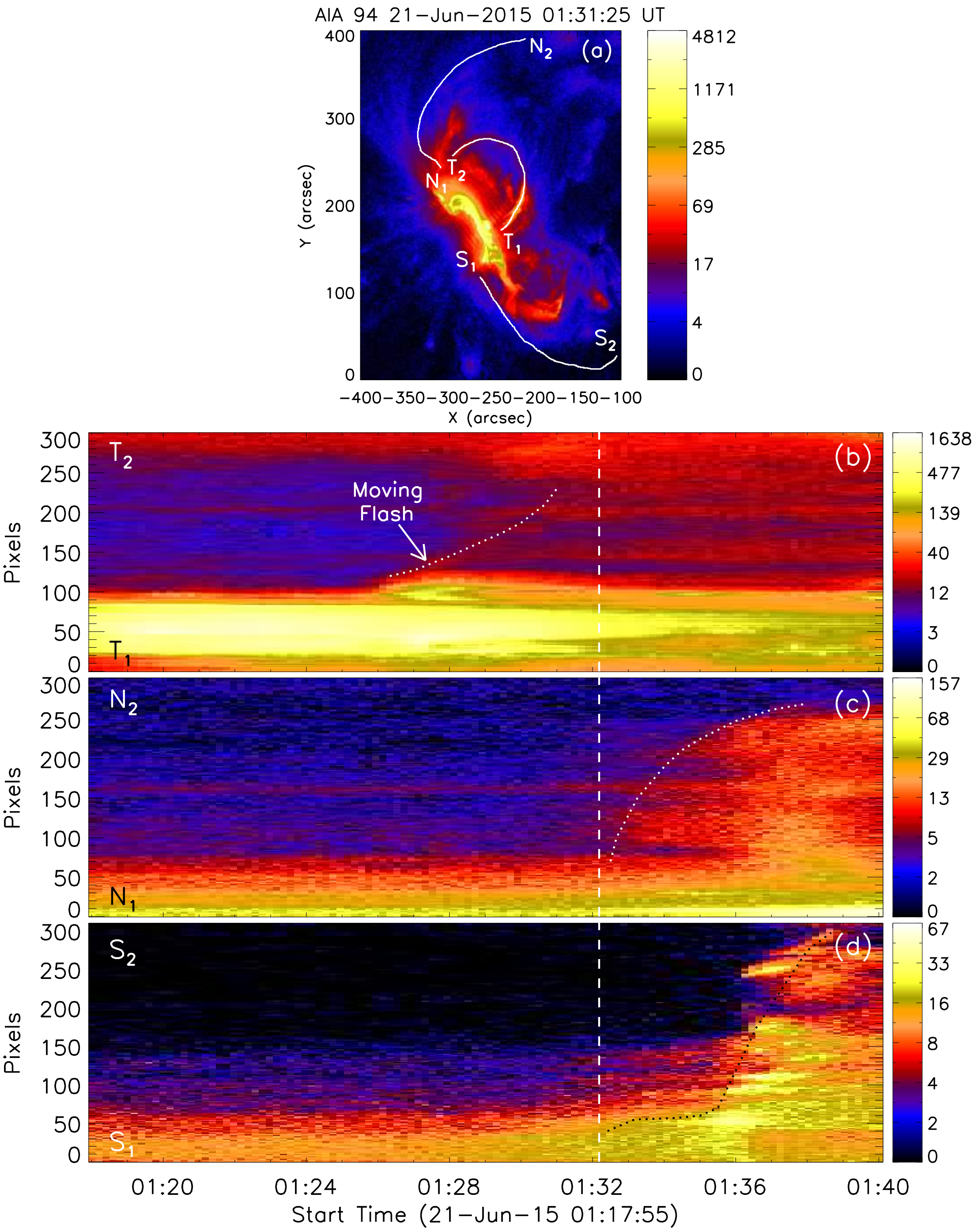

Figure 3.7: Panel (a): AIA 94 Å images prior to the onset of the hot channel eruption. The three curves (marked by T_1T_2, N_1N_2, and S_1S_2) indicate three slits along which time-slice diagrams are computed. Panels (b)–(d): Time-slice diagrams corresponding to the slits T_1T_2, N_1N_2, and S_1S_2, respectively. The dotted curve in panel (b) indicate the anti-clockwise motion of the subtle brightness from the precursor location to the northern leg of the hot channel. Dotted curves in panels (c) and (d) highlight the eruptive motion of the hot channel. The dashed vertical line in panels (b) and (d) indicate the estimated time of the arrival of the brightness to the northern leg of the hot channel along T_1T_2.

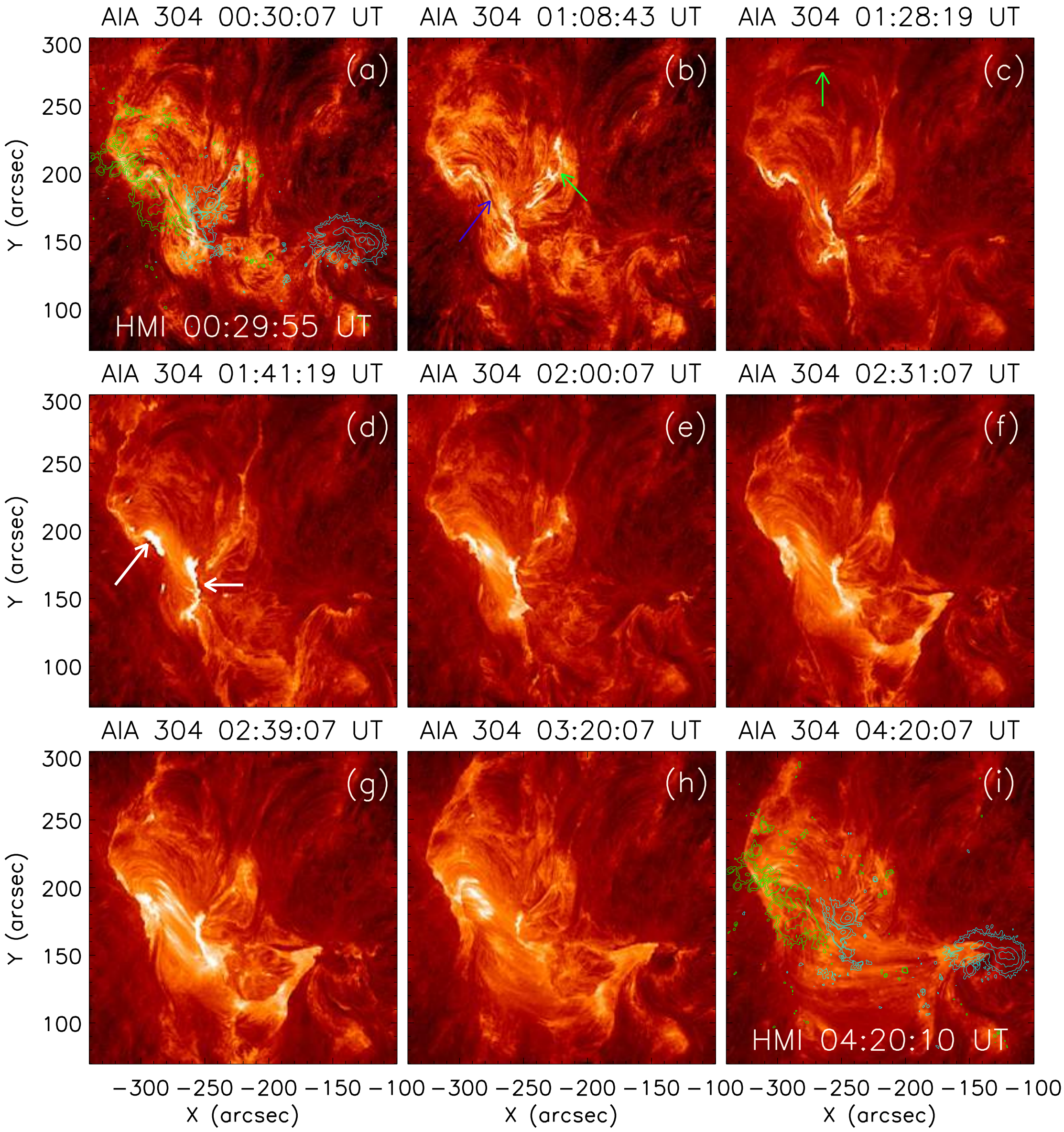

Figure 3.8: Series of AIA 304 Å images displaying different phases of the M-class flare. A filament was observed (indicated by the blue arrow in panel (b)) which was co-spatial to the hot channel (cf. Figure 3.6(b)). The remote brightening and the moving flash are indicated by the green arrow in panels (b) and (c), respectively. The white arrows in panel (d) mark the two flare ribbons during the impulsive phase of the flare. Co-temporal HMI LOS magnetogram contours are overplotted in panels (a) and (i) at $\pm(500, 800, 1500, 2000)$ G. Green and sky contours refer to positive and negative polarity, respectively. All the images are derotated to 21 Jun 2015 00:30 UT.

3.2.5 Identification of small-scale pre-eruption processes

EUV images of the AR (Figures 3.6 and 3.8) clearly suggest that the earliest flare brightening occurred at a remote location to the west of the pre-existing hot channel (i.e., magnetic flux rope), which evolved with time but remained within a localized region. As discussed earlier, we interpret this brightening as GOES SXR precursor as it was followed by the activation and eruption of the hot channel as a sequence of causally linked activities. Here we further recall that this region region of precursor brightening was associated with rapidly evolving dispersed magnetic field of positive and negative polarities which included MMFs besides the emergence and cancellation of magnetic flux (Figure 3.4). In Figure 3.9, we further investigate the precursor activities and its relation to the small-scale magnetic field changes. The region of precursor brightening over an HMI magnetogram is highlighted by the box in Figure 3.9(a) and co-temporal overplots of the AIA 94 Å images with the magnetograms are shown in Figures 3.9(b1)–(b3). We identified several instances of flux emergence and cancellation of both polarities within the region of the precursor brightening (indicated by the arrows of different colors and the boxes in Figures 3.9(b1)–(b3)). In Figure 3.9(c), we show the evolution of LOS magnetic flux from the precursor region on 21 June 2015 from 00:00 UT till the onset of the impulsive phase of the flare at ≈01:20 UT. We find that magnetic flux of both positive and negative polarities exhibited episodic increase and decrease from the region, further implying significant small-scale flux variations. Notably, the overall trend of positive flux in this region displayed a slow decay while the negative flux increased initially up to ≈00:25 UT and decayed gradually thereafter.

3.2.6 Morphology and evolution of photospheric longitudinal current

Electric current density on the photosphere, being a direct consequence of flux emergence and decay as well as photospheric motions, is expected to provide important insights toward understanding the onset of flares. The longitudinal component of current density (j_z) on the photosphere can be calculated from horizontal components of magnetic field (B_x and B_y) using the Ampere's law (Tan et al., 2006; Kontogiannis et al., 2017):

$$j_z = \frac{1}{\mu_\circ}\left(\frac{dB_y}{dx} - \frac{dB_x}{dy}\right) \tag{3.1}$$

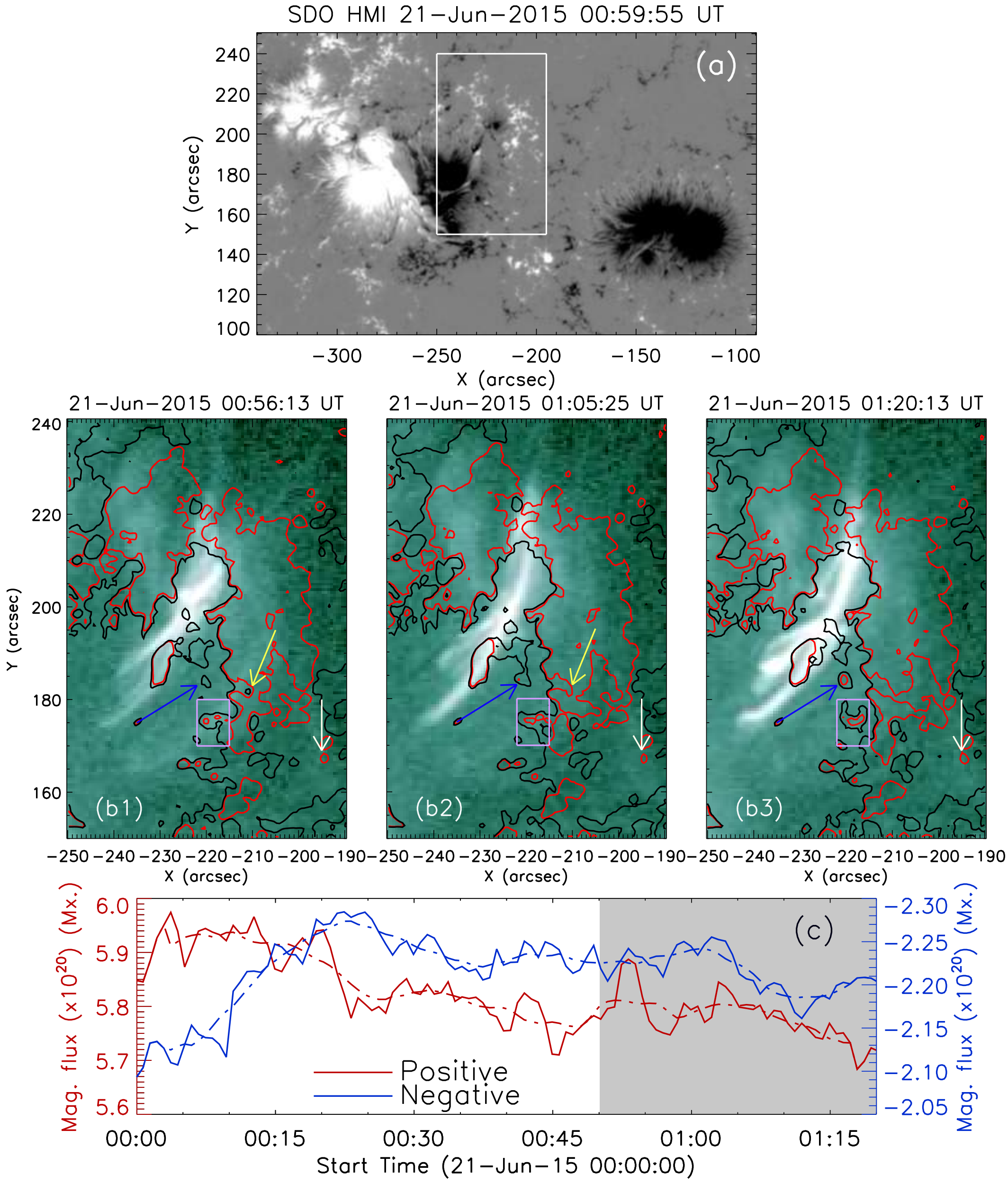

Figure 3.9: Panel (a): HMI LOS magnetogram of NOAA 12371 prior to the onset of the M-class flare. The box in panel (a) outlines the region that displayed small-scale magnetic field changes along with MMFs. Panels (b1)–(b3): AIA 94 Å images of the region, shown within the box in panel (a), overplotted with co-temporal LOS magnetograms. Black and red contours refer to negative and positive polarities, respectively. Contour levels are ±25 G. The arrows and the boxes in these panels indicate different instances of flux emergence and decay in this region prior to the triggering of the flare. All the images in panels (a) and (b1)–(b3) are derotated to 21 Jun 2015 01:00 UT. In panel (c), we display the variation of magnetic flux in the region within the box in panel (a) on 21 Jun 2015 from 00:00 UT up to the onset of the flare at ≈01:20 UT. The shaded region in panel (c) denotes the interval of precursor enhancements observed in GOES SXR channels.

Photospheric current (I_z) is derived from current density (j_z) by multiplying j_z with the area of one pixel ($\approx$13.14$\times$10^{10} m^2 for HMI vector magnetograms of the 'hmi.sharp_cea_720s' series). In Figure 3.10, we plot the temporal evolution of average I_z for the overall AR (Figure 3.10(b)) as well as the location of precursor brightening (Figure 3.10(c)). From the spatial distribution of I_z prior to the hot channel activation (Figure 3.10(a)), we find large concentration of positive and negative currents along the narrow strip delineated by the PIL with the maximum and minimum values of I_z in the AR being 2.09$\times$10^{10} A and -2.24$\times$10^{10} A, respectively. It is noteworthy that the region displaying precursor brightenings in the corona and underlying MMFs in the photosphere (i.e., the triggering region; shown within the box in Figure 3.10(a)) exhibited a complex distribution of I_z.

The spatial distribution of I_z in the triggering region of the AR (within the box in Figure 3.10(a)) suggests that small-scale regions of both positive and negative I_z were mostly distributed randomly. However, a few regions of relatively strong photospheric current of both polarities situated close to each other forming a structure with the apparent shape of 'A' formed by I_z was very clear in the region during the pre-flare phase (outlined by pink-black dashed lines in Figure 3.11(b)). Notably, the left arm of the structure was completely made of negative I_z regions while the right arm was consisted of the positive I_z in the northern part and negative I_z in the southern part. The connecting part of the arms in the 'A' was consisted of positive I_z. A comparison of the timings of the I_z-maps of the triggering region with GOES SXR evolution (Figure 3.11(a)) reveals that during the SXR precursor enhancement, in the northern tip of the structure (outlined by the oval shape in Figures 3.11(b)–(g)), I_z of opposite polarities became very close to each other (Figures 3.11(b) and (c)) which may be ideal for dissipation of current in the form of magnetic reconnection. With the evolution of the flare (Figures 3.11(c)–(g)), the closely situated regions with high-I_z at the tip of the 'A' significantly decayed and the left arm of the 'A' became fragmented (see region inside the box in Figures 3.11(b)–(g)). We further spotted another interesting feature in Figures 3.11(b)–(g) in the form of appearance and decay of a positive current region which are indicated by the black arrows.

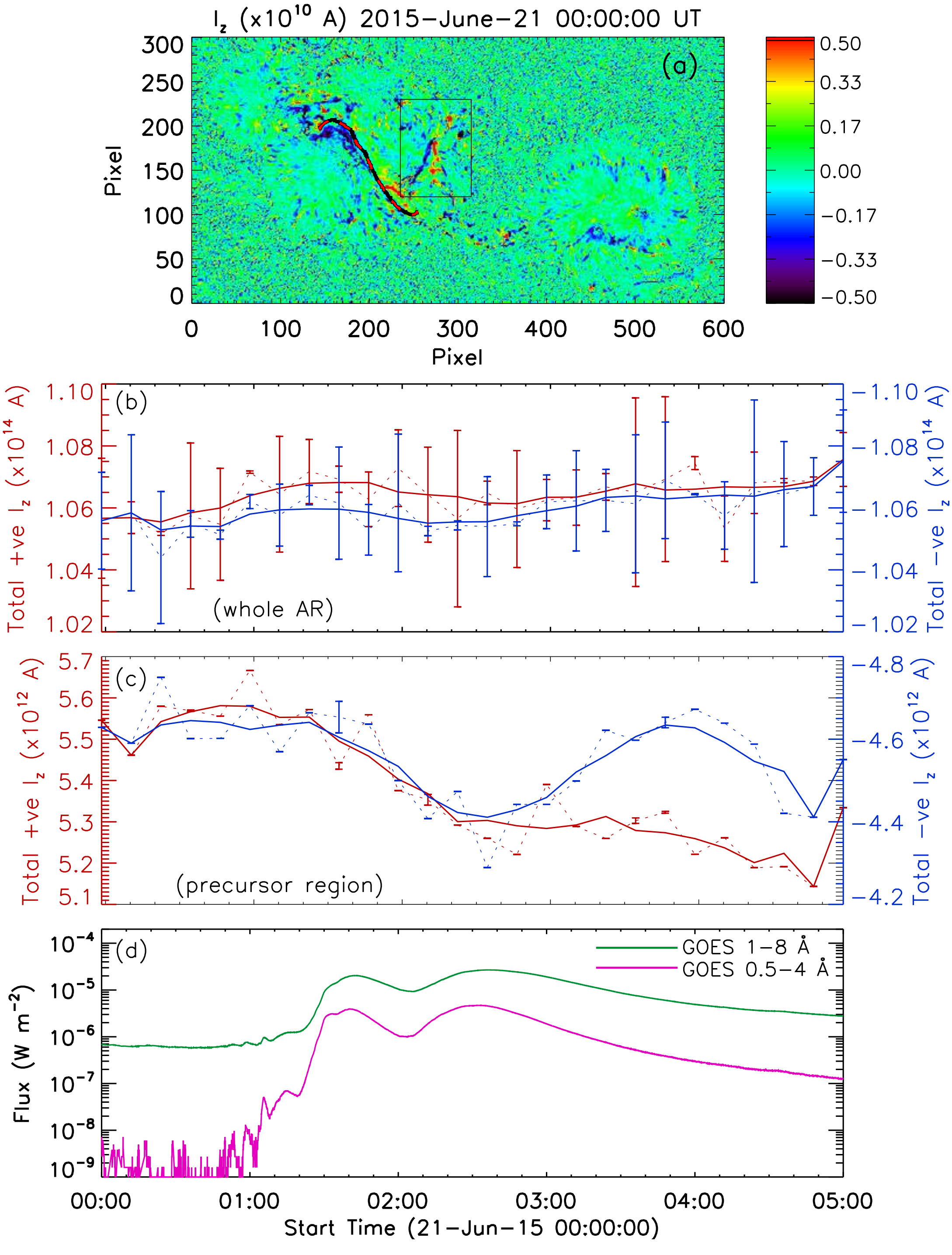

Figure 3.10: Panel (a): Distribution of longitudinal component of the photospheric current in NOAA 12371 on 21 June 2015 00:00 UT. The region associated with precursor brightening is enclosed by the box in panel (a). Note that, for better visualization, we have saturated the I_z values at $\pm 0.5 \times 10^{10}$ A in panel (a). The approximate location of the hot channel is indicated by the red-black dashed line in panel (a). In panel (b) and panel (c), we plot the variation of vertical component of photospheric current within the entire AR and within the box in panel (a), respectively. The vertical bars represent 1σ uncertainty in the calculation. For comparison, we have plotted the variation of GOES SXR channels in panel (d).

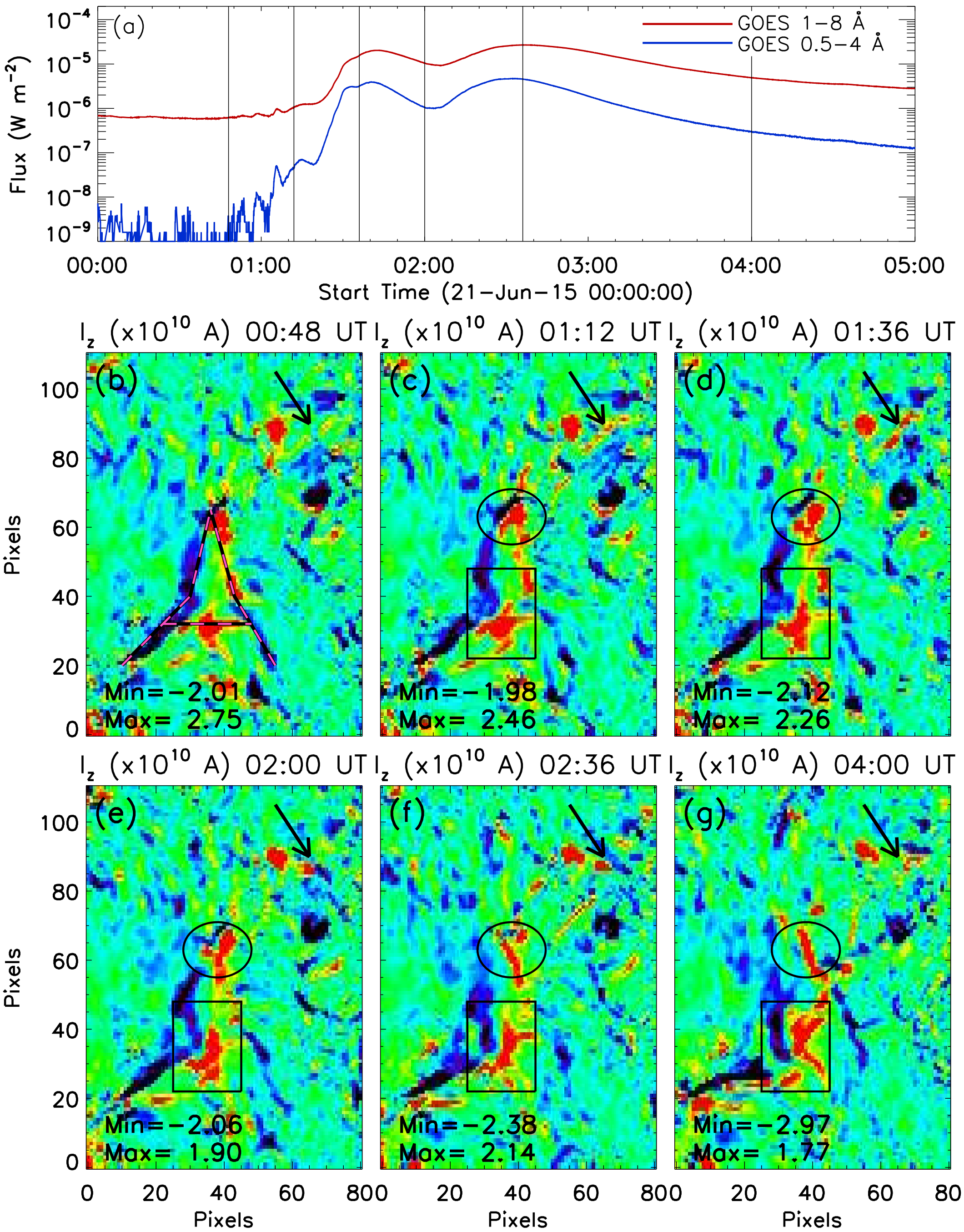

Figure 3.11: Panel (a): GOES SXR lightcurves showing the evolution of the M-class flare. In panels (b)–(g), we plot the distribution of vertical component of photospheric current over the region shown within the box in Figure 3.10a at six different times as indicated by the black lines in panel (a). Notably, on a whole, few regions of strong current of opposite polarity constitute a structure similar to the English letter 'A' which is outlined by the black-pink dashed lines in panel (b). We highlight few major changes in the distribution of current by the arrow, oval and box in panels (c)–(g). For better visualization, values of I_z are saturated at $\pm0.5\times10^{10}$ A. Maximum and minimum values of I_z with order of 10^{10} A within the selected FOV are indicated in each of these panels.

3.2.7 Non-linear Force Free Field (NLFFF) extrapolation results

Modeled coronal magnetic configuration

In order to understand the coronal connectivities between the photospheric magnetic polarities of the AR, we performed NLFFF extrapolation based on an optimization technique (see Section 2.3.2). For the purpose, we selected an HMI magnetogram at 01:00 UT on 21 June 2015 which represents the photospheric configuration prior to the onset of eruption (Figure 3.12(a)). The following values of the free parameters (see Chapter 2.3.2) were used for the extrapolation:

$\nu = 0.01$; $w_{los} = 1$; $w_{trans} = \frac{B_{trans}}{max(B_{trans})}$;

$\mu_1 = \mu_2 = 1$; $\mu_3 = 0.001$; $\mu_4 = 0.01$

The residual errors were obtained as

$< |f_i| >= 3.78 \times 10{-}4$; $\theta_J = 7.22°$.

The NLFFF-modeled coronal configuration readily revealed the presence of an extended flux rope over the PIL (shown by sky-colored lines in Figures 3.12(b)–(d)) which was enveloped by a set of low-lying coronal loops (shown by blue lines in Figures 3.12(b)–(d)) connecting the opposite polarity regions of the trailing sunspot group. Importantly, the modeled flux rope is situated at the same location where the hot coronal channel was identified in the AIA images (cf. Figure 3.12(b) and 3.6(a), (b)). The coronal configuration associated with the remote region of precursor brightening is manifested by the pink lines in Figure 3.12. We further identified a second set of closed field lines (shown by the yellow lines) connecting the opposite polarity regions in the trailing sunspot group, a part of which were situated at a very close proximity to the pink lines (see Figure 3.12(c)). Notably, the anti-clockwise motion of the brightening from the precursor location, clearly revealed by the time-slice diagram shown in Figure 3.7(a), matches reasonably well with the footpoints of the yellow lines. We also note that, a few of the yellow and pink lines displayed a drastic change in the field-line linkage. In literature, such structures are termed as quasi-separatrix layers (QSLs) and are characterized by high squashing factor (Q; see, Priest & Démoulin, 1995). The Q value of this region is found to be higher than 10^9 (shown by the neon-green colored patch and the black arrow in Figure 3.12(c)).

To have a further insight of the anti-clockwise motion of the brightening prior to the eruption of the hot channel, we show the photospheric regions with a Q value greater than 10^7 by red color in Figures 3.12(b)–(e). We find that, the footpoints of the yellow lines perfectly match with regions of high Q values (Figure 3.12(c)) which implies that the anti-clockwise motion of brightening from the precursor location was a slipping reconnection (see e.g., Démoulin et al., 1997; Craig & Effenberger, 2014; Janvier et al., 2016).

From the coronal connectvities in the whole AR, shown from the top and side views in Figures 3.12(d) and (e), respectively, we readily note the presence of a set of relatively large-scale coronal loops that connected the positive regions of the trailing sunspot group to the leading negative sunspot group (shown by green lines in Figure 3.12(d)–(e)). Further, a part of the green lines originating at the positive polarity region terminated at the adjacent negative polarity region of the same sunspot group. Notably, these two sets of green lines constituted a second QSL characterized by $\log(Q) > 8$ within the AR (indicated by a black arrow and the blue colored patch in Figure 3.12(d)). Interestingly, Jing et al. (2017) reported the occurrence of a large-scale slipping reconnection on 22 June 2015 from the same region of the second QSL. This implies that despite producing the eruption of a halo CME associated with a complex M-class flare on 21 June 2015, the large-scale magnetic structure of NOAA 12371 remained mostly preserved on the next day.

Evolution of Magnetic Free Energy

The magnetic free energy (E_F) associated with an AR is considered as an important factor in order to understand the energy budget of the flares originated from that AR. E_F can be estimated by the formula:

$$E_\mathrm{F} = E_\mathrm{N} - E_\mathrm{P} = \int_v \frac{{B_\mathrm{N}}^2}{8\pi} \mathrm{d}v - \int_v \frac{{B_\mathrm{P}}^2}{8\pi} \mathrm{d}v \tag{3.2}$$

where E_N and E_P are non-potential energy and potential energy, respectively. In this work, we calculated magnetic energy by employing the magnetic virial theorem (Klimchuk et al., 1992). According to this theorem, the magnetic energy stored in a coronal force-free magnetic field is given by the surface integral at the

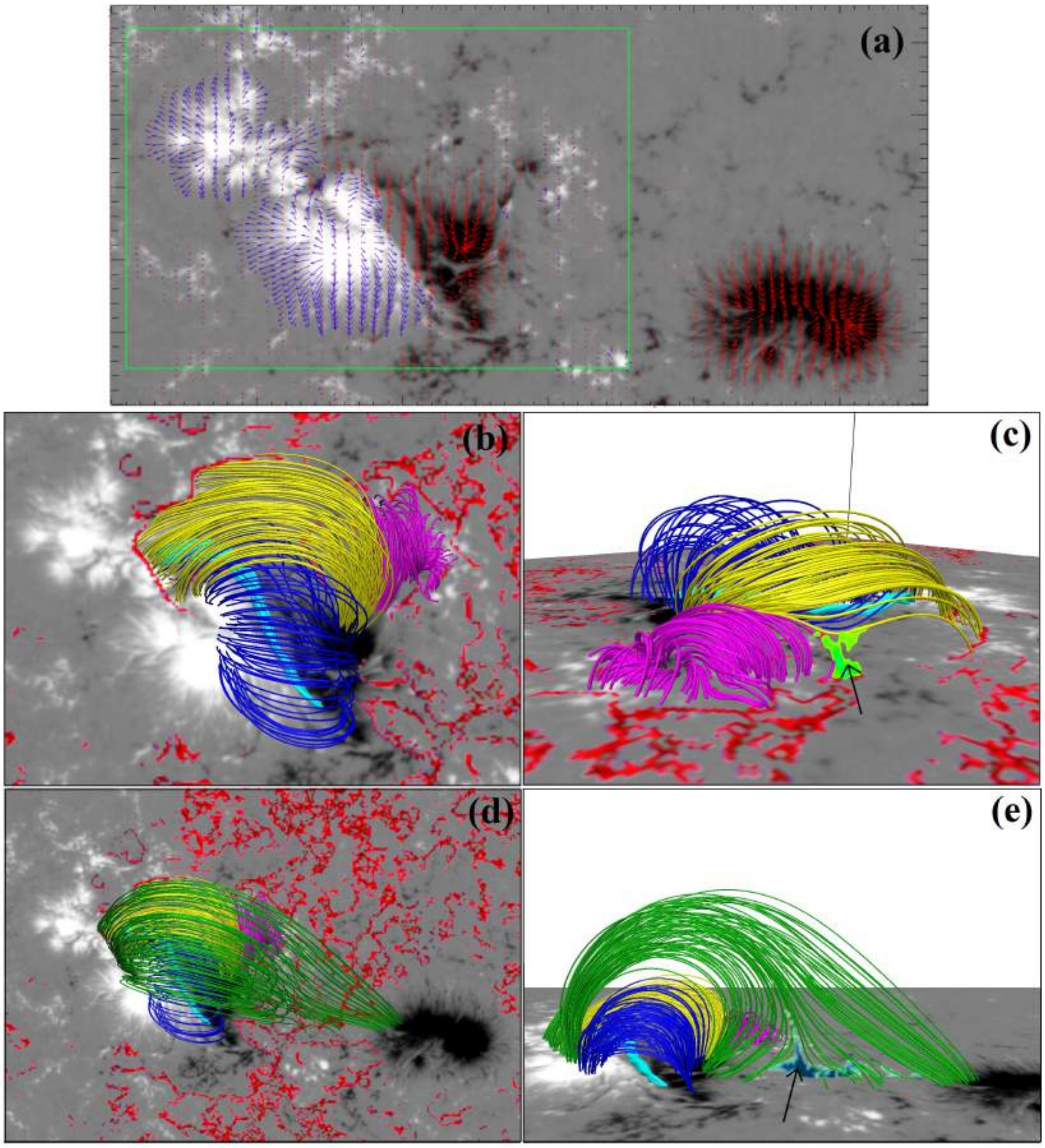

Figure 3.12: Panel (a): CEA projected vertical component (B_z) of the HMI vector magnetogram of NOAA 12371 at 01:00 UT on 21 June 2015. Blue and red arrows over the magnetogram indicate the horizontal component of magnetic field associated with positive and negative (B_z), respectively. Panels (b)–(e): Modeled coronal magnetic configuration based on the NLFFF extrapolation results of the vector magnetogram shown in panel (a). Different sets of NLFFF field lines associated with the trailing sunspot group, i.e., within the green box in panel (a), from top and side views, are shown in panels (b) and (c), respectively. The neon-green colored region (also marked by the black arrow) indicate regions characterized by $\log(Q) > 9$. In panels (d) and (e), we show the top and side view of the model lines in the whole FOV as in panel (a). The blue regions (also marked by the black arrow) in panel (d) indicate a region possessing high Q value ($\log(Q) > 8$). The background white boundary behind the green lines in panel (d) direct to the north. In all the panels, photospheric regions shown by red color are characterized by $\log(Q) > 7$.

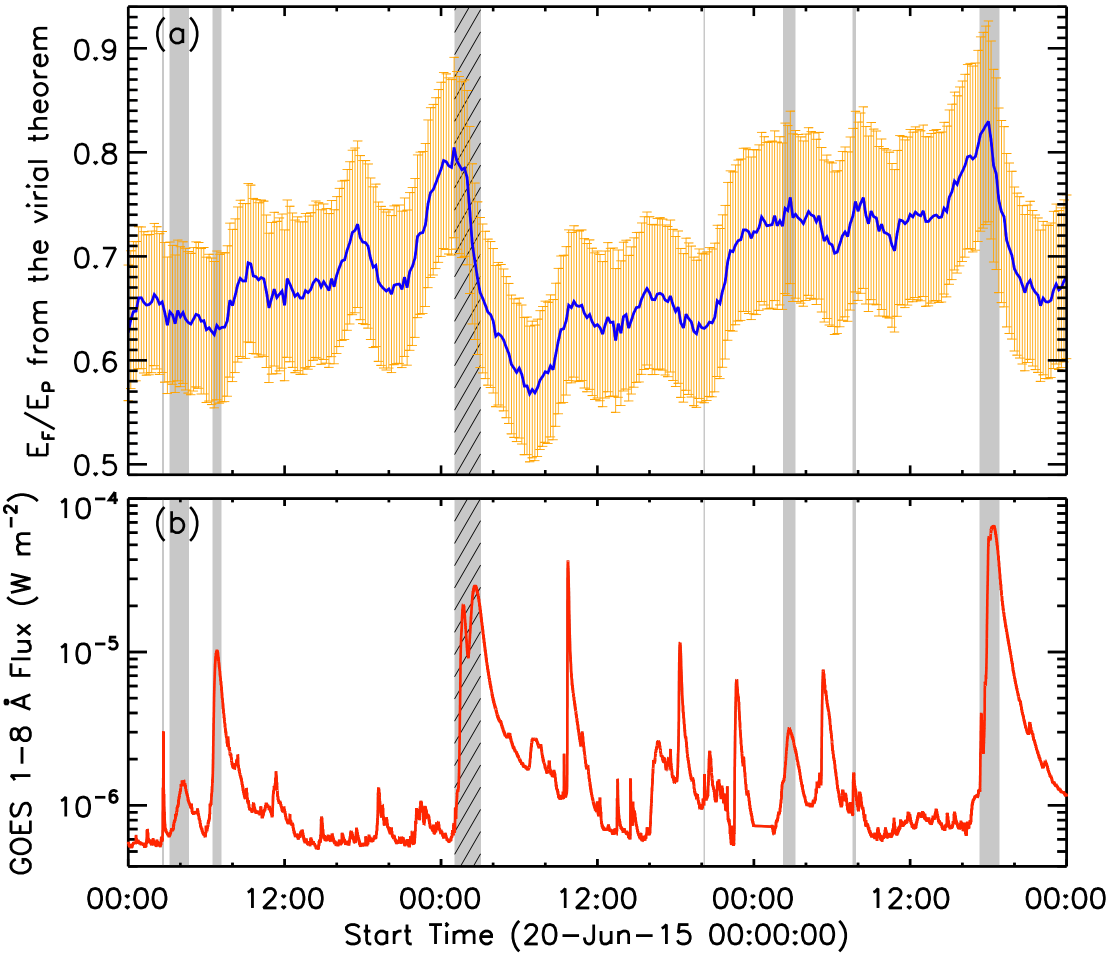

Figure 3.13: Panel (a): Evolution of magnetic free energy during 20–22 June, 2015, calculated by virial theorem. 1σ error in the calculation of free energy is plotted by yellow bars. For comparison, GOES 1–8 Å SXR flux variation is plotted in panel (b). The shaded intervals represent the durations of C-, and M-class flares originated from NOAA 12371. The striped dashed interval indicates the duration of the flare.

photospheric boundary involving the three vector magnetic field components, i.e.,

$$E = \frac{1}{4\pi} \int_{z=0} (xB_{\rm x} + yB_{\rm y}) B_{\rm z} {\rm d}x{\rm d}y \tag{3.3}$$

where $B_{\rm x}$, $B_{\rm y}$, and $B_{\rm z}$ are the x-, y-, and z-components of the photospheric magnetic field, respectively. Here, the three components of photospheric vector magnetic field were obtained from the 'hmi.sharp_cea_720s' series of HMI/SDO. The magnetograms were then pre-processed as described in Section 2.3.2 and the references therein. The evolution of the free magnetic energy stored in NOAA 12371 normalized by the corresponding potential energy during the most active phase of NOAA 12371 (i.e., 20-22 June, 2015) is shown in Figure 3.13(a). For reference, we have also plotted the GOES 1–8 Å SXR flux variation during the whole period in Figure 3.13(b). Notably, in this duration, the AR produced three M-class flares: class M1.0 on 20 June, class M2.6 on 21 June and class M6.5 on 22 June. From these figures, we find that prior to the M2.6 and M6.5 class flares, magnetic free energy accumulated in NOAA 12371 was over 80% of the corresponding potential energy, which significantly decreased after the flares and reached local minima at ≈57% and ≈65% of the corresponding potential energies, respectively. Interestingly, we observed no significant change in magnetic free energy before and after the M-class flare on 20 June.

3.2.8 Discussion

In this work, we carried out a multi-wavelength analysis of the flux rope eruption on 21 June 2015 from NOAA 12371 with a particular emphasis on the pre-flare period and their role on triggering the eruption. Although the automated catalog of GOES flares[1] has enrolled two flares on 21 June 2015, the evolution of the AR from the hot channel to the formation of large post-flare arcade during the two GOES peaks clearly suggests the GOES flaring events as a single flux rope eruption, i.e., a dual-peaked long duration flare.

The temporal evolution of the GOES SXR flux readily reveals that the flare was associated with two-stage precursor emission. Comparison of GOES SXR fluxes with AIA observations confirms that both the episodes of the pre-flare subtle flux enhancements were caused by localized brightenings occurring from a nearby region situated to the west of the hot channel (Figures 3.6, 3.8 and 3.9). These localized brightenings suggests energy release at small-scale within the same AR that can provide potential trigger for eruption by destabilizing a stable flux rope (Fárník et al., 1996; Fárník & Savy, 1998; Warren & Warshall, 2001; Fárník et al., 2003; Sterling & Moore, 2005; Chifor et al., 2007; Kim et al., 2008; Liu et al., 2009; Joshi et al., 2011, 2016a, 2017a; Dhara et al., 2017; Woods et al., 2018; Hernandez-Perez et al., 2019b; Mitra & Joshi, 2019). In view of the location of the pre-flare energy release, being within the spatial extension of the AR but clearly separated from the hot channel (i.e., the flux rope), the present case is a good example of adjacent

[1]https://www.swpc.noaa.gov/products/solar-and-geophysical-activity-summary

pre-flare activity. Further, the temporal and spatial evolution of the event suggests that pre-flare emission essentially acted as the precursor to the main eruption.

An important aspect of this study is to investigate the origin of the pre-flare activities and their spatial relation with the eruption of the flux rope. Modeled coronal configuration (Figure 3.12) suggests that the triggering region, (i.e., the region of precursor activity) was characterized by highly sheared small-scale coronal magnetic loops (pink lines in Figure 3.12). Small scale electric currents are generated on the photosphere within the region of sheared magnetic field, which can lead to the onset of solar flares (Zhang & Low, 2005). Tan et al. (2006) carried out an investigation of the evolution of photospheric currents during two M-class flares occurring from two different ARs. They found that although both the ARs were subjected to rapid flux emergence, the two flares differed significantly in the evolution of photospheric longitudinal current. Their analysis revealed that, during one flare the longitudinal electric current density dropped rapidly; while it increased during the other flare. This result led them to conclude that rapid emergence of current carrying flux may be responsible for the increasing longitudinal current while decrease of electric current can be resulted by dissipation of magnetic free energy. Our analysis suggests that in the triggering location, a few localized regions with high values of vertical component of photospheric electric current with opposite polarities were situated very close to each other (Figure 3.11). One particular set of such regions with opposite polarity longitudinal current became adjacent to each other (within the oval in Figures 3.11(b), (c)) during one pre-flare SXR enhancement, implying that the initial reconnection most likely occurred from this location. Once the reconnection began, it induced further reconnection events in the nearby stressed magnetic field lines of the region resulting in the enhancement of plasma temperature. Reconnection events at the pre-flare location most likely induced a slipping reconnection in the yellow field lines (Figure 3.12) carrying energy from the precursor location to the northern leg of the hot channel leading to its destabilization. The entire mechanism suggested here is analogous to the domino effect that involve a sequence of destabilizing processes that eventually cause a large-scale eruption (Zuccarello, F. et al., 2009).

Evolution of magnetic flux suggests that the AR experienced significant flux emergence for ≈10 hrs and cancellation thereafter for ≈2 hrs prior to the onset of the flare (Figures 3.1(c)–(d)). Notably, in the entire duration, the AR did not produce any flaring activity (cf. Figures 3.1(c), (d) and (e)) suggesting the emergence of magnetic flux in the trailing sunspot region and the subsequent phase of its decay prior to the onset of the flare possibly resulted in the build up of the flux rope along the PIL. This result is supportive of the flux cancellation model proposed by van Ballegooijen & Martens (1989) which states that flux cancellation at the PIL of a sheared magnetic arcade leads to the formation of flux ropes. The build up of the flux rope over the PIL in the trailing sunspot group of NOAA 12371 prior to the M-class flare on 21 June 2015 was observationally inferred by continuous brightening up of the hot channel as observed in AIA 94 Å channel images (Figure 3.6(a)–(c)). Our analysis suggests that the hot channel continued to acquire the magnetic field and stress in response to the flux cancellation for an extended period of time during the pre-flare phase. As a result, the flux rope had already reached to a meta-stable state prior to the onset of the flare which allowed immediate eruption of it once triggered by the slipping reconnection. This type triggering can be explained by the "tether-weakening" model proposed by Moore & Roumeliotis (1992). According to this model, a meta-stable flux rope can be triggered by activities occurring adjacent to it, i.e., off the main PIL (see e.g., Sterling et al., 2007; Yang & Chen, 2019).

3.3 Triggering and evolution of eruptive X-class flaring activity in NOAA 11875

In order to understand how the eruption characteristics of flux ropes are influenced by pre-flare activities, we carried out a multi-wavelength observation of a flux rope eruption leading to the formation of a halo CME, associated with an X1.0 flare. Notably, the flare was preceded by a couple of distinct pre-flare periods of SXR flux enhancements. We further observed a period of mild SXR flux enhancement immediately prior to the start of the impulsive energy release during the X1.0 flare, a characteristic of the 'precursor phase' (Zhang & Dere, 2006).

3.3.1 Overview of NOAA 11875

The eruptive flare under study occurred from NOAA 11875. The AR emerged on the eastern limb of the Sun on 16 October 2013 as a $\beta\gamma$-type sunspot[2]. It gradually transformed into a more complex $\beta\gamma\delta$-type on 22 October and remained so until its remaining passage on the visible Sun till 30 October. In its lifetime, NOAA 11875 produced a total of 2 X-class, 11 M-class flare besides many C-class ones[3]. Notably, the eruptive X1.0 flare occurred on 28 October 2013 when the AR was situated close to the western limb of the Sun at the heliographic co-ordinates ~N07W66[4].

We analyzed the observation of NOAA 11875 on 28 October 2013 from 00:30 UT to 04:30 UT, during which the AR underwent activation and eruption of a hot channel in association with an X1.0 flare. In Figure 3.14, we present multi-wavelength view of the AR prior to the erupting event. The photospheric HMI white light image suggests that the AR was consisted of a major leading sunspot and few trailing spots of much smaller sizes (Figure 3.14(a)). Comparison of a co-temporal HMI LOS magnetogram (Figure 3.14(b)) with the while light image indicates that the major leading sunspot had a complex fine structure with multiple umbrae of opposite polarity within a common penumbra i.e., δ-spots while the trailing spots were mostly of positive polarity. AIA 171 Å image gives information about the coronal connectivities associated with the AR. Interestingly, we find a filament structure in the AR (indicated by the brown arrow in Figure 3.14(c)) and a set of open field lines originating from the trailing part of the AR (marked by the black arrows in Figure 3.14(c)). AIA 94 Å image indicates a hot coronal channel near the filament (indicated by the red arrow in Figure 3.14(d)) which forms the core of the AR. Notably, comparison of AIA 171 and 94 Å images also indicate that the region of open field lines was also connected with the core of the AR (containing the filament) by a set of hot coronal loops.

[2] www.helioviewer.org
[3] http://www.lmsal.com/solarsoft/latest_events_archive.html
[4] https://www.solarmonitor.org/index.php?date=20131028&region=11875

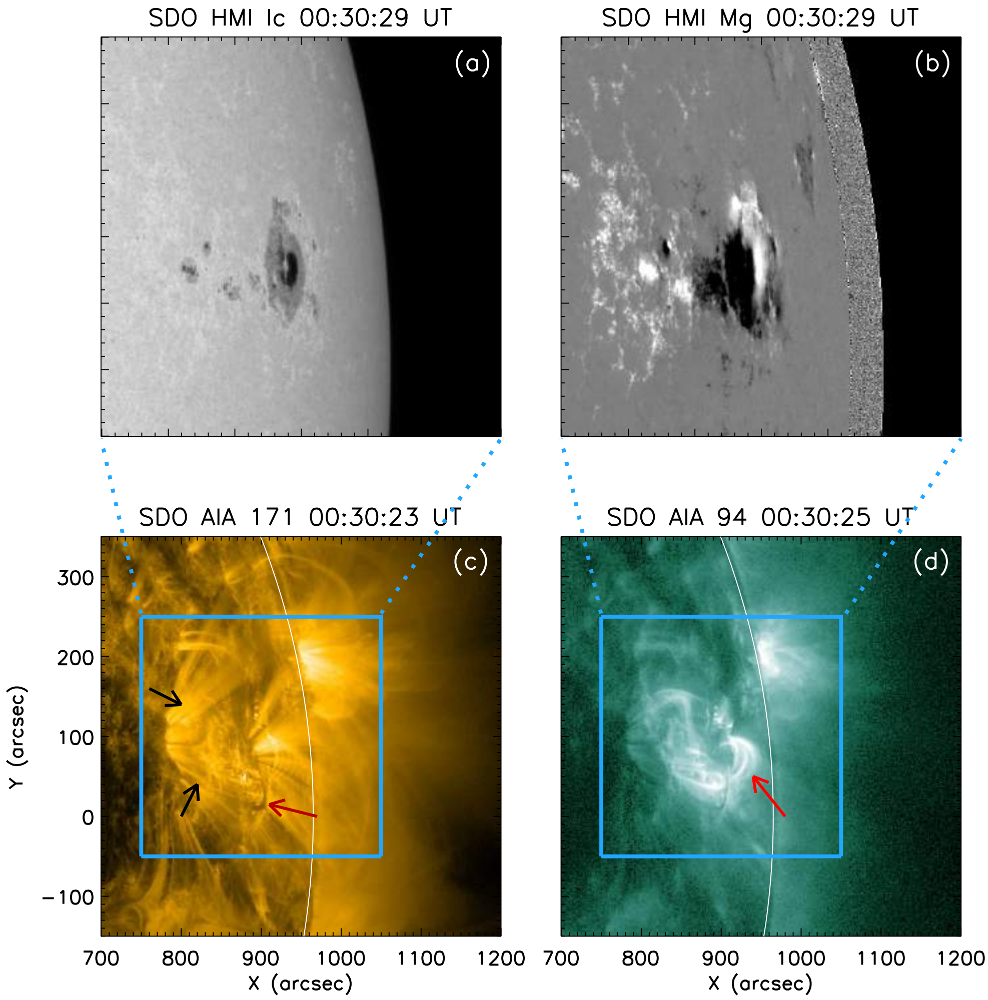

Figure 3.14: Panel (a): HMI white light image of the active region NOAA 11875 prior to the eruptive flare. Panel (b): Co-temporal HMI LOS magnetogram of NOAA 11875. Panels (c)–(d): AIA EUV images of the AR in 171 Å and 94 Å , respectively. FOV of panels (a) and (b) is indicated by the sky colored boxes in panels (c) and (d). The black arrows in panel (c) indicate few open coronal lines. The brown arrow indicate the filament during the pre-flare phase. The red arrow in panel (d) indicate the hot coronal loops near the filament.

3.3.2 Evolutionary phases of the X1.0 flare

We have shown the time variation of the GOES SXR flux in 1–8 Å and 0.5–4 Å channels within our studied interval in Figure 3.15(a). Based on the time variation, the overall evolution of the X1.0 flare can readily be summarized by three distinct phases: a pre-flare phase characterized by two temporally well separated episodes of SXR flux enhancement with peaks ‘P1’ and ‘P2’ (indicated by the two dotted lines in Figure 3.15(a)), a precursor phase when the XSR flux increased gradually and the X1.0 flare including the impulsive and gradual phases. According to GOES, the onset of the impulsive phase of the X1.0 flare occurred at ≈01:53 UT.

Table 3.2: Summary of the evolutionary phases of the eruptive X1.0 flare

Sr. No.	Phase	Interval	Remarks
1	Pre-flare	00:45 UT– 01:37 UT	Two peaks were observed in the GOES SXR flux at ≈00:59 UT ('P1') and ≈01:30 UT ('P2').
2	Precursor	01:37 UT– 01:53 UT	Activation of the hot coronal channel began and it underwent a slow rise.
3	Impulsive	01:53 UT– 02:02 UT	The eruption of the hot channel experienced rapid acceleration; multiple X-ray sources were observed from footpoint and looptop locations.
4	Gradual	02:02 UT– 02:58 UT	Dense post-flare arcade was formed.

After a period of rapid enhancement of flux in both the GOES X-ray channels, lasting for ≈9 min, the flare reached at its peak flux at ≈02:02 UT which was followed by a slow decrease of SXR flux in both the GOES channels, i.e., the flare moved into the gradual phase. A summary of different evolutionary phases of the X1.0 flare is given in Table 3.2.

Our observation revealed that a complex structure situated close to the northern leg of the hot coronal channel (shown inside the boxes in Figures 3.15(b)–(d)) brightened up during the first pre-flare event (i.e., P1). Notably, activity from this region was clearly captured in both high and low temperature AIA passband filter images (highlighted by the boxes in Figures 3.15(b)–(d)). Interestingly, during the second pre-flare event (P2), we observed intensified brightness from a compact loop system from the trailing part of the AR (shown inside the white boxes in Figures 3.15(e)–(g)), i.e., location of energy release during the two pre-flare SXR enhancements were completely different, although both the locations resided within the overall extent of the AR. It is noteworthy that AIA 304 Å images during the P_2 event revealed two ribbon-like brightening (shown within the box in Figure 3.15(g)), co-spatial to the loop-like brightening, suggesting emission from the footpoints of the hot loops. The precursor phase of the flare was characterized by the activation and slow rise of the hot channel (Figures 3.15(h)–(j)). The hot channel completely erupted during the X1.0 flare which is indicated by white arrows in Figures 3.15(k) and (l).

Figure 3.16 shows the temporal evolution of AIA (E)UV intensities (Figure

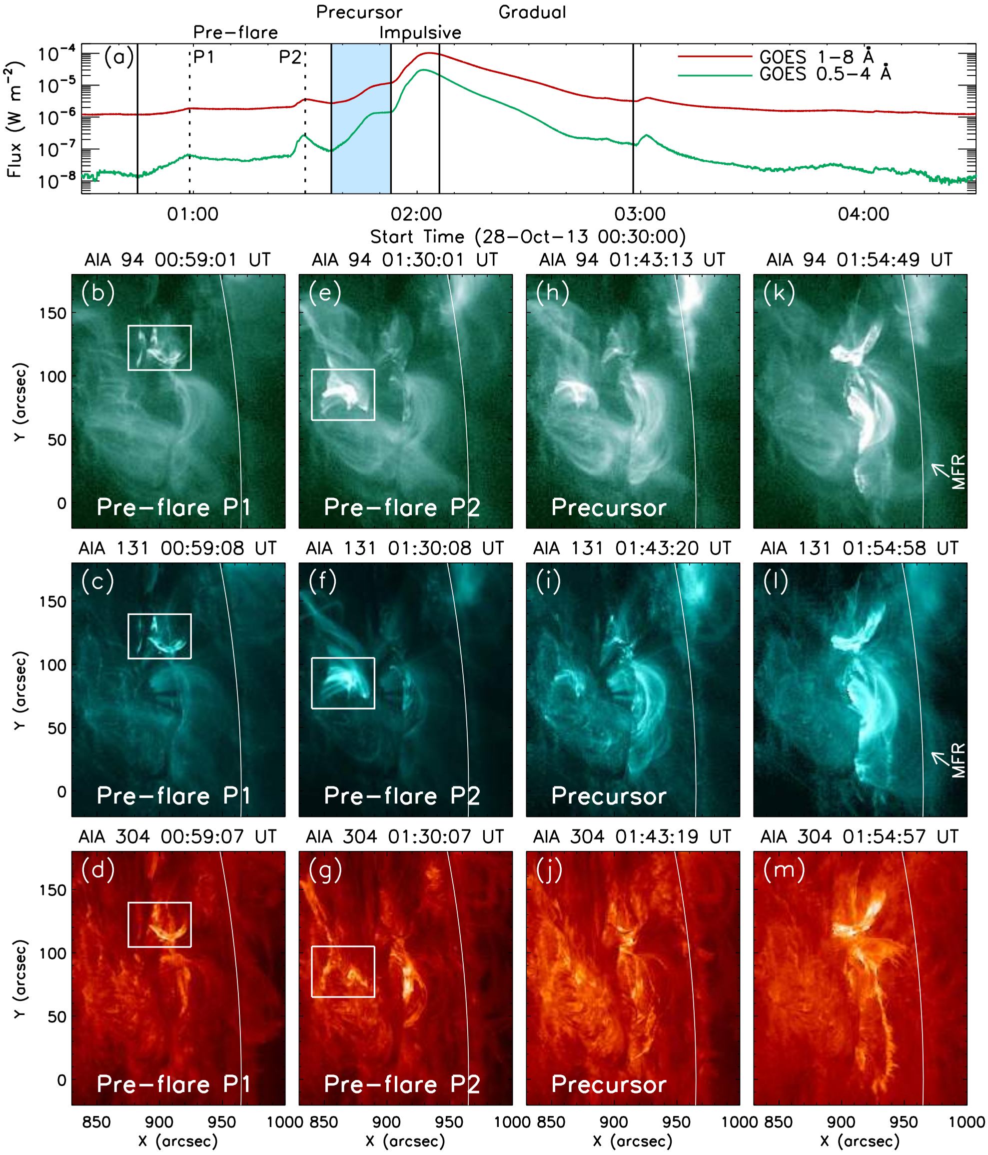

Figure 3.15: Panel (a): GOES SXR flux variation in 1–8 Å (red curve) and 0.5–4 Å (green curve) channels on 2013 October 28 from 00:30 UT to 04:30 UT that includes different phases prior to and during the X1.0 flare. The pre-flare phase was characterized by two episodes of SXR flux enhancements with peaks 'P1' and 'P2' which are indicated by the dashed lines. The sky colored shaded area indicates the precursor phase when the activation of the hot channel (i.e., flux rope) began and it underwent a slow-rise phase. Panels (b)–(m): AIA EUV images of the active region NOAA 11875 in 94 Å (panels (b), (e), (h), (k)), 131 Å (panels (c), (f), (i), (l)), and 304 Å (panels (d), (g), (j), (m)). These representative images show various phases of the X1.0 flare: two pre-flare peaks P1 and P2 (panels (b)–(d) and (e)–(g), respectively); precursor phase (panels (h)–(j)), and the eruption of the hot channel during the impulsive phase of the X1.0 flare (panels (k)–(m)). The white boxes in panels (b)–(d) indicate pre-flare activity during P1 from a complex localized region adjacent to the northern leg of the hot channel. The white boxes in panels (e)–(g) indicate pre-flare activity during P2 from the trailing part of the AR. The white arrows in panels (k) and (l) indicate the erupting flux rope.

3.16(a)) and RHESSI X-ray counts (Figure 3.16(b)). For comparison, we have overplotted GOES SXR flux variation in both 1–8 Å and 0.5–4 Å channels in Figure 3.16(b). Comparison of multi-wavelength and multi-instrument lightcurves clearly indicates that the pre-flare event P1 was very prominent in RHESSI 3–6 keV and 6–12 keV channels. However, only the 304 Å channel among other AIA-(E)UV channels displayed a small peak during P1. RHESSI missed observation during ≈01:13 UT– 01:45 UT due to 'South Atlantic Anomaly' (SAA; Heirtzler, 2002), which included the pre-flare event P2. Notably, the AIA 94 Å and 304 Å lightcurves displayed a small increment during this period. We noted a general agreement between all the lightcurves during the main phase of the X1.0 flare. RHESSI time profiles underwent a sudden rise of HXR flux at ≈01:53 UT implying the onset of the impulsive phase of the X1.0 flare. The impulsive build up phase of the X1.0 flare was characterized by a very interesting phenomena in the RHESSI high energy channels of $\gtrsim$25 keV in the form of multiple short-lived spikes during ≈01:55 UT– 02:00 UT (see the green, yellow and violet lines in Figure 3.16(b)). Counts in the high energy channels of RHESSI ($\gtrsim$50 keV) decreased suddenly after ≈02:00 UT while counts in the low energy channels ($\lesssim$50 keV) underwent gradual decay (decay rate was faster for the 25–50 keV channel than the other channels).

Pre-flare phase

The two SXR pre-flare events (P1 and P2) were spatially and temporally well-separated from each other (Figure 3.15(a) and Section 3.3.2). In order have a better understanding of the locations and structural evolutions of pre-flare events, we look into AIA 94 Å images of the activity site (Figure 3.17). These images readily reveal that a small region situated at the north of the AR underwent a complex evolution during P1 (zoomed in images of the region are shown in the insets in Figures 3.17(b) and (c)). We observed strong RHESSI 6–12 keV sources residing at the same location during P1 (co-temporal RHESSI 6–12 keV contours are plotted in Figure 3.17(a) and in the inset in Figures 3.17(c)). During the P_2 event (i.e., ≈01:28 UT–≈01:40 UT), we observed moderately intense loop brightening from a nearby region situated to the east of the main flaring site (identified

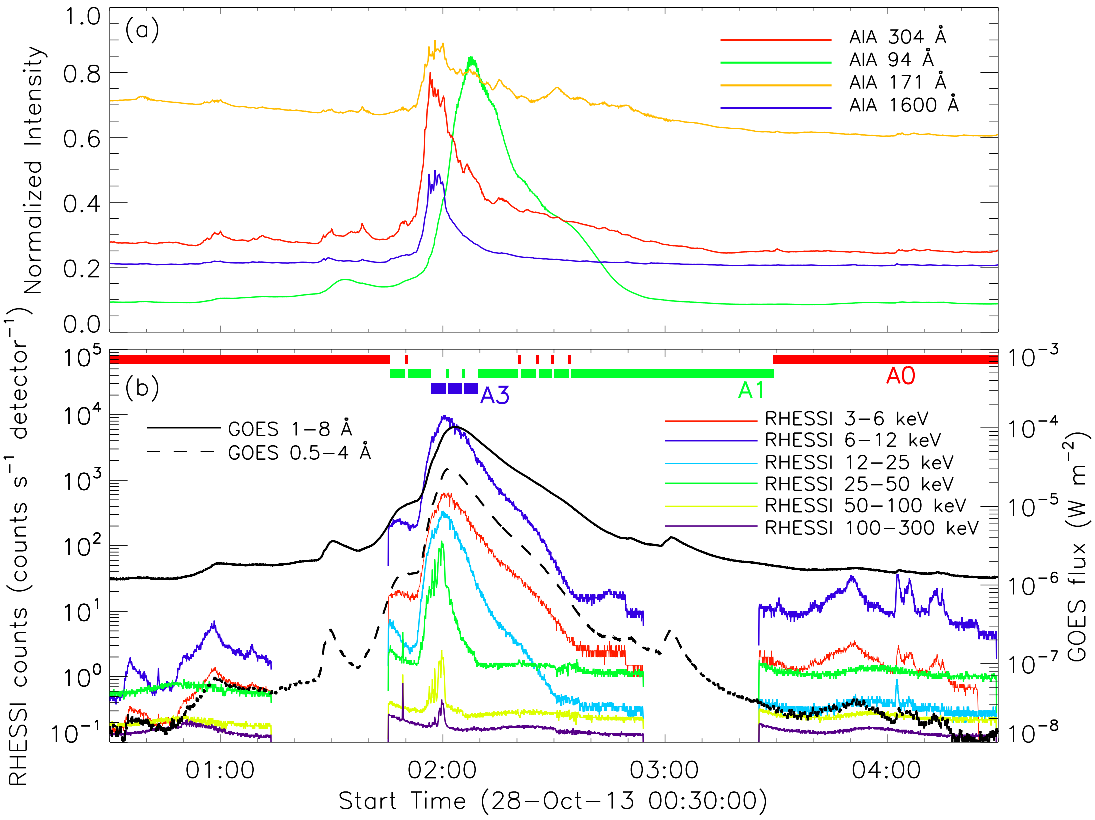

Figure 3.16: Panel (a): AIA lightcurves on 2013 October 28 during 00:30–04:30 UT normalized by the corresponding peak fluxes. For clear visualization, AIA lightcurves have been further normalized by 0.8, 0.85, 0.9, and 0.5 for 304 Å, 94 Å, 171 Å, and 1600 Å, respectively. Panel (b): Temporal evolution of RHESSI and GOES X-ray fluxes in the same interval as in panel (a). RHESSI did not observe during ≈01:14 UT– ≈01:45 UT and ≈02:54 UT– ≈03:25 UT. RHESSI fluxes have been normalized by factors of $\frac{1}{2}$, $\frac{1}{20}$, $\frac{1}{10}$, $\frac{1}{100}$, and $\frac{1}{500}$ for 3–6 keV, 12–25 keV, 25–50 keV, 50–100 keV, and 100-300 keV, respectively. The red, green, and blue bars at the top of panel (b) indicate RHESSI attenuator states A0, A1, and A3, respectively.

by the presence of the hot channel indicated by the arrow in Figure 3.17(a)) but within the AR (indicated by the arrows in Figures 3.17(d) and (e)). Comparison of GOES time profiles (Figure 3.15(a)) and AIA images (Figure 3.17) confirms the association of SXR pre-flare enhancements with localized energy release events within the AR. In Figure 3.17(f), we plot an AIA 94 Å image of the AR where the erupting hot channel can be identified clearly (indicated by the white arrow). The two dashed boxes in Figure 3.17 indicates the locations of the two pre-flare activities, which provides decisive evidence that the two pre-flare events prior to the X1.0 flare recorded by GOES occurred in the same AR but from two different

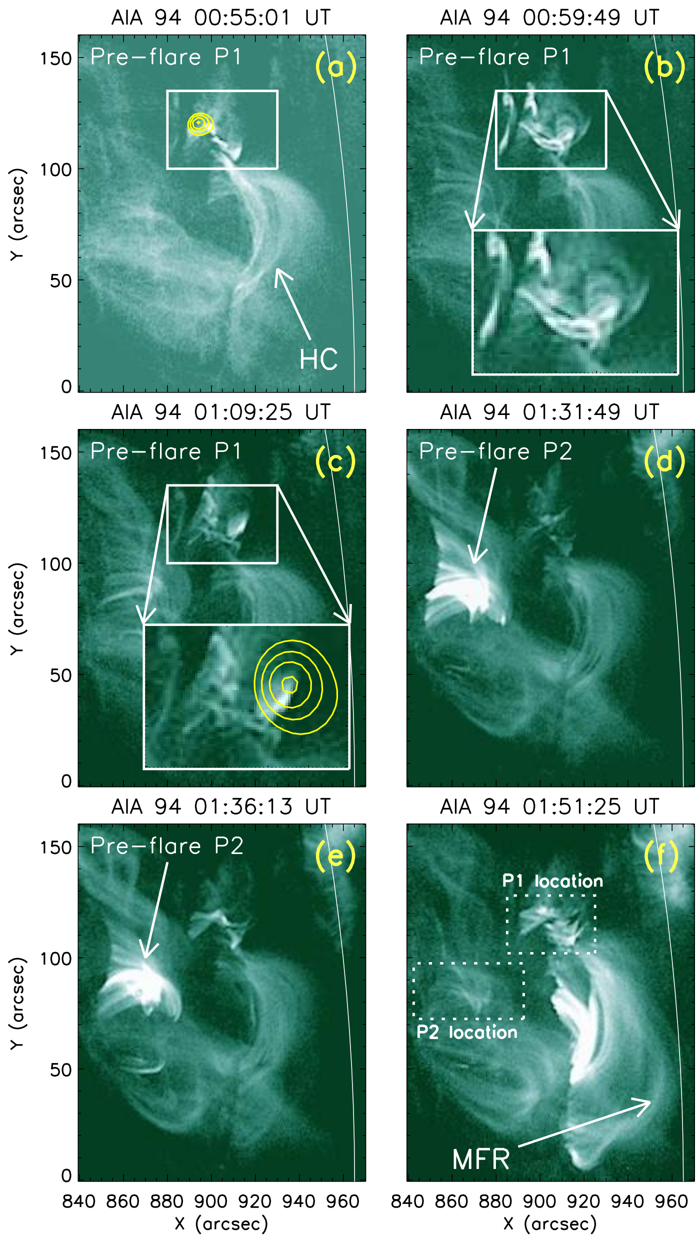

Figure 3.17: Panels (a)–(c): AIA 94 Å images showing evolution during the pre-flare event P1. During pre-flare event P1, activities were observed from a complex structure situated at the northern end of the hot channel which is outlined by the white boxes. Insets in panels (b) and (c) show zoomed in images of the region enclosed within the boxes. RHESSI observation was available during pre-flare event P1. In panel (a) and the inset in panel (c), we plot co-temporal RHESSI 6–12 keV contours. Contour levels are 35%, 50%, 70%, and 95% of the corresponding peak flux. Panels (d)–(e): AIA 94 Å images during the pre-flare event P2. Activities during P2 were observed in the form of loop brightening which is indicated by the white arrows. Panel (f): AIA 94 Å at ≈01:51 UT when flux rope eruption was very prominently observed in hot AIA pass band filters. The eruption of the magnetic flux rope is indicated by the arrow in panel (f). For comparison, the locations of pre-flare activities during the P1 and P2 are shown by the white boxes with dotted lines in this panel.

locations. It is worth mentioning that, while the location of pre-flare event P2 displayed activity only during P2, the location of pre-flare event P1 was associated with continuous small scale activity throughout the pre-flare phase, precursor phase, and even during the impulsive phase of the X1.0 flare.

Precursor phase

Following the two pre-flare events, we observed a phase during ≈01:37 UT to ≈01:53 UT characterized by a gradual rise of SXR flux in both the GOES channels when the hot channel underwent activation and exhibited a slow but steady expansion (Figure 3.15(a)). EUV images revealed that emission from the core field region, containing the activated hot channel significantly intensified during this phase (Figures 3.15(h)–(j)). The slowly accelerating hot channel was most prominently observed in the AIA images of hot 94 Å (Figures 3.18(b)–(d)) and 131 Å (Figures 3.19(a)–(d)) channels. This phase was further characterized by X-ray emission up to ≈50 keV from the hot core field region while the slowly rising hot channel steadily moved to larger heights (Figure 3.18(c)–(d) and Figure 3.19(b)–(d)). Further, the location of pre-flare event P1 consistently displayed activities including localized brightening and plasma ejection throughout the precursor phase (indicated by the yellow arrows in Figures 3.18(a), (c), and (d)). Notably, an intense 50–100 keV HXR source was observed from the location of P1 during the late precursor phase (Figure 3.18(d)) suggesting strong non-thermal emission from the location.

To further investigate the eruptive evolution of the hot channel, we specified a narrow slit along direction of its eruption (shown by the white line $\overline{S_1S_2}$ in Figure 3.20(a)) and plotted its time evolution between ≈01:35 UT–02:00 UT in Figure 3.20(b). The time-slice diagram reveals that initially the hot channel experienced a very gradual rise with a speed of ≈14 km s^{-1} up to ≈01:53 UT, which was followed by rapid acceleration (≈1.41 km s^{-2}) between ≈01:52 UT and 01:54 UT as the flare moved into the impulsive phase (the interval is marked by the two blue dotted lines in Figure 3.20(b)).

The X1.0 flare and eruption of the hot channel

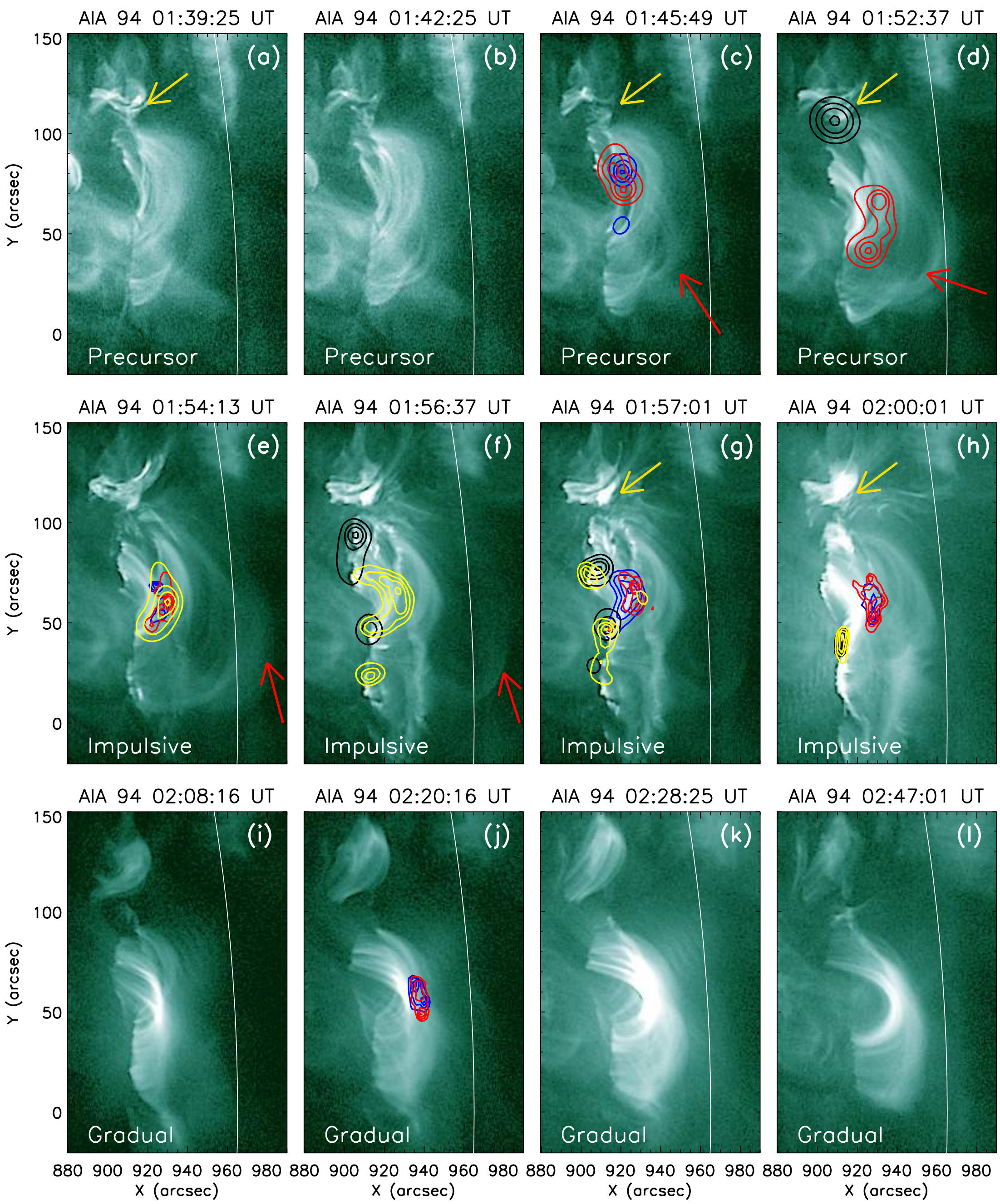

Figure 3.18: Representative AIA 94 Å images showing various evolutionary phases (precursor, impulsive, and gradual) during the X1.0 flare. The red arrows in panels (c)–(d) indicate the slow rise of the hot channel during the precursor phase which erupted during the subsequent impulsive phase of the X1.0 flare (indicated by the red arrows in panels (e) and (f)). From the location of pre-flare events 'P1' (cf. Figure 3.17(f)), we observed localized brightening and plasma ejection throughout the precursor and impulsive phase which is indicated by yellow arrows in panels (a), (c), (d), (g), and (h). Co-temporal RHESSI contours of 6–12 keV (blue), 12–25 keV (red), 25–50 keV (yellow), and 50–100 keV (black) energy bands are overplotted in selected panels. The contour levels are 30%, 50%, 70%, and 95% of the corresponding peak fluxes.

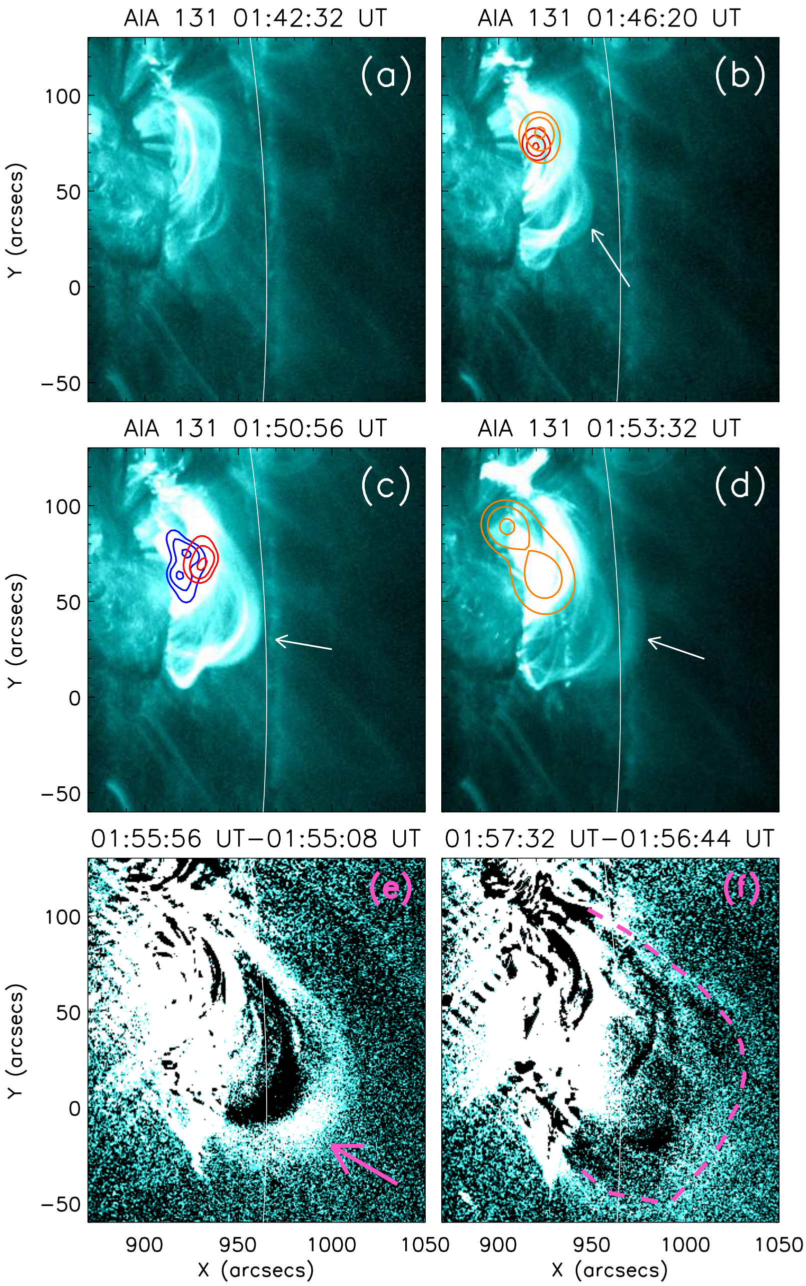

Figure 3.19: Representative AIA 131 Å direct (panels (a)–(d)) and running difference (panels (e)–(f)) images showing the hot channel eruption during the X1.0 flare. White arrows in panels (b)–(d) and pink arrow in panel (e) indicate the erupting the hot channel. In panel (f), the erupting hot channel has been outlined by a pink dashed curve. Co-temporal RHESSI contours of 6–12 keV (blue), 12–25 keV (red), and 25–50 keV (orange) energy bands are overplotted in panels (b)–(d). Contour levels are 50%, 70%, and 95% of the corresponding peak fluxes.

Onset of the impulsive phase of the X1.0 flare occurred at ≈01:53 UT (Figure 3.15(a)) when the slowly rising hot channel experienced a complete eruption (Figure 3.20(b)). Eruptive expansion of the hot channel led to the formation of post-reconnection arcade began underneath it, as explained in the CSHKP model. Co-temporal RHESSI images suggested intense HXR emission up to ≈50 keV energies from the apex of the post-reconnection arcade (Figures 3.18(e)–(h)). The impulsive phase of the X1.0 flare was further characterized by strong footpoint HXR sources up to ≈100 keV energies (Figure 3.18(f)–(h)). As the hot channel moved into higher coronal heights, its brightness steadily decreased and it slowly became indistinct in direct imaging after ≈01:56 UT (the erupting hot channel is indicated by red arrows in Figures 3.18(e)–(f)). However, we could track the erupting hot channel in AIA 131 Å running difference images till ≈01:57 UT (indicated by the pink arrow and pink dashed curve in Figures 3.19(e)–(f)), respectively). The flare moved into the gradual phase after ≈02:02 UT. During this phase, the post-flare arcade slowly increased in height and continued to emit hot, intense diffused emission (Figures 3.18(i)–(l)). RHESSI sources of energies up to 25 keV were observed from the top of the post-flare arcade (Figure 3.18(j)).

The time-slice diagram (Figure 3.20(b)) suggests that after undergoing a slow expansion during the precursor phase, the hot channel exhibited fast eruption with a linear speed of ≈183 km s^{-1} during the impulsive phase. The eruption of the hot channel resulted in a halo CME which was captured in the LASCO C2 and C3 coronagraph observations (Figure 3.21). The CME was first detected by LASCO C2 at 02:24 UT[5] when the leading edge of the CME reached a coronal height of ≈3.82 R$_\odot$. LASCO C3 observed the CME until 07:30 UT at ≈22.91 R$_\odot$. Within the field of view (FOV) of LASCO, the CME was propagating toward the position angle 296° with a linear speed of ≈695 km s^{-1} and a slow deceleration of 12.1 m s^{-2}.

3.3.3 RHESSI spectroscopy

To understand the HXR spectral evolution of the X1.0 flare during the impulsive phase, we carried out RHESSI spectroscopic analysis. For the purpose, we used energy bins of $\frac{1}{3}$ keV from 6 to 15 keV, 1 keV from 15 to 100 keV, and 5 keV from 100 to 300 keV energies. At the start of the impulsive phase of the X1.0 flare, the attenuator of RHESSI was set at A1 (i.e., thin shutter; Figure 3.16(b)). At ≈01:56

[5]https://cdaw.gsfc.nasa.gov/CME_list/UNIVERSAL/2013_10/yht/20131028.022405.w360h.v0695.p296g.yht

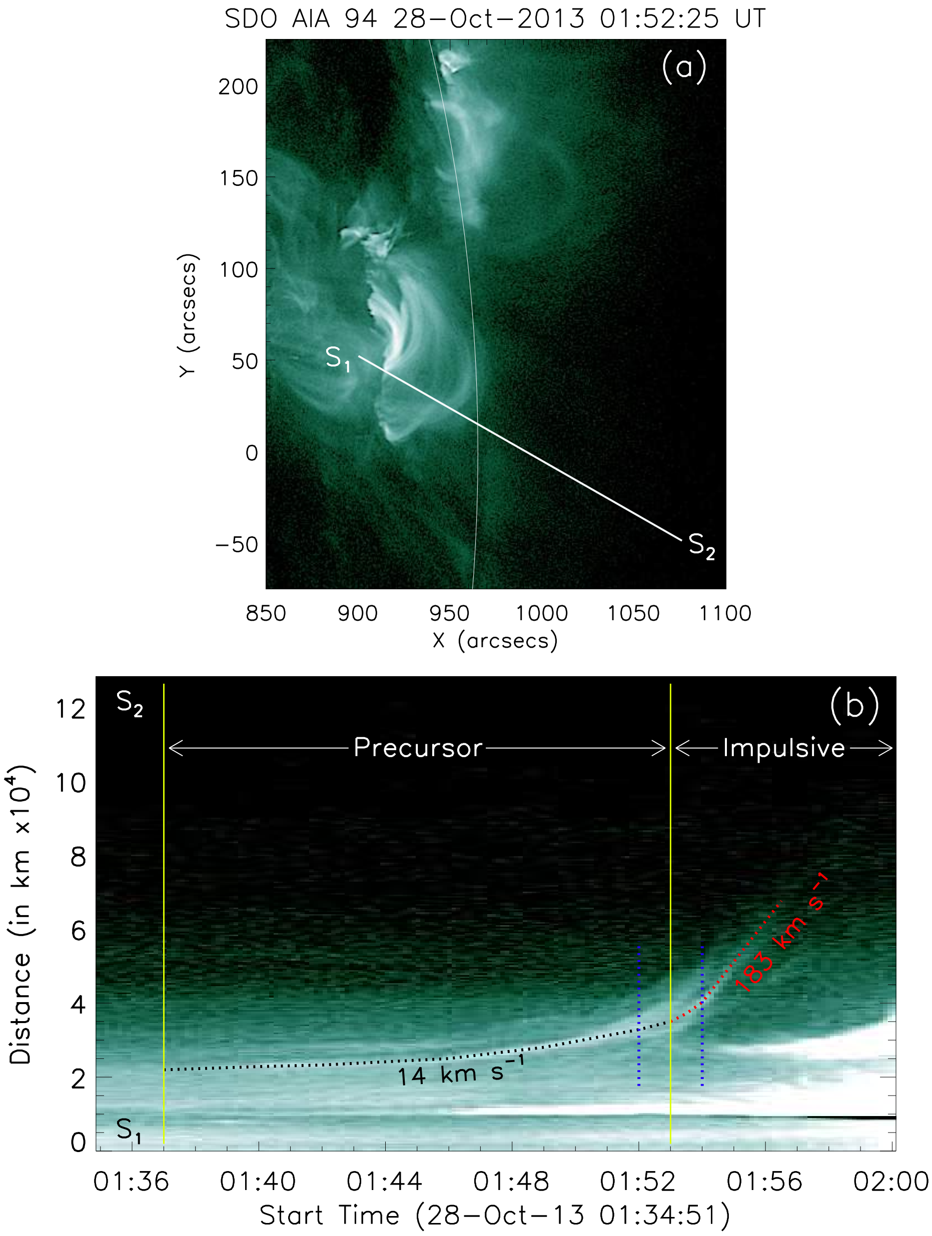

Figure 3.20: Panel (a): An AIA 94 Å image of NOAA 11875 during the precursor phase showing a straight line along which time-slice diagram was constructed. Panel (b): Time-slice diagram showing two phase acceleration of the erupting hot channel along the slit indicated in panel (a). 'S_1' and 'S_2' in panels (a) and (b) indicate the orientation of the slit in the time-slice diagram. The hot channel was found to be slowly elevating during the precursor phase of the flare (≈01:37 UT–01:53 UT) with a linear speed of ≈14 km s^{-1}. Afterwards, the flare entered into the impulsive phase (see Figure 3.15(a)) during which the hot channel underwent eruption with a linear speed of ≈183 km s^{-1}. Notably, the hot channel was subjected to a transition phase during ≈01:52 UT– 01:54 UT (indicated by the vertical blue dotted lines in panel (b)) when it moved continuously from the state of slow rise to eruptive expansion with a rapid acceleration of ≈1.41 km s^{-2}.

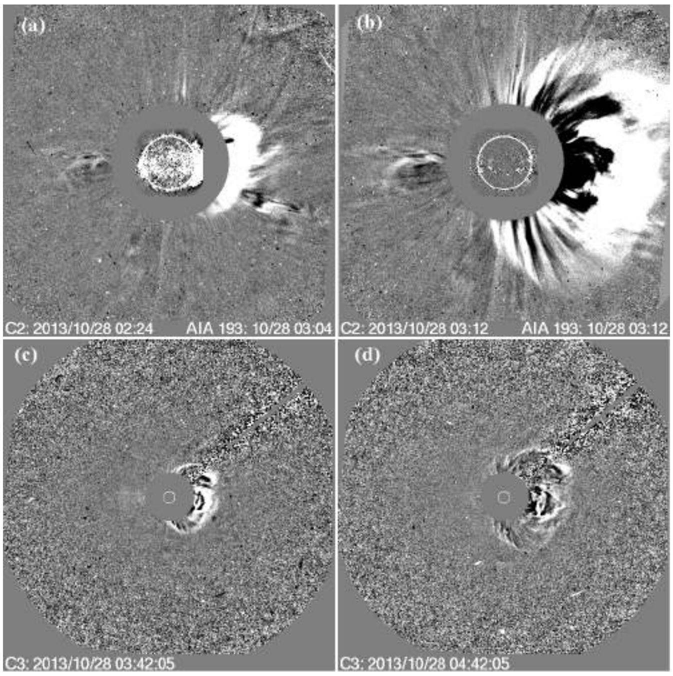

Figure 3.21: Running difference images obtained from LASCO C2 (panels (a), (b)) and C3 (panels (c), (d)) showing the propagation of the halo CME originated during the X1.0 flare from NOAA 11875. The linear speed of the CME calculated within the LASCO field of view is 695 km s^{-1}.

UT, the attenuator state was changes to A3 (i.e., both thin and thick shutters) and remained so until ≈02:09 UT except two short intervals of ∼1 minute (at ≈02:00 UT and ≈02:05 UT) when the attenuator state was changed to A1. After ≈02:09 UT, the attenuator state was changed to A1 as the flare had moved into the gradual phase. The time intervals for spectral analysis were chosen to be 20 s. Notably, RHESSI measurements during the impulsive phase of the X1.0 flare were contaminated by two periods of low energy radiation-belt particle events. To restrict the spectroscopic measurements from contamination due to the particle events, we confined our spectroscopic analysis between 01:57 and 02:01 UT. Spectral fits were obtained using a forward-fitting method implemented in the idl-based Object Spectral Executive code (OSPEX; Schwartz et al., 2002). For creating the spectrum, we used the combined RHESSI front detectors 1–9 excluding 2 and 7 (see Smith et al., 2002; Holman et al., 2011). Two fitting models were used: line emission from an isothermal plasma and thick-target bremsstrahlung from non-thermal electrons interacting with the chromosphere (Holman et al., 2003). From these fits, we derived the temperature (T) and emission measure (EM) of the hot flaring plasma, as well as the non-thermal electron spectral index (δ) for the non-thermal component and break energy (E_B) between the thermal and the non-thermal components.

In Figure 3.22, we show few spatially integrated, background-subtracted RHESSI

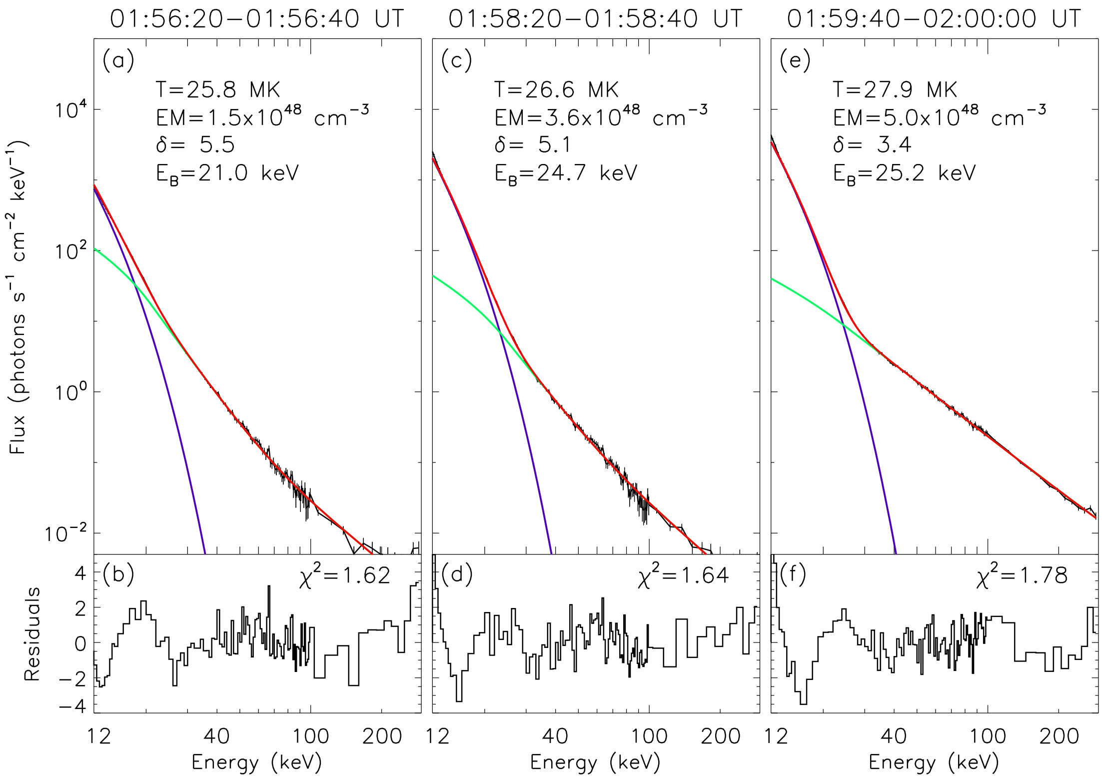

Figure 3.22: Representative RHESSI X-ray spectra during the impulsive phase of the X1.0 flare along with their respective residuals. These spectra were fitted with a combination of an isothermal component (blue line) and a thick-target bremsstrahlung model (green line). The red lines indicate the sum of the two components. The energy range chosen for fitting is [12–295] keV. The notations used in different panels are as follows: T: temperature obtained from the isothermal component, EM: emission measure, δ: power law index for the non-thermal fitting, E_B: break energy separating thermal energy from non-thermal energy, χ^2: goodness of the fitting.

spectra along with their respective fits and residuals for three selected intervals. We find that both temperature and emission measure increased during the impulsive phase and reached at ≈28 MK and $\approx 5 \times 10^{48}$ cm^{-3}, respectively, at the peak phase. At this time, as expected, with the evolution of the flare during the impulsive phase, the low energy cut-off (i.e., break energy E_B) increased progressively up to ≈25 keV. During the impulsive rise and peak of hard X-ray flux (Figures 3.22(c) and (e)), the hardness of non-thermal component increased highly with spectral index (δ) ≈3.4.

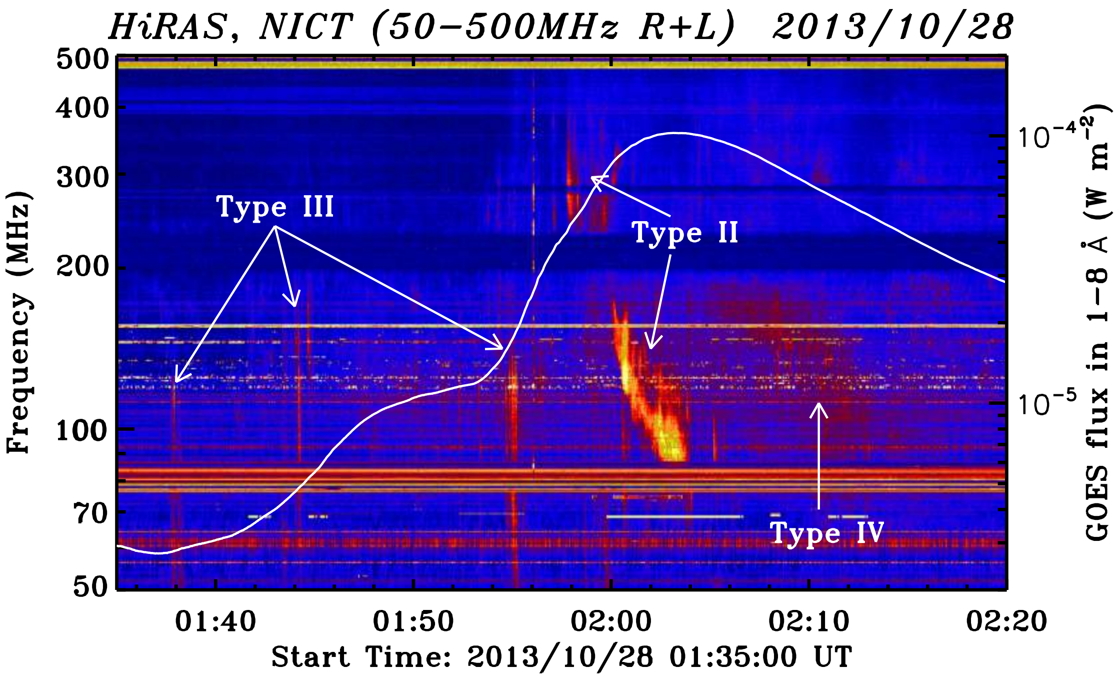

Figure 3.23: Dynamic radio spectrum recorded by the HiRAS spectrograph on 2013 October 28 from 01:35 UT– 02:20 UT within the frequency range 50–500 MHz, showing many discrete type III bursts between ≈01:37 UT–01:55 UT, a split-band harmonic of type II burst between ≈01:58 UT–02:04 UT and a faint type IV spectra during ≈02:05 UT–02:14 UT. For reference, we have overplotted GOES SXR flux variation in the 1–8 Å range by the white curve.

3.3.4 Dynamic radio spectrum

The impulsive phase of the X1.0 flare exhibited a spectacular display of different types of radio structures in the dynamic spectra (Figure 3.23). A series of type III bursts were recorded by HiRAS during ≈01:37 UT–01:55 UT followed by a split-band type II burst. Since, the AR was situated at the limb, it is likely that the observed split-band of type II was the harmonic as the fundamental part of type II bursts originated near solar limbs get severely attenuated (Gopalswamy, 2013). A brief brightening was recorded at ≈01:58 UT within frequency range ≈210–400 MHz. Observation within the frequency range ≈200–210 MHz was rejected throughout the interval by HiRAS. The type II burst was very clear between ≈02:00 UT–02:04 UT within the frequency range ≈75–180 MHz. However, from the apparent drift of the type II bands and dynamics of the erupting hot channel, it can be understood that the brief brightening within frequency range ≈210–400 MHz was an early extension of the type II. The type II burst was followed by a faint dynamic type IV signatures between ≈02:05 UT and 02:14 UT within the frequency range ≈70–180 MHz.

3.4 Discussion

In this work, we carried out a multi-wavelength analysis of different evolutionary phases of an X1.0 flare associated with the activation and eruption of a hot channel from NOAA 11875, with an aim to provide a detailed understanding of the activities during the pre-flare phase, a relatively less studied and ill-understood aspect of the overall flare evolution.

We thoroughly studied the prolonged pre-flare phase of a duration of ≈52 min (≈00:45 UT– ≈01:37 UT; Figure 3.16), which was characterized by two distinct SXR peaks, P1 and P2, occurred ≈38 min and ≈7 min, respectively, prior to the onset of the main flare. Comparison of GOES time profiles with AIA EUV images confirmed that both the pre-flare events occurred from two spatially well-separated locations within the AR (Figure 3.15). While the location of the first pre-flare event (i.e., P1) was adjacent to one leg of the hot channel, the second pre-flare event (i.e., P2) occurred from a remote location suggesting it to belong to the category of the distinct pre-flare activities (Fárník et al., 1996).

Here it is also noteworthy that, while the location of P2 was associated with EUV brightening during the pre-flare event P2 only, the location of P1 underwent continuous EUV brightening throughout the pre-flare phase and even during the later precursor and impulsive phases of the flare. Further, the location of the pre-flare event 'P1' was associated with consistent EUV brightening along with thermal X-ray sources (Figure 3.17) suggesting continuous small-scale reconnection events in a localized region. The proximity of the location of 'P_1' to the location of the hot channel signifies that the continuous reconnection activities from this location most likely resulted into the complete destabilization and eruption of the hot channel (i.e., the pre-existing flux rope). In this way, our results can be interpreted in the light of multiple pre-flare events prior to a major flare of X-class analyzed by Joshi et al. (2013). Their work revealed that the activities during the pre-eruption phase were characterized by three localized episodes of energy release occurring in the vicinity of a filament that produced intense heating along with non-thermal emission. Based on these observations, Joshi et al. (2013) concluded that localized magnetic reconnections beneath the flux rope in the pre-eruption phase played an important role in destabilizing the filament through the tether-cutting process. From the spatial and temporal characteristics of pre-flare activities occurring at the location P1, we conclude that continuous, small-scale reconnection events in the vicinity of the northern leg of the hot channel would result in restructuring of the magnetic field configuration in a localized region besides reducing the magnetic flux near one of the footpoints of the magnetic flux rope. This process would progressively lead toward establishing the conditions favorable for the destabilization of the flux rope and subsequent large-scale eruption.

An important objective of this study lies in the detection of a pre-existing stable, hot EUV channel. The hot channel was in stable condition for at least ≈67 min before it was activated during the precursor phase (Figure 3.14(d)). Contemporary studies have established that hot coronal channels are one of the observational evidences of flux ropes (see e.g., Chen, 2011; Cheng et al., 2014a; Song et al., 2015b; Joshi et al., 2017a, 2018; Mitra et al., 2018). Notably, observations showing prior formation of flux ropes that remain stable during the pre-eruption phase are still uncommon with availability of only a few such reported incidences (Cheng et al., 2014a; Song et al., 2015c). The exact topology and formation process of flux ropes are still unclear and debatable. According to the mechanism proposed by van Ballegooijen & Martens (1989), flux cancellation through the photospheric converging and shearing motions leads into the formation of flux rope which has been subsequently supported by the numerical studies by Amari et al. (1999, 2000) where the twisted flux rope remains stable for a period before erupting. Many studies have also recommended the in-situ formation of flux ropes in the corona by magnetic reconnection, i.e., the flux rope builds up with the initiation of the flare itself (Cheng et al., 2011; Song et al., 2014; Chintzoglou et al., 2015; Wang et al., 2017a). Another class of model suggests that flux ropes are generated in the convection zone of the Sun and then emerges into the solar atmosphere by buoyancy (Caligari et al., 1995; Fan, 2001; Archontis et al., 2004; Martínez-Sykora et al., 2008). With the detection of a pre-existing hot channel right from the beginning of the studied interval and subsequent occurrence of small-scale energy release processes at adjacent and remote locations, our observational results support the scenario of flux rope emergence from the convection zone. During the impulsive phase of the X1.0 flare, the hot channel became activated and erupted resulting into a halo CME (Figures 3.18, 3.19, and 3.21). With a high proneness towards eruption and association with CMEs, hot channels are believed to be the earliest signatures of CMEs (Canfield et al., 1999; Pevtsov, 2002; Gibson et al., 2004, 2006; Liu et al., 2007, 2010; Cheng et al., 2014b; Kumar et al., 2016; Joshi et al., 2017a, 2018; Liu et al., 2018b; Mitra et al., 2018; Hernandez-Perez et al., 2019b); our observations are consistent with these earlier studies.

Further, the early dynamical evolution of the hot channel, characterized by its slow yet steady rise with a speed of ≈14 km s^{-1}, is of special interest. This relatively brief precursor phase of ≈16 minutes was associated with a gradual increase of the emission intensity from the flaring region. The temporal association between the slow rise phase of the flux rope and the precursor flare emission can be considered to be very important toward understanding the origin of CMEs (Zhang et al., 2001, 2004; Zhang & Dere, 2006). The early slow rise phase essentially marks the CME initiation in the source AR which is found to be well correlated with the mild and consistent precursor phase emission, commonly observed as gradually rising SXR flux (Zhang & Dere, 2006). It has been suggested that the precursor phase activities correspond to the dynamical formation of a current sheet underneath the flux rope that subsequently reconnects to trigger the onset of the main phase of the eruptive flare (Zhou et al., 2016). Our analysis readily supports this scenario as the hot channel underwent an abrupt transition from the state of slow rise to the fast acceleration as a continuous process which precisely bifurcates the precursor and impulsive phase of the eruptive flare (cf. Figures 3.20(b) and 3.15(a)).

We observed strong HXR sources of energies up to ≈100 keV from the flaring location during the early impulsive phase (Figure 3.18). In particular, the detection of a very high energy HXR source at the adjacent pre-flare (i.e., P_1) location (Figures 3.18(d), 3.17) is of high significance and rather surprising, since pre-flare activities are generally observed to be associated with only thermal emissions (see e.g., Hernandez-Perez et al., 2019b; Sahu et al., 2020). Detection of HXR source from pre-flare location essentially imply strong reconnection and restructuring of the magnetic field lines. This is supported by small-scale plasma ejection from this region (Figure 3.18).

The late impulsive phase of the X1.0 flare was characterized by a fast eruption of the flux rope in association with strong non-thermal high energy HXR sources (>50 keV) the footpoint location and relatively lower energy X-ray sources ($\lesssim$ 25 keV) from the apex of the post-reconnection arcade (Figure 3.18). Notably, the 25–50 keV HXR sources, probably containing mix of thermal and non-thermal emissions, were detected from both looptop and footpoint locations (Figures 3.18(e)–(h)). High energy HXR footpoint sources can be interpreted in terms of 'thick target bremsstrahlung' model (Brown, 1971; Hudson, 1972; Syrovatskii & Shmeleva, 1972; Emslie, 1983), which suggests that highly accelerated electrons from the site of magnetic reconnection in the corona are injected downward into the transition region and the chromospheric layers along the post reconnection magnetic field lines with relativistic speed. The relativistic electrons collide with cool and dense chromospheric plasma and deposit their energy with the production of HXR footpoint sources (Korchak, 1967a,b; Cline et al., 1968; Moza et al., 1986; Brown et al., 2002; O'Flannagain et al., 2015; Reep et al., 2016). Two basic models of HXR flares– impulsive injection and continuous injection models differ on the time-scale of electron acceleration. According to the impulsive injection model proposed by Takakura & Kai (1966), electrons are accelerated in multiple episodes of short time-scales in magnetic traps (i.e., magnetic loops). In contrast, the continuous injection model suggests continuous acceleration of electrons in dense chromosphere (Kundu, 1963; Acton, 1968; Kane & Anderson, 1970; Brown, 1971). In the view of multiple spikes in HXR time profiles during the impulsive phase (Figure 3.16(b)) and multiple type III bursts observed during the build up phase of the X1.0 flare (Figure 3.23), our analysis suggests occurrence of discrete events of particle acceleration during the impulsive phase. The overall distribution of low energy looptop and high energy footpoint X-ray sources, observed in our work, is in agreement with the CSHKP model of solar eruptive flares and also consistent with the general energy release scenario developed during the RHESSI era (Krucker et al., 2003; Veronig et al., 2006; Joshi et al., 2007, 2013).

The slowly evolving flux rope experienced rapid acceleration ($\approx$1.41 km s^{-2}) increasing its eruption speed to $\approx$183 km s^{-1} during the onset of the impulsive phase. The brief phase of rapid acceleration is co-temporal with the onset time of multiple HXR bursts observed in the high energy channels ($\gtrsim$25 keV) of RHESSI (cf. Figures 3.20, 3.18 and 3.16(b)) and a series of type III radio bursts (Figure 3.23). Type III radio bursts are produced by near-relativistic electrons propagating along the open magnetic field lines in the corona, restructured by the magnetic reconnection (Bastian et al., 1998; Reid & Ratcliffe, 2014; Chen et al., 2018a). The appearance of strong looptop and footpoint HXR sources during the impulsive phase implies rapid dissipation of magnetic energy in the current sheet as a result of an increase in the rate of magnetic reconnection (Sui & Holman, 2003) which is also likely to be responsible for the fast acceleration of the flux rope. While studying full CME kinematics including the initiation and impulsive acceleration phase of two fast halo CMEs and the associated flares, Temmer et al. (2008) found a close synchronization between the CME acceleration profile and the flare energy release as indicated by the RHESSI HXR flux onsets. They interpreted their results in terms of a feedback relationship between CME dynamics and reconnection events in the current sheet beneath the CME. Similar results were reported by many subsequent studies (see e.g., Zhang et al., 2012; Song et al., 2015a; Joshi et al., 2016a).

3.5 Summary and conclusion

In this chapter, we have presented two case studies of eruptive flaring activities that were associated with pre-flare events. By these studies, we aim to extend our understanding of pre-flare processes which form an ill-understood aspect of solar eruptions. In particular, we explore the effects of small-scale activities toward the development and activation of magnetic flux ropes and its subsequent large-scale eruption. In both the events under study, the pre-flare activity occurred adjacent to the main flaring site. In the following, we summarize the results obtained on the basis of multi-wavelength observations and associated numerical analysis of the two eruptive flares.

1. Our analysis revealed that magnetic flux ropes can exist within AR for extended period in stable conditions. Small-scale reconnection activities in the vicinity of a flux rope are observed to indirectly cause the slow-activation of the flux rope. Further, extended periods of photospheric flux cancellation can result in a gradual increase in the non-potential energy in flux ropes which eventually lead to the activation of it. During the course of the activation, temperature of flux ropes slowly increases and they begin to emit in the hot EUV channels e.g., AIA 94, 131 Å etc. Such activated, coherent flux rope structures have been recognized as 'coronal hot channel' (Zhang et al., 2012; Cheng et al., 2013). Detection of coronal hot channels can therefore be interpreted as the earliest signatures of a CME in the source region.

2. The present works have also provided significant information on the origin of pre-flare activities. We found that small-scale reconnection activities are initiated from regions exhibiting strong photospheric longitudinal currents of opposite polarities within close proximity. Zhang (1995) noted that strong photospheric currents can be generated in the regions of highly sheared magnetic field. Notably, the longitudinal electric current density at the precursor location decreased significantly with the onset of magnetic reconnection, suggesting rapid dissipation of stored non-potential energy of the region which would, in turn, reduce the shear of the magnetic field.

3. Our study have provided significant clarity on the understanding of the processes of the triggering of flux ropes by adjacent/overlapping pre-flare activities. Precursor reconnection activity occurring away from activated flux ropes can induce a series of small-scale activities which can eventually lead to the destabilization of the flux rope, which is analogous to the 'domino effect' (Zuccarello, F. et al., 2009).

4. We would like to emphasize on the detection of the HXR sources of energies up to ≈100 keV from the precursor location (Figure 3.18). Detection of strong non-thermal emission from the precursor location is conspicuous. Our finding, therefore, suggests that occasionally pre-flare activities also cause brief yet significant episodes of particle acceleration.

Chapter 4

Quasi-circular Ribbon Flares and Aspects of 3D Magnetic Reconnection

4.1 Introduction

Traditionally, solar eruptive flares have been observed to be associated with a pair of ribbon-like brightenings identified in chromospheric Hα images, situated on the opposite sides of the polarity inversion line (PIL). According to the CSHKP model (Carmichael, 1964; Sturrock, 1966; Hirayama, 1974; Kopp & Pneuman, 1976), magnetic reconnection along a vertical current sheet beneath an erupting prominence is primarily responsible for the ribbon-like emission. During reconnection, a part of the released energy results in accelerating electrons. The highly accelerated electrons are then projected with almost relativistic speeds along the post-reconnection magnetic loops toward the lower, denser chromospheric layer of the Sun along the reconnected field lines (Shibata & Magara, 2011). The accelerated electrons collide with the dense chromospheric plasma giving rise to a pair of hard X-ray (HXR) sources at the footpoints of the post-reconnection loops (Musset et al., 2015; Joshi et al., 2017a). In addition to the HXR emission, thermal conduction causes a sudden increase of chromospheric plasma temperature at the footpoints of the post-reconnection arcade, resulting in a pair of ribbon like brightening which can be observed in Extreme Ultra-violet (EUV) and op-

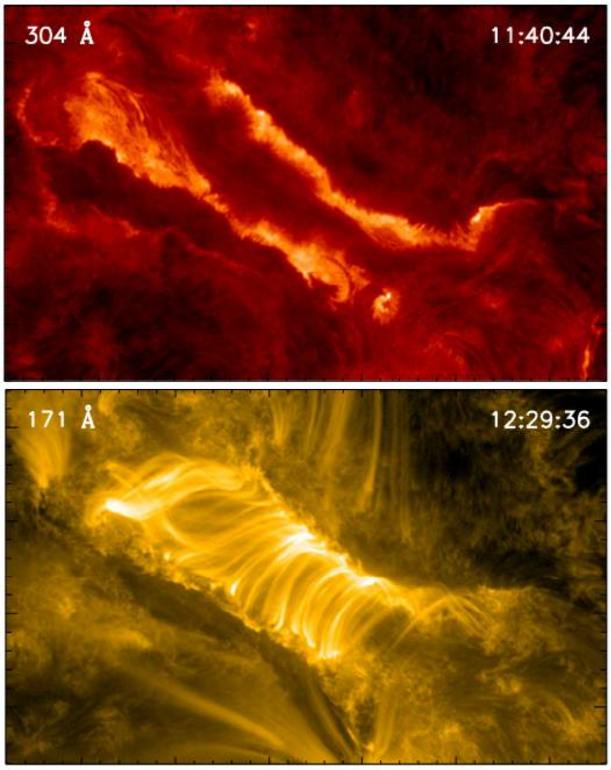

Figure 4.1: Characteristic evolution of parallel-ribbon flare in EUV. The top panel shows set of flare ribbons observed in chromospheric temperatures. The bottom panel shows a highly structured loop arcade, i.e., post reconnection arcade, connecting the two ribbons. Figure is adopted from Cheng & Qiu (2016).

tical wavelengths (top panel of Figure 4.1). As the flare progresses, the coronal loop arcade connecting the conjugate flare ribbons are gradually filled with hot chromospheric material via the process of chormospheric evaporation (see Fletcher et al., 2011). This results in intense thermal radiation from the post-reconnection arcade observable in the Soft X-ray (SXR) and EUV wavelengths (bottom panel of Figure 4.1).

The pre-flare configuration of such two-ribbon flares usually involve bipolar photospheric regions consisting of sheared and twisted coronal magnetic field as explained in Figure 4.2. In a bipolar magnetic configuration, shear in the coronal magnetic field build up stored in response to photospheric motion that include shearing motion, rotational motion etc. (Zhang, 1995). Shear in the magnetic field can naturally lead to the formation of small-scale current sheets in the system. According to the three dimensional standard flare model (Aulanier et al., 2012, 2013; Janvier et al., 2013, 2014), reconnection at these small-scale current sheets is responsible for the development of a flux rope from the sheared arcade. During the course of the flare, the formed flux rope is erupted and the inner legs of the sheared field lines which surround the erupting flux tube eventually reconnect beneath it forming near-potential post-flare loop-arcade (Aulanier et al., 2012). A simple

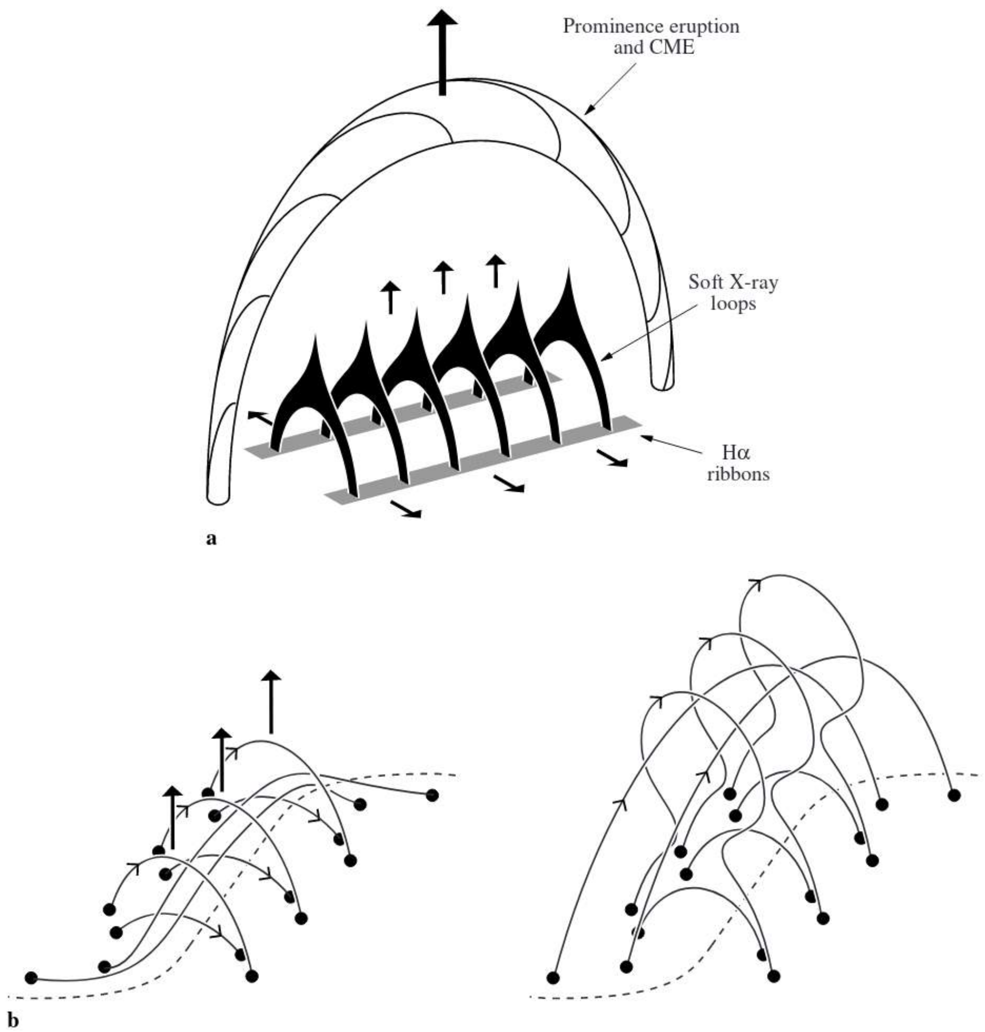

Figure 4.2: Overall picture for an eruptive two-ribbon flare. Top: Key observational features of two-ribbon eruptive flares and their spatial coupling. Bottom: Magnetic configuration showing the initial rise of a sheared arcade due to nonequilibrium (left) and the onset of reconnection below the rising flux tube (right). Figure is adopted from Priest & Forbes (2002).

cartoon showing the initial sheared magnetic field and post-reconnection potential magnetic loop system is shown in the bottom panel of Figure 4.2.

Morphologically, a completely different category of flares is circular (or quasi-circular) ribbon flares (Masson et al., 2009) which are identified by a single, closed circular/quasi-circular/elliptical-shaped flare ribbon (see Figure 4.3). Such flares usually occur from the 'anemone'-type ARs which are characterized on the photosphere by a compact magnetic region surrounded by magnetic regions of opposite polarity (Shibata et al., 1994). The coronal configuration of such ARs involve fan-spine configurations in 3D null-point topology (Lau & Finn, 1990; Sun et al., 2013). In Section 4.1.1, we discuss different aspects of a typical coronal fan-spine

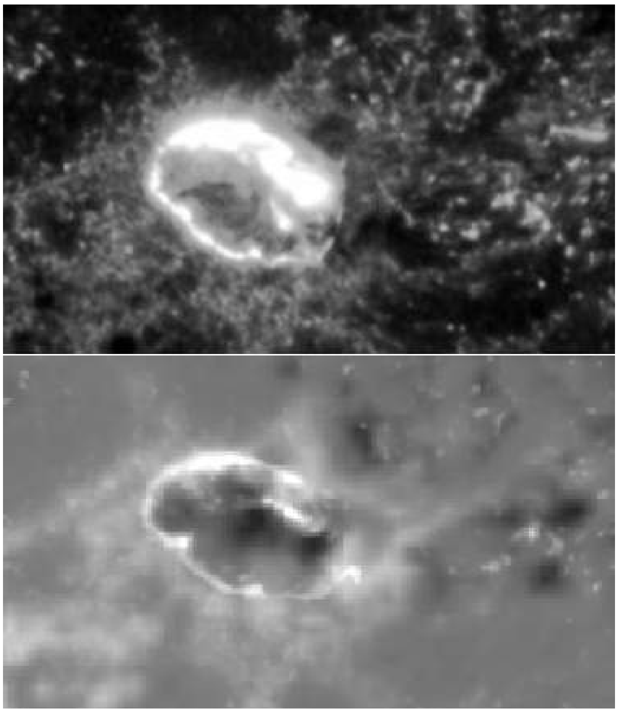

Figure 4.3: Top panel: A circular ribbon flare observed in TRACE (Handy et al., 1999) 1600 Å passband. Bottom panel: Association of the circular ribbon with photospheric magnetogram. Figure is adopted from Masson et al. (2009).

configuration in a null point topology. Notably, coronal null points belong to a special set of three-dimensional topological features present in the solar corona. We provide a brief introduction of the general three-dimensional topological features of solar corona in Section 4.1.2.

In the recent years, with the advancements of observational facilities and numerical techniques, a number of intriguing flaring activities have been reported that involved both the circular and parallel ribbons where the parallel ribbons reside within the periphery of the circular ribbon (e.g., Joshi et al., 2015, 2017b; Hernandez-Perez et al., 2017; Li et al., 2017; Xu et al., 2017; Li et al., 2018a,b; Hou et al., 2019; Shen et al., 2019). Such events usually develop as a small flux rope erupts within a fan-dome structure which then triggers reconnection at the null-point. We discuss different evolutionary aspects of typical flares associated with both circular and parallel ribbons in Section 4.1.3.

The quasi-circular ribbon flares sometimes occur successively at the same location of an AR. Such events are classically included in the category of homologous flares. In Section 4.2, we present a detailed study of four homologous quasi-circular ribbon flares in NOAA 11977. We perform a comprehensive analysis on coronal magnetic field modeling to address the cause of flare initiations and understand various 3D topological features associated with these complex events.

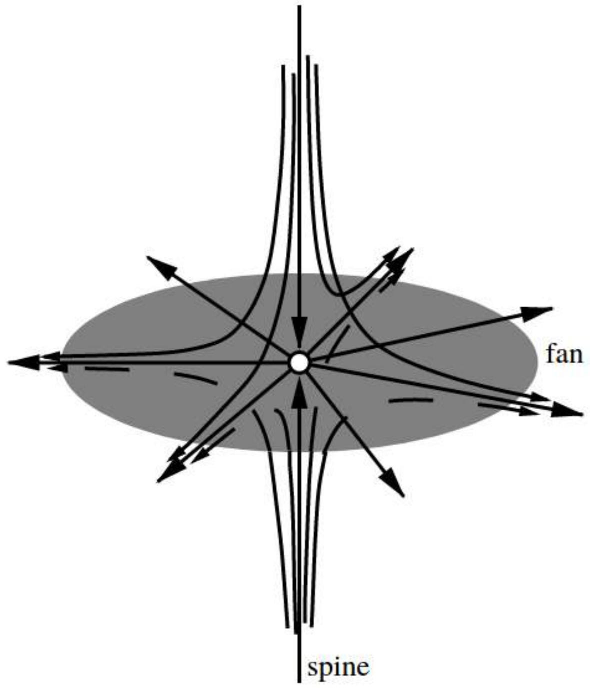

Figure 4.4: Schematic depictions of the magnetic configuration associated with a simplest (potential) positive null point. Two spine field lines directed toward the null (white circle) appear as dark lines with arrow heads next to the null. The central portion of the horizontal fan surface is colored grey, and contains fan field lines directed outward like spokes on a wheel. Dashed lines show a few of the field lines on either side of the fan surface. Figure is adopted from Longcope (2005).

4.1.1 Configuration of a typical null-point topology in a spine-fan configuration

Coronal null-points are locations in the solar corona, where the strengths of all the three components of magnetic field become locally zero (see review by Longcope, 2005). Magnetic field beyond the immediate neighborhood of the null-point is characterized by a spine line and a fan surface. Depending on the sign of the null-point (positive or negative), magnetic field lines approach the null-point along the spine line and move away from it along the fan surface (for positive null; see Figure 4.4); or, approach the null along the fan surface and recede from it along the spine line (negative null).

In the context of such 3D null-point configurations generating fan and spine lines, the anemone-type ARs where a compact magnetic region is surrounded by magnetic regions of opposite polarity (see, Shibata et al., 1994) are of special significance (Figure 4.5(a)). The inner compact region is connected with the surrounding opposite polarity region by small-scale closed magnetic loops (shown by the yellow colored field lines in Figure 4.5(b)–(d)) while a set of relatively large field lines connect the surrounding polarity to a remote region of polarity similar to that of the inner compact region (shown by the red colored field lines in Figure 4.5(b)–(d)). In this way, the two sets of field lines constitute two sets of fan

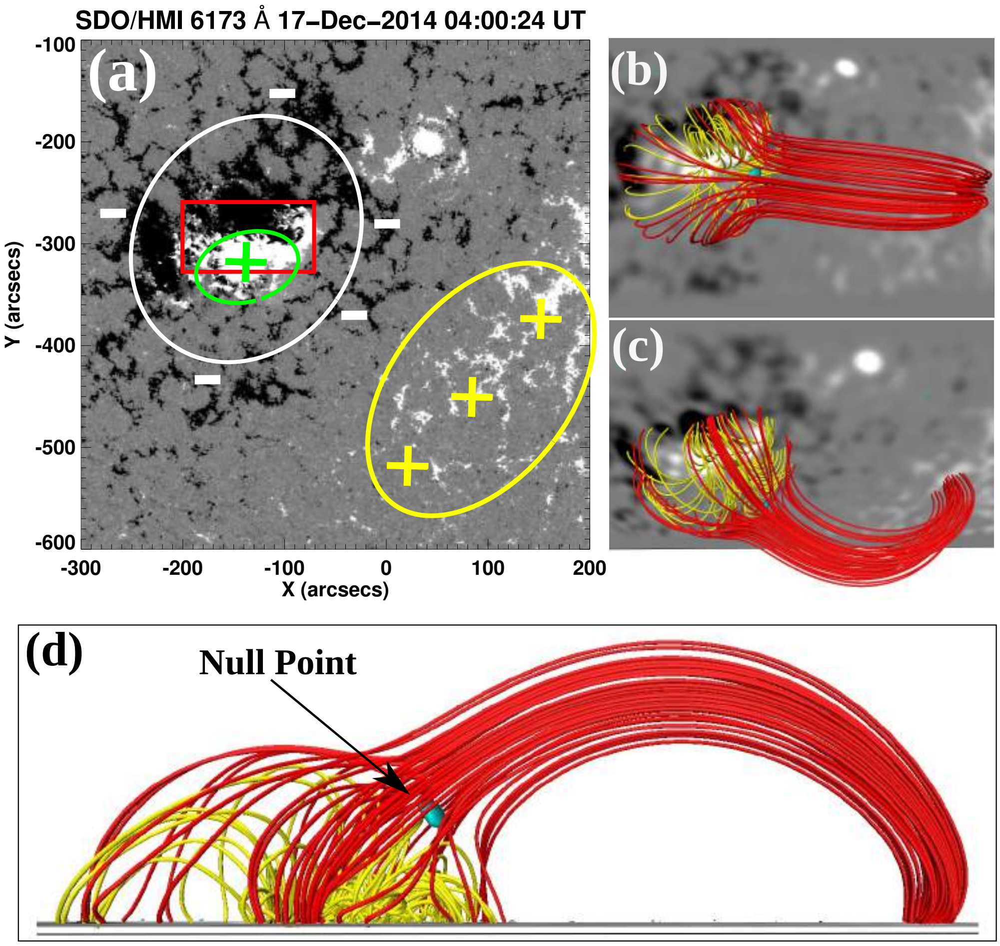

Figure 4.5: Photospheric configuration of an anemone type active region. The central positive polarity and the surrounding negative polarity regions are represented by the green and white ellipse, respectively. The remote positive polarity region is enclosed by the yellow ellipse. Figure is adopted from Joshi et al. (2021).

lines (inner and outer fan lines) and two sets of spine lines (inner and outer spine lines). The two sets of fan lines are separated by a dome-shaped surface (i.e., fan separatrix; Figure 4.6) characterized by high degree of squashing factor (Q; see, Priest & Démoulin, 1995; Titov et al., 2002), which intersects the spine lines at the null-point (Sun et al., 2013). The location of the null-point is highlighted by the cyan-colored iso-surface in Figure 4.5(d).

The distribution of magnetic decay index within the fan-dome is particularly interesting. Since, a null point resides on the fan dome, it is expected that magnetic field below it will experience a rapid decay. Therefore, magnetic decay index reaches the value $n \geq 1.5$ within relatively short height in a region encompassed by the fan-spine configuration. In Figure 4.6, the yellow-colored iso-surface encloses the region of torus instability i.e., $n > 1.5$ which suggests that the region of

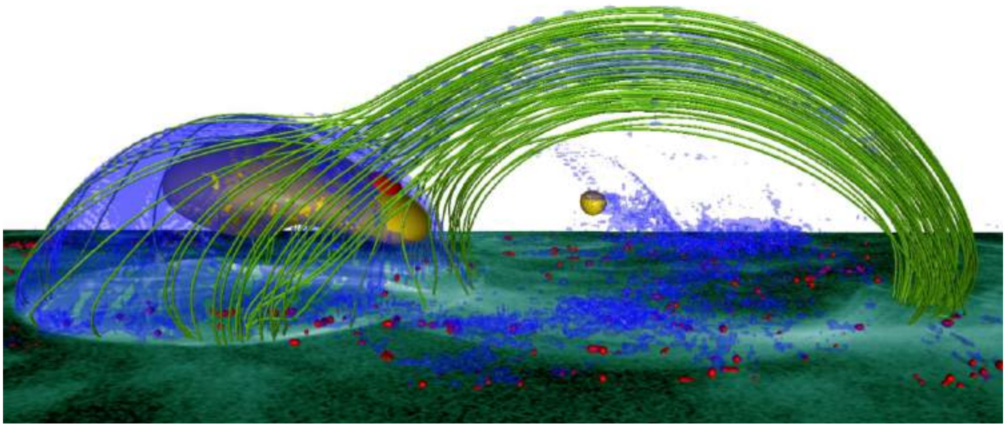

Figure 4.6: Fan separatrix surface of a fan-spine configuration associated with 3D null-point and distribution of decay index within the fan-dome. The yellow colored iso-surface encloses a region characterized by magnetic decay index $n > 1.5$. The fan separatrix (shown by the blue colored surface) between the outer fan lines (shown by the green colored field lines) and inner field lines (not shown in order to the simplicity of visualization) is characterized by $log(Q) = 5$. The location of the null point is indicated by the red colored iso-surface which is situated at the intersection of the spine lines and the fan separatrix. Figure is adopted from Joshi et al. (2021).

high decay index within a fan dome resides just beneath its top part, having an intersection with the null point.

4.1.2 Coronal three dimensional topological features

Coronal null points, being defined as a point where strength of all the three components of magnetic field is zero, creates a local discontinuity in the solar corona. In general, domains corresponding to drastic changes in the magnetic field connectivity gradient are identified as quasi-separatrix layers (QSLs; see e.g., Janvier et al., 2013). While the values of Q corresponding to QSLs are high ($\gg$2; see, Aulanier et al., 2005), null-points can be characterised by $Q \rightarrow \infty$. The finite values of Q at the QSLs imply that although magnetic fields show drastic change in the connectivity they are still continuous, which is contrary to the cases of null-points where magnetic field becomes discontinuous. In complex photospheric configurations, e.g., those formed by two bipolar sunspots, a pair of photospheric null-points of opposite signs may exist which are connected by ‘separators’ (Titov et al., 2002). A separator can be identified by narrow elongated strips of high Q-values, i.e., a QSL, with a pair of null-points at both of its ends. Further, a generalisation of the concept of separator lines reveals a special geometrical feature called 'Hyperbolic Flux Tubes' (HFTs; Titov et al., 2002) which can be understood as the intersection of two QSLs. The middle of an HFT is characterized by 'X'-type cross section comprised of high Q-values. Such structures of high Q-values are preferred sites for the formation of current sheets and initiation of magnetic reconnection (Titov et al., 2003). Moreover, magnetic field lines can constantly change their connectivities along the QSLs as a consequence of local diffusion in the region, allowing neighboring field lines to exchange connectivities (Aulanier et al., 2006). This can be observed as an apparent slipping or flipping motion of loop connectivities and are termed as 'slipping reconnection' (see e.g., Priest & Démoulin, 1995; Aulanier et al., 2006; Janvier et al., 2013).

4.1.3 Evolutionary aspects of typical circular-ribbon flares associated with parallel ribbons

The key ingredients of a typical flare coupling circular and parallel ribbons are schematically given in Figure 4.7, which is adopted from Sun et al. (2013). A flux rope (shown by the pink lines) is situated along a sheared PIL between opposite polarity regions of the anemone type AR formed as the negative polarity region N1 is surrounded by positive polarity regions highlighted by P1 and P2. Here, a single null point exists in the domain above the N1 (indicated by an arrow in Figure 4.7(a)), through which a spine field line (shown by red lines) links N1 and a second negative polarity region N2. The presence of N2 enables the overall coronal configuration to be a closed-fan-spine configuration where the yellow-colored lines form the fan lines and red-colored line form the spine line. Notably, the null point is situated at the intersection between the fan and spine lines. Absence of the N2 region would result in the outer spine line being open i.e., open-fan-spine configuration. The fan separatrix divides the domain into two flux systems; it intersects the lower boundary to form a quasi-circular footprint.

Analysis of the degree of squashing factor (Q; Demoulin et al., 1996; Titov et al., 2002) provides an excellent representation of the footprints of the fan-spine configuration (Figure 4.7(b)). High-Q regions i.e., QSLs readily include the circular footprint of the fan dome, relatively localized high-Q footprints of the inner and

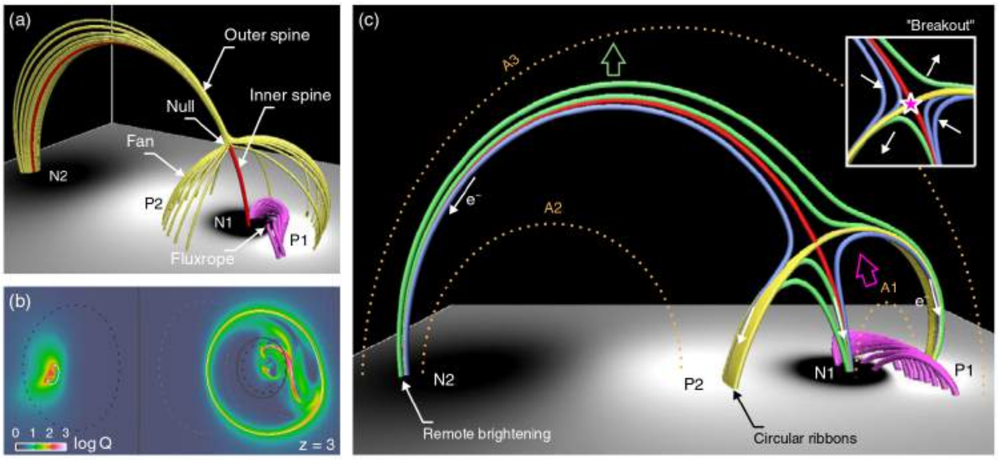

Figure 4.7: Panel (a): Magnetic skeleton of a model fan-spine configuration. Four flux patches exist at the lower boundary (P1/N1 and P2/N2, P for positive, N for negative). A flux rope (pink) resides above the P1/N1 polarity inversion line (PIL). The domain contains a null point above N1. The spine (red) and the fan (yellow) are marked. Panel (b): Logarithm squashing degree Q on the plane $z = 3$. Red and yellow delineate the quasi-separatrix layer (QSL) footprint. Dotted lines are contours of the normal magnetic field; gray solid lines are the PILs. Panel (c): Two-dimensional representation of the magnetic system illustrating possible physical processes pertinent to typical circular ribbon flares. Field lines undergo slipping-type reconnection within the fan QSL (yellow). At the null, blue field lines undergo breakout-type reconnection (inset). Energized particles or intense heat flux propagate along the fan and spine QSLs, resulting in circular ribbon and remote chromospheric brightening. The flux rope may eventually erupt and open the fan. Post-reconnection loops of various configurations (A1, A2, and A3) may form. Figure is adopted from Sun et al. (2013).

outer spine, and an S (or inverse S)-shaped pattern due to the left (or right)-hand twisted flux rope Savcheva et al. (2012).

In most of the reported cases, activation and eruption of the flux rope occurs in association with standard flare reconnection giving rise to the parallel flare ribbons. Considering the PIL corresponding to the flux rope is highly sheared and flux emergence is primarily responsible in the formation of anemone type AR, the triggering of flux rope usually takes place in response to tether-cutting reconnection. Further, since magnetic field rapidly decays within the fan dome, initially triggered flux rope easily enters the region of torus instability which further supports the eruption of the flux rope. The erupting flux rope then triggers magnetic reconnection at the coronal null point causing the circular ribbon brightening. In Figure 4.8, a typical circular flare ribbon associated with parallel ribbons in shown. In this context it is worth mentioning that, in rare cases it has also been observed

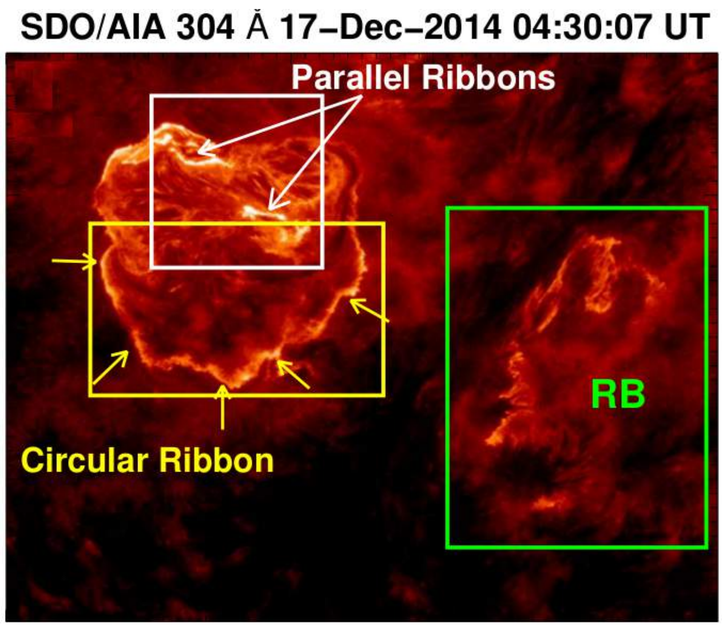

Figure 4.8: An AIA 304 Å image showing a circular flare ribbon associated with parallel and remote ribbons. Figure is adopted from Joshi et al. (2021).

that null-point is triggered first which eventually leads to the eruption of the flux rope (see e.g., Joshi et al., 2021).

The null-point reconnection itself is a complex, multi-stage mechanism which initially includes slipping reconnection at the quasi-separatrix surface at the fan-dome giving rise to the circular or quasi-circular ribbon and during the subsequent stage, interchange reconnection takes place between the inner close fan lines and the outer open spine lines causing the remote brightening (Figure 4.8; see also Masson et al., 2009). In response to the interchange reconnection at the coronal null-point, collimated ejection of plasma i.e., coronal jets or Hα-surges have been identified in several studies (Pariat et al., 2009a, 2010).

Since, the null-point is situated well above the core field, the null-point reconnection is analogous to the breakout type reconnection (Antiochos et al., 1999). Reconnection at the null point enables the flux systems below and above the fan to interact. In the model shown in Figure 4.7, the blue field lines reconnect and become the green ones (inset of Figure 4.7(c)). Following the null-point reconnection, part of the P1 flux that originally linked to N1 above the flux rope maps to N2 (Sun et al., 2013). Simultaneously, part of the P2 flux now changes its linking from N2 to N1. As a result, flare emission from the remote region (N1) is observed.

Table 4.1: Summary of the homologous, quasi-circular flares occurred on 2014 February 16

Flare Id.	Location	Flare timing (UT) Start/ Peak/ End	GOES class	Remarks
F_1	S10E00	09:20/09:26/ 09:29	M1.1	Observation of quasi-circular ribbon
F_2	S10W01	13:48/14:00/14:05	C3.4	Observation of shortened quasi-circular ribbon
F_3	S10W03	17:35/17:38/17:40	C1.2	Observation of arc-shaped ribbon
F_4	S10W04	19:20/19:23/19:28	C1.7	Observation of arc-shaped ribbon

4.2 Homologous quasi-circular ribbon flares in NOAA 11977

The four homologous quasi-circular ribbon flares reported in this chapter, originated on 16 February 2014 within an interval of ≈11 hours from a complex magnetic configuration within NOAA 11977. Interestingly, all the four flares were relatively less energetic, as only the first flare was of low GOES M-class while the rest three flares were of C-class category. A summary of the four flares is presented in Table 4.1. In Section 4.2.1, we provide a comprehensive overview of the structure and evolution of NOAA 11977 and discuss the evolution of the four homologous flares in Section 4.2.2.

4.2.1 NOAA 11977: structure and evolution

The AR under observation, NOAA 11977 was first detected on 2014 February 11 when it appeared on the eastern limb of the Sun as a simple α-type AR. Initially it evolved quickly and transformed successively into more complex β and $\beta\gamma$-type by 2014 February 14. Interestingly, although it maintained its $\beta\gamma$-type magnetic complexity for the next four days, the sunspot-area of the AR started to decay from the next day i.e., 2014 February 15. The most important aspect of this AR, in view of the present study developed on 2014 February 16 in the form of an intriguing, complex bipolar configuration which formed in the westernmost part of the AR. Notably, once developed, this region, after producing one M and three C-class flares on 2014 February 16 within an interval of ≈11 (see Table 4.1) decayed completely by the end of the day. The magnetic complexity of the overall

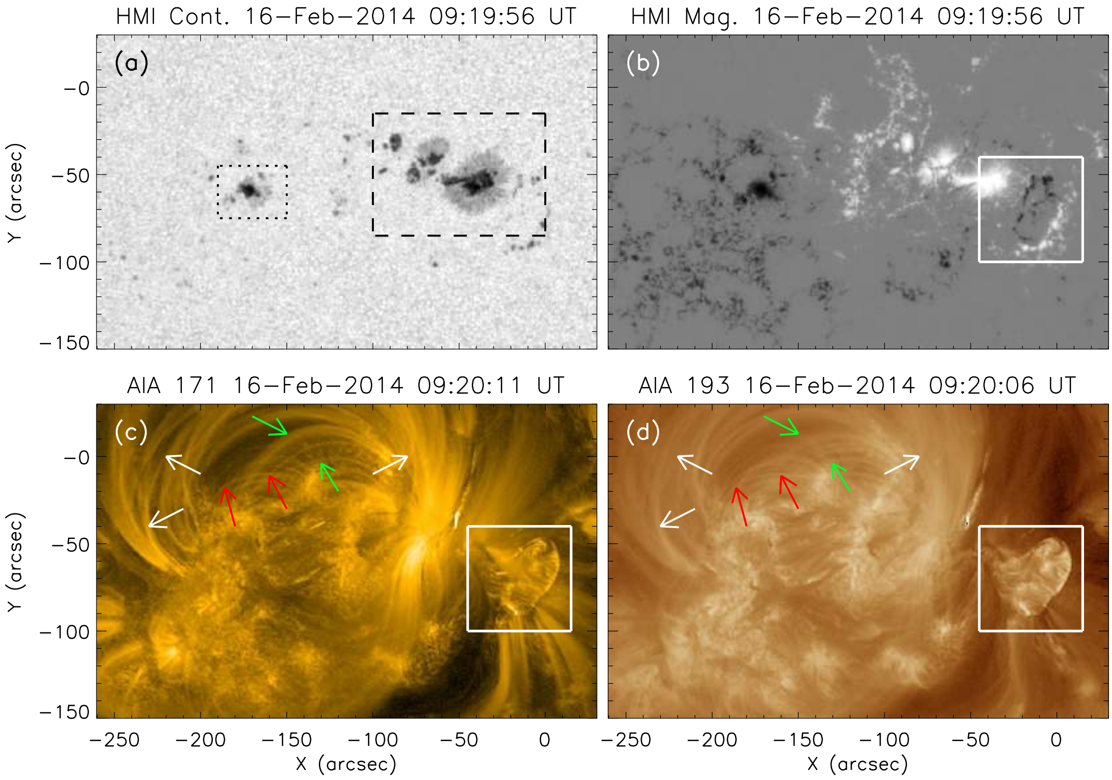

Figure 4.9: The morphology of the active region NOAA 11977 on the photosphere (panels (a) and (b)) and different coronal temperatures (panels (c) and (d)). The flaring activity occurred from the region shown within the white box in panels (b)–(d).

decaying AR reduced gradually to β-type on 2014 February 19 and further to the simplest α-type on 2014 February 23, few hours before its disappearance over the western limb of the Sun.

Photospheric and coronal configurations

We compare the photospheric and corresponding coronal structures of NOAA 11977 in Figure 4.9. We readily observe that, the AR was comprised of a few prominent sunspots along with many pores (Figure 4.9(a)). Further, a comparison of the co-temporal magnetogram (Figure 4.9(b)) with the white light image (Figure 4.9(a)) distinctly reveals that the overall sunspot groups of the AR can be easily grouped in two subregions: the positive polarity leading sunspot group and the negative polarity trailing sunspot group (shown by the dashed and dotted boxes in Figure 4.9(a), respectively). In general, the leading part of the AR was mostly dominated by positive polarity while the trailing part of the AR was consisted of mainly dispersed negative polarity magnetic field regions. However, the most interesting aspect of the AR, in the context of the present analysis, developed in the extreme western part of it where magnetic patches of positive and negative polarities formed a complex magnetic configuration similar to a geological 'atoll' (within the white box in Figure 4.9(b)). AIA images suggest that the AR, on the whole, consisted of different sets of coronal loops of varying spatial extents and projected heights. In Figures 4.9(c) and (d), we identify and indicate some of these loops by arrows of different colors (white, green, and red).

Notably, the coronal structures over the photospheric atoll region (outlined by the white boxes in Figures 4.9(c) and (d)) were clearly distinguishable from the rest of the AR in view of its peculiar morphology. The EUV images of the particular region clearly revealed enhanced structured oval-shaped brightening within a sharp boundary. All the four events of 2014 February 16 occurred within this region.

Formation of the 'magnetic atoll' region

In order to achieve a comprehensive understanding of the formation and development of the magnetic atoll region, we looked into a series of LOS magnetogram (Figures 4.10(a)–(f)) corresponding to the photospheric region (shown within the white box in Figure 4.9(b)). Considering the diffused brightening region to be intrinsically related with the magnetic atoll region, we further observed co-temporal AIA 304 Å images of the same region (Figures 4.10(g)–(l)). Our observations revealed that the development of the atoll region began from the late hours of 2014 February 15 when a few small negative polarity flux regions emerged at the western side of the leading sunspot (the emerging negative polarity regions are indicated by the yellow arrows in Figure 4.10(a)). Emergence of negative polarity magnetic flux kept continued in this region and by the first hour of 2014 February 16, a relatively large magnetic patch of negative polarity was developed. We have indicated the relatively large negative polarity patch by the blue arrow in Figure 4.10(c). Co-temporal AIA 304 Å images suggest that the distinct oval-shaped region displaying enhanced-diffused brightening started to build-up from around this time onward (cf. Figures 4.10(i) and (c)). Gradually, as emergence of negative flux continued, the diffused EUV emission from the region became more prominent and its boundary extended spatially (cf. Figures 4.10(i)–(l)). Notably, along with the emergence of negative flux patches, the atoll region also experienced emergence of positive flux which surrounded the negative polarity patches in the south-west direction (cf. the regions indicated by the pink arrows in Figures 4.10(c) and (f)). In general, the atoll region can be characterized by newly emerged and spatially dispersed prominent patches of negative magnetic flux surrounded by positive polarity regions from two sides i.e., northeast (by the positive polarity sunspot) and southwest (by the dispersed positive polarity patches). Apart from the emerging magnetic features, we also identified several instances of flux cancellation within the magnetic atoll region, a few events of such instances of flux changes are indicated by blue, red, and green arrows in Figures 4.10(c)–(f). Notably, AIA 304 Å images suggests the formation of a filament channel during the early hours of 2014 February 16 along the north-eastern boundary of the diffused brightening region (indicated by the green arrow in Figure 4.10(j)). Comparison of AIA 304 Å images with co-temporal LOS HMI magnetograms reveal that the filament channel was situated along the PIL between the positive polarity sunspot and dispersed negative polarity patches of the magnetic atoll region.

4.2.2 Four successive flares from the magnetic atoll region

Four successive quasi-circular ribbon flare originated from the magnetic atoll region on 2014 February 16 within an interval of ≈11 hours. In Figure 4.11(a), we plot SXR flux in the GOES 1–8 Å channel along with EUV intensities of AIA 94 and 304 Å channels from 2014 February 16 00:00 UT–20:00 UT which displays the onset and temporal evolutions of the four flares (a summary of the temporal evolution of the four events are presented in Table 4.1). The general agreement of the multi-wavelength lightcurves suggest that the onset of the first flare originating from the atoll region initiated at ≈09:20 UT. Following a brief rise phase of ≈6 minutes, this short lived flare of GOES class M1.1 reached to its peak at ≈09:26 UT. Interestingly, the second flare, having a lower GOES class (C3.4) than the first flare of GOES class M1.1, had a longer rise phase than the first flare. After its initiation at ≈13:48 UT, the GOES C3.4 flare reached its peak intensity after a relatively extended rise phase of ≈12 minutes. The last two flares originating from

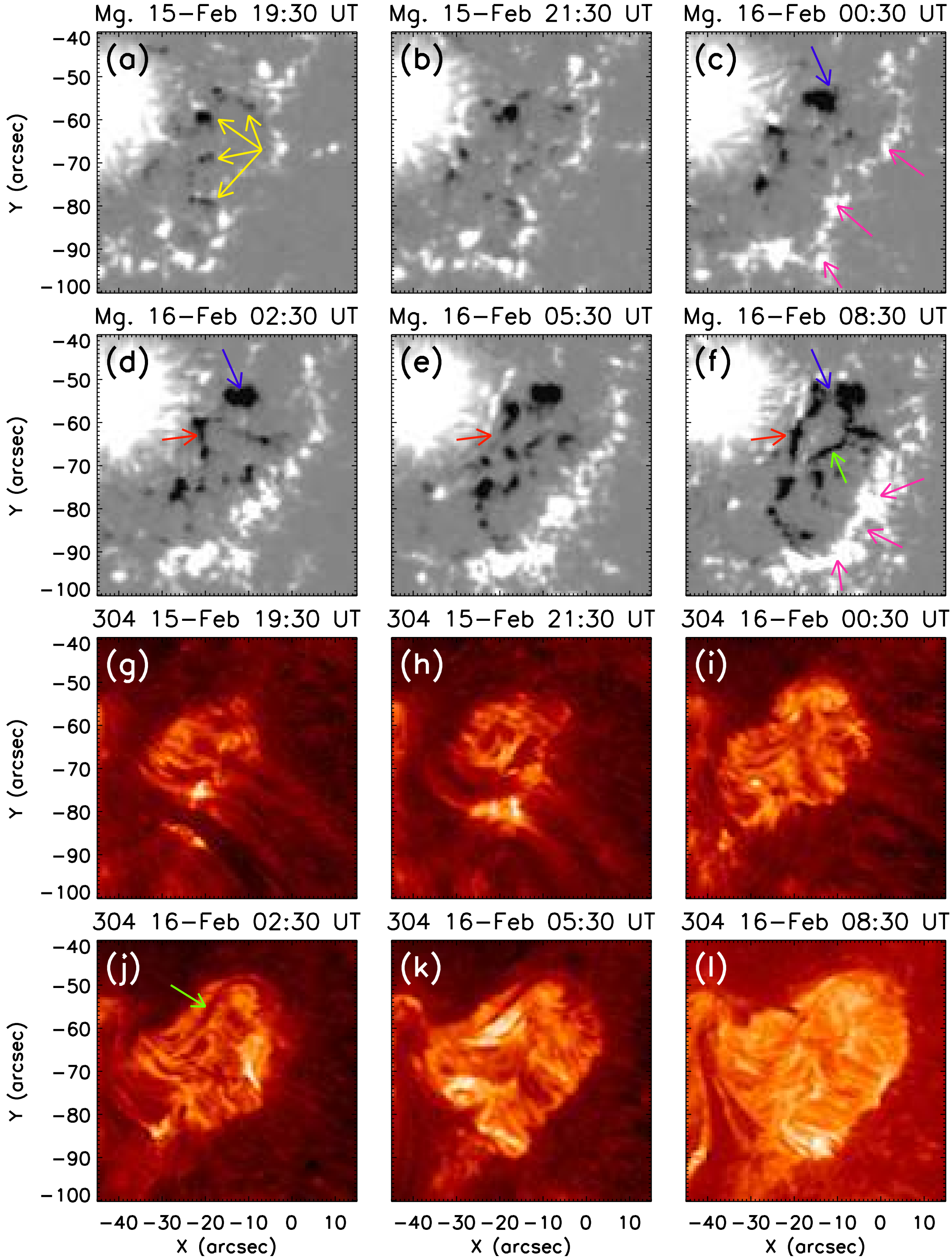

Figure 4.10: Series of HMI LOS magnetograms showing the development of the magnetic 'atoll' region (panels (a)–(f)). Arrows of different color indicate few prominent locations of negative magnetic flux emergence. Panels (g)–(l) are AIA 304 Å images associated with the magnetic atoll region displaying the formation of the diffused circular brightening region. All the images are derotated to 2014 February 16 09:20 UT.

this region were rather impulsive and short lived. According to the GOES 1–8 Å flux profile, these C-class flares originated at ≈17:35 UT and 19:20 UT while their impulsive phases lasted for only ≈3 minutes each. In Figure 4.11(a), we indicate the durations of the four flares by gray-shaded intervals and assign the notations 'F_1', 'F_2', 'F_3' and 'F_4' to the flares in the chronological order.

To understand the extent of the ribbon-brightenings during the four flares, we plot AIA 94 (Figures 4.11(b)–(e))and 304 Å (Figures 4.11(f)–(i)) images of the diffused brightening region during the peak phases of the flares. These multi-wavelength EUV images revealed that, all the four flares were characterized by some degree of ribbon-like brightening along the circumference of the diffused brightening region. Quite prominent signatures of an extended quasi-circular ribbon brightening were observed during F_1, which we have delineated by the red dotted curve in Figure 4.11(b) and the green arrows in Figure 4.11(f). The quasi-circular ribbon brightening significantly shortened during F_2, which was primarily situated along the western boundary of the diffused brightening region (indicated by the red dotted curve in Figure 4.11(c) and the green arrows in Figure 4.11(g)). The shortening of the circular ribbon during F_2 was possibly a result of the decay of the magnetic atoll region. During F_3 and F_4, the flare ribbons further shortened and only a small portion of the western boundary of the diffused brightening region displayed enhanced emission. We have indicated this arc-shaped flare brightening by the yellow arrows in Figures 4.11(d)–(e) and the green arrows in Figures 4.11(h)–(i).

To understand the spatial connection of the quasi-circular ribbons with the magnetic atoll region, we have further plotted the pre-flare HMI LOS magnetograms corresponding to all the four flares in Figures 4.11(j)–(m), respectively. From the co-temporal AIA 304 Å contours plotted over the LOS magnetograms, it becomes clear that the quasi-circular ribbon brightening during the F_1 flare was co-spatial with the positive polarity flux regions situated at the boundary of the photospheric atoll region. As the ribbon-brightening shortened during the subsequent flares, they primarily extended along the northern part of the positive polarity region situated at the western boundary of the atoll region, while the main flare kernels connected the positive polarity sunspot with the negative polarity re-

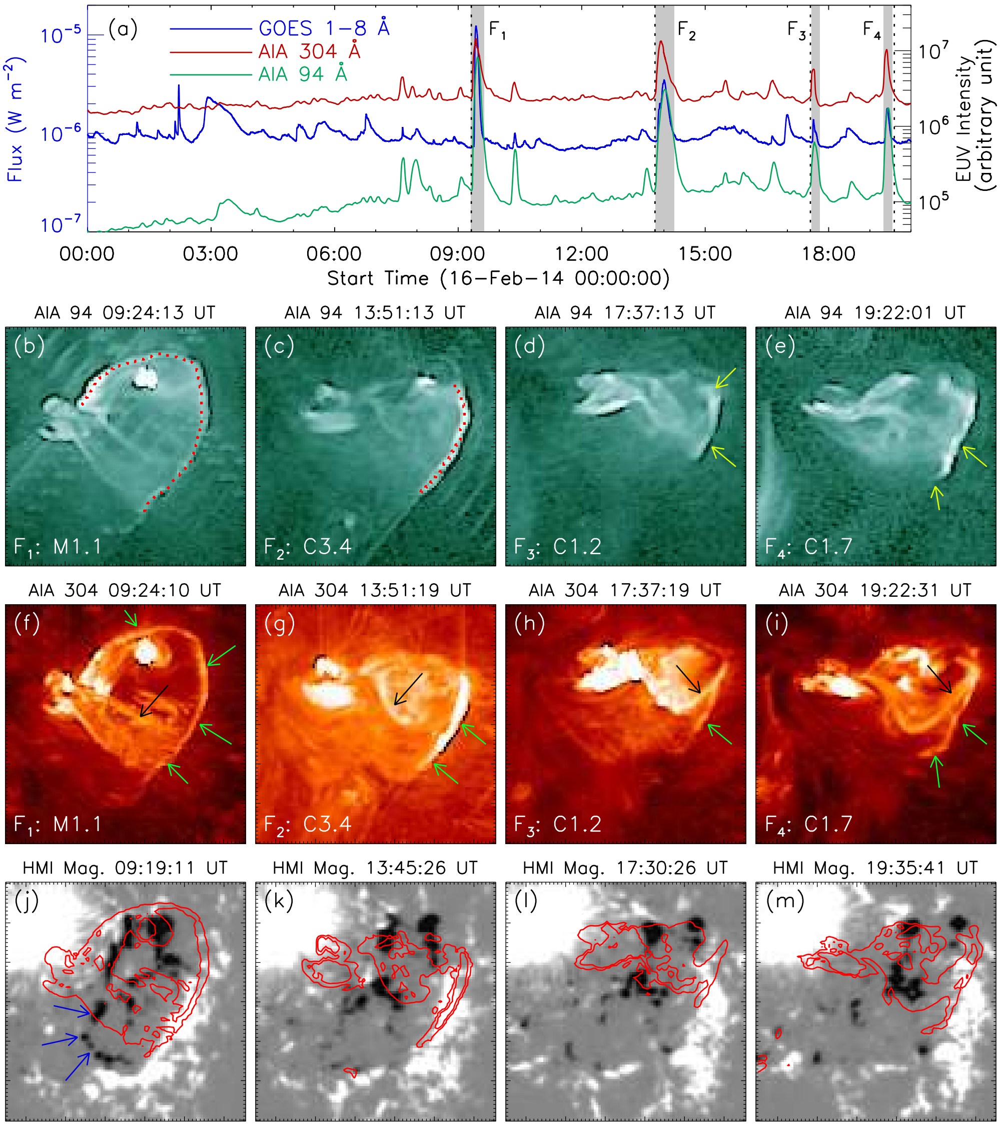

Figure 4.11: Panel (a): GOES 1–8 Å flux (blue curve), AIA 304 Å (red curve) and AIA 94 Å (green curve) intensities showing the onset and evolution of four flares (‘F_1’, ‘F_2’, ‘F_3’ and ‘F_4’) from the diffused brightening region. Panels (b)–(e): AIA 94 Å images of the diffused brightening region during the peak phases of the four flares. The red dotted curves in panels (b) and (c) indicate the quasi-circular ribbon observed during F_1 and F_2 while the yellow arrows in panels (d)–(e) indicate arc-shaped ribbons during F_3 and F_4 flares, respectively. Panels (j)–(i): AIA 304 Å images showing the peak phases of the four flares. The green arrows in different panels indicate the quasi-circular (panel (f)), semi-circular (panel (g)) and arc-shaped (panels (h) and (i)) ribbons observed during the flares. The black arrows indicate the erupting filament. Panels (j)–(m): HMI LOS magnetograms of the ‘magnetic atoll’ region prior to the onset of the F_1–F_3 flares (panels (j)–(l)) and after the F_4 flare (panel (m)). The blue arrows in panel (j) indicate few negative flux region which disappeared with time. Contours of co-temporal EUV intensities in AIA 304 Å are overplotted on the bottom row. Contour levels are [4, 80]%, [12, 60]%, [11, 60]% and [9, 40]% of the corresponding peak intensities in panels (j), (k), (l) and (m), respectively.

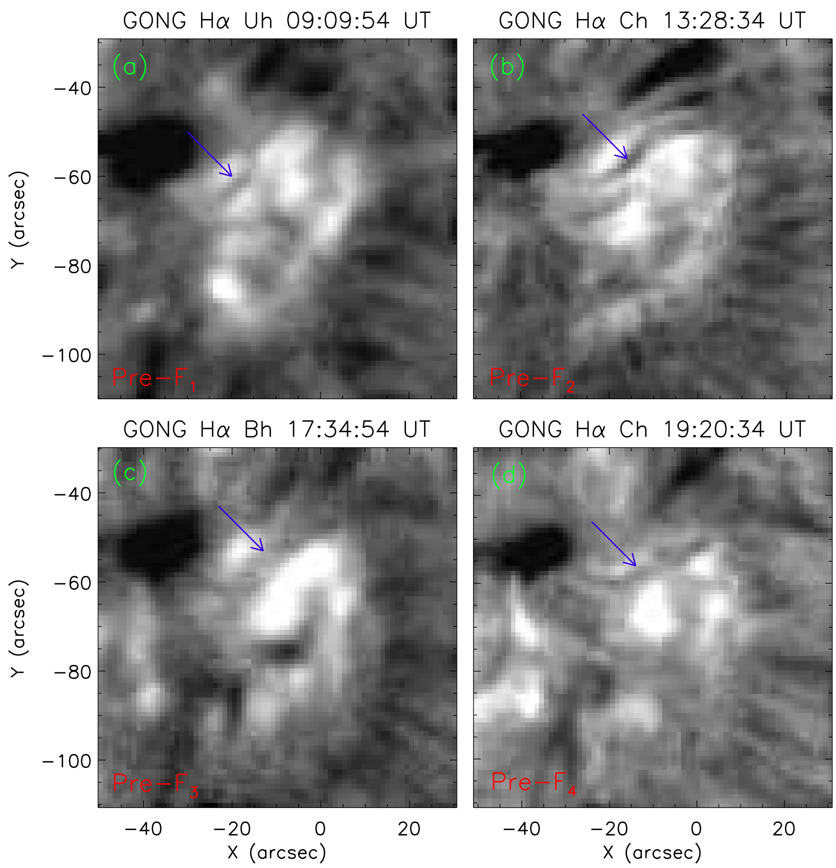

Figure 4.12: Selective of Hα images of the diffused brightening region during the pre-flare phases of the quasi-circular ribbon flares, recorded by different stations of the GONG network. The corresponding GONG stations are indicated in the titles in each panel as Uh (Udaipur Solar Observatory, India), Ch (Cerro Tololo Inter-American Observatory, Chile) and Bh (Big Bear Solar Observatory, USA). The blue arrows indicate the presence of small filaments prior to the flares.

gions of the atoll region. From the LOS magnetograms, it also becomes evident that the negative polarity flux regions from the magnetic atoll region continuously decayed with the evolution of each flares. This cancellation of negative flux was much more prominent in the southern part of the atoll region than the northern part (cf. the negative flux regions indicated by blue arrows in Figures 4.11(j) and (m)).

To confirm the presence of filaments prior to the flares, over the filament channel that was developed along the northern boundary of the diffused brightening region (Figure 4.10(j) and and Section 4.2.1), we looked into the pre-flare chromospheric images of the diffused brightening region in the Hα passband (Figures 4.12). We clearly identified impressions of the filaments from these images which implies recursive development of filaments at the filament channel, activation of which might have been responsible for the initiation of the quasi-circular ribbon flares.

Since, photospheric magnetic activities play a crucial role towards the origin of flaring activity, we examined the evolution of photospheric flux within the magnetic atoll region (enclosed by the box in Figure 4.13(a)) over its lifetime that also included the time-span of the four quasi-circular ribbon flares. For a detailed understanding of the influence of photospheric flux on the on origin of the flares, we emphasized on the small-scale flux changes within the atoll region (in Figures 4.13(b_1)–(b_8)) and the temporal evolution of flux from it (Figure 4.13(c)) by analyzing HMI LOS magnetograms. From the series of the LOS magnetograms of the atoll region, we clearly identified several instances of small-scale flux cancellation of both polarities. We have highlighted a few of such instances by arrows and ovals of different colors in Figures 4.13(b_1)–(b_8). The pre-flare phase of F_1 (Figures 4.13(b_1)–(b_2)) was characterized by cancellation of positive flux at the region of the PIL between the positive polarity sunspot and the negative polarity regions, i.e., the photospheric location associated with the filament. In particular, we observed distinct episodes of positive flux cancellation at the northern boundary of the magnetic atoll region (cf. the regions within the yellow ovals in Figures 4.13(b_1) and (b_2)). During the interval between F_1 and F_2, we identified multiple instances of flux cancellation of both polarities at the same PIL region (cf. the arrow heads of the red, blue and green arrows in Figures 4.13(b_3)–(b_4)). Between F_3 and F_4, a significant part of a relatively prominent negative flux region got decayed (cf. the region enclosed by the green ovals in Figures 4.13(b_5)–(b_6)). During the interval, we further observed cancellation of positive flux in the atoll region which is highlighted within the orange ovals in Figures 4.13(b_5)–(b_6). This region was further associated with flux cancellation during the interval between F_3 and F_4 flares which is indicated by the red ovals in Figures 4.13(b_7)–(b_8). We also observed cancellation of small negative fluxes from the atoll region in this duration which are indicated by the blue arrows in Figures 4.13(b_7)–(b_8).

Following its development, the atoll region experienced a significant decrease of negative flux (Figures 4.11(j)–(m) and 4.13(b_1)–(b_8)) which can be readily recognized by the temporal evolution of negative flux (blue curve in Figure 4.13(c)).

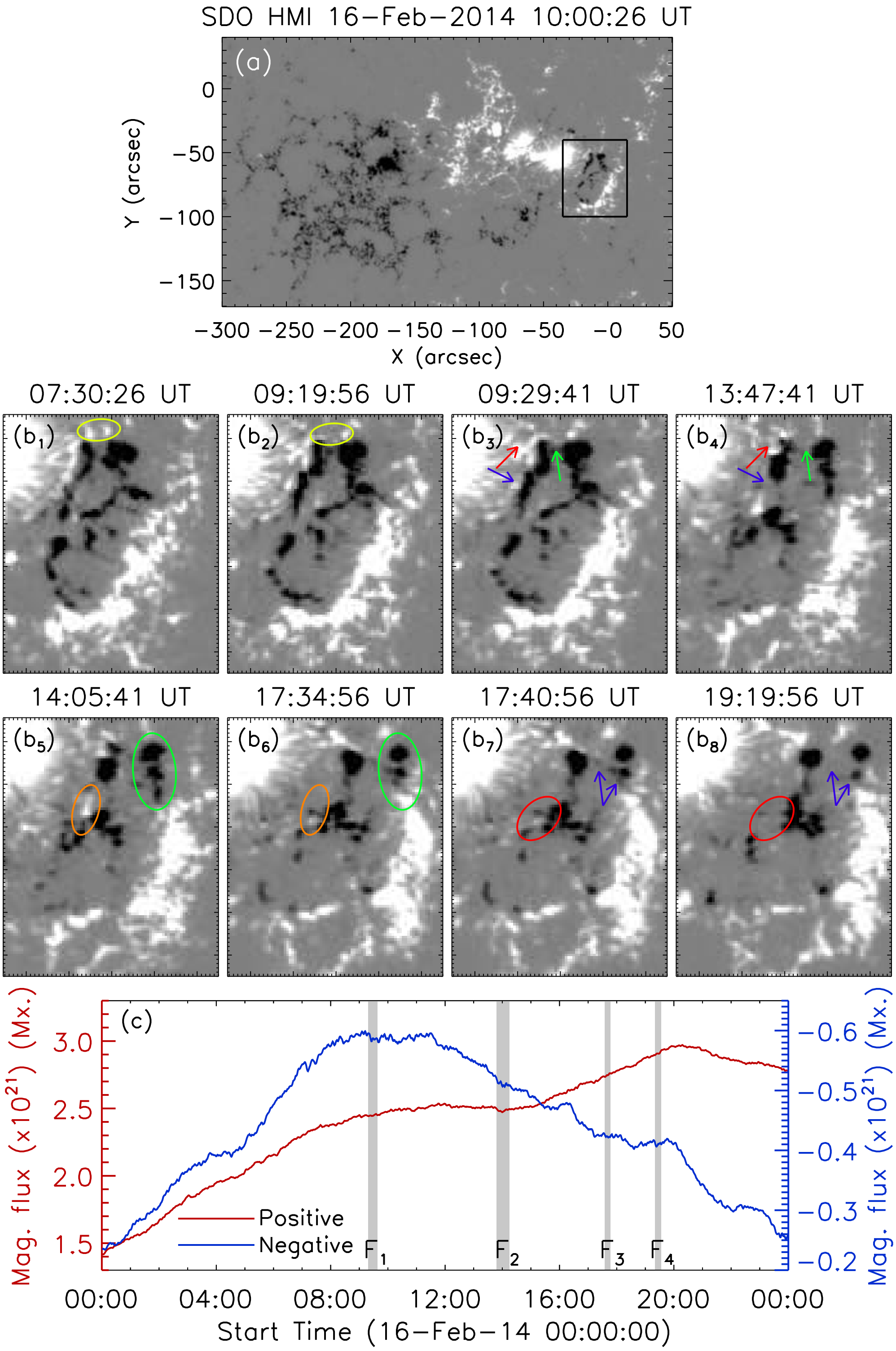

Figure 4.13: Panel (a): LOS magnetogram of the active region NOAA 11977 where the magnetic atoll region is enclosed within the black box. Panels (b_1)–(b_8): Selective LOS magnetograms of the atoll region displaying several instances of flux cancellation. We have indicated few of such flux cancellation by arrows and ovals of different colours in different panels. Panel (c): Evolution of magnetic flux in the magnetic atoll region indicated in panel (a). The shaded intervals in panel (c) indicate the durations of flares occurred from the magnetic atoll region.

The flux profiles suggest that in the first part of 2014 February 16, the flaring region (enclosed by the black box in Figure 4.13(a)), underwent a rapid increase of negative flux beside relatively moderate positive flux enhancement (see 00:00 UT – 08:00 UT in Figure 4.13(c)) suggesting the rapid development of the atoll region and the associated diffused brightening region. The first flare (F_1) initiated when negative flux reached to its peak; following which, negative flux from the region remained relatively unchanged for ≈3 hours and then continuously decayed till ≈19:30 UT. After this time, negative flux maintained an approximately constant level for ≈1.5 hours when the last flare from this region (F_4) took place. From ≈20:00 UT, negative flux primarily decayed characterizing the decay of the overall diffused brightening region. On the other hand, positive flux within the atoll region displayed a stepwise enhancement till ≈20:00 UT after which it decayed slowly till the end of the period of our calculation.

4.2.3 Morphological evolution of quasi-circular ribbon flares

All the four flares originating from the oval-shaped diffused brightening region initiated with the activation and eruption of the filaments that developed over the filament channel along the PIL at the northern boundary of the diffused brightening region (Figure 4.10(j)). Further, all the four flares were characterized by the onset of quasi-circular ribbon brightening along the boundary of the diffused brightening region (Figure 4.11). The quasi-circular ribbon was the most prominent and extended during F_1 of GOES class M1.1, which progressively decreased during the subsequent flares (i.e., F_2–F_4; see, Section 4.2.2 and Figure 4.11). Despite the difference in the extent of the quasi-circular ribbons, all the four flares displayed similarities in their onset and evolutions. Importantly, the F_2–F_4 events evolved with a complete blow-out type eruption of filamentary material from the diffused brightening region while such catastrophic eruptive features were not observed during F_1. In this section, we focus on the detailed morphological evolution of F_1 and F_2 flares.

Filament eruption and quasi-circular ribbon during F_1

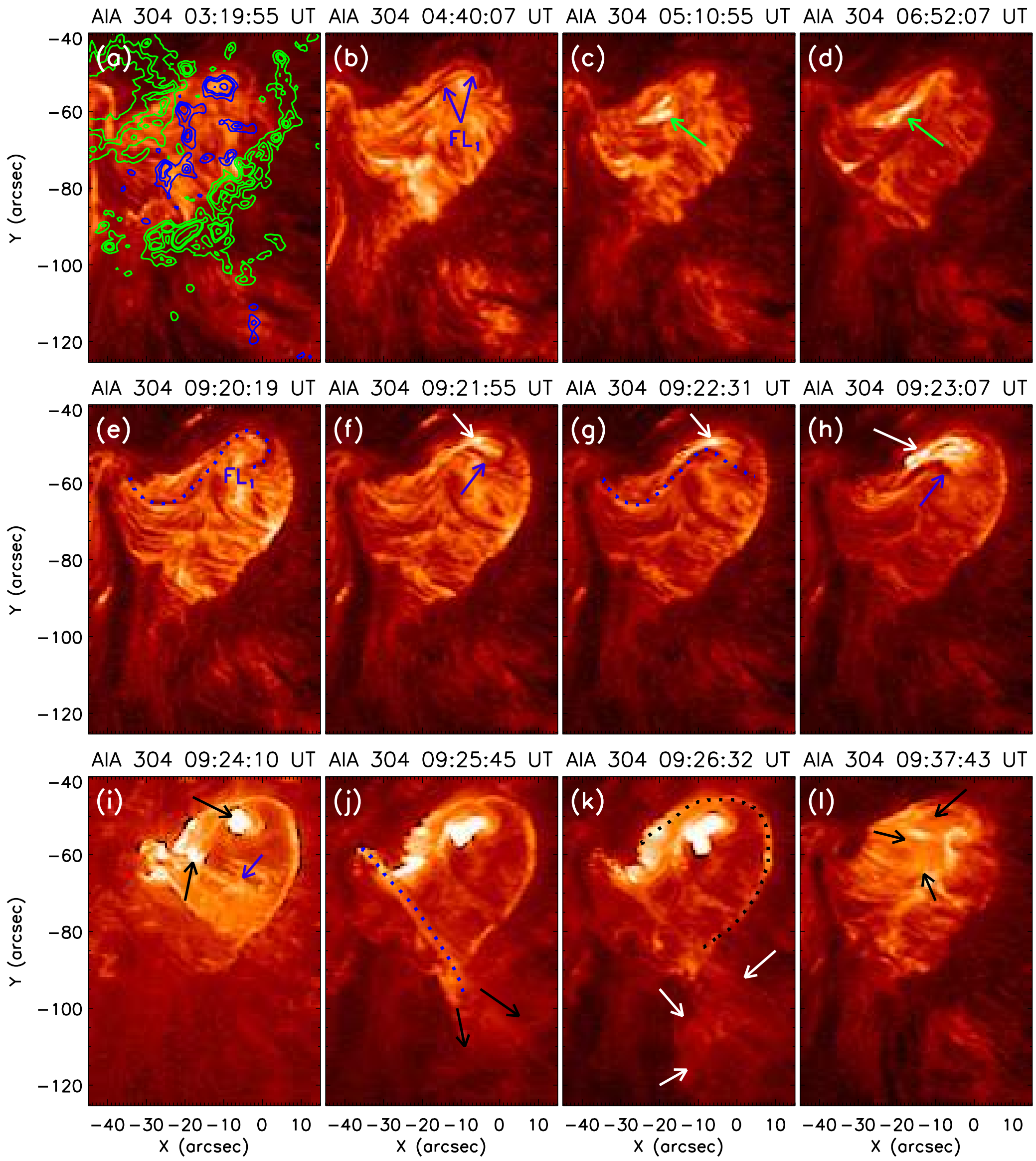

Figure 4.14: Representative AIA 304 Å images depicting filament eruption and associated M1.1 flare. The two blue arrows indicate a filament which is referred to as 'FL_1'. The green arrows in panels (c) and (d) indicate small-scale brightenings observed at the location of the filament. In panel (e), we outline the 'S' shaped filament by dotted curve. The filament during its initial eruption phase is shown by blue arrows in panels (f) and (h) and blue dotted line in panel (g). The white arrows in panels (c)–(h) indicate initial flare brightening beneath the northern end of the erupting filament. The final stage of filament eruption from the active region is outlined by the blue arrow in panel 9i) and blue dotted curve in panel (j). The black arrows in panel (e) indicate parallel flare brightening during the impulsive phase of the flare. The black arrows in panel (j) and white arrows in panel (k) indicate erupting plasma. The black dotted curve in panel (k) indicate the quasi-circular ribbon. Co-temporal LOS HMI magnetogram contours at levels ±[300, 500, 1000] G are plotted in panel (a). Green and blue contours refer to positive and negative polarity, respectively.

In order to investigate the detailed evolution of the M1.1 flare (i.e., the F_1 event) and associated eruption of the filament, we plot a series of AIA 304 Å images of the diffused brightening region (Figure 4.14). These images suggest that the impression of the filament at the northern boundary of the diffused brightening region was first identified at around ≈02:30 UT (Section 4.2.1 and Figure 4.10). The filament is indicated by the blue arrows in Figure 4.14(b); referred as FL_1 henceforth. A comparison of AIA 304 Å image with the co-temporal LOS magnetograms in Figure 4.14(a) immediately confirms that the filament was situated along the PIL between the positive polarity sunspot and the dispersed negative magnetic field regions. During the extended period prior to the activation of the filament, we observed a series of localized small-scale brightenings associated with it (indicated by the green arrows in Figures 4.14(c) and (d)). The filament became most prominent at ≈09:20 UT (indicated by the blue dotted curve in Figure 4.14(e)) which was soon followed by a subtle enhancement in the brightness at the northern leg of the filament suggesting the earliest signatures of its activation at ≈09:21 UT (indicated by the white arrow in Figure 4.14(f)). The activation of the filament was immediately followed by eruption from its northern end (indicated by the blue arrow in Figure 4.14(f)). The enhanced brightening advanced southward (cf. the white arrowheads in Figures 4.14(d) and (c)) as the erupting front of the filament induced a zipping-like upward erupting motion toward the southern part of the filament also. The southward induced eruption of the filament is further outlined by the blue dotted curve in Figure 4.14(g) and indicated by the blue arrows in Figures 4.14(h) and (i). The eruption of the filament was characterized by two localized spot-like bright structures formed at both sides of the filament (indicated by the black arrows in Figure 4.14(i)) at around 09:24 UT, which resembles with 'standard flare ribbons' originating at highly sheared bipolar regions. At the same time, a circular ribbon brightening appeared along the boundary of the diffused brightening region. After ≈09:25 UT, the filamentary structure (FL_1) appeared as a straight, long structure with one end still attached to its initial location (outlined by the blue dotted curve in Figure 4.14(j)). Interestingly, during this time, it was observed as a bright structure suggesting strong heating of the filamentary materials during the flaring process. The open end of the filamentary structure was associated with plasma eruption after ≈09:25 UT. We have indicated the direction of the erupting plasma by the arrows in Figure 4.14(j). Notably, both the parallel and circular ribbon brightening increased up to ≈09:27 UT (the circular ribbon brightening is outlined by the black dotted curve in Figure 4.14(g)) after which, flare brightenings from the AR slowly decreased while eruption continued (indicated by the white arrows in Figure 4.14(k)). After ≈09:32 UT, a set of post-flare arcade developed at the location of the initial filament (indicated by black arrows in Figure 4.14(l)) which sustained till ≈09:42 UT.

Filament eruption and shortened quasi-circular ribbon during F_2

During the evolution of the flare F_1, the filament situated at the northern boundary of the diffused brightening region, i.e., FL_1, underwent partial eruption. However, the corresponding PIL showed the presence of a filament channel throughout the lifetime of the diffused brightening region. Interestingly, before the initiation of the flare F_2, we observed signatures of a second filament (henceforth referred as FL_2) near the location of the first filament, i.e., FL_1. In Figure 4.15(a), we have indicated FL_1 by a blue dotted curve and FL_2 by a green arrow. Similar to the pre-flare phase prior to F_1, we observed localized, small-scale brightenings during the pre-flare phase of F_2 also (indicated by the yellow arrows in Figures 4.15(a) and (b)). As the episodes of localized brightenings continued, the filament FL_1 gradually became more prominent with time (indicated by the blue arrow in Figure 4.15(b)). Few minutes prior to the onset of F_2, the filament FL_2 evolved rapidly and both the filaments got intertwined to each other, constituting a double-decker filament system. The two filaments in the double-decker system are indicated by two dotted curves in Figure 4.15(c). Notably, this double-decker system is confirmed by the presence of two intertwined flux ropes (Section 4.2.4). Here, it worth mentioning that the north-western end of FL_2 was associated with narrow collimated plasma eruption even before the flare was initiated (indicated by the yellow arrow in Figure 4.15(c)). Onset of the flare F_2 took place as the filament FL_1 went through a complete eruption at ≈13:51 UT. The erupting FL_1 is outlined by a blue dotted curve in Figure 4.15(e). At the same time, a part of the western boundary of the diffused brightening region became very bright implying the formation of a circular

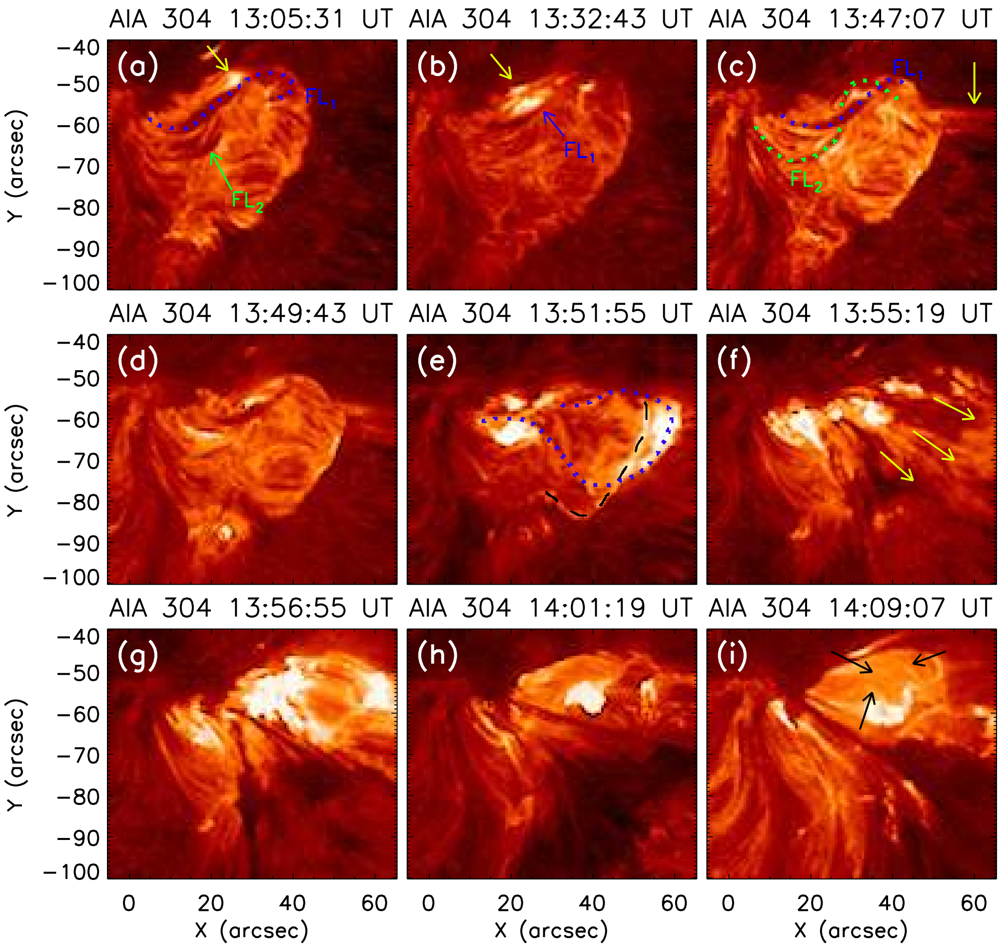

Figure 4.15: Representative AIA 304 Å images depicting the eruption of the filament and associated C3.4 flare. The filament FL_1 is indicated by the blue dotted curve in panel (a) and blue arrow in panel (b). A second filament ('FL_2) is indicated by the green arrow in panel (a). The yellow arrows in panels (a) and (b) indicate small-scale brightenings at the location of the filaments during the pre-flare phase. The blue and green dotted lines in panel (c) indicate the double-decker flux rope configuration formed by FL_1 and FL_2. The yellow arrow in panel (c) indicate jet-like plasma ejection prior to the onset of the flare. The blue dotted curve in panel (e) indicate erupting filament while the black dashed curve in the same panel indicate a quasi-circular ribbon during the F_2 flare. The yellow arrows in panel (f) indicate the direction of the erupting plasma during the flare. The black arrows in panel (i) indicate post-flare arcade.

ribbon (highlighted by the black dashed curve in Figure 4.15(e)). Following the eruption of FL_1, the AR became partially masked by the cool erupting plasma (the direction of erupting plasma is indicated by yellow arrows in Figure 4.15(f)). After ≈14:06 UT, a post-flare arcade developed in the flaring region (indicated by black arrows in Figure 4.15(i)) which suggests the flare progressed to the gradual phase.

Table 4.2: Summary of the parameters for assessing the quality of NLFFF extrapolation

Time of extrapolation	$< \lvert f_i \rvert >$	θ_J
09:22 UT	6.79×10^{-4}	8.35°
13:46 UT	7.26×10^{-4}	8.24°
17:34 UT	6.93×10^{-4}	7.88°
18:58 UT	6.58×10^{-4}	7.59°

4.2.4 Coronal Magnetic Field Modeling

Extrapolation set up

In order to investigate the coronal magnetic configurations prior to the onset of the quasi-circular ribbon flares, we employed optimization based NLFFF extrapolation method (See Section 2.3.2) with a particular focus to the magnetic atoll (i.e., flaring) region. As the boundary condition, we used vector magnetograms from the 'hmi.sharp_cea_720s' series at four times: 09:22 UT (prior to F_1; Figure 4.16), 13:46 UT (prior to F_2; Figure 4.17), 17:34 UT (prior to F_3; Figure 4.18(a)–(d1)) and 18:58 UT (prior to F_4; Figure 4.18(e)–(h1)) on 2014 February 16. In all the four instances of coronal magnetic field extrapolation conducted in this work, we used the following values of the free parameters (Section 2.3.2):

$\nu = 0.01$; $\quad w_{los} = 1$; $\quad w_{trans} = \frac{B_{trans}}{max(B_{trans})}$;

$\mu_1 = \mu_2 = 1$; $\quad \mu_3 = 0.001$; $\quad \mu_4 = 0.01$.

In Table 4.2, we have listed the values of the residual errors corresponding to all the four extrapolations, which can be used as the assessment of the NLFFF solutions. Here we clarify that, although the extrapolations were conducted over the entire AR (Figure 4.13(a)), in this section and in Figures 4.16–4.18, we have only shown and discussed the modeled coronal configuration associated with the atoll region.

Pre-flare coronal magnetic connectivities

NLFFF-modeled coronal field lines at 09:22 UT readily indicates the presence of a flux rope at the location of FL_1. The flux rope is shown by the blue lines in Figures 4.16(a) and (d). For a better understanding of the structure and morphology of the flux rope, we have further shown only the flux rope from top and side views in Figure 4.16(b) and (c), respectively, where different field lines are plotted in dif-

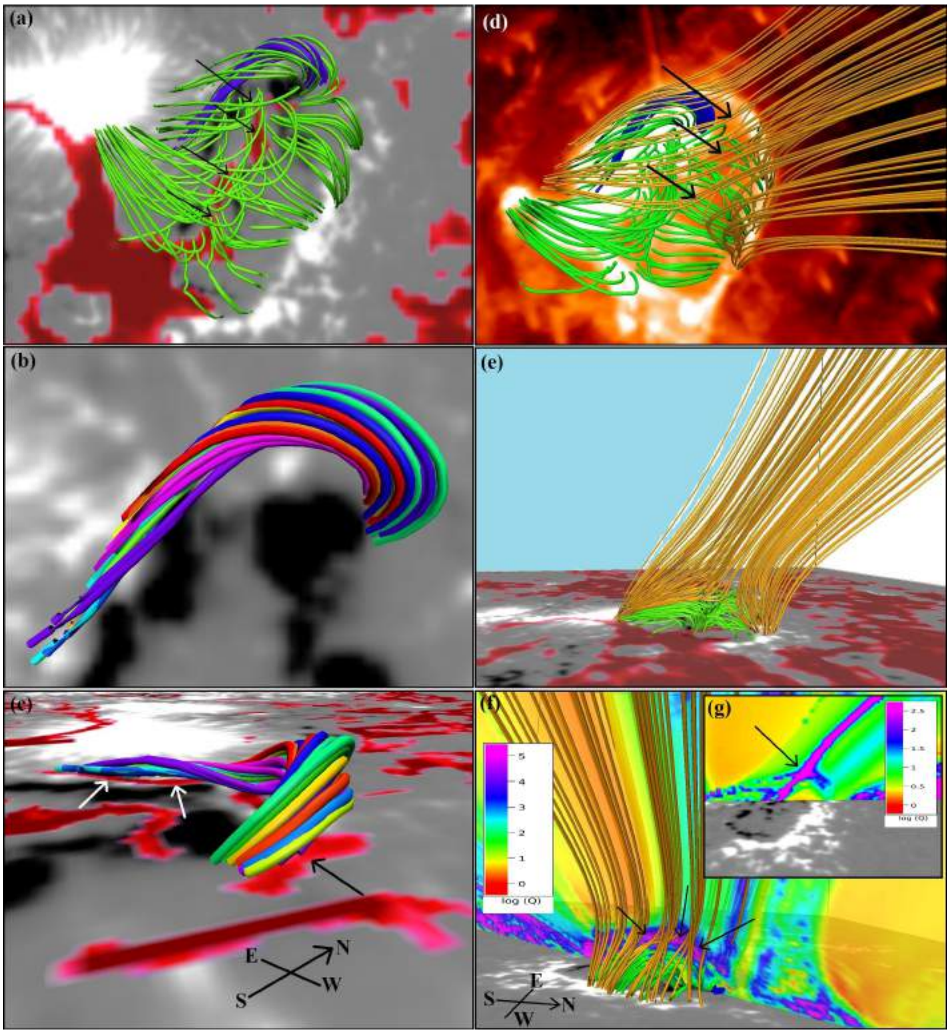

Figure 4.16: Non-linear Force Free Field extrapolation results of the magnetic atoll region prior to the flare F_1 (at 09:22 UT) showing the presence of a flux rope and closed magnetic loops within the region (green lines) besides large open field lines originating from the outer magnetic patches of the atoll region (yellow lines). To understand the structures of the flux ropes clearly, we provide zoomed views of the flux rope with multiple colors in panels (b) (top view) and (c) (side view). The red patches over the background HMI magnetogram in panels (a), (c), and (e) represent regions with high Q-value ($log(Q)$ > 2). The arrows in panel (c) highlight the close association between the legs of the flux rope and photospheric regions with high Q-value. The Y-Z tilted vertical surface in panel (f) drawn along the yellow lines represent the distribution of Q-values. In panel (g), the distribution of Q is shown along a plane passing across the magnetic atoll region i.e., along X-Z plane. The arrow in panel (g) indicate an 'X'-shape formed by the regions of high Q. For reference, we have included the color-table showing the distribution of $log(Q)$ values in the box in panels (f) and (g). Top boundary in panels (a), (b), (d) as well as the sky-colored boundary in panel (e) represent north. We have plotted a compass for representing the direction in panels (c) and (f). An AIA 304 Å image of 09:26 UT has been plotted in the background in panel (d).

ferent colors. The flux rope was found to be enveloped by a set of highly sheared low-coronal closed loops (shown by the green lines in Figure 4.16). Notably, these low-coronal closed loops connected the outer positive polarity patches of the atoll region to the central dispersed negative polarity regions. The green lines were further surrounded by a second set of open field lines (shown by yellow color in Figures 4.16(d)–(f)) which originated from the outer positive polarity regions. It is worth mentioning that the boundary of the diffused, nearly-circular flare brightening observed during the F_1 flare apparently delineated the footpoints of the open field lines (cf. the modeled yellow lines and the background AIA 304 Å image in Figure 4.16(d)). In this way, the entire structure made of the green and yellow lines resembles a spine-fan-like configuration. Notably, although few low-lying null-points were located by trilinear method (see Section 2.3.5) close to the bottom boundary of the extrapolation volume, we could not find presence of any null-point near or within our region of interest. The lack of null point within the coronal configuration associated with the atoll region suggests that the configuration differed from the typical 3D spine-fan configuration. The laterally extended nature of the spine-like lines (indicated by the black arrows in Figures 4.16(a) and (d)) further provided evidence in this direction as it is uncharacteristic of the spine-fan configuration in null point topology. In Figure 4.16(e), we have shown the complete coronal configuration from a side angle for an overall visualization. This atypical, spine-fan-like configuration was also recognized prior to the onset of F_2 which is indicated by the black arrows in Figures 4.17(d)–(e)). Our extrapolation results further revealed that this spine-fan-like configuration decayed significantly in the spatial extent afterwards (Figures 4.18(a) and (e)) vis-à-vis changes in the corresponding photospheric magnetic field structure of the magnetic atoll region (Figures 4.11(j)–(m)).

Notably, the model field structure during the pre-flare phase of F_2 revealed two sets of twisted field lines, i.e., flux ropes, which were intertwined with each other forming a double-decker flux rope configuration (shown by blue and pink colors in Figures 4.17(a)–(c)). While the twisted field lines shown in blue were similar to the flux rope identified during the pre-flare phase of F_1 (i.e., FL_1), the apparent twist associated with it was found to be more than the previous flux rope (see

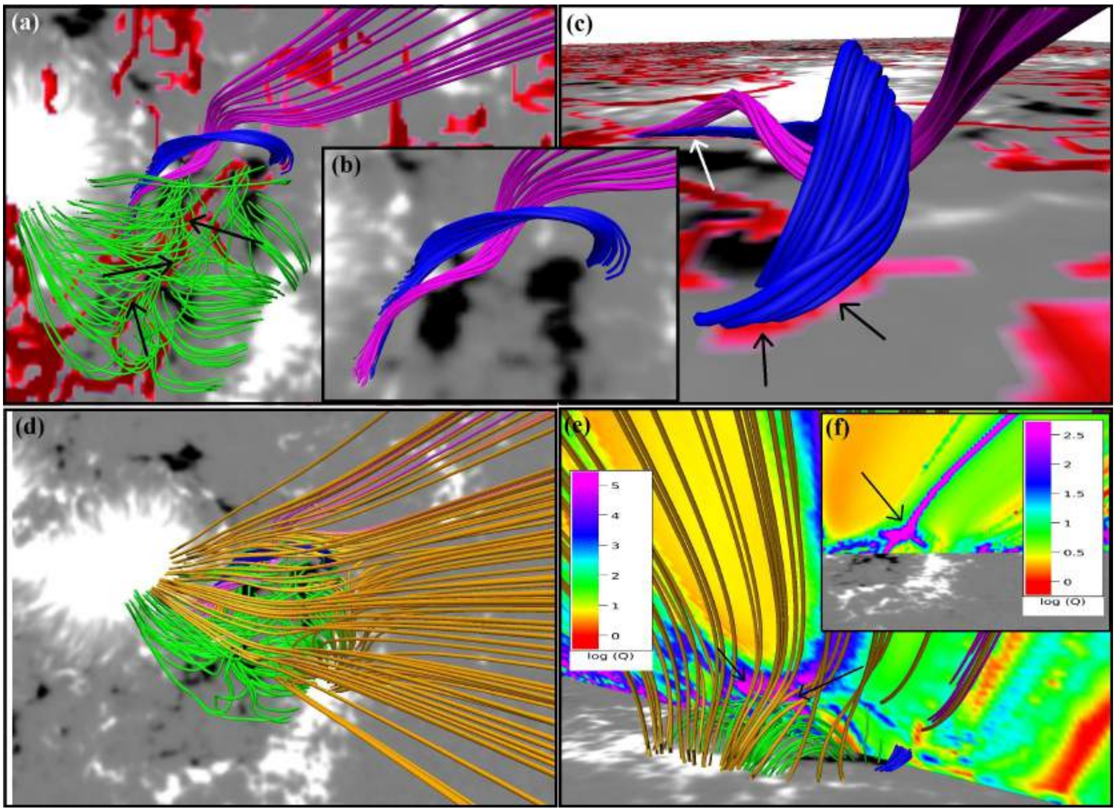

Figure 4.17: Non-linear Force Free Field extrapolation results on the magnetic atoll region prior to the F_2 flare (at 13:46 UT) showing the presence of a flux rope (blue lines) and closed magnetic loops within the region (green lines) as well as large open field lines originating from magnetic patches of the atoll region (yellow lines). A set of twisted field lines having origin in the south-western end of the polarity inversion line and extending north-westward as a part of open field lines i.e., 'open flux rope' are shown in pink color. In panels (b) and (c), only the two flux ropes are shown from top and side views, respectively. The red patches over the background HMI magnetogram in panels (a) and (c) represent regions with high Q-value ($log(Q) > 2$). The arrows in panel (c) highlight the close association between the legs of the flux ropes and photospheric regions with high Q. Panels (e) and (f) are same as Figures 4.16(f) and (g), respectively. Top boundary in panels (a), (b) and (d) represent north. Top boundary in panel (c) represents east.

Table 4.3). The other set of twisted field lines (shown in pink color) was rather interesting as the northern end, the field lines of the flux rope become a part of the open lines instead of terminating on the photosphere (cf. the open end of the pink lines in Figures 4.17(a) and the open yellow lines in Figure 4.17(d)). We further note that, the location of the pink lines was same as the apparent location of FL_2 (cf. Figures 4.17(b) and 4.15(c)). The double-decker flux rope configuration is shown from top and side views in Figures 4.17(b) and (c), for a better visualization. In Figure 4.18, we have shown the modeled magnetic configuration above the

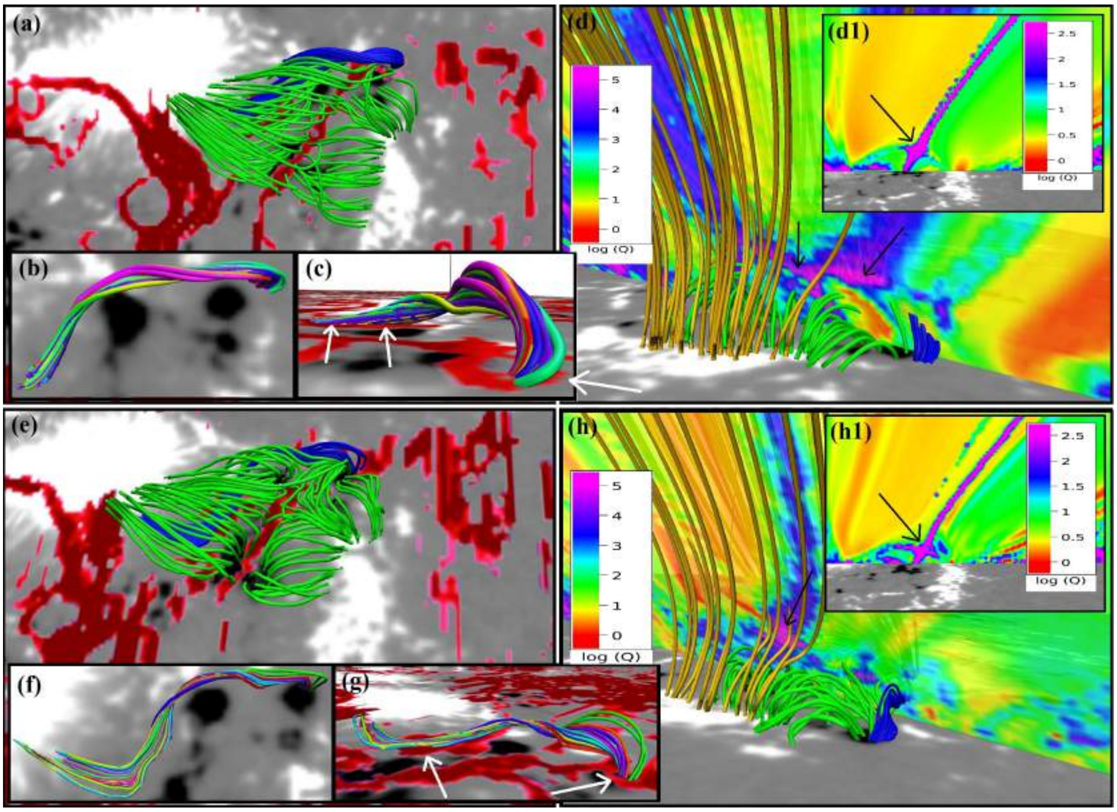

Figure 4.18: NLFFF extrapolation results showing the coronal configurations prior to the F_3 (at 17:34 UT; panels (a)–(d1)) and F_4 flare (at 18:58 UT; panels (e)–(h1). Panels (a) and (e) show the flux ropes (in blue color) and the inner fan-like lines (in green color) from top view. The flux ropes prior to the F_3 and F_4 flares are exclusively shown in multiple colors from the top view in panels (b) and (f), respectively, and from side views in panels (c) and (g), respectively. Panels (d)–(d1) and (h)–(h1) are same as Figures 4.16(f)–(g), respectively. The arrows in panels (c) and (g) highlight the close association between the legs of the flux ropes and photospheric regions with high Q.

magnetic atoll region prior to the onset of the F_3 (Figures 4.18(a)–(d1)) and F_4 (Figures 4.18(e)–(h1)) flares. NLFFF extrapolation results suggested that, similar to F_1, prior to the F_3 and F_4 flares also, single flux rope structures are identified from the modeled coronal magnetic field which are shown from top views in Figures 4.18(a), (b) and 4.18(e), (f), respectively, and side views in Figures 4.18(c) and (g), respectively.

Distribution of Squashing factor (Q)

NLFFF modeling revealed a complex coronal magnetic configuration prior to the successive four flares where the overall coronal structures despite resembling a fan-spine-like configuration, lacked a coronal null-point. In order to further investigate this peculiar fan-spine-like configuration, we computed QSL-maps within the extrapolated region. The photospheric regions associated with high-Q ($log(Q) > 2$) regions are shown by the red colored patches in the relevant panels in Figures 4.16–4.18. From Figures 4.16(a), 4.17(a), 4.18(a) and (e), it becomes evident that the high-Q regions within the magnetic atoll region were situated along the elongated footpoint locations of the green lines (indicated by the black arrows in Figures 4.16(a) and 4.17(a)) which further provides substantial evidence for the laterally extended nature of the spine-like lines. Notably, the footpoint regions of the flux ropes were also found to be associated with high Q-values which can be inferred from the red colored patches indicated by the arrows in Figures 4.16(c), 4.17(c), 4.18(c) and (g).

To understand the variation of Q-values along the laterally extended spine-like lines, we drew tilted vertical planes passing through the outer spine-like lines (i.e., the yellow lines shown in Figures 4.16(d)–(e), 4.17(d)); distribution of Q along which are shown in Figure 4.16(f), 4.17(e) and 4.18(d) and (h). These Q-maps clearly reveals that immediately over the inner fan-like lines (shown by green color), the Q-values approached maximum ($log(Q) \gtrsim 5$) signifying drastic change in the magnetic connectivity between the green and the yellow lines. The extended arc-shaped high Q region (shown in purple color and the arrows in Figures 4.16(f), 4.17(e) 4.18(d) and (h)) in the absence of coronal nulls, suggests the presence of an HFT between the green and yellow lines. In Figure 4.16(g), we plot Q-values along a plane that crosses perpendicularly the tilted plane of Figure 4.16(f), i.e., it shows the variation of Q across the spine-fan-like configuration. From this panel, we readily observe the 'X'-shape formed by high Q-values (indicated by the black arrow) which further confirms the presence of the HFT in the coronal magnetic configuration above the atoll region. Notably, similar configurations are also found prior to the onset of the subsequent flares (indicated by the arrow in Figures 4.17(f), 4.18(d1) and (h1)); however, with the decay of the magnetic atoll region, the extended coronal region of high Q-values over the inner fan-like lines (indicated by arrows in Figures 4.16(f), 4.17(e) and 4.18(d)), gradually reduced and concentrated to a point-like structure prior to the onset of the F_4 flare (indicated by the black arrow in Figure 4.18(h)).

Table 4.3: Summary of the twist number $|T_w|$ and critical height (h_{crit}) for magnetic decay index $n = 1.0$ and 1.5, prior to the four flares from the magnetic atoll region

Flare Id.	$\|T_w\|$	$h_{crit}(n = 1.0)$ (Mm)	$h_{crit}(n = 1.5)$ (Mm)	Maximum height of the flux rope (Mm)
F_1	$\approx$0.93$\pm$0.11	$\approx$15	$\approx$25	$\approx$4
F_2	$\approx$1.12$\pm$0.18	$\approx$19	$\approx$30	$\approx$4
F_3	$\approx$1.20$\pm$0.20	$\approx$17	$\approx$28	$\approx$5
F_4	$\approx$1.22$\pm$0.20	$\approx$17	$\approx$27	$\approx$4

Twist number and magnetic decay index

GONG Hα and AIA 304 Å images provided observational evidence of filaments prior to each of the quasi-circular ribbon flares, which underwent eruptions during the evolutions of the flares (Figures 4.12, 4.14, 4.15). NLFFF extrapolation results further confirmed the presence of flux ropes at the apparent locations of the filaments (Figures 4.16, 4.17, 4.18). However, both the imaging and modeling analysis qualitatively suggested that twist of all flux ropes increased successively from F_1 to F_4. Therefore, in order to have a quantitative assessment of the twists of the flux ropes, we compared distribution of twist number (T_w; Berger & Prior, 2006, see also Section 2.3.4) associated with the location of the flux ropes within the extrapolation volume. The average twist numbers (T_w) associated with the flux ropes corresponding to consecutive flares prior to their onset (F_1–F_4) are provided in Table 4.3. Analysis of T_w-maps quantitatively confirmed that T_w increased successively from F_1 to F_4. While T_w prior to F_1 was only $\approx$0.93, it increased to $\approx$1.22 prior to the onset of F_4.

To understand how the horizontal magnetic field changed with height over the flux ropes, we calculated magnetic decay index (n). For this purpose, we considered the PILs over which the flux ropes were situated and computed average decay index along vertical surfaces above it. Variation of magnetic decay index with height, averaged over the lengths of the PILs are shown in Figure 4.19, where the critical heights at which the value of decay index reached $n = 1.0$ ($h_{crit}(n = 1.0)$) and $n = 1.5$ ($h_{crit}(n = 1.5)$) are indicated by the dotted and dashed vertical lines. In Table 4.3, we have summarized the values of h_{crit} and approximate maximum heights of the flux ropes before the onset of all the four flares. Our calculations

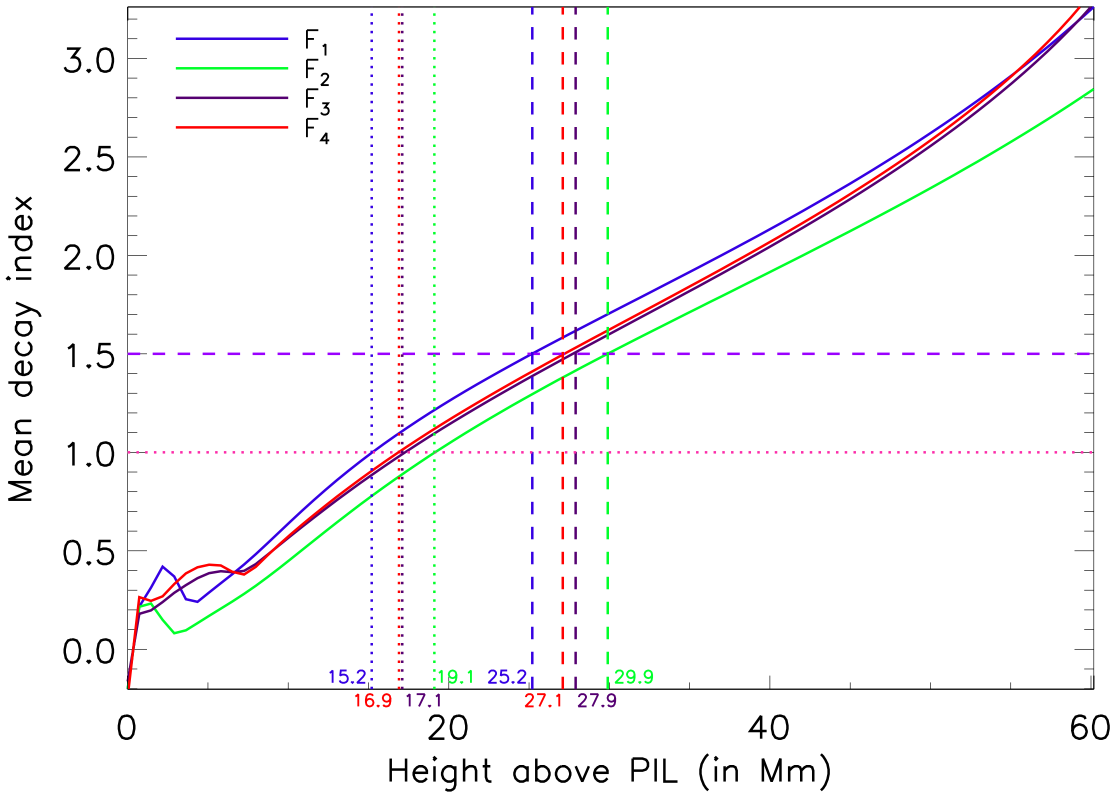

Figure 4.19: Plot of decay index (n) above the PIL as a function of height, prior to the four events. The values of decay index $n = 1.0$ and 1.5 are indicated by the pink dotted and purple dashed horizontal lines. The critical heights corresponding to the values $n = 1.0$ and 1.5 prior to the flares are represented by the dotted and dashed vertical lines, respectively, and noted at the bottom of the plot. Colors of these vertical lines and the values of critical heights corresponding to the events are synchronized with the colors of the decay index plots.

suggest that prior to the F_1 flare, h_{crit} was ≈25 Mm while it slightly increased to ≈27–30 Mm prior to the subsequent flares. However, the maximum heights of the flux ropes prior to the onset of the flares were found to be only ≈4–5 Mm (Table 4.3) which were much less compared to the critical heights.

4.2.5 Discussions

In this chapter, we present a detailed analysis of four successive flares from NOAA 11977 which were associated with some extent of quasi-circular ribbons. These flares (denoted as F_1, F_2, F_3, F_4; in the order of their occurrence) originated on a single day within a period of ≈11 hour (see Table 4.1) from a complex photospheric configuration. The coronal configuration of the flaring region was characterized by an elongated fan-spine-like structure that involved a hyperbolic flux tube (HFT). In EUV images, we identified the fan-spine-like configuration in the form of a diffused EUV brightening region spread within a circular base prior to F_1. In the course of the four flares, the length of the elongated fan-spine-like structure gradually decayed, resulting in the decomposition and simplification of the prominent quasi-circular brightening.

The interesting coronal configuration that facilitated the four morphologically similar flares, was developed over several hours prior to the onset of the flare F_1. Comparison of EUV images with co-temporal magnetograms revealed that the development the structure was eventually correlated with the formation of the magnetic atoll region (Figure 4.10). Further, prior to the F_1 event, the overall configuration composed of negative polarity patches (indicated by the red and blue arrows in Figure 4.10(f)) and the western positive polarity region (indicated by the pink arrows in Figure 4.10(f)) can be characterized by a geometric stadium shape[1] with the longitudinal dimension lying along northwest-southeast (NW-SE) direction (Figure 4.10(f)). In general, the overall photospheric structure of the flaring region i.e., the magnetic atoll region, consisted of a longitudinally stretched magnetic patch bounded by regions of opposite polarity on both sides. Coronal magnetic field reconstruction revealed a complex configuration characterized by open field lines originating from the positive polarity regions enclosing an extended fan-like structure (Figures 4.16–4.18). In this way, the overall coronal magnetic configuration resembled the topology of pseudo-streamers (Wang et al., 2007; Titov et al., 2011, 2012; Masson et al., 2014) albeit in a much smaller spatial scale. Notably, since pseudo-streamers connect coronal holes of the same polarity, involving even number of PILs, two-dimensional depiction of the cross-section of pseudo-streamers indicate the presence of X-shaped high Q-structures (Titov et al., 2012), which may represent true 3D null-points or topological structures such as separators connecting multiple null-points, HFTs etc. (Gibson et al., 2017). In the absence of any null-point, the coronal magnetic configuration, derived from our analysis, can be physically well interpreted by considering a small-scale pseudo-streamer involving an HFT.

The presence of the HFT in the flaring region was further confirmed by their

[1] http://mathworld.wolfram.com/Stadium.html

cross-sectional X-shaped high Q-regions (Figures 4.16(g), 4.17(f), 4.18(d1) and (h1)). The high Q values of these regions imply high gradient of magnetic field (i.e., QSLs) within the diffused brightening region. Intense current sheets are formed naturally around QSLs as gradient in magnetic field contributes toward the generation of current (Lau & Finn, 1990; Priest & Titov, 1996; Aulanier et al., 2005; Démoulin, 2007). Using MHD simulations, formation of electric current has also been demonstrated in magnetic flux ropes, coronal sigmoids, beneath an erupting flux rope etc. (see, e.g., Wilmot-Smith et al., 2009; Pariat et al., 2009b; Aulanier et al., 2009). Therefore, we interpret the diffused EUV brightness of the flaring region in terms of joule heating due to the dissipation of the currents associated with the QSL formed by the inner fan-like lines.

As clearly revealed in the AIA images, the quasi-circular ribbon brightening during the four flares, formed along the boundary of the dome shaped diffused brightening region (DBR). Further, all the four flares initiated as a filament, residing close to the northern edge of the DBR underwent activation and eruption (Figures 4.12, 4.14 and 4.15). Correspondingly, NLFFF extrapolation results revealed the presence of flux ropes within the fan-spine-like configuration close to its northern boundary (Figures 4.16–4.18). This provides a conclusive evidence that the triggering of the quasi-circular ribbon flares were caused by the interaction of the erupting flux rope with the fan-like separatrix surface. Using MHD simulations, it has been established that stressed QSL regions can give rise to slipping reconnections even without the presence of a coronal null-point and for sufficiently thin QSLs and high resistivities, the field line footpoints can slip-run at super-Alfvénic speeds along the intersection of the QSLs (slip running reconnection; Aulanier et al., 2006). While studying a circular ribbon in association with a coronal null-point topology, Masson et al. (2009) observed that slip-running reconnection and null-point reconnection can occur sequentially. They also found that Q is a highly effective parameter which determines which mode of reconnection will occur in a null-point topology: cut-paste type null-point reconnetion occurs when the value of Q reaches infinity and slipping (or slip-running) reconnection occurs for lesser values of Q. As observational signature of slipping/slip-running reconnection, circular ribbon and remote brightening can be highlighted (Masson et al., 2009); while the null-point reconnection usually gives rise to collimated eruptions i.e., coronal jets or Hα surges (Pariat et al., 2009a, 2010).

In this context, the association of flux ropes and QSLs is worth mentioning. In all the four cases (Figures 4.16(c), 4.17(c), 4.18(c) and (g)), we observed the legs of the flux ropes to be associated with high photospheric Q-values. High Q-values at the boundaries of flux ropes essentially associated with two different sets of magnetic field lines: one set forming the flux rope and the other set forming the relatively potential, ambient magnetic field (see e.g., Savcheva et al., 2012; Zhao et al., 2016; Janvier et al., 2016; Guo et al., 2019).

Activations of the filaments prior to the onset of the four flares were characterized by localized brightenings beneath the filaments (Figure 4.14 and 4.15). Further, we identified several instances of flux cancellation from the PIL region during pre-flare phases of all the flares (Figure 4.13). We interpret these findings as the observational signatures of the tether-cutting model of solar eruptions (Moore & Roumeliotis, 1992; Moore et al., 2001). We also explored the possibility of torus and kink instabilities as the triggering mechanism, by computing the decay index and twist numbers. Our analysis suggests that the critical decay height for n =1.5 above the PIL of the flux rope prior to all the four flares remained consistent within the heights of ≈25–30 Mm (Table 4.3). Statistical surveys concerning the torus instability as the triggering mechanism for eruptive flares by Wang et al. (2017b); Baumgartner et al. (2018) revealed the critical decay height to lie within the ranges of ≈36±17 Mm and 21±10 Mm. Therefore, the results of the magnetic decay index analysis suggest the decay height to be in well agreement with the statistically established values, pointing toward a favorable role played by torus instability. However, it should be mentioned that calculation of critical decay height by considering the average decay index over the PIL is rather a simplistic approach. Detailed studies devoted to the analysis of decay index (see e.g., Zuccarello et al., 2014, 2017; Myshyakov & Tsvetkov, 2020) have shown that a flux rope eruption can take place even when the critical height (h_{crit}) becomes sufficiently low in a few discrete locations over the flux rope. Further, theoretical studies have shown that the critical height strongly depend on the magnetic topology (Kliem et al., 2014). Notably, in view of the fan-spine-like structure, the coronal magnetic configuration reported in this study presented a much complex configuration compared to the general cases of sheared bipolar configurations. Rapid decay of magnetic field within the fan-surface is expected which in turns results in high values of magnetic decay index (see e.g., Joshi et al., 2021). Average twist numbers associated with the flux ropes were found to increase successively from ≈0.93 prior to F_1 to ≈1.22 prior to F_4 (Table 4.3). Although, the increase in twist suggest higher storage of magnetic free energy in the flux ropes, the critical value of twist number for resulting in the destabilization of the flux ropes was statistically established to be $|T_w|$ ≈2 (Duan et al., 2019). Therefore, we could not find any conclusive evidence for kink instability as the triggering mechanism for the homologous flares reported in this chapter.

Importantly, although a prominent circular ribbon developed during the M-class flare (i.e., the F_1 event), we did not observe any signature of magnetic reconnection at null-point-like configuration (i.e., jet/surge, breakout type eruption etc.). AIA 304 Å images clearly revealed the erupting filament to undergo an apparent sliding/zipping motion which initiated from its northern end and propagated toward the southern direction. We observed eruption of plasma only when the sliding end of the filament eventually reached the southern boundary of the diffused brightening region. These observational features led us to conclude that the occurrence of the circular ribbon during the F_1 flare was the manifestation of predominantly QSL-reconnection, rather than the interchange-type reconnection between the inner and outer fan-like lines. Contrary to the M1.1 flare, all the subsequent flares (F_2–F_4) underwent complete eruption of the filaments, clearly implying reconnection at the HFT. In this context, we remember that twist number associated with the flux ropes successively increased from F_1 to F_4. Further, we observed almost consistent cancellation of negative flux within the magnetic atoll region following the onset of F_1 flare. While the increasing twist number suggests storage of more free energy in the flux ropes, the flux cancellation events signify decrease in the constraining energy of the fan-spine configuration following the F_1 flare. Therefore, we speculate that excess energy stored in the flux rope (in the form of higher twist number) and less energy stored in the constraining magnetic field resulted in the complete destruction of the fan-spine-like configuration during the subsequent C-class flares; while, during the M1.1 flare, less twisted flux rope did not have enough energy to trigger interchange type reconnection at the HFT.

4.3 Concluding remarks

In this chapter, we explore different aspects of magnetic reconnection in 3D by thoroughly analyzing the homologous, eruptive,quasi-circular ribbon flares originating from a complex photospheric magnetic configuration which was characterized by elongated parasitic negative polarity regions surrounded by positive polarity regions (i.e., a magnetic atoll region). The corresponding coronal magnetic field depicted a fan-spine-like configuration that involved a hyperbolic flux tube (HFT) that lacked a coronal null point. All the four flares initiated as a flux rope developed over the PIL at the northern edge of the atoll region underwent activation and eruption within the fan dome. The localized brightenings observed from the location of the filament as well as small-scale flux cancellation from the PIL region provided supports the tether-cutting model of solar eruption. Interaction between the erupting flux rope and the fan-like-separatrix surface resulted in the circular ribbon brightening during the flares.

The overall evolution of the ribbon brightenings during the quasi-circular ribbon flares was in line with most of the previously reported cases of circular ribbon flares, i.e., onset of the parallel ribbons followed by the onset of the circular/quasi-circular ribbons. However, the coronal configuration associated with the magnetic atoll region differed from typical coronal configurations governing circular ribbons, in view of the absence of the null point. To our end, we emphasize that, the reporting of the occurrence of quasi-circular ribbon flares from complex fan-spine-like configurations including HFTs provides important addition to the existing knowledge of flaring activities originating from complex 3D magnetic structures. Further studies involving theoretical and observational analyses of similar events are essential to reach to a general understanding of the complex coronal configurations in the solar atmosphere.

Chapter 5

Reconnection in a Quadrupolar Coronal Configuration and Magnetic Confinement of Flux Ropes

5.1 Introduction

Solar ARs, which are ideal locations for storing non-potential magnetic energy, are preferable sites for solar transient phenomena i.e., flares, CMEs etc. (see review by Priest & Forbes, 2002). Since the explosive energy release during such catastrophic events occur in response to magnetic reconnection at current sheets, their locations are associated with high magnetic gradient (Schrijver, 2009). Naturally, in view of the strong magnetic gradients across the polarity inversion lines (PILs), the δ-spots where multiple, segmented umbra of opposite polarities are surrounded by a common penumbrae (Künzel, 1960), are observed to be associated with the largest solar flares (see e.g., Zirin & Liggett, 1987; Schrijver, 2007). Unsurprisingly, all the historical flaring events which were subjected to extensive studies, occurred from complex ARs involving δ-spots, e.g., NOAA 11429 (e.g., Liu et al., 2014; Wang et al., 2014; Chintzoglou et al., 2015; Syntelis et al., 2016; Patsourakos et al., 2016; Zheng et al., 2017; Yang et al., 2018; Baker et al., 2019; Zhou et al., 2019), NOAA 11158 (e.g., Schrijver et al., 2011; Sun et al., 2012; Wang et al., 2012; Liu

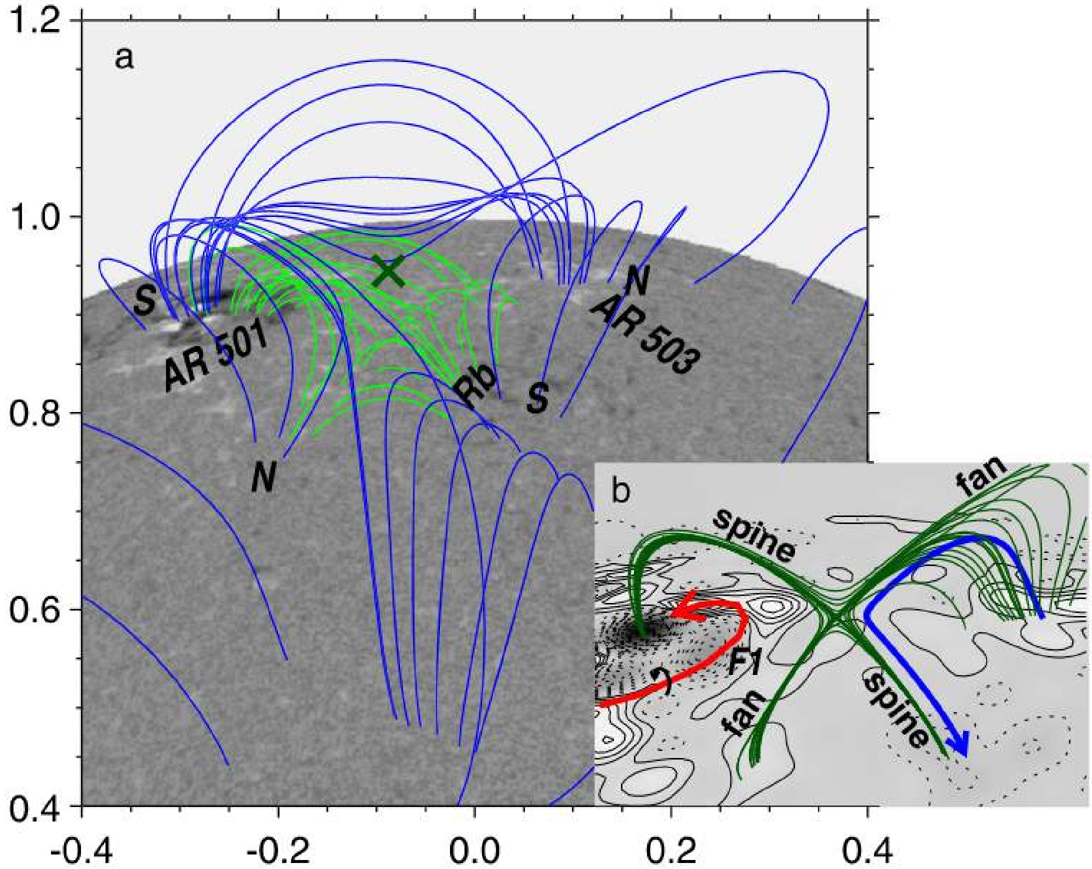

Figure 5.1: A quadrupolar magnetic configuration developed by two interacting active regions. Panel (a): Field lines in the large-scale environment of the quadrupolar coronal magnetic configuration. The magnetic null point in the configuration is denoted with the dark-green slanted cross. Panel (b): A selected set of field lines in the quadrupolar configuration passing close to the magnetic null point shown in the same scale as in panel (a). The contour levels of the radial magnetic component in panel (b) are symmetric relative to zero in steps of 31 G; dotted: −(15,46,...,728)G, continuous: +(15,46,...,139)G. The axes are in solar radii from the solar disk center. Figure is adopted from Uralov et al. (2014).

et al., 2012a; Vemareddy et al., 2012; Dalmasse et al., 2013; Tziotziou et al., 2013; Janvier et al., 2014; Kazachenko et al., 2015; Zhang et al., 2016; Lumme et al., 2019), NOAA 12673 (Chapter 6 of this thesis is dedicated to the evolution of the AR and flaring activities occurring from it), etc.

δ-sunspots are generally developed as two or more bipolar regions collide and emerge into each other (Zhongxian & Jingxiu, 1994). Merging of two bipolar ARs create the so called 'quadrupolar' magnetic regions (Toriumi & Takasao, 2017). With highly sheared PILs and excess storage of magnetic free energy, quadrupolar ARs are frequently observed to generate large flares (e.g., Mandrini et al., 2006; Schrijver et al., 2011; Joshi et al., 2016b; Lee et al., 2016; Liu et al., 2016a).

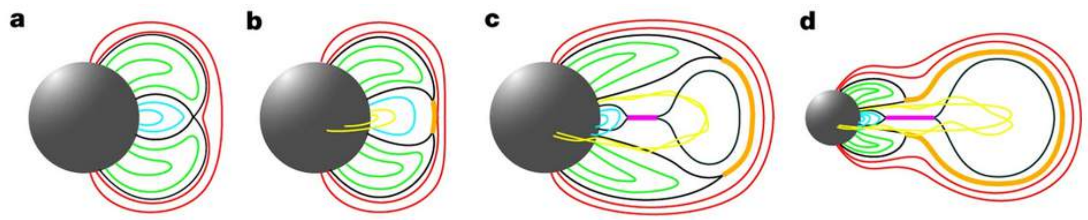

Figure 5.2: Essential steps in the breakout type CME eruption. Black field lines show separatrices (or quasi-separatrices) dividing different regions of the magnetic field (red, green, blue). Yellow field lines show the core of the filament/flux rope. Orange shading denotes the breakout current sheet, pink shading the flare current sheet. Figure is adopted from Wyper et al. (2017).

Since, quadrupolar ARs involve multiple PILs, the coronal configuration associated with such quadrupolar configurations are often characterized by the presence of a coronal null point (Longcope, 2005). In Figure 5.1, we have shown the coronal magnetic configuration associated with a typical quadrupolar AR, that involved a null point.

Presence of null point in the quadrupolar configuration forms the key ingredients of the breakout model of solar eruption (Antiochos et al., 1999; Karpen et al., 2012). The null point creates four distinct domain of the magnetic field in its neighborhood (Figure 5.2(a)): a central arcade straddling the equator (blue field lines), two arcades associated with the neutral lines i.e., side lobes (green field lines), and a overlying flux system (red lines). The four domains are separated by two separatrices (shown by the black lines). Notably, the null is situated at the intersection of the two separatrices. The relatively potential magnetic fluxes of the side lobes (i.e., the green field lines) and the overlying magnetic flux (i.e., the red lines) provide confinement to the expansion of the sheared core field (i.e., the blue flux system). Reconnection at the null weakens the confinement enabling the sheared core to expand outward that leads to the formation of the CME (Antiochos et al., 1999).

In this chapter, we discuss different aspects of quadrupolar magnetic configuration in association with the triggering of an impulsive M-class flare in NOAA 11302. The flaring region was a complex δ-type. However, despite critical dramatic evolution, the flare proceeded with a failed eruption. The present study also attempts to understand the factors involved in the confinement of the activated flux ropes.

5.2 δ-sunspot region and quadrupolar configuration

The AR under consideration, NOAA 11302, on the day of our study was located at the heliographic location ≈N15E35. In Figure 5.3, we show different photospheric and coronal aspects of the AR using multi-wavelength images from different observing instruments and NLFFF extrapolation results. The AR consisted of three separate but prominent sunspot groups which were aligned in the northeast–southwest (NE–SW) direction in a linear distribution (Figure 5.3(a)). Co-temporal magnetograms (Figure 5.3(b)) suggest that the easternmost sunspot group was of predominantly positive polarity; while, the westernmost sunspot group was mostly composed of negative flux. The bipolar central sunspot group is particularly interesting and important for this study. From the intensity contours overplotted in Figure 5.3(b), it becomes evident that the central sunspot group was composed of fragmented umbrae of opposite polarities within a single penumbra; a characteristics of the δ-type ARs (Künzel, 1960). Notably, the M-class flare and associated failed eruption reported in this chapter, originated from this sunspot group. We identified a small, faint filament in the chromospheric Hα image of the AR, one leg of which was attached to the central sunspot group (indicated by the red arrow in Figure 5.3(c)). A particularly interesting structure was revealed in the hot EUV observations e.g., AIA 94 and 131 Å channels, which appeared to be composed of a few localized coronal loops that connected opposite polarity flux regions of the central sunspot group (indicated by the red arrow in Figure 5.3(d)).

The coronal structures suggested by the EUV and Hα images, in both small and large scales, were readily validated by NLFFF modeling results (Figure 5.3(e)). The localized hot structure situated over the central sunspot group (indicated by the red arrow in Figure 5.3(d)) was revealed to be a well-defined quadrupolar coronal configuration associated with a 3D null point situated at a height of ≈8 Mm. In Figure 5.3(e), the different domains of magnetic loops constituting the quadrupolar configuration are shown by blue, green, pink and sky-colored lines while the null point is shown by the red patch (also indicated by the black arrow). Further, we identified a magnetic flux rope in the central sunspot region (shown

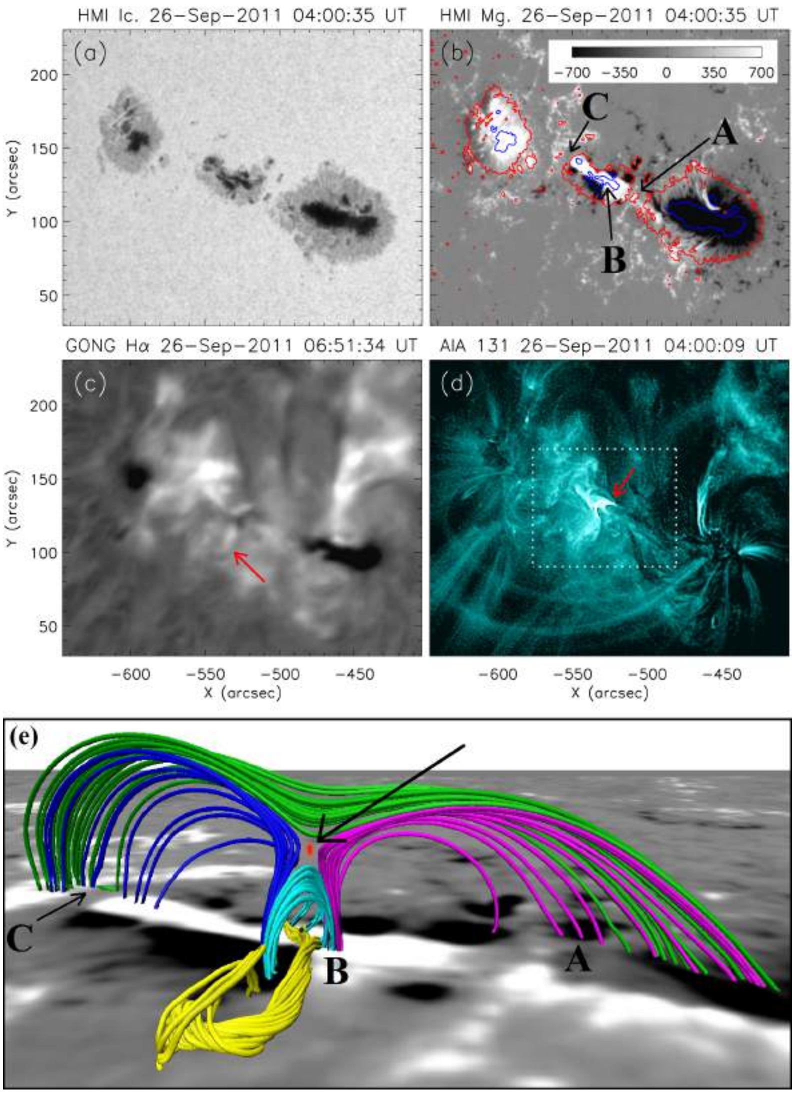

Figure 5.3: Panel (a): HMI white-light image of NOAA 11302 on 2011 September 26 04:00 UT. Panel (b): Cotemporal HMI line-of-sight (LOS) magnetogram. Magnetic flux density in *Gauss* is color-coded as the color-bar shown in the inset. The blue and red contours in panel (b) indicates the spatial extent of the umbrae and penumbrae of the sunspot groups as observed in white light. The contour levels are 35% and 75% of the maximum white light emission, respectively. Panel (c): GONG Learmonth Hα image of the active region showing the presence of multiple filaments. The red arrow indicates a faint filament which was involved in the M-class flare under study. Panel (d): AIA 131 Å image of the active region showing a set of significantly bright, small coronal loops during the pre-flare phase (indicated by the red arrow). The white dotted boxes in panel (d) indicate the field of view of Figures 5.5(b)–(m). Panel (e): NLFFF extrapolation results of the flaring region showing a flux rope (displayed by the yellow lines) and four sets of coronal loops connecting different photospheric flux regions associated with the quadrupolar configuration of the central sunspot group. The red patch (indicated by the black arrow) represent a coronal null point. The stamps A, B, and C in panels (b) and (e) are for comparison between the field of views (FOVs) of the corresponding panels.

by the yellow lines in Figure 5.3(e)) which can be well considered as the magnetic structure of the filament indicated by the red arrow in Figure 5.3(c).

5.3 Temporal Evolution of X-ray and EUV Emission

For understanding the temporal evolution of the flaring region (indicated by the white dotted box in Figure 5.3(c)) during the extend period of our observation, we looked into the X-ray flux variations in the 1–8 Å and 0.5–4 Å channels of GOES and multiple energy channels of RHESSI covering the energy range 3–25 keV (Figure 5.4(a)) as well as EUV flux variations derived from different AIA channels (Figure 5.4(b)) within the interval 04:00 UT – 05:15 UT on 2011 September 26. In Figure 5.4. Notably, this duration included an extended phase prior to the onset of the M4.0 flare as well as the impulsive and a part of the gradual phase of it. GOES did not observe the Sun during 05:15 UT – 06:25 UT which covered most of the declining phase of the flare[1]. RHESSI missed the initial phase of our observing period (till ∼04:13 UT) due to 'RHESSI night'.

The X-ray flux variations in Figure 5.4(a), particularly the GOES 0.5–4 Å channel and low energy RHESSI channels, readily indicate the occurrence of a number of episodes of small flux-enhancements prior to the onset of the M-class flare, i.e., during ≈04:04 UT – 04:53 UT. Interestingly, the SXR peaks and associate brightening from the quadrupolar location varied significantly and on the basis of intensity and compactness of the EUV and X-ray sources, the extended pre-flare period of observation can be divided into two phases: 'Phase 1': 04:04 UT – 04:39 UT (highlighted by light yellow background in Figure 5.4) and 'Phase 2': 04:39 UT – 04:53 UT (highlighted by light purple background in Figure 5.4). Accordingly, we identified the individual flux peaks during these two sub-periods by $P1_1$–$P1_6$ and $P2_1$–$P2_4$, respectively. After ≈05:06 UT, emission in X-ray and EUV increased rapidly, suggesting the onset of the flare. The impulsive phase of the flare lasted for only ≈1 min leading the flare to reach its peak at ≈05:08 UT. Interestingly, EUV lightcurves only in the hot 94 and 131 Å channels displayed

[1] https://www.swpc.noaa.gov/products/goes-x-ray-flux

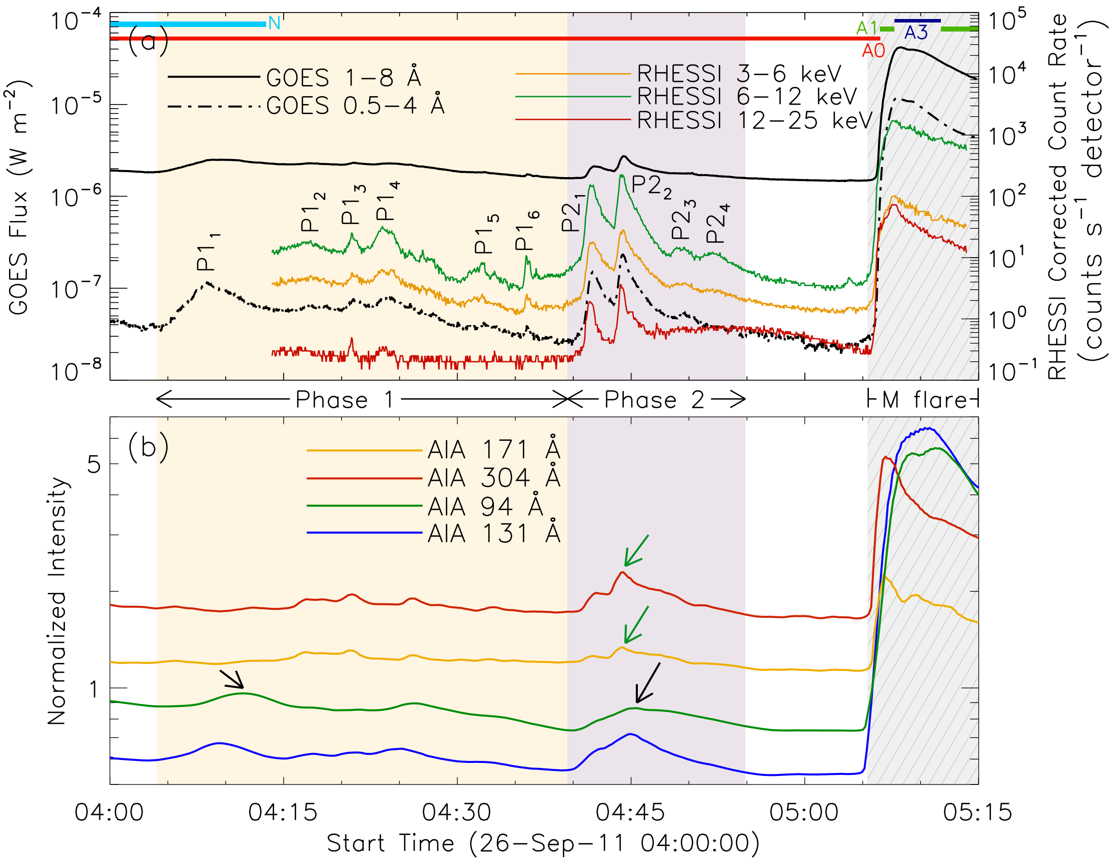

Figure 5.4: Panel (a): Evolution of X-ray flux in different GOES and RHESSI channels showing the extended pre-flare phase along with the evolution of the M4.0 flare. For better visualization, RHESSI fluxes are normalized by $\frac{1}{2}$ and $\frac{1}{20}$ for 3–6 keV and 12–25 keV channels. The horizontal bars at the top represent the status of RHESSI observation and attenuator states. Panel (b): Normalized AIA EUV intensity variations in the same duration as in panel (a). For better visualization, AIA 171, 304, 94 and 131 Å channels are scaled by factors of 1.2, 1.8, 0.9, and 0.6, respectively. The light yellow and light purple shaded intervals represent the durations of the two pre-flare periods of SXR flux enhancements which are further identified as 'Phase 1' and 'Phase 2', respectively. Individual SXR peaks during Phase 1 and Phase 2 are identified as $P1_1$–$P1_6$ and $P2_1$–$P2_4$, respectively. The hatched light grey-shaded interval represents the impulsive and early gradual phase of the M2.4 flare. The two green arrows in panel (b) indicate the intensity enhancement in AIA 171 and 304 Å channels during '$P2_2$' while the two black arrows indicate mild enhancement in the intensities in AIA 94 and 131 Å channels during $P1_1$ and $P2_2$.

appreciable enhancements during Phase 1. However, Phase 2 was associated by emission enhancements in all the AIA EUV channels.

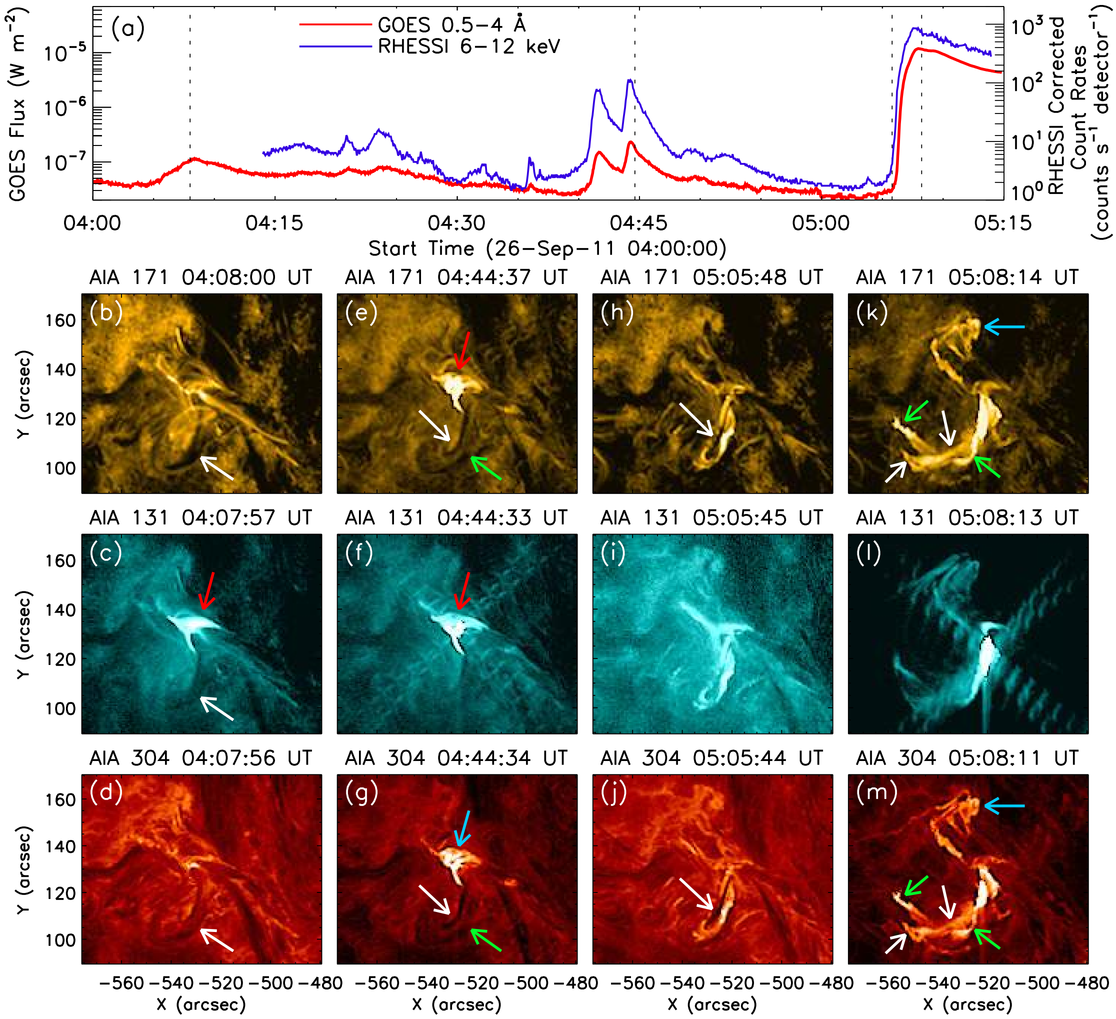

Figure 5.5: Panel (a): SXR flux in the GOES 0.5–4 Å (red curve) and RHESSI 6–12 keV (blue curve) channels. Panels (b)–(m): Multi-wavelength evolution of the core AR in AIA 171 Å (panels (b), (e), (h), (k)), 131 Å (panels (c), (f), (i), (l)) and 304 Å (panels (d), (g), (j), (m)). For comparison, four dashed lines are drawn in panel (a) corresponding to the time-informations of the images of the four columns. The white and green arrows in different panels indicate filaments during different phases within the studied interval. The red arrows in different panels and the sky-colored arrow in panel (g) indicate the location of pre-flare brightening. The sky-colored arrows in panels (k) and (m) indicate a remote brightening observed during the peak phases of the flare. The field-of-view of these panels are shown by the dotted boxes in Figures 5.3(d).

5.4 Multi-wavelegth Imaging of Coronal Energy Release: Onset and Consequences

Figure 5.5 shows a few representative AIA 171, 131, and 304 Å images of the flaring region providing an overview during different prominent episodes of energy release with respect to the GOES and RHESSI soft X-ray time-evolution.

EUV images during the $P1_1$ peak (Figures 5.5(b)–(d); see also Figure 5.4) readily suggest a localized brightening (indicated by the red arrow in Figure 5.5(c)) situated at the northern end of the filament (indicated by the white arrows in Figure 5.5(b)–(d)). Notably, NLFFF extrapolation results revealed the presence of the quadrupolar configuration in association with the coronal null point at the same location (Figure 5.3), suggesting null point reconnection to be responsible for the flux enhancements. Although during the $P1_1$ peak, we observed appreciable brightening from the quadrupolar brightening only in the hot AIA channels (e.g., 131 Å channel), all the AIA EUV channel images significant brightening from the same location during $P2_1$ and $P2_2$ peaks (Figures 5.5(e)–(g); indicated by the red and sky-colored arrows). Notably, during Phase 2 signatures of a second filament (indicated by the green arrows in Figure 5.5(e), (g)) became prominent close to the previously observed filament (indicated by white arrows in Figure 5.5(e), (g) and also in Figures 5.5(b)–(d)). At ≈05:06 UT, the first filament underwent activation which marked the onset of the M-class flare. During the process of the activation, the appearance of the filament changed from absorption to emission lines suggesting the rapid enhancement of its temperature. With the evolution of the impulsive phase, the filament initially displayed a brief eruptive motion and extended spatially along its length. However, the eruption of the filament came to an halt within ≈2 min resulting in the formation of a complex intertwined structure consisting of both the activated filaments. The peak phase of the flare was characterized by the intense emission from the initial location of the small filament as well as from the intertwined activate-filament structure. Notably, during this time we further observed quite intense emission from a second location situated remotely to the north of the filaments (indicated by the sky-colored arrows in Figures 5.5(k) and (m)). A summary of the different evolutionary phases is provided in Table 5.1.

5.4.1 Episoidic Energy Release at Null Point Topology

Comparison of Figures 5.4(a) and (b) readily suggests that the pre-flare flux peaks were more in agreement with hot AIA channel intensity variations (i.e., 94 and 131 Å) compared to the low temperature channels (i.e., 304 and 171 Å). There-

Table 5.1: Summary of the pre- to postflare evolution of NOAA 11302 on 2011 September 26

Sr. No.	Phase	Flux Peaks	Time (≈ UT)	Remarks
1	Phase 1 (04:04 UT – 04:39 UT)	$P1_1$ $P1_2$ $P1_3$ $P1_4$ $P1_5$ $P1_6$	04:08 04:17 04:21 04:24 04:32 04:36	Brightening in compact loop system associated with coronal null point topology. RHESSI missed observation of $P1_1$ due to 'RHESSI night'. Localized RHESSI sources within the energy range 3–25 keV from at the location during subsequent SXR peaks.
2	Phase 2 (04:39 UT – 04:53 UT)	$P2_1$ $P2_2$ $P2_3$ $P2_4$	04:41 04:44 04:49 04:52	Highly compact X-ray sources up to ≈25 keV energy from the location of null point. Eruption of small loop-like structures from the null point configuration during $P2_1$ and $P2_2$.
3	Impulsive (05:06 UT – 05:08 UT)			Activation and failed eruption of one filament. Development of intertwined double-decker flux rope system. X-ray sources up to energy ≈50 keV from the location of the activated filaments.
4	Gradual (05:08 UT – 05:13 UT)			Brightening of a highly structured loop system. Intense EUV emission from flare ribbons and post-reconnection loop arcade. Multiple ribbon-like brightening from regions situated north of the core flaring location.

fore, in order to have a thorough understanding of the activities during Phase 1 and Phase 2, we examine the AIA 131 Å images (shown in Figures 5.6 and 5.7, respectively). From these figures, it becomes clear that repetitive X-ray/EUV peaks during Phases 1 and 2 were essentially linked with an episodic, impulsive brightening of the compact loop structure which was formed by a quadrupolar configuration involving a null point (see Figure 5.3(e)).

In Figure 5.6(a), the bright loops are highlighted by the red dashed curves while

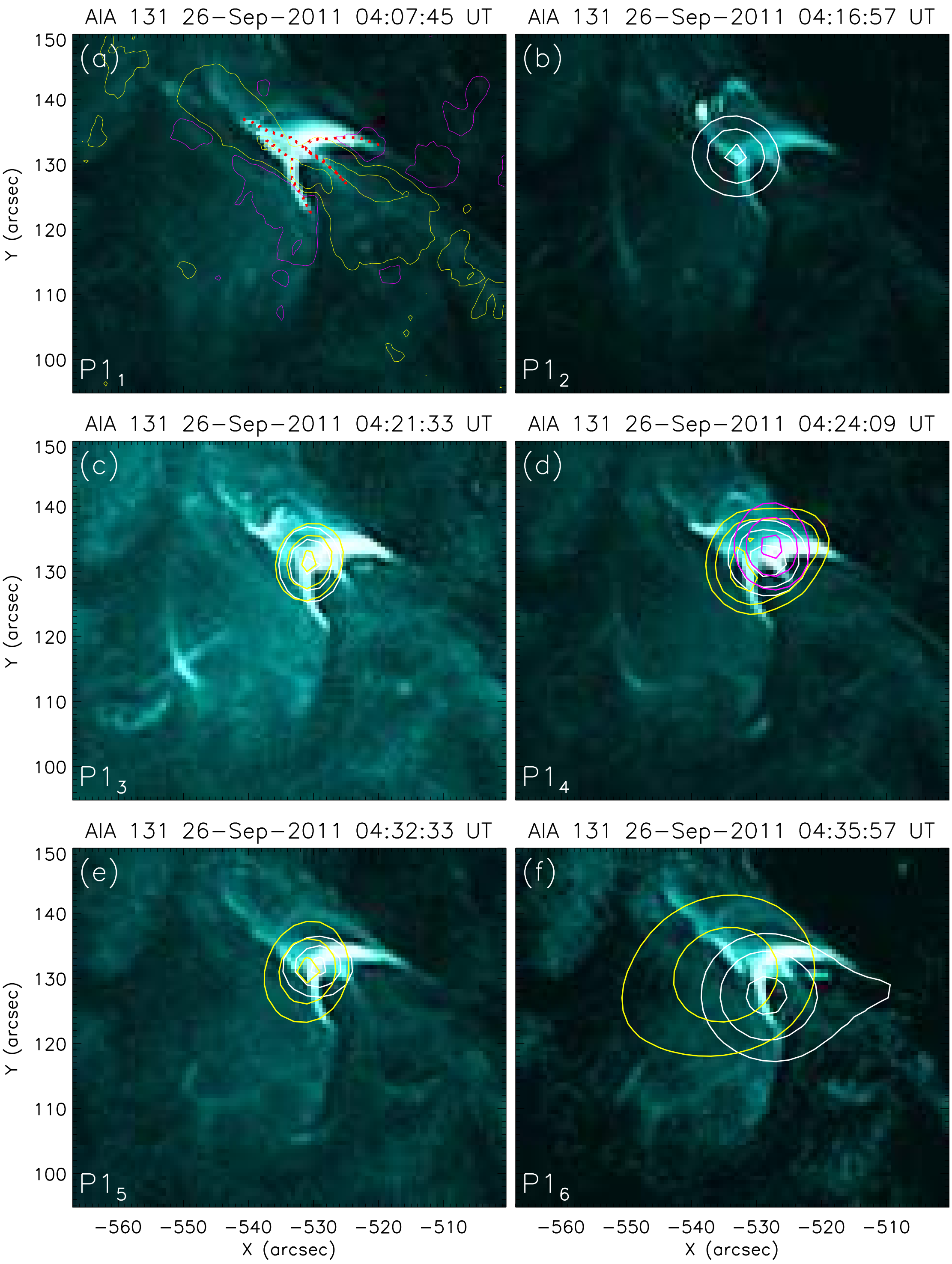

Figure 5.6: Evolution of Phase 1 in the AIA 131 Å channel. The red dotted curves in panel (a) indicate the coronal loops involved in the null point topology, during the different flux peaks of Phase 1 (i.e., $P1_1$–$P1_6$). Contours of a co-temporal HMI LOS Magnetograms are overplotted in panel (a). Contour levels are ±[400, 1400] G. Yellow and purple contours refer to positive and negative field, respectively. Co-temporal RHESSI contours of 3–6 keV (white), 6–12 keV (yellow), and 12–25 keV (pink) energy bands are plotted over panels (b)–(f). Contour levels are 55%, 75%, and 95% of the corresponding peak flux.

the co-temporal LOS magnetogram is overplotted with contours. A comparison between the HMI contours and the dashed curves confirms that the bright coronal loops were connecting different opposite polarity regions of the central sunspot group (see also Figures 5.3(b), (d)). This compact location was associated with clear X-ray sources up to 25 keV during the subsequent peaks of Phase 1 i.e., $P1_2$–$P1_6$. Interestingly, although this compact location underwent continuous X-ray emission and enhanced EUV brightening, the apparent magnetic configuration of the structure remained mostly unchanged. The loop brightness from the compact system significantly increased during Phase 2 (Figure 5.7; see also (Figure 5.4(b)). Further, during this phase, RHESSI sources became more compact compared to Phase 1 and emissions were noted in higher energies (12–25 keV) which strongly suggest that reconnection activities at the null-point were more energetic during Phase 2 in comparison to Phase 1. As a consequence of null point reconnection, we observed eruptions of small loop-like structures from the compact system during the X-ray peaks of Phase 2 (indicated by the yellow arrows in Figures 5.7(b) and (c)) which can be explained as the restructuring of the magnetic configuration in the vicinity of the null point.

5.4.2 Failed Eruption of the Filament and Associated M4.0 Flare

After a prolonged pre-flare period characterized by repetitive small-scale events of energy release, the main flare of GOES class M4.0 initiated at ≈05:06 UT. Figure 5.8 presents a series of representative AIA 94 Å images displaying the evolution of the core region during the impulsive and gradual phase of the flare. Notably, prior to the onset of the flare, AIA 94 Å images, which samples the solar corona in high temperature (≈6 MK), showed faint signatures of the filament. However, with the onset of the flare, the filament underwent activation and we observed bright emission along a narrow but elongated stretch beneath the entire length of the filament (indicated by the black arrow in Figure 5.8(b)). The impulsive phase of the flare was characterized by a brief eruption of the filament toward the projected eastern direction (shown by red arrows in Figures 5.8(b)–(e)). The flaring location was associated with strong X-ray sources up to energy ≈50 keV

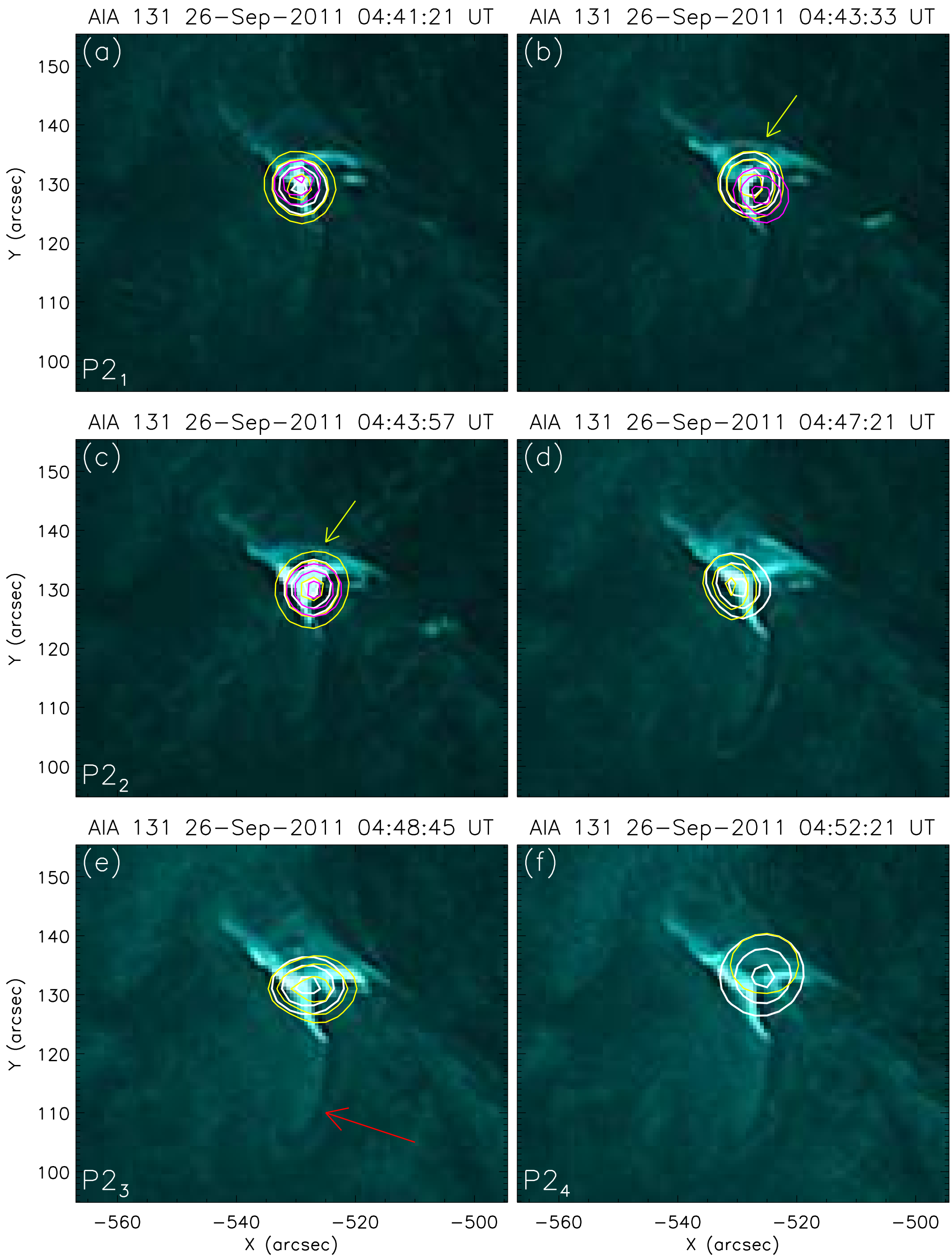

Figure 5.7: Evolution of Phase 2 in AIA 131 Å channel. Panels (a), (c), (e), and (f) are during $P2_1$–$P2_4$ peaks, respectively. Contours of co-temporal RHESSI sources in 3–6 keV (white), 6–12 keV (yellow) and 12–25 keV (pink) energy bands are plotted in selected panels. Contour levels are 55%, 75%, and 95% of the corresponding peak flux. Yellow arrows in panels (b) and (c) indicate small-loop like erupting structures. The red arrow in panel (e) indicate the filament which underwent activation during the M-class flare.

which were mostly concentrated around the initial location of the flare. After the brief phase of eruption, as the flare moved into the gradual phase, the filament interacted with a set of closed low-coronal loops lying above the core region. This low-coronal loop system connected the negative polarity regions of the central sunspot region to the dispersed positive polarity region situated to the north of the central sunspot group (cf. the loop system indicated by the blue arrow in Figure 5.8(f) with the HMI LOS magnetogram contours). Interaction of the erupting flux rope with the low-coronal loop system most likely ceased the eruption of the filament leading the flare in the 'failed eruptive' category. The gradual phase of the flare was characterized by significant brightening of the loop-system as well as intense EUV emission from the post-reconnection arcade during the gradual phase.

For investigating the activities at the lower atmospheric layers of the Sun during the flare, we looked into the AIA 304 Å images (Figure 5.9). In these images, we readily noted impressions of two clear filaments prior to the onset of the flare, which were spatially well separated (indicated by the yellow arrows in Figure 5.9(a)). During the impulsive phase, which was characterized by the brief eruption of one filament, we observed intense emission from the core location of the flaring region (Figures 5.9(b)–(c)). As the flare moved into the gradual phase, both the filaments got activated and composed an intertwined structure that resembled a double-decker flux rope system. In Figure 5.9(d), we indicate the two hot filaments of the double-decker configuration by the green and sky-colored arrows. During the gradual phase, the double-decker structure slowly reduced in spatial extent (indicated by the yellow arrows in Figure 5.9(e)) and a post-reconnection arcade was developed (within the green dashed box in Figure 5.9(f)).

During the peak phase, formation of a few ribbon-like brightening from regions north to the filament is noteworthy (indicated by the white arrows in Figure 5.9(d)). Emission from these structures significantly increased during the gradual phase. We carried out topological analysis in order to investigate the physical connections of these extended brightenings with the flaring processes which is presented in Section 5.5.1.

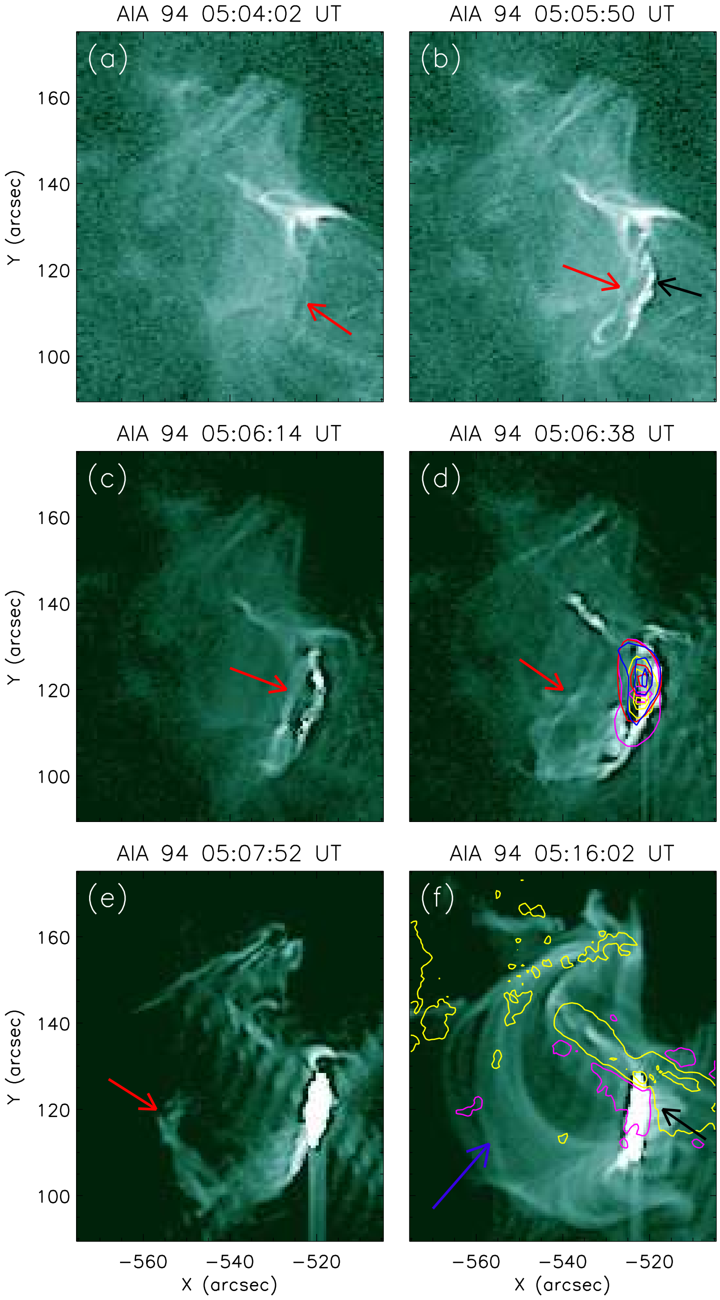

Figure 5.8: Series of AIA 94 Å images depicting the evolution of the M-class flare. The black arrow in panel (b) indicate the localized brightening suggesting the onset of the flare. The red arrows in panels (a)–(e) indicate the filament during different phases of its failed eruption. The black arrow in panel (f) indicate emission from the flare arcade. The blue arrow in panel (f) indicate highly structured coronal loops overlying the post-reconnection arcade. Contours of HMI LOS magnetogram are overplotted in panel (f). Contour levels are ±(500, 1500) G. Yellow and pink contours refer to positive and negative flux, respectively. Contours of co-temporal RHESSI sources in 3–6 keV (pink), 6–12 keV (yellow), 12–25 keV (red), and 25–50 keV (blue) energy bands are plotted in selected panels. Contour levels are 50%, 80%, and 95% of the corresponding peak flux.

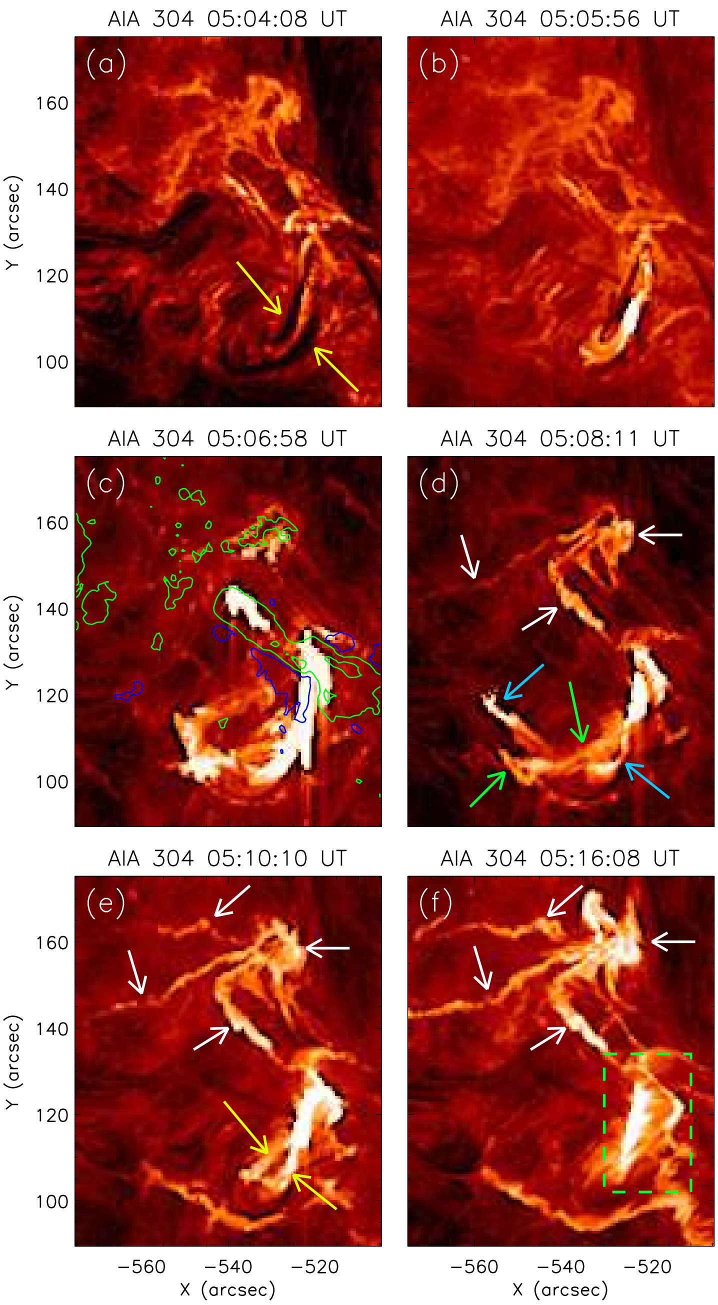

Figure 5.9: Series of AIA 304 Å images depicting the evolution of the M-class flare. The yellow arrows in panel (a) indicate the two filaments prior to the onset of the flare. The sky-blue and green arrows in panel (d) indicate the two filaments during the peak phase of the flare. The yellow arrows in panel (e) indicate the two filaments after the failed eruption. The green dashed box in panel (f) outline the core region during the gradual phase of the flare where intense emission from the flare ribbons and post-reconnection arcade can be identified. The white arrows in panels (d)–(f) indicate ribbon-like brightenings observed during the gradual phase of the flare. Contours of HMI LOS magnetogram are overplotted in panel (c). Contour levels are ±(500, 1500) G. Green and blue contours refer to positive and negative flux, respectively.

5.5 Coronal Magnetic Field Modeling

5.5.1 Pre-flare Coronal Configuration and Post-flare arcade

Figure 5.10 presents NLFFF-extrapolated coronal field lines associated with NOAA 11302 prior to the onset of the M4.0 flare. For the extrapolation, we used the following values of the free parameters (see Chapter 2.3.2):

$\nu = 0.01;$ $\quad w_{los} = 1;$ $\quad w_{trans} = \frac{B_{trans}}{max(B_{trans})};$

$\mu_1 = \mu_2 = 1;$ $\quad \mu_3 = 0.001;$ $\quad \mu_4 = 0.01.$

The residual errors assessing the NLFFF solutions were obtained as follows:

$< |f_i| >= 4.06 \times 10^{-4};$ $\quad \theta_J = 6.76°$

In order to compare the NLFFF-extrapolation results with the co-temporal coronal loops observed in EUV images, co-temporal LOS magnetogram and AIA 171 Å image of the AR are plotted in Figures 5.10(a) and (b), respectively. From the HMI LOS magnetogram contours plotted on top of AIA 171 Å image (Figure 5.10(b)), it becomes clear that the filament was situated along the PIL within the central sunspot region. Further, we note a set of large coronal loops that extended upto high coronal heights, which are indicated by the sky-colored arrows. Further, the presence of a different filament within the AR is also noteworthy which remained uninvolved in the reported flaring activity. In Figure 5.10(b), this second filament is indicated by a black arrow.

NLFFF-modeled coronal magnetic lines showed excellent agreement with the observed coronal loops (Figure 5.10(c)). The sky-colored modeled lines correlate well with the large scale coronal loops observed in AIA 171 Å images (indicated by the sky-colored arrows in Figure 5.10(b)) while the flux rope shown by light yellow color in Figure 5.10(d) represents the magnetic configuration of the filament indicated by the black arrow in 5.10(b) which is further demonstrated by AIA 304 Å image in the background of Figure 5.10(d). The flux ropes shown by yellow and pink color constitute a double-decker flux rope which is exactly co-spatial with the two filament observed during the M4.0 flare, while, the yellow colored flux rope underwent the failed eruption. The quadrupolar coronal configuration associated with the central sunspot group is shown by blue colored lines.

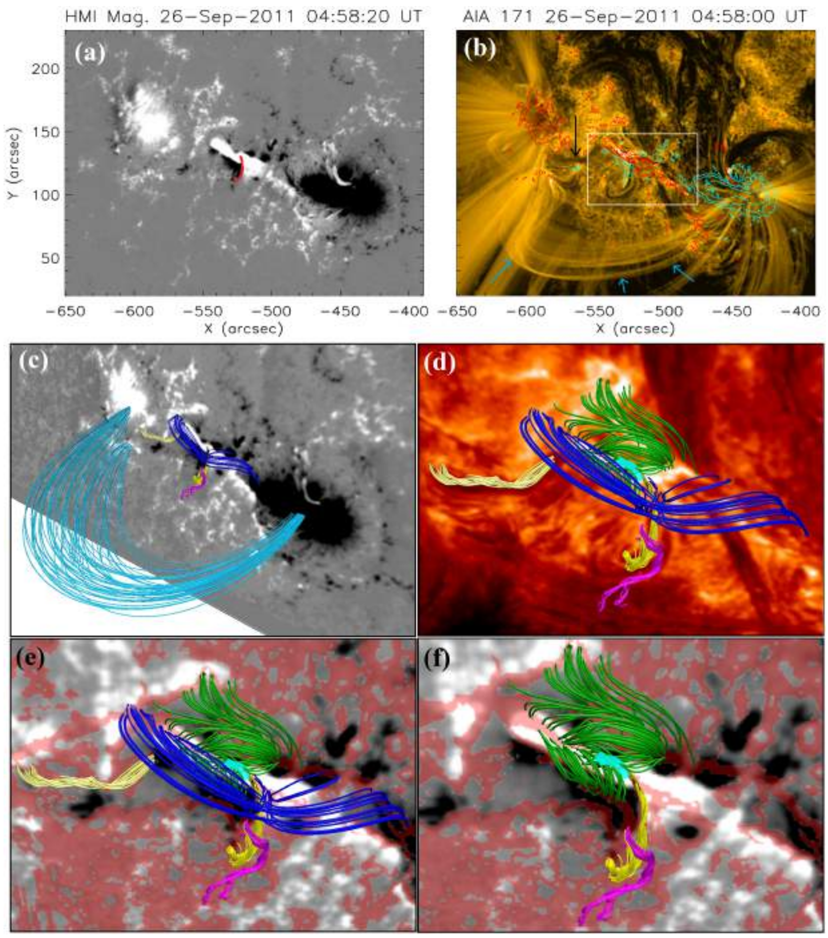

Figure 5.10: Panel (a): HMI LOS magnetogram of NOAA 11302. Panel (b): Co-temporal AIA 171 Å image. The flaring region is outlined by the white box. The sky-blue colored arrows indicate a set of large, high-lying coronal loops above the flaring region. Contours of the LOS magnetograms are plotted over the AIA 171 Å image at levels of ±[500, 1000, 1500] G. Red and cyan contours refer to positive and negative polarities, respectively. Panel (c): NLFFF-extrapolated magnetic field lines showing the important coronal connectivities in the overall active region. In panels (d)–(f), we show only the model field lines in the flaring region. The bright yellow and pink lines represent two flux ropes. The northern part of the flux rope shown by bright yellow, was enveloped by the blue lines. A set of field lines (shown by green color) situated to the north of the flux rope shown in bright yellow, was associated with a high squashing factor. The sky-colored patch in panels (d)–(f) within the region of green lines is characterized by $\log(Q) = 3$. The light yellow lines in panels (d) and (e) represent another flux rope which was present in the active region but did not take part in the flaring activity. In panel (f), we show the same model coronal loops except the blue and light yellow lines for better visualization of the green lines. The color template used in the background magnetograms is same as in Figure 5.3(b). Background of panel (d) is AIA 304 Å image. The reddish colored patches over the background in panels (e)–(f) is characterized by $\log(Q) = 2$. The red curve in panel (a) approximately denotes the axis of the bright-yellow flux rope, which is used for the magnetic decay index analysis shown in Figure 5.12.

Here we recall that, we observed multiple ribbon-like brightenings during the gradual phase of the flare, which were situated to the north of the core region (indicated by the white arrow in Figure 5.9(f); Section 5.4.2). Notably, the footpoints of the green colored modeled lines match well with the extended ribbon-like brightening (Figure 5.10(d)). Further, few of the green lines, exactly above the northern leg of the flux rope shown in bright yellow, was characterized by high values of the squashing factor ($\log(Q) = 3$) which is represented by the sky-colored patch in Figures 5.10(d)–(f). In general, the footpoints of the green lines were associated with high Q values which is evident from the background red colored patches representing $\log(Q) = 2$, in Figures 5.10(e)–(f).

Different panels of Figure 5.11 show the association of the double-decker flux ropes and the quadrupolar coronal configuration from different viewing angles. The configuration, from the top view (Figure 5.11(a)), clearly reveals that the null point (indicated by the red arrow in Figures 5.11(a)) was situated above only the yellow colored flux rope. The null point is further indicated by the orange arrow in Figure 5.11(b) and by the black arrow in Figure 5.11(c). Notably, for a better visualization, we have shown the different coronal magnetic model lines associated with the quadrupolar configuration in different colors. Here, we remember that, during a gradual phase of the flare as the eruption of the filament came to a halt, a set of relatively large coronal loops became very bright (indicated by the blue arrow in Figure 5.8(f)), which seems to be well manifested by the sky-blue colored model lines shown in Figure 5.11(d). Therefore, we believe that during the impulsive phase of the flare, the bright yellow flux rope, while erupting toward east, most likely interacted with the sly-blue colored lines, giving rise to the enhanced emission from the highly structured lines.

5.5.2 Decay Index and Twist Number

In order to investigate the coronal condition responsible for the failed eruption, we calculated the magnetic decay index (n) within the extrapolation volume. Theoretically, if a current ring of major radius R is embedded in an external magnetic field, then the ring experiences a radially outward 'hoop force', because of its curvature (see Myers et al., 2016). In stable condition, this hoop force is balanced by

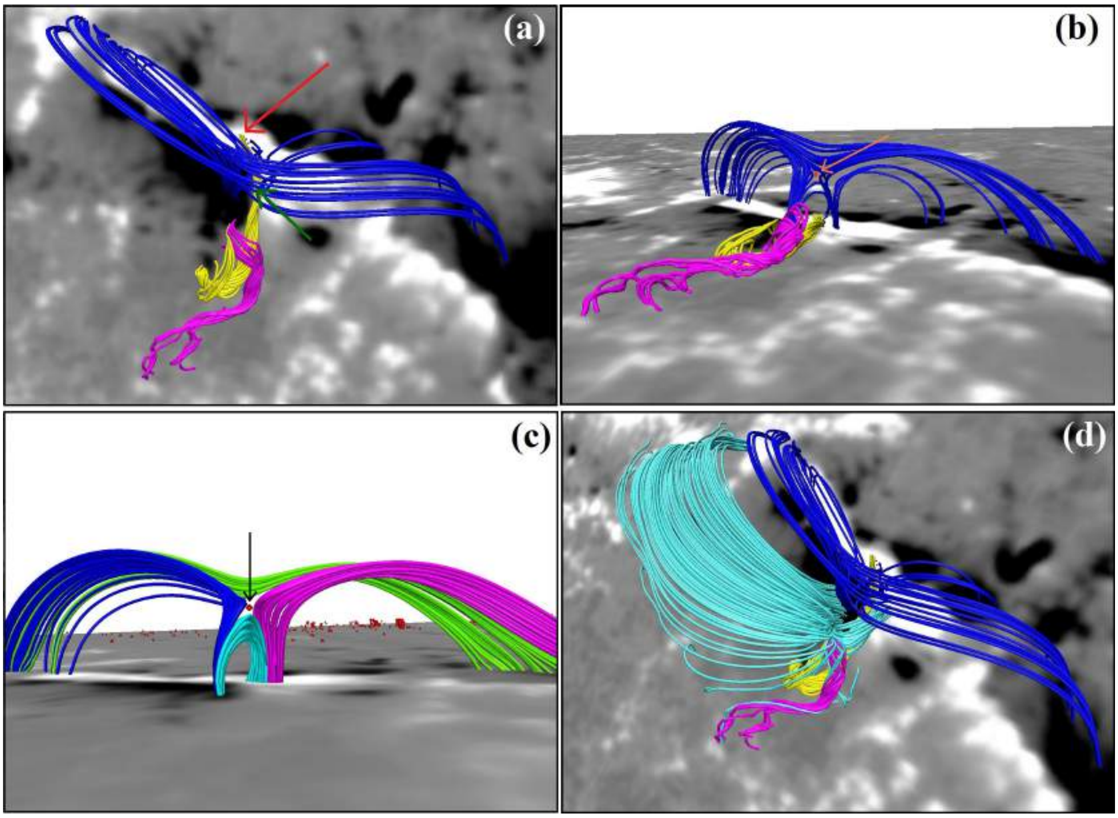

Figure 5.11: Modeled coronal configuration involved in the pre-flare activities and the M-class flare including the two flux ropes (shown in bright yellow and pink color) and the low-coronal closed loops connecting the multi-polar photospheric configuration (shown in blue color in panels (a), (b), (d) and in multiple colors in panel (c)). The northern leg of the yellow-colored flux rope is indicated by the red arrows in panels (a). The red-colored patch within the blue lines (also indicated by the orange arrow in panel (b)) is characterized by log(Q) = 8.5 which represents a coronal null point. The green arrow in panel (a) indicate the approximate location of the null point. In panel (c), only the representative magnetic lines involved in the null point configuration are shown. For a better representation, the four domains of magnetic field lines are shown in different colors. The black arrow indicates the null point. The sky-colored lines in panel (d) represent the set of coronal loops that intensified during the gradual phase of the flare (indicated by the blue arrow in Figure 5.8(f)). The color template used in the background magnetograms is same as in Figure 5.3(b).

the inwardly directed Lorentz force. If the Lorentz force due to the external field decreases faster with R than the hoop force, the system becomes unstable due to the torus instability (Bateman, 1978). The decay rate of the external magnetic field is quantified by the magnetic decay index (n). Considering the fact that the toroidal component (directed along the axis of the flux rope) of magnetic field does not contribute to the strapping force (see Myers et al., 2015), in the ideal current-wire approach, the magnetic decay index is calculated as

$$n = -\frac{d\log(B_p)}{d\log(h)} \tag{5.1}$$

where B_p is the external poloidal field (along the transverse direction of the flux rope axis) and h is the height.

However, in reality, flux ropes are observed to significantly differ from the simplified shape of a semi-circular current-wire (Démoulin & Aulanier, 2010). In view of this, we first manually determined the approximate 2D projected flux rope axis on the photosphere which is shown by the red curve in Figure 5.10(a). The 3D magnetic field vector at each pixel on the vertical surface above the axis were then decomposed into two components: along the direction of the axis i.e., the toroidal component; and perpendicular to the axis i.e., the poloidal component. This perpendicular component was used in Equation 5.1 for the computation of the magnetic decay index.

The distribution of the magnetic decay index (Figure 5.12) suggests the presence of an extended region of high magnetic decay index within a very low height above the flux rope (depicted by the red colored patch in Figure 5.12(a)). This region of high decay index was immediately enveloped by a relatively more extended region where the decay index rapidly decreased reaching to values as low as ≈–3 (the region shown in blue in Figure 5.12(a)) above which the value of decay index steadily increased and reached to 1.5 again at a quite high coronal layer (indicated by the yellow curve in the top portion of Figure 5.12(a)). In Figure 5.12(b), we show the variation of the decay index averaged over the length of the axis of the double-decker filament with height, which reveals that the average value of decay index in the high corona reached the values of 1.0 and 1.5 at heights of ≈43 Mm and ≈64 Mm, respectively.

In order to explore the applicability of kink instability as the triggering mechanism of the flux ropes, we computed the twist number within the extrapolation volume using the IDL-based code developed by Liu et al. (2016b). The twist number (T_w; Berger & Prior, 2006) associated with a flux rope is defined as

$$\tau_w = \int_L \frac{(\nabla \times \vec{B}) \cdot \vec{B}}{4\pi B^2} dl \ , \tag{5.2}$$

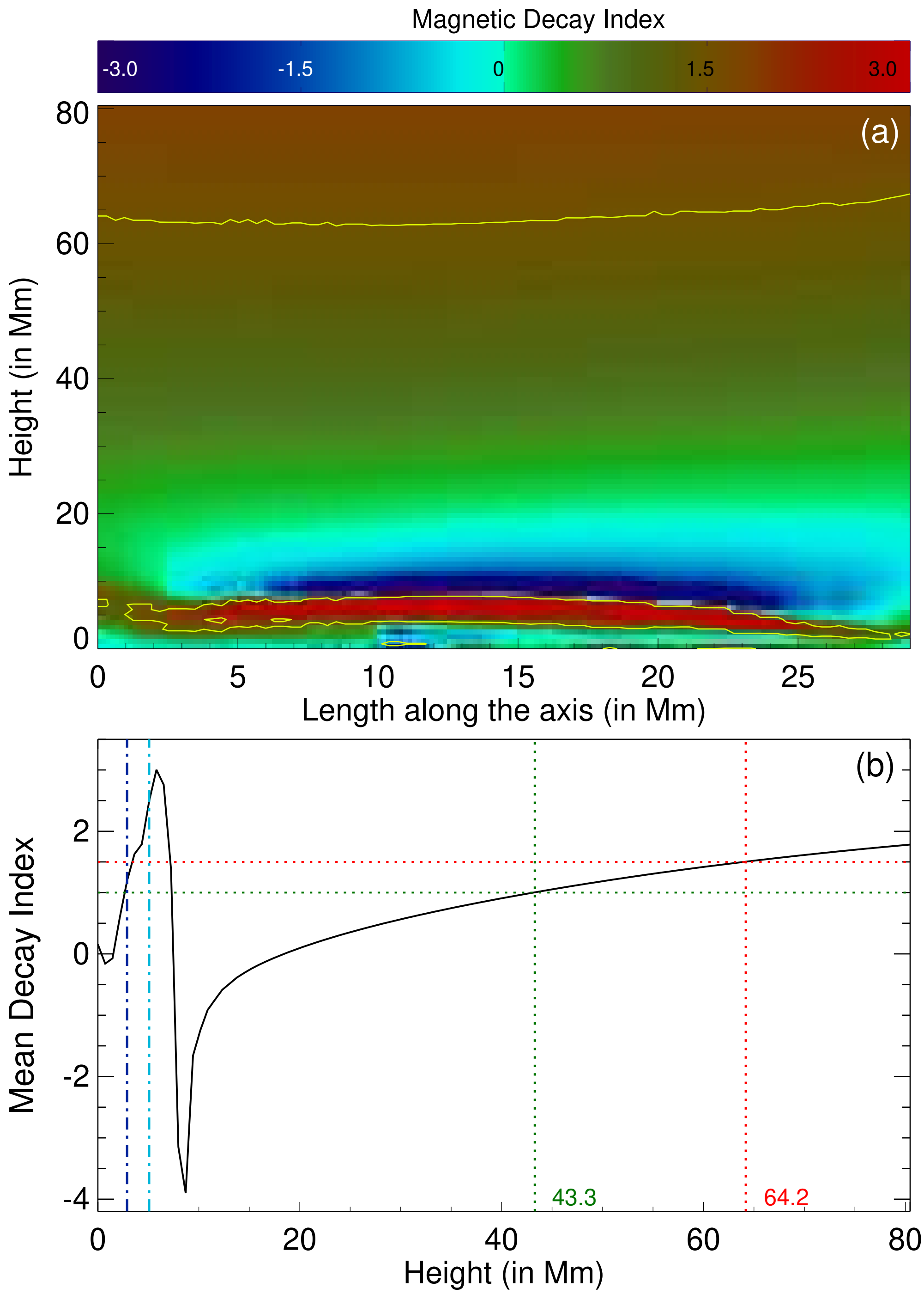

Figure 5.12: Panel (a): Distribution of magnetic decay index with height above the axis of the yellow-colored flux rope (indicated by the red curve in Figure 5.10(a)). The yellow curves refer to n=1.5. The variation of decay index with height, averaged over the flux rope axis, is shown in panel (b). The green and red dotted lines indicate the critical heights corresponding to n=1.0 and n=1.5, respectively. The blue and sky-colored dash-dotted lines indicate the maximum heights of the yellow and pink-colored flux ropes, respectively.

where L denotes the length of the flux rope. Our calculations suggest that both the flux ropes in the double-decker flux rope system were associated with a positive twist. The average value of twist number associated with the yellow and pink flux ropes were found to be ≈1.5 and ≈1.7, respectively. A statistical survey conducted by Duan et al. (2019) revealed the critical value of $|\tau_w|$ for kink instability to be 2 which suggests kink instability was not responsible for the activation of the filament during the onset of the M4.0 flare.

5.6 Discussion

In this chapter, we have presented a detailed multi-wavelength analysis of the triggering and evolution of an M-class flare from NOAA 11302 and investigate the probable causes of the failed filament eruption associated with it. The AR was comprised of three prominent and distinct sunspot groups arranged in a linear manner. The central sunspot group, despite being the smallest among the three, was the only bipolar region and contained δ-spots (Figure 5.3). Notably, the reported flare occurred from this sunspot group.

The M-class flare was characterized by the initial triggering and eventual failed eruption of a filament. Although, one filament underwent the failed eruption, we identified clear signatures of two distinct filaments in the flaring region prior to the onset of the M-class flare (Figure 5.5, 5.9(a)). During the impulsive phase of the flare, both filaments got activated, extended spatially and developed into a complex structure where both the filaments were intertwined with each other (Figure 5.5(k)–(m), 5.9(d)). NLFFF-reconstructed coronal magnetic fields revealed the presence of two flux ropes at the flaring region, in a double-decker configuration. The contemporary concept of double-decker flux rope system was first reported by Liu et al. (2012b) and only a handful of articles have reported such complex structures since then (e.g., Cheng et al., 2014a; Kliem et al., 2014; Dhakal et al., 2018; Wang et al., 2018; Tian et al., 2018; Awasthi et al., 2019; Zheng et al., 2019; Mitra et al., 2020b; Mitra & Joshi, 2021). Despite the small number of reportings, double-decker flux rope systems can be mostly divided into two categories. While most of the reported double-decker flux rope systems were identified as two vertically well separated filaments with one of them undergoing eruption (e.g., Liu et al., 2012b; Dhakal et al., 2018; Tian et al., 2018; Awasthi et al., 2019; Zheng et al., 2019), the second category comprises complex pre-flare sigmoidal structures involving intertwined flux ropes (Cheng et al., 2014a; Mitra et al., 2020b; Mitra & Joshi, 2021). In the first category, triggering and eruption of flux ropes are generally caused by photospheric activity i.e., shearing and/or rotating motion. Further, in this case, the activation of one flux rope in the double-decker system may or may not influence the stability of the other flux rope (see e.g., Liu et al., 2012b). On the other hand, in the case of intertwined flux ropes, interaction between the two flux ropes mostly cause activation and eruption of the system. Although, the two filaments observed in this study were spatially well separated during the pre-flare phase, they extended longitudinally and got intertwined with each other during the impulsive phase. Further, the onset of the flare in this case, followed clear pre-flare activities occurring at a separate location than the filaments, which were identified in the SXR flux evolution and the AIA EUV imaging observations. In view of this, the double-decker system, reported in this study, seems to have characteristics of both the categories of double-decker systems discussed above. Such complex and intriguing behavior of magnetic flux ropes challenges our general understanding of solar magnetic fields and their evolution during transient activities.

We observed multiple episodes of flux enhancements in the SXR wavelengths prior to the onset of the flare (Figure 5.4). Comparison of SXR lightcurves with EUV images of the AR revealed that the pre-flare flux enhancements originated in the form of a localized brightening from a location situated above the northern footpoints of the filaments. NLFFF-modeled field lines revealed a quadrupolar coronal configuration at the same location, that included a coronal null point (Figures 5.3(e), 5.11). Such a pre-flare coronal configuration is in agreement with the scenario prescribed in the breakout model of solar eruptions (Antiochos et al., 1999; Karpen et al., 2012). According to this model, small-scale pre-flare reconnection at the null point will remove the overlying constraining magnetic flux by reconfiguring them into 'side lobe magnetic flux' (see Figure 1 in Karpen et al., 2012). In view of this, we interpret the observed pre-flare episodic brightening of the coronal loops associated with the null point to be observational evidences of the breakout model for the activation of the flux rope.

We identified the location of the null point by pointing out the location of the highest value of the degree of squashing factor (Q). Null points are essentially singular points in the corona where all the components of magnetic field vanishes (Aschwanden, 2005). Theoretically, a null point can be characterized by $Q \rightarrow \infty$ as it works as a separator between different topological domains of magnetic field (see e.g., Longcope & Klapper, 2002). However, numerical techniques used to calculate Q-values will always return finite values, thus we can expect a coronal null point to be associated with high degree of Q-values (Pariat & Démoulin, 2012). In a number of studies concerning coronal null points and their evolution, the coronal null points were found to be associated with a wide range of Q-values ($\sim 10^4$–10^{12}; see, Yang et al., 2015; Liu et al., 2020; Qiu et al., 2020; Prasad et al., 2020). In the present study, the null point was observed to be associated with a value of $Q \approx 10^{8.5}$. Regions with smaller Q are identified as 'Quasi-separatrix layers' (QSL; Aulanier et al., 2006). Notably, we observed multiple ribbon-like brightenings from the locations to the north of the main flaring region during the gradual phase of the M-class flare (Figure 5.9(d)–(f)). Model coronal configuration suggested the presence of a set of coronal loops which connected the locations of the remote ribobn-brightenings to the northern footpoint region of the flux rope (shown by the green colored lines in Figures 5.10(d)–(f)). Our calculation further revealed high Q-values associated with the green model lines (Figure 5.10(d)–(f)). These observations are suggestive that the remote brightenings during the M-class flare were the observational manifestations of slip-running reconnection influenced by the QSLs.

The most important aspect of this study was to investigate the probable causes of the failed eruption of the activated flux rope. Our analysis of decay index (n) readily revealed the presence of a high-n region only a few Mm above the flux rope, extending over the entire length of its axis (Figure 5.12). This suggests high influence of torus instability toward the eruption of the flux rope. However, the coronal configuration above the flux rope was characterized by the presence of a null point (Figure 5.11). Magnetic field is expected to undergo strong decay below null points leading to higher values of magnetic decay index. However, the decay index profile of the height range ≈7–20 Mm above the flux ropes (Figure 5.12(a)) presented a very interesting scenario, where the value of n was negative. The specific cases, in which the variations of decay index with height is characterized by initial increase of n followed by a rapid decay and steady increase of it afterward, are referred to as 'saddle'-like profiles (Wang et al., 2017a). Such saddle-like profiles of the decay index produces a favorable condition for failed eruption of flux ropes since the toroidal strapping force (responsible to constraint the erupting magnetic structure) increases in height after an initial decrease (see e.g., Wang et al., 2017a; Filippov, 2020b). However, a number of studies have reported successful eruption of flux ropes despite the coronal decay index profile being saddle-like (e.g., Cheng et al., 2011; Wang et al., 2017a; Filippov, 2020a) suggesting the involvement of other factors towards such successful eruption. Among a number of parameters such as, Lorentz force, non-potentiality of the source region etc., the value of decay index in the saddle bottom is believed to be important in determining the eruption profile of flux ropes (Liu et al., 2018b). Inoue et al. (2018) investigated a successful flux rope eruption through a saddle-like decay index profile by numerical simulation and found that the feedback relation between the eruption of the flux rope and reconnection rate beneath it, enabled the flux rope to pass through the torus stable zone. The event reported in this chapter presents a good example of a failed eruption due to a saddle-like decay index profile of the corona above the flux rope. We recognize the specialty of this event to be the presence of the negative decay index region above the torus unstable zone within a low height ($\lesssim$20 Mm; Figures 5.12(c), (e)), which is rarely observed (see Filippov, 2020a). The negative value of the magnetic decay index not only decelerated the eruption of the flux rope but also repelled it back downward resulting the failed eruption during the event.

5.7 Concluding remarks

The present study explores an intriguing case of the failed eruption of a 'torus unstable' complex double-decker flux rope system. We show that the continuation of a flux rope eruption against the overlying coronal fields is essentially controlled by the extended decay index profile characterizing the strength of strapping field through the larger coronal heights above the flux rope axis. Investigations on the failed eruptions of flux ropes, especially the torus unstable ones, are crucial for predicting the occurrence of CME and subsequent space weather forecast. In this context, in addition to classical torus instability, some additional factors have been assessed to understand the cause of the failed eruption which are worth discussing (Myers et al., 2015; Zhong et al., 2021). Based on the results of laboratory experiment, Myers et al. (2015) found that the failed eruption can also occur when the guide magnetic field i.e., the toroidal field (the ambient field that runs along the flux rope) is strong enough to prevent the flux rope from kinking. Under these conditions, the guide field interacts with electric currents in the flux rope to produce a dynamic toroidal field tension force that halts the eruption. The study by Zhong et al. (2021) presents a data-driven magnetohydrodynamic simulation for a confined eruption. They showed a Lorentz force component, resulting from the radial magnetic field or the non-axisymmetry of the flux rope, which can essentially constrain the eruption. In the light of above studies and our work, we understand that the ultimate fate of solar eruptions is determined by a complex interplay of coronal magnetic fields involving the magnetic flux rope, core and envelope fields.

Chapter 6

Magnetic Characteristics and Onset of Eruption in δ-sunspot Region NOAA 12673

6.1 Introduction

Ever since the first observation of solar flare by Carrington (1859) and the discovery of magnetic field in the sunspots by Hale (1908), the close relationship between the production of solar flares and the magnetic characteristics of ARs has been extensively discussed and investigated (Toriumi & Wang, 2019). After a meticulous investigation over the years, an understanding has been developed: some ARs are particularly high flare productive and few ARs are 'flare-quiet'. Statistical studies have shown that the most flare productive ARs are usually associated with the 'δ-spots' (Jaeggli & Norton, 2016). Therefore, a few questions naturally develop which include:

- What are the morphological and magnetic properties that enable only a few ARs to be extremely flare productive?

- What are the properties responsible for different flare energetics originating from the same AR?

NOAA 12673 was one of the most flare productive solar ARs of cycle 24. It underwent a rapid evolution in magnetic complexity which resulted in tremendous flare productivity. Multi-instrument observations of NOAA 12673, coupled with modeling analysis of coronal magnetic fields, have provided us with a unique opportunity to investigate various physical parameters that play vital role in the onset of large flares and influence the early CME dynamics. Notably, NOAA 12673 produced the largest flare of the cycle, an X9.3 flare on 6 September 2017. Interestingly, NOAA 12673 appeared on the eastern limb of the Sun as a simple unipolar sunspot. However, it quickly evolved into the most complex type and produced a series of large eruptive flares. Being one of the most flare productive AR of the solar cycle 24, NOAA 12673 was subjected to extensive investigations focusing on multiple aspects including case studies of a few flares as well as the long term evolution of the AR itself (see e.g., Yang et al., 2017; Gary et al., 2018; Guo et al., 2018; Hou et al., 2018; Liu et al., 2018a,d, 2019; Mitra et al., 2018; Romano et al., 2018, 2019; Seaton & Darnel, 2018; Verma, 2018; Veronig et al., 2018; Moraitis et al., 2019; Duan et al., 2019; Li et al., 2019; Chen et al., 2020). In this chapter, we thoroughly investigate the evolution and magnetic characteristics of NOAA 12673. We briefly examine the evolutions of two homologous X-class flares on 6 September 2017 and corresponding coronal magnetic field configurations. We further present detailed multi-wavelength analysis of two homologous M-class eruptive flares originating from it on 7 September 2017.

6.2 Evolution of NOAA 12673

Figure 6.1 provides an overview of the transit of NOAA 12673 through the visible hemisphere of the Sun. Figures 6.2 and 6.3 show the build up of the AR with a better visualization. NOAA 12673 appeared on the eastern limb of the Sun on 28 August 2017 as a simple positive polarity sunspot. In view of its single unipolar sunspot (Figure 6.2(a)), it was classified as an α-type AR. It remained α-type till the late hours of 2 September (Figure 6.1(a), (b), also indicated by an arrow in Figure 6.3(a)) following which we observed rapid flux emergence of both polarities first from the south-eastern location of the sunspot (indicated by the oval shape in Figure 6.3(b)) and then from the eastern and north-eastern sides on 3 September (Figure 6.3(c)). Accordingly, continuum images suggested appearance of a few pores from the south eastern (Figure 6.2(b)) and north eastern sides (Figure

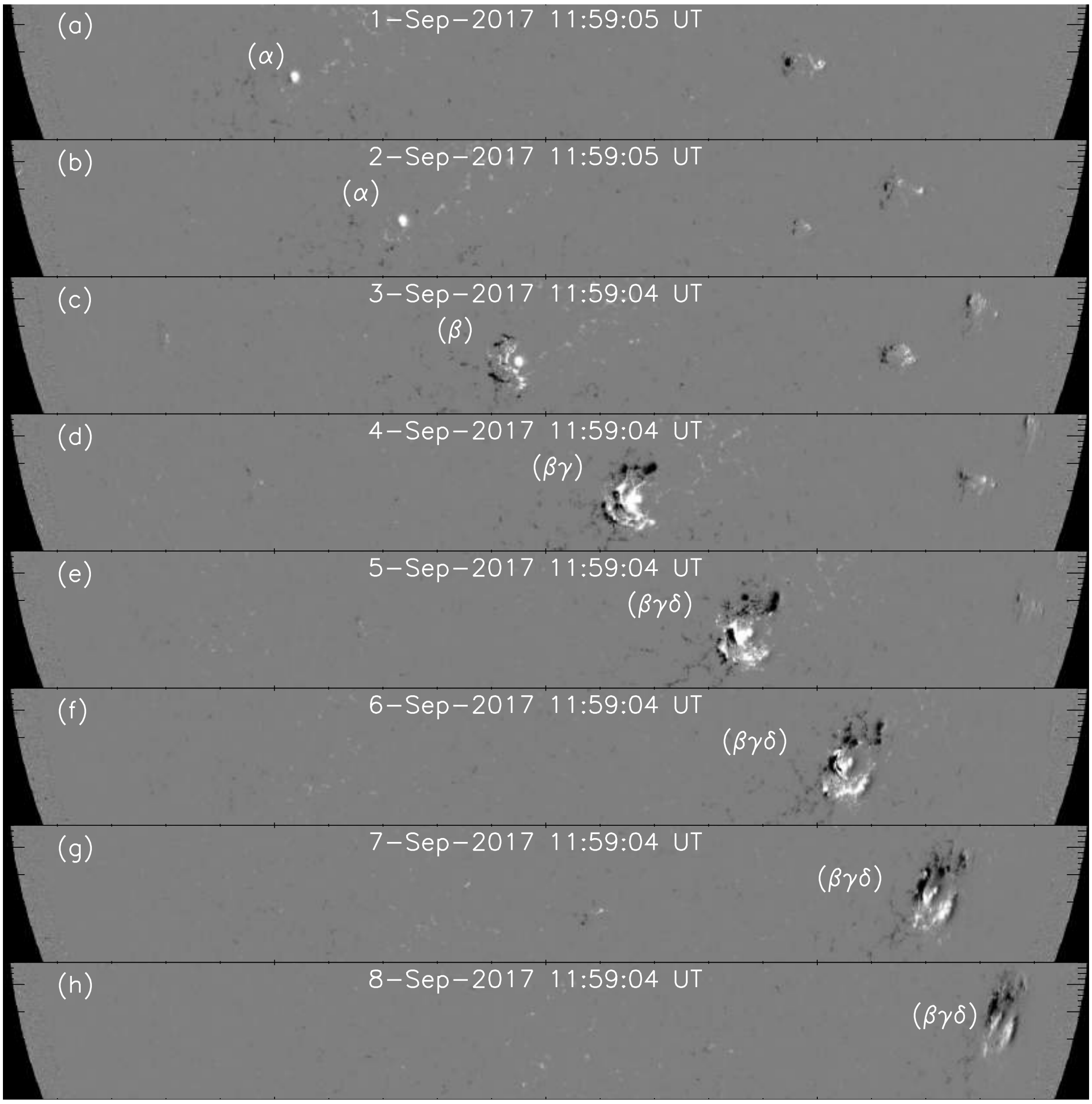

Figure 6.1: Evolution of the active region NOAA 12673 through its transit over the visible hemisphere of the Sun. The corresponding magnetic classification of active region is noted in each panel.

6.2(c)). From 3 September onward, the AR experienced rapid flux emergence, resulting the magnetic classification of the AR to move from α to β-category (Figure 6.1(c)). Importantly, the rate of flux emergence in this AR was greater than any other known ARs (Sun & Norton, 2017). Along with rapid flux emergence, the AR underwent continuous photospheric activity including shearing and rotational motion (Li et al., 2019) which led to rapid evolution of the AR to the $\beta\gamma$-category on 4 September (Figures 6.1(d), 6.2(d), 6.3(d)) and to the most complex $\beta\gamma\delta$-category on 5 September (Figures 6.1(e), 6.2(e), 6.3(e)). Flux emergence continued till 6 September following which we observed decay of the AR, although the magnetic classification remained $\beta\gamma\delta$-type till the completion of the AR's transit through

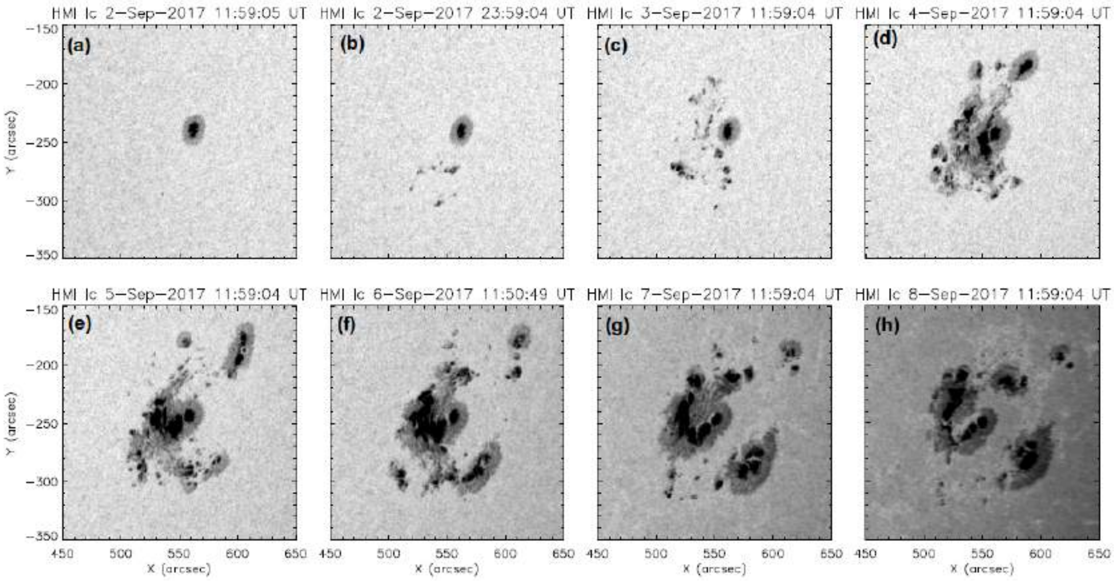

Figure 6.2: Series of HMI continuum images showing the build up and evolution of the active region NOAA 12673. All the images were rotated to the co-ordinate corresponding to 6 September 2017 12:00 UT.

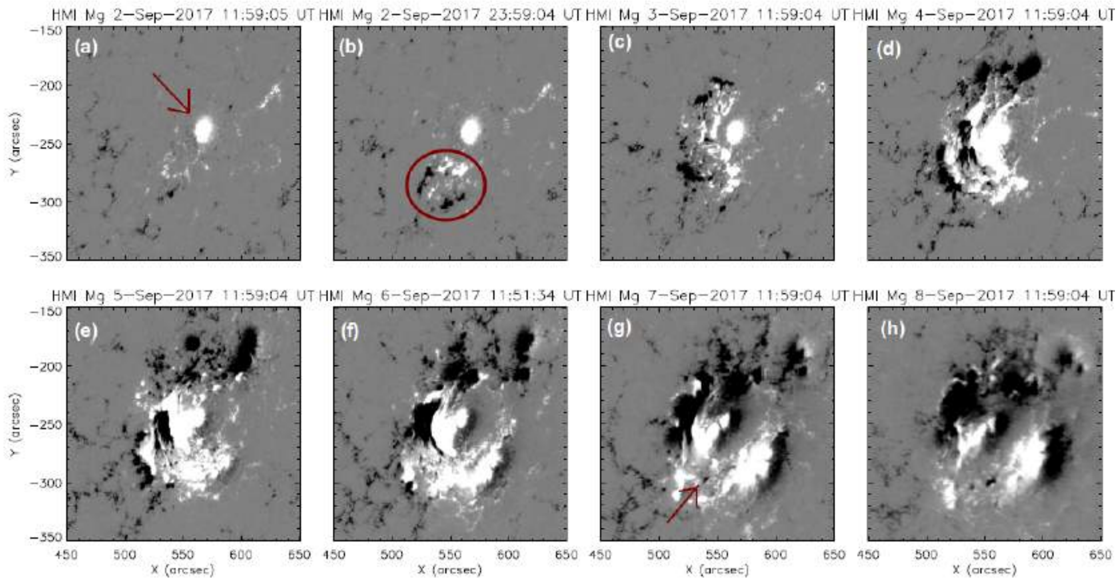

Figure 6.3: Series of HMI continuum images showing the build up and evolution of the active region NOAA 12673. All the images were rotated to the co-ordinate corresponding to 6 September 2017 12:00 UT. The arrow in panel (a) indicate the positive polarity sunspot. The oval shape in panel (b) indicates the initial flux emergence on 3 September 2017.

the visible hemisphere of the Sun (Figures 6.1(f)–(h), 6.2(f)–(h), 6.3(f)–(h)).

6.3 Flaring activity from NOAA 12673

In total, NOAA 12673 produced 4 X-class and 27 M-class flares along with numerous smaller events. In Table 6.1, a summary of the flares of GOES class M and above is given. From Table 6.1 we find that the first M class flare from NOAA 12673 originated on 4 September 2017 suggesting that the AR remained flare quiet for ≈6 days after its appearance. Importantly, after producing the first M-class flare, the AR produced 12 further M-class flares within 2 days before producing the first X-class flare.

The first X-class flare from NOAA 12673 (GOES class X2.2; Verma, 2018; Romano et al., 2018; Yan et al., 2018; Liu et al., 2018b; Mitra et al., 2018; Zou et al., 2019) originated on 6 September and within ≈3 hours after its initiation, the AR produced the largest flare of the solar cycle 24, having GOES class X9.3 (Verma, 2018; Romano et al., 2018; Yan et al., 2018; Mitra et al., 2018; Zou et al., 2020). After producing two X-class flares on 6 September, NOAA 12673 produced two more X-class flares, one on 7 September 2017 and the last one on 10 September 2017. This extraordinary AR moved to the other side of the Sun on 10 September 2017 when the last X-class flare (of GOES class X8.2) was within the impulsive phase (see e.g., Gary et al., 2018; Veronig et al., 2018; Reeves et al., 2020; Zhao et al., 2021).

As we found from Figure 6.1, the AR started evolving from 3 September 2017 after a few initial days of very less apparent activities. Further, it moved too close to the western limb of the Sun after 8 September 2017. Since, magnetic field observation loses reliability close to the solar limb, our following analysis were limited between 2 September and 8 September. In Figure 6.4, we plot the disk-integrated SXR flux variation between 2 and 8 September to understand the overall activity level from NOAA 12673. Notably, during the initial phase of the AR's transit, we observed the presence of one more AR (see Figure 6.1(a)–(d)). However, during the most flaring phase, NOAA 12673 was the only AR on the solar disk suggesting the SXR evolution was predominantly caused by NOAA 12673.

Figure 6.4 suggests that the background SXR level remained at a constant level till ≈12:00 UT on 3 September 2017 despite multiple short-lived SXR peaks. We denote this period as 'Phase 1' when the AR was devoid of any major activity

Table 6.1: Summary of the large flares (GOES class M1 or above) originated from the active region NOAA 12673

Flare Id.	Date (Sep '17)	AR conf.	Location	Flare timing (UT) Start/ Peak/ End	GOES class
F_1	4	$\beta\gamma$	S10W04	05:36/ 05:49/ 06:05	M1.2
F_2			S10W08	15:11/ 15:30/ 15:33	M1.5
F_3			S07W11	18:05/ 18:22/ 18:31	M1.0
F_4			S09W11	18:46/ 19:37/ 19:52	M1.7
F_5			S10W11	19:59/ 20:02/ 20:06	M1.5
F_6			S10W11	20:28/ 20:33/ 20:37	M5.5
F_7			S09W12	22:10/ 22:14/ 22:19	M1.7
F_8	5	$\beta\gamma\delta$	S09W14	01:03/ 01:08/ 01:11	M4.2
F_9			S09W15	03:42/ 03:51/ 04:04	M1.0
F_{10}			S11W18	04:33/ 04:53/ 05:07	M3.2
F_{11}			S11W19	06:33/ 06:40/ 06:43	M3.8
F_{12}			S10W23	17:37/ 17:43/ 17:51	M1.5
F_{13}	6	$\beta\gamma\delta$	S08W32	08:57/ 09:10/ 09:17	X2.2
F_{14}			S09W34	11:53/ 12:02/ 12:10	X9.3
F_{15}			S08W36	15:51/ 15:56/ 16:03	M2.5
F_{16}			S08W38	19:21/ 19:30/ 19:35	M1.4
F_{17}			S08W40	23:33/ 23:39/ 23:44	M1.2
F_{18}	7	$\beta\gamma\delta$	S08W44	04:59/ 05:02/ 05:08	M2.4
F_{19}			S07W46	09:49/ 09:54/ 09:58	M1.4
F_{20}			S07W46	10:11/ 10:15/ 10:18	M7.3
F_{21}			S08W48	14:20/ 14:36/ 14:55	X1.3
F_{22}			S11W54	23:50/ 23:59/ 00:14 (8 Sep)	M3.9
F_{23}	8	$\beta\gamma\delta$	S09W55	02:19/ 02:24/ 02:29	M1.3
F_{24}			S07W55	03:39/ 03:43/ 03:45	M1.2
F_{25}			S09W57	07:40/ 07:49/ 07:58	M8.1
F_{26}			S09W63	15:09/ 15:47/ 16:04	M2.9
F_{27}			S08W69	23:33/ 23:44/ 23:56	M2.1
F_{28}	9	$\beta\gamma\delta$	S11W70	04:14/ 04:28/ 04:43	M1.1
F_{29}			S08W74	11:50/ 11:04/ 11:42	M3.7
F_{30}			S09W88	22:04/ 23:53/ 01:30 (10 Sep)	M1.2
F_{31}	10	$\beta\gamma\delta$	S08W88	15:35/ 16:06/ 16:31	X8.2

(Figure 6.4) The background SXR level steadily increased from ≈12:00 UT on 3 September till ≈20:00 UT on 4 September till the onset of the M5.5 flare. This period can be classified as 'Phase 2' when the AR underwent rapid flux emergence (Figure 6.3) and became magnetically complex which led to the overall increase in SXR emission. Following the M5.5 flare, we observed a temporary decay in the GOES background flux till ≈06:00 UT on 6 September. This period is referred as 'Phase 3'. After this time, SXR emission from the AR rapidly increased leading

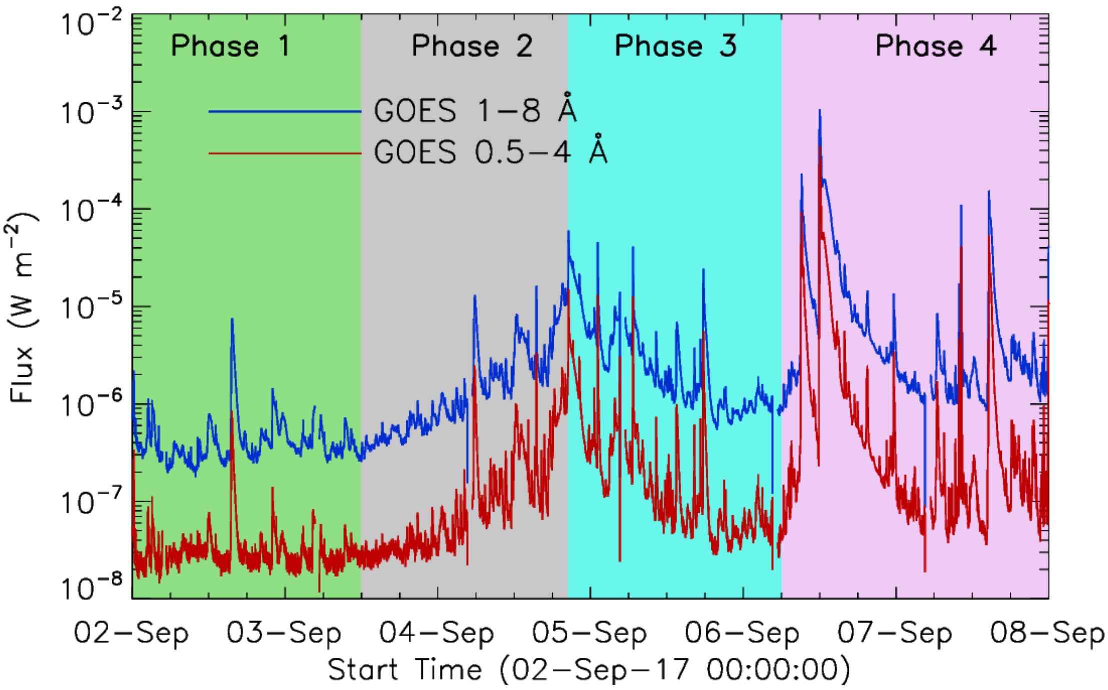

Figure 6.4: GOES SXR flux in the 1–8 Å (blue) and 0.5–4 Å (red) channels showing the occurrence of the flares during 2–8 September 2017. On the basis of the background SXR trend, the entire duration has been divided into four phases.

to the onset of the two X-class flares on 6 September 2017. This period can be classified as 'Phase 4' which is characterized as the most flare productive period of NOAA 12673.

EUV images of the AR provided important insights in the context of coronal magnetic field configuration of the AR during its different phases (Figure 6.5). AIA EUV channels at different sampling temperatures suggested significant spatial extension of the AR toward developing into a sigmoid structure, over the course of the AR's lifetime. Interestingly, during Phase 2 (second column in Figure 6.5), a highly localized region situated around the central part of the sigmoid displayed the most intense EUV emission (indicated by the black arrow in Figure 6.5(b)). However, during Phase 4, we observed intense emission from the entire sigmoidal structure (last column of Figure 6.5). In the following section, employing photospheric longitudinal current maps, we investigate the evolution of NOAA 12673 and explore the reasons for the higher flare productivity.

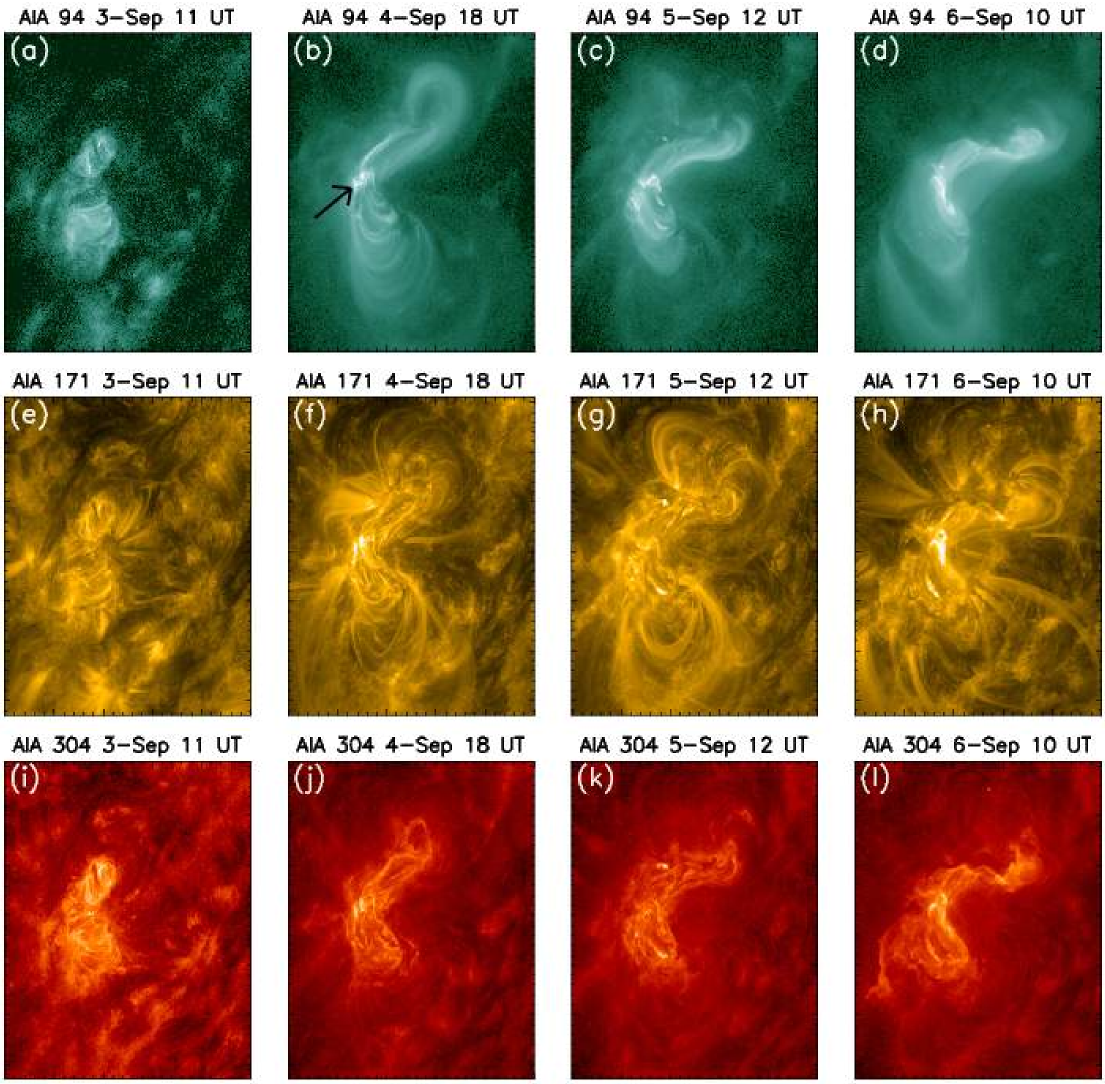

Figure 6.5: Representative AIA 94 Å (top row), 171 Å (middle row), and 131 Å (bottom row) images showing the EUV evolution of the active region during different activity phases of the active region. The four columns correspond to the four phases respectively.

6.4 Evolution of longitudinal current maps

The vertical component of photospheric current density (j_z) is computed by taking the 2D curl of the horizontal components of magnetic field (see Equation 3.1). Photospheric current (I_z) is derived from current density (j_z) by multiplying j_z with the area of one pixel ($\approx 13.14\times10^{10}$ m^2 for HMI vector magnetograms of the 'hmi.sharp_cea_720s' series).

In Figure 6.6, we plot the I_z-maps of NOAA 12673 during Phase 1. We remember that, during the major part of this phase, the AR was mostly consisted of a unipolar sunspot (Figures 6.1, 6.2, 6.3). Consequently, I_z-maps did not reveal any

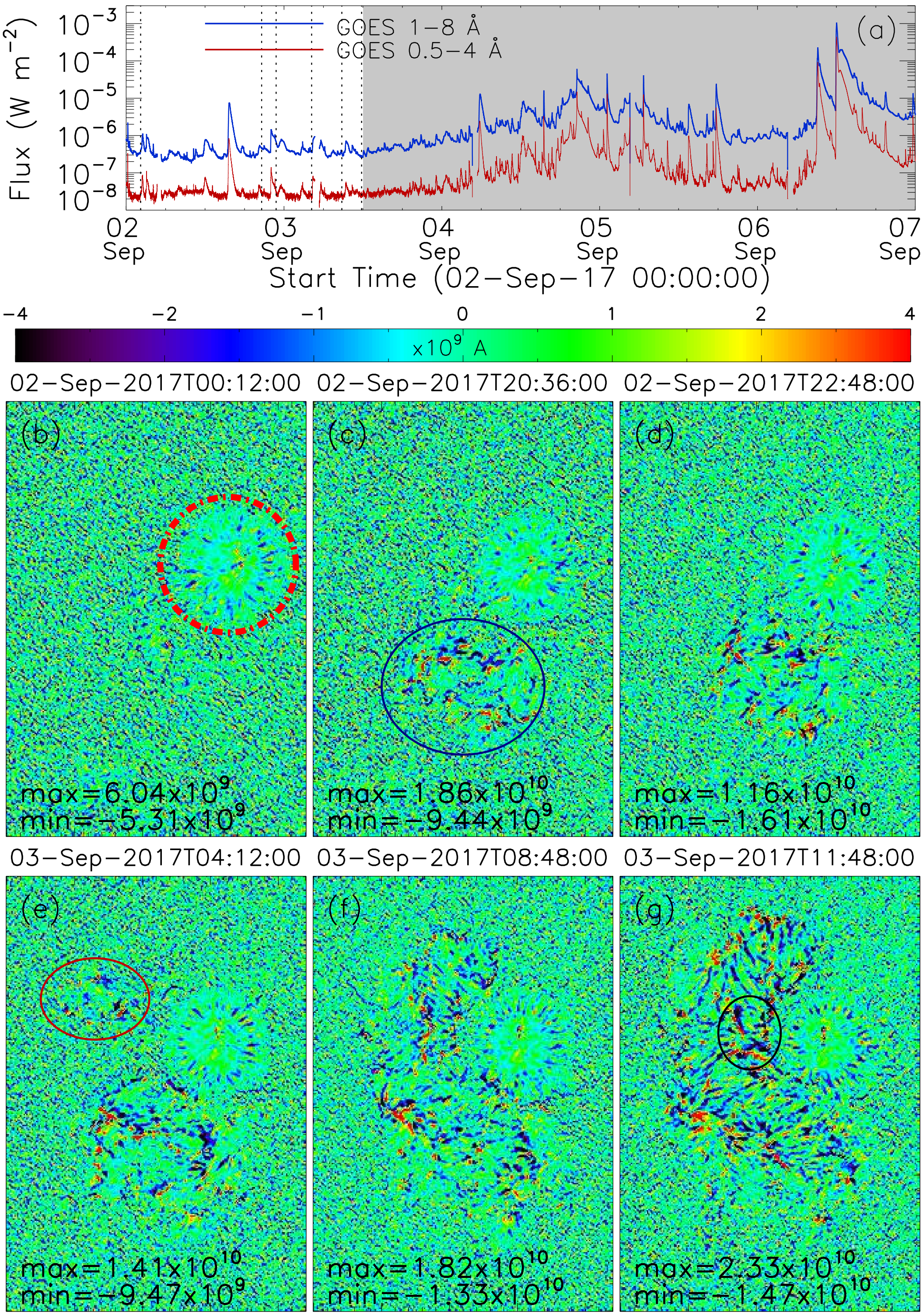

Figure 6.6: Panel (a): GOES 1–8 Å (blue curve) and 0.5–4 Å (red curve) showing the temporal evolution of the active region NOAA 12673 between 2–7 September 2017. Only Phase 1 is not gray-shaded. Panels (b)–(g): I_z-maps of NOAA 12673 during six representative intervals showing the evolution of longitudinal photospheric current during Phase 1. The time-stamps of the I_z-maps are indicated in Panel (a) by six dotted lines.

strong current location on the AR (Figure 6.6(b); the sunspot area is outlined by the red dash-dotted circle). As the AR underwent rapid flux emergence during the later part of Phase 1, we observe gradual accumulation of current at the locations of flux emergence. Interestingly, the values of maximum and minimum longitudinal photospheric currents increased by $\approx$4 and $\approx$3 times, respectively, during Phase 1 (cf., Figures 6.6(b) and (g)). We have highlighted different locations of current formations by oval shapes in the different panels of Figure 6.6.

Although, the values of current increased significantly by the end of Phase 1, the I_z-maps did not reveal any mention-worthy current-structures in Phase 1. During Phase 2, we observed development of a few interesting structures composed of strong photospheric currents (Figure 6.7). As flux emergence occurred to the eastern direction of the positive polarity sunspot (indicated by the black arrow on the I_z map in Figure 6.7(a)), it is expected that the photospheric strong current regions would also develop on the eastern part of the AR. The most noticeable development in the I_z-maps of NOAA 12673 during Phase 2 was in the form of an elongated negative ribbon-like current structure (indicated by the brown arrows in Figures 6.7(c)–(g)). Apart from this 'current ribbon' structure, we observed the development of opposite polarity currents in a close proximity over a localized area at the eastern part of the AR (indicated by the black arrows in Figures 6.7(e)–(g); cf., this location with the location indicated by the pink arrow in Figure 6.7(b)).

NOAA 12673 moved into Phase 3 following the M5.5 flare which initiated at $\approx$20:28 UT on 4 September 2017. As expected, complex arrangements of strong photospheric currents decreased after the impulsive phase of the M5.5 flare (cf., Figure 6.7(g) and Figure 6.8(b)). However, since flux emergence continued during this phase, we observed important evolution of photospheric longitudinal currents in the I_z-maps of Phase 3 (Figure 6.8). The location of mixed current directions (indicated by black arrow in Figure 6.8(b)) underwent through constant development of positive current while the negative current remained mostly consistent (indicated by black arrows in Figures 6.8(c), (d), (f)). The location indicated by the blue arrows in Figures 6.8(b), (c) and (e) is also noteworthy. Here, we observed initial development of currents of both signs which seem to underwent decay afterward. Further, the thickness of the elongated negative current structure

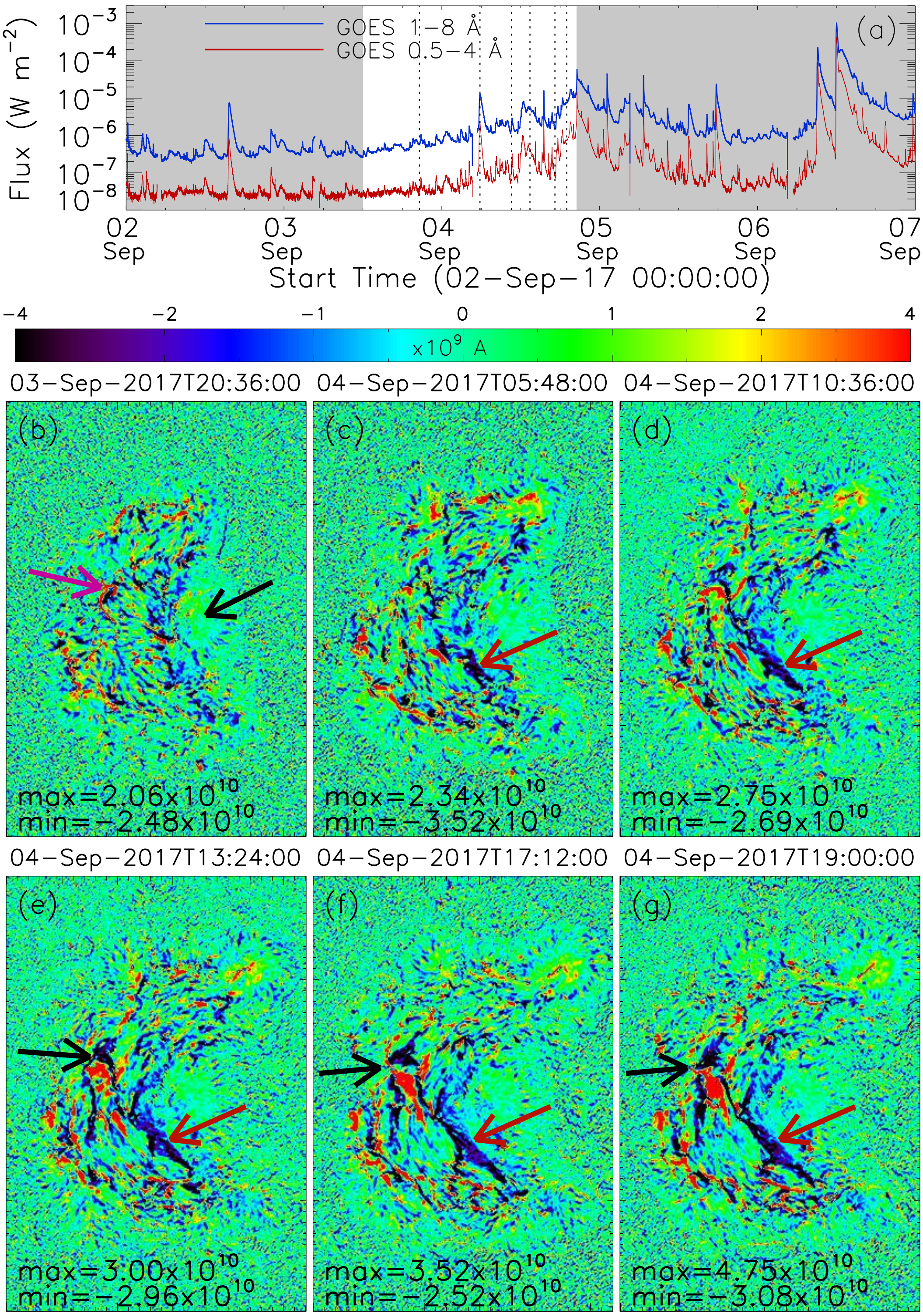

Figure 6.7: Same as Figure 6.6 but for Phase 2. Different arrows in different panels indicate few instances of current development and cancellation.

which developed during Phase 2 (indicated by the brown arrow in Figure 6.7(g)) significantly decayed during Phase 3 and reduced to an extremely narrow current strip by the end of the phase (indicated by brown arrows in Figures 6.8(e)–(g)).

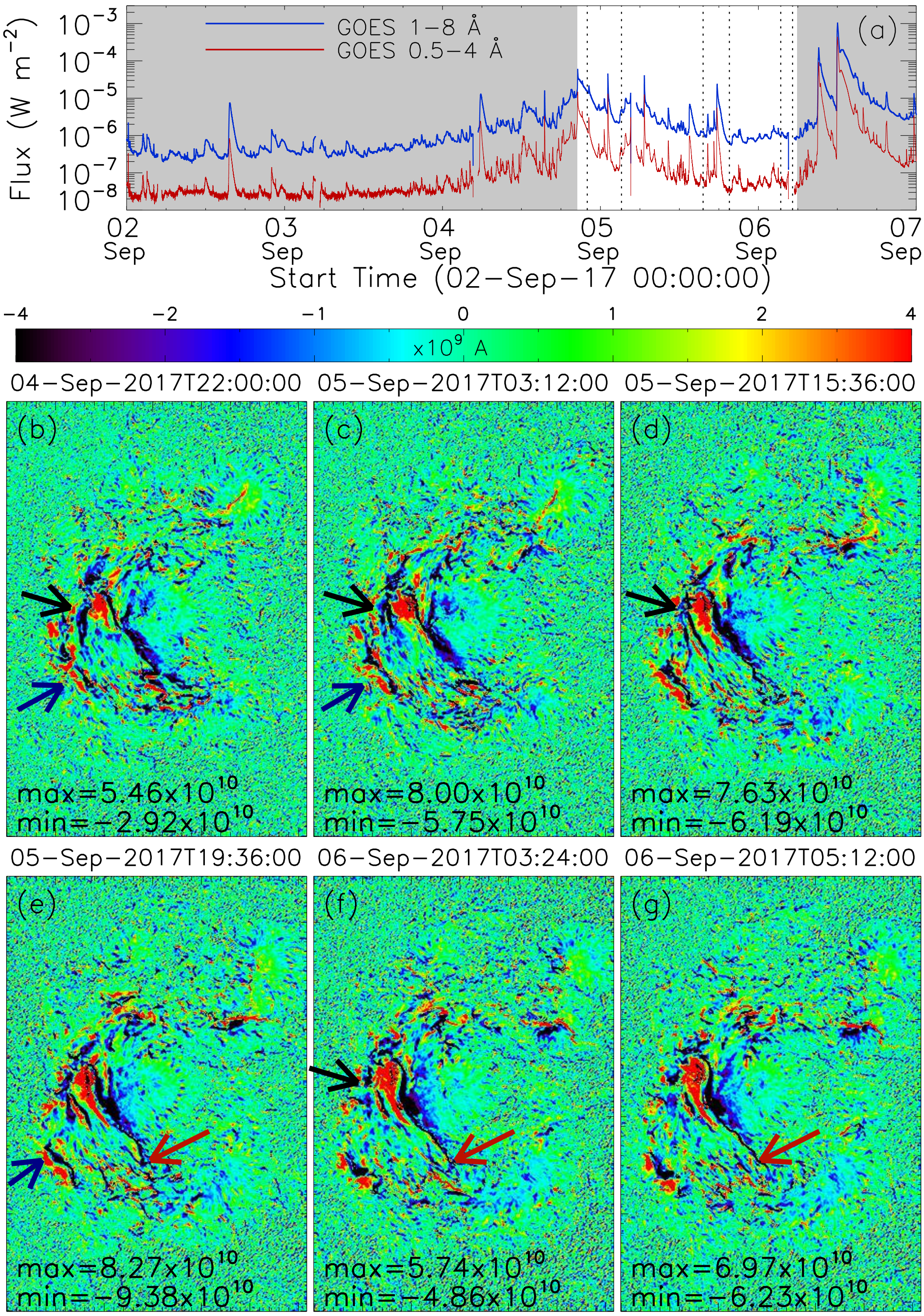

Figure 6.8: Same as Figure 6.6 but for Phase 3. Different arrows in different panels indicate few instances of current development and cancellation.

The circular positive polarity patch situated close to the northern end of the negative current ribbon-like structure, gradually elongated southward in parallel to the negative current structure (cf., Figures 6.8(b), (g)).

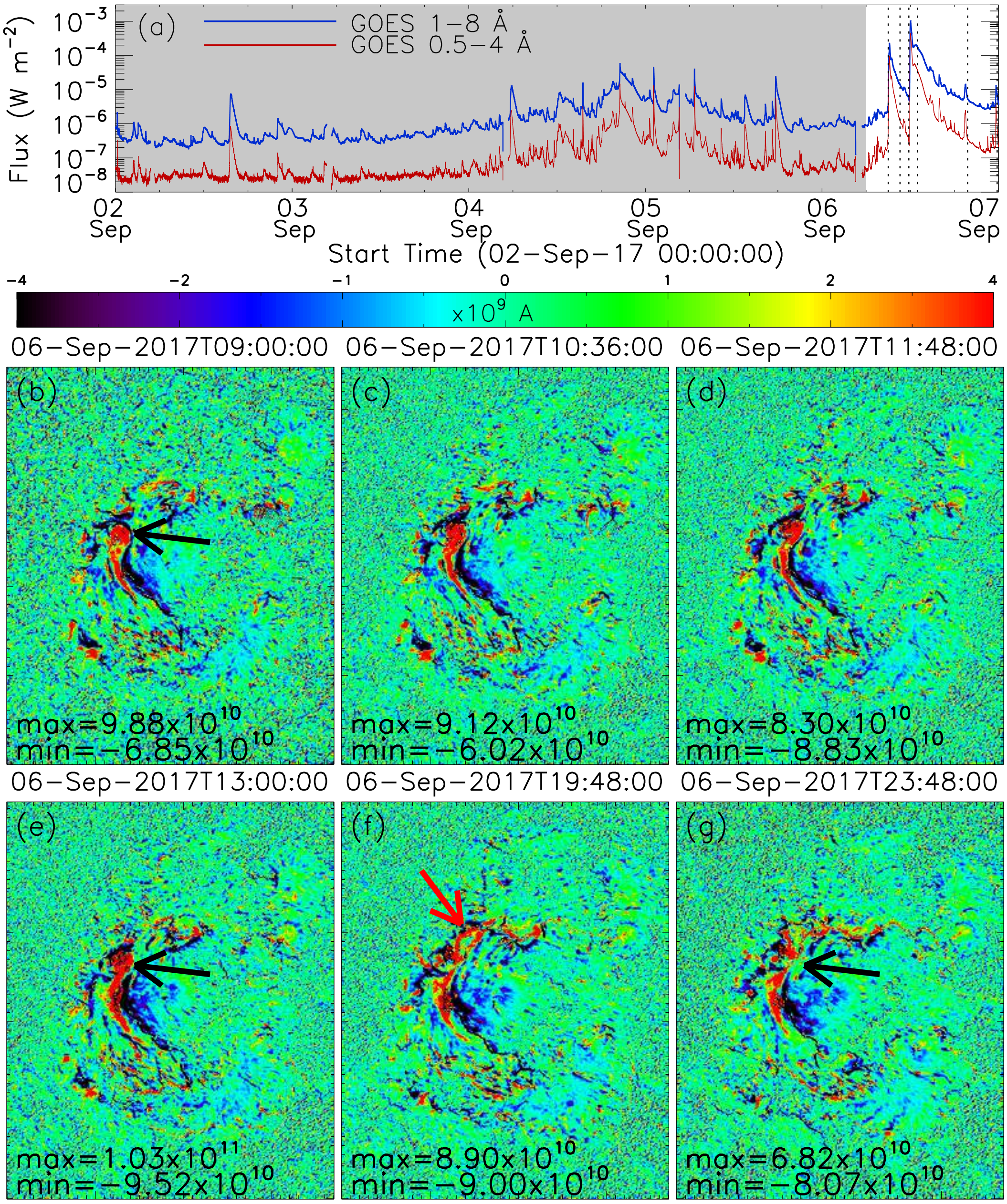

Figure 6.9: Same as Figure 6.6 but for Phase 4. Different arrows in different panels indicate few instances of current development and cancellation.

Phase 4 of the AR can be readily characterized as the most flare productive period during the evolution of NOAA 12673. As expected, the photospheric currents reached to the maximum values during this phase (Figure 6.9) in comparison to the prior phases. Particularly, the location indicated by the black arrow in Figure 6.9(b) is important which was characterized by extremely close proximity of localized strong current patches of opposite direction, prior to the onset of the X2.2 flare. Notably, the X2.2 flare was initiated from this location (see e.g., Mitra et al., 2018). Following the X2.2 flare, the complex arrangement of photospheric current decayed, as well as the maximum and minimum values of currents also decayed (cf., Figures 6.9(b), (c)). Further, prior to the onset of the X9.3 flare, the elongated ribbon-like parallel-shaped structure composed of positive and negative currents became most prominent (cf., Figures 6.9(b) and (d)). It is noteworthy that the X9.3 flare initiated as the flux rope situated along the sharp PIL between the positive polarity sunspot and the negative flux regions, underwent eruption (see e.g., Mitra et al., 2018). The ribbon-like opposite currents structure, therefore, can be explained as the photospheric manifestations of the flux rope. Following the X9.3 flare, currents of both polarities from this ribbon-shaped structure decayed significantly (cf., Figures 6.9(d), (g)). Interestingly, we observed an oval-shaped positive current structure situated to the north of the current ribbon structure (indicated by the red arrow in Figure 6.9(f)) which decayed within a few hours (see Figure 6.9(g)). Further, the arc-shaped positive current (indicated by the black arrow in Figure 6.9(e)) completely decayed by the end of Phase 4 (indicated b the black arrow in Figure 6.9(g)).

6.5 Circumstances during X-class flares on 6 September 2017

Characteristics of δ-spot of NOAA 12673

The magnetic complexity of NOAA 12673 evolved into the $\beta\gamma\delta$-type on 5 September 2017. The δ-type sunspots are identified as fragmented umbrae of opposite polarities sharing a common penumbra (Künzel, 1960). Such complex ARs are usually associated with very high magnetic gradient across the PILs. To understand the magnetic nature of the δ-spots of NOAA 12673, in Figure 6.10, we plot co-temporal white light image and magetogram of the AR prior to its most flaring phase and calculate magnetic gradient across the PIL associated with the bipolar region. The white light image suggests the presence of a few segmented umbrae within the central sunspot area which were surrounded by a single penumbra (Figure 6.10(a)). Comparison of the white light image and the magnetogram (cf., Figures 6.10(a) and (b)) suggests a few of these fragmented umbrae to have negative polarity and a few to be associated with positive polarity. Figure 6.10(c) readily suggests that LOS magnetic strength sharply changed from ≈1500 G to ≈ −1000 G within a distance of ≈1 arcsec across the PIL. Consequently, the PIL region was associated with the highest magnetic gradient with a value ≈2.4×10^3 G Mm^{-1}. This confirms NOAA 12673 to be associated with all the characteristic properties of typical δ-type sunspots prior to the onset of the X-class flares.

Temporal evolution of the X-class flares

Two homologous X-class flares originated from NOAA 12673 on 6 September 2017 with GOES classes X2.2 and X9.3 (see Table 6.1). To understand the temporal evolutions of the two flares we plot GOES SXR and AIA (E)UV lightcurves in Figure 6.11 (panels (a) and (b), respectively). Both SXR and (E)UV lightcurves suggest the onset of the impulsive phase of the X2.2 flare at ≈08:57 UT. Following the peak emission at ≈09:10 UT, the X-ray flux of both the GOES channels (1–8 Å and 0.5–4 Å) gradually decreased till ≈11:55 UT and thereafter rapidly increased, implying the onset of the X9.3 flare. Within a brief ≈9 minutes, the flare reached to the peak emission at ≈12:02 UT. In a complete agreement with the SXR fluxes, the abrupt increase of flare emission was observed in the AIA (E)UV emission also (Figure 6.11(b). After ≈12:02 UT, flux in both SXR and (E)UV energies decreased suggesting the flare's progression to the gradual phase.

EUV imaging of the X2.2 flare

In order to understand the evolution of the X2.2 flare, we plot a few representative AIA 94 Å and 304 Å images in Figure 6.12. The EUV images prior to the onset of the flare (Figures 6.12(a) and (d)) readily confirms that the coronal configuration associated with the AR took the shape of an impressive 'inverse-S' i.e., a prominent coronal sigmoid (the sigmoidal structure is highlighted by the dotted curve in Figure 6.12(a)). Notably, the sigmoid encompassed the entire stretch of the AR and axis of the sigmoid was associated with the PIL between the positive and negative flux regions. The onset of the X2.2 flare took place with intense emission from a relatively localized 'question mark (?)' shaped structure from the center of the sigmoid (indicated by the white arrow in Figure 6.12(b)). Careful inspection suggests this emitting structure to be composed of a few loop-like features which suggests this structure to be a coronal hot channel i.e., an activated flux rope.

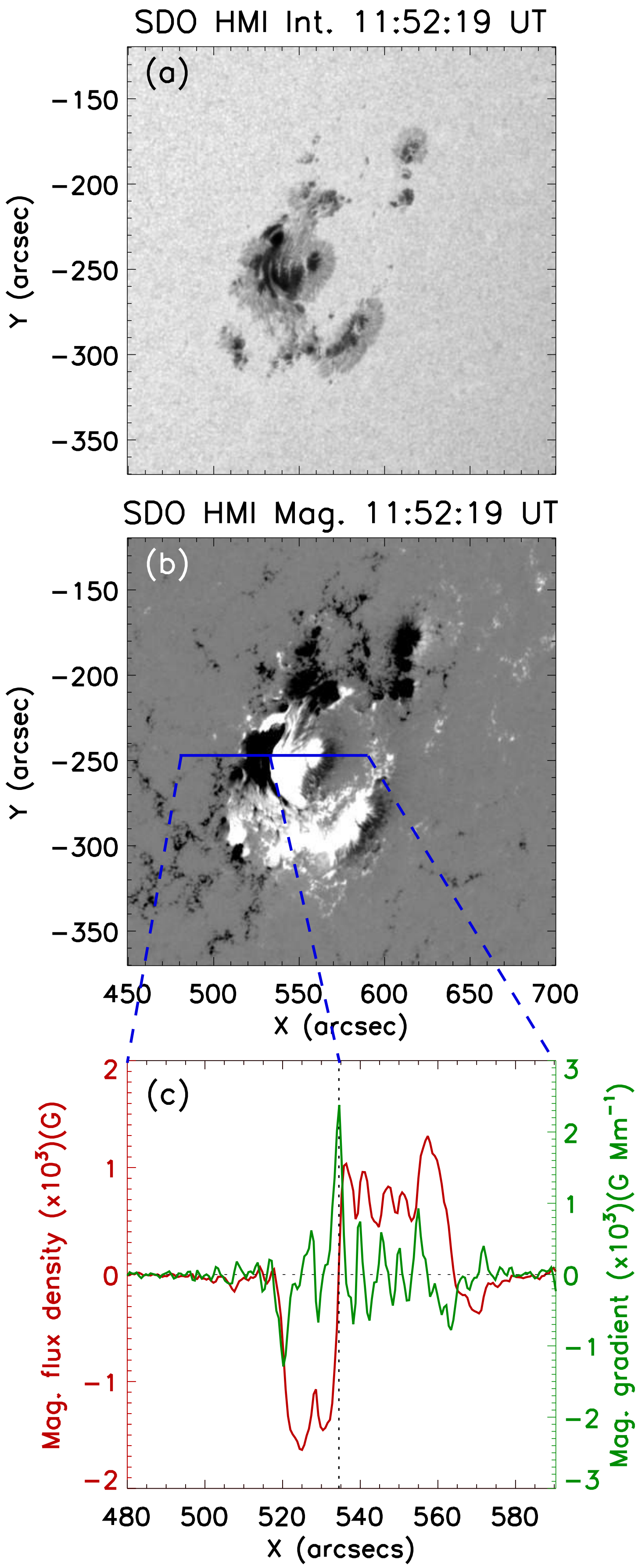

Figure 6.10: Panel (a): HMI continuum image of the active region NOAA 12763 prior to the onset of the X-class flares on 6 September 2017, showing multiple, fragmented umbrae within a single penumbrae. Panel (b): co-temporal HMI LOS magnetogram of NOAA 12673. Panel (c): LOS magnetic flux density (red) and magnetic gradient (green) computed along the blue slit in panel (b).

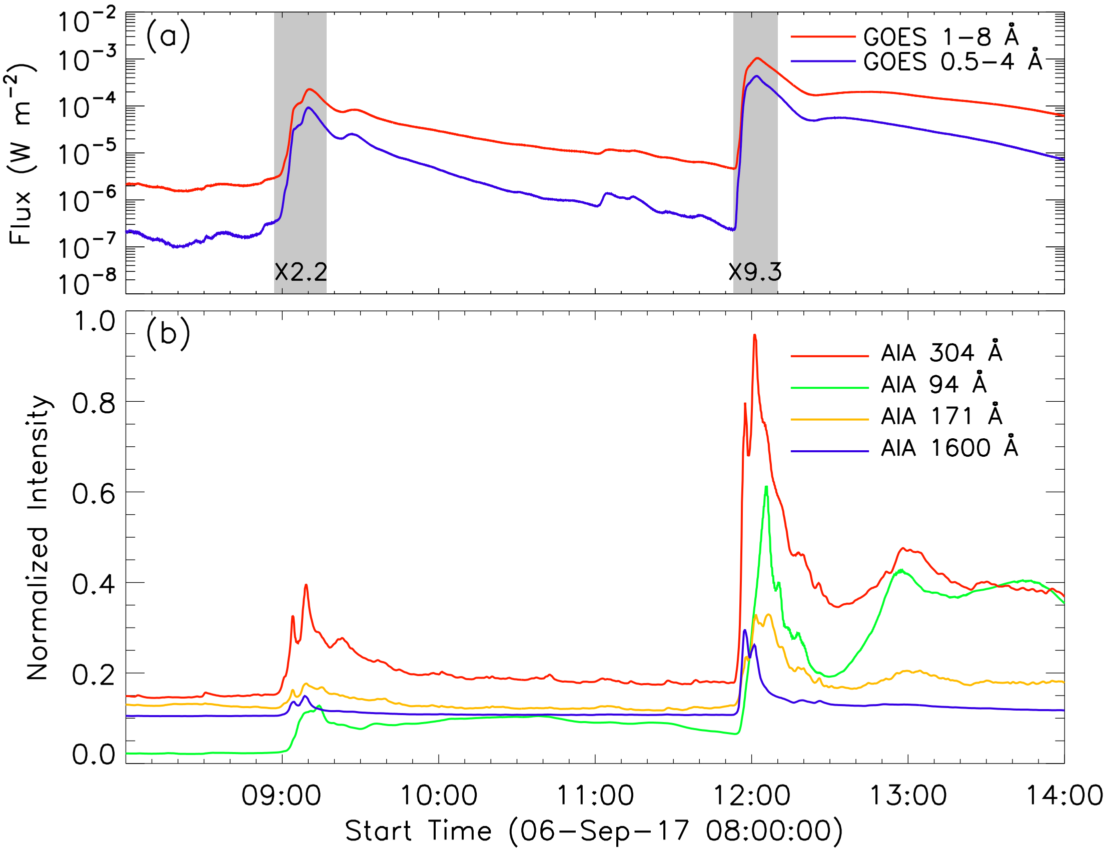

Figure 6.11: Panel (a): GOES X-ray flux profiles in 1–8 Å and 0.5–4 Å from 08:00 UT to 14:00 UT on 6 September 2017 covering the occurrence of two X-class flares. The flaring intervals are highlighted by the gray-shaded intervals which also mentions the corresponding GOES flare classes. Panel (b): (E)UV lightcurves from different AIA channels, normalized by corresponding peak intensities. For a better visualization, the AIA lightcurves have been scaled by factors of 1, 0.65, 0.33, and 0.33 for 304 Å, 94 Å, 171 Å, and 1600 Å channels, respectively.

During the impulsive phase of the flare, this flux rope underwent partial eruption (Mitra et al., 2018) but the overall coronal configuration of the AR remained mostly unchanged (cf. Figures 6.12(b), (e) with 6.12(c), (f)).

EUV imaging of the X9.3 flare

After the X2.2 flare, the sigmoidal structure underwent a gradual expansion and rise in the intensity of emission (cf. Figure 6.13(a) and 6.12(c)). Notably, prior to the onset of the X9.3 flare, the hot channel appeared as a thin, elongated thread-like structure at the central part of the sigmoid (indicated by the red arrow in Figure 6.13(b)). Notably, the flare initiated with a localized spot-like brightening at the northern footpoint of the hot channel (indicated by the white arrow

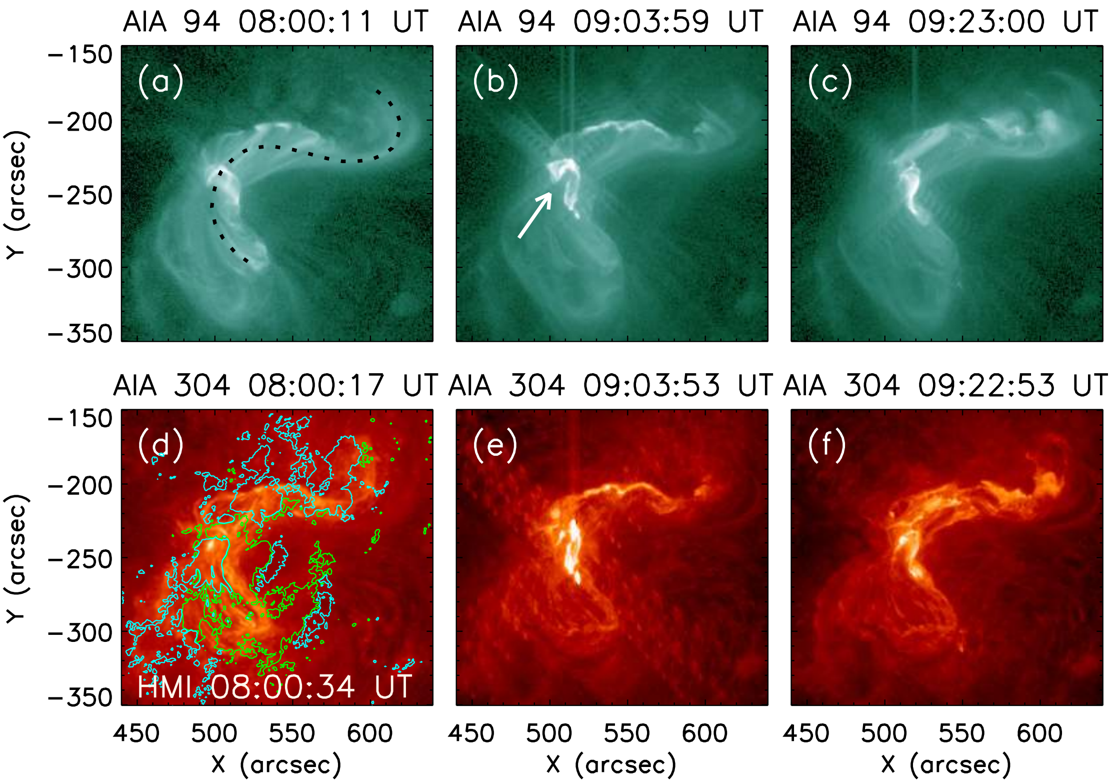

Figure 6.12: AIA 94 Å (panels (a)–(c)) and 304 Å (panels (d)–(f)) showing the evolution of the X2.2 flare on 6 September 2017. The dashed curve in panel (a) highlights the pre-flare sigmoidal structure. The arrow in panel (b) indicates a hot channel. Co-temporal HMI LOS magnetogram contours are plotted over panel (d). The green and sky-blue contours refer to positive and negative field, respectively. Contour levels are ±150 G.

in Figure 6.13(b)). Almost simultaneously we observed prominent signatures of filament eruption which initially ascended with the hot channel (indicated by the arrow in the inset of Figure 6.13(f)). Following the eruption, we observed formation of two prominent flare ribbons which were situated very close to each other (shown within the inset of Figure 6.13(g)). The narrow post-reconnection arcade connecting these flare ribbons is indicated by the yellow arrow in Figure 6.13(c). Importantly, the gradual phase of the flare was characterized by the formation of a large-scale loop arcade that encompassed the entire stretch of the AR (indicated by the blue arrows in Figures 6.13(d) and (h)). AIA 304 Å images of this phase revealed the formation of large-scale flare ribbons at the footpoints of the large loop-arcade which are indicated by the green arrows in Figure 6.13(h).

Model coronal configurations prior to the X-class flares

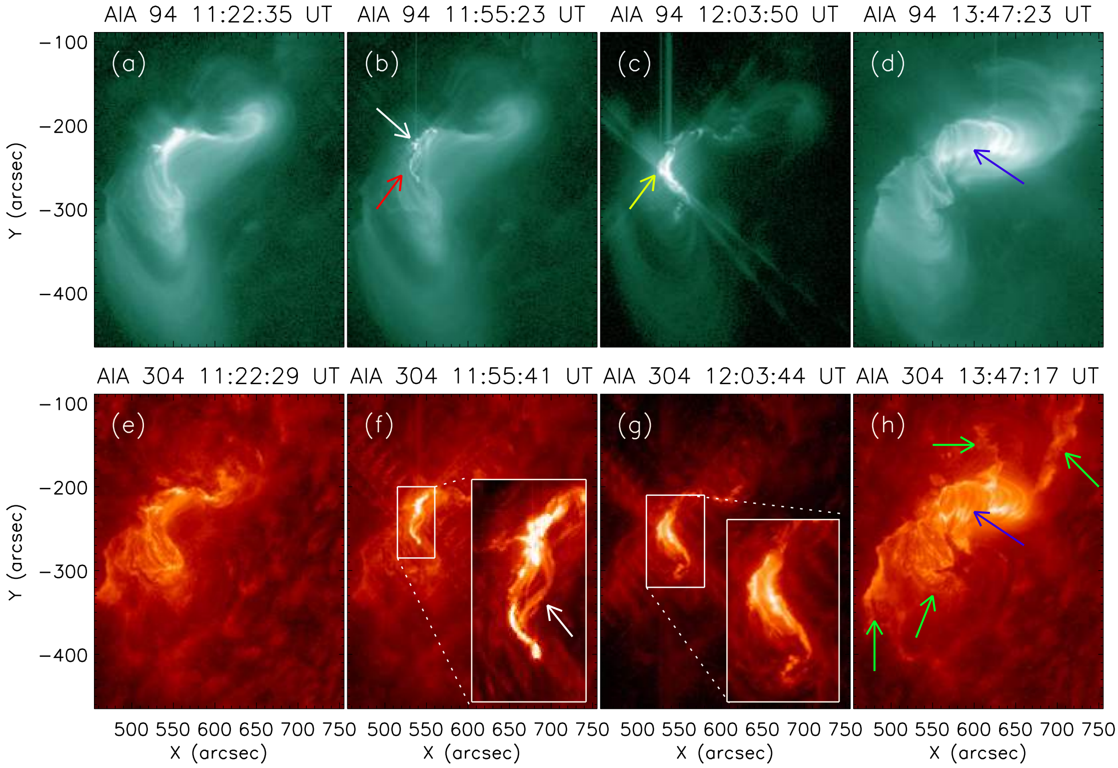

Figure 6.13: AIA 94 Å (panels (a)–(d)) and 304 Å (panels (e)–(h)) showing the evolution of the X9.3 flare on 6 September 2017. The red arrow in panel (b) indicates a thin hot channel. The white arrow in panel (b) indicates the location of the earliest brightening prior to the eruption of the hot channel. The yellow arrow in panel (c) indicates intense thermal emission from the location of the hot channel. The blue arrows in panels (d) and (h) indicate a large-scale post-reconnection arcade encompassing almost the entire span of the active region. The white arrow in the inset of panel (f) indicates the erupting hot filament. The green arrows in panel (h) indicate a set of large-scale flare ribbons during the gradual phase of the X9.3 flare.

In order to understand the coronal magnetic configuration leading to the onset of the two X-class flares, we carried out NLFFF extrapolation at 08:48 UT and 11:48 UT (prior to the onset of the X2.2 and X9.3 flares, respectively). In both the instances, we used the following values of the free parameters (see Chapter 2.3.2):

$$\nu = 0.01; \qquad w_{los} = 1; \qquad w_{trans} = \frac{B_{trans}}{max(B_{trans})};$$

$$\mu_1 = \mu_2 = 1; \qquad \mu_3 = 0.001; \qquad \mu_4 = 0.01$$

In Table 6.2, we have listed the values of the residual errors corresponding to all the four extrapolations, which can be used as the assessment of the NLFFF solutions.

The modeled magnetic field configuration prior to the onset of the X2.2 flare (Figures 6.14(a) and (b)) readily indicates the presence of a flux rope extending over the PIL (shown by the green lines) with northern and southern footpoints

Table 6.2: Summary of the parameters for assessing the quality of NLFFF extrapolation

Time of extrapolation	$< \lvert f_i \rvert >$	θ_J
08:48 UT	6.59×10^{-4}	5.67°
11:48 UT	6.59×10^{-4}	6.56°

fixed at negative and positive polarity regions of the central sunspot region, respectively. Notably, the appearance of the hot channel, observed just prior to the onset of the X2.2 flare, was almost precisely the same as the shape of the flux rope (see Figure 6.12(b)). Further, photospheric longitudinal currents of this period displayed a pair of ribbon-like structures composed of positive and negative currents (Figure 6.9(a)). The location next to the northern footpoints of the flux rope was characterized by a complex coronal structure similar to the fan-spine configuration that involved a magnetic null point. The two sets of fan-spine lines are depicted by the blue and pink lines in Figures 6.14(a) and (b) and the coronal null point is indicated by a black arrow in Figure 6.14(b). Here we remember that the corresponding photospheric location was associated with strong vertical currents of opposite directions situated in a close proximity (Figure 6.9(a).

The overall model magnetic configuration prior to the onset of the X9.3 flare at the core region of NOAA 12673 (Figures 6.14(c)–(d)) was similar to that corresponding to the X2.2 flare. However, the flux rope prior to the X9.3 flare (shown by the green lines in Figures 6.14(c)–(d)) appeared to be magnetically more twisted than that of the X2.2 flare. The overall fan-spine configuration prior to the X9.3 flare is shown by the blue and yellow lines in Figures 6.14(c) and (d). Notably, the northern footpoint of the flux rope itself appeared to be involved in the fan-spine configuration. In Figure 6.14(d), the null point involved in the fan-spine configuration is indicated by a black arrow. Here we remember that, the X9.3 initiated with a point-like brightening from the northern footpoint location of the hot channel (Figure 6.13(b)).

The presence of the null point close to the northern footpoint of the flux rope is supportive of the breakout model for solar eruptions (Antiochos et al., 1999; Karpen et al., 2012). During the impulsive phases of the X-class flares, the flux ropes underwent eruption and we observed intense EUV emission from this region

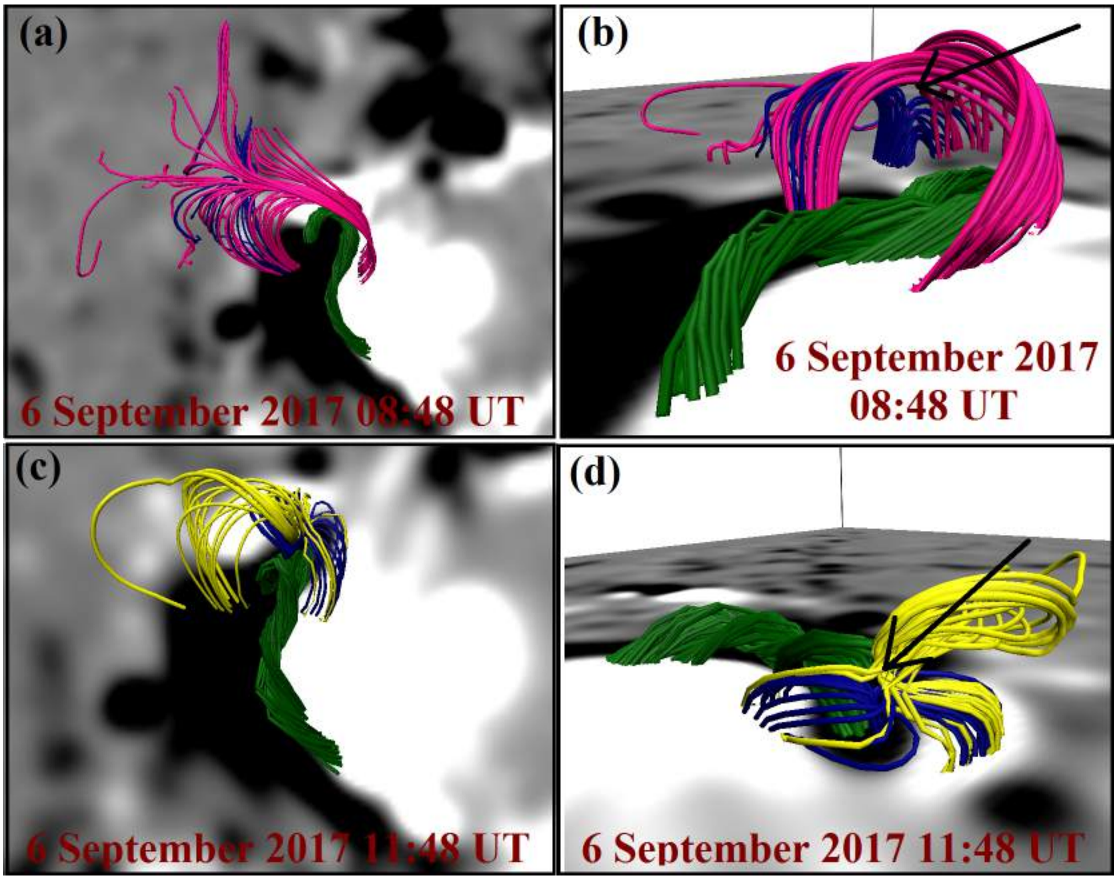

Figure 6.14: NLFFF-reconstructed coronal magnetic field configuration prior to the X2.2 flare (top panel) and X9.3 flare (bottom panel). In all the panels, the green lines represent magnetic flux ropes. The arrows in panels (b) and (d) indicate coronal null points.

(Figure 6.5(d), (h), (l); see also, Mitra et al., 2018).

6.6 Homologous M-class flares from minisigmoid of NOAA 12673

On 7 September 2017, NOAA 12673 produced two highly impulsive homologous M-class flares which were extremely intriguing in view of their association with a highly localized sigmoidal region. Both the events (M1.4 and M7.3 flares) were eruptive and exhibited complex dynamical evolution. In this section, we present our thorough multi-wavelength imaging and numerical analysis for investigating the origin and evolution of the eruptive events.

6.6.1 Event overview

To understand the temporal evolutions of the two M-class flares, we look at the GOES SXR fluxes in the 1–8 and 0.5–4 Å channels on 7 September 2017 from 09:45 to 10:30 UT (Figure 6.15(a); red and blue curves, respectively). The GOES SXR lightcurves suggest the first M-class flare (GOES class M1.4; indicated by an arrow in Figure 6.15(a)) to initiate at ≈09:51 UT. After the initiation, the flare emission underwent a brief period of slow rise during ≈09:51–09:53 UT. Notably, such slow rise in the flare missions often preceding the impulsive flare phase are identified as precursor phase (see, e.g., Veronig et al., 2002; Mitra & Joshi, 2019). Following ≈09:53 UT, SXR fluxes in both the GOES channels (i.e., 1–8 and 0.5–4 Å) underwent a rapid enhancement til ≈09:54 UT manifesting the short-lived impulsive phase. The flare reached at its peak at ≈09:54 UT which was followed by gradual decay of SXR fluxes. Flare emission continuously decayed till ≈10:14 UT except a subtle rise at ≈09:57 UT. SXR profiles further showed an abrupt rise from ≈10:14 UT, indicating the onset of the second M-class flare. The second M-class flare of GOES class M7.3 followed a brief impulsive phase of ≈2 min reaching to the peak emission at ≈10:16 UT. After ≈10:16 UT, flare emission steadily decreased and reached the pre-flare fluxes at ≈10:30 UT which marked the end of our observing period. Within our observing period, RHESSI missed observation till ≈09:59 UT due to 'South Atlantic Anomaly' (SAA; Hajdas et al., 2004) and then again from ≈10:24 UT due to 'RHESSI night'. Importantly, although RHESSI missed the M1.4 flare entirely, it provided continuous observational data during ≈09:59–10:24 UT that covered the interval between the two flares and the M7.3 flare almost entirely (Figure 6.15(b)). On the basis of the time evolution observed from the GOES SXR lightcurves in combination with the available RHESSI observations, we divided the entire duration (09:45–10:30 UT) into three periods: periods I and III cover the M1.4 and M7.3 flares with the associated eruptions, respectively, whereas period II covers a rather quiet phase in between the two M-class flares (Figure 6.15(a)).

(E)UV fluxes derived from different AIA channels integrated over the AR during the observing duration (Figure 6.15(c)) were in a general agreement with the GOES SXR flux variation, signifying the large influence of SXR emission from

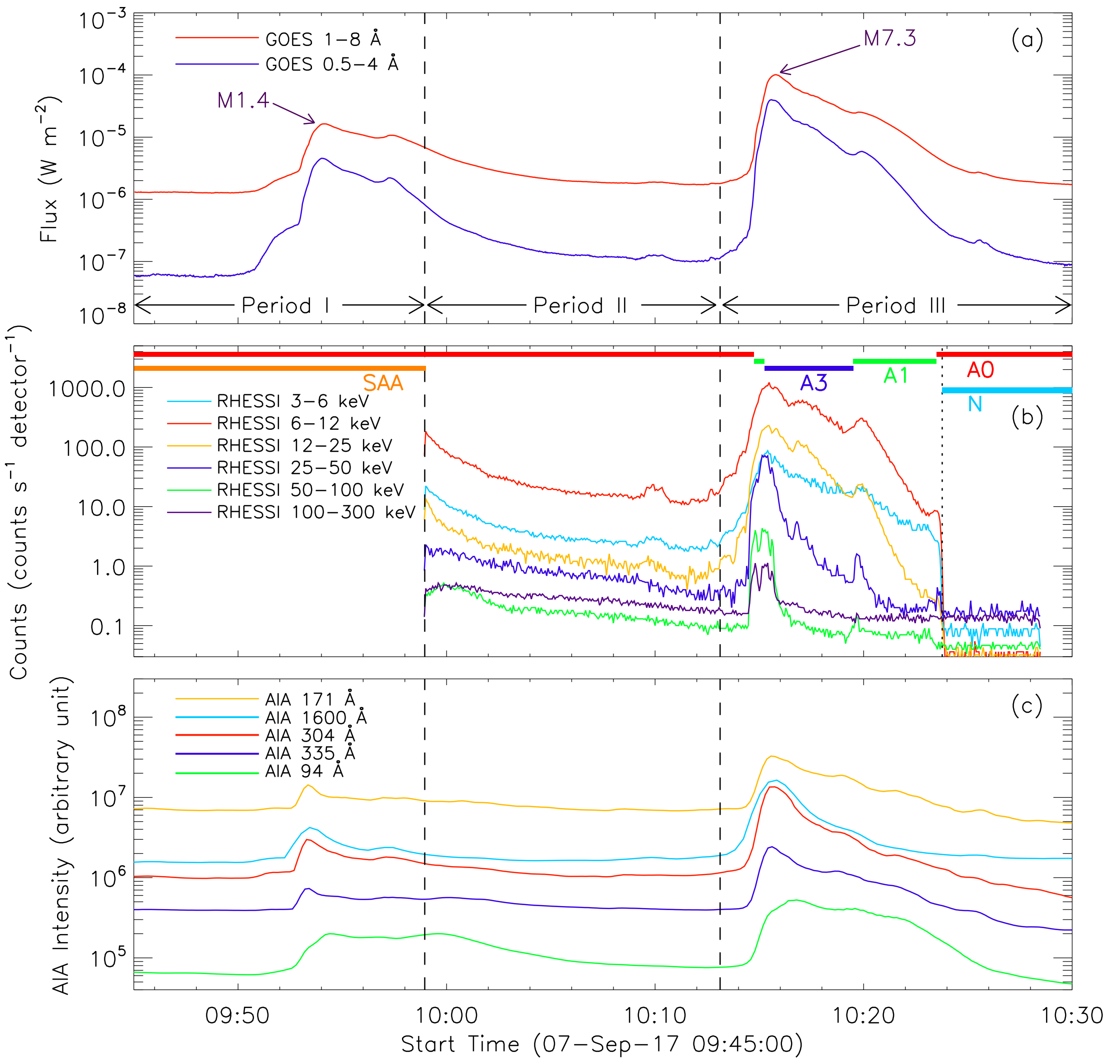

Figure 6.15: Panel (a): GOES SXR flux in the 1–8 Å (red curve) and 0.5–4 Å (blue curve) bands on 2017 September 7 from 09:45 to 10:30 UT, covering the two M-class flares under study. Panel (b): RHESSI X-ray fluxes normalized by factors of 10 , 30 , 100 , and 100 for the 12–25, 25–50, 50–100, and 100–300 keV energy bands, respectively. The horizontal red, green, and dark blue bars indicate the RHESSI attenuator states (A0, A1, and A3, respectively). The orange and light blue horizontal bars indicate the durations missed by RHESSI due to the SAA and 'RHESSI night', respectively. Panel (c): AIA (E)UV lightcurves. For clear visualization, the AIA lightcurves in channels 171 and 94 Å are scaled by 2 and 10 , respectively.

NOAA 12673 on the the disk-integrated GOES measurement. Temporal variations in all AIA (E)UV channels suggest the initiation of the M1.4 flare at ≈09:52 UT and the M7.3 flare at ≈10:14 UT. We have summarized the different phases of the flares in the studied interval in Table 6.3.

The morphology and multi-layer configuration of the AR at ≈09:45 UT on 7

Table 6.3: Chronology of Events during the Two M-class Flares that Occurred on 7 September 2017

Sr. No.	Evolutionary Stages	Time (UT)	Obs. Instr./ Wavelength	Remarks
1	Pre-flare phase	09:45	AIA (E)UV and HMI	Emission from a very localized inverted 'S' structure. We call it 'minisigmoid'.
2	Init. of M1.4 flare	09:49	GOES 1–8 Å	
3	Init. of plasma ejection during M1.4 flare	09:53	AIA 94 Å and 304 Å	Collimated ejection of plasma from the core of the minisigmoid toward the east.
4	End of M1.4 flare	09:58	GOES 1–8 Å	Appearance of a small filament in the minisigmoid region. Start of RHESSI observation at ≈09:59 UT.
5	Initiation of the M7.3 flare	10:11 UT	GOES 1–8 Å	
6	Init. of first phase of plasma ejection during M7.3 flare	10:14	AIA 304 Å	Collimated plasma ejection from the core of the minisigmoid toward the east. RHESSI sources of energies up to ≈100 keV from the minisigmoid region.
7	Init. of second phase of plasma ejection during M7.3 flare	10:16	AIA 304 Å	Eruption from the southern end of the filament, ejection of plasma toward the south.
8	Merging of the ejected plasma	10:22	AIA 335 Å	Strange deflection of ejected plasma from east to southwest direction.
9	End of M7.3 flare	10:18	GOES 1–8 Å	
10	Detection of CME	10:24	LASCO C2	

September 2017 is shown in Figure 6.16. Notably, after producing the two X-class flares on 6 September 2017 (see Section 6.3), the AR underwent significant decay in the overall sunspot area (cf., Figures 6.2(f) and (g)). As a consequence, prior to the onset of the homologous M-class flares on 7 September 2017, NOAA 12673 consisted of two major sunspots along with a few pores. A comparison between co-temporal continuum image and magnetogram (Figures 6.16(a) and (b), respectively) readily reveals that the southwestern sunspot group was primarily of positive polarity, while main, larger sunspot group was composed of mixed polarity fluxes. The northern localized part of the mixed polarity sunspot shown

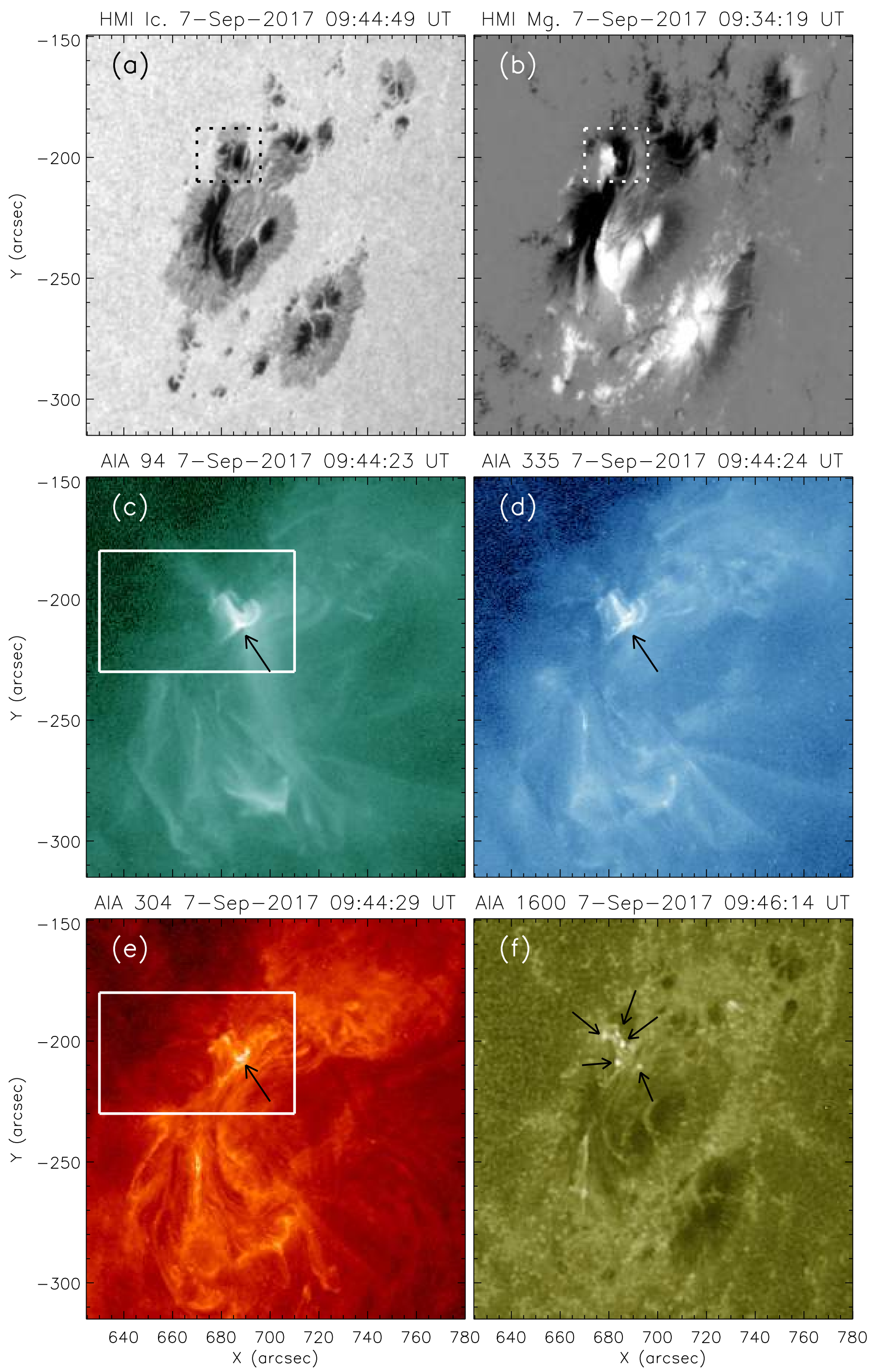

Figure 6.16: Panel (a): HMI white-light image of NOAA 12673 on 2017 September 7 09:44 UT. Panel (b): cotemporal HMI magnetogram. Panels (c)–(e): AIA EUV images of the AR in 94, 335, and 304 Å respectively, showing the morphology of the AR in the corona and chromosphere. Panel (f): AIA UV image of the AR in 1600 Å. The dashed boxes in panels (a) and (b) indicate the photospheric region associated with the two M-class flares. The boxes in panels (c) and (e) indicate the FOV of the AR plotted in Figures 3, 5, and 6. The arrows in panels (c)–(e) indicate the minisigmoid region, whereas the arrows in panel (f) indicate brightenings at the location of the minisigmoid.

within the dotted boxes in Figures 6.16(a) and (b) was particularly interesting. The corresponding coronal images displayed an intriguing semicircular arc-shaped structure similar to an inverted 'S'. In view of its shape and highly localized spatial extension, this structure can be considered as a minisigmoidal region. The minisigmoidal structure was prominently visible in the AIA EUV images (indicated by the black arrows Figures 6.16(c)–(e)), although it was not clearly identified in the UV images. However, AIA 1600 Å image displayed a few bright dots at the location co-spatial to the minisigmoid (indicated by the black arrows in Figure 6.16(f)). Notably, both the M-class flares originated from this minisigmoid region. In Sections 6.6.2–6.6.4, we focus on EUV images of the region outlined by the boxes in Figures 6.16(c) and (e), to understand the origin and evolution of the homologous flares.

6.6.2 Period I: evolution of the M1.4 Flare

To understand the evolution of the M1.4 flare, we look into series of AIA 94 and 304 Å images (Figures 6.17(a)–(i) and 6.17(j)–(r), respectively). As we discussed in Section 6.6.1, the pre-flare coronal configuration was characterized by the presence of a reverse 'S'-shaped minisigmoid. Notably, the minisigmoid appeared more prominently in the hot AIA channels (e.g., 94 Å) over the other AIA channels sampling relatively cooler atmospheric plasma (i.e., AIA 304 Å), in terms of its relative brightness compared to the ambient medium. The minisigmoid structure (outlined by a dashed curve in Figure 6.17(a)) significantly brightened up after ≈09:50 UT marking the onset of the M1.4 flare (cf., Figures 6.17(a) and (b)). We note a localized kernel-like brightening in the western leg of the minisigmoid at ≈09:53 UT (shown by the blue arrow in Figure 6.17(c)). Interestingly, emission from the kernel-like bright point was much prominent in the AIA 304 Å images (indicated by the blue arrow in Figure 6.17(l)) which is suggestive that the earliest episodes of energy release during the initiation of the M1.4 flare took place in lower, i.e., chromospheric, heights. The occurrence of the bright point was immediately followed by ejection of plasma from the middle of the minisigmoid (shown by the white arrow in Figure 6.17(c)). The ejection of plasma can be characterized as a very narrow and collimated motion i.e., a jet-like eruption. The direction of the jet-

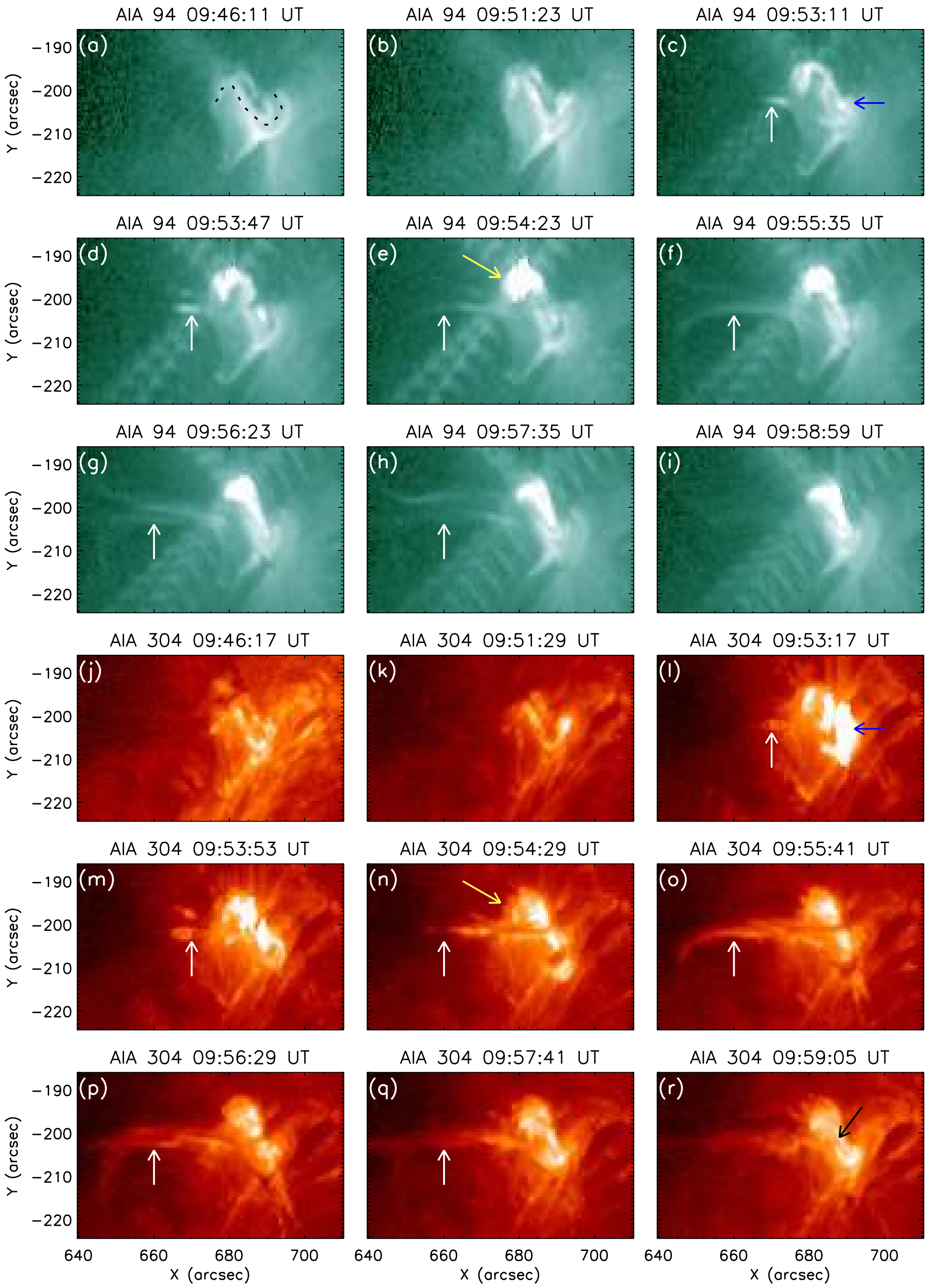

Figure 6.17: Series of AIA 94 (panels (a)–(i)) and 304 (panels (j)–(r)) Å images showing the time evolution of the M1.4 flare. The minisigmoid structure identified in the pre-flare phase is outlined by the dashed black dotted curve in panel (a). The white arrows in different panels indicate the ejected jet-like plasma. The blue arrows in panels (c) and (l) indicate a newly emerged brightening in the western end of the minisigmoid that led to the flare onset. The yellow arrows in panels (e) and (n) indicate the brightening in the eastern end of the minisigmoid during the peak phase of the M1.4 flare. The black arrow in panel (r) indicates a newly formed filament structure during the decaying phase of the M1.4 flare.

like eruption was quite interesting. The ejecting plasma, after initially progressing the eastward direction for a distance of $\approx 40''$, abruptly changed its direction mostly toward south. In Figures 6.17(c)–(h) and (l)–(q), we have indicated the progress of the ejected plasma by the white arrows. Notably, this jet-like plasma ejection was observed more clearly in AIA 304 Å images compared to the AIA 94 Å images. This is suggestive of plasma being ejected from lower atmospheric layers which underwent partial heating during the ejection process. Notably, during the peak phase of the flare, the eastern leg of the minisigmoid evolved as the brightest location in the entire AR (indicated by the yellow arrows in Figures 6.17(e) and (n)). AIA 304 Å images of the decay phase of the M1.4 flare suggest the appearance of the small filament within the minisigmoid structure, which is indicated by the black arrow in Figure 6.17(r).

6.6.3 Period II: quiet phase between the two M-class flares

We observed the appearance of a small filament along the axis of the minisigmoid structure during the late phase of the M1.4 flare (Section 6.6.2). Following the flare, i.e., during the period II of the study (see Figure 6.15), this filament became prominent. Notably, as mentioned in Section 6.6.1, RHESSI observation with the attenuator state A0 (i.e., high sensitivity at low energies) was available during this period. Figure 6.18 shows a few representative AIA 304 Å images of period II which were overplotted with RHESSI X-ray contours within the energy ranges 3–6 (shown by light blue contours) and 6–12 (shown by dark blue contours) keV. From Figure 6.18 it becomes evident that X-ray emission in the 6–12 keV range was concentrated along the axis of the minisigmoid (Figure 6.18(a)). Notably, X-ray emission in the 3–6 keV energy range at $\approx$10:00 UT was characterized by two distinct sources situated on either sides of the filament. During this period, the filament became much prominent (indicated by the black arrow in Figure 6.18(e)), we observed highly localized 6–12 keV RHESSI sources concentrated around the projected apex of the filament. Further, at $\approx$10:12 UT, the 6–12 keV emission was characterized by an interesting arrangement consisting of an intense source at the top of the filament and two weaker sources on the either sides of it (Figure 6.18(f)).

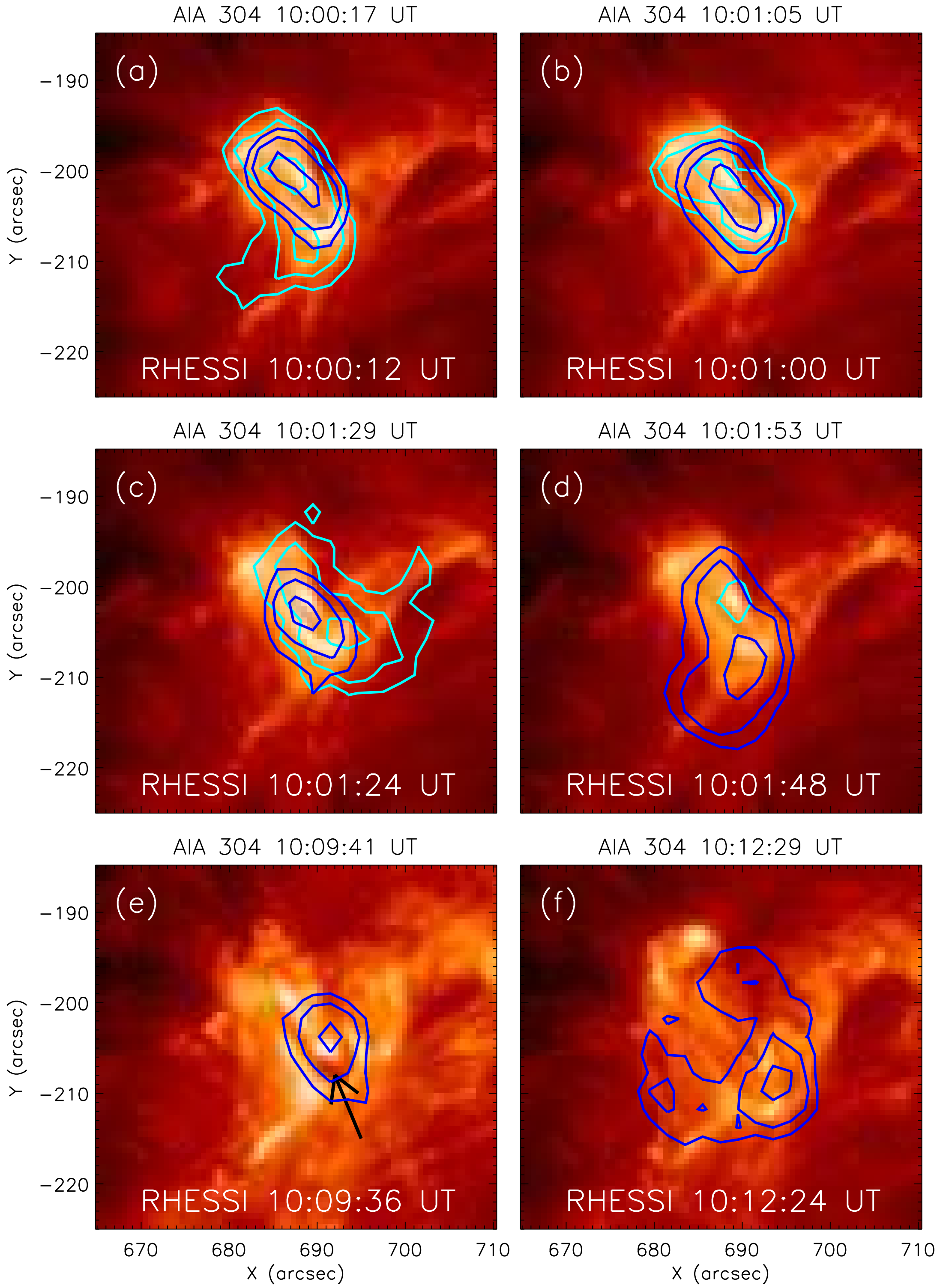

Figure 6.18: Series of AIA 304 Å images of the flaring region during the relatively quiet period between the two M-class flares. Contours of RHESSI 3–6 (light blue) and 6–12 (dark blue) keV are overplotted on each panel. Contour levels are set as 70%, 80%, and 95% of the corresponding peak flux. The arrow in panel (e) indicates a developing filament from the minisigmoid structure prior to the onset of the M7.3 flare.

6.6.4 Period III: evolution of the M7.3 flare and the filament eruption

GOES SXR fluxes, after decreased steadily during period II, rapidly increased from ≈10:14 UT marking the onset of the M7.3 flare (Figure 6.15). Notably, prior to the onset of the flare, the newly developed filament became distinctly visible in both the coronal and chromospheric images of the minisigmoid (indicated b brown and blue arrows in Figures 6.19(a), (j) and 6.20(a)). Interestingly, the filament appeared in the absorption line more prominently in the hot coronal AIA channels (e.g., AIA 94 and 335 Å) compared to cooler AIA 304 Å images (cf., Figure 6.19(a), 6.20(a) with Figure 6.19(j)). Contrary to the M1.4 flare, where the initial flare brightening was observed at the western end of the minisigmoid, the M7.3 flare brightening was mostly concentrated at the northern end of it. Similar to the M1.4 flare, the M7.3 flare was also associated with a narrow jet-like plasma ejection. Signatures of the jet-like ejection was first observed in the AIA 304 Å images at ≈10:15 UT (Figures 6.19(l)) followed by its appearance in the AIA 335 and 94 Å images chronologically (indicated by yellow arrows in Figures 6.20(c)–(f) and 6.19(d)–(g)). Notably, during the initial phases of the jet-like eruption, we observed a slow but steady upward motion of the filament in all AIA EUV channels suggesting a causal relation of the jet-like eruption with the activation of the filament. We have indicated the upward moving filament by brown arrows in Figures 6.19(c), (d), 6.20(b)–(d) and by blue arrows in Figures 6.19(l), (m). The filament brightened up after ≈10:15 UT which caused the M7.3 flare to reach its peak emission. During the flare, we observed hard X-ray emission of energies up to ≈100 keV which is shown by contours of different colors plotted over different panels of Figure 6.19. In general, similar to EUV brightenings, X-ray emission was also concentrated at the northern end of the minisigmoid structure. Following 10:15 UT, we observed an interesting evolution in the AIA 304 and 335 Å images in view of the development of a cusp-like structure by the rising filament (indicated by the black arrows in Figures 6.19(n) and 6.20(f)). This cusp-like structure was associated with the initiation of a second phase of plasma eruption at ≈10:16 UT. During the same time, ejected plasma during the first phase of eruption changed direction from eastward to southward and plasma ejected during both the two

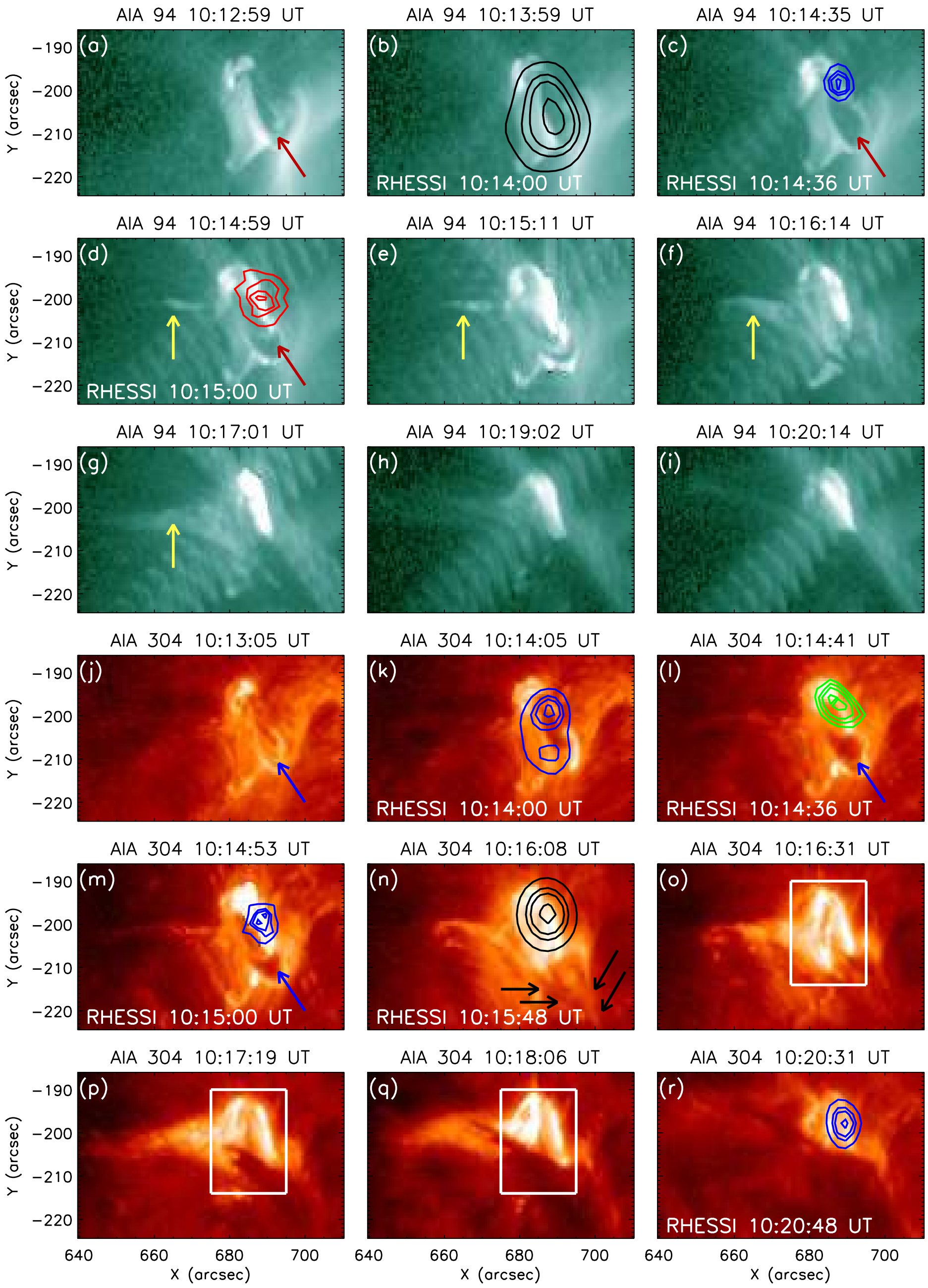

Figure 6.19: Series of AIA 94 (panels (a)–(i)) and 304 (panels (j)–(r)) Å images showing the time evolution of the M7.3 flare. The brown and blue arrows in different panels indicate the development of the filament. The yellow arrows in panels (d)–(g) indicate the first phase of plasma ejection during the M7.3 flare. The black arrows in panel (n) indicate a second phase of the eruption during the flare. The white boxes in panels (o)–(q) indicate a postflare arcade observed from an edge-on view. Contours of RHESSI 6–12 (blue), 12–25 (black), 25–50 (red), and 50–100 (green) keV are overplotted in different panels. Contour levels are set as 50%, 70%, 80%, and 95% of the corresponding peak flux for the 6–12, 12–25, and 25–50 keV energy bands and 60%, 70%, 80%, and 95% of the corresponding peak flux for the 50–100 keV band.

phases partially occulted the bright flaring emission of the M7.3 flare. After 10:16 UT, observation of the source AR was only possible in the AIA UV channels (e.g., AIA 1600 Å) since they primarily image the lower atmospheric layers of the Sun. AIA 1600 Å images of this time were characterized by the bright ribbon-like structures situated on the opposite sides of the filament which were visible till ≈10:20 UT (indicated by the red arrows in Figures 6.20(j)–(l)). However, a comparison with the co-temporal AIA 304 Å images (outlined by the white boxes in Figures 6.19(o)–(q)) suggest that the bright structures might possibly be a mixture of emissions coming from the flare ribbons as well as post-flare arcades viewed from an edge-on angle. By 10:20 UT, the flare had moved into the gradual phase and we did not observe any significant morphological changes in the AR thereafter, except for a short-lived brightening found in the western end of the sigmoid region at ≈10:26 UT (shown by the blue arrow in Figure 6.20(o)). In this context, it is worth noting that the GOES SXR lightcurves displayed a subtle peak in both the 1–8 and 0.5–4 Å channels at the same time (see Figure 6.15).

6.6.5 Development of the CME from the erupting filament

We discussed the initial phases of plasma ejection during both the M-class flares in Sections 6.6.2 and 6.6.4. Interestingly, we observed jet-like plasma ejection during the M1.4 flare for only a few minutes as the ejection signatures became too weak to be identified in the AIA (E)UV images. However, during the M7.3 flare, the combination of the two-phase plasma eruption continued to produce a CME. In this section, we focus on the dynamics of the plasma ejection during the M7.3 flare (Figure 6.21) and the corresponding CME (Figure 6.22). As discussed in Sections 6.6.2 and 6.6.4, the initial phases of plasma ejection was characterized by collimated (i.e., jet-like) eruption propagating toward the eastern direction (indicated by the red arrow in Figures 6.21(b) and (c)). However, the erupting plasma changed its direction dramatically toward the southwest. We have approximately outlined the direction-change of the erupting plasma by a sky-blue colored curve in Figure 6.21(e). The second phase of plasma ejection during the M7.3 flare initiated from the apparent cusp-like structure at the western end of the minisigmoid region after ≈10:16 UT (see Section 6.6.4). Plasma ejected during the two phases

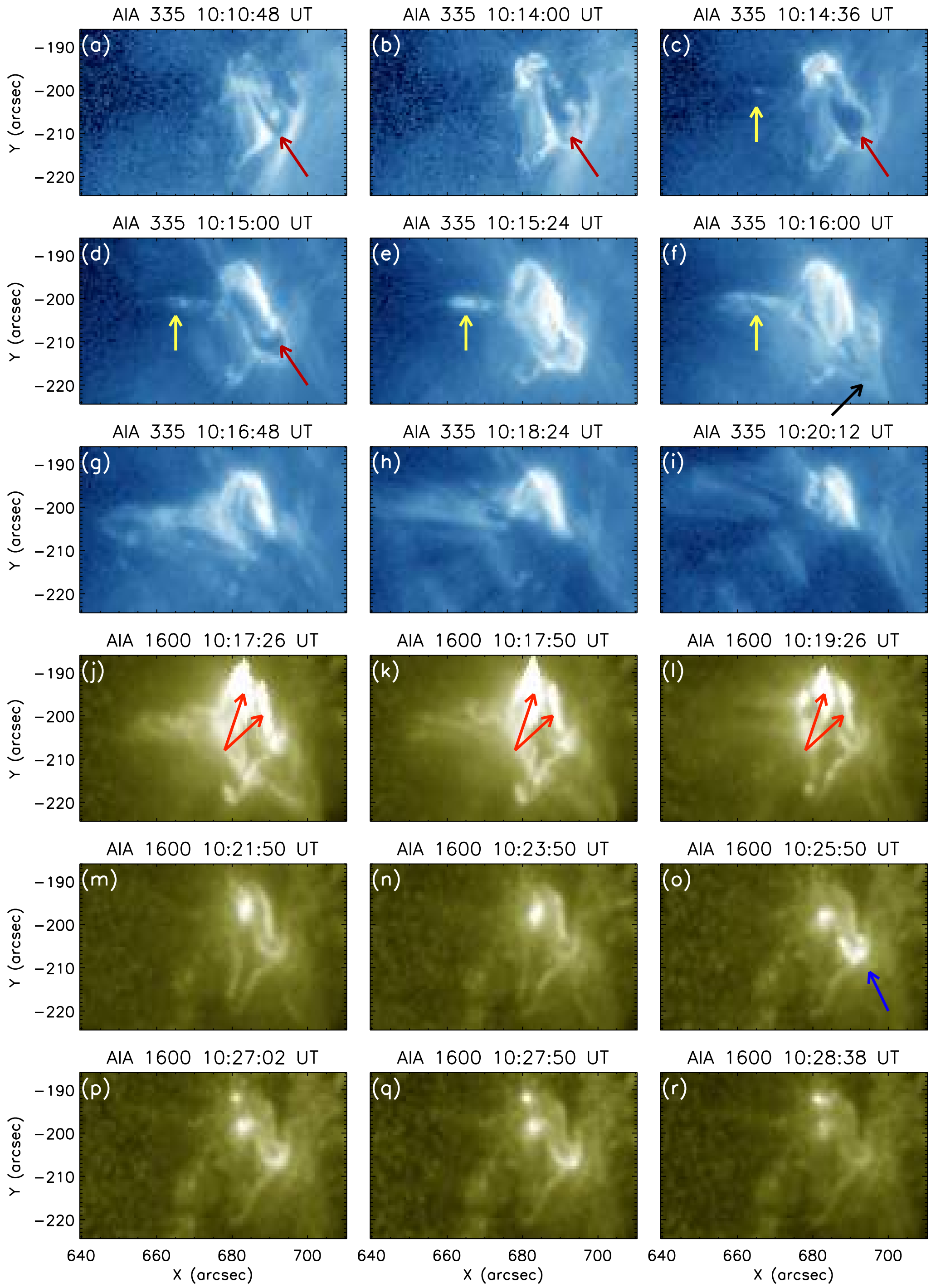

Figure 6.20: Series of AIA 335 (panels (a)–(i)) and 1600 (panels (j)–(r)) Å images showing the time evolution of the M7.3 flare. Brown arrows in panels (a)–(d) indicate the emergence of a small filament structure in the pre-flare phase. Yellow arrows in panels (c)–(f) indicate the ejecting plasma. The black arrow in panel (f) indicate the direction of a second stream of ejecting plasma. The red arrows in panels (j)–(l) indicate flare ribbon-like structures formed during the M7.3 flare. The blue arrow in panel (o) indicates a subtle brightening occurring in the decay phase of the flare that was probably responsible for the small enhancement in the GOES SXR lightcurves (see Figure 6.15).

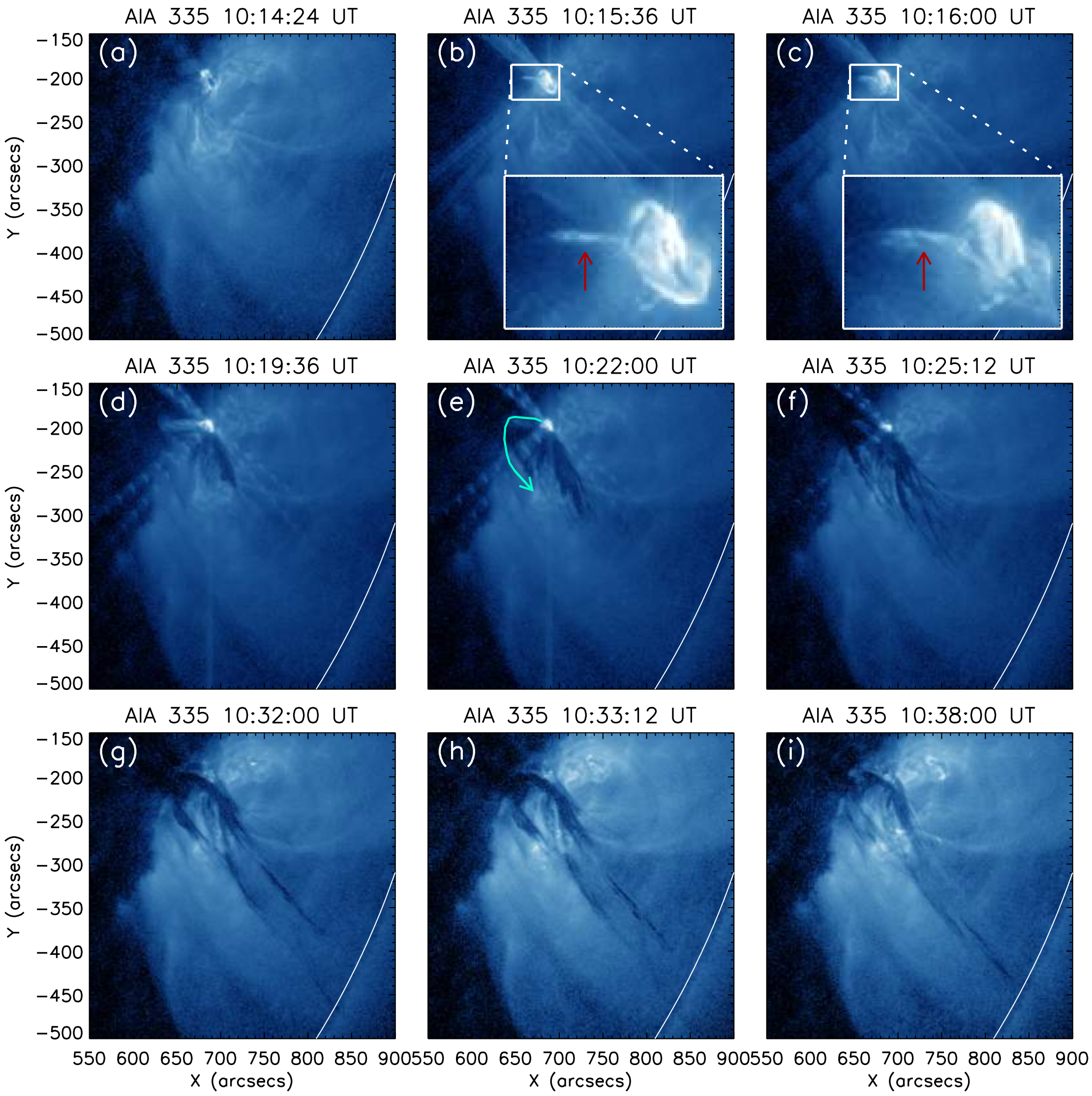

Figure 6.21: Series of AIA 335 Å images showing large-scale eruption of plasma from NOAA 12673 during the M7.3 flare. The red arrows in panels (b) and (c) indicate the initial phases of the ejecting plasma moving toward the east. The curve in panel (e) outlines the unusual turning of the ejecting plasma from east to southwest. The ejected plasma during the M7.3 flare resulted in a CME of medium speed and small angular width.

got mingled up and thereafter proceeded toward the south-western direction (Figures 6.21(d)–(i)) to constitute a CME. Within the LASCO field of view, the CME (Figure 6.22) was propagating along the central PA of 254° having an angular width of 32° with a linear speed of 470 km s^{-1}.

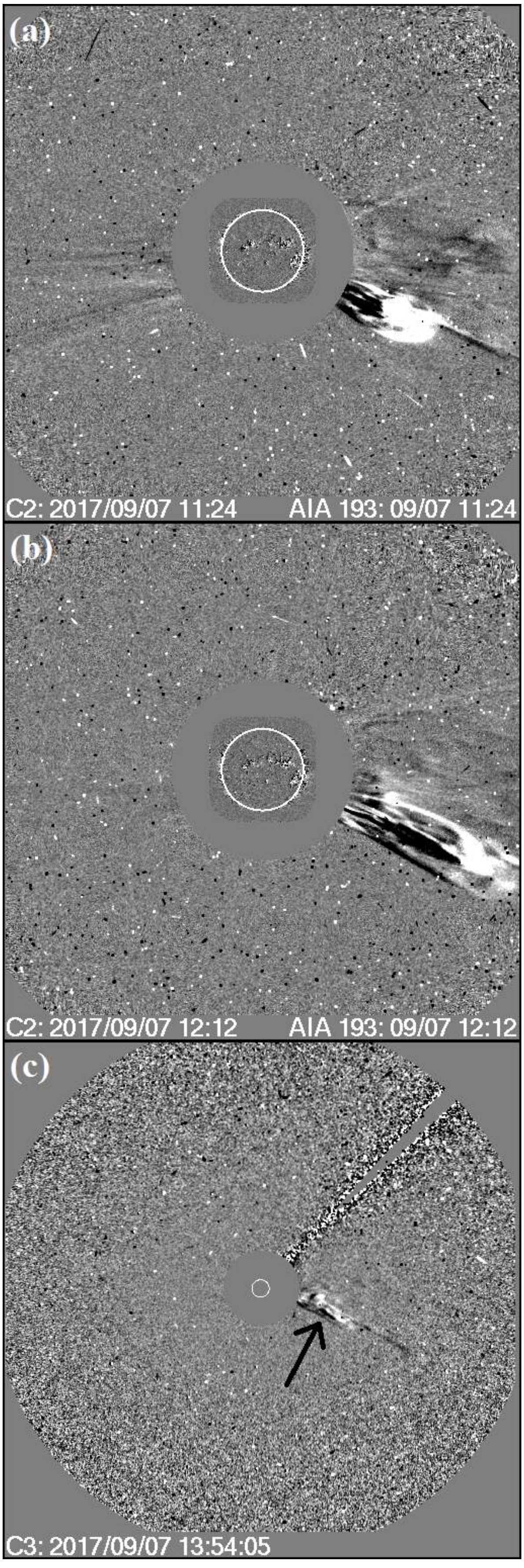

Figure 6.22: LASCO observations of the CME that developed from the plasma ejection during the M7.3 flare. Panels (a) and (b) present observations from the C2 coronagraph (1.5–6 R.), while panel (c) shows observations from the C3 coronagraph (3.7–30 R.). The CME is indicated by the black arrow in panel (c). The CME was first observed by LASCO at 10:24 UT and was observed until 16:18 UT.

6.6.6 Structure and evolution of the magnetic configuration of NOAA 12673

During the course of the two M-class flares, the photospheric morphology of NOAA 12673 (Figure 6.23(a)) remained without any major changes, although the flux content in it varied significantly. To understand the influence of photospheric flux emergence and cancellation on the flaring activities, we plot LOS photospheric flux variation within the flaring region (shown by the dashed box in Figure 6.23(a)) between 08:00 UT and 10:30 UT on 7 September 2017 (Figure 6.24(b)). The flux variation readily indicates that the negative flux underwent a monotonic decrease from ≈08:40 to ≈09:49 UT (shown by the blue curve in Figure 6.24(b)) with a decay rate of $\approx 2.41 \times 10^{16}$ Mx s^{-1}. Positive flux, however, underwent periodic flux emergence and cancellation, having two distinguishable phases of flux decrease (≈08:35–08:40 and ≈09:17–09:28 UT). The two M-class flaring intervals (indicated by the dashed and dashed–dotted lines) were characterized by drastic decrease of flux of both polarities which seems to be manifestations of artifacts driven by the flaring activities.

6.6.7 Large-scale magnetic field modeling

Large-scale magnetic field configurations, such as open magnetic field lines represented by coronal holes (CHs; Cranmer, 2009), may strongly influence the early propagation of CMEs and cause significant deflections of their original direction of motion (Gopalswamy et al., 2009; Heinemann et al., 2019). To investigate if the change in the direction of erupting plasma in the low coronal layers was influenced by the open field configuration, we carried out global magnetic field reconstruction using the PFSS model[1] and compare it with AIA EUV images (Figures 6.24). A few PFSS extrapolated magnetic field lines concentrated around the AR is shown in Figure 6.24(b), where the location of NOAA 12673 is indicated by a black arrow. PFSS extrapolation results readily indicate the presence of multiple open field lines (shown by the blue lines in Figure 6.24(b)). Notably, a few open field lines originating close to the northern and western sides of the flaring region, strongly

[1]https://www.lmsal.com/~derosa/pfsspack/

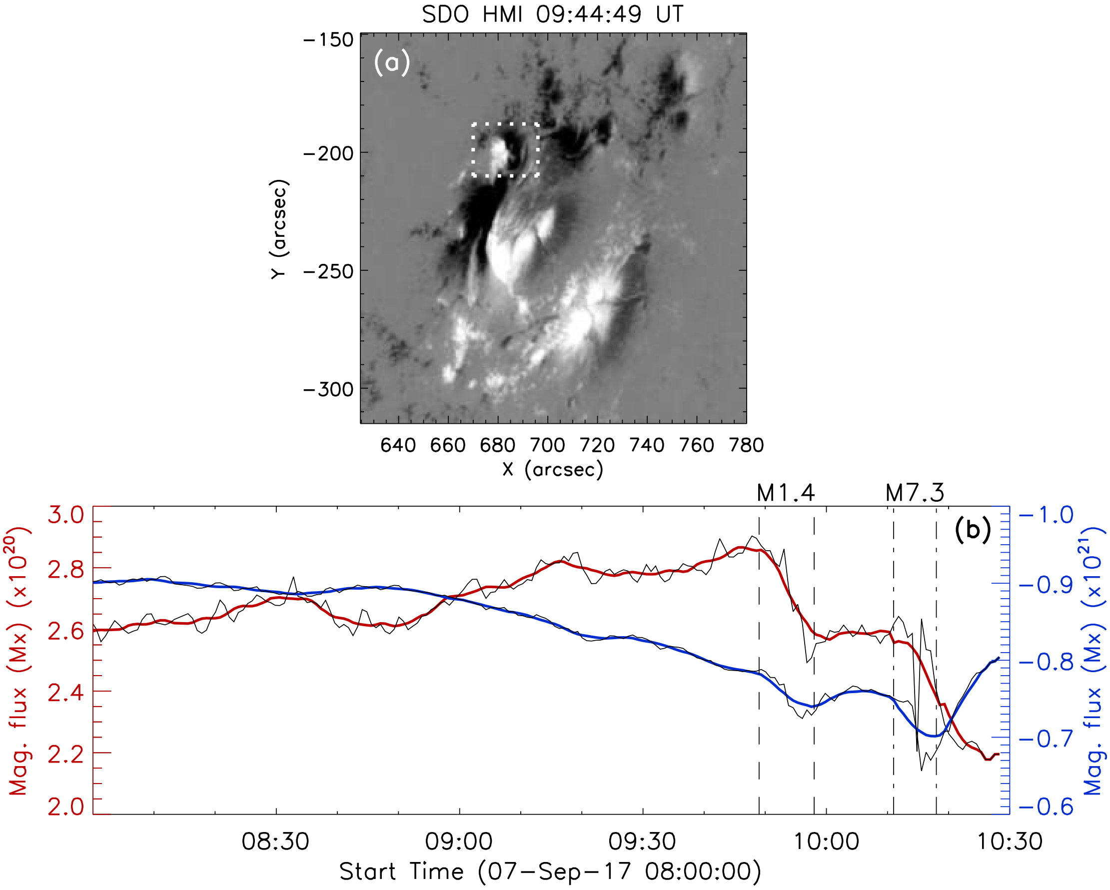

Figure 6.23: Panel (a): HMI magnetogram of NOAA 12673 on 2017 September 7 at 09:45 UT. The time evolution of the photospheric magnetic flux of the whole AR and inside the selected region within the dotted box in panel (a) is plotted in panel (b). The dashed lines in panel (b) mark the starting and ending time of the M1.4 flare as observed by GOES, and the dashed–dotted lines mark the starting and ending time of the M7.3 flare as observed by GOES.

deflected toward the southwest direction. Here we recall that the ejected plasma associated with the M7.3 flare and the eventual CME propagated along the same direction (see Figure 6.22). Interestingly, AIA 193 Å images during the peak of the M1.4 flare did not reveal any unambiguous observational signature of CHs (Figure 6.24(a)); although a small but prominent CH region was identified at the location of modeled open field lines after one solar rotation (indicated by the white arrow in Figure 6.24(c)).

6.6.8 NLFFF extrapolation results

In order to understand the coronal configuration associated with the flaring region, we carried out NLFFF coronal magnetic field modeling (Figure 6.25) at 09:46 UT,

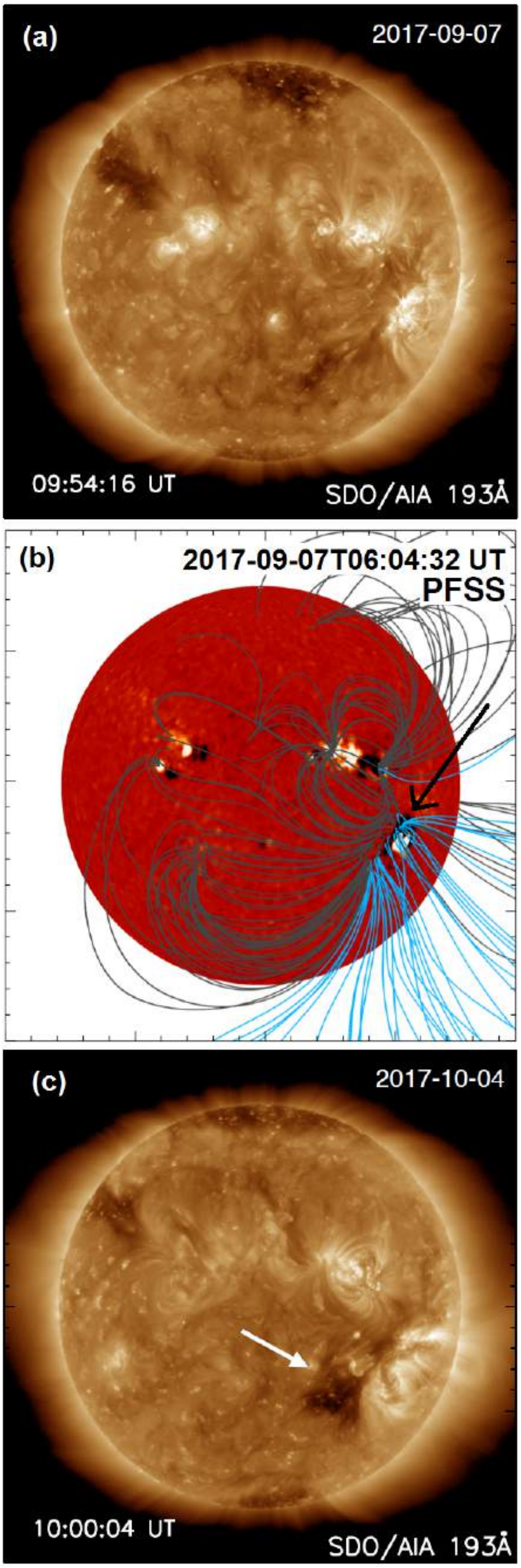

Figure 6.24: A PFSS extrapolation of the global magnetic field (panel (b)), together with AIA 193 Å images during the events under study (panel (a)) and one solar rotation later on 2017 October 4 (panel (c)). Gray and blue field lines indicate closed and open magnetic field lines, respectively. The open field lines originating to the north and west sides of the flaring AR are observed as the signature of a CH one solar rotation later (indicated by the white arrow).

i.e., prior to the onset of the M1.4 flare. The following values of the free parameters (see Chapter 2.3.2) were used for the extrapolation:

$\nu = 0.01;$ $\quad w_{los} = 1;$ $\quad w_{trans} = \frac{B_{trans}}{max(B_{trans})};$

$\mu_1 = \mu_2 = 1;$ $\quad \mu_3 = 0.001;$ $\quad \mu_4 = 0.01$

The residual errors were obtained as

$< |f_i| >= 5.09 \times 10{-}4;$ $\quad \theta_J = 6.74°.$

For comparison, we plot a pre-flare HMI LOS magnetogram of NOAA 12673 in Figure 6.25(a) where we specify a small part by the blue box for plotting the coronal connectivities (Figure 6.25(b)). Notably, the homologous M-class flares on 7 September 2017 originated from the highly localized bipolar location (enclosed by the green box in Figure 6.25(a)) close to the northern part of the region inside the blue box. For plotting the model field lines, we focused on the the region within the green box. Here we considered that this region was associated with the coronal configurations involved in the flare-associated brightenings which contained part of the flux rope (observed as the small filament) that underwent magnetic reconnection.

The NLFFF extrapolation results revealed the presence of two small magnetic flux ropes along the PIL between the bipolar region enclosed by the green box in Figure 6.25(a). The PIL is highlighted by a red curve in Figure 6.25(a). In Figure 6.25(b)–(c), we plot the two flux ropes by blue and green lines. Notably, the two flux ropes were intertwined with each other, forming a ‘double-decker flux rope system’. For a better visualization, we plot only the double-decker flux rope system in Figure 6.25(c). Further, the NLFFF-modeled magnetic field within the blue box in Figure 6.25(a) was characterized by relatively large-scale closed loops connecting the central positive polarity region with the northern negative flux regions (shown by the yellow lines in Figure 6.25(b)).

6.6.9 Magnetic decay index and twist number

To explore the influence of torus instability on the flare associated eruption (Section 1.9.2), we computed the magnetic decay index using the potential magnetic field extrapolation results of NOAA 12673 (Figures 6.25(d)–(e)). For the purpose, we manually determined the approximate 2D projection of the axis of the

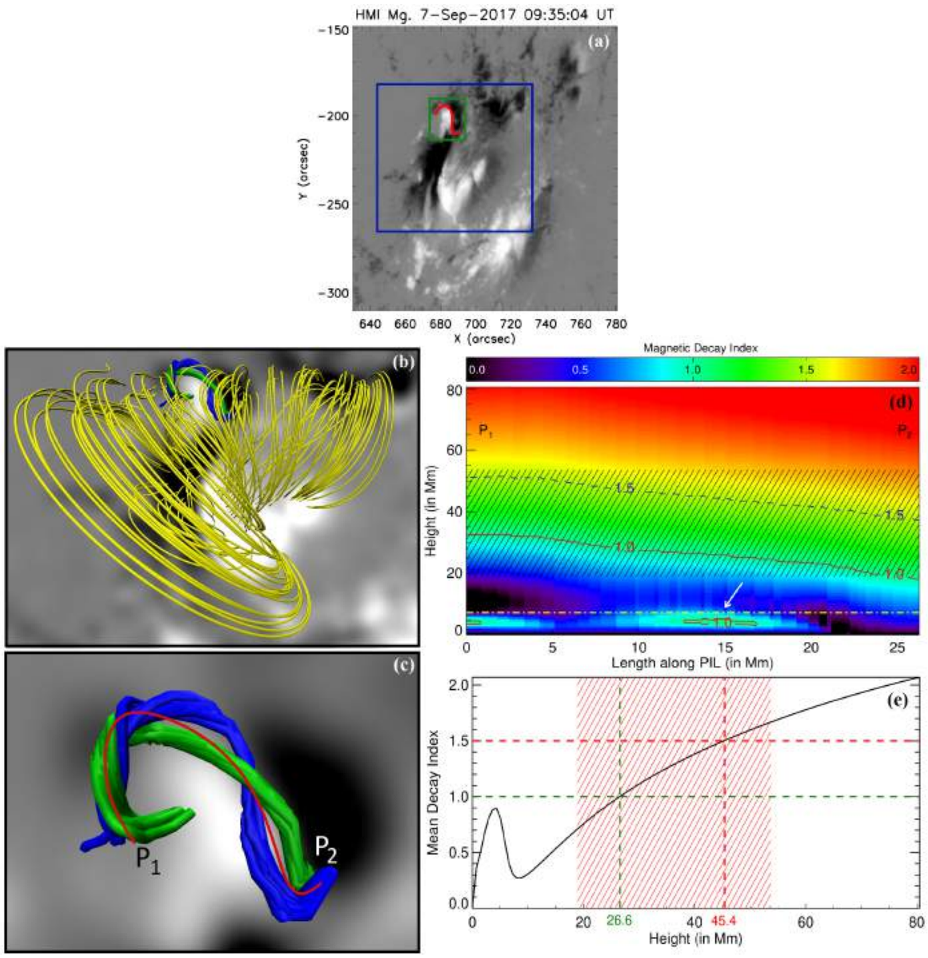

Figure 6.25: Panel (a): HMI LOS magnetogram showing the photospheric configuration of NOAA 12673 prior to the flaring activity. Panel (b): NLFFF extrapolation results at 2017 September 7 09:45 UT showing coronal connectivities between different parts of the complex AR. Multiple flux ropes were identified in the extrapolation volume and are shown by blue and green lines. The NLFFF extrapolated field lines are drawn over the photospheric region shown inside the blue box in panel (a). In panel (c), we only show the two flux ropes situated in the flaring region within the AR, constituting a double-decker flux rope system. The FOV of panel (c) is approximately indicated in panel (a) by the green box. Panel (d): distribution of magnetic decay index (n) above the PIL, indicated by the red curves in panels (a) and (c). The yellow dashed–dotted line in panel (d) approximately indicates the height of the double-decker flux rope system. The blue dashed and red solid curves in panel (d) refer to contours of n=1.0 and 1.5, respectively. The white arrow in panel (d) indicates a region within the height of the flux ropes characterized by decay index n≈1.0, which is higher than the surrounding region. Panel (e): variation of mean decay index with height above the PIL. The green and red dashed lines in panel (e) mark the heights corresponding to n=1.0 and 1.5, respectively. The hatched regions in panels (d) and (e) indicate the range of critical decay index height for torus instability as found by Wang et al. (2017a).

double-decker flux rope system (shown by the red curves in Figures 6.25(a) and (c)). In Figure 6.25(d), we plot the variation of the magnetic decay index in a vertical 2D plane above the flux rope axis. For a better understanding, two contours were plotted on the vertical plane characterizing the decay index values n=1.0 and 1.5. Further, we indicate the approximate height of the double-decker system by a yellow dashed–dotted line in Figure 6.25(d). The distribution of decay index above the axis of the double-decker flux rope system readily suggested that a few segments of the double-decker flux rope system were characterized by n$\gtrsim$1.0. Further, we highlighted the statistically established height range of critical decay index (n=1.5) associated with torus instability (Wang et al., 2017a). We find that, above the double-decker axis, both the heights corresponding to decay index values n=1.0 and 1.5 lie well within the statistically found height range. We plot the variation of decay index averaged over the length of the PIL with height in Figure 6.25(e). The average decay index initially increased reaching to the value of ≈0.9 within a short height of ≈5 Mm but then underwent a sharp decrease till the height of ≈9 Mm reaching to the value n≈0.3. Above this height (≈9 Mm), the average decay index increased steadily and reached to the values n=1.0 and 1.5 at the heights of ≈27 and 45 Mm, respectively, which is well within the statistically established range of critical height for torus instability.

We further explored the possibility of kink instability for the triggering of the flux rope, by computing the twist number (T_w) within the flaring region. Our calculations revealed that both the flux ropes within the double-decker system were associated with a negative twist. The average values of $|T_w|$ associated with the double-decker system was found to be ≈1.0. Extensive statistical work by Duan et al. (2019) concerning the torus and kink instabilities as the triggering mechanisms of flux ropes revealed that the critical value for the onset of kink instability is given by a twist number $|T_w| \approx 2.0$. In view of this result, we could not establish any conclusive evidence of kink instability as a possible triggering mechanism in our event.

6.7 Discussion

6.7.1 Evolution of NOAA 12763

In this chapter, we present a synoptic study of the evolution and flaring activity of NOAA 12673 which was the most flare productive AR of the minimum phase of the solar cycle 24. We also discuss case studies of a few prominent and representative flares occurring from the AR, besides briefly highlighting the evolution and coronal configuration of the largest flare of cycle 24.

NOAA 12673 appeared on the eastern limb of the Sun as a simple positive polarity α-type sunspot on 28 August 2017 (Figure 6.1(a)). Notably, by analyzing the synoptic maps of several Carrington Rotations, Muhamad et al. (2022) found that the predecessor of the AR was formed at least in July 2017 which was identified as NOAA 12665. Their analysis further suggested that NOAA 12673 survived at least two more Carrington Rotations, till November 2017. However, the transit of NOAA 12673 was the most flare productive phase of the AR in comparison to its preceding and succeeding rotations (see Table 2 in Muhamad et al., 2022). Although NOAA 12673 appeared as a α-type sunspot, it underwent rapid flux emergence of both polarities which led to the evolution of the AR toward the most complex $\beta\gamma\delta$-type (Figures 6.1, 6.2, 6.3). Hou et al. (2018) identified emergence of at least five magnetic dipoles within the AR between 3 and 6 September 2017, interaction of which led to the formation of highly shearing and rotational motion of the photospheric fields. The photospheric motions during the build up phase of the AR was studied in details by Vemareddy (2019). By thorough investigations of the velocity fields of the AR, Vemareddy (2019) observed persistent shearing and converging motions of magnetic flux around the polarity inversion line (PIL). Rapid photospheric flux emergence led to major helicity injection in the coronal field which in turns led to the development of a coronal sigmoid by 4 September.

Development of strong photospheric currents is in direct relation with photospheric motions. The AR underwent rapid build up of photosheric current following 3 September 2017 which was hand-in-hand with the rapid flux emergence episodes (Figures 6.6–6.9). Notably, during Phases 2–4, we observed the development of strong currents of opposite polarities in close proximity (Figure 6.7).

Such locations characterized by close proximity of opposite polarity currents have previously been observed to be highly probable locations for initiating magnetic reconnection (Mitra et al., 2020a). Interestingly, during Phase 2, an elongated structure of strong negative polarity current was observed to develop along the PIL between the central positive polarity and the trailing negative polarity regions.

On 6 September 2017, NOAA 12673 produced 2 X-class flares within an interval of ≈3 hours, the latter one of class X9.3 being the largest flare of cycle 24. Our analysis reveals that prior to the onset of the X9.3 flare, a positive polarity current region was developed in parallel to the previously developed negative current structure (see Figure 6.9 showing photospheric I_z-maps during phase 4 of the AR). Importantly, we observed a high magnetic field gradient across the PIL which further implies the formation of strong current sheets. NLFFF-modeled coronal configurations revealed the presence of well developed flux ropes situated along the PIL at the site of the X-class flares (Figure 6.14). We interpret the ribbon-like current structures as the photospheric signatures of well developed flux ropes. Further, the northern footpoint of flux ropes preceding the onsets of the X-class flares on 6 September 2017, were situated very close to the coronal null point of a fan-spine configurations. Notably, the flux rope itself appeared to be involved in the null point configuration during the pre-flare phase of the X9.3 flare, which clearly suggests the continuous build up of magnetic complexities in NOAA 12673. It is noteworthy that the extent of photospheric current ribbons and magnitude of currents within them were observed to remain largely uninfluenced even after the occurrence of the large X2.2 flare, which suggests a dominant role played by magnetic flux emergence in the region.

6.7.2 Homologous M-class flares on 7 September 2017

Both the M-class flares from NOAA 12673 on 2017 September 7 originated as a result of successive activation of a filament. As discussed in Figure 6.15, both M-class flares were highly impulsive with the respective impulsive phases lasting for only ≈4 and ≈2 minutes. The EUV images of the flaring site revealed that the flares occurred from a localized region situated at the northern part of the main sunspot group of NOAA 12763 (indicated within the boxes in Figures 6.16(c) and (e)). Hot coronal images (i.e., AIA 94 Å) suggested the flaring region to have a clear reverse-S shaped structure implying the presence of a coronal sigmoid (see Manoharan et al., 1996; Rust & Kumar, 1996). However, while coronal sigmoids are usually observed as relatively large structures having spatial extensions extending over ≈100 Mm (see, e.g., Tripathi et al., 2009; Joshi et al., 2017a; Mitra et al., 2018, 2020a), the sigmoid reported in this study had a characteristic length of only ≈20 Mm (≈30″). Inspired by the much smaller length of the sigmoid, we can justifiably refer it a 'minisigmoid'. Even with the much smaller scale, we clearly observed development and activation of a small filament within it, activation of which produced the two eruptive flares (Figures 6.17 and 6.19).

Sigmoids are associated with twisted or helical magnetic structures, i.e., magnetic flux ropes or filament channels (Gibson et al., 2002). Magnetic flux ropes are complex structures lying above PILs in the solar atmosphere where a set of magnetic field lines wrap around along its central axis more than once (Gibson & Fan, 2006). NLFFF-modeled magnetic field lines suggested the presence of two flux ropes at the flaring location on 7 September (Figure 6.25). Notably, the flux ropes appeared to be wrapping around each other forming a so-called double-decker flux rope system. Notably, we have reported a double-decker structure in Chapter 5 also. Our multi-wavelength investigations of the failed eruption presented in Chapter 5 of this thesis suggested the pre-flare double-decker system to be composed of two well-separated filaments but at much larger spatial scales. During the impulsive phase of the flare, as the filaments got activated, they extended spatially and got intertwined with each other. The two flux ropes in the double-decker system reported in this chapter, however, were intertwined with each other even during the pre-flare phase which further supports the extreme magnetic complexity of NOAA 12673.

Eruptive flares from sigmoidal regions are usually characterized by a co-called 'sigmoid-to-arcade' evolution (see e.g., Joshi et al., 2017a; Mitra et al., 2018) as the eruption of the flux rope induces magnetic reconnection beneath it leading to the formation of the post-reconnection arcade. However, the sigmoidal structures reported in this chapter survived after the eruptive flares (Figures 6.20(m)–(r)) suggesting only one flux rope from the double-decker system to undergo eruption during the flares. Such evolution of the double-decker flux ropes seems to be common, particularly in the cases of intertwined double-decker flux rope systems (see e.g., Cheng et al., 2014a). In this context, it is worth mentioning that in the previous reports of double-decker flux rope structures, signatures of two flux ropes (or filaments) were clearly observed in optical and/or (E)UV images. However, we were unable to distinctly resolve the observational signatures of the two flux ropes within the double-decker system presented in this study. We attribute this to the highly localized nature of the structure, making it hard to distinguish even with the high resolutions of AIA images (see Figures 6.17 and 6.19). Here, we also consider the influence of projection effects in view of the location of the AR being ∼S07W46 (see Table 6.1) during the flares. Importantly, AIA 1600 Å images during the pre-flare phase revealed a few bright spots co-spatial to the minisigmoid which may possibly represented the footpoints of the two flux ropes of the double-decker configuration. Notably, we observed the appearance of the minisigmoid in the AIA 94 Å images only ≈1.5 hours prior to the onset of the M1.4 flare, which seems to be a much shorter time compared to the lifetimes of previously reported intertwined double-decker systems (≈40 hr; see Cheng et al., 2014a).

We observed compact localized brightenings at the sigmoidal region region prior to the onset of the M-class flares. Initiation of both the flares were immediately associated with collimated jet-like plasma ejection (Figures 6.17 and 6.19). The highly sheared bipolar photospheric region associated with the flare underwent flux cancellation of both the polarities prior to the flares (Figure 6.23(b)) which can be interpreted as the observational signatures of photospheric flux cancellation at the PIL (van Ballegooijen & Martens, 1989). Flux cancellation at the PILs have been recognized to initiate small-scale magnetic reconnections leading to the formation of flux ropes (see, e.g., Amari et al., 2010; Xue et al., 2017; Panesar et al., 2018; Mitra et al., 2020a). Further, we interpret the localized (E)UV brightenings underneath the apparent location of the filament body prior to the onset of the flares as the evidence for the tether-cutting model of solar eruptions (Moore & Roumeliotis, 1992; Moore et al., 2001). Among the observable signatures of tether-cutting reconnection, compact EUV and hard X-ray brightenings beneath an erupting flux rope (or middle of the sigmoid) and collimated plasma outflows may be highlighted (Raftery et al., 2010; Liu et al., 2013; Chen et al., 2014, 2016, 2018b). While investigating the onset processes of a solar eruption, Chen et al. (2018b) observed clear signatures of flux cancellation from the flaring region, bidirectional jets, and change in the topology of the hot loops during the precursor phase. They inferred these signatures as the tether-cutting models. Although the events reported in this study evolved with unidirectional jets, the locations of the occurrences of the jets were observed to be closely associated with the initial brightenings beneath the filaments (Figures 6.17(e) and (m) and 6.20(d)). This further supports the tether-cutting reconnection between the two flux ropes in the double-decker flux rope system as the triggering mechanism for the activation of the flux ropes.

The horizontal components of magnetic field above the double-decker configuration underwent a rapid decay with height resulting in the condition of torus instability to be achieved within a low height (Figure 6.25(d)). The condition of torus instability has been extensively used to explain the eruptive nature of ARs (see, e.g., Liu, 2008; Aulanier et al., 2010; Démoulin & Aulanier, 2010; Thalmann et al., 2015; Zuccarello et al., 2017; Liu et al., 2018c; Sarkar & Srivastava, 2018). On the basis of a statistical study, Wang et al. (2017a) found the critical height (h_{crit}) of torus instability for successful eruption to be within the range $h_{crit} = 36.3 \pm 17.4$ Mm above the PIL. During the pre-flare phase of the M-class flares reported in this chapter, the condition of torus instability (n_{crit}=1.0–1.5) was achieved at heights of h_{crit} ≈27–45 Mm above the PIL, which is in basic agreement with the statistical results reported in Wang et al. (2017a, $h_{crit} = 36.3 \pm 17.4$ Mm) and Baumgartner et al. (2018, $h_{crit} = 21 \pm 10$ Mm).

6.8 Summary and Conclusion

In summary, NOAA 12673 underwent rapid flux emergence along with photospheric motions including shearing and rotational motions. In response to the photopsheric motions, strong horizontal current regions developed within the AR which were probable locations for the initiation of magnetic reconnection leading to subsequent large-scale currents. Further, the continuous shearing and rotational motion resulted in the injection of high non-potential energy within the AR enabling it to produce a series of large flares including the largest flare of the cycle 24. As a consequence of the high shear in the AR, a flux rope was developed over the PIL in a close proximity of a fan-spine configuration involving a coronal null point, prior to the onset of the X-class flares on 6 September. In view of the coronal null point above a highly sheared core field region which also contained magnetic flux ropes, the triggering of the X-class flares can be interpreted by the breakout model of solar eruptions.

While the X-class flares on 6 September 2017 encompassed the entire extension of NOAA 12673 (Mitra et al., 2018) on the very next day the AR produced two homologous impulsive eruptive M-class flares from a highly localized part of the AR. The associated coronal images revealed the presence of a minisigmoid region, which suggests that the storage of sufficient energy within even smaller flux rope structures can also lead to CME initiation, provided the overlying magnetic field configuration is favorable for its further expansion in the corona. Our analysis also reveals the presence of a compact intertwined double-decker flux rope configuration, unveiling the venue for the storage of magnetic free energy within the spatially localized regions in solar corona.

Chapter 7

Conclusions and Future Prospectus

With a combination of multi-wavelength obeservations and coronal field modeling, the thesis aims to explore important aspects related to the onset and evolution of solar transient phenomena at a wide range of spatial, temporal, and spectral scales. As the modern society is rapidly developing an irreversible dependence on the space technologies, a detailed understanding of solar eruptive activities is crucial. This chapter highlights the work presented in this thesis and discuss scope for the future work which I am interested to pursue in my post-doctoral endeavor.

7.1 Summary and conclusions

The prime objectives of this thesis include investigations of the triggering mechanisms of large-scale solar eruptions and understanding the mechanisms responsible for the activation and eruption of magnetic flux ropes. We focused on the pre-flare activities i.e, the small-scale energy release events occurring prior to main energy release phase of eruptive flares. In Chapter 1, we discussed various aspects of solar transient phenomena and presented the objectives of the Ph.D. thesis. Elaborate descriptions of the sources of the multi-wavelength observational data and numerical techniques are given in Chapter 2.

In Chapter 3, we explored the pre-flare processes. We presented two case studies which were associated with multiple episodes of pre-flare activities originating within or in the vicinity of the main flaring site. The results of our investigations suggest that continuous small-scale reconnection activities close to a flux rope can result in the slow activation and eruption of it by adding flux content to the flux rope as well as reducing the strapping magnetic field confining the flux rope. Further, flux ropes are strengthened in response to flux cancellation at the polarity inversion line (PIL) for prolonged periods. The resulting slow activation of flux ropes can be identified in the SXR lightcurves as a gradual rise in SXR flux prior to the impulsive phase of flares, known as the precursor phase. Activated, hot flux ropes are identified as coherent structures in the EUV images corresponding to extremely high temperatures e.g., AIA 94 Å and 131 Å channels, which are called coronal hot channels. Therefore, observations of hot channels in the active regions (ARs) can be interpreted as the earliest signatures of CMEs in the source regions. Complete destabilization of activated flux ropes can be achieved by delivering even small energy to the system by small-scale pre-flare activities originating within or near the quasi-stable flux ropes. We would also like to mention that we detected HXR sources of energies as high as ≈100 keV associated with pre-flare activities. This suggests that occasionally pre-flare activities also cause brief yet significant events of particle acceleration.

In Chapter 4, we focused on the signatures of magnetic reconnection in 2D and 3D in the context of solar flares. The chapter starts with a discussion on different varieties of circular ribbon flares and advancements of our theoretical understanding on 3D topological features. We present the results of our thorough multi-wavelength analysis of four homologous quasi-circular ribbon eruptive flares, onset of which was driven by repeated eruption of filaments from a filament channel situated within the periphery of circular ribbon structures. By employing NLFFF coronal modeling, we investigated and compared the coronal magnetic configuration associated with the filament and the circular ribbons. The flaring region was characterized by a fan-spine-like structure that developed over a complex photospheric configuration where dispersed negative polarity regions were surrounded by positive polarity regions. This unique photospheric configuration is analogous to the geological 'atoll' regions. The magnetic structure of the filament was manifested by well developed flux ropes. Prior to the eruption of the filaments, we observed localized brightening from the location of the filament as well as flux cancellation at the PIL, which are supportive of the tether-cutting model for flux rope activation. While the ascend of the flux ropes was characterized by highly localized (almost spot-like) flare ribbons, structured post-reconnection arcades were developed following the eruption of the flux ropes. Such evolutions are in line with the CSHKP model which explains eruptive flares in terms of 2D magnetic reconnection. We, therefore, interpret that all the four quasi-circular ribbon flares were triggered by the flux rope eruptions inside the fan-spine-like configuration. However, the most important result of this study was in view of the absence of null points in the 3D structure. Instead of a coronal null point, we observed the presence of a hyperbolic flux tube (HFT) between the fan and spine quasi-separatrix layers (QSLs). We emphasize that the occurrence of quasi-circular ribbon flares from complex fan-spine-like configurations involving HFTs, explored by us, provide a novel idea in the context of 3D coronal structures and flaring activities originating from them.

Understanding the factors responsible for failed eruptions is important not only for understanding the basics of coronal magnetic fields but also for space weather prediction purposes. One of the major objectives of the thesis has been to investigate the magnetic configurations of erupting and non-erupting flares. For this purpose, we carried out comprehensive analysis of a failed eruptive flare originating from quadrupolar magnetic configuration which are frequently observed to produce large eruptive flares. The quadrupolar configuration involved a 3D coronal null which was situated above a filament. Soft X-ray (SXR) lightcurves revealed a number of periods of pre-flare flux enhancement prior to the large-scale flaring process. Comparison of EUV images with the SXR time profiles suggested the pre-flare activities to be associated with magnetic reconnections at the null point supporting the predictions of the breakout model of solar eruption. The distribution of magnetic decay index above the magnetic flux rope was characterized by a saddle-type profile where the values of decay index initially increased reaching to the conditions of torus instability within much lower heights. However, following the initial increase, magnetic decay index values decreased rapidly reaching to negative values before steadily increasing again. Based on this important observation, we propose that the negative value of the magnetic decay index not only decelerated the eruption of the flux rope but also repelled it back downward resulting in the failed eruption. On the basis of these results, we conclude that the ultimate fate of solar eruptions is determined by a complex interplay of coronal magnetic fields involving the magnetic flux rope, core and envelope fields. This study is presented in Chapter 5.

In Chapter 6, we presented a comprehensive study of the magnetic characteristics and eruptivity of the historical active region NOAA 12673. Notably, this AR was among the most flare productive ARs which also produced the largest solar flare of the solar cycle 24, an X9.3 flare on 6 September 2017. After appearing as a simple α-type AR, NOAA 12763 experienced consistent flux emergence of both polarities as well as photospheric shearing and rotational motions. The photospheric motions led to the formation of strong horizontal current regions of both polarities on the photosphere, a few of which were situated in close proximity. Such close proximity of opposite polarities are preferred locations for the initiation of magnetic reconnection. Continuous flux emergence and photospheric motion also injected strong helicity and non-potential energy in the system which led the AR to evolve as one of the most flare productive ARs. NLFFF extrapolation results prior to the onset of the two X-class flares (GOES classes X2.2 and X9.3) on 6 September 2017, revealed the presence of well developed flux ropes over the PIL. Notably, along with the flux rope, the core magnetic field was associated with a fan-spine configuration involving a coronal null point, prior to the X2.2 flare. Prior to the onset of the X9.3 flare, the northern footpoint of flux rope essentially got involved in the fan-spine configuration while the flux rope itself appeared to be more developed compared to that prior to the X2.2 flare. Thus, we believe that the direct involvement of the more developed flux rope in the null point configuration resulted in higher flare class of the second X-class flare over the first one. Further, we carried out multi-wavelength and modeling analysis of two homologous eruptive M-class flare that originated from a highly localized part of NOAA 12673. Coronal images revealed the presence of a highly localized coronal sigmoid at the flare location, which can be justifiably termed as a minisigmoid. Further, NLFFF extrapolation results suggested the presence of two intertwined flux ropes in a double-decker flux rope configuration, which were co-spatial to the minisigmoid. Magnetic decay index profile above the axis of the double-decker flux rope configuration exhibited a favorable condition for the successful eruption of a torus unstable flux rope. Presence of the double-decker structure within the minisigmoid and the occurrence of homologous flares from it suggests that the magnetic complexity of AR is strongly linked with the flare productivity rather than the area or strength of the corresponding magnetic flux region.

In essence, the thesis explored the magnetic configurations associated with flaring activities as well as investigated their initiation and evolution, considering events of a wide spatial, temporal and morphological varieties. The thesis has provided a few novel ideas on 3D coronal magnetic field topologies and destabilization processes of magnetic flux ropes in solar ARs.

7.2 Future Works

In future, I would like to continue our research work in line of the topics addressed in the thesis. The future work will also aim at further strengthening the new ideas proposed in my thesis work. This will be achieved by exploring new data from recently launched and upcoming space missions and ground-based observing facilities. I enlist a few anticipated research topics in the following.

- I plan to carry out a series of subsequent studies on failed eruptions of torus unstable flux ropes in order to reach to further understandings on the mechanism(s) of successful/failed solar eruptions.

- We will emphasize on understanding the small-scale energetic processes in solar corona, such as A and sub-A-class flares; compact jets; etc., by exploring the events of the rising phase of solar cycle 25 exhibiting prolonged periods of low solar activity. In particular, I plan to utilize the unprecedented data from the Solar X-Ray Monitor on Board the Chandrayaan-2 Orbiter (XSM; Mithun et al., 2020) and The Spectrometer Telescope for Imaging X-rays (STIX; Krucker et al., 2020) on board the Solar Orbiter.

- We will put special focus on investigating the magnetic configurations associated with quasi-circular ribbon flares in order to advance our understanding on those observational features which are beyond the scope of the standard 2D model of solar flares. To this end, I also plan to investigate the evolution of complex 3D magnetic structures associated with circular ribbon flares by using numerical simulation techniques.

- Solar radio bursts are very effective probes of the physical state of the flaring atmosphere, providing an important diagnostic tool for magnetic structures and flare-accelerated electrons. In future studies, I would like to explore microwave and radio observations of solar flares to address the particle acceleration processes.

Bibliography

Acton, L. W. 1968, *Astrophys. J.*, 152, 305

Amari, T., Aly, J. J., Mikic, Z., & Linker, J. 2010, *Astrophys. J. Lett.*, 717, L26

Amari, T., Canou, A., Aly, J.-J., Delyon, F., & Alauzet, F. 2018, *Nature*, 554, 211

Amari, T., Luciani, J. F., Aly, J. J., Mikic, Z., & Linker, J. 2003, *Astrophys. J.*, 585, 1073

Amari, T., Luciani, J. F., Mikic, Z., & Linker, J. 1999, *Astrophys. J. Lett.*, 518, L57

—. 2000, *Astrophys. J. Lett.*, 529, L49

Antiochos, S. K., Dahlburg, R. B., & Klimchuk, J. A. 1994, *Astrophys. J. Lett.*, 420, L41

Antiochos, S. K., DeVore, C. R., & Klimchuk, J. A. 1999, *Astrophys. J.*, 510, 485

Archontis, V., Moreno-Insertis, F., Galsgaard, K., Hood, A., & O'Shea, E. 2004, *Astron. Astrophys.*, 426, 1047

Aschwanden, M. J. 2005, Physics of the Solar Corona. An Introduction with Problems and Solutions (2nd edition)

Aulanier, G., Démoulin, P., Schrijver, C. J., et al. 2013, *Astron. Astrophys.*, 549, A66

Aulanier, G., Janvier, M., & Schmieder, B. 2012, *Astron. Astrophys.*, 543, A110

Aulanier, G., Pariat, E., & Démoulin, P. 2005, *Astron. Astrophys.*, 444, 961

Aulanier, G., Pariat, E., Démoulin, P., & DeVore, C. R. 2006, *Solar Phys.*, 238, 347

Aulanier, G., Török, T., Démoulin, P., & DeLuca, E. E. 2010, *Astrophys. J.*, 708, 314

Aulanier, G., Török, T., Démoulin, P., & DeLuca, E. E. 2009, The Astrophysical Journal, 708, 314

Awasthi, A. K., Liu, R., & Wang, Y. 2019, *Astrophys. J.*, 872, 109

Baker, D., van Driel-Gesztelyi, L., Brooks, D. H., et al. 2019, *Astrophys. J.*, 875, 35

Bastian, T. S., Benz, A. O., & Gary, D. E. 1998, *Annual Review of Astronomy & Astrophysics*, 36, 131

Bateman, G. 1978, MHD instabilities

Baumgartner, C., Thalmann, J. K., & Veronig, A. M. 2018, *Astrophys. J.*, 853, 105

Benz, A. O. 2017, Living Reviews in Solar Physics, 14, 2

Berger, M. A., & Prior, C. 2006, Journal of Physics A Mathematical General, 39, 8321

Bobra, M. G., Sun, X., Hoeksema, J. T., et al. 2014, *Solar Phys.*, 289, 3549

Borrero, J. M., Tomczyk, S., Kubo, M., et al. 2011, *Solar Phys.*, 273, 267

Brown, J. C. 1971, *Solar Phys.*, 18, 489

Brown, J. C., Aschwanden, M. J., & Kontar, E. P. 2002, Solar Physics, 210, 373

Brueckner, G. E., Howard, R. A., Koomen, M. J., et al. 1995, Solar Physics, 162, 357

Cairns, I. H., Knock, S., Robinson, P., & Kuncic, Z. 2003, Space Science Reviews, 107, 27

Caligari, P., Moreno-Insertis, F., & Schussler, M. 1995, *Astrophys. J.*, 441, 886

Canfield, R. C., Hudson, H. S., & McKenzie, D. E. 1999, *Geophys. Res. Lett.*, 26, 627

Carmichael, H. 1964, NASA Special Publication, 50, 451

Carrington, R. C. 1859, *Mon. Not. Roy. Astron. Soc.*, 20, 13

Chandra, R., Schmieder, B., Aulanier, G., & Malherbe, J. M. 2009, *Solar Phys.*, 258, 53

Chatterjee, P., & Fan, Y. 2013, *Astrophys. J. Lett.*, 778, L8

Chen, B., Yu, S., Reeves, K. K., & Gary, D. E. 2020, *Astrophys. J. Lett.*, 895, L50

Chen, B., Yu, S., Battaglia, M., et al. 2018a, *Astrophys. J.*, 866, 62

Chen, H., Duan, Y., Yang, J., Yang, B., & Dai, J. 2018b, *Astrophys. J.*, 869, 78

Chen, H., Zhang, J., Cheng, X., et al. 2014, *Astrophys. J. Lett.*, 797, L15

Chen, H., Zhang, J., Li, L., & Ma, S. 2016, *Astrophys. J. Lett.*, 818, L27

Chen, P. F. 2011, Living Reviews in Solar Physics, 8, 1

Chen, P. F., & Shibata, K. 2000, *Astrophys. J.*, 545, 524

Cheng, J. X., & Qiu, J. 2016, The Astrophysical Journal, 825, 37

Cheng, X., Ding, M. D., Zhang, J., et al. 2014a, *Astrophys. J.*, 789, 93

—. 2014b, *Astrophys. J.*, 789, 93

Cheng, X., Zhang, J., Ding, M. D., Guo, Y., & Su, J. T. 2011, *Astrophys. J.*, 732, 87

Cheng, X., Zhang, J., Ding, M. D., Liu, Y., & Poomvises, W. 2013, *Astrophys. J.*, 763, 43

Chifor, C., Mason, H. E., Tripathi, D., Isobe, H., & Asai, A. 2006, *Astron. Astrophys.*, 458, 965

Chifor, C., Tripathi, D., Mason, H. E., & Dennis, B. R. 2007, *Astron. Astrophys.*, 472, 967

Chintzoglou, G., Patsourakos, S., & Vourlidas, A. 2015, *Astrophys. J.*, 809, 34

Cline, T. L., Holt, S. S., & Hones, Jr., E. W. 1968, *J. Geophys. Res.*, 73, 434

Craig, I. J. D., & Effenberger, F. 2014, *Astrophys. J.*, 795, 129

Cranmer, S. R. 2009, Living Reviews in Solar Physics, 6, 3

Dalmasse, K., Pariat, E., Valori, G., Démoulin, P., & Green, L. M. 2013, *Astron. Astrophys.*, 555, L6

del Zanna, G., Berlicki, A., Schmieder, B., & Mason, H. E. 2006, *Solar Phys.*, 234, 95

Démoulin, P. 2007, Advances in Space Research, 39, 1367

Démoulin, P., & Aulanier, G. 2010, *Astrophys. J.*, 718, 1388

Démoulin, P., Bagala, L. G., Mandrini, C. H., Henoux, J. C., & Rovira, M. G. 1997, *Astron. Astrophys.*, 325, 305

Demoulin, P., Henoux, J. C., Priest, E. R., & Mand rini, C. H. 1996, *Astron. Astrophys.*, 308, 643

DeRosa, M. L., Wheatland, M. S., Leka, K. D., et al. 2015, *Astrophys. J.*, 811, 107

Dhakal, S. K., Chintzoglou, G., & Zhang, J. 2018, *Astrophys. J.*, 860, 35

Dhara, S. K., Belur, R., Kumar, P., et al. 2017, *Solar Phys.*, 292, 145

Domingo, V., Fleck, B., & Poland, A. I. 1995, *Solar Phys.*, 162, 1

Doschek, G. A., & Warren, H. P. 2005, *Astrophys. J.*, 629, 1150

Duan, A., Jiang, C., He, W., et al. 2019, *Astrophys. J.*, 884, 73

Emslie, A. G. 1983, *Astrophys. J.*, 271, 367

Fan, Y. 2001, *Astrophys. J.*, 554, L111

—. 2009, *Astrophys. J.*, 697, 1529

Fárník, F., Hudson, H., & Watanabe, T. 1996, *Solar Phys.*, 165, 169

Fárník, F., Hudson, H. S., Karlický, M., & Kosugi, T. 2003, *Astron. Astrophys.*, 399, 1159

Fárník, F., & Savy, S. K. 1998, *Solar Phys.*, 183, 339

Filippov, B. 2020a, *Mon. Not. Roy. Astron. Soc.*, 494, 2166

Filippov, B. P. 2020b, Astronomy Reports, 64, 272

Fletcher, L., & Hudson, H. S. 2002, *Solar Phys.*, 210, 307

Fletcher, L., Dennis, B. R., Hudson, H. S., et al. 2011, *Space Sci. Rev.*, 159, 19

Forbes, T. G. 2000, *J. Geophys. Res.*, 105, 23153

Forbes, T. G., & Acton, L. W. 1996, *Astrophys. J.*, 459, 330

Forsyth, R. J., Bothmer, V., Cid, C., et al. 2006, Space Science Reviews, 123, 383

Gallagher, P. T., Dennis, B. R., Krucker, S., Schwartz, R. A., & Tolbert, A. K. 2002, *Solar Phys.*, 210, 341

Gary, D. E., Chen, B., Dennis, B. R., et al. 2018, *Astrophys. J.*, 863, 83

Gary, G. A., & Hagyard, M. J. 1990, *Solar Phys.*, 126, 21

Gibson, S. E. 2018, Living Reviews in Solar Physics, 15, 7

Gibson, S. E., Dalmasse, K., Rachmeler, L. A., et al. 2017, *Astrophys. J. Lett.*, 840, L13

Gibson, S. E., & Fan, Y. 2006, Journal of Geophysical Research (Space Physics), 111, A12103

Gibson, S. E., Fan, Y., Mandrini, C., Fisher, G., & Demoulin, P. 2004, *Astrophys. J.*, 617, 600

Gibson, S. E., Fan, Y., Török, T., & Kliem, B. 2006, *Space Sci. Rev.*, 124, 131

Gibson, S. E., Fletcher, L., Del Zanna, G., et al. 2002, *Astrophys. J.*, 574, 1021

Gilbert, H. R., Alexander, D., & Liu, R. 2007, *Solar Phys.*, 245, 287

Gopalswamy, N. 2013, Type II Solar Radio Bursts (American Geophysical Union (AGU)), 123–135

Gopalswamy, N., Mäkelä, P., Xie, H., Akiyama, S., & Yashiro, S. 2009, Journal of Geophysical Research (Space Physics), 114, A00A22

Gosling, J. T., Bame, S. J., McComas, D. J., & Phillips, J. L. 1990, *Geophys. Res. Lett.*, 17, 901

Guo, J., Dumbović, M., Wimmer-Schweingruber, R. F., et al. 2018, Space Weather, 16, 1156

Guo, Y., Xu, Y., Ding, M. D., et al. 2019, *Astrophys. J. Lett.*, 884, L1

Hajdas, W., Eggel, C., Wigger, C., et al. 2004, in ESA Special Publication, Vol. 536, ESA Special Publication, 607

Hale, G. E. 1908, *Astrophys. J.*, 28, 315

Handy, B. N., Acton, L. W., Kankelborg, C. C., et al. 1999, *Solar Phys.*, 187, 229

Harvey, J. W., Hill, F., Hubbard, R. P., et al. 1996, Science, 272, 1284

Harvey, J. W., Bolding, J., Clark, R., et al. 2011, in AAS/Solar Physics Division Abstracts #42, AAS/Solar Physics Division Meeting, 17.45

Haynes, A. L., & Parnell, C. E. 2007, Physics of Plasmas, 14, 082107

Heinemann, S. G., Temmer, M., Farrugia, C. J., et al. 2019, *Solar Phys.*, 294, 121

Heirtzler, J. 2002, Journal of Atmospheric and Solar-Terrestrial Physics, 64, 1701

Hernandez-Perez, A., Su, Y., Thalmann, J., et al. 2019a, *Astrophys. J. Lett.*, 887, L28

Hernandez-Perez, A., Su, Y., Veronig, A. M., et al. 2019b, *Astrophys. J.*, 874, 122

Hernandez-Perez, A., Thalmann, J. K., Veronig, A. M., et al. 2017, *Astrophys. J.*, 847, 124

Hirayama, T. 1974, Solar Physics, 34, 323

Högbom, J. A. 1974, *Astron. Astrophys. Suppl.*, 15, 417

Holman, G. D., Sui, L., Schwartz, R. A., & Emslie, A. G. 2003, *Astrophys. J. Lett.*, 595, L97

Holman, G. D., Aschwanden, M. J., Aurass, H., et al. 2011, *Space Sci. Rev.*, 159, 107

Hou, Y., Li, T., Yang, S., & Zhang, J. 2019, *Astrophys. J.*, 871, 4

Hou, Y. J., Zhang, J., Li, T., Yang, S. H., & Li, X. H. 2018, *Astron. Astrophys.*, 619, A100

Hudson, H. S. 1972, *Solar Phys.*, 24, 414

Hudson, H. S., Bougeret, J.-L., & Burkepile, J. 2006, Space Science Reviews, 123, 13

Hurford, G. J., & Curtis, D. W. 2002, *Solar Phys.*, 210, 101

Hurford, G. J., Schmahl, E. J., Schwartz, R. A., et al. 2002, *Solar Phys.*, 210, 61

Inoue, S., Kusano, K., Büchner, J., & Skála, J. 2018, Nature Communications, 9, 174

Isenberg, P. A., Forbes, T. G., & Demoulin, P. 1993, *Astrophys. J.*, 417, 368

Jaeggli, S. A., & Norton, A. A. 2016, *Astrophys. J. Lett.*, 820, L11

Janvier, M., Aulanier, G., Bommier, V., et al. 2014, *Astrophys. J.*, 788, 60

Janvier, M., Aulanier, G., Pariat, E., & Démoulin, P. 2013, *Astron. Astrophys.*, 555, A77

Janvier, M., Savcheva, A., Pariat, E., et al. 2016, *Astron. Astrophys.*, 591, A141

Jing, J., Liu, R., Cheung, M. C. M., et al. 2017, *Astrophys. J. Lett.*, 842, L18

Joshi, B., Ibrahim, M. S., Shanmugaraju, A., & Chakrabarty, D. 2018, *Solar Phys.*, 293, 107

Joshi, B., Kushwaha, U., Cho, K.-S., & Veronig, A. M. 2013, *Astrophys. J.*, 771, 1

Joshi, B., Kushwaha, U., Veronig, A. M., & Cho, K.-S. 2016a, *Astrophys. J.*, 832, 130

Joshi, B., Kushwaha, U., Veronig, A. M., et al. 2017a, *Astrophys. J.*, 834, 42

Joshi, B., Manoharan, P. K., Veronig, A. M., Pant, P., & Pandey, K. 2007, *Solar Phys.*, 242, 143

Joshi, B., Veronig, A. M., Lee, J., et al. 2011, *Astrophys. J.*, 743, 195

Joshi, N. C., Filippov, B., Schmieder, B., et al. 2016b, *Astrophys. J.*, 825, 123

Joshi, N. C., Joshi, B., & Mitra, P. K. 2021, *Mon. Not. Roy. Astron. Soc.*, 501, 4703

Joshi, N. C., Liu, C., Sun, X., et al. 2015, *Astrophys. J.*, 812, 50

Joshi, N. C., Sterling, A. C., Moore, R. L., Magara, T., & Moon, Y.-J. 2017b, *Astrophys. J.*, 845, 26

Joshi, N. C., Zhu, X., Schmieder, B., et al. 2019, *Astrophys. J.*, 871, 165

Kane, S. R. 1974, in IAU Symposium, Vol. 57, Coronal Disturbances, ed. G. A. Newkirk, 105

Kane, S. R., & Anderson, K. A. 1970, *Astrophys. J.*, 162, 1003

Karpen, J. T., Antiochos, S. K., & DeVore, C. R. 2012, *Astrophys. J.*, 760, 81

Kawabata, Y., Iida, Y., Doi, T., et al. 2018, *Astrophys. J.*, 869, 99

Kazachenko, M. D., Fisher, G. H., Welsch, B. T., Liu, Y., & Sun, X. 2015, *Astrophys. J.*, 811, 16

Kim, S., Moon, Y. J., Kim, Y. H., et al. 2008, *Astrophys. J.*, 683, 510

Kliem, B., & Török, T. 2006, Physical Review Letters, 96, 255002

Kliem, B., Török, T., Titov, V. S., et al. 2014, *Astrophys. J.*, 792, 107

Klimchuk, J. A., Canfield, R. C., & Rhoads, J. E. 1992, *Astrophys. J.*, 385, 327

Kondo, T., Isobe, T., Igi, S., Watari, S., & Tokumaru, M. 1995, Journal of the Communications Research Laboratory, 42, 111

Kontogiannis, I., Georgoulis, M. K., Park, S.-H., & Guerra, J. A. 2017, *Solar Phys.*, 292, 159

Kopp, R. A., & Pneuman, G. W. 1976, *Solar Phys.*, 50, 85

Korchak, A. A. 1967a, *Soviet Astron.*, 11, 258

—. 1967b, Soviet Physics Doklady, 12, 192

Krucker, S., Hurford, G. J., & Lin, R. P. 2003, *Astrophys. J.*, 595, L103

Krucker, S., Battaglia, M., Cargill, P. J., et al. 2008, *Astron. Astrophys. Rev.*, 16, 155

Krucker, S., Hurford, G. J., Grimm, O., et al. 2020, *Astron. Astrophys.*, 642, A15

Kumar, S., Bhattacharyya, R., Joshi, B., & Smolarkiewicz, P. K. 2016, *Astrophys. J.*, 830, 80

Kundu, M. R. 1963, *Space Sci. Rev.*, 2, 438

Künzel, H. 1960, Astronomische Nachrichten, 285, 271

Kushwaha, U., Joshi, B., Veronig, A. M., & Moon, Y.-J. 2015, *Astrophys. J.*, 807, 101

Lau, Y.-T., & Finn, J. M. 1990, *Astrophys. J.*, 350, 672

Lee, J., Liu, C., Jing, J., & Chae, J. 2016, *Astrophys. J. Lett.*, 829, L1

Lee, J., White, S. M., Liu, C., Kliem, B., & Masuda, S. 2018, *Astrophys. J.*, 856, 70

Leka, K. D., Barnes, G., Crouch, A. D., et al. 2009, *Solar Phys.*, 260, 83

Lemen, J. R., Title, A. M., Akin, D. J., et al. 2012, *Solar Phys.*, 275, 17

Li, H., Jiang, Y., Yang, J., et al. 2017, *Astrophys. J.*, 836, 235

Li, H., Yang, J., Jiang, Y., et al. 2018a, *Astrophys. Space Sci.*, 363, 26

Li, Q., Yan, X., Wang, J., et al. 2019, *Astrophys. J.*, 886, 149

Li, T., Yang, S., Zhang, Q., Hou, Y., & Zhang, J. 2018b, *Astrophys. J.*, 859, 122

Lin, J., & Forbes, T. G. 2000, *J. Geophys. Res.*, 105, 2375

Lin, J., Forbes, T. G., Isenberg, P. A., & Démoulin, P. 1998, *Astrophys. J.*, 504, 1006

Lin, R. P., Dennis, B. R., Hurford, G. J., et al. 2002, *Solar Phys.*, 210, 3

Liu, C., Deng, N., Lee, J., et al. 2013, *Astrophys. J. Lett.*, 778, L36

Liu, C., Lee, J., Yurchyshyn, V., et al. 2007, *Astrophys. J.*, 669, 1372

Liu, C., Prasad, A., Lee, J., & Wang, H. 2020, *Astrophys. J.*, 899, 34

Liu, C., Deng, N., Liu, R., et al. 2012a, *Astrophys. J. Lett.*, 745, L4

Liu, L., Cheng, X., Wang, Y., & Zhou, Z. 2019, *Astrophys. J.*, 884, 45

Liu, L., Cheng, X., Wang, Y., et al. 2018a, *Astrophys. J. Lett.*, 867, L5

Liu, L., Wang, Y., Zhou, Z., et al. 2018b, *Astrophys. J.*, 858, 121

—. 2018c, *Astrophys. J.*, 858, 121

Liu, R., Chen, J., Wang, Y., & Liu, K. 2016a, Scientific Reports, 6, 34021

Liu, R., Kliem, B., Török, T., et al. 2012b, *Astrophys. J.*, 756, 59

Liu, R., Liu, C., Wang, S., Deng, N., & Wang, H. 2010, *Astrophys. J.*, 725, L84

Liu, R., Kliem, B., Titov, V. S., et al. 2016b, *Astrophys. J.*, 818, 148

Liu, W., Jin, M., Downs, C., et al. 2018d, *Astrophys. J. Lett.*, 864, L24

Liu, W., Wang, T.-J., Dennis, B. R., & Holman, G. D. 2009, *Astrophys. J.*, 698, 632

Liu, Y. 2008, *Astrophys. J. Lett.*, 679, L151

Liu, Y. D., Richardson, J. D., Wang, C., & Luhmann, J. G. 2014, *Astrophys. J. Lett.*, 788, L28

Longcope, D. W. 2005, Living Reviews in Solar Physics, 2, 7

Longcope, D. W., & Klapper, I. 2002, *Astrophys. J.*, 579, 468

Lumme, E., Kazachenko, M. D., Fisher, G. H., et al. 2019, *Solar Phys.*, 294, 84

Mackay, D. H., & van Ballegooijen, A. A. 2006, *Astrophys. J.*, 641, 577

MacTaggart, D., Prior, C., Raphaldini, B., Romano, P., & Guglielmino, S. L. 2021, Nature Communications, 12, 6621

Mandrini, C. H., Demoulin, P., Schmieder, B., et al. 2006, *Solar Phys.*, 238, 293

Manoharan, P. K., van Driel-Gesztelyi, L., Pick, M., & Demoulin, P. 1996, *Astrophys. J. Lett.*, 468, L73

Martin, S. F. 1998, *Solar Phys.*, 182, 107

Martínez-Sykora, J., Hansteen, V., & Carlsson, M. 2008, *Astrophys. J.*, 679, 871

Masson, S., McCauley, P., Golub, L., Reeves, K. K., & DeLuca, E. E. 2014, *Astrophys. J.*, 787, 145

Masson, S., Pariat, E., Aulanier, G., & Schrijver, C. J. 2009, The Astrophysical Journal, 700, 559

Masuda, S., Kosugi, T., Hara, H., Tsuneta, S., & Ogawara, Y. 1994, *Nature*, 371, 495

Mertz, L. N., Nakano, G. H., & Kilner, J. R. 1986, Journal of the Optical Society of America A, 3, 2167

Metcalf, T. R. 1994, *Solar Phys.*, 155, 235

Metcalf, T. R., Hudson, H. S., Kosugi, T., Puetter, R. C., & Pina, R. K. 1996, *Astrophys. J.*, 466, 585

Mithun, N. P. S., Vadawale, S. V., Sarkar, A., et al. 2020, *Solar Phys.*, 295, 139

Mitra, P. K., & Joshi, B. 2019, *Astrophys. J.*, 884, 46

—. 2021, *Mon. Not. Roy. Astron. Soc.*, 503, 1017

Mitra, P. K., Joshi, B., & Prasad, A. 2020a, *Solar Phys.*, 295, 29

Mitra, P. K., Joshi, B., Prasad, A., Veronig, A. M., & Bhattacharyya, R. 2018, *Astrophys. J.*, 869, 69

Mitra, P. K., Joshi, B., Veronig, A. M., et al. 2020b, *Astrophys. J.*, 900, 23

Moore, R. L., & Labonte, B. J. 1980, in IAU Symposium, Vol. 91, Solar and Interplanetary Dynamics, ed. M. Dryer & E. Tandberg-Hanssen, 207–210

Moore, R. L., & Roumeliotis, G. 1992, in Lecture Notes in Physics, Berlin Springer Verlag, Vol. 399, IAU Colloq. 133: Eruptive Solar Flares, ed. Z. Svestka, B. V. Jackson, & M. E. Machado, 69

Moore, R. L., Sterling, A. C., Hudson, H. S., & Lemen, J. R. 2001, *Astrophys. J.*, 552, 833

Moraitis, K., Sun, X., Pariat, É., & Linan, L. 2019, *Astron. Astrophys.*, 628, A50

Moza, K. L., Koul, P. K., Rausaria, R. R., & Khosa, P. N. 1986, Journal of Astrophysics and Astronomy, 7, 39

Muhamad, J., Nurzaman, M. Z., Dani, T., & Pamutri, A. R. 2022, Research in Astronomy and Astrophysics, 21, 312

Musset, S., Vilmer, N., & Bommier, V. 2015, *Astron. Astrophys.*, 580, A106

Myers, C. E., Yamada, M., Ji, H., et al. 2015, *Nature*, 528, 526

Myers, C. E., Yamada, M., Ji, H., et al. 2016, Physics of Plasmas, 23, 112102

Myshyakov, I., & Tsvetkov, T. 2020, *Astrophys. J.*, 889, 28

O'Flannagain, A. M., Brown, J. C., & Gallagher, P. T. 2015, *Astrophys. J.*, 799, 127

Panesar, N. K., Sterling, A. C., & Moore, R. L. 2018, *Astrophys. J.*, 853, 189

Parenti, S. 2014, Living Reviews in Solar Physics, 11, 1

Pariat, E., Antiochos, S. K., & DeVore, C. R. 2009a, The Astrophysical Journal, 691, 61

—. 2010, The Astrophysical Journal, 714, 1762

Pariat, E., & Démoulin, P. 2012, *Astron. Astrophys.*, 541, A78

Pariat, E., Masson, S., & Aulanier, G. 2009b, The Astrophysical Journal, 701, 1911

Patsourakos, S., Georgoulis, M. K., Vourlidas, A., et al. 2016, *Astrophys. J.*, 817, 14

Pesnell, W. D., Thompson, B. J., & Chamberlin, P. C. 2012, *Solar Phys.*, 275, 3

Pevtsov, A. A. 2002, *Solar Phys.*, 207, 111

Pontin, D. I. 2012, Philosophical Transactions of the Royal Society A: Mathematical, Physical and Engineering Sciences, 370, 3169

Prasad, A., Dissauer, K., Hu, Q., et al. 2020, arXiv e-prints, arXiv:2009.11109

Priest, E. 2014, Magnetohydrodynamics of the Sun, doi:10.1017/CBO9781139020732

Priest, E. R., & Démoulin, P. 1995, *J. Geophys. Res.*, 100, 23443

Priest, E. R., & Forbes, T. G. 2002, *Astron. Astrophys. Rev.*, 10, 313

Priest, E. R., & Titov, V. S. 1996, Philosophical Transactions of the Royal Society of London Series A, 354, 2951

Qiu, Y., Guo, Y., Ding, M., & Zhong, Z. 2020, *Astrophys. J.*, 901, 13

Raftery, C. L., Gallagher, P. T., McAteer, R. T. J., Lin, C.-H., & Delahunt, G. 2010, *Astrophys. J.*, 721, 1579

Reep, J. W., Bradshaw, S. J., & Holman, G. D. 2016, *Astrophys. J.*, 818, 44

Reeves, K. K., & Forbes, T. G. 2005, *Astrophys. J.*, 630, 1133

Reeves, K. K., Polito, V., Chen, B., et al. 2020, *Astrophys. J.*, 905, 165

Reid, H. A. S., & Ratcliffe, H. 2014, Research in Astronomy and Astrophysics, 14, 773

Romano, P., Elmhamdi, A., Falco, M., et al. 2018, *Astrophys. J. Lett.*, 852, L10

Romano, P., Elmhamdi, A., & Kordi, A. S. 2019, *Solar Phys.*, 294, 4

Rust, D. M., & Kumar, A. 1996, *Astrophys. J. Lett.*, 464, L199

Sahu, S., Joshi, B., Mitra, P. K., Veronig, A. M., & Yurchyshyn, V. 2020, *Astrophys. J.*, 897, 157

Sarkar, R., & Srivastava, N. 2018, *Solar Phys.*, 293, 16

Savcheva, A. S., van Ballegooijen, A. A., & DeLuca, E. E. 2012, *Astrophys. J.*, 744, 78

Schou, J., Scherrer, P. H., Bush, R. I., et al. 2012, *Solar Phys.*, 275, 229

Schrijver, C. J. 2007, *Astrophys. J. Lett.*, 655, L117

—. 2009, Advances in Space Research, 43, 739

Schrijver, C. J., Aulanier, G., Title, A. M., Pariat, E., & Delannée, C. 2011, *Astrophys. J.*, 738, 167

Schwartz, R. A., Csillaghy, A., Tolbert, A. K., et al. 2002, *Solar Phys.*, 210, 165

Schwenn, R. 2006, Living Reviews in Solar Physics, 3, 2

Seaton, D. B., & Darnel, J. M. 2018, *Astrophys. J. Lett.*, 852, L9

Shen, Y., Qu, Z., Zhou, C., et al. 2019, *Astrophys. J. Lett.*, 885, L11

Shibata, K. 1997, in ESA Special Publication, Vol. 404, Fifth SOHO Workshop: The Corona and Solar Wind Near Minimum Activity, ed. A. Wilson, 103

Shibata, K., & Magara, T. 2011, Living Reviews in Solar Physics, 8, 6

Shibata, K., Masuda, S., Shimojo, M., et al. 1995, *Astrophys. J. Lett.*, 451, L83

Shibata, K., Nitta, N., Strong, K. T., et al. 1994, *Astrophys. J. Lett.*, 431, L51

Shibata, K., & Yokoyama, T. 1999, *Astrophys. J. Lett.*, 526, L49

Shibata, K., Yokoyama, T., & Shimojo, M. 1996, Advances in Space Research, 17, 197

Shiota, D., Isobe, H., Chen, P. F., et al. 2005, *Astrophys. J.*, 634, 663

Smith, D. M., Lin, R. P., Turin, P., et al. 2002, *Solar Phys.*, 210, 33

Song, H. Q., Chen, Y., Zhang, J., et al. 2015a, *Astrophys. J. Lett.*, 804, L38

—. 2015b, *Astrophys. J. Lett.*, 808, L15

—. 2015c, *Astrophys. J.*, 808, L15

Song, H. Q., Zhang, J., Chen, Y., & Cheng, X. 2014, *Astrophys. J. Lett.*, 792, L40

Staude, J. 1990, Astronomische Nachrichten, 311, 106

Sterling, A. C. 2000, *Solar Phys.*, 196, 79

Sterling, A. C., Harra, L. K., & Moore, R. L. 2007, *Astrophys. J.*, 669, 1359

Sterling, A. C., & Moore, R. L. 2005, *Astrophys. J.*, 630, 1148

Sterling, A. C., Moore, R. L., & Freeland, S. L. 2011, *Astrophys. J. Lett.*, 731, L3

Sturrock, P. A. 1966, *Nature*, 211, 695

Sturrock, P. A. 1968, Symposium - International Astronomical Union, 35, 471–479

Sui, L., & Holman, G. D. 2003, *Astrophys. J. Lett.*, 596, L251

Sun, X., Hoeksema, J. T., Liu, Y., et al. 2013, *Astrophys. J.*, 778, 139

—. 2012, *Astrophys. J.*, 748, 77

Sun, X., & Norton, A. A. 2017, Research Notes of the American Astronomical Society, 1, 24

Švestka, Z., & Cliver, E. 1992, Eruptive Solar Flares (IAU Colloq. 133), Vol. 399, ed. Z. Švestka, BV Jackson, & ME Machado

Syntelis, P., Gontikakis, C., Patsourakos, S., & Tsinganos, K. 2016, *Astron. Astrophys.*, 588, A16

Syrovatskii, S. 1971, Sov. Phys. JETP, 33, 933

Syrovatskii, S. I., & Shmeleva, O. P. 1972, *Soviet Astron.*, 16, 273

Takakura, T., & Kai, K. 1966, *Pub. Astron. Soc. Japan*, 18, 57

Tan, B., Ji, H., Huang, G., et al. 2006, *Solar Phys.*, 239, 137

Tandberg-Hanssen, E., ed. 1995, Astrophysics and Space Science Library, Vol. 199, The nature of solar prominences

Temmer, M., Veronig, A. M., Vršnak, B., et al. 2008, *Astrophys. J. Lett.*, 673, L95

Temmer, M., Veronig, A. M., Vršnak, B., & Miklenic, C. 2007, *Astrophys. J.*, 654, 665

Tenerani, A., Velli, M., Rappazzo, A. F., & Pucci, F. 2015, *Astrophys. J. Lett.*, 813, L32

Thalmann, J. K., Moraitis, K., Linan, L., et al. 2019, *Astrophys. J.*, 887, 64

Thalmann, J. K., Su, Y., Temmer, M., & Veronig, A. M. 2015, *Astrophys. J. Lett.*, 801, L23

Tian, Z., Shen, Y., & Liu, Y. 2018, *New Astronomy*, 65, 7

Titov, V. S., Forbes, T. G., Priest, E. R., Mikić, Z., & Linker, J. A. 2009, *Astrophys. J.*, 693, 1029

Titov, V. S., Galsgaard, K., & Neukirch, T. 2003, The Astrophysical Journal, 582, 1172

Titov, V. S., Hornig, G., & Démoulin, P. 2002, Journal of Geophysical Research (Space Physics), 107, 1164

Titov, V. S., Mikić, Z., Linker, J. A., Lionello, R., & Antiochos, S. K. 2011, *Astrophys. J.*, 731, 111

Titov, V. S., Mikic, Z., Török, T., Linker, J. A., & Panasenco, O. 2012, *Astrophys. J.*, 759, 70

Tolbert, K., & Schwartz, R. 2020, OSPEX: Object Spectral Executive, ascl:2007.018

Toriumi, S., & Takasao, S. 2017, *Astrophys. J.*, 850, 39

Toriumi, S., & Wang, H. 2019, Living Reviews in Solar Physics, 16, 3

Tripathi, D., Kliem, B., Mason, H. E., Young, P. R., & Green, L. M. 2009, *Astrophys. J. Lett.*, 698, L27

Tsuneta, S., Hara, H., Shimizu, T., et al. 1992, *Pub. Astron. Soc. Japan*, 44, L63

Tziotziou, K., Georgoulis, M. K., & Liu, Y. 2013, *Astrophys. J.*, 772, 115

Uralov, A. M., Grechnev, V. V., Rudenko, G. V., et al. 2014, *Solar Phys.*, 289, 3747

van Ballegooijen, A. A., & Martens, P. C. H. 1989, *Astrophys. J.*, 343, 971

Vemareddy, P. 2019, *Astrophys. J.*, 872, 182

Vemareddy, P., Ambastha, A., & Maurya, R. A. 2012, *Astrophys. J.*, 761, 60

Verma, M. 2018, *Astron. Astrophys.*, 612, A101

Veronig, A., Vršnak, B., Temmer, M., & Hanslmeier, A. 2002, *Solar Phys.*, 208, 297

Veronig, A. M., Karlický, M., Vršnak, B., et al. 2006, *Astron. Astrophys.*, 446, 675

Veronig, A. M., Podladchikova, T., Dissauer, K., et al. 2018, *Astrophys. J.*, 868, 107

Wang, D., Liu, R., Wang, Y., et al. 2017a, *Astrophys. J. Lett.*, 843, L9

—. 2017b, *Astrophys. J. Lett.*, 843, L9

Wang, R., Liu, Y. D., Yang, Z., & Hu, H. 2014, *Astrophys. J.*, 791, 84

Wang, S., Liu, C., Liu, R., et al. 2012, *Astrophys. J. Lett.*, 745, L17

Wang, Y., Su, Y., Shen, J., et al. 2018, *Astrophys. J.*, 859, 148

Wang, Y. M., Sheeley, N. R., J., & Rich, N. B. 2007, *Astrophys. J.*, 658, 1340

Warren, H. P., & Warshall, A. D. 2001, *Astrophys. J.*, 560, L87

Webb, D. F., & Howard, T. A. 2012, Living Reviews in Solar Physics, 9, 3

Wheatland, M. S., Sturrock, P. A., & Roumeliotis, G. 2000, *Astrophys. J.*, 540, 1150

White, S. M., Benz, A. O., Christe, S., et al. 2011, *Space Sci. Rev.*, 159, 225

Wiegelmann, T. 2004, *Solar Phys.*, 219, 87

Wiegelmann, T., Inhester, B., & Sakurai, T. 2006, *Solar Phys.*, 233, 215

Wiegelmann, T., & Sakurai, T. 2021, Living Reviews in Solar Physics, 18, 1

Wiegelmann, T., Thalmann, J. K., & Solanki, S. K. 2014, *Astron. Astrophys. Rev.*, 22, 78

Wiegelmann, T., & Inhester, B. 2010, A&A, 516, A107

Wilmot-Smith, A. L., Hornig, G., & Pontin, D. I. 2009, The Astrophysical Journal, 704, 1288

Woods, M. M., Inoue, S., Harra, L. K., et al. 2018, *Astrophys. J.*, 860, 163

Woods, T. N., Eparvier, F. G., Hock, R., et al. 2012, *Solar Phys.*, 275, 115

Wyper, P. F., Antiochos, S. K., & DeVore, C. R. 2017, *Nature*, 544, 452

Xu, Z., Yang, K., Guo, Y., et al. 2017, *Astrophys. J.*, 851, 30

Xue, Z., Yan, X., Yang, L., Wang, J., & Zhao, L. 2017, *Astrophys. J. Lett.*, 840, L23

Yan, X. L., Wang, J. C., Pan, G. M., et al. 2018, *Astrophys. J.*, 856, 79

Yang, B., & Chen, H. 2019, *Astrophys. J.*, 874, 96

Yang, K., Guo, Y., & Ding, M. D. 2015, *Astrophys. J.*, 806, 171

Yang, S., Büchner, J., Skála, J., & Zhang, H. 2018, *Astron. Astrophys.*, 613, A27

Yang, S., Zhang, J., Zhu, X., & Song, Q. 2017, *Astrophys. J. Lett.*, 849, L21

Yashiro, S., Akiyama, S., Gopalswamy, N., & Howard, R. A. 2006, *Astrophys. J. Lett.*, 650, L143

Yashiro, S., Gopalswamy, N., Akiyama, S., Michalek, G., & Howard, R. A. 2005, Journal of Geophysical Research (Space Physics), 110, A12S05

Yashiro, S., Gopalswamy, N., Michalek, G., et al. 2004, Journal of Geophysical Research (Space Physics), 109, A07105

Yokoyama, T., Akita, K., Morimoto, T., Inoue, K., & Newmark, J. 2001, *Astrophys. J. Lett.*, 546, L69

Zhang, H. 1995, *Astron. Astrophys.*, 304, 541

Zhang, H., Brandenburg, A., & Sokoloff, D. D. 2016, *Astrophys. J.*, 819, 146

Zhang, J., Cheng, X., & Ding, M.-D. 2012, Nature Communications, 3, 747

Zhang, J., & Dere, K. P. 2006, *Astrophys. J.*, 649, 1100

Zhang, J., Dere, K. P., Howard, R. A., Kundu, M. R., & White, S. M. 2001, *Astrophys. J.*, 559, 452

Zhang, J., Dere, K. P., Howard, R. A., & Vourlidas, A. 2004, *Astrophys. J.*, 604, 420

Zhang, M., & Low, B. C. 2005, *Annual Review of Astronomy & Astrophysics*, 43, 103

Zhao, J., Gilchrist, S. A., Aulanier, G., et al. 2016, *Astrophys. J.*, 823, 62

Zhao, J., Liu, W., & Vial, J.-C. 2021, *Astrophys. J. Lett.*, 921, L26

Zheng, J.-C., Yang, Z.-L., Guo, J.-P., et al. 2017, Research in Astronomy and Astrophysics, 17, 081

Zheng, R., Yang, S., Rao, C., et al. 2019, *Astrophys. J.*, 875, 71

Zhong, Z., Guo, Y., & Ding, M. D. 2021, Nature Communications, 12, 2734

Zhongxian, S., & Jingxiu, W. 1994, *Solar Phys.*, 149, 105

Zhou, G. P., Tan, C. M., Su, Y. N., et al. 2019, *Astrophys. J.*, 873, 23

Zhou, G. P., Zhang, J., & Wang, J. X. 2016, *Astrophys. J. Lett.*, 823, L19

Zirin, H. 1988, Astrophysics of the sun

Zirin, H., & Liggett, M. A. 1987, *Solar Phys.*, 113, 267

Zou, P., Jiang, C., Feng, X., et al. 2019, *Astrophys. J.*, 870, 97

Zou, P., Jiang, C., Wei, F., et al. 2020, *Astrophys. J.*, 890, 10

Zuccarello, F. P., Chandra, R., Schmieder, B., Aulanier, G., & Joshi, R. 2017, *Astron. Astrophys.*, 601, A26

Zuccarello, F. P., Seaton, D. B., Mierla, M., et al. 2014, *Astrophys. J.*, 785, 88

Zuccarello, F., Romano, P., Farnik, F., et al. 2009, *Astron. Astrophys.*, 493, 629

Publications attached with the thesis

1. **Mitra, P. K.** & Joshi, B., 2019, *"Preflare Processes, Flux Rope Activation, Large-scale Eruption, and Associated X-class Flare from the Active Region NOAA 11875"*, **Astrophysical Journal**, 884, 1.

2. **Mitra, P. K.**, Joshi, B. & Prasad, A., 2020, *"Identification of Pre-flare Processes and Their Possible Role in Driving a Large-scale Flux Rope Eruption with Complex M-class Flare in the Active Region NOAA 12371"*, **Solar Physics**, 295, 29.

3. **Mitra, P. K.**, Joshi, B., Veronig, A. M., Chandra, R., Dissauer, K. & Wiegelmann, T., 2020, *"Eruptive-Impulsive Homologous M-class Flares Associated with Double-decker Flux Rope Configuration in Minisigmoid of NOAA 12673"*, **Astrophysical Journal**, 900, 23.

4. **Mitra, P. K.**, Joshi, B., 2021, *"Successive occurrences of quasi-circular ribbon flares in a fan-spine-like configuration involving hyperbolic flux tube"*, **Monthly Notices of the Royal Astronomical Society**, 503, 1017.

5. **Mitra, P. K.**, Joshi, B., Veronig, A. M., & Wiegelmann, T., 2022, *"Multi-wavelength Signatures of Episodic Null Point Reconnection in a Quadrupolar Magnetic Configuration and the Cause of Failed Flux Rope Eruption"*, **Astrophysical Journal**, 926, 143.

The Astrophysical Journal, 884:46 (16pp), 2019 October 10 https://doi.org/10.3847/1538-4357/ab3a96

Preflare Processes, Flux Rope Activation, Large-scale Eruption, and an Associated X-class Flare from the Active Region NOAA 11875

Prabir K. Mitra[1,2] and Bhuwan Joshi[1]
[1] Udaipur Solar Observatory, Physical Research Laboratory, Udaipur 313 001, India; prabir@prl.res.in
[2] Department of Physics, Gujarat University, Ahmedabad 380 009, India
Received 2019 June 11; revised 2019 July 30; accepted 2019 August 11; published 2019 October 11

Abstract

We present a multiwavelength analysis of the eruption of a hot coronal channel associated with an X1.0 flare (SOL2013-10-28T02:03) from the active region NOAA 11875 by combining observations from Atmospheric Imaging Assembly/*Solar Dynamics Observatory* (*SDO*), Helioseismic and Magnetic Imager/*SDO*, *Reuven Ramaty High Energy Solar Spectroscopic Imager*, and Hiraiso Radio Spectrograph. EUV images at high coronal temperatures indicated the presence of a hot channel at the core of the active region from the early preflare phase evidencing the preexistence of a quasi-stable magnetic flux rope. The hot channel underwent an activation phase after a localized and prolonged preflare event occurring adjacent to one of its footpoints. Subsequently, the flux rope continued to rise slowly for ≈16 minutes during which soft X-ray flux gradually built-up characterizing a distinct precursor phase. The flux rope transitioned from the state of slow rise to the eruptive motion with the onset of the impulsive phase of the X1.0 flare. The eruptive expansion of the hot channel is accompanied by a series of type III radio bursts in association with the impulsive rise of strong hard X-ray nonthermal emissions that included explicit hard X-ray sources of energies up to ≈50 keV from the coronal loops and ≈100 keV from their footpoint locations. Our study contains evidence that preflare activity occurring within the spatial extent of a stable flux rope can destabilize it toward eruption. Moreover, sudden transition of the flux rope from the state of slow rise to fast acceleration precisely bifurcated the precursor and the impulsive phases of the flare, which points toward a feedback relationship between early coronal mass ejection dynamics and the strength of the large-scale magnetic reconnection.

Key words: Sun: activity – Sun: corona – Sun: filaments, prominences – Sun: flares – Sun: X-rays, gamma rays

Supporting material: animation

1. Introduction

Magnetic flux ropes (MFRs) are defined as sets of magnetic field lines, which are twisted along a common central axis usually more than once (Gibson & Fan 2006). MFRs are observed to be levitated along the polarity inversion line with the two legs tied in the opposite polarity regions. With a high storage of magnetic free energy, MFRs are one of the essential ingredients of large-scale solar transient phenomena, i.e., flares and coronal mass ejections (CMEs; Jing et al. 2010). Earth-directed CMEs cause geomagnetic storms which may disrupt the spacecraft stationed in near-Earth orbits and the communication system on Earth (Forsyth et al. 2006; Webb & Howard 2012). As the core of CMEs, MFRs have been studied extensively in recent years and remain one of the most contemporary topics in solar physics.

Different solar features, viz., filaments, prominences, filament channels, hot coronal channels, etc., essentially form the observational counterparts of MFRs. Filaments are thread-like structures found as dark features in the chromospheric images of the Sun. These are cool, dense materials supported in the corona against gravity by a sheared magnetic field with a dip (Antiochos et al. 1994) or helically twisted field lines (Priest et al. 1989). When these structures are observed on the limb, they are called prominences because they appear bright compared to the background. Filament channels are long-lived, narrow lanes between extended areas of magnetic field of opposite polarities where a filament (or prominence) can be formed (Engvold 1997; Gaizauskas et al. 1997). Hot coronal channels were first reported by Zhang et al. (2012) and Cheng et al. (2013) as coherent structures found in high temperature passband filter images. Hot channels are often found to appear in association with coronal sigmoids that are observed in EUV images (Cheng et al. 2014b; Joshi et al. 2017, 2018; Mitra et al. 2018). It is noteworthy that one footpoint of the hot coronal channel may originate in a strong magnetic field region with the other footpoint terminating in a weaker magnetic field (Cheng & Ding 2016). Below the hot channel, a filament channel is often observed confirming its association with MFRs (Chen et al. 2014a). An observational survey performed by Nindos et al. (2015) revealed that almost half of the major eruptive flares are associated with a preflare hot channel.

Successful eruption of an MFR is essential for the origin of a CME. According to the "standard flare model" (also known as CSHKP model; Carmichael 1964; Sturrock 1966; Hirayama 1974; Kopp & Pneuman 1976), once an MFR undergoes eruptive expansion, magnetic reconnection sets in between the inflow magnetic field lines. During magnetic reconnection, the stored magnetic energy is released in the form of intense heating within a localized region and nonthermal emissions (Shibata & Magara 2011). Multiwavelength observations of solar flares demonstrate complex temporal, spatial, and spectral variabilities in the energy release processes (Fletcher et al. 2011; Benz 2017). The CSHKP model is successful in explaining most of the commonly observed signatures of a flare, such as, flare ribbons; looptop and footpoint X-ray sources; cusp structure following the passage of the filament; post-flare loop arcade; etc. However, it remains silent to the topics of flux rope formation and triggering of the eruption process. It is also noteworthy that in view of the spatial evolution of the looptop and footpoint sources during the early impulsive phases, many flares do not comply with the CSHKP model (see, e.g., Veronig et al. 2006; Joshi et al. 2009, 2012). Further, the morphological and dynamical evolution of flare ribbons could be very complex (see, e.g., Sui & Holman 2003; Dalmasse et al. 2015; Joshi et al. 2017, 2019; Mitra et al. 2018).

The triggering mechanism of flux ropes is one of the most debated topics among solar physicists. Years of observation and corresponding theoretical understanding have led to two different classes of models for the triggering mechanism: reconnection based triggering and ideal instability. Two representative reconnection based triggering mechanisms—tether-cutting and breakout models—rely on different preflare magnetic configurations. The tether-cutting model involves two highly sheared arcades in a bipolar active region where triggering occurs in the form of initial reconnection beneath the sheared arcades when a newly emerged bipole interacts with them (Moore & Roumeliotis 1992; Moore et al. 2001). The breakout model, on the other hand, requires a complex multipolar active region with one or more preexisting magnetic nulls well above the core field containing a sheared arcade. Initial reconnection, according to the breakout model, occurs in those magnetic nulls, which reduces downward tension on the flux rope setting it in an eruptive motion (Antiochos et al. 1999). Over the years, several case studies have provided support for the tether-cutting model (see, e.g., Liu et al. 2007, 2013; Chen et al. 2014b, 2018b; Xue et al. 2017; Yang et al. 2018). Similarly, several observational studies and simulations have supported the breakout model of solar eruption (see, e.g., Manoharan & Kundu 2003; Gary & Moore 2004; Joshi et al. 2007; Aurass et al. 2011; Chen et al. 2016; Mitra et al. 2018).

The ideal instability models for triggering mechanisms do not rely on initial reconnection for eruption of MFRs. Two basic instability models—torus instability (Kliem & Török 2006) and kink instability (Török et al. 2004)—predict the onset of eruption of an MFR when some critical values are reached. According to the torus instability model, an MFR may attain eruptive expansion if the overlying magnetic field experiences a sharp decay with height. The critical value is decided by the parameter "decay index" ($n = -\frac{\log(B_{ex})}{\log(z)}$, where B_{ex} and z are the overlying magnetic field and height, respectively) and several studies have shown the critical value of the decay index to lie within the range [1.1–1.5] (Démoulin & Aulanier 2010; Olmedo & Zhang 2010). The kink instability model suggests eruption of an MFR if its twist increases beyond a critical value of $\approx 3.5\pi$. However, several studies have shown that both these instability criteria may lead to failed eruption of an MFR (Liu 2008; Song et al. 2014b) and often both the torus and kink instabilities are simultaneously required for a successful eruption of an MFR (Liu 2008; Vemareddy & Zhang 2014).

During a flare, a huge amount of magnetic energy is released in the form of thermal and nonthermal energies radiating across the entire electromagnetic spectrum, i.e., from γ-rays to radio waves. Thermal signatures of flares include optical, ultra-violet (UV), extreme ultra-violet (EUV), and soft X-ray (SXR) brightenings from post-reconnection loop arcades and flare ribbons (see the review by Fletcher et al. 2011). Nonthermal signatures of flares include hard X-ray (HXR), microwave, and radio bursts, which individually carry evidence of different physical mechanisms during a flare (Krucker et al. 2008; White et al. 2011). Careful observation and rightful analysis of flare HXR sources can be used to constraint the location of magnetic reconnection and particle acceleration (Masuda et al. 1994; Benz 2017) whereas type III and type II radio bursts can indirectly provide information on the restructuring of coronal field and early phases of CME propagation (Wild 1950; Cairns et al. 2003; Reid & Ratcliffe 2014).

In this work, we present a multiwavelength study of the eruption of a hot coronal channel which led to an X1.0 flare, using high cadence and high spatial resolution observations from the Atmospheric Imaging Assembly (AIA; Lemen et al. 2012). The flaring region was associated with multiple hard X-ray sources of energies up to $\approx$100 keV. The Hiraiso Radio Spectrograph (HiRAS; Kondo et al. 1995) revealed a complex set of metric radio bursts: a series of type III during the early rise phase, a set of prominent split-band type II harmonic band around the peak phase and a type IV burst during the decay phase. An important objective of the study lies in understanding the preflare processes and their relevance to the subsequent phases of CME initiation and main flaring event. The study provides an unambiguous detection of a preexisting MFR in the active region and shows its various activation stages that lead to a standard CME-producing X-class flares. The availability of solar X-ray observations from the *Reuven Ramaty High Energy Solar Spectroscopic Imager* (*RHESSI*; Lin et al. 2002) during part of the preflare phase and most of the X-class flare provided us with an opportunity to explore the sites of energization, heating, and particle acceleration. Section 2 provides details of the observational data and analysis techniques used in this article. Multiwavelength results involving EUV, X-ray and radio observations are explained in Section 3. We discuss and interpret our results in Section 4. The major highlights and conclusions of the study are provided in Section 5.

2. Observational Data and Methods

For observing the Sun in (E)UV wavelengths, we use high resolution ($0\farcs6$ pixel^{-1}), 4096 × 4096 pixel full disk observations from the AIA (Lemen et al. 2012) on board the *Solar Dynamics Observatory* (*SDO*; Pesnell et al. 2012). AIA observes the Sun in seven EUV channels (94, 131, 171, 193, 211, 304, and 335 Å), 2 UV channels (1600 and 1700 Å), and 1 white light channel (4500 Å). Temporal cadences are 12 s for the EUV filters, 24 s for the UV filters, and 3600 s for the white light filter. For photospheric observation, we use 45 s cadence line-of-sight (LOS) magnetograms and intensity images observed by the Helioseismic and Magnetic Imager (HMI; Schou et al. 2012) on board *SDO*, which takes continuous full disk observation of the solar photosphere with a spatial resolution of $0\farcs5$ pixel^{-1}.

CME associated with the erupting hot channel was observed by the C2 and C3 instruments of the Large Angle and Spectrometric Coronagraph (LASCO; Brueckner et al. 1995) on board the *Solar and Heliospheric Observatory* (Domingo et al. 1995). C2 and C3 are white light coronagraphs imaging from 1.5 to 6 $R_\odot$ and from 3.7 to 30 $R_\odot$, respectively.

The *RHESSI* (Lin et al. 2002) provided information about the X-ray sources associated with the flaring region. *RHESSI* observes the full Sun with an unprecedented spatial resolution (as fine as $\sim 2\farcs3$) and energy resolution (1–5 keV) in the energy range 3 keV–17 MeV. For imaging of the X-ray sources using *RHESSI* observation, we use the PIXON algorithm

(Metcalf et al. 1996) with the natural weighting scheme for front detector segments 2–9 (excluding 7). For construction of *RHESSI* spectra, we use the front detector segments 1–9 excluding 2 and 7 (which have lower energy resolution and high threshold energies, respectively; see Smith et al. 2002; Holman et al. 2011). The spectra were deconvolved with the full detector response matrix (i.e., off-diagonal elements were included; Smith et al. 2002).

Dynamic radio spectra within the frequency range 50–500 MHz were obtained from the Hiraiso Radio Spectrograph (HiRAS; Kondo et al. 1995), which is operated by the National Institute of Information and Communications Technology, Japan.[3]

3. Multiwavelength Observations and Results

3.1. Active Region NOAA 11875

The active region (AR) NOAA 11875 emerged on the eastern limb of the Sun on 2013 October 16 as a $\beta\gamma$-type sunspot.[4] On October 22, it transformed into a more complex $\beta\gamma\delta$-type and remained so until its disappearance from the western limb of the Sun on October 30. In its lifetime, it produced 2 X-class, 11 M-class besides many C-class flares.[5]

We have studied the active region NOAA 11875 on 2013 October 28 from 00:30 UT to 04:30 UT while it was situated close to the western limb of the Sun at the heliographic coordinates ∼N07W66.[6] In this duration, the active region underwent activation and eruption of a hot channel in association with an X1.0 flare. In Figure 1, we present a multiwavelength view of the AR prior to the erupting event. The photospheric HMI white light image suggests that the active region consisted of a major leading sunspot and few trailing spots of much smaller sizes (Figure 1(a)). Comparison of a cotemporal HMI LOS magnetogram (Figure 1(b)) with the while light image indicates that the major leading sunspot had a complex fine structure with multiple umbrae of opposite polarity within a common penumbra, i.e., δ-spots while the trailing spots were mostly of positive polarity. The AIA 171 Å image gives information about the coronal connectivities associated with the AR. Interestingly, we find a filament structure in the AR (indicated by the brown arrow in Figure 1(c)) and a set of open field lines originating from the trailing part of the AR (marked by the black arrows in Figure 1(c)). AIA 94 Å image indicates a hot coronal channel near the filament (indicated by the red arrow in Figure 1(d)), which forms the core of the AR. Notably, comparison of AIA 171 and 94 Å images indicates that the region of open field lines was also connected with the core of the AR (containing the filament) by a set of hot coronal loops.

3.2. Evolutionary Phases of the X1.0 Flare

Figure 2(a) displays the time variation of the *GOES* SXR flux in 1–8 and 0.5–4 Å channels within our studied interval. The temporal evolution of the X1.0 flare can readily be summarized by three phases: a preflare phase showing two distinct episodes of SXR flux enhancement with peaks "P1" and "P2" (indicated by the two dotted lines in Figure 2(a)), a precursor phase and the X1.0 flare. According to *GOES*, the onset of the impulsive phase of the X1.0 flare occurred at ≈01:53 UT which was characterized by rapid enhancement of flux in both the *GOES* X-ray channels and eruption of hot coronal channel. The flare reached its peak flux at ≈02:02 UT, which was followed by a gradual phase when SXR flux in both *GOES* channels decreased slowly.

During the first preflare event (P1), a complex structure, situated near the northern leg of the hot coronal channel (shown inside the boxes in Figures 2(b)–(d)) brightened up which could be observed in both high and low temperature AIA passband filter images. In Figures 2(b)–(d), we have plotted AIA 94 Å, 131 Å, and 304 Å images, respectively, during the peak of the preflare event P1. During the second preflare event (P2), localized intensified brightness was observed from the trailing part of the AR (shown inside the white boxes in Figures 2(e)–(g)). AIA 94 Å (Figure 2(e)) and AIA 131 Å (Figure 2(f)) images during the preflare event P2 suggest that energy release involving a compact loop system probably led to the enhancement in *GOES* SXR flux during the second preflare event. From the cotemporal AIA 304 Å image (Figure 2(g)), we observed two ribbon like brightenings which outlined the footpoints of the intensified loops. In Figures 2(h)–(j), we have plotted AIA 94 Å, 131 Å, and 304 Å images, respectively, during the precursor phase of the flare when the activation of the hot channel began and it underwent a slow rise phase. The subsequent eruption of the hot channel was clearly identified in AIA 94 and 131 Å images (indicated by white arrows in Figures 2(k) and (l)).

In Figure 3, we plot temporal evolution of AIA (E)UV intensities (Figure 3(a)) and *RHESSI* X-ray counts (Figure 3(b)). For comparison, we have overplotted *GOES* SXR flux variation in both 1–8 and 0.5–4 Å channels in Figure 3(b). Comparison of *GOES*, *RHESSI*, and AIA light curves clearly indicates that the preflare event P1 was very prominent in *RHESSI* 3–6 keV and 6–12 keV channels while only the 304 Å channel among other AIA channels displayed a small peak at the time of preflare event P1. *RHESSI* did not observe during ≈01:13 UT–01:45 UT, which included the preflare event P2. A small increment during this period was observed in the AIA 94 and 304 Å light curves. Interestingly, the preflare event P2 was more prominent in the high energy *GOES* channel of 0.5–4 Å than the lower energy channel of 1–8 Å. AIA light curves show a general agreement with *RHESSI* and *GOES* time profiles during the main phase of the X1.0 flare. *RHESSI* time profiles reveal a sudden rise of HXR flux at ≈01:53 UT implying the onset of the impulsive phase of the X1.0 flare. The impulsive build up phase of the X1.0 flare was associated with a very interesting phenomena in the *RHESSI* high energy channels of ≳25 keV in the form of multiple short-lived spikes during ≈01:55 UT–02:00 UT (see the green, yellow, and violet lines in Figure 3(b)). Here we note that, counts in the high energy channels of *RHESSI* (≳50 keV) underwent a sudden fall after ≈02:00 UT while counts in the low energy channels (≲50 keV) displayed gradual decay (the decay rate was faster for the 25–50 keV channel than the other channels).

3.2.1. Preflare Phase

The two SXR preflare events (P1 and P2) were separated by a time span of ≈30 minutes (Figure 2(a) and Section 3.1). In order to understand the location and structures of preflare events, we provide a few representative AIA 94 Å images of the activity site in Figure 4. From these images we find that a small region situated at the north of the AR underwent a

[3] http://sunbase.nict.go.jp/solar/denpa/index.html
[4] www.helioviewer.org
[5] http://www.lmsal.com/solarsoft/latest_events_archive.html
[6] https://www.solarmonitor.org/index.php?date=20131028&region=11875

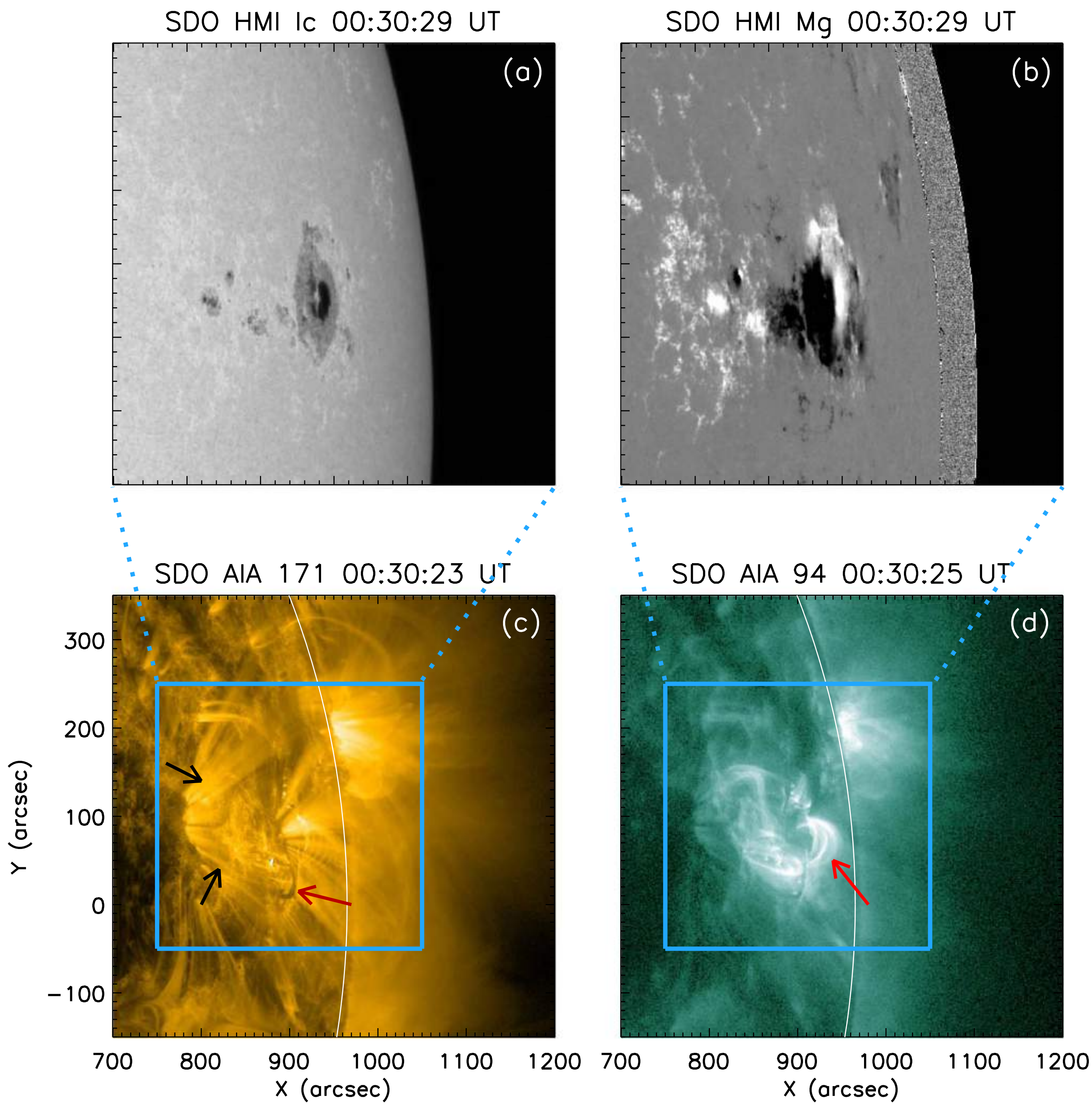

Figure 1. Panel (a): HMI white light image of the active region NOAA 11875 prior to the eruptive flare. Panel (b): cotemporal HMI LOS magnetogram of AR11875. Panels (c)–(d): AIA EUV images of the AR in 171 Å and 94 Å, respectively. FOV of panels (a) and (b) is indicated by the sky colored boxes in panels (c) and (d). The black arrows in panel (c) indicate few open coronal lines. The brown arrow indicates the filament during the preflare phase. The red arrow in panel (d) indicates the hot coronal loops near the filament.

complex evolution during the preflare event P1 (zoomed in images of the region are shown in the insets in Figures 4(b) and (c)). Strong *RHESSI* 6–12 keV sources were observed to reside at that region during the preflare event P1 (cotemporal *RHESSI* 6–12 keV contours are plotted in Figure 4(a) and in the inset in Figures 4(c)). During ≈01:28 UT to ≈01:40 UT, we observed loop brightening from a nearby eastern region within the AR, which is indicated by the arrows in Figures 4(d) and (e). Comparison of *GOES* time profiles (Figure 2(a)) and AIA images (Figure 4) confirms the association of SXR preflare enhancements with localized energy release events within the AR. In Figure 4(f), we plot an AIA 94 Å image of the AR where the erupting hot channel can be identified clearly (indicated by the white arrow). For a comparison, we have also marked the locations of the two preflare events in Figure 4(f) from which it becomes clear that the two preflare events prior

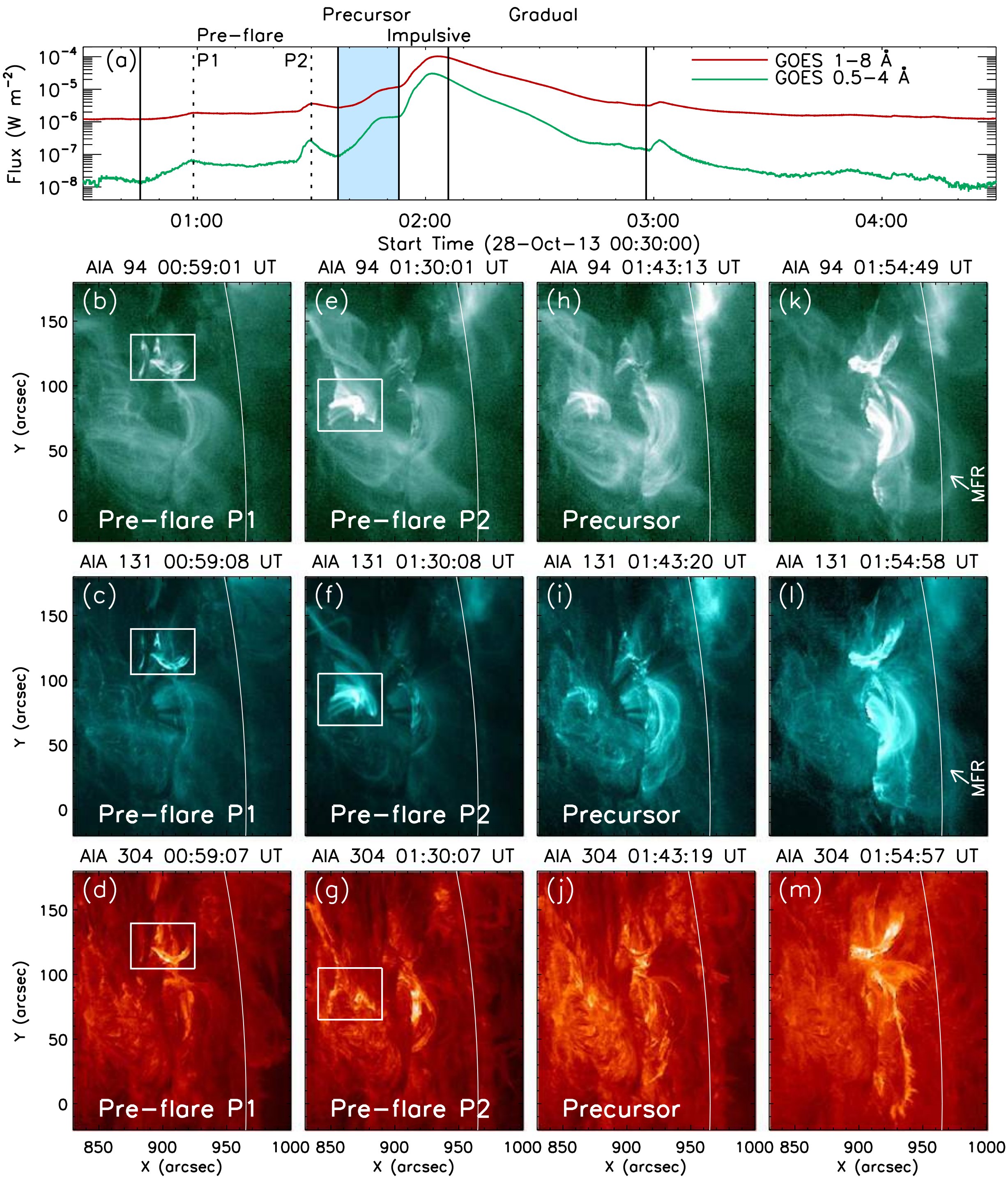

Figure 2. Panel (a): *GOES* SXR flux variation in 1–8 Å (red curve) and 0.5–4 Å (green curve) channels on 2013 October 28 from 00:30 UT to 04:30 UT that includes different phases prior to and during the X1.0 flare. The preflare phase was characterized by two episodes of SXR flux enhancements with peaks "P1" and "P2," which are indicated by the dashed lines. The sky colored shaded area indicates the precursor phase when the activation of the hot channel (i.e., flux rope) began and it underwent a slow rise phase. Panels (b)–(m): AIA EUV images of the active region NOAA 11875 in 94 Å (panels (b), (e), (h), (k)), 131 Å (panels (c), (f), (i), (l)), and 304 Å (panels (d), (g), (j), (m)). These representative images show various phases of the X1.0 flare: two preflare peaks, P1 and P2 (panels (b)–(d) and (e)–(g), respectively); precursor phase (panels (h)–(j)), and eruption of the hot channel during the impulsive phase of the X1.0 flare (panels (k)–(m)). The white boxes in panels (b)–(d) indicate preflare activity during P1 from a complex localized region adjacent to the northern leg of the hot channel. The white boxes in panels (e)–(g) indicate preflare activity during P2 from the trailing part of the AR. The white arrows in panels (k) and (l) indicate the erupting flux rope. The video starts at 2013 October 28 00:30 UT and ends the same day at 04:30 UT. The video duration is 44 s.

(An animation of this figure is available.)

to the X1.0 flare recorded by *GOES* occurred in the same AR but from two different locations. It is worth mentioning that, while the location of preflare event P2 displayed activity only during P2, the location of preflare event P1 was associated with continuous small-scale activity throughout the preflare phase, the precursor phase, and even during the impulsive phase of the X1.0 flare.

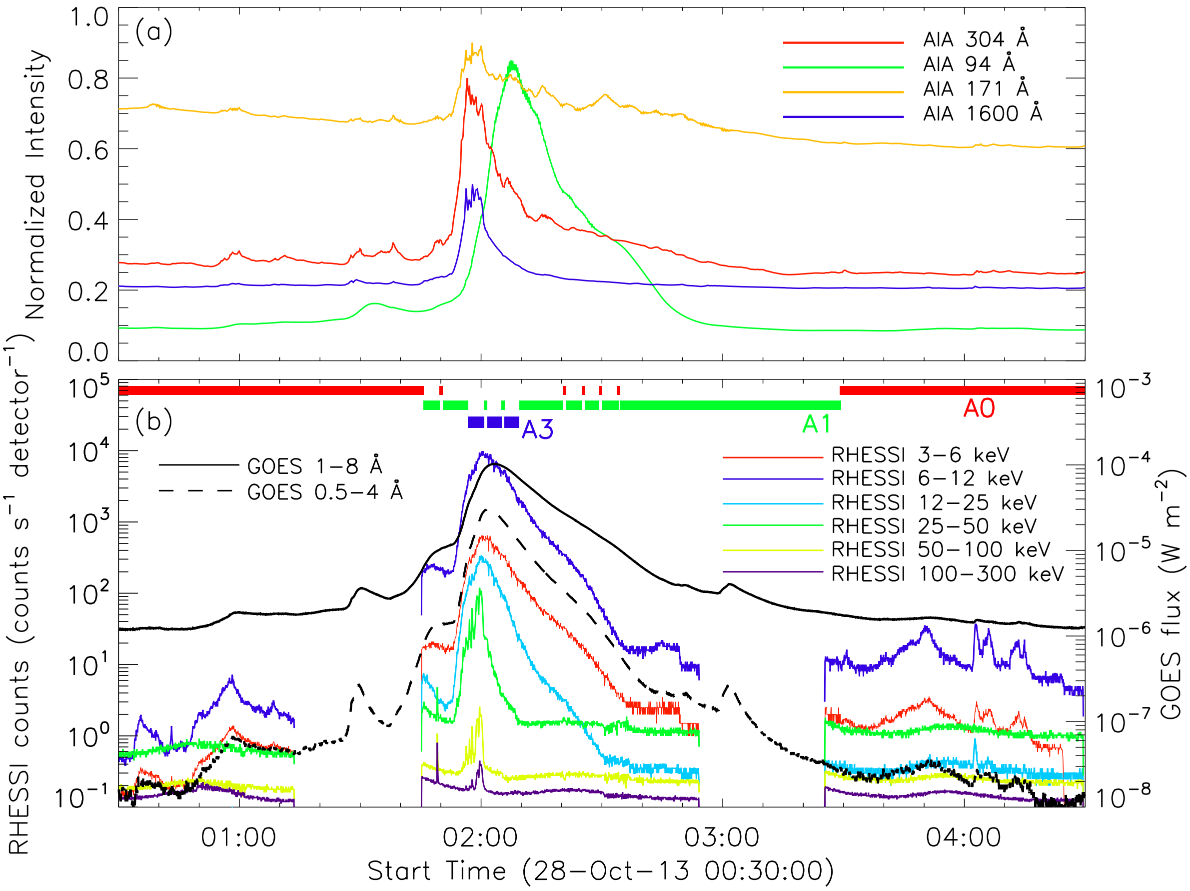

Figure 3. Panel (a): AIA light curves on 2013 October 28 during 00:30–04:30 UT normalized by the corresponding peak fluxes. For clear visualization, AIA light curves have been further normalized by 0.8, 0.85, 0.9, and 0.5 for 304 Å, 94 Å, 171 Å, and 1600 Å, respectively. Panel (b): temporal evolution of *RHESSI* and *GOES* X-ray fluxes in the same interval as in panel (a). *RHESSI* did not observe during ≈01:14 UT to ≈01:45 UT and ≈02:54 UT to ≈03:25 UT. *RHESSI* fluxes have been normalized by factors of $\frac{1}{2}$, $\frac{1}{20}$, $\frac{1}{10}$, $\frac{1}{100}$, and $\frac{1}{500}$ for 3–6 keV, 12–25 keV, 25–50 keV, 50–100 keV, and 100–300 keV, respectively. The red, green, and blue bars at the top of panel (b) indicate *RHESSI* attenuator states A0, A1, and A3, respectively.

3.2.2. Precursor Phase

The X1.0 flare was associated with a distinct precursor phase during ≈01:37 UT to ≈01:53 UT when the hot channel underwent activation and exhibited a slow but steady expansion. During this phase, *GOES* SXR flux displayed a gradual rise in both the 1–8 and 0.5–4 Å channels (Figure 2(a)). EUV images reveal that the core field region, containing the activated hot channel, became very bright compared to the rest of the AR during this phase (Figures 2(h)–(j)). The slowly accelerating hot channel was identified in the AIA images of hot 94 Å (Figures 5(b)–(d)) and 131 Å (Figures 6(a)–(d)) channels. We found X-ray emission up to ≈50 keV from the hot core field region during this phase while the slowly rising hot channel steadily moved to larger heights (Figures 5(c)–(d) and 6(b)–(d)). We observed consistent activities from the location of preflare event P1 that included localized brightening and plasma ejection throughout the precursor phase (indicated by the yellow arrows in Figures 5(a), (c), and (d)). Notably, a strong 50–100 keV HXR source was observed from the location of P1 during the late precursor phase (Figure 5(d)).

To further investigate the altitude evolution of the hot channel, we specify a narrow slit along the white line $\overline{S_1S_2}$ in Figure 7(a) and plot its time evolution between ≈01:35 UT and 02:00 UT in Figure 7(b). The time–slice diagram reveals that the hot channel experienced a very gradual rise with a speed of ≈14 km s^{-1} up to ≈01:53 UT. Also we note that, between ≈01:52 UT and 01:54 UT (the interval is marked by the two blue dotted lines in Figure 7(b)), the hot channel was subjected to a rapid acceleration (≈1.41 km s^{-2}) as the flare moved into the impulsive phase.

3.2.3. The X1.0 Flare and Eruption of the Hot Channel

The impulsive phase of the X1.0 flare started at ≈01:53 UT (Figure 2(a)). During this interval, the slowly rising hot channel entered into the eruptive phase (Figure 7(b)). As the hot channel started erupting, formation of the post-flare arcade began underneath it. The cotemporal *RHESSI* images reveal intense HXR emission up to ≈50 keV energies from the apex of the post-flare arcade (Figures 5(e)–(h)). During the peak phase of the X1.0 flare, along with the coronal HXR sources, strong HXR sources up to ≈100 keV energies were observed from the footpoint of the arcades (Figures 5(f)–(h)). As the hot channel moved into higher coronal heights, it lost its brightness and slowly became indistinct in direct images after ≈01:56 UT (the erupting hot channel is indicated by red arrows in Figures 5(e)–(f). In Figures 6(e)–(f), we plot running difference AIA 131 Å images where we indicate the

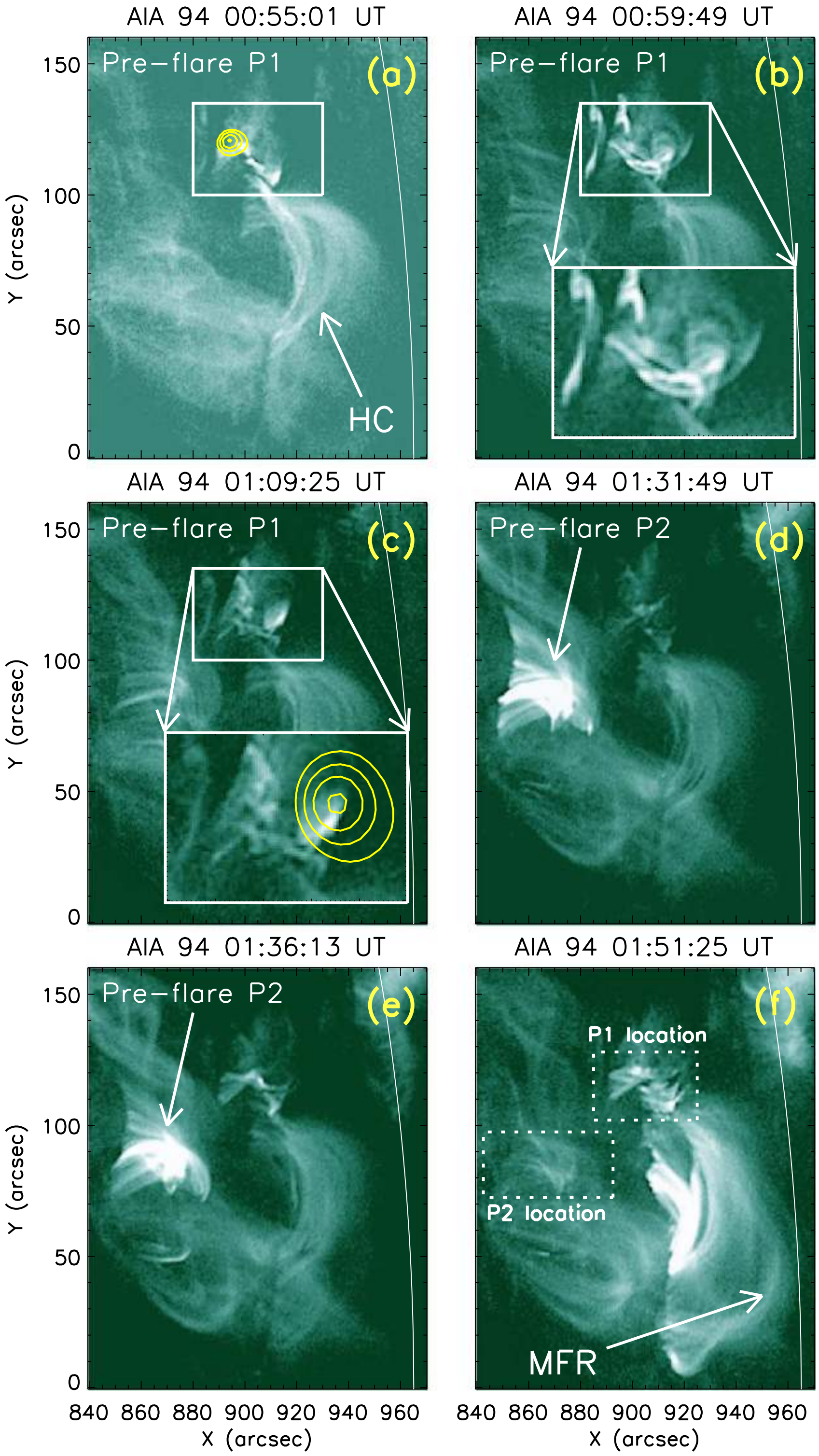

Figure 4. Panels (a)–(c): AIA 94 Å images showing evolution during the preflare event P1. During preflare event P1, activities were observed from a complex structure situated at the northern end of the hot channel, which is outlined by the white boxes. Insets in panels (b) and (c) show zoomed in images of the region enclosed within the boxes. *RHESSI* observation was available during preflare event P1. In panel (a) and the inset in panel (c), we plot cotemporal *RHESSI* 6–12 keV contours. Contour levels are 35%, 50%, 70%, and 95% of the corresponding peak flux. Panels (d)–(e): AIA 94 Å images during the preflare event P2. Activities during P2 were observed in the form of loop brightening, which is indicated by the white arrows. Panel (f): AIA 94 Å at ≈01:51 UT when flux rope eruption was very prominently observed in hot AIA passband filters. The eruption of the magnetic flux rope (MFR) is indicated by the arrow in panel (f). For comparison, the locations of preflare activities during the P1 and P2 are shown by the white boxes with dotted lines in this panel.

hot channel by a pink arrow and a dashed pink line, respectively. The flare moved into the gradual phase after ≈02:02 UT. During this phase, the post-flare arcade slowly increased in height and continued to emit hot, intense diffused emission (Figures 5(i)–(l)). *RHESSI* sources of energies up to 25 keV were observed from the top of the post-flare arcade (Figure 5(j)).

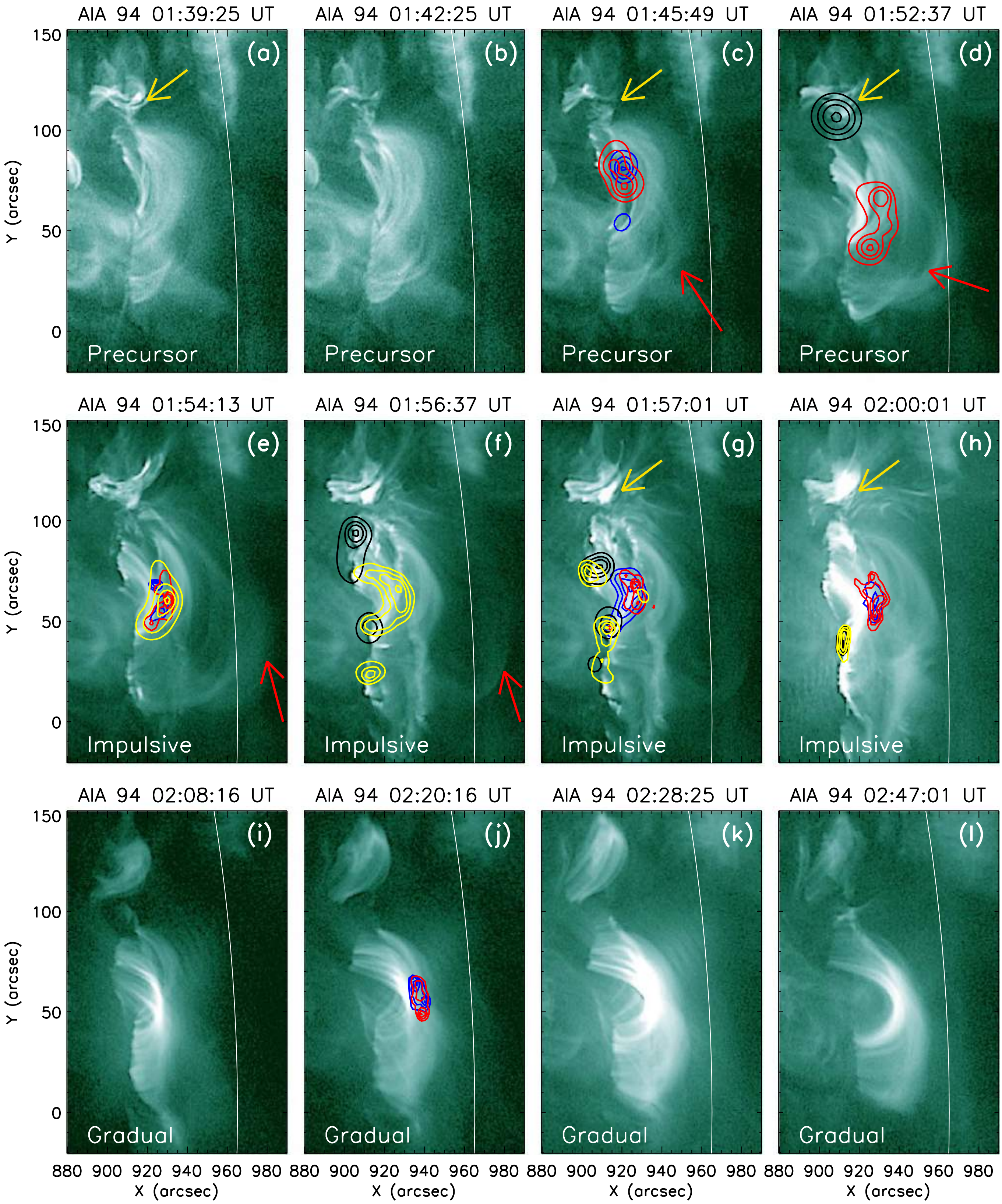

Figure 5. Representative AIA 94 Å images showing various evolutionary phases (precursor, impulsive, and gradual) during the X1.0 flare. The red arrows in panels (c)–(d) indicate the slow rise of the hot channel during the precursor phase, which erupted during the subsequent impulsive phase of the X1.0 flare (indicated by the red arrows in panels (e) and (f)). From the location of preflare events "P1" (see Figure 4(f)), we observed localized brightening and plasma ejection throughout the precursor and impulsive phase, which is indicated by yellow arrows in panels (a), (c), (d), (g), and (h). Cotemporal *RHESSI* contours of 6–12 keV (blue), 12–25 keV (red), 25–50 keV (yellow), and 50–100 keV (black) energy bands are overplotted in selected panels. The contour levels are 30%, 50%, 70%, and 95% of the corresponding peak fluxes.

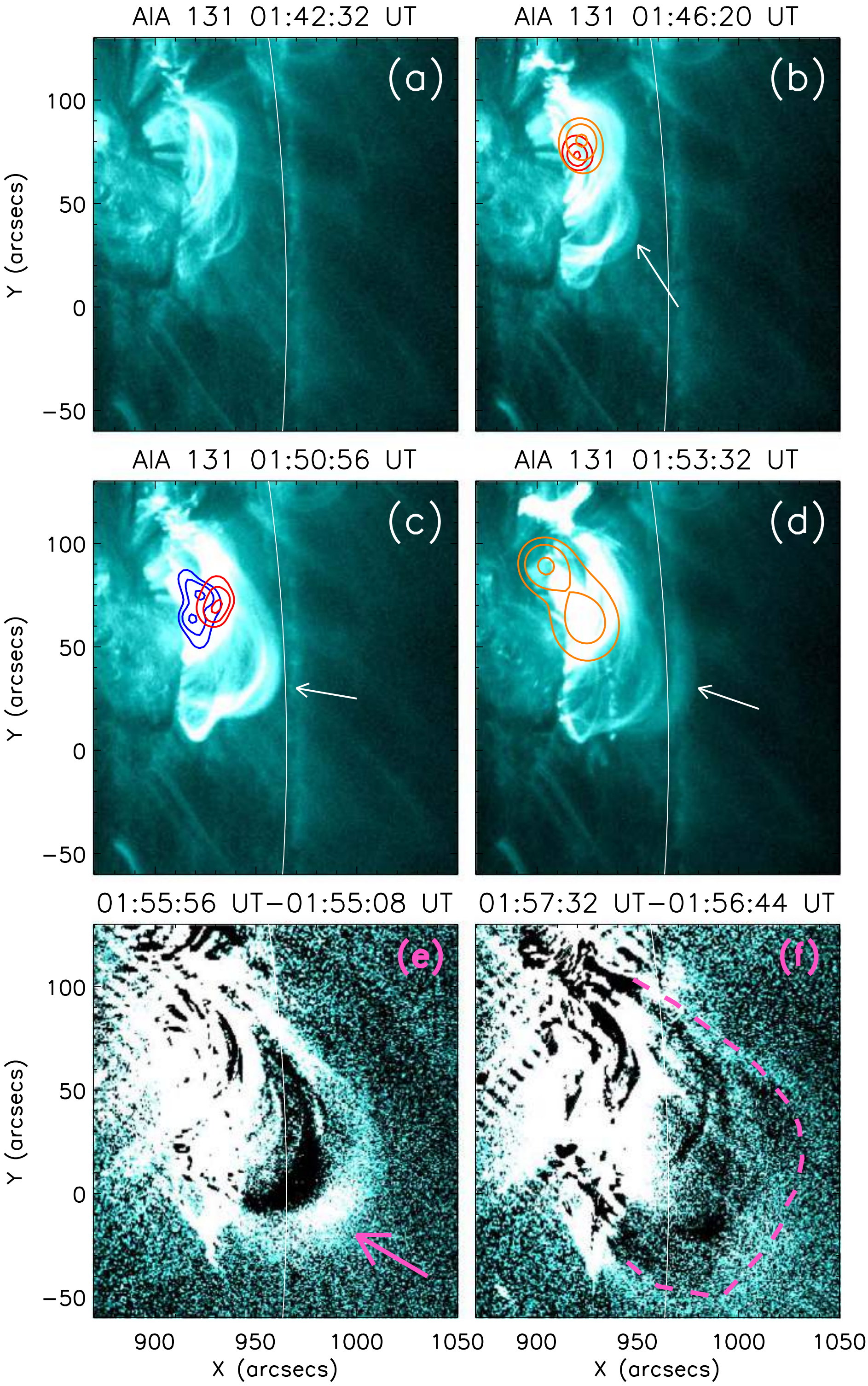

Figure 6. Representative AIA 131 Å direct (panels (a)–(d)) and running difference (panels (e)–(f)) images showing the hot channel eruption during the X1.0 flare. White arrows in panels (b)–(d) and the pink arrow in panel (e) indicate the erupting hot channel. In panel (f), the erupting hot channel has been outlined by a pink dashed curve. Cotemporal *RHESSI* contours of 6–12 keV (blue), 12–25 keV (red), and 25–50 keV (orange) energy bands are overplotted in panels (b)–(d). Contour levels are 50%, 70%, and 95% of the corresponding peak fluxes.

The time–slice diagram (Figure 7(b)) suggests that after undergoing a slow expansion during the precursor phase, the hot channel exhibited fast eruption with a linear speed of $\approx 183\ \mathrm{km\ s^{-1}}$ during the impulsive phase. The eruption of the hot channel resulted in a halo CME which was captured in the LASCO C2 and C3 coronagraph observations (Figure 8). The CME was first detected by LASCO C2 at 02:24 UT[7] when the

[7] https://cdaw.gsfc.nasa.gov/CME_list/UNIVERSAL/2013_10/yht/20131028.022405.w360h.v0695.p296g.yht

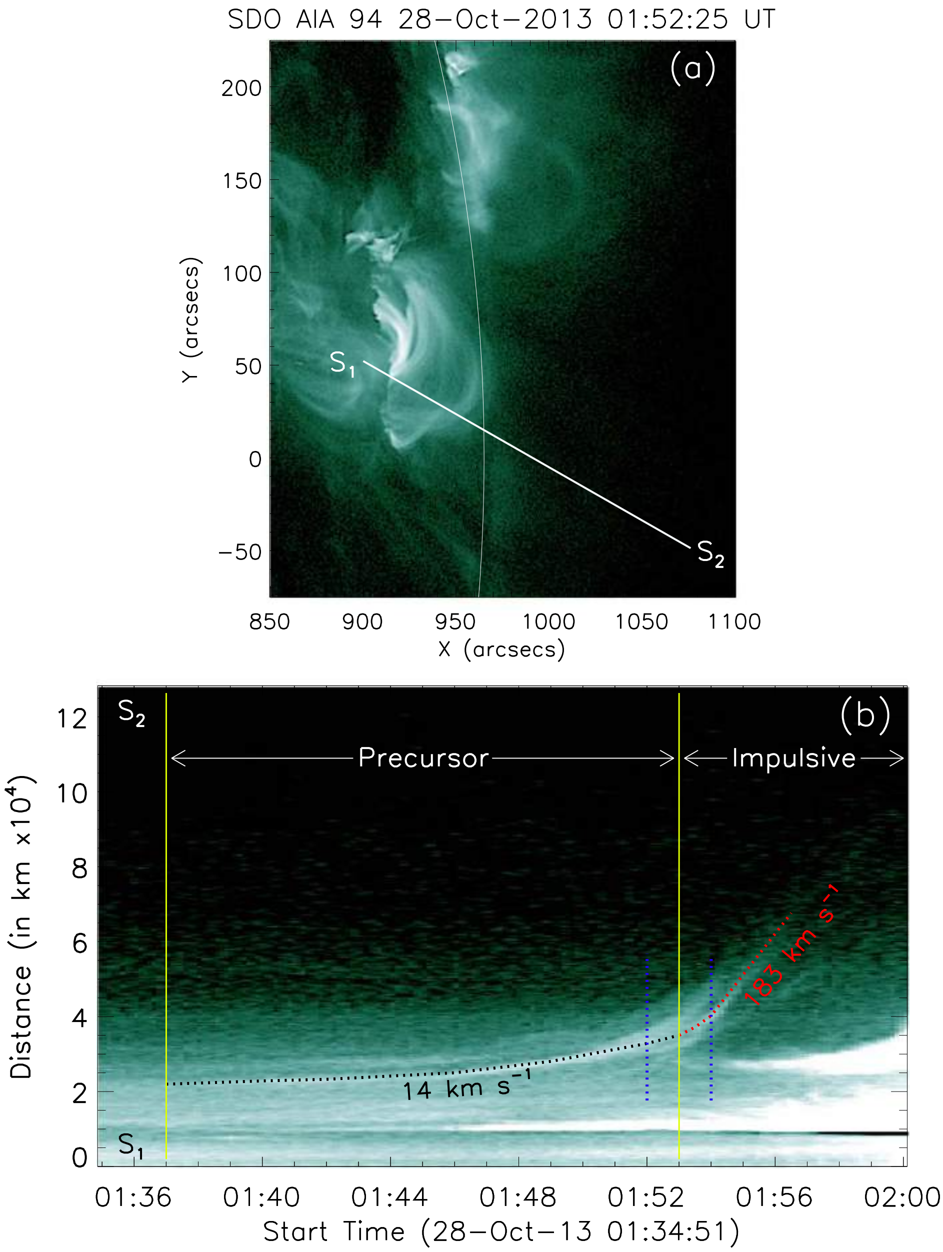

Figure 7. Panel (a): an AIA 94 Å image of AR11875 during the precursor phase showing a straight line along which the time–slice diagram was constructed. Panel (b): time–slice diagram showing two phase acceleration of the erupting hot channel along the slit indicated in panel (a). "S_1" and "S_2" in panels (a) and (b) indicate the orientation of the slit in the time–slice diagram. The hot channel was found to be slowly elevating during the precursor phase of the flare (≈01:37 UT–01:53 UT) with a linear speed of ≈14 km s^{-1}. Afterwards, the flare entered into the impulsive phase (see Figure 2(a)) during which the hot channel underwent eruption with a linear speed of ≈183 km s^{-1}. Notably, the hot channel was subjected to a transition phase during ≈01:52 UT–01:54 UT (indicated by the vertical blue dotted lines in panel (b)) when it moved continuously from the state of slow rise to eruptive expansion with a rapid acceleration of ≈1.41 km s^{-2}.

leading edge of the CME reached a coronal height of ≈3.82 $R_\odot$. LASCO C3 observed the CME until 07:30 UT at ≈22.91 $R_\odot$. Within the field of view of LASCO, the CME was propagating toward the position angle 296° with a linear speed of ≈695 km s^{-1} and a slow deceleration of 12.1 m s^{-2}.

3.3. RHESSI *Spectroscopy*

To study the HXR spectral evolution of the X1.0 flare during the impulsive phase, we conducted *RHESSI* spectroscopy. For this purpose, we used energy bins of $\frac{1}{3}$ keV from 6 to 15 keV, 1 keV from 15 to 100 keV, and 5 keV from 100 to 300 keV energies. At the start of the impulsive phase of the X1.0 flare, the attenuator of *RHESSI* was set at A1 (i.e., thin shutter; Figure 3(b)). At ≈01:56 UT, the attenuator state was changed to A3 (i.e., both thin and thick shutters) and remained so until ≈02:09 UT except for two short intervals of ∼1 minute (at ≈02:00 UT and ≈02:05 UT) when the attenuator state was changed to A1. After ≈02:09 UT, the attenuator state was changed to A1 as the flare moved into the gradual phase. The time intervals for spectral analysis were chosen to be 20 s. Notably, *RHESSI* measurements during the impulsive phase of the X1.0 flare were contaminated by two periods of low energy radiation-belt particle events. To restrict the spectroscopic

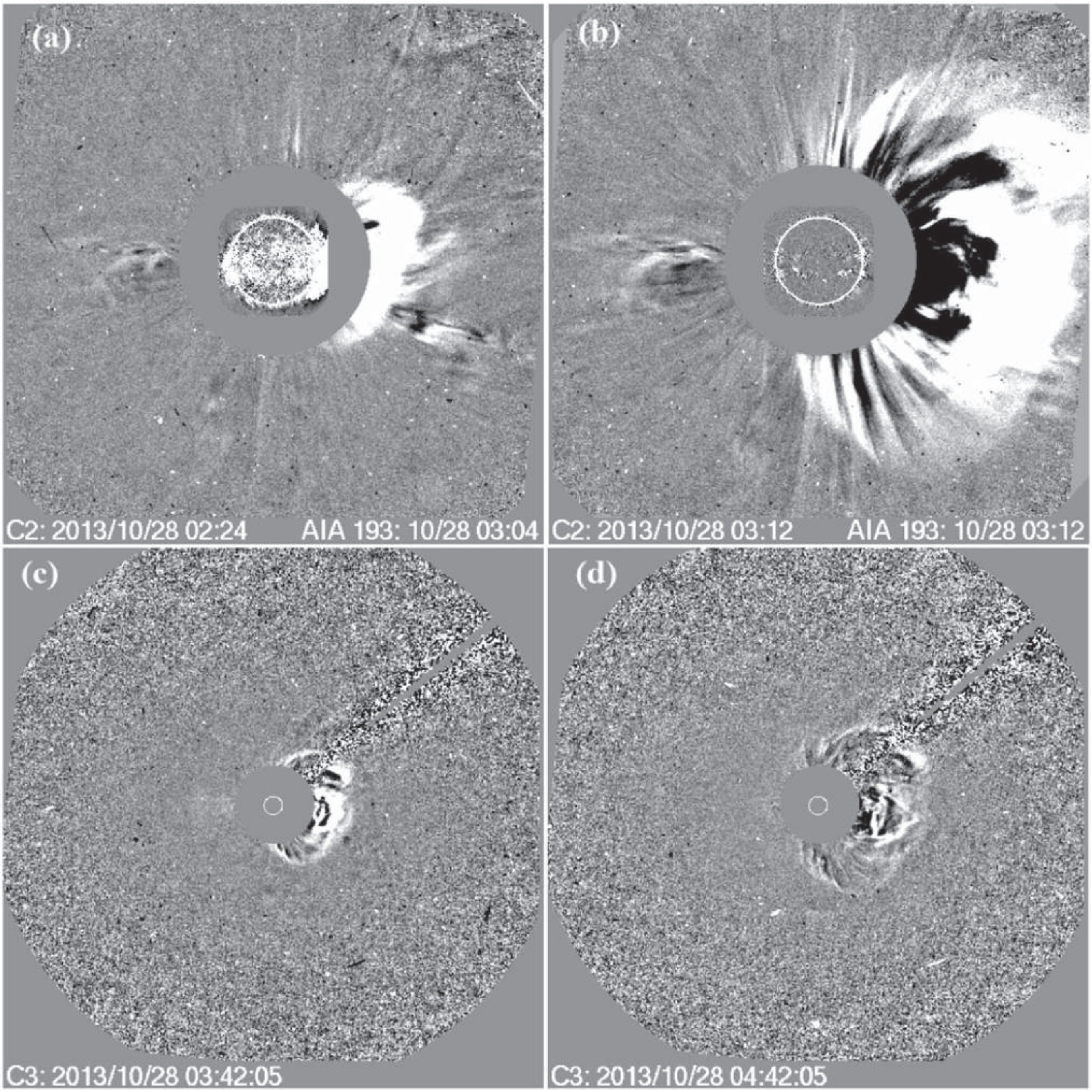

Figure 8. Running difference images obtained from LASCO C2 (panels (a) and (b)) and C3 (panels (c) and (d)) showing the propagation of the halo CME originated during the X1.0 flare from AR11875. The linear speed of the CME calculated within the LASCO field of view is 695 km s^{-1}.

measurements from contamination due to the particle events, we confined our spectroscopic analysis between 01:57 and 02:01 UT. Spectral fits were obtained using a forward-fitting method implemented in the idl-based Object Spectral Executive code (OSPEX; Schwartz et al. 2002). To create the spectrum, we used the combined *RHESSI* front detectors 1–9 excluding 2 and 7 (see Smith et al. 2002; Holman et al. 2011). Two fitting models were used: line emission from an isothermal plasma and thick-target bremsstrahlung from nonthermal electrons interacting with the chromosphere (Holman et al. 2003). From these fits, we derived the temperature (T) and emission measure (EM) of the hot flaring plasma, as well as the nonthermal electron spectral index (δ) for the nonthermal component and break energy (E_B) between the thermal and the nonthermal components.

In Figure 9, we show few spatially integrated, background-subtracted *RHESSI* spectra along with their respective fits and residuals for three selected intervals. We find that both temperature and emission measure increased during the impulsive phase and reached $\approx$28 MK and $\approx 5 \times 10^{48}$ cm^{-3}, respectively, at the peak phase. At this time, as expected, with the evolution of the flare during the impulsive phase, the low

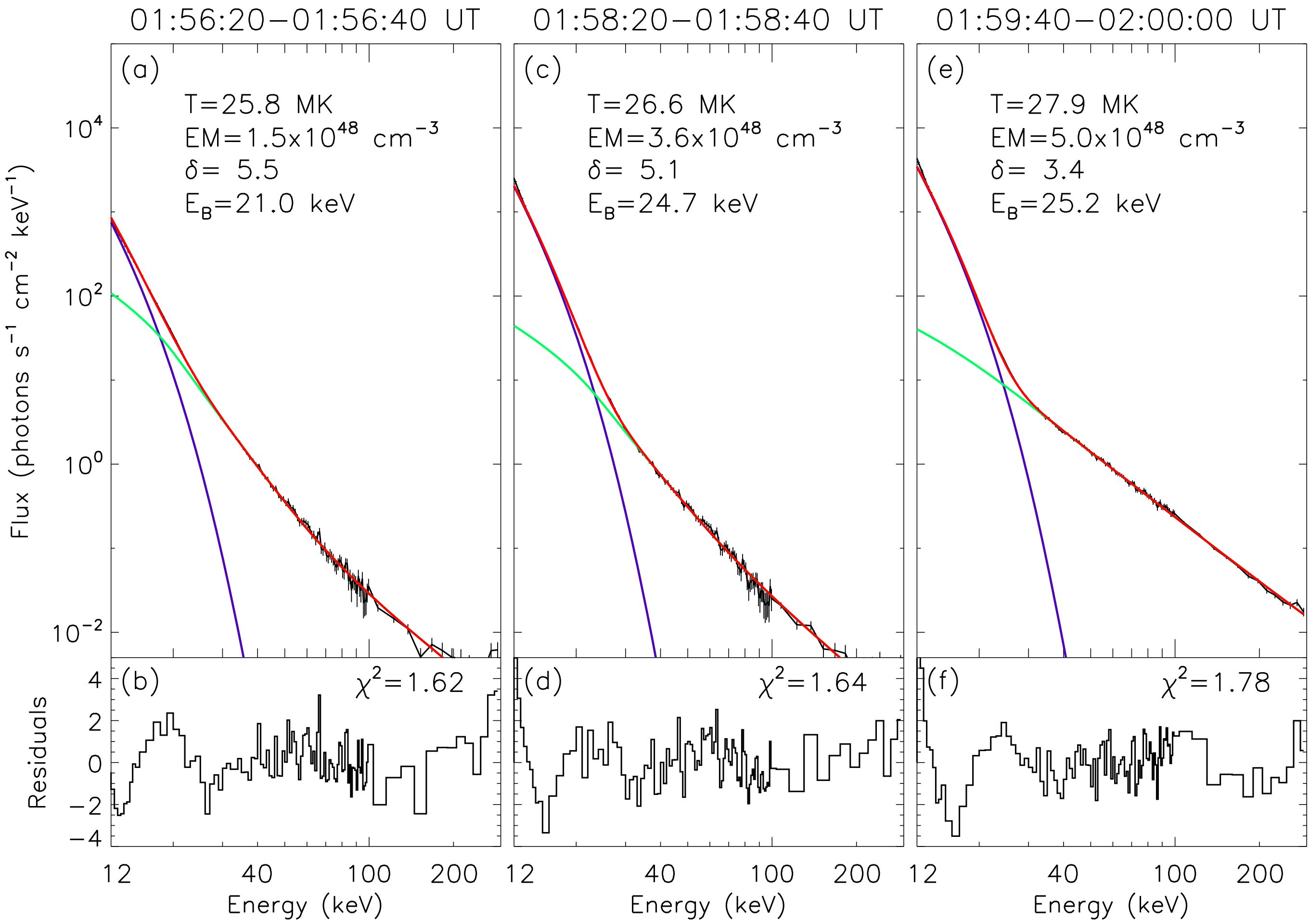

Figure 9. Representative *RHESSI* X-ray spectra during the impulsive phase of the X1.0 flare along with their respective residuals. These spectra were fitted with a combination of an isothermal component (blue line) and a thick-target bremsstrahlung model (green line). The red lines indicate the sum of the two components. The energy range chosen for fitting is [12–295] keV. The notations used in different panels are as follows. T: temperature obtained from the isothermal component; EM: emission measure; δ: power-law index for the nonthermal fitting; E_B: break energy separating thermal energy from nonthermal energy; χ^2: goodness of the fitting.

energy cutoff (i.e., break energy E_B) increased progressively up to ≈25 keV. During the impulsive rise and peak of hard X-ray flux (Figures 9(c) and (e)), the hardness of the nonthermal component increased highly with spectral index (δ) ≈ 3.4.

3.4. Dynamic Radio Spectrum

The impulsive phase of the X1.0 flare exhibited a spectacular display of different types of radio structures in the dynamic spectra (Figure 10). A series of type III bursts were recorded by HiRAS during ≈01:37 UT–01:55 UT followed by a split-band type II burst. Because the AR was situated at the limb, it is likely that the observed split-band of type II was the harmonic as the fundamental part of type II bursts that originated near solar limbs get severely attenuated (Gopalswamy 2013). A brief brightening was recorded at ≈01:58 UT within frequency range ≈210–400 MHz. Observation within the frequency range ≈200–210 MHz was rejected throughout the interval by HiRAS. The type II burst was very clear between ≈02:00 UT and 02:04 UT within the frequency range ≈75–180 MHz. However, from the apparent drift of the type II bands and dynamics of the erupting hot channel, it can be understood that the brief brightening within frequency a range of ≈210–400 MHz was an early extension of the type II. The type II burst was followed by a faint dynamic type IV signatures between ≈02:05 UT and 02:14 UT within the frequency range ≈70–180 MHz.

4. Discussion

In this article, we present a multiwavelength analysis of the evolutionary phases of an X1.0 flare associated with the activation and eruption of a hot channel from active region NOAA 11875. On the day of reported activity, i.e., 2013 October 28, the AR was situated near the western limb of the Sun at heliographic coordinates of ∼N07W66. We provide a detailed investigation of the activities during the preflare phase, a relatively less studied and ill-understood aspect of the overall flare evolution. The activation and steady, slow rise of the preexisting hot channel accompanied the precursor phase of the X-class flare while its eruption proceeded with the impulsive and peak phases. We have summarized different evolutionary phases of the X1.0 flare in Table 1.

Our study distinctively reveals the manifestation of a prolonged preflare phase of ≈52 minute duration (≈00:45 UT to ≈01:37 UT; Figure 2). Further, the preflare phase is characterized by two distinct SXR peaks, P1 and P2, occurring ≈38 minutes and ≈7 minutes, respectively, prior to the onset of the flux rope activation. Comparison of *GOES* time profiles

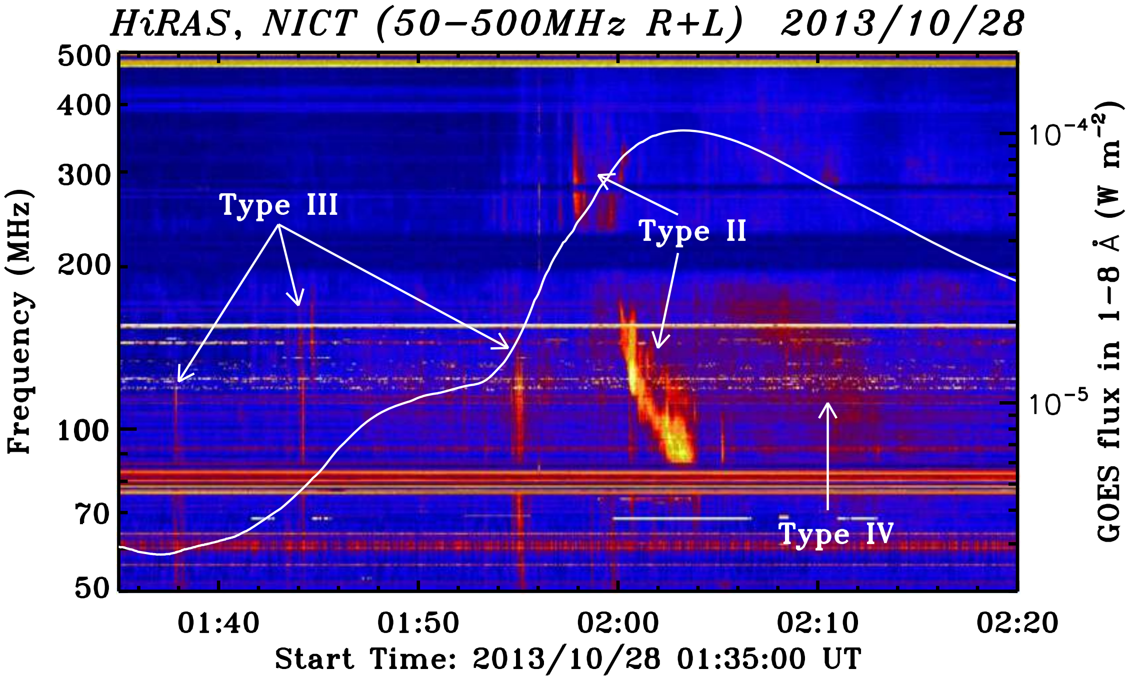

Figure 10. Dynamic radio spectrum recorded by the HiRAS spectrograph on 2013 October 28 from 01:35 UT to 02:20 UT within the frequency range of 50–500 MHz, showing many discrete type III bursts between ≈01:37 UT and 01:55 UT, a split-band harmonic of type II burst between ≈01:58 UT and 02:04 UT and a faint type IV spectra during ≈02:05 UT–02:14 UT. For reference, we have overplotted *GOES* SXR flux variation in the 1–8 Å range by the white curve.

Table 1
Summary of the Evolutionary Phases of the Eruptive X1.0 Flare

Sr. No.	Phase	Interval	Remarks
1	Preflare	00:45 UT–01:37 UT	Two peaks were observed in the *GOES* SXR flux at ≈00:59 UT ("P1") and ≈01:30 UT ("P2").
2	Precursor	01:37 UT–01:53 UT	Activation of the hot coronal channel began and it underwent a slow rise.
3	Impulsive	01:53 UT–02:02 UT	The eruption of the hot channel experienced rapid acceleration; multiple X-ray sources were observed from footpoint and looptop locations.
4	Gradual	02:02 UT–02:58 UT	Dense post-flare arcade was formed.

with AIA EUV images confirmed that both the preflare events occurred from different locations within the AR (Figure 2). While the location of the first preflare event (i.e., P1) was adjacent to the hot channel, the location of the second preflare event (i.e., P2) was a distant one. Notably, while the location of P2 was associated with EUV brightening during the preflare event P2 only, the location of P1 experienced continuous EUV brightening throughout the preflare phase and even during the later precursor and impulsive phases of the flare. Statistical studies, conducted with the *Yohkoh*-SXT images, of the preflare locations with respect to the main flare sites by Fárník et al. (1996) and Fárník & Savy (1998) revealed an abundance of "adjacent" cases while the "distant" preflare sources were found to be rather uncommon. However, while discerning the locations of preflare localized emissions over the large-scale main flare brightenings, we should also consider that the *SDO*/AIA images have much better temporal and spatial resolutions compared to the *Yohkoh* images.

Preflare activities prior to a flare are considered to be important in order to understand the physical conditions that lead to flares and associated eruptions (Fárník et al. 1996, 2003; Fárník & Savy 1998; Chifor et al. 2006, 2007; Joshi et al. 2011, 2013). Contemporary studies, dealing with the analysis of X-ray images and spectra during the mild preflare X-ray emission (Joshi et al. 2013; Hernandez-Perez et al. 2019), suggest the preflare phase is associated with the events of small-scale magnetic reconnection that can potentially destabilize the flux ropes as described in different models of solar eruptions (i.e., tether-cutting and breakout reconnection models). Our analysis suggests that the location of the preflare event "P1" was associated with consistent EUV brightening along with thermal X-ray sources (Figure 4) suggesting continuous small-scale reconnection events in a localized region that resulted in the eruption of the hot channel (i.e., the preexisting flux rope). Our results can be interpreted in the light of multiple preflare events prior to a major flare of X-class analyzed by Joshi et al. (2013). Their work revealed that the activities during the preeruption phase were characterized by three localized episodes of energy release occurring in the vicinity of a filament that produced intense heating along with nonthermal emission. Based on these observations, Joshi et al. (2013) concluded that localized magnetic reconnections beneath the flux rope in the preeruption phase played an important role in destabilizing the active region filament through the tether-cutting process. From the spatial and temporal characteristics of preflare activities occurring at the location P1, we conclude that continuous, small-scale reconnection events in the vicinity of the northern leg of the hot channel would result in restructuring of the magnetic field configuration in a localized region besides reducing the magnetic flux near one of the footpoints of the MFR. This process would progressively lead to establishing the conditions favorable for the destabilization of the MFR and subsequent large-scale eruption.

An important aspect of present observations lies in the detection of a stable, hot EUV channel that preexisted in the active region corona at least ≈67 minutes before its activation during the precursor phase (Figure 1(d)). Contemporary studies have established that hot coronal channels are one of the observational pieces of evidence of MFRs (see, e.g., Chen 2011; Cheng et al. 2014a; Song et al. 2015b; Joshi et al. 2017, 2018; Mitra et al. 2018). Notably, observations showing prior formation of flux ropes that remain stable during the preeruption phase are still uncommon with availability of only a few such reported incidences (Cheng et al. 2014a; Song et al. 2015b). The exact topology and formation process of MFRs are still unclear and debatable. According to the mechanism proposed by van Ballegooijen & Martens (1989), flux cancellation through the photospheric converging and shearing motions leads to the formation of MFR, which has been subsequently supported by the numerical studies by Amari et al. (1999, 2000) where the twisted flux rope remains stable for a period before erupting. Many studies have also recommended the in situ formation of MFRs in the corona by magnetic reconnection, i.e., the MFR builds up with the initiation of the flare itself (Cheng et al. 2011; Song et al. 2014a; Chintzoglou et al. 2015; Wang et al. 2017). Another class of model suggests that MFRs are generated in the convection zone of the Sun and then emerge into the solar atmosphere by buoyancy (Caligari et al. 1995; Fan 2001; Archontis et al. 2004; Martínez-Sykora et al. 2008). With the detection of a preexisting hot channel right from the beginning of the studied interval and subsequent occurrence of small-scale energy release processes at adjacent and remote locations, our observational results support the scenario of flux rope emergence from the convection zone. During the impulsive phase of the X1.0 flare, the hot channel became activated and erupted resulting in a halo CME (Figures 5, 6, and 8). With high proneness toward eruption and association with CMEs, hot channels are believed to be the earliest signatures of CMEs (Canfield et al. 1999; Pevtsov 2002; Gibson et al. 2004, 2006; Liu et al. 2007, 2010, 2018; Cheng et al. 2014b; Kumar et al. 2016; Joshi et al. 2017, 2018; Mitra et al. 2018; Hernandez-Perez et al. 2019); our observations are consistent with these earlier studies.

We would like to further emphasize on the early dynamical evolution of the hot channel, which is characterized by its slow yet steady rise with a speed of ≈14 km s^{-1}. This phase lasted for a period of 16 minutes during which the intensity of the flaring region increased gradually. The temporal association between the slow rise phase of the MFR and the precursor flare emission is of great significance to understanding the origin of CMEs (Zhang et al. 2001, 2004; Zhang & Dere 2006). The early slow rise phase essentially marks the CME initiation in the source active region which is found to be well correlated with the mild and consistent precursor phase emission, commonly observed as gradually rising SXR flux (Zhang & Dere 2006). It has been suggested that the precursor phase activities correspond to the dynamical formation of a current sheet underneath the MFR that subsequently reconnects to trigger the onset of the main phase of the eruptive flare (Zhou et al. 2016). Our analysis readily supports this scenario as the hot channel underwent an abrupt transition from the state of slow rise to the fast acceleration as a continuous process which precisely bifurcates the precursor and impulsive phase of the eruptive flare (see Figures 7(b) and 2(a)).

The early impulsive phase and the eruption of the flux rope was associated with strong HXR sources of energies up to ≈100 keV (Figure 5). We further emphasize the appearance of a very high energy HXR source at the adjacent preflare location (Figures 5(d), 4). Appearance of such high energy HXR sources from a preflare location is rather surprising. In addition, we note that HXR sources were primarily concentrated at the northern part of the AR, which is also the preflare location P1 (Figures 4(a), (c) and 5(c)–(d)) suggesting strong reconnection and restructuring of the magnetic field lines. This is supported by small-scale plasma ejection from this region (Figure 5).

During the late impulsive phase, which is accompanied with fast eruption of the flux rope, nonthermal high energy HXR sources (>50 keV) were observed from the footpoint location while lower energy X-ray sources ($\lesssim$25 keV) were observed from the apex of the post-flare arcade (Figure 5). Notably, 25–50 keV HXR sources, probably containing a mix of thermal and nonthermal emissions, were found from both looptop and footpoint locations (Figures 5(e)–(h)). High energy HXR footpoint sources can be interpreted in terms of a "thick-target bremsstrahlung" model (Brown 1971; Hudson 1972; Syrovatskii & Shmeleva 1972; Emslie 1983). According to this model, highly accelerated electrons from the site of magnetic reconnection in the corona are injected downward into the transition region and the chromospheric layers along the post-reconnection magnetic field lines with relativistic speed. The relativistic electrons collide with cool and dense chromospheric plasma and deposit their energy with the production of HXR footpoint sources (Korchak 1967a, 1967b; Cline et al. 1968; Moza et al. 1986; Brown et al. 2002; O'Flannagain et al. 2015; Reep et al. 2016). Two basic models of HXR flares–impulsive injection and continuous injection models differ on the timescale of electron acceleration. According to the impulsive injection model proposed by Takakura & Kai (1966), electrons are accelerated in multiple episodes of short timescales in magnetic traps (i.e., magnetic loops). In contrast, the continuous injection model suggests continuous acceleration of electrons in dense chromosphere (Kundu 1963; Acton 1968; Kane & Anderson 1970; Brown 1971). In the view of multiple spikes in HXR time profiles during the impulsive phase (Figure 3(b)) and multiple type III bursts observed during the build up phase of the X1.0 flare (Figure 10), our analysis suggests the occurrence of discrete events of particle acceleration during the impulsive phase. The overall distribution of low energy looptop and high energy footpoint X-ray sources, observed in our work, is in agreement with the CSHKP model of solar eruptive flares and also consistent with the general energy release scenario developed during the *RHESSI* era (Krucker et al. 2003; Veronig et al. 2006; Joshi et al. 2007, 2013).

During the impulsive phase of the X1.0 flare, the MFR underwent fast acceleration (≈1.41 km s^{-2}) with the enhancement of its eruption speed to ≈183 km s^{-1}. The brief but rapid acceleration phase of the flux rope is cotemporal with the onset time of multiple HXR bursts observed in the high energy channels ($\gtrsim$25 keV) of *RHESSI* (see Figures 7, 5, and 3(b)) and a series of type III radio bursts (Figure 10). Type III radio bursts are produced by near-relativistic electrons propagating along the open magnetic field lines in the corona, restructured by the magnetic reconnection (Bastian et al. 1998; Reid & Ratcliffe 2014; Chen et al. 2018a). The appearance of strong looptop and footpoint HXR sources during the impulsive phase implies rapid dissipation of magnetic energy in the current sheet as a result of an increase in the rate of magnetic reconnection (Sui & Holman 2003), which is also likely to be responsible for the fast acceleration of the flux rope. While studying full CME kinematics including the initiation and impulsive acceleration phase of two fast halo CMEs and the associated flares, Temmer et al. (2008) found a close synchronization between the CME acceleration profile and the flare energy release as indicated by the *RHESSI* HXR flux onsets. They interpreted their results in terms of a feedback relationship between CME dynamics and reconnection events in the current sheet beneath the CME. Similar results were reported by many subsequent studies (see, e.g., Zhang et al. 2012; Song et al. 2015a; Joshi et al. 2016).

5. Summary and Conclusions

We provide a comprehensive investigation of the unveiling and subsequent eruption of an MFR, which we observationally recognized in the form of an EUV hot channel. This quasi-static hot channel was observed from at least 67 minutes before its activation, evidencing the preexistence of the MFR in the corona much prior to the CME initiation. These observations readily support the idea that hot channel structures can be regarded as the earliest signatures of a CME in the source active region. Our work also focuses on the preflare activity and its role in the destabilization of a stable MFR. The prolonged preflare phase exhibited two distinct SXR peaks which are characterized by small-scale energy release processes within the confined regions. With respect to the preexisting MFR, one of the preflare events occurred at an "adjacent" location while the second one was a "remote" activity but within the active region. Importantly, the adjacent preflare event took place near one of the footpoints of the MFR. The activation of MFR occurred with the strong intensity enhancement at the adjacent preflare activity location at HXR energies besides EUV brightening. These observations imply toward the role of preflare magnetic reconnections in the destabilization of a stable MFR. The destabilization of an MFR can be characterized by a gradual rise in the *GOES* SXR flux during the precursor phase of a flare accompanied by slow elevation of the MFR. A current sheet is formed underneath the destabilized MFR that subsequently reconnects to trigger the onset of the "standard" flare. With the signatures of the initiation of large-scale magnetic reconnection triggered by the eruptive MFR, such as, high energy nonthermal HXR sources and multiple type III radio bursts, the MFR underwent a transition from slow to fast motions, which points toward a feedback relationship between the initial CME acceleration and strength of the large-scale magnetic reconnection.

The authors would like to thank the *SDO* and *RHESSI* teams for their open data policy. *SDO* and *RHESSI* are NASA's missions under the Living With a Star (LWS) and SMall EXplorer (SMEX) programs, respectively. The authors would also like to thank the NICT team for providing the HiRAS dynamic spectrum. The authors acknowledge the constructive comments and suggestions of the anonymous referee, which improved the presentation and scientific content of the article.

ORCID iDs

Prabir K. Mitra https://orcid.org/0000-0002-0341-7886
Bhuwan Joshi https://orcid.org/0000-0001-5042-2170

References

Acton, L. W. 1968, ApJ, 152, 305
Amari, T., Luciani, J. F., Mikic, Z., & Linker, J. 1999, ApJL, 518, L57
Amari, T., Luciani, J. F., Mikic, Z., & Linker, J. 2000, ApJL, 529, L49
Antiochos, S. K., Dahlburg, R. B., & Klimchuk, J. A. 1994, ApJL, 420, L41
Antiochos, S. K., DeVore, C. R., & Klimchuk, J. A. 1999, ApJ, 510, 485
Archontis, V., Moreno-Insertis, F., Galsgaard, K., Hood, A., & O'Shea, E. 2004, A&A, 426, 1047
Aurass, H., Mann, G., Zlobec, P., & Karlický, M. 2011, ApJ, 730, 57
Bastian, T. S., Benz, A. O., & Gary, D. E. 1998, ARA&A, 36, 131
Benz, A. O. 2017, LRSP, 14, 2
Brown, J. C. 1971, SoPh, 18, 489
Brown, J. C., Aschwanden, M. J., & Kontar, E. P. 2002, SoPh, 210, 373
Brueckner, G. E., Howard, R. A., Koomen, M. J., et al. 1995, SoPh, 162, 357
Cairns, I. H., Knock, S., Robinson, P., & Kuncic, Z. 2003, SSRv, 107, 27
Caligari, P., Moreno-Insertis, F., & Schussler, M. 1995, ApJ, 441, 886
Canfield, R. C., Hudson, H. S., & McKenzie, D. E. 1999, GeoRL, 26, 627
Carmichael, H. 1964, NASSP, 50, 451
Chen, B., Bastian, T. S., & Gary, D. E. 2014a, ApJ, 794, 149
Chen, B., Yu, S., Battaglia, M., et al. 2018a, ApJ, 866, 62
Chen, H., Duan, Y., Yang, J., Yang, B., & Dai, J. 2018b, ApJ, 869, 78
Chen, H., Zhang, J., Cheng, X., et al. 2014b, ApJL, 797, L15
Chen, P. F. 2011, LRSP, 8, 1
Chen, Y., Du, G., Zhao, D., et al. 2016, ApJL, 820, L37
Cheng, X., & Ding, M. D. 2016, ApJS, 225, 16
Cheng, X., Ding, M. D., Zhang, J., et al. 2014a, ApJL, 789, L35
Cheng, X., Ding, M. D., Zhang, J., et al. 2014b, ApJ, 789, 93
Cheng, X., Zhang, J., Ding, M. D., Liu, Y., & Poomvises, W. 2013, ApJ, 763, 43
Cheng, X., Zhang, J., Liu, Y., & Ding, M. D. 2011, ApJL, 732, L25
Chifor, C., Mason, H. E., Tripathi, D., Isobe, H., & Asai, A. 2006, A&A, 458, 965
Chifor, C., Tripathi, D., Mason, H. E., & Dennis, B. R. 2007, A&A, 472, 967
Chintzoglou, G., Patsourakos, S., & Vourlidas, A. 2015, ApJ, 809, 34
Cline, T. L., Holt, S. S., & Hones, E. W., Jr. 1968, JGR, 73, 434
Dalmasse, K., Chandra, R., Schmieder, B., & Aulanier, G. 2015, A&A, 574, A37
Démoulin, P., & Aulanier, G. 2010, ApJ, 718, 1388
Domingo, V., Fleck, B., & Poland, A. I. 1995, SoPh, 162, 1
Emslie, A. G. 1983, ApJ, 271, 367
Engvold, O. 1997, in Filament Channels in the Corona, ed. Z. Mouradian & M. Stavinschi (Dordrecht: Springer Netherlands), 125
Fan, Y. 2001, ApJL, 554, L111
Fárník, F., Hudson, H., & Watanabe, T. 1996, SoPh, 165, 169
Fárník, F., Hudson, H. S., Karlický, M., & Kosugi, T. 2003, A&A, 399, 1159
Fárník, F., & Savy, S. K. 1998, SoPh, 183, 339
Fletcher, L., Dennis, B. R., Hudson, H. S., et al. 2011, SSRv, 159, 19
Forsyth, R. J., Bothmer, V., Cid, C., et al. 2006, SSRv, 123, 383
Gaizauskas, V., Zirker, J. B., Sweetland, C., & Kovacs, A. 1997, ApJ, 479, 448
Gary, G. A., & Moore, R. L. 2004, ApJ, 611, 545
Gibson, S. E., & Fan, Y. 2006, JGRA, 111, A12103
Gibson, S. E., Fan, Y., Mandrini, C., Fisher, G., & Demoulin, P. 2004, ApJ, 617, 600
Gibson, S. E., Fan, Y., Török, T., & Kliem, B. 2006, SSRv, 124, 131
Gopalswamy, N. 2013, Type II Solar Radio Bursts (Washington, DC: American Geophysical Union), 123
Hernandez-Perez, A., Su, Y., Veronig, A. M., et al. 2019, ApJ, 874, 122
Hirayama, T. 1974, SoPh, 34, 323
Holman, G. D., Aschwanden, M. J., Aurass, H., et al. 2011, SSRv, 159, 107
Holman, G. D., Sui, L., Schwartz, R. A., & Emslie, A. G. 2003, ApJL, 595, L97
Hudson, H. S. 1972, SoPh, 24, 414
Jing, J., Tan, C., Yuan, Y., et al. 2010, ApJ, 713, 440
Joshi, B., Ibrahim, M. S., Shanmugaraju, A., & Chakrabarty, D. 2018, SoPh, 293, 107
Joshi, B., Kushwaha, U., Cho, K.-S., & Veronig, A. M. 2013, ApJ, 771, 1
Joshi, B., Kushwaha, U., Veronig, A. M., & Cho, K.-S. 2016, ApJ, 832, 130
Joshi, B., Kushwaha, U., Veronig, A. M., et al. 2017, ApJ, 834, 42
Joshi, B., Manoharan, P. K., Veronig, A. M., Pant, P., & Pandey, K. 2007, SoPh, 242, 143

Joshi, B., Veronig, A., Cho, K. S., et al. 2009, ApJ, 706, 1438
Joshi, B., Veronig, A., Manoharan, P. K., & Somov, B. V. 2012, in Multi-scale Dynamical Processes in Space and Astrophysical Plasmas, ed. M. P. Leubner & Z. Vörös (Berlin: Springer), 29
Joshi, B., Veronig, A. M., Lee, J., et al. 2011, ApJ, 743, 195
Joshi, N. C., Zhu, X., Schmieder, B., et al. 2019, ApJ, 871, 165
Kane, S. R., & Anderson, K. A. 1970, ApJ, 162, 1003
Kliem, B., & Török, T. 2006, PhRvL, 96, 255002
Kondo, T., Isobe, T., Igi, S., Watari, S., & Tokimura, M. 1995, J. Commun. Res. Lab., 42, 111
Kopp, R. A., & Pneuman, G. W. 1976, SoPh, 50, 85
Korchak, A. A. 1967a, SvA, 11, 258
Korchak, A. A. 1967b, SPhD, 12, 192
Krucker, S., Battaglia, M., Cargill, P. J., et al. 2008, A&ARv, 16, 155
Krucker, S., Hurford, G. J., & Lin, R. P. 2003, ApJL, 595, L103
Kumar, S., Bhattacharyya, R., Joshi, B., & Smolarkiewicz, P. K. 2016, ApJ, 830, 80
Kundu, M. R. 1963, SSRv, 2, 438
Lemen, J. R., Title, A. M., Akin, D. J., et al. 2012, SoPh, 275, 17
Lin, R. P., Dennis, B. R., Hurford, G. J., et al. 2002, SoPh, 210, 3
Liu, C., Deng, N., Lee, J., et al. 2013, ApJL, 778, L36
Liu, C., Lee, J., Yurchyshyn, V., et al. 2007, ApJ, 669, 1372
Liu, R., Liu, C., Wang, S., Deng, N., & Wang, H. 2010, ApJL, 725, L84
Liu, T., Su, Y., Cheng, X., van Ballegooijen, A., & Ji, H. 2018, ApJ, 868, 59
Liu, Y. 2008, ApJL, 679, L151
Manoharan, P. K., & Kundu, M. R. 2003, ApJ, 592, 597
Martínez-Sykora, J., Hansteen, V., & Carlsson, M. 2008, ApJ, 679, 871
Masuda, S., Kosugi, T., Hara, H., Tsuneta, S., & Ogawara, Y. 1994, Natur, 371, 495
Metcalf, T. R., Hudson, H. S., Kosugi, T., Puetter, R. C., & Pina, R. K. 1996, ApJ, 466, 585
Mitra, P. K., Joshi, B., Prasad, A., Veronig, A. M., & Bhattacharyya, R. 2018, ApJ, 869, 69
Moore, R. L., & Roumeliotis, G. 1992, in IAU Coll. 133: Eruptive Solar Flares, ed. Z. Svestka, B. V. Jackson, & M. E. Machado (Berlin: Springer), 69
Moore, R. L., Sterling, A. C., Hudson, H. S., & Lemen, J. R. 2001, ApJ, 552, 833
Moza, K. L., Koul, P. K., Rausaria, R. R., & Khosa, P. N. 1986, JApA, 7, 39
Nindos, A., Patsourakos, S., Vourlidas, A., & Tagikas, C. 2015, ApJ, 808, 117
O'Flannagain, A. M., Brown, J. C., & Gallagher, P. T. 2015, ApJ, 799, 127
Olmedo, O., & Zhang, J. 2010, ApJ, 718, 433
Pesnell, W. D., Thompson, B. J., & Chamberlin, P. C. 2012, SoPh, 275, 3
Pevtsov, A. A. 2002, SoPh, 207, 111
Priest, E. R., Hood, A. W., & Anzer, U. 1989, ApJ, 344, 1010
Reep, J. W., Bradshaw, S. J., & Holman, G. D. 2016, ApJ, 818, 44
Reid, H. A. S., & Ratcliffe, H. 2014, RAA, 14, 773
Schou, J., Scherrer, P. H., Bush, R. I., et al. 2012, SoPh, 275, 229
Schwartz, R. A., Csillaghy, A., Tolbert, A. K., et al. 2002, SoPh, 210, 165
Shibata, K., & Magara, T. 2011, LRSP, 8, 6
Smith, D. M., Lin, R. P., Turin, P., et al. 2002, SoPh, 210, 33
Song, H. Q., Chen, Y., Zhang, J., et al. 2015a, ApJL, 804, L38
Song, H. Q., Chen, Y., Zhang, J., et al. 2015b, ApJL, 808, L15
Song, H. Q., Zhang, J., Chen, Y., & Cheng, X. 2014a, ApJL, 792, L40
Song, H. Q., Zhang, J., Cheng, X., et al. 2014b, ApJ, 784, 48
Sturrock, P. A. 1966, Natur, 211, 695
Sui, L., & Holman, G. D. 2003, ApJL, 596, L251
Syrovatskii, S. I., & Shmeleva, O. P. 1972, SvA, 16, 273
Takakura, T., & Kai, K. 1966, PASJ, 18, 57
Temmer, M., Veronig, A. M., Vršnak, B., et al. 2008, ApJL, 673, L95
Török, T., Kliem, B., & Titov, V. S. 2004, A&A, 413, L27
van Ballegooijen, A. A., & Martens, P. C. H. 1989, ApJ, 343, 971
Vemareddy, P., & Zhang, J. 2014, ApJ, 797, 80
Veronig, A. M., Karlický, M., Vršnak, B., et al. 2006, A&A, 446, 675
Wang, W., Liu, R., Wang, Y., et al. 2017, NatCo, 8, 1330
Webb, D. F., & Howard, T. A. 2012, LRSP, 9, 3
White, S. M., Benz, A. O., Christe, S., et al. 2011, SSRv, 159, 225
Wild, J. P. 1950, AuSRA, 3, 541
Xue, Z., Yan, X., Yang, L., Wang, J., & Zhao, L. 2017, ApJL, 840, L23
Yang, B., Yang, J., Bi, Y., et al. 2018, ApJ, 861, 135
Zhang, J., Cheng, X., & Ding, M.-D. 2012, NatCo, 3, 747
Zhang, J., & Dere, K. P. 2006, ApJ, 649, 1100
Zhang, J., Dere, K. P., Howard, R. A., Kundu, M. R., & White, S. M. 2001, ApJ, 559, 452
Zhang, J., Dere, K. P., Howard, R. A., & Vourlidas, A. 2004, ApJ, 604, 420
Zhou, G. P., Zhang, J., & Wang, J. X. 2016, ApJL, 823, L19

Solar Phys (2020) 295:29
https://doi.org/10.1007/s11207-020-1596-2

Identification of Pre-flare Processes and Their Possible Role in Driving a Large-scale Flux Rope Eruption with Complex M-class Flare in the Active Region NOAA 12371

Prabir K. Mitra[1,2] · **Bhuwan Joshi**[1] · **Avijeet Prasad**[3]

Received: 19 October 2019 / Accepted: 3 February 2020

Abstract In this article, we study the origin of precursor flare activity and investigate its role towards triggering the eruption of a flux rope which resulted into a dual-peak M-class flare (SOL2015-06-21T02:36) in the active region NOAA 12371. The flare evolved in two distinct phases with peak flux levels of M2.1 and M2.6 at an interval of ≈ 54 min. The active region exhibited striking moving magnetic features (MMFs) along with sunspot rotation. Nonlinear force-free field (NLFFF) modelling of the active region corona reveals a magnetic flux rope along the polarity inversion line in the trailing sunspot group which is observationally manifested by the co-spatial structures of an active region filament and a hot channel identified in the 304 and 94 Å images, respectively, from the *Atmospheric Imaging Assembly* (AIA). The active region underwent a prolonged phase of flux enhancement followed by a relatively shorter period of flux cancellation prior to the onset of the flare which led to the build up and activation of the flux rope. Extreme ultra-violet (EUV) images reveal localised and structured pre-flare emission, from the region of MMFs, adjacent to the location of the main flare. Our analysis reveals strong, localised regions of photospheric currents of opposite polarities at the precursor location, thereby making the region susceptible to small-scale magnetic reconnection. Precursor reconnection activity from this location most likely induced a slipping reconnection towards the northern leg of the hot channel which led to the destabilisation of the flux rope. The application of magnetic virial theorem suggests that there was an overall growth of magnetic free energy in the active region during the prolonged pre-flare phase which decayed rapidly after the hot channel eruption and its successful transformation into a halo coronal mass ejection (CME).

Electronic supplementary material The online version of this article (https://doi.org/10.1007/s11207-020-1596-2) contains supplementary material, which is available to authorized users.

P.K. Mitra
prabir@prl.res.in

1 Udaipur Solar Observatory, Physical Research Laboratory, Udaipur 313 001, India

2 Department of Physics, Gujarat University, Ahmedabad 380 009, India

3 Center for Space Plasma and Aeronomic Research, The University of Alabama in Huntsville, Huntsville, AL 35899, USA

Published online: 12 February 2020

Keywords Active Regions, Magnetic Fields · Flares, Dynamics, Pre-Flare Phenomena, Relation to Magnetic Field · Magnetic fields, Models · X-Ray Bursts, Association with Flares

1. Introduction

Solar flares belong to the most spectacular phenomena occurring in the solar system. During a flare, catastrophic energy release of the order as high as $10^{27} - 10^{32}$ erg occurs in the solar atmosphere within tens of minutes. The released energy manifests its signatures in the entire electromagnetic spectrum in the form of heat and particle acceleration (see reviews by Fletcher *et al.*, 2011; Benz, 2017). Major flares are often associated with large-scale eruption of plasma from the solar corona known as coronal mass ejection (CME). Earth-directed CMEs are known to cause geomagnetic storms and other hazardous effects at the near-Earth environment. The precise understanding of the magnetic configuration of the flare producing active regions (ARs) during the pre-flare phase and its role in triggering the large-scale eruptions are among the most critical topics studied in the solar physics community (see *e.g.*, Mitra and Joshi, 2019).

The "standard flare model", also known as CSHKP model (Carmichael, 1964; Sturrock, 1966; Hirayama, 1974; Kopp and Pneuman, 1976), recognizes the presence of magnetic flux rope (MFR) in the AR corona as the prerequisite for the initiation of eruptive flares. An MFR is recognised as sets of magnetic field lines which are twisted around its central axis more than once (Gibson and Fan, 2006). These complex structures are believed to be formed as a result of flux cancellation over the polarity inversion line (PIL) through photospheric shearing and converging motions (van Ballegooijen and Martens, 1989); however, the exact mechanism for flux rope formation is still unclear and debatable. Observationally, MFRs have been identified in the form of different solar features, such as, filaments, prominences, filament channels, hot coronal channels, and coronal sigmoids. Filaments are threadlike structures which are observed as dark long narrow features in the chromospheric images of the Sun (Zirin, 1988; Martin, 1998). When these structures are observed over the limb, they appear brighter than the background sky and are called prominences (Tandberg-Hanssen, 1995; Parenti, 2014). Filament channels are voids without plages or chromospheric fine structures such as spicules or fibrils *etc.* (Martres and Michard, 1966; Gaizauskas *et al.*, 1997). These are long, narrow, extended structures situated over the PIL where filaments or prominences are formed (Engvold, 1997).

While filaments and filament channels are observed in the absorption lines of choromospheric images, sigmoids and hot channels are observed in the emission line features of the solar corona. Sigmoids are "S" (or inverted "S") shaped structures that are observed in the soft X-ray (SXR) and the extreme ultra-violet (EUV) images of the Sun (Rust and Kumar, 1996; Manoharan *et al.*, 1996). Hot channels are coherent structures observed in the high temperature pass-band EUV images of the solar corona (Zhang, Cheng, and Ding, 2012; Cheng *et al.*, 2013). These are often found in association with coronal sigmoids (see *e.g.*, Cheng *et al.*, 2014a; Joshi *et al.*, 2017; Mitra *et al.*, 2018). Their frequent co-existence with filaments confirms that filaments and hot channels are different observational manifestations of MFRs lying in the chromospheric and coronal heights, respectively (Cheng *et al.*, 2014b). However, the most important feature of hot channels and coronal sigmoids is their frequent association with CMEs which has been suggested by several case studies and statistical surveys (see *e.g.*, Nindos *et al.*, 2015).

The temporal evolution of a typical eruptive flare can be summarized in three phases: pre-flare/precursor phase, impulsive phase, and gradual phase. While the processes occurring during the impulsive and gradual phases are broadly explained by the CSHKP model (Shibata, 1996), the pre-flare phase is still ill-understood. Pre-flare activities are considered to be important in order to understand the physical conditions that lead to flares and associated eruptions (see *e.g.*, Fárník, Hudson, and Watanabe, 1996; Chifor *et al.*, 2006; Joshi *et al.*, 2011). Although it is well understood that a significant fraction of all the major flares are associated with pre-flare events, the causal relation between them requires investigation in detail through multi-wavelength case studies. Thanks to the high resolution and high cadence observations of the *Atmospheric Imaging Assembly* (AIA; Lemen *et al.*, 2012) and the *Helioseismic and Magnetic Imager* (HMI; Schou *et al.*, 2012) on board the *Solar Dynamics Observatory* (SDO; Pesnell, Thompson, and Chamberlin, 2012), in the recent years, there has been a progress in understanding the short-lived pre-flare events and precursor emission.

In this article we present a detailed multi-wavelength analysis of the pre-flare processes associated with a dual-peak M-class flare on 21 June 2015. The reported events occurred in the AR NOAA 12371 which was among the prominent ARs of the Solar Cycle 24. The M-class flares produced by this AR on 21 and 22 June 2015 have been subjected to a number of studies (see *e.g.*, Manoharan *et al.*, 2016; Cheng and Ding, 2016; Jing *et al.*, 2017; Vemareddy, 2017; Piersanti *et al.*, 2017; Bi *et al.*, 2017; Lee *et al.*, 2017; Wang *et al.*, 2018; Lee *et al.*, 2018; Kuroda *et al.*, 2018; Joshi *et al.*, 2018; Gopalswamy *et al.*, 2018; Liu *et al.*, 2019). Our rigorous analysis aims to provide a clear understanding of the pre-flare energy release processes and the role of the pre-flare activity in triggering the flux rope eruption during the complex M-class flare that displayed characteristics of a long duration event (LDE) of energy release. Section 2 provides a detailed account of the observational data and analysis techniques used in this article. In Section 3, we discuss the evolution of the AR NOAA 12371 in detail. The results obtained on the basis of multi-wavelength analysis and photospheric measurements are discussed in Section 4. Nonlinear force-free field (NLFFF) extrapolation results and evolution of magnetic free energy in the AR are provided in Section 5. We discuss and interpret our results in Section 6.

2. Observational Data and Methods

Solar observation in EUV wavelengths were obtained from the *Atmospheric Imaging Assembly* (AIA; Lemen *et al.*, 2012) on board the *Solar Dynamics Observatory* (SDO; Pesnell, Thompson, and Chamberlin, 2012). Among the seven EUV filters of AIA (94 Å, 131 Å, 171 Å, 193 Å, 211 Å, 304 Å, and 335 Å), we have focused on the 4096×4096 pixel full-disk solar images in the 94 and 304 Å channels at a spatial resolution of $0.''6$ pixel^{-1} and temporal cadence of 12 s.

For studying the photospheric structures and their evolution, we have used intensity and magnetogram images taken by the *Helioseismic and Magnetic Imager* (HMI; Schou *et al.*, 2012) on board SDO. HMI produces full-disk line of sight (LOS) intensity (continuum) and magnetogram images of 4096×4096 pixels at a spatial resolution of $0.''5$ pixel^{-1} and 45 s temporal cadence while the vector magnetograms are produced with a temporal cadence of 720 s.

Coronal magnetic field extrapolation has been carried out by employing the optimisation based nonlinear force-free field (NLFFF) extrapolation method developed by Wiegelmann and Inhester (2010), Wiegelmann *et al.* (2012), using photospheric vector magnetograms from the "hmi.sharp_cea_720s" series of HMI/SDO at a spatial resolution of $1.''0$ pixel^{-1}

as boundary conditions. Extrapolations have been done in a Cartesian volume of $474 \times 226 \times 226$ pixels which translates to a physical volume with dimensions $\approx 344 \times 164 \times 164$ Mm. Using NLFFF extrapolation results, we calculated the squashing factor (Q) in the extrapolation-volume by employing the code introduced by Liu *et al.* (2016). For visualizing the extrapolated coronal field lines, we have used Visualization and Analysis Platform for Ocean, Atmosphere, and Solar Researchers (VAPOR; Clyne *et al.*, 2007) software.

X-ray observation during the flare was provided by the *Reuven Ramaty High Energy Solar Spectroscopic Imager* (RHESSI; Lin *et al.*, 2002). RHESSI observed the full Sun with an unprecedented spatial resolution (as fine as $\approx 2.''3$) and energy resolution (1 – 5 keV) in the energy range 3 – 17 MeV. For imaging of the X-ray sources using RHESSI observation, we have used the CLEAN algorithm (Hurford *et al.*, 2002) with the natural weighting scheme for front detector segments 2 – 9 (excluding 7).

3. Magnetic Structure of the Active Region NOAA 12371

3.1. Morphology and Build up of Magnetic Complexity

The AR NOAA 12371 appeared on the eastern limb of the Sun during the last hours of 15 June 2015 as a moderately complex β-type sunspot. Flaring activity from the AR was noted to start from 16 June 2015. Interestingly, despite producing numerous B and C class flares alongside few M-class ones, it did not produce any X-class flare. By 18 June 2015, it gradually became a more complex $\beta\gamma$-type sunspot (Figure 1a) and produced its first M-class flare on the same day. The AR evolved into the most complex $\beta\gamma\delta$-type (Figure 1b) on the next day, *i.e.* 19 June 2015. The highest flaring activity from the AR was observed during 20 – 22 June 2015. In this duration, it produced 3 M-class flares along with many C- and B-class flares. The AR started to decay after 22 June 2015. In Table 1, we summarise various evolutionary aspects of NOAA 12371 during its disk passage during 18 – 25 June 2015 which are collected from the NOAA Solar Region Summary (SRS) reports.[1] The magnetic configuration of the AR reduced to $\beta\gamma$-type on 25 June 2015 (Figure 1h) and even further to β-type on 29 June 2015 just before it went on to the far side of the Sun from the western limb. During its lifetime on the visible hemisphere of the Sun, it produced a total of 5 M-class flares, which are also listed in Table 1. Notably, the AR produced the largest flare of class M7.9 on 25 June 2015 when it had entered into the declining phase. However, in terms of space weather manifestations, the most interesting eruptive flare from the AR occurred on 21 June 2015. This event followed the characteristics of a long duration flare with peak GOES flux reaching a level of M2.6 and a fast CME[2] with linear speed of 1366 km s^{-1}.

3.2. Evolution of Photospheric Magnetic Flux

To have a comprehensive understanding of the photospheric magnetic activities during the prolonged phase of energy build up and subsequent flaring activity on 21 June 2015, we have thoroughly examined large as well as small-scale changes in the LOS magnetograms. During this period, the AR was consisted of two major sunspot groups (Figure 2a). A comparison of the white light image of the AR with a co-temporal magnetogram (*cf.* Figures 2a and b) reveals that almost all of the leading sunspot group of the AR was consisted of

[1] See https://www.swpc.noaa.gov/products/solar-region-summary.

[2] See https://cdaw.gsfc.nasa.gov/CME_list/index.html.

Table 1 Evolution of the AR NOAA 12371 during its peak activity period and summary of the major flares produced by it.

Sr. No.	Date	Heliographic co-ordinates	AR configuration	Area (Millionth of hemisphere)	GOES flare class (peak time (UT))
1	2015 June 18	≈ N12E53	$\beta\gamma$	≈ 520	M3.0 (17:36)
2	2015 June 19	≈ N12E39	$\beta\gamma\delta$	≈ 810	–
3	2015 June 20	≈ N13E27	$\beta\gamma\delta$	≈ 1020	M1.0 (06:48)
4	2015 June 21	≈ N13E14	$\beta\gamma\delta$	≈ 1120	M2.6 (02:36)
5	2015 June 22	≈ N13W00	$\beta\gamma\delta$	≈ 1180	M6.5 (18:23)
6	2015 June 23	≈ N13W13	$\beta\gamma\delta$	≈ 1070	–
7	2015 June 24	≈ N12W28	$\beta\gamma\delta$	≈ 950	–
8	2015 June 25	≈ N11W40	$\beta\gamma$	≈ 740	M7.9 (08:16)

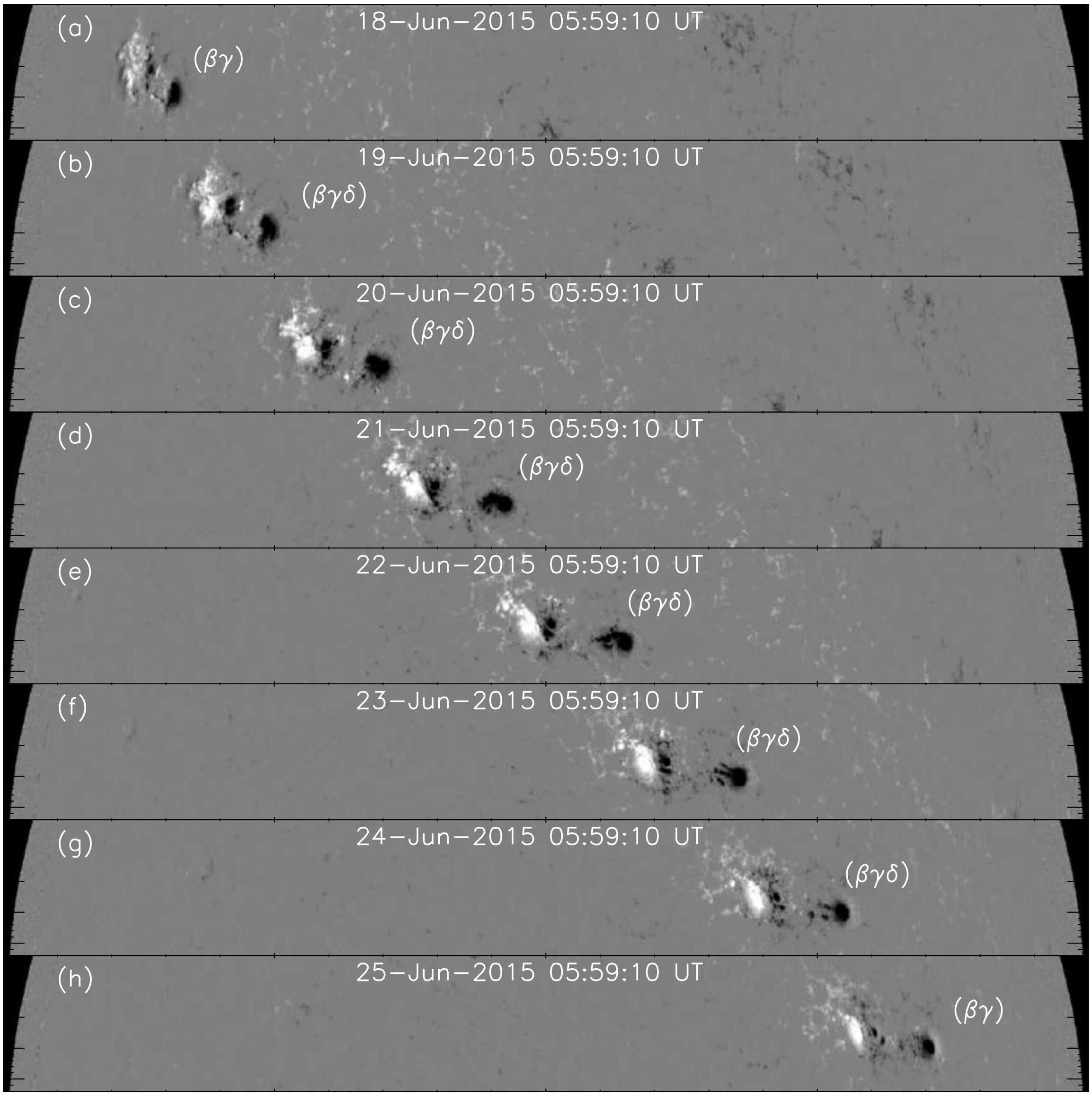

Figure 1 Line-of-sight (LOS) magnetograms showing the synoptic overview of the photospheric magnetic structure of the AR NOAA 12371 during 18 – 25 June 2015. Magnetic configuration of the active region on each day is annotated in the corresponding panel.

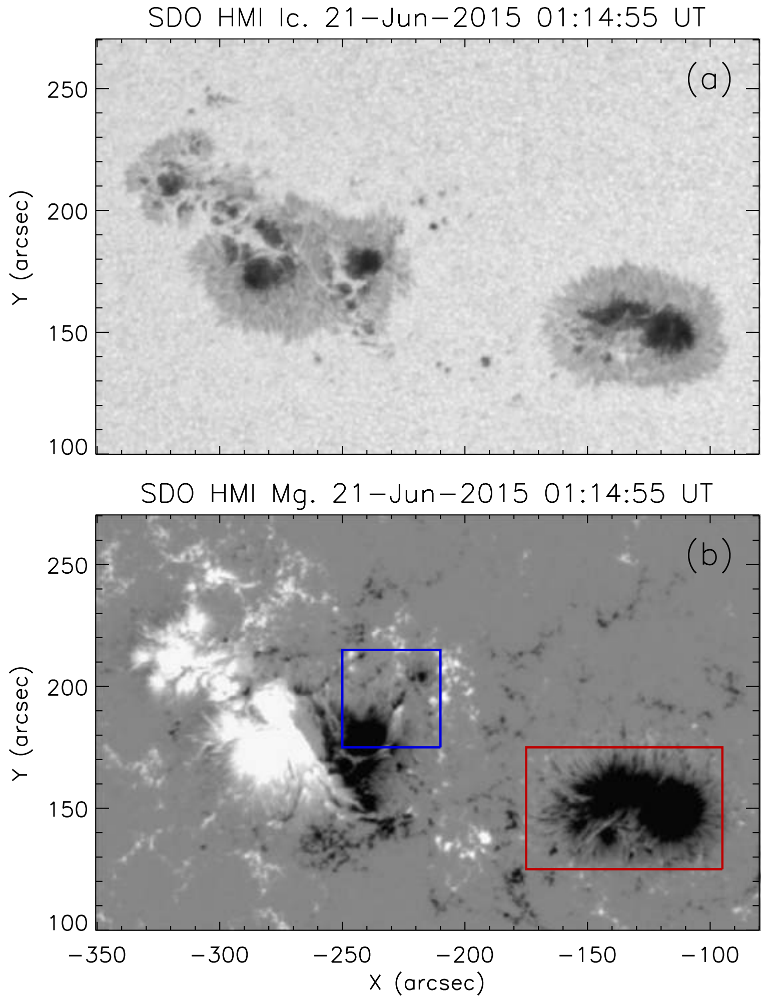

Figure 2 (**a**): A white light image of the AR during the pre-flare phase of the M-class flare on 21 June 2015. (**b**): A co-temporal LOS magnetogram. The blue and red boxes indicate two regions that showed striking photospheric changes. An animation of this figure is provided in the supplementary materials.

negative polarity while the trailing sunspot group was of mixed polarities forming δ-type configuration. In this manner, the overall photospheric configuration of magnetic polarities of the AR made it a $\beta\gamma\delta$ sunspot region.

In Figure 3, we plot the evolution of the LOS magnetic flux through the whole AR as well as only from the trailing sunspot region from 20 June 2015 12:00 UT to 21 June 2015 05:00 UT. The trailing sunspot group has been shown in the box in Figure 3a. Notably, the eruptive flare under investigation was triggered from this region. The evolution of the trailing sunspot group of the AR can be inferred by comparing Figures 3b1 and 3b2 which present enlarged view of the selected region at two different times. The area marked by dashed circles shows rapidly evolving magnetic elements and moving magnetic features (MMFs) which are discussed in the next subsection. From Figure 3c, we readily find that both the positive and negative flux from the AR increased during $\approx$ 13:30 – 23:00 UT on 20 June 2015 and thereafter decreased till the onset of the flare at $\approx$01:05 UT on 21 June 2015. Based on the flux variations, we have divided the whole interval in two phases: "phase 1"; when the active region displayed flux enhancement in both the polarities, and "phase 2"; when flux of both polarities decayed. Evolution of magnetic flux in the trailing sunspot group, (*i.e.* the flaring region) displayed similar variation as the entire AR (Figure 3d). In phase 1, flux of both polarities increased; however, increase of positive flux was more than that of negative flux. Flux of both polarities decayed at similar rate during phase 2. To have an understanding of flaring activity in the AR, we have plotted the variation of GOES SXR flux along with AIA 94 Å light curve from 20 June 2015 12:00 UT to 21 June 2015

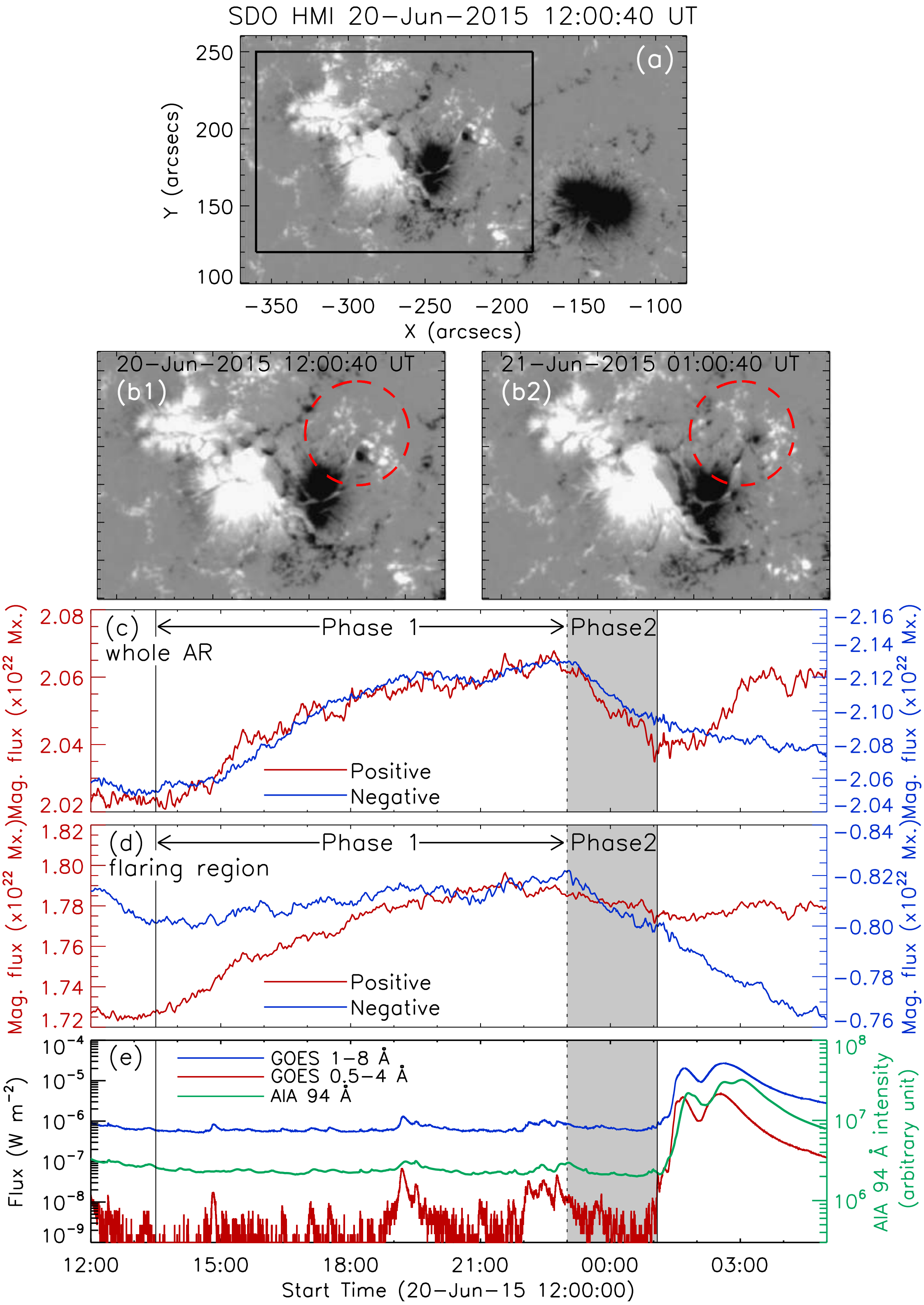

Figure 3 (**a**): HMI LOS magnetogram of AR 12371. We outline the flaring region in the AR by the black box. (**b1**) and (**b2**): the flaring region as indicated by the black box in (**a**), at two different times with a time-gap of ≈ 23 hours. The red dashed circles in these two panels mark the region with striking moving magnetic features (MMFs). (**c**): Evolution of magnetic flux in the whole AR from 20 June 2015 12:00 UT to 21 June 2015 05:00 UT. (**d**): Evolution of magnetic flux in the flaring region (within the box in (**a**)). In (**e**), we plot GOES SXR light curves in both the channels as well as the AIA 94 Å intensity profile. In (**c**) – (**e**), the interval marked as "phase 1" depicts flux emergence of both polarities in the AR as well as flaring region. The "phase 1" was followed by a period of flux cancellation of both polarities ("phase 2"; the shaded region) which lasts up to the initiation of the M-class flare on 21 June 2015.

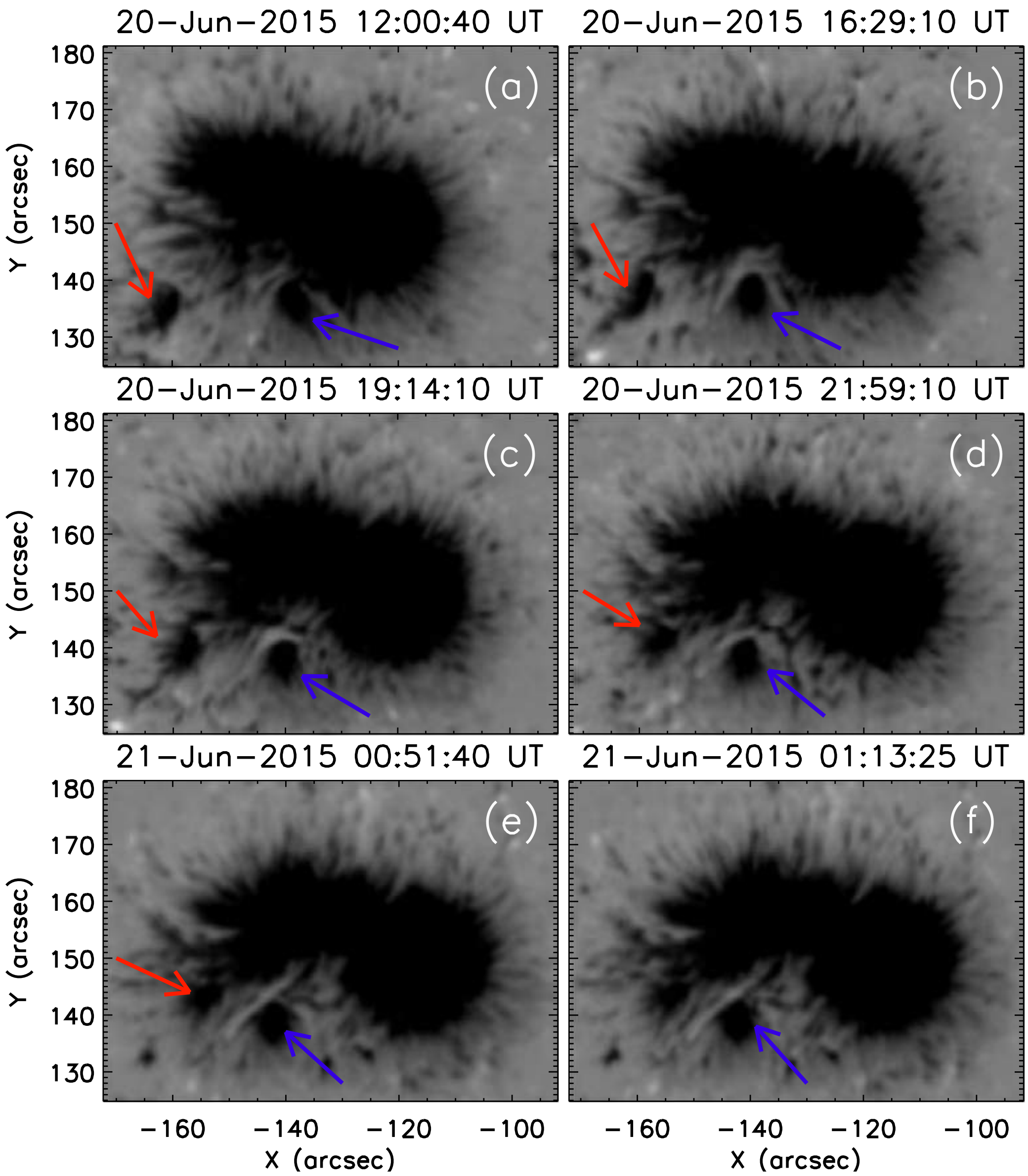

Figure 4 Series of LOS magnetograms showing the evolution of the leading sunspot group of the AR (shown within the red box in Figure 2b). We have identified a small, nearly circular patch that exhibited significant clockwise rotation (indicated by the blue arrows) and another small magnetic patch displayed converging motion towards the sunspot (indicated by the red arrows).

05:00 UT in Figure 3e. We find that, during the selected interval, there was no appreciable enhancement of SXR and EUV fluxes prior to the onset of the M-class flare on 21 June 2015 at ≈ 01:05 UT.

3.3. Sunspot Rotation and Moving Magnetic Features

The AR NOAA 12371 underwent significant morphological changes prior to the reported flare, which include MMFs, emerging/cancelling flux elements, and sunspot rotation. To highlight these features, we have identified two sub-regions in the AR with most prominent photospheric changes which are marked by the red and blue coloured boxes in Figure 2b. The leading sunspot group of the AR (inside the red box in Figure 2b) was associated with a very interesting display of morphological evolution (see the animation associated with Figure 2). We note that the extension of the leading sunspot group along the east-west direction

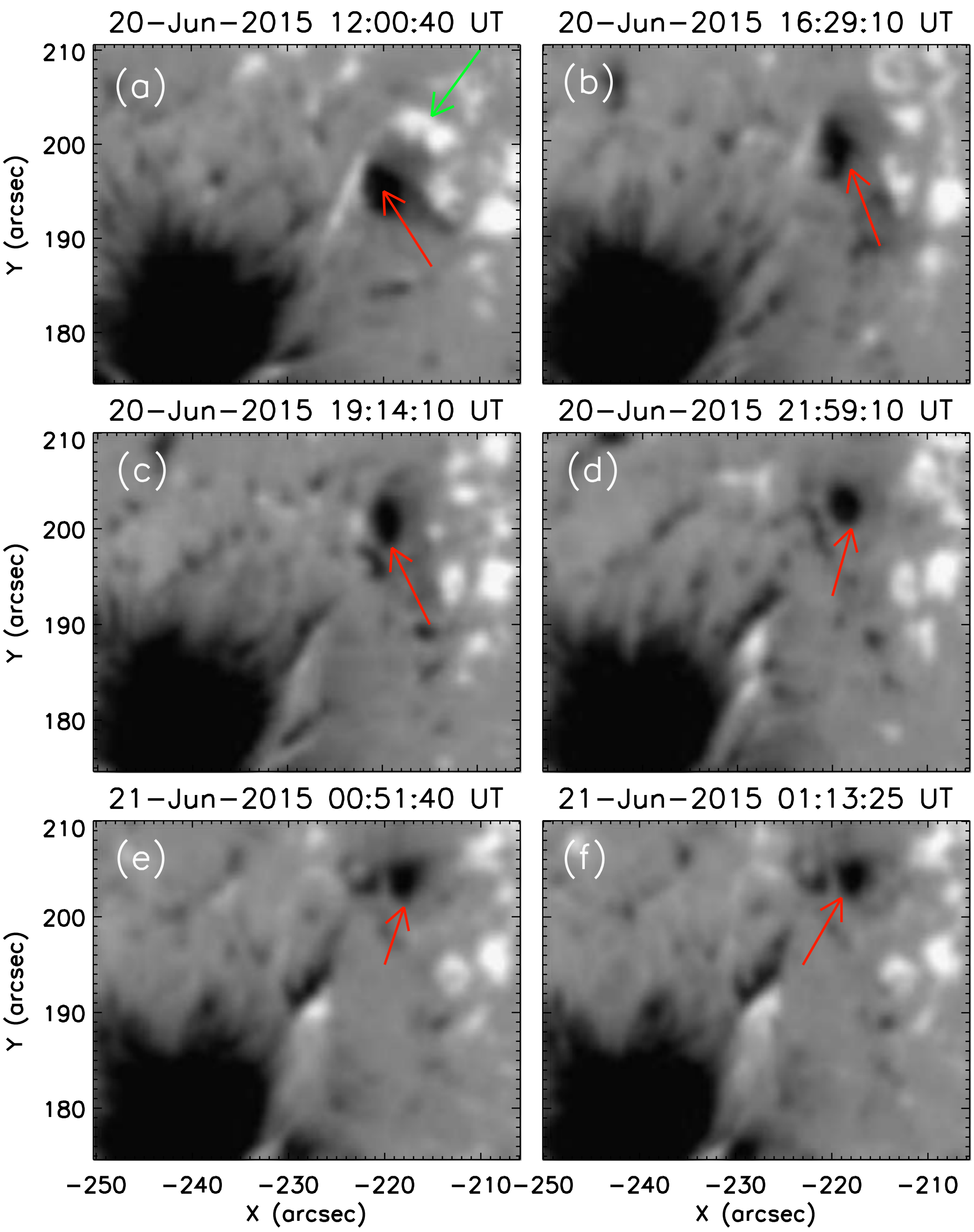

Figure 5 Series of LOS magnetograms of the selected region shown within the blue box in Figure 2b showing striking and rapidly evolving MMFs along with flux emergence and cancellation. The red arrows indicate an MMF of a negative polarity. The green arrow indicates a region associated with cancellation of positive flux.

increased from $\approx 55''$ at 20 June 2015 12:00 UT to $\approx 65''$ prior to the onset of the flare. During the same time, the north–south extension of the leading sunspot group decreased from $\approx 40''$ to $\approx 35''$ (*cf.* Figures 4a and f). Further, a small circular element of negative polarity (indicated by the blue arrows in Figure 4) exhibited continuous motion along the southern boundary of the leading sunspot group. The diagonal expansion of the region alongside the motions of the small patch suggest "clockwise rotation" of the overall leading sunspot group. We also identify a distinct patch of small magnetic region (indicated by the red arrows in Figure 4) which, after initially exhibiting constant converging motion toward the major sunspot, merged with it during the final hours of 20 June 2015 (Figure 4e).

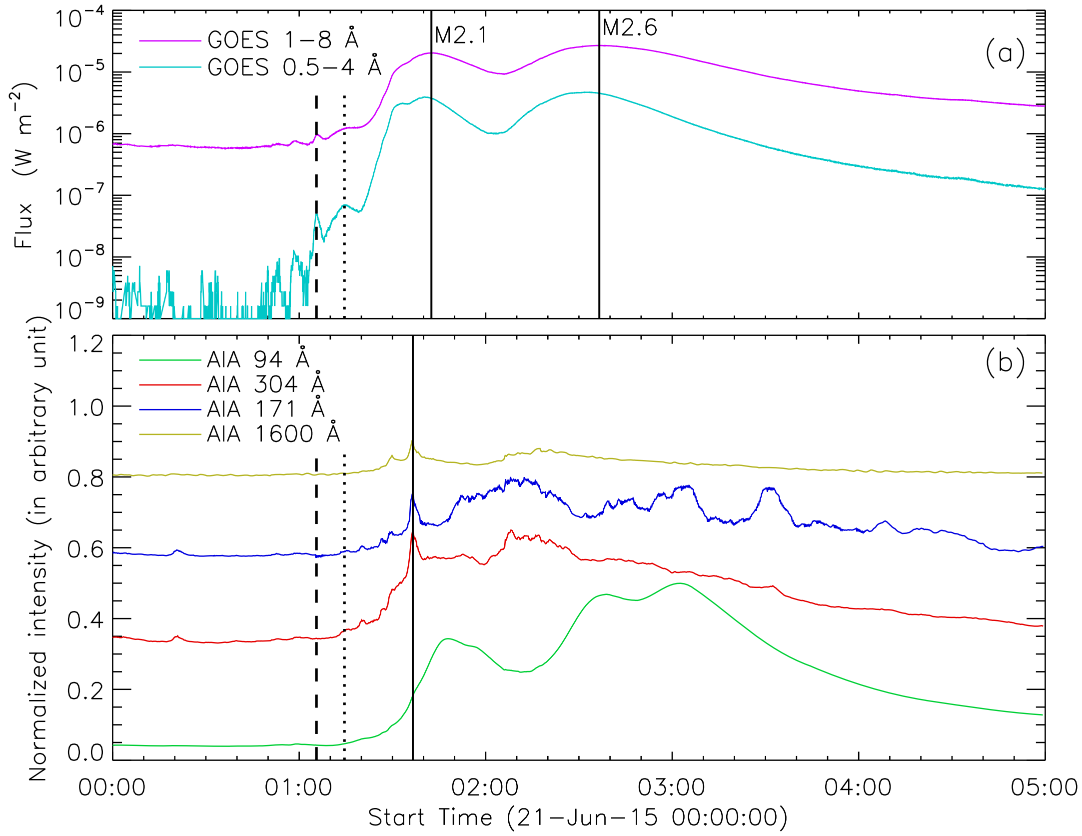

Figure 6 (**a**): GOES SXR flux variation in the 1 – 8 Å (magenta) and 0.5 – 4 Å (green) channels showing the initiation and evolution of the dual-peak M-class flare on 21 June 2015. (**b**): Normalized intensity variations in the 94 Å (green), 304 Å (red), 171 Å (blue), and 1600 Å (yellow) channels of AIA during the flare. For better visualisation, the AIA channels are scaled by factors of 0.5, 0.65, 0.8, and 0.9, respectively. The dashed and dotted lines in both the panels indicate two precursor events identified in the GOES SXR channels prior to the initiation of the main flare. The two peaks of the main flare are indicated by the solid lines in (**a**) during which GOES 1 – 8 Å flux attained levels of M2.1 and M2.6, respectively. The solid line in (**b**) indicates an impulsive but short-lived intensity enhancement observed in the AIA 304, 171, and 1600 Å channels. An animation of this figure is provided in the supplementary materials.

In Figure 5, we show the evolution of the region inside the blue box (Figure 2b) where we have indicated two particular features by red and green arrows. The red arrows indicate a striking MMF element of negative polarity which also shows significant morphological changes (see animation with Figure 2). The green arrows mark persistent cancellation of a positive flux element as the negative MMF moves toward north–west direction.

4. Multi-wavelength Observations of the Eruptive Flare

4.1. Overview of the Event

The temporal evolution of the M-class flare on 21 June 2015 is depicted by the flux variation in the *Geostationary Operational Environmental Satellite* (GOES) 1 – 8 Å and 0.5 – 4 Å channels which are plotted between 21 June 2015 00:00 UT and 05:00 UT in Figure 6a. The GOES profiles suggest that the eruptive flare evolved in two phases. According to the GOES 1 – 8 Å time profile, the event started at ≈ 01:20 UT while the peaks of the two subsequent episodes of energy release were recorded at 01:42 and 02:36 UT during which the flux rose to the levels of M2.1 and M2.6, respectively. Further, the flare was associated with two brief pre-flare flux enhancements at ≈ 01:05 and ≈ 01:14 UT (indicated by the dashed and dotted lines, respectively, in Figure 6). Profile of GOES 0.5 – 4 Å channel clearly shows that, while the flux enhancement during the first pre-flare peak was quite impulsive and short-lived, it was relatively gradual during the second pre-flare peak. Based on the temporal and spatial characteristics (discussed in the next subsection) of the episodic pre-flare enhancements, we refer to them as SXR precursors.

In Figure 6b, we display the intensity variation of AIA (E)UV channels on 21 June 2015 from 00:00 UT to 05:00 UT. We note that none of the AIA intensity profiles exhibited enhancement during the first GOES precursor while a subtle enhancement was observed during the second precursor in the AIA 304 and 171 Å channels (*cf.* the dashed and dotted lines in Figure 6a and b). Intensity in all the AIA channels, except the 94 Å channel, displayed a sharp peak at ≈ 01:36 UT (indicated by the solid line in Figure 6b) while the second peak in these AIA channels was rather gradual. The intensity variation in the AIA 94 Å channel diverged from other AIA channels in the timing and extended duration of the peaks. Interestingly, the AIA 94 Å channel displayed three distinct peaks, first and second ones of which were consistent with the GOES M2.1 and the GOES M2.6 peaks, respectively. The highest of the three AIA 94 Å peaks occurred during the gradual phase of the M-class flare. The flare moved into the gradual phase after ≈ 03:00 UT in all the AIA (E)UV and GOES SXR channels.

4.2. Two-phase Flare Emission and Flux Rope Eruption

In Figure 7, we plot a series of AIA 94 Å images displaying the AR NOAA 12371 during different phases of the M-class flare. We readily observe the presence of a prominent hot channel at the core of the AR during the pre-flare phase (indicated by the yellow arrow in Figure 7b). Comparison of the location of the hot channel with the HMI LOS magnetogram contours in Figure 7a confirms that the hot channel was lying over the PIL in the trailing sunspot of the AR. After ≈ 00:52 UT, we observed a localized yet prominent brightening from a location near to the hot channel (indicated by the red arrow in Figure 7b). We note that hard X-ray (HXR) emission of energies up to ≈ 25 keV originated from this location of pre-flare EUV brightenings. The examination of series of AIA 94 Å images suggest that the brightness of this localized region initially increased up to ≈ 01:05 UT and then decreased till ≈ 01:10 UT before increasing again. These pre-flare episodic brightenings observed in AIA 94 Å images are exactly co-temporal with the GOES SXR precursors observed at ≈ 01:05 UT and ≈ 01:14 UT (*cf.* Figure 6a). A very interesting phenomena was observed around ≈ 01:28 UT in terms of anti-clockwise motion of brightness depicting a narrow semicircular path from the northern end of the region of precursor brightening to the northern leg of the hot channel. This moving flash in indicated by the red arrows in Figures 7c and d. The flare entered into the impulsive rise phase by ≈ 01:20 UT as the hot channel got activated. During this time, we noted HXR emission of energies up to ≈ 25 keV predominantly from the northern part of the hot channel. The progression of brightness from the adjacent precursor region to the northern leg of the hot channel was immediately followed by eruption of the hot channel, *i.e.* the eruption was triggered. In Figure 7d, we indicate the direction of the hot channel eruption by the blue arrows. The eruption phase was followed by formation of post-flare arcade in the trailing sunspot (Figures 7e and f) which are associated with HXR emission of energies up to ≈ 25 keV. A second phase of the eruption was observed between ≈ 01:53 UT and ≈ 02:05 UT followed by further restructuring of the AR loops at even larger scales, as inferred from the formation of large post-flare arcade

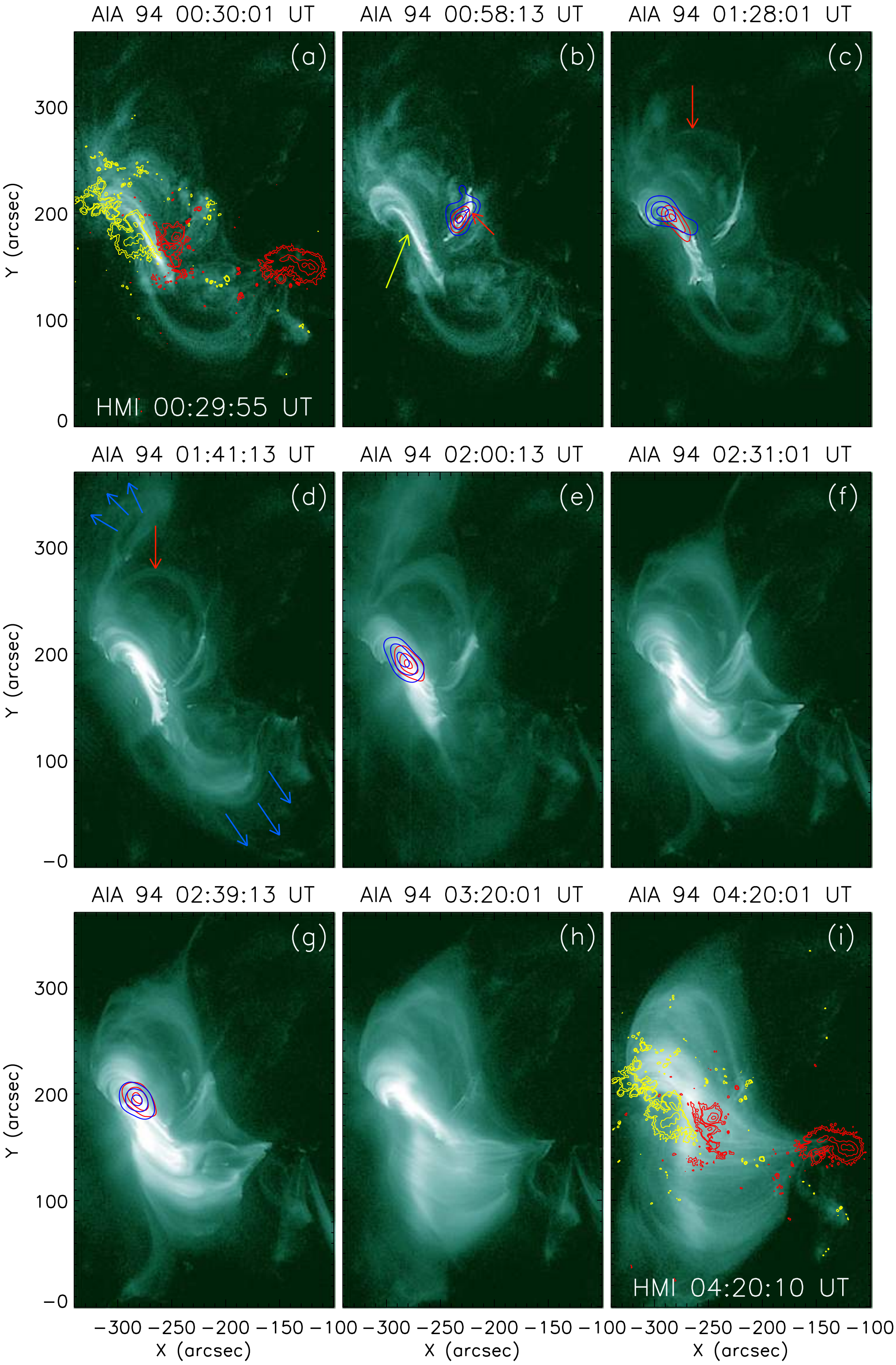

Figure 7 Series of AIA 94 Å images showing the evolution of the M-class flare on 21 June 2015 from the AR NOAA 12371. A distinct hot channel was observed during the pre-flare phase over the polarity inversion line in the AR which is marked by the yellow arrow in (**b**). A remote brightening observed prior to the onset of the flare is indicated by the red arrow in (**b**). The red arrows in (**c**) and (**d**) indicate a moving flash connecting the remote region and the northern leg of the hot channel. The blue arrows in (**d**) indicate the direction of erupting plasma during the impulsive phase of the flare. Co-temporal HMI LOS magnetogram contours are overplotted in (**a**) and (**i**) at ±(500, 800, 1500, 2000) G. Red and yellow contours refer to negative and positive polarities, respectively. Co-temporal RHESSI contours in the energy bands 6 – 12 keV (red) and 12 – 25 keV (blue) are overplotted in selective panels. Contour levels are 60%, 80% and 95% of the corresponding peak flux. All the images are derotated to 21 Jun 2015 00:30 UT.

connecting the trailing sunspot with the leading sunspot. The large post-flare arcade was associated with strong diffused emission till ≈ 02:40 UT (Figure 7g) when the flare reached its second peak. The active region did not show any significant morphological change afterwards till the end of our studied period except the brightness of the large post-flare arcade slowly reduced as the flare had moved into the gradual phase (Figures 7h, i). The above observations led Joshi *et al.* (2018) to conclude that two distinct phases of magnetic reconnection occurred successively at two separate locations and heights of the AR corona in the wake of single, large hot channel eruption. Based on the temporal and spatial proximity of the two distinct energy release phases along with spectral characteristics of emission, Lee *et al.* (2018) has termed the two-phases of energy release as the signature of a "composite flare" triggered by the flux rope eruption.

To have a further clarification on the triggering of the hot channel eruption, we selected three slits and computed time-slice diagrams along them (Figure 8). These time-slice diagrams can be effectively used to observe the time evolution of plasma eruption and brightness progression along the selected slits (see also the animation associated with Figure 8). From Figure 8b, we find that the motion of brightness (apparent signatures of slipping reconnection) from the precursor location started at ≈ 01:26 UT. We have highlighted the motion of the brightness in Figure 8b by a dotted curve. The estimated time of the arrival of the brightness at the T_2 point is indicated by the dashed vertical line in Figures 8b – c. From Figures 8c and d, it becomes evident that the eruption started immediately after the progression of brightness reached the core of the AR, *i.e.* the eruption was triggered by the processes linked with the moving brightness.

In Figure 9, we display a series of AIA 304 Å channel showing the evolution of the AR during the M-class flare. A filament (marked by the blue arrow in Figure 9b) was observed to lie along the PIL in the trailing sunspot region (*cf.* Figure 9b with HMI LOS contours in Figure 9a) which is co-spatial with the location of the hot channel observed in the AIA 94 Å channel images (*cf.* Figures 9b and 7b). The adjacent precursor activity was observed in the AIA 304 Å images also (Figure 9b and c). During the impulsive phase of the M-class flare, a clear set of flare ribbons formed in the trailing sunspot region (indicated by the arrows in Figure 9d). As expected from the standard flare scenario, the separation between the two ribbons increased, albeit rather slowly, with time and a dense post-flare arcade was eventually formed connecting the two ribbons (Figures 9d – h).

4.3. Small-scale Pre-eruption Processes

From AIA EUV images (Figures 7 and 9) it is clearly understood that the earliest flare brightening occurred at the west of the pre-existing hot channel, (*i.e.* MFR) which evolved with time but remained within a localized region. As discussed earlier, we identify this brightening as GOES SXR precursor (see Figure 6a). This was followed by the activation and eruption of the hot channel as a sequence of activities. We recall that this region of precursor brightening was associated with rapidly evolving dispersed magnetic field of positive and negative polarities in which MMFs were observed besides emergence and cancellation of magnetic flux (Figure 5). The precursor activities and its relation to the small-scale magnetic field changes are further analysed in Figure 10. In Figure 10a, we highlight the region of precursor brightening over the HMI magnetogram by the box and show co-temporal overplots of the AIA 94 Å images with the magnetograms in Figures 10b1 – b3. We identify several instances of flux emergence and cancellation of both polarities which are indicated by the arrows of different colours and the boxes in Figures 10b1 – b3. In Figure 10c, we show the evolution of LOS magnetic flux from the region shown within the box in Figure 10a on 21 June 2015 from 00:00 UT till the onset of the impulsive phase of the flare

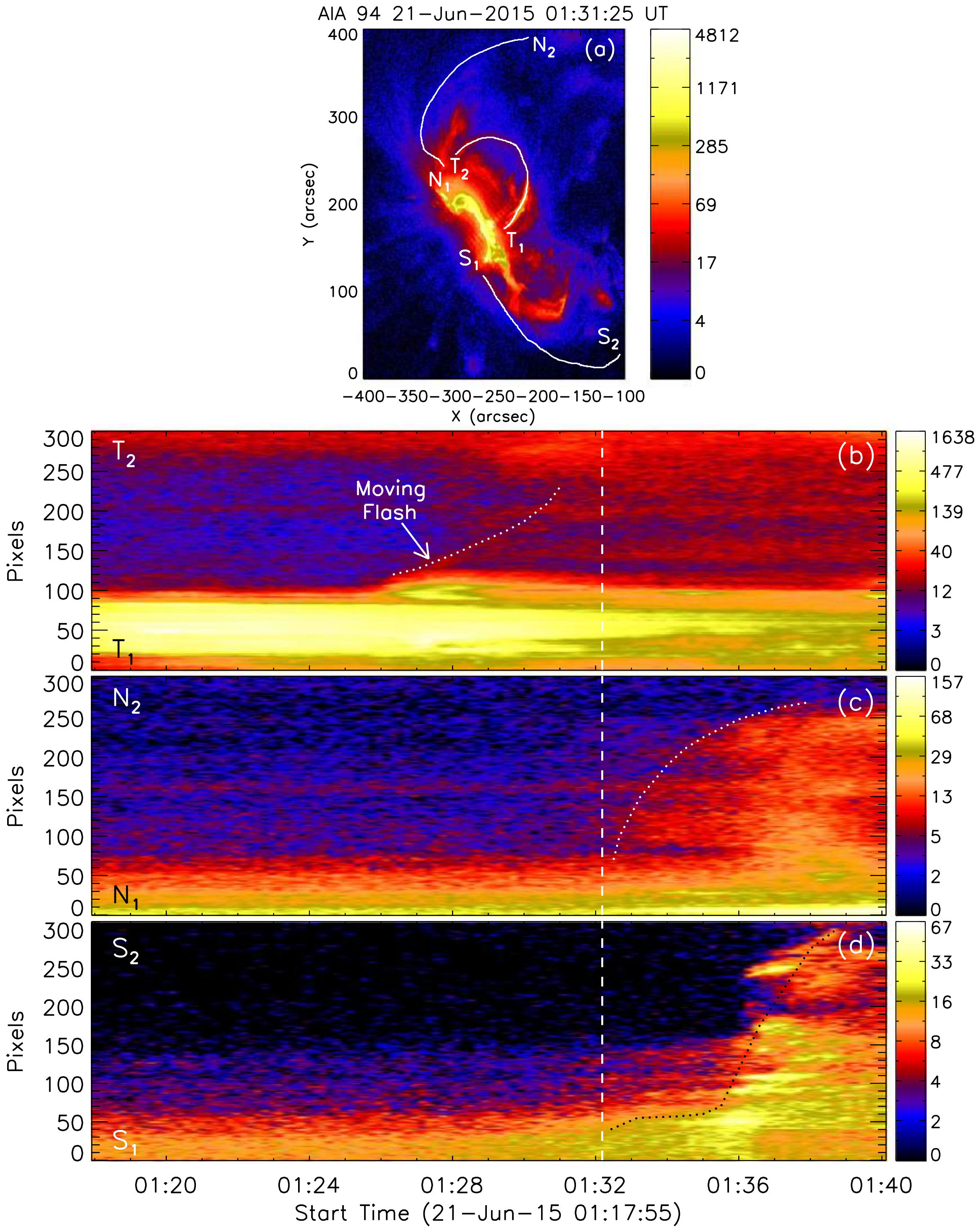

Figure 8 (**a**): AIA 94 Å images prior to the onset of the hot channel eruption. The three curves (marked by T_1T_2, N_1N_2, and S_1S_2) indicate three slits along which time-slice diagrams are computed. (**b**) – (**d**): Time-slice diagrams corresponding to the slits T_1T_2, N_1N_2, and S_1S_2, respectively. The dotted curve in (**b**) indicate the anti-clockwise motion of the subtle brightness from the precursor location to the northern leg of the hot channel. Dotted curves in (**c**) and (**d**) highlight the eruptive motion of the hot channel. The dashed vertical line in (**b**) – (**d**) indicate the estimated time of the arrival of the brightness to the northern leg of the hot channel along T_1T_2. An animation of this figure is provided in the supplementary materials.

at ≈ 01:20 UT. We find that magnetic flux of both positive and negative polarities exhibited episodic increase and decrease from the region, further implying significant small-scale flux variations. Notably, the overall trend of positive flux in this region displayed a slow

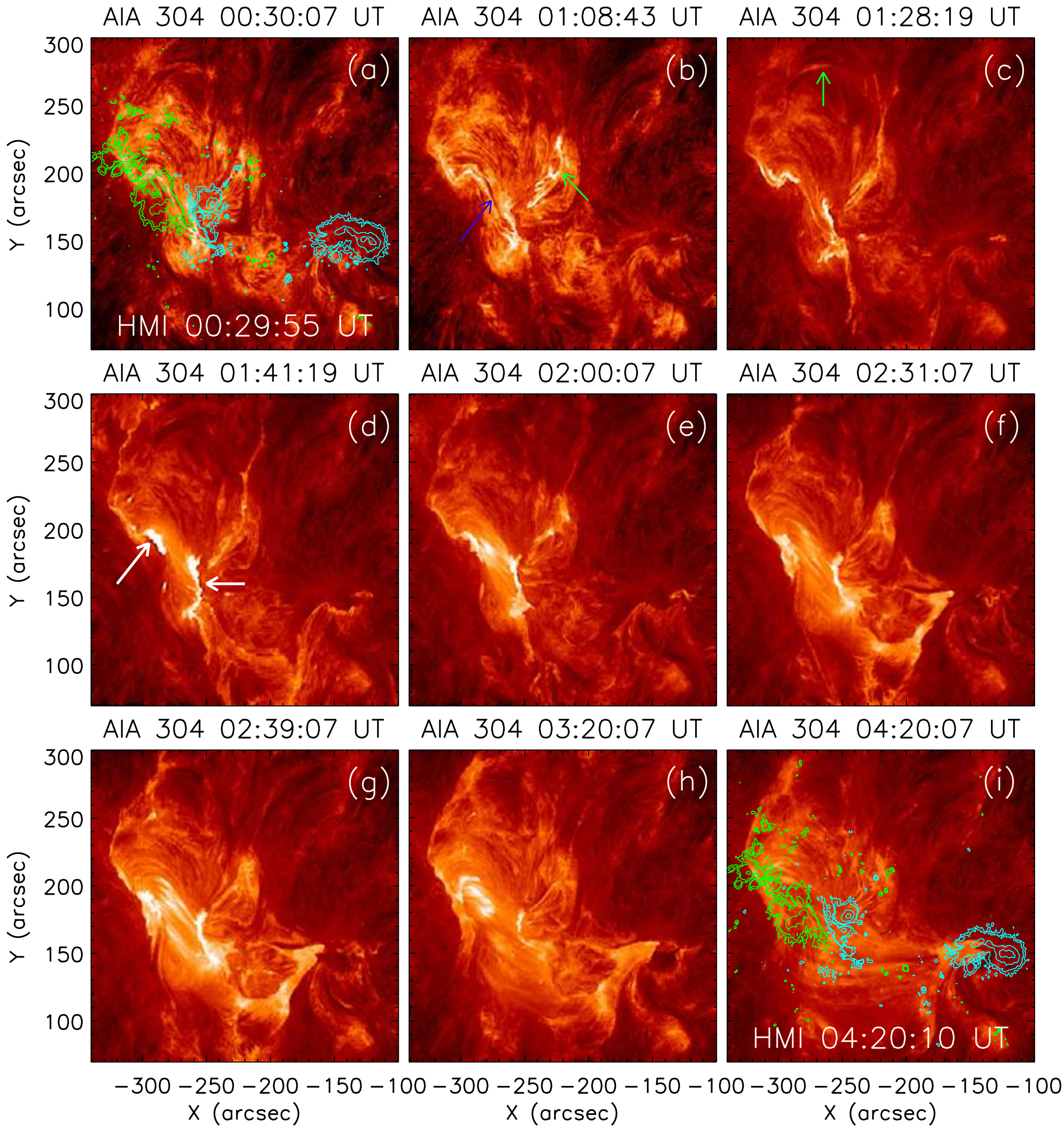

Figure 9 Series of AIA 304 Å images displaying different phases of the M-class flare. A filament was observed (indicated by the blue arrow in (**b**)) which was co-spatial to the hot channel (*cf.* Figure 7b). The remote brightening and the moving flash are indicated by the green arrow in (**b**) and (**c**), respectively. The white arrows in (**d**) mark the two flare ribbons during the impulsive phase of the flare. Co-temporal HMI LOS magnetogram contours are overplotted in (**a**) and (**i**) at $\pm(500, 800, 1500, 2000)$ G. Green and sky contours refer to positive and negative polarity, respectively. All the images are derotated to 21 Jun 2015 00:30 UT.

decay while the negative flux increased initially up to $\approx$00:25 UT and decayed gradually thereafter.

4.4. Morphology and Evolution of Photospheric Longitudinal Current

Electric current density on the photosphere, being a direct consequence of flux emergence and decay as well as photospheric motions, is expected to provide important insights toward understanding the onset of flares. The longitudinal component of current density (j_z) on the photosphere can be calculated from horizontal components of magnetic field (B_x and B_y)

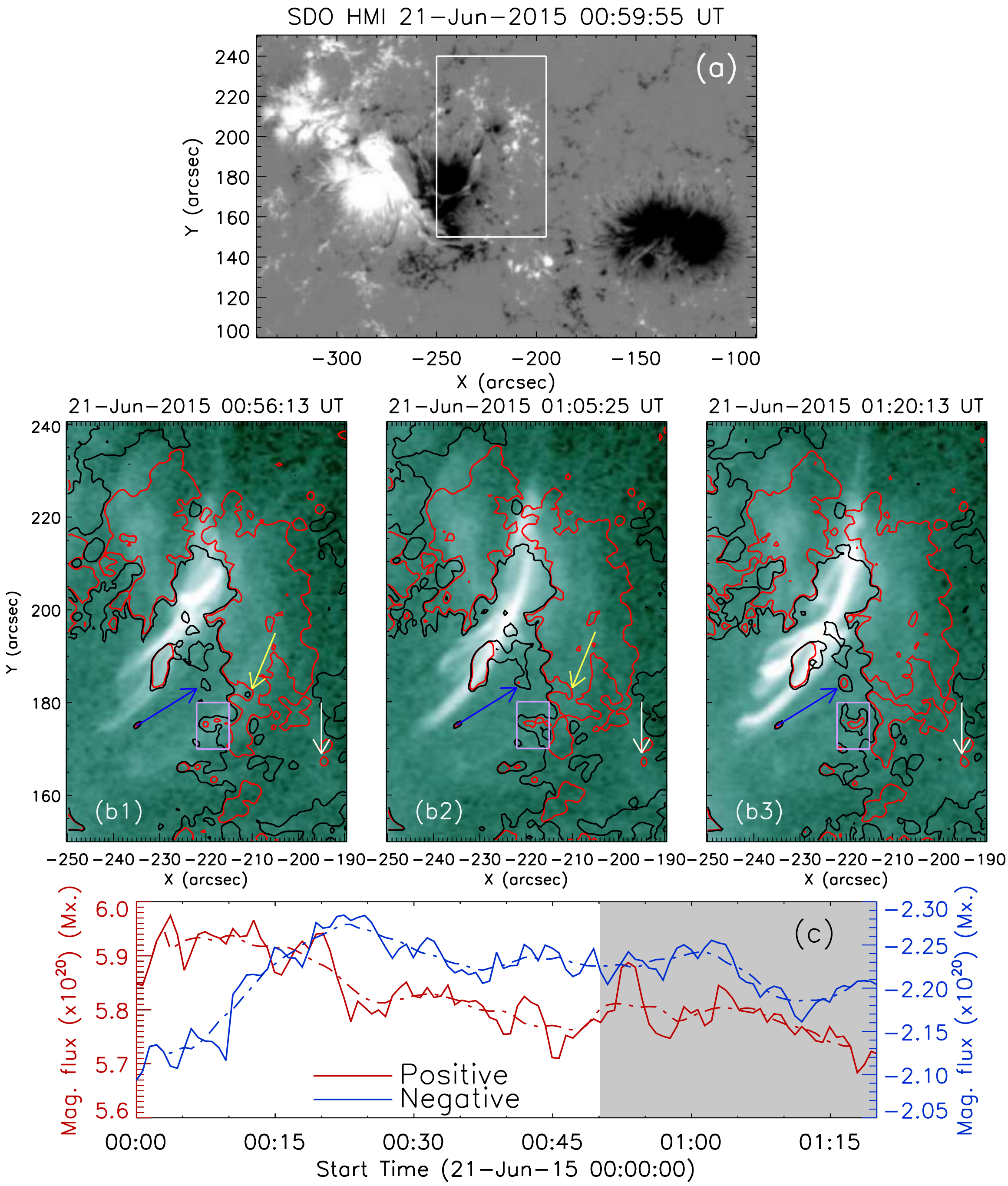

Figure 10 (**a**): HMI LOS magnetogram of AR 12371 prior to the onset of the M-class flare reported in this article. The box in (**a**) outlines the region that displayed small-scale magnetic field changes along with MMFs. (**b1**) – (**b3**): AIA 94 Å images of the region, shown within the box in (**a**), are overplotted with co-temporal LOS magnetograms. Black and red contours refer to negative and positive polarities, respectively. Contour levels are ±25 G. The arrows and the boxes in these panels indicate different instances of flux emergence and decay in this region prior to the triggering of the flare. All the images in (**a**) and (**b1**) – (**b3**) are derotated to 21 Jun 2015 01:00 UT. In (**c**), we display the variation of magnetic flux in the region within the box in (**a**) on 21 Jun 2015 from 00:00 UT up to the onset of the flare at ≈ 01:20 UT. The shaded region in (**c**) denotes the interval of precursor enhancements observed in GOES SXR channels.

using Ampere's law (Tan *et al.*, 2006; Kontogiannis *et al.*, 2017):

$$j_z = \frac{1}{\mu_\circ}\left(\frac{\mathrm{d}B_y}{\mathrm{d}x} - \frac{\mathrm{d}B_x}{\mathrm{d}y}\right) \quad (1)$$

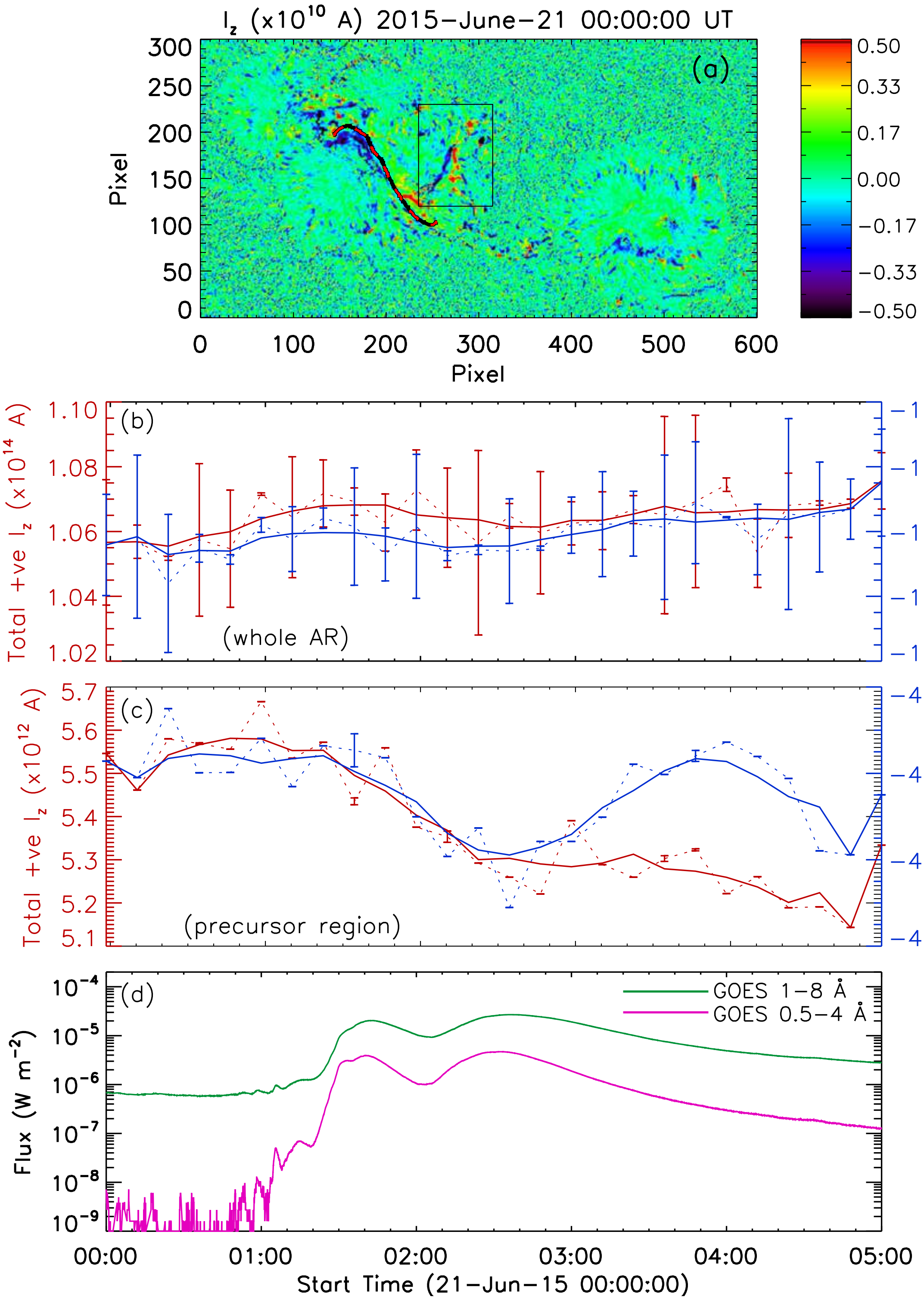

Figure 11 (**a**): Distribution of longitudinal component of the photospheric current in AR 12371 on 21 June 2015 00:00 UT. The region associated with precursor brightening is enclosed by the box in (**a**). Note that, for better visualisation, we have saturated the I_z values at $\pm 0.5 \times 10^{10}$ A in (**a**). The approximate location of the hot channel is indicated by the red-black dashed line in (**a**). In (**b**) and (**c**), we plot the variation of vertical component of photospheric current within the entire AR and within the box in (**a**), respectively. The vertical bars represent 1σ uncertainty in the calculation. For comparison, we have plotted the variation of GOES SXR channels in (**d**).

From current density (j_z), we derive current (I_z) by multiplying j_z with the area of one pixel, *i.e.* $\approx 13.14 \times 10^{10}$ m^2. In Figure 11, we plot the temporal evolution of average I_z for the overall active region (Figure 11b) as well as the location of precursor brightening (Figure 11c). From the spatial distribution of I_z prior to the hot channel activation (Figure 11a), we find large concentration of positive and negative currents along the narrow strip delineated by the PIL with the maximum and minimum values of I_z in the active region being 2.09×10^{10} A and -2.24×10^{10} A, respectively. It is noteworthy that the region displaying precursor brightenings in the corona and underlying MMFs in the photosphere exhibited a complex distribution of I_z. We have indicated this region in the box in Figure 11a and identify this as the triggering region. We find that in the overall AR, both positive and negative currents experienced a slow variation. Both the positive and negative components of I_z slowly increased during the pre-flare phase of the flare and decreased once the flare onset took place.

In Figure 12, we show the evolution of the spatial distribution of I_z in the triggering region of the AR (within the box in Figure 11a). For convenience, we have plotted GOES SXR light curves in Figure 12a where the timings of the Figures 12b – g are indicated by the vertical lines. We find that, in the triggering location, small-scale regions of both positive and negative I_z were mostly distributed randomly. However, an interesting structure of the shape “A” formed by I_z was very clear in the region during the pre-flare phase (outlined by pink–black dashed lines in Figure 12b). In the “A” shaped distribution, the left arm was completely made of negative I_z while the right arm was consisted of the positive I_z in the northern part and negative I_z in the southern part. The connecting part of the arms in the “A” was consisted of positive I_z. During the SXR precursor enhancement, in the northern tip of the structure (outlined by the oval shape in Figures 12b – g), I_z of opposite polarities became very close to each other (Figures 12b and c) which may be ideal for dissipation of current in the form of magnetic reconnection. As Figures 12d – g suggest, with the evolution of the flare, strength of I_z at the tip of the “A” significantly decreased and the left arm of the “A” became fragmented (see region inside the box in Figures 12b – g). We spotted another interesting feature from Figures 12b – g in the form of appearance and decay of a positive current region which we indicate by the black arrows.

5. Nonlinear Force Free Field Extrapolation Results

5.1. Modelled Coronal Magnetic Configuration

In order to understand the coronal connectivities between the photospheric magnetic polarities of the AR, we performed a nonlinear force-free field (NLFFF) extrapolation. For the purpose, we selected an HMI magnetogram at 01:00 UT on 21 June 2015 which represents the photospheric configuration prior to the onset of eruption (Figure 13a). In Figures 13b and c, we display different sets of NLFFF lines associated with the trailing sunspot group, from top and side views, respectively. The NLFFF extrapolation results readily suggest the presence of an extended flux rope (shown by sky-coloured lines) over the PIL which was enveloped by a set of low coronal closed loops (shown by blue lines) connecting the opposite polarity regions of the trailing sunspot group. Importantly, the modelled flux rope is situated at the same location where the hot coronal channel was identified in the AIA images (*cf.* Figure 13b and 7a). The coronal configuration associated with the precursor brightening region is displayed by the pink lines in Figure 13. Further, we identified a set of closed field lines (shown by the yellow lines) connecting the opposite polarity regions in the trailing

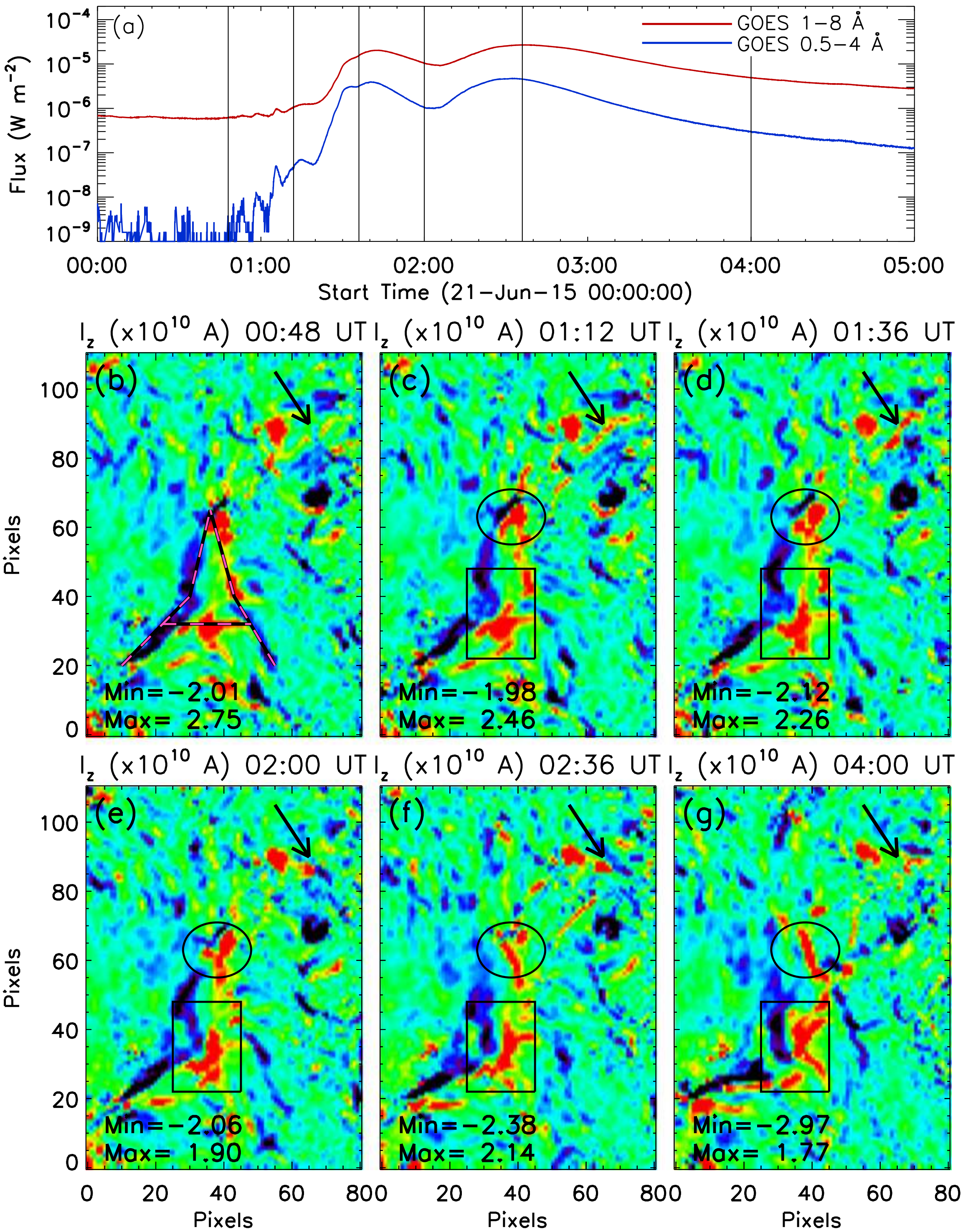

Figure 12 (**a**): GOES SXR light curves showing the evolution of the M-class flare. In (**b**) – (**g**), we plot the distribution of vertical component of photospheric current over the region shown within the box in Figure 11a at six different times as indicated by the black lines in (**a**). Notably, on a whole, few regions of strong current of opposite polarity constitute a structure similar to the letter "A" which is outlined by the black-pink dashed lines in (**b**). We highlight few major changes in the distribution of current by the arrow, oval and box in (**c**) – (**g**). For better visualisation, values of I_z are saturated at $\pm 0.5 \times 10^{10}$ A. Maximum and minimum values of I_z with order of 10^{10} A within the selected FOV are indicated in each of these panels.

sunspot group, a part of which are situated at a very close proximity to the pink lines (see Figure 13c). Notably, the anti-clockwise motion of the brightness from the precursor location, clearly revealed by the time-slice diagram shown in Figure 8a, matches reasonably well

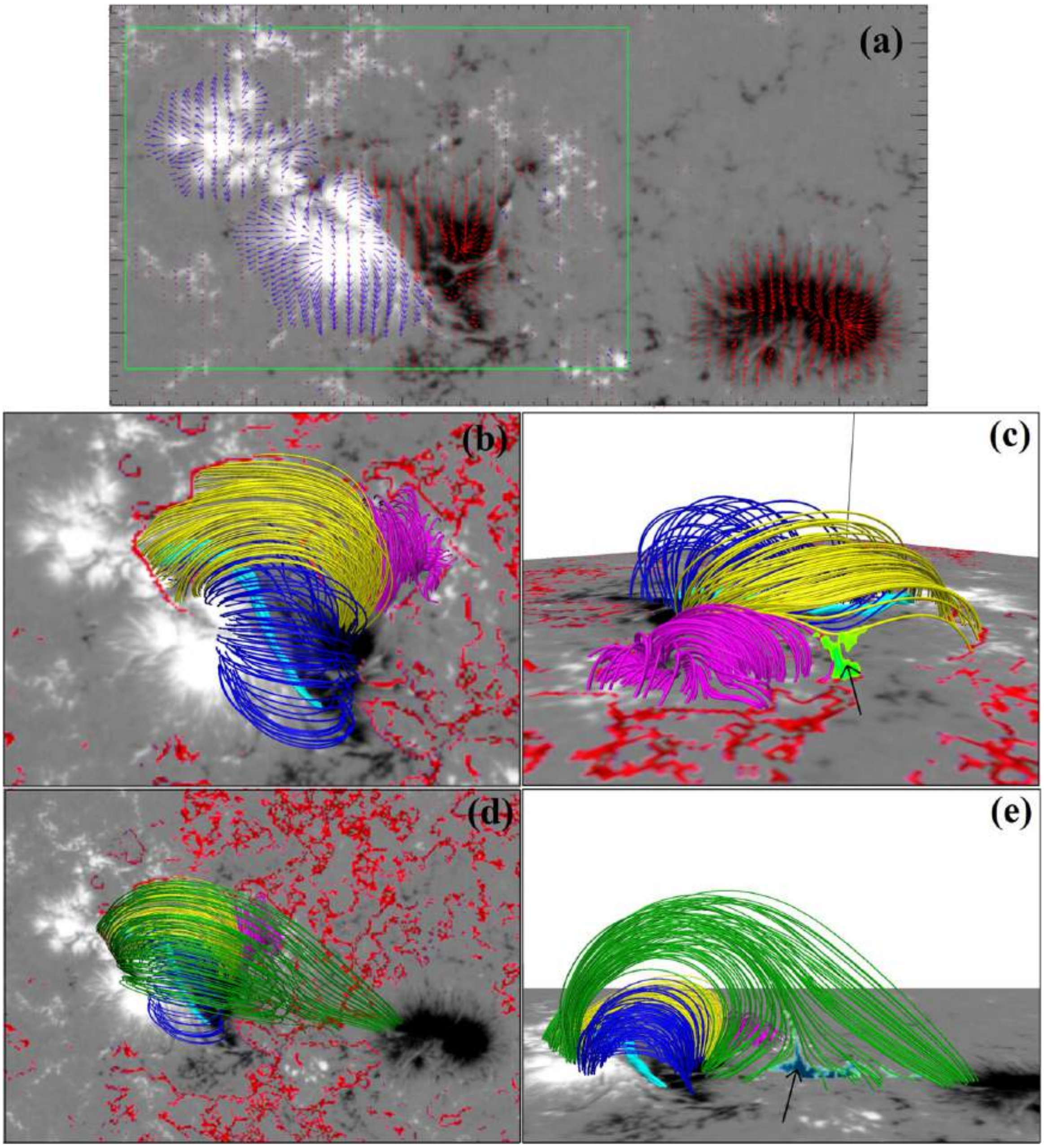

Figure 13 (**a**): CEA projected vertical component (B_z) of the HMI vector magnetogram of the AR NOAA 12371 at 01:00 UT on 21 June 2015. Blue and red arrows over the magnetogram indicate the horizontal component of magnetic field associated with positive and negative (B_z), respectively. (**b**) – (**e**): Modelled coronal magnetic configuration based on the NLFFF extrapolation results of the vector magnetogram shown in (**a**). Different sets of NLFFF field lines associated with the trailing sunspot group, *i.e.* within the green box in (**a**), from top and side views, are shown in (**b**) and (**c**), respectively. The neon-green coloured region (also marked by the black arrow) indicate regions characterised by $\log(Q) > 9$. In (**d**) and (**e**), we show the top and side view of the model lines in the whole FOV as in (**a**). The blue regions (also marked by the black arrow) in (**d**) indicate a region possessing high Q value ($\log(Q) > 8$). The background white boundary behind the green lines in (**d**) direct to the north. In all the panels, photospheric regions shown by a red colour are characterised by $\log(Q) > 7$.

with the footpoints of the yellow lines. We also note that a few of the yellow and pink lines displayed a drastic change in the field-line linkage. In literature, such structures are termed quasi-separatrix layers (QSLs) and are characterised by high squashing factor (Q; see, Priest and Démoulin, 1995). The Q value of this region is found to be higher than 10^9 (shown by the neon-green coloured patch and the black arrow in Figure 13c).

To have a further insight of the anti-clockwise motion of the brightening prior to the eruption of the hot channel, we show the photospheric regions with a Q value greater than 10^7 by a red colour in Figures 13b – e. We find that the footpoints of the yellow lines perfectly match with regions of high Q values (Figure 13c) which implies that the anti-clockwise motion of brightness from the precursor location was a slipping reconnection (see *e.g.*, Démoulin *et al.*, 1997; Craig and Effenberger, 2014; Janvier *et al.*, 2016).

In Figures 13d and e, we display the coronal connectivities in the whole AR from top and side views, respectively. We note the presence of large coronal loops that connected the positive regions of the trailing sunspot group to the leading negative sunspot group (shown by green lines in Figure 13d – e). Also, a part of the green lines originating at the positive polarity region were connected with the adjacent negative polarity region of the same sunspot group. These two sets of green lines constituted a second QSL ($\log(Q) > 8$) which we have indicated by a black arrow and the blue coloured patch in Figure 13d. The observations of spatial progression of brightness within the same region (Figures 7f – g, 9f – h and animation associated with Figure 6) are consistent with the scenario of slipping reconnection. Interestingly, the same region of high Q value was associated with a large-scale slipping reconnection event during the M-class flare on 22 June 2015 (Jing *et al.*, 2017) which implies that the large-scale magnetic structure associated with the active region remained preserved on the next day despite the eruption of a halo CME on 21 June 2015.

5.2. Evolution of Magnetic Free Energy

The magnetic free energy (E_{F}) associated with an AR is important in order to understand the energy budget of the flares originated from that AR. E_{F} can be estimated by the formula

$$E_{\mathrm{F}} = E_{\mathrm{N}} - E_{\mathrm{P}} = \int_v \frac{{B_{\mathrm{N}}}^2}{8\pi}\,\mathrm{d}v - \int_v \frac{{B_{\mathrm{P}}}^2}{8\pi}\,\mathrm{d}v \tag{2}$$

where E_{N} and E_{P} are non-potential energy and potential energy, respectively. We have calculated magnetic energy stored in the active region NOAA 12371 by employing the magnetic virial theorem (Klimchuk, Canfield, and Rhoads, 1992). According to this theorem, the magnetic energy stored in a coronal force-free magnetic field is given by the surface integral at the photospheric boundary involving the three vector magnetic field components, *i.e.*

$$E = \frac{1}{4\pi}\int_{z=0} (x B_{\mathrm{x}} + y B_{\mathrm{y}}) B_{\mathrm{z}}\,\mathrm{d}x\,\mathrm{d}y \tag{3}$$

where B_{x}, B_{y}, and B_{z} are the x-, y-, and z-components of the photospheric magnetic field, respectively. We obtained the 3 components of photospheric magnetic field from the vector magnetograms of the “hmi.sharp_cea_720s” series. The magnetograms were then preprocessed as described in Wiegelmann, Inhester, and Sakurai (2006). We plot the evolution of the free magnetic energy stored in the AR NOAA 12371 normalised by the corresponding potential energy in Figure 14a during the most active phase of AR 12371 (20 – 22 June, 2015). For reference, we have plotted GOES 1 – 8 Å SXR flux for the whole duration in Figure 14b. In this duration, the AR produced 3 M-class flares: class M1.0 on 20 June, class M2.6 on 21 June and class M6.5 on 22 June (see Table 1). From Figure 14a, we find that prior to the M2.6 and M6.5 class flares, magnetic free energy in the AR 12371 was over 80% of the corresponding potential energy. After both the flares, free energy decreased and reached local minima at $\approx 57\%$ and $\approx 65\%$ of the corresponding potential energies, respectively. Interestingly, we did not find any significant decrease in magnetic free energy during and after the M-class flare on 20 June, neither free energy increased prior to the flare.

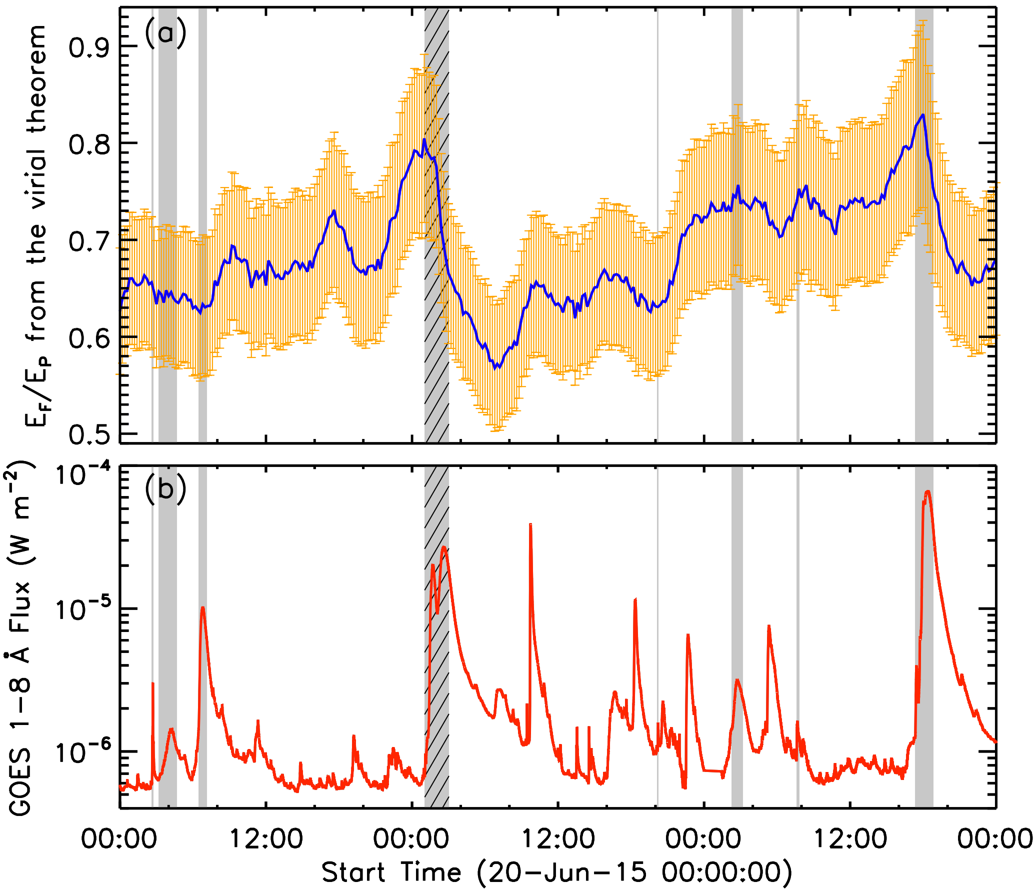

Figure 14 (**a**): Evolution of magnetic free energy during 20 – 22 June, 2015, calculated by virial theorem. 1σ error in the calculation of free energy is plotted by yellow bars. For comparison, GOES 1 – 8 Å SXR flux variation is plotted in (**b**). The shaded intervals represent the durations of C-, and M-class flares originated from AR NOAA 12371. The striped dashed interval indicates the duration of the flare reported in this article.

6. Discussion

We present a multi-wavelength analysis of the flux rope eruption on 21 June 2015 from the active region NOAA 12371 with a particular emphasis on its triggering mechanism. The automated catalogue of GOES flares[3] has enrolled two flares on 21 June 2015. However, from the evolution of the active region from the hot channel to the formation of large post-flare arcade during the two GOES peaks, we can convincingly call the GOES flaring events as flux rope eruption, *i.e.* a dual-peaked long duration event.

The temporal evolution of the GOES SXR flux suggests that the flare was associated with two-stage precursor emission. Comparison of GOES SXR fluxes with AIA observations confirms that both the episodes of the subtle flux enhancements prior to the flare were caused by localised brightenings in a nearby region situated to the west of the hot channel (Figures 7, 9, and 10). These localised brightenings indicate energy release at small-scale within the same active region that can provide potential trigger for eruption by destabilizing a stable MFR (Fárník, Hudson, and Watanabe, 1996; Fárník and Savy, 1998; Warren and Warshall, 2001; Fárník *et al.*, 2003; Sterling and Moore, 2005; Chifor *et al.*, 2007; Kim *et al.*, 2008; Liu *et al.*, 2009; Joshi *et al.*, 2011, 2016, 2017; Woods *et al.*, 2017; Dhara *et al.*, 2017; Woods *et al.*, 2018; Hernandez-Perez *et al.*, 2019; Mitra and Joshi, 2019). Based on

[3] See https://www.swpc.noaa.gov/products/solar-and-geophysical-activity-summary.

the location of small-scale energy release compared to main flaring event, pre-flare events can be categorized in three classes: co-spatial, adjacent/overlapping, and distant (Fárník, Hudson, and Watanabe, 1996; Fárník and Savy, 1998); the present case being an example of adjacent pre-flare activity. Further, the temporal and spatial evolution of the event suggests that pre-flare emission essentially acted as the precursor to the main eruption.

An important aspect of this study is to investigate the origin of the pre-flare activities and their spatial relation with the eruption of the MFR. NLFFF extrapolation results (Figure 13) suggests that the triggering region, (*i.e.* the region of precursor activity) was associated with coronal magnetic loops with high shear (pink lines in Figure 13). Zhang (1995) demonstrated that sheared magnetic field leads to the formation of electric current on the photosphere which can be accompanied by flares. Tan *et al.* (2006) investigated evolution of photospheric current during two flares of classes M1.0 and M8.7 occurring from two different ARs. Although both ARs were subjected to rapid flux emergence, the two flares differed significantly in the evolution of photospheric longitudinal current. Their analysis revealed that, for the M1.0 flare, the longitudinal electric current density dropped rapidly; while it increased for the case of the M8.7 flare. They concluded rapid emergence of current carrying flux to be responsible for the increasing longitudinal current during the M8.7 flare while their explanation for the decrease of electric current for the M1.0 flare the was dissipation of magnetic free energy in the solar atmosphere. Our analysis suggests that in the triggering location, a few localized regions with high values of vertical component of photospheric electric current with opposite polarities were situated very close to each other (Figure 12). During the GOES pre-flare peaks, one particular set of regions with opposite polarity longitudinal current became adjacent to each other (within the oval in Figures 12b, c) suggesting that the initial reconnection most likely occurred from this location. Once the reconnection began, it induced further reconnection events in the nearby stressed magnetic field lines of the region resulting in the enhancement of plasma temperature. These reconnection events most likely induced a slipping reconnection in the yellow field lines (Figure 13) carrying energy from the precursor location to the northern leg of the hot channel leading to its destabilisation. The entire mechanism suggested here is analogous to the domino effect that involve a sequence of destabilising processes that eventually cause a large-scale eruption (Zuccarello, F. *et al.*, 2009).

The AR experienced significant flux emergence for ≈ 10 hrs and cancellation thereafter for ≈ 2 hrs prior to the onset of the flare (Figures 3c and d). However, GOES SXR and AIA EUV light curves suggests absence of flaring activity in the AR during this prolonged period (*cf.* Figures 3c, d and e) which signifies continuous storage of magnetic energy into the flaring environment without significant dissipation by reconnection events. Therefore, the emergence of magnetic flux in the trailing sunspot region and the subsequent phase of its decay prior to the onset of the flare possibly resulted in the build up of the MFR along the PIL. This is supportive of the flux cancellation model proposed by van Ballegooijen and Martens (1989) which states that flux cancellation at the PIL of a sheared magnetic arcade leads to the formation of MFRs. The build up of the MFR over the PIL in the trailing sunspot group of AR 12371 prior to the M-class flare on 21 June 2015 was observationally inferred by continuous brightening up of the hot channel as observed in AIA 94 Å channel images (Figure 7a – c). Our analysis suggests that the hot channel continued to acquire the magnetic field and stress in response to the flux cancellation for an elongated period of time during the pre-flare phase. As a result, the MFR had already reached to a meta-stable state prior to the onset of the flare which allowed immediate eruption of it once triggered by the slipping reconnection. This type triggering can be explained by the "tether-weakening" model proposed by Moore and Roumeliotis (1992). According to this model, a meta-stable flux rope can be triggered by activities occurring adjacent to it, *i.e.* off the main PIL (see *e.g.,* Sterling, Harra, and Moore, 2007; Yang and Chen, 2019).

It is very interesting to note that the flare originated from the same AR on the next day, (*i.e.* 22 June 2015) proceeded with the formation and eruption of a hot channel from the trailing sunspot group (see Cheng and Ding, 2016; Wang *et al.*, 2017; Awasthi *et al.*, 2018), similar to the AIA observations of the M-class flare on 21 June, being investigated here. Also, in both the cases, the flux rope eruptions resulted into halo CMEs. However, the underlying flux rope structure of the hot channel bore differences between the events of 21 June and 22 June. By employing NLFFF extrapolation technique, Awasthi *et al.* (2018) observed multiple braided flux ropes with different degrees of coherency over the PIL during the pre-flare phase, which were separated in height. They also found evidence of small-scale reconnection events among the different flux rope branches which resulted into further braiding among the flux rope threads. While Awasthi *et al.* (2018) found the internal structure of the MFR on 22 June 2015 to be complex braided magnetic field, our result suggests coherent twisted field as the structure of the MFR. Further, there seems to have differences in the time-sequence and activities associated with the early stages of the MFR activation. Using high resolution observations of the precursor phase of the M6.5 flare on 22 June 2015 from the 1.6-m *New Solar Telescope*, Wang *et al.* (2017) found two episodes of small-scale precursor brightening at the magnetic channel prior to the large-scale eruption of the MFR. Based on these observations, they concluded that low-atmospheric small-scale energy release events possibly triggered the eruption which supports the model proposed by Kusano *et al.* (2012).

During the build up of the flux rope in the trailing sunspot prior to the M-class flare on 21 June, magnetic free energy stored in the AR increased significantly for a period of ≈ 5 hours which drastically reduced during the flare (Figure 14). The M-class flare occurring on the next day from the same AR was subjected to similar type of magnetic energy evolution. These results clearly refer to a direct correlation between accumulation of free energy in the AR and build up of MFR with excess free energy in the form of their twisted (or, braided) magnetic structures.

In summary, the AR NOAA 12371 went through an elaborate phase of flux enhancement followed by a duration of significant flux cancellation which led to build up of an MFR along the PIL in the trailing sunspot group. The AR was associated with highly dynamical features including photospheric motions (*i.e.* MMFs) and rotation which led to formation of localized regions of high photospheric current densities. Two well identified precursor events preceded the flux rope activation. The precursor region, spatially separated from the location of the MFR, exhibited strong photospheric longitudinal currents of opposite polarities in very close proximity and was connected directly to the MFR through magnetic loops. More importantly, we found evidence for slipping reconnection from the precursor region to the flux rope activation site which eventually destabilised the quasi-evolving MFR, resulting a halo CME and M-class flaring activities. Our study especially addresses the build-up phase of the MFR and the role of precursor activities toward driving the eruption. In future, we aim to study the slipping reconnection in the context of physical processes during the pre-flare and early flare evolution.

Acknowledgements The authors would like to thank the SDO and RHESSI teams for their open data policy. SDO is NASA's mission under the Living With a Star (LWS) program. RHESSI was the sixth mission in the SMall EXplorer (SMEX) program of NASA. The authors are also thankful to Dr. Thomas Wiegelmann for providing the NLFFF code. AP acknowledges partial support of NASA grant 80NSSC17K0016 and NSF award AGS-1650854. We also acknowledge the constructive comments and useful suggestions of the anonymous referee, which improved the presentation and scientific content of the article.

Disclosure of Potential Conflicts of Interest The authors declare that they have no conflict of interest.

Publisher's Note Springer Nature remains neutral with regard to jurisdictional claims in published maps and institutional affiliations.

References

Awasthi, A.K., Liu, R., Wang, H., Wang, Y., Shen, C.: 2018, Pre-eruptive magnetic reconnection within a multi-flux-rope system in the solar corona. *Astrophys. J.* **857**(2), 124. DOI. ADS.

Benz, A.O.: 2017, Flare observations. *Living Rev. Solar Phys.* **14**, 2. DOI. ADS.

Bi, Y., Yang, J., Jiang, Y., Hong, J., Xu, Z., Qu, Z., Ji, K.: 2017, The photospheric vortex flows during a solar flare. *Astrophys. J. Lett.* **849**(2), L35. DOI. ADS.

Carmichael, H.: 1964, A process for flares. *NASA Spec. Publ.* **50**, 451. ADS.

Cheng, X., Ding, M.D.: 2016, Spectroscopic diagnostics of solar magnetic flux ropes using iron forbidden line. *Astrophys. J. Lett.* **823**(1), L4. DOI. ADS.

Cheng, X., Zhang, J., Ding, M.D., Liu, Y., Poomvises, W.: 2013, The driver of coronal mass ejections in the low corona: a flux rope. *Astrophys. J.* **763**, 43. DOI. ADS.

Cheng, X., Ding, M.D., Zhang, J., Sun, X.D., Guo, Y., Wang, Y.M., Kliem, B., Deng, Y.Y.: 2014a, Formation of a double-decker magnetic flux rope in the sigmoidal solar active region 11520. *Astrophys. J.* **789**(2), 93. DOI. ADS.

Cheng, X., Ding, M.D., Zhang, J., Srivastava, A.K., Guo, Y., Chen, P.F., Sun, J.Q.: 2014b, On the relationship between a hot-channel-like solar magnetic flux rope and its embedded prominence. *Astrophys. J. Lett.* **789**, L35. DOI. ADS.

Chifor, C., Mason, H.E., Tripathi, D., Isobe, H., Asai, A.: 2006, The early phases of a solar prominence eruption and associated flare: a multi-wavelength analysis. *Astron. Astrophys.* **458**, 965. DOI. ADS.

Chifor, C., Tripathi, D., Mason, H.E., Dennis, B.R.: 2007, X-ray precursors to flares and filament eruptions. *Astron. Astrophys.* **472**, 967. DOI. ADS.

Clyne, J., Mininni, P., Norton, A., Rast, M.: 2007, Interactive desktop analysis of high resolution simulations: application to turbulent plume dynamics and current sheet formation. *New J. Phys.* **9**(8), 301. http://stacks.iop.org/1367-2630/9/i=8/a=301.

Craig, I.J.D., Effenberger, F.: 2014, Current singularities at quasi-separatrix layers and three-dimensional magnetic nulls. *Astrophys. J.* **795**(2), 129. DOI. ADS.

Démoulin, P., Bagala, L.G., Mandrini, C.H., Henoux, J.C., Rovira, M.G.: 1997, Quasi-separatrix layers in solar flares. II. Observed magnetic configurations. *Astron. Astrophys.* **325**, 305. ADS.

Dhara, S.K., Belur, R., Kumar, P., Banyal, R.K., Mathew, S.K., Joshi, B.: 2017, Trigger of successive filament eruptions observed by sdo and stereo. *Solar Phys.* **292**(10), 145. DOI.

Engvold, O.: 1997, In: Mouradian, Z., Stavinschi, M. (eds.) *Filament Channels in the Corona*, Springer, Dordrecht, 125. 978-94-011-5492-5. DOI.

Fárník, F., Hudson, H., Watanabe, T.: 1996, Spatial relations between preflares and flares. *Solar Phys.* **165**, 169. DOI. ADS.

Fárník, F., Savy, S.K.: 1998, Soft X-ray pre-flare emission studied in Yohkoh-SXT images. *Solar Phys.* **183**, 339. DOI. ADS.

Fárník, F., Hudson, H.S., Karlický, M., Kosugi, T.: 2003, X-ray and radio observations of the activation stages of an X-class solar flare. *Astron. Astrophys.* **399**, 1159. DOI. ADS.

Fletcher, L., Dennis, B.R., Hudson, H.S., Krucker, S., Phillips, K., Veronig, A., Battaglia, M., Bone, L., Caspi, A., Chen, Q., Gallagher, P., Grigis, P.T., Ji, H., Liu, W., Milligan, R.O., Temmer, M.: 2011, An observational overview of solar flares. *Space Sci. Rev.* **159**, 19. DOI. ADS.

Gaizauskas, V., Zirker, J.B., Sweetland, C., Kovacs, A.: 1997, Formation of a solar filament channel. *Astrophys. J.* **479**(1), 448. DOI.

Gibson, S.E., Fan, Y.: 2006, Coronal prominence structure and dynamics: a magnetic flux rope interpretation. *J. Geophys. Res.* **111**, A12103. DOI. ADS.

Gopalswamy, N., Mäkelä, P., Akiyama, S., Yashiro, S., Xie, H., Thakur, N.: 2018, Sun-to-Earth propagation of the 2015 June 21 coronal mass ejection revealed by optical, EUV, and radio observations. *J. Atmos. Solar-Terr. Phys.* **179**, 225. DOI. ADS.

Hernandez-Perez, A., Su, Y., Veronig, A.M., Thalmann, J., Gömöry, P., Joshi, B.: 2019, Pre-eruption processes: heating, particle acceleration, and the formation of a hot channel before the 2012 October 20 M9.0 limb flare. *Astrophys. J.* **874**, 122. DOI. ADS.

Hirayama, T.: 1974, Theoretical model of flares and prominences. *Solar Phys.* **34**(2), 323. DOI.

Hurford, G.J., Schmahl, E.J., Schwartz, R.A., Conway, A.J., Aschwanden, M.J., Csillaghy, A., Dennis, B.R., Johns-Krull, C., Krucker, S., Lin, R.P., McTiernan, J., Metcalf, T.R., Sato, J., Smith, D.M.: 2002, The RHESSI imaging concept. *Solar Phys.* **210**(1), 61. DOI. ADS.

Janvier, M., Savcheva, A., Pariat, E., Tassev, S., Millholland, S., Bommier, V., McCauley, P., McKillop, S., Dougan, F.: 2016, Evolution of flare ribbons, electric currents, and quasi-separatrix layers during an X-class flare. *Astron. Astrophys.* **591**, A141. DOI. ADS.

Jing, J., Liu, R., Cheung, M.C.M., Lee, J., Xu, Y., Liu, C., Zhu, C., Wang, H.: 2017, Witnessing a large-scale slipping magnetic reconnection along a dimming channel during a solar flare. *Astrophys. J. Lett.* **842**(2), L18. DOI. ADS.

Joshi, B., Veronig, A.M., Lee, J., Bong, S.-C., Tiwari, S.K., Cho, K.-S.: 2011, Pre-flare activity and magnetic reconnection during the evolutionary stages of energy release in a solar eruptive flare. *Astrophys. J.* **743**, 195. DOI. ADS.

Joshi, B., Kushwaha, U., Veronig, A.M., Cho, K.-S.: 2016, Pre-flare coronal jet and evolutionary phases of a solar eruptive prominence associated with the M1.8 flare: SDO and RHESSI observations. *Astrophys. J.* **832**, 130. DOI. ADS.

Joshi, B., Kushwaha, U., Veronig, A.M., Dhara, S.K., Shanmugaraju, A., Moon, Y.-J.: 2017, Formation and eruption of a flux rope from the sigmoid active region NOAA 11719 and associated M6.5 flare: a multi-wavelength study. *Astrophys. J.* **834**, 42. DOI. ADS.

Joshi, B., Ibrahim, M.S., Shanmugaraju, A., Chakrabarty, D.: 2018, A major geoeffective CME from NOAA 12371: initiation, CME-CME interactions, and interplanetary consequences. *Solar Phys.* **293**, 107. DOI. ADS.

Kim, S., Moon, Y.-J., Kim, Y.-H., Park, Y.-D., Kim, K.-S., Choe, G.S., Kim, K.-H.: 2008, Preflare eruption triggered by a tether-cutting process. *Astrophys. J.* **683**(1), 510. DOI. ADS.

Klimchuk, J.A., Canfield, R.C., Rhoads, J.E.: 1992, The practical application of the magnetic virial theorem. *Astrophys. J.* **385**, 327. DOI. ADS.

Kontogiannis, I., Georgoulis, M.K., Park, S.-H., Guerra, J.A.: 2017, Non-neutralized electric currents in solar active regions and flare productivity. *Solar Phys.* **292**(11), 159. DOI.

Kopp, R.A., Pneuman, G.W.: 1976, Magnetic reconnection in the corona and the loop prominence phenomenon. *Solar Phys.* **50**, 85. DOI. ADS.

Kuroda, N., Gary, D.E., Wang, H., Fleishman, G.D., Nita, G.M., Jing, J.: 2018, Three-dimensional forward-fit modeling of the hard X-ray and microwave emissions of the 2015 June 22 M6.5 flare. *Astrophys. J.* **852**(1), 32. DOI. ADS.

Kusano, K., Bamba, Y., Yamamoto, T.T., Iida, Y., Toriumi, S., Asai, A.: 2012, Magnetic field structures triggering solar flares and coronal mass ejections. *Astrophys. J.* **760**(1), 31. DOI. ADS.

Lee, J., White, S.M., Jing, J., Liu, C., Masuda, S., Chae, J.: 2017, Thermal and nonthermal emissions of a composite flare derived from NoRH and SDO observations. *Astrophys. J.* **850**(2), 124. DOI. ADS.

Lee, J., White, S.M., Liu, C., Kliem, B., Masuda, S.: 2018, Magnetic structure of a composite solar microwave burst. *Astrophys. J.* **856**(1), 70. DOI. ADS.

Lemen, J.R., Title, A.M., Akin, D.J., Boerner, P.F., Chou, C., Drake, J.F., Duncan, D.W., Edwards, C.G., Friedlaender, F.M., Heyman, G.F., Hurlburt, N.E., Katz, N.L., Kushner, G.D., Levay, M., Lindgren, R.W., Mathur, D.P., McFeaters, E.L., Mitchell, S., Rehse, R.A., Schrijver, C.J., Springer, L.A., Stern, R.A., Tarbell, T.D., Wuelser, J.-P., Wolfson, C.J., Yanari, C., Bookbinder, J.A., Cheimets, P.N., Caldwell, D., Deluca, E.E., Gates, R., Golub, L., Park, S., Podgorski, W.A., Bush, R.I., Scherrer, P.H., Gummin, M.A., Smith, P., Auker, G., Jerram, P., Pool, P., Soufli, R., Windt, D.L., Beardsley, S., Clapp, M., Lang, J., Waltham, N.: 2012, The Atmospheric Imaging Assembly (AIA) on the Solar Dynamics Observatory (SDO). *Solar Phys.* **275**, 17. DOI. ADS.

Lin, R.P., Dennis, B.R., Hurford, G.J., Smith, D.M., Zehnder, A., Harvey, P.R., Curtis, D.W., Pankow, D., Turin, P., Bester, M., Csillaghy, A., Lewis, M., Madden, N., van Beek, H.F., Appleby, M., Raudorf, T., McTiernan, J., Ramaty, R., Schmahl, E., Schwartz, R., Krucker, S., Abiad, R., Quinn, T., Berg, P., Hashii, M., Sterling, R., Jackson, R., Pratt, R., Campbell, R.D., Malone, D., Landis, D., Barrington-Leigh, C.P., Slassi-Sennou, S., Cork, C., Clark, D., Amato, D., Orwig, L., Boyle, R., Banks, I.S., Shirey, K., Tolbert, A.K., Zarro, D., Snow, F., Thomsen, K., Henneck, R., McHedlishvili, A., Ming, P., Fivian, M., Jordan, J., Wanner, R., Crubb, J., Preble, J., Matranga, M., Benz, A., Hudson, H., Canfield, R.C., Holman, G.D., Crannell, C., Kosugi, T., Emslie, A.G., Vilmer, N., Brown, J.C., Johns-Krull, C., Aschwanden, M., Metcalf, T., Conway, A.: 2002, The Reuven Ramaty High-Energy Solar Spectroscopic Imager (RHESSI). *Solar Phys.* **210**, 3. DOI. ADS.

Liu, W., Wang, T.-J., Dennis, B.R., Holman, G.D.: 2009, Episoidic X-ray emmision accompanying the activation of an eruptive prominence: evidence of episodic magnetic reconnection. *Astrophys. J.* **698**(1), 632. DOI.

Liu, R., Kliem, B., Titov, V.S., Chen, J., Wang, Y., Wang, H., Liu, C., Xu, Y., Wiegelmann, T.: 2016, Structure, stability, and evolution of magnetic flux ropes from the perspective of magnetic twist. *Astrophys. J.* **818**(2), 148. DOI. ADS.

Liu, R., Wang, Y., Lee, J., Shen, C.: 2019, Impacts of EUV wavefronts on coronal structures in homologous coronal mass ejections. *Astrophys. J.* **870**(1), 15. DOI. ADS.

Manoharan, P.K., van Driel-Gesztelyi, L., Pick, M., Démoulin, P.: 1996, Evidence for large-scale solar magnetic reconnection from radio and X-ray measurements. *Astrophys. J. Lett.* **468**, L73. DOI. ADS.

Manoharan, P.K., Maia, D., Johri, A., Induja, M.S.: 2016, Interplanetary consequences of coronal mass ejection events occurred during 18 – 25 June 2015. In: Dorotovic, I., Fischer, C.E., Temmer, M. (eds.) *Coimbra Solar Physics Meeting: Ground-Based Solar Observations in the Space Instrumentation Era*, *Astronomical Society of the Pacific Conference Series* **504**, 59. ADS.

Martin, S.F.: 1998, Conditions for the formation and maintenance of filaments (Invited Review). *Solar Phys.* **182**(1), 107. DOI. ADS.

Martres, M., Michard, R.: 1966, Soru-iscovici. *Ann. Astrophys.* **29**, 249.

Mitra, P.K., Joshi, B.: 2019, Preflare processes, flux rope activation, large-scale eruption, and associated X-class flare from the active region NOAA 11875. *Astrophys. J.* **884**(1), 46. DOI. ADS.

Mitra, P.K., Joshi, B., Prasad, A., Veronig, A.M., Bhattacharyya, R.: 2018, Successive flux rope eruptions from δ-sunspots region of NOAA 12673 and associated X-class eruptive flares on 2017 September 6. *Astrophys. J.* **869**(1), 69.

Moore, R.L., Roumeliotis, G.: 1992, Triggering of eruptive flares – destabilization of the preflare magnetic field configuration. In: Svestka, Z., Jackson, B.V., Machado, M.E. (eds.) *IAU Colloq. 133: Eruptive Solar Flares*, *Lecture Notes in Physics, Berlin Springer Verlag* **399**, 69. DOI. ADS.

Nindos, A., Patsourakos, S., Vourlidas, A., Tagikas, C.: 2015, How common are hot magnetic flux ropes in the low solar corona? A statistical study of EUV observations. *Astrophys. J.* **808**(2), 117. DOI.

Parenti, S.: 2014, Solar prominences: observations. *Living Rev. Solar Phys.* **11**(1), 1. DOI.

Pesnell, W.D., Thompson, B.J., Chamberlin, P.C.: 2012, The Solar Dynamics Observatory (SDO). *Solar Phys.* **275**(1), 3. DOI.

Piersanti, M., Alberti, T., Bemporad, A., Berrilli, F., Bruno, R., Capparelli, V., Carbone, V., Cesaroni, C., Consolini, G., Cristaldi, A., Del Corpo, A., Del Moro, D., Di Matteo, S., Ermolli, I., Fineschi, S., Giannattasio, F., Giorgi, F., Giovannelli, L., Guglielmino, S.L., Laurenza, M., Lepreti, F., Marcucci, M.F., Martucci, M., Mergè, M., Pezzopane, M., Pietropaolo, E., Romano, P., Sparvoli, R., Spogli, L., Stangalini, M., Vecchio, A., Vellante, M., Villante, U., Zuccarello, F., Heilig, B., Reda, J., Lichtenberger, J.: 2017, Comprehensive analysis of the geoeffective solar event of 21 June 2015: effects on the magnetosphere, plasmasphere, and ionosphere systems. *Solar Phys.* **292**(11), 169. DOI. ADS.

Priest, E.R., Démoulin, P.: 1995, Three-dimensional magnetic reconnection without null points: 1. Basic theory of magnetic flipping. *J. Geophys. Res.* **100**(A12), 23443. DOI.

Rust, D.M., Kumar, A.: 1996, Evidence for helically kinked magnetic flux ropes in solar eruptions. *Astrophys. J. Lett.* **464**, L199. DOI. ADS.

Schou, J., Scherrer, P.H., Bush, R.I., Wachter, R., Couvidat, S., Rabello-Soares, M.C., Bogart, R.S., Hoeksema, J.T., Liu, Y., Duvall, T.L., Akin, D.J., Allard, B.A., Miles, J.W., Rairden, R., Shine, R.A., Tarbell, T.D., Title, A.M., Wolfson, C.J., Elmore, D.F., Norton, A.A., Tomczyk, S.: 2012, Design and ground calibration of the Helioseismic and Magnetic Imager (HMI) instrument on the Solar Dynamics Observatory (SDO). *Solar Phys.* **275**, 229. DOI. ADS.

Shibata, K.: 1996, New observational facts about solar flares from YOHKOH studies – evidence of magnetic reconnection and a unified model of flares. *Adv. Space Res.* **17**(4-5), 9. DOI. ADS.

Sterling, A.C., Harra, L.K., Moore, R.L.: 2007, New evidence for the role of emerging flux in a solar filament's slow rise preceding its CME-producing fast eruption. *Astrophys. J.* **669**(2), 1359. DOI. ADS.

Sterling, A.C., Moore, R.L.: 2005, Slow-rise and fast-rise phases of an erupting solar filament, and flare emission onset. *Astrophys. J.* **630**(2), 1148. DOI.

Sturrock, P.A.: 1966, Model of the high-energy phase of solar flares. *Nature* **211**, 695. DOI. ADS.

Tan, B., Ji, H., Huang, G., Zhou, T., Song, Q., Huang, Y.: 2006, Evolution of electric currents associated with two m-class flares. *Solar Phys.* **239**(1), 137. DOI.

Tandberg-Hanssen, E.: 1995, *Physical Parameters of the Prominence Plasma*, Springer, Dordrecht, 81. 978-94-017-3396-0. DOI.

van Ballegooijen, A.A., Martens, P.C.H.: 1989, Formation and eruption of solar prominences. *Astrophys. J.* **343**, 971. DOI. ADS.

Vemareddy, P.: 2017, Successive homologous coronal mass ejections driven by shearing and converging motions in solar active region NOAA 12371. *Astrophys. J.* **845**(1), 59. DOI. ADS.

Wang, H., Liu, C., Ahn, K., Xu, Y., Jing, J., Deng, N., Huang, N., Liu, R., Kusano, K., Fleishman, G.D., Gary, D.E., Cao, W.: 2017, High-resolution observations of flare precursors in the low solar atmosphere. *Nat. Astron.* **1**, 0085. DOI. ADS.

Wang, J., Liu, C., Deng, N., Wang, H.: 2018, Evolution of photospheric flow and magnetic fields associated with the 2015 June 22 M6.5 flare. *Astrophys. J.* **853**(2), 143. DOI. ADS.

Warren, H.P., Warshall, A.D.: 2001, Ultraviolet flare ribbon brightenings and the onset of hard X-ray emission. *Astrophys. J.* **560**(1), L87. DOI.

Wiegelmann, T., Inhester, B.: 2010, How to deal with measurement errors and lacking data in nonlinear force-free coronal magnetic field modelling? *Astron. Astrophys.* **516**, A107. DOI. ADS.

Wiegelmann, T., Inhester, B., Sakurai, T.: 2006, Preprocessing of vector magnetograph data for a nonlinear force-free magnetic field reconstruction. *Solar Phys.* **233**(2), 215. DOI.

Wiegelmann, T., Thalmann, J.K., Inhester, B., Tadesse, T., Sun, X., Hoeksema, J.T.: 2012, How should one optimize nonlinear force-free coronal magnetic field extrapolations from SDO/HMI vector magnetograms? *Solar Phys.* **281**, 37. DOI. ADS.

Woods, M.M., Harra, L.K., Matthews, S.A., Mackay, D.H., Dacie, S., Long, D.M.: 2017, Observations and modelling of the pre-flare period of the 29 March 2014 X1 flare. *Solar Phys.* **292**(2), 38. DOI. ADS.

Woods, M.M., Inoue, S., Harra, L.K., Matthews, S.A., Kusano, K., Kalmoni, N.M.E.: 2018, The triggering of the 2014 March 29 filament eruption. *Astrophys. J.* **860**(2), 163. DOI. ADS.

Yang, B., Chen, H.: 2019, Filament eruption and its reformation caused by emerging magnetic flux. *Astrophys. J.* **874**(1), 96. DOI. ADS.

Zhang, H.: 1995, Formation of magnetic shear and an electric current system in an emerging flux region. *Astron. Astrophys.* **304**, 541. ADS.

Zhang, J., Cheng, X., Ding, M.-D.: 2012, Observation of an evolving magnetic flux rope before and during a solar eruption. *Nat. Commun.* **3**, 747. DOI. ADS.

Zirin, H.: 1988, *Astrophysics of the Sun*. ADS.

Zuccarello, F., Romano, P., Farnik, F., Karlicky, M., Contarino, L., Battiato, V., Guglielmino, S.L., Comparato, M., Ugarte-Urra, I.: 2009, The X17.2 flare occurred in NOAA 10486: an example of filament destabilization caused by a domino effect. *Astron. Astrophys.* **493**(2), 629. DOI.

The Astrophysical Journal, 900:23 (20pp), 2020 September 1 https://doi.org/10.3847/1538-4357/aba900

Eruptive–Impulsive Homologous M-class Flares Associated with Double-decker Flux Rope Configuration in Minisigmoid of NOAA 12673

Prabir K. Mitra[1,2], Bhuwan Joshi[1], Astrid M. Veronig[3], Ramesh Chandra[4], K. Dissauer[3,5], and Thomas Wiegelmann[6]
[1] Udaipur Solar Observatory, Physical Research Laboratory, Udaipur 313 001, India; prabir@prl.res.in
[2] Department of Physics, Gujarat University, Ahmedabad 380 009, India
[3] Institute of Physics & Kanzelhöhe Observatory, University of Graz, Universitätsplatz 5, A-8010 Graz, Austria
[4] Department of Physics, DSB Campus, Kumaun University, Nainital 263 002, India
[5] NorthWest Research Associates, 3380 Mitchell Lane, Boulder, CO 80301, USA
[6] Max-Planck-Institut für Sonnensystemforschung, Justus-von-Liebig-Weg 3, D-37077 Göttingen, Germany
Received 2020 January 15; revised 2020 July 20; accepted 2020 July 22; published 2020 August 27

Abstract

We present a multiwavelength analysis of two homologous, short-lived, impulsive flares of GOES class M1.4 and M7.3 that occurred from a very localized minisigmoid region within the active region NOAA 12673 on 2017 September 7. Both flares were associated with initial jetlike plasma ejection that for a brief amount of time moved toward the east in a collimated manner before drastically changing direction toward the southwest. Nonlinear force-free field extrapolation reveals the presence of a compact double-decker flux rope configuration in the minisigmoid region prior to the flares. A set of open field lines originating near the active region that were most likely responsible for the anomalous dynamics of the erupted plasma gave the earliest indication of an emerging coronal hole near the active region. The horizontal field distribution suggests a rapid decay of the field above the active region, implying high proneness of the flux rope system toward eruption. In view of the low coronal double-decker flux ropes and compact extreme ultraviolet brightening beneath the filament, along with associated photospheric magnetic field changes, our analysis supports the combination of initial tether-cutting reconnection and subsequent torus instability for driving the eruption.

Unified Astronomy Thesaurus concepts: Solar active region filaments (1977); Solar corona (1483); Solar activity (1475); Solar x-ray flares (1816)

Supporting material: animations

1. Introduction

Flares are transient activities occurring in the solar atmosphere in which a huge amount of energy is released within a short time, i.e., a few minutes to a few hours. Earth-directed coronal mass ejections (CMEs), along with their associated eruptive flares, are known to produce hazardous effects in the near-Earth environment and drive geomagnetic storms. Magnetic reconnection, a topological reconfiguration of the magnetic field in a plasma medium (Priest & Forbes 2000), is widely accepted to be the fundamental energy release process during solar transient activities. In the process of reconnection, magnetic energy is rapidly converted into plasma heating, bulk motions, and kinetic energy of nonthermal particles (Priest & Forbes 2002; Shibata & Magara 2011). Eruptive flares and their associated CMEs are, therefore, responsible for large-scale changes in the magnetic structure of the solar atmosphere. With a complex mechanism involving large-scale magnetic fields and its direct consequences on the Earth's atmosphere, flares and CMEs have been widely studied over the years and are still a prominent field of interest (e.g., reviews by Fletcher et al. 2011; Benz 2017; Green et al. 2018).

The "standard flare model," also known as the CSHKP model (Carmichael 1964; Sturrock 1966; Hirayama 1974; Kopp & Pneuman 1976), considers the existence of a prominence as a prerequisite for the initiation of eruptive flares. Theoretical models suggest that the basic structure of a prominence/filament is composed of magnetic flux rope (MFR), defined as a set of twisted magnetic field lines wrapped around its central axis more than once (Gibson & Fan 2006). Further, the MFR is identified as the dark cavity in the three-part structure of CMEs (e.g., Riley et al. 2008). Once the MFR is dynamically activated by external triggering or some kind of instability and set into an eruptive motion, magnetic reconnection begins in a vertical current sheet formed beneath the MFR, causing intense flare emission. The CSHKP model successfully incorporates several key features of eruptive flares: flare ribbons, loop-top and footpoint sources, hot cusp, postflare loop arcade, etc. However, the processes that are responsible for the formation of the MFR and triggering mechanisms for the eruptive flares are still important and debatable in solar physics. Also, in many eruptive flares, the spatial evolution of loop-top sources and flare ribbons during the early phases exhibits significant deviation from the classical scenario described in the CSHKP model, which points toward a much more complicated energy release process in complex magnetic configuration (e.g., Veronig et al. 2006; Joshi et al. 2009, 2017a; Dalmasse et al. 2015; Gou et al. 2017; see also review by Joshi et al. 2012).

It is essential to note that the CSHKP model is a 2D model; therefore, it is not designed to accommodate the 3D structures and configurations—e.g., sheared arcades, J-shaped flare ribbons, flux ropes, complex flare loops, etc.—that are important in the understanding of solar flares. To implement these features in a general flare model, the CSHKP model has been extended to three dimensions on the basis of a series of numerical simulations (Aulanier et al. 2012, 2013; Janvier et al. 2013, 2014). These MHD simulation results suggest that in the highly sheared preflare magnetic configuration, small-scale current sheets could be generated in the regions of high magnetic gradients, i.e., quasi-separatrix layers (Titov et al. 2002). Reconnections in these current sheets are responsible for the formation of MFRs from the sheared arcades, as well as destabilization. During the eruption of the MFRs, the inner legs of the sheared arcades that envelop the MFR straighten vertically beneath the erupting MFR and eventually reconnect, resulting in the formation of postflare arcades.

The successful eruption of an MFR is essential for generating a CME. There are two basic groups of models describing the activation and eruption of an MFR from its stable state: models invoking ideal MHD instabilities and models invoking magnetic reconnection (see, e.g., reviews by Priest & Forbes 2002; Aulanier 2014; Green et al. 2018). In the ideal instability model, a preexisting MFR can erupt if the background magnetic field displays a rapid decay with height (torus instability; Kliem & Török 2006) or the rope's twist number increases beyond a critical value (kink instability; Török et al. 2004). Two representative reconnection models, namely, tether-cutting and magnetic breakout, use different preflare magnetic configurations of the active region (AR) while describing the eruption of an MFR. The tether-cutting model requires a bipolar magnetic field configuration, with the earliest reconnection (i.e., triggering process) taking place deep in the sheared core fields (Moore & Roumeliotis 1992; Moore et al. 2001). The breakout model involves a multipolar topology containing one or more preexisting coronal null points (Karpen et al. 2012). In this case, the CME onset is triggered by reconnection occurring well above the core region that reduces the tension of the overlying field (Antiochos et al. 1999). Irrespective of the triggering mechanism, once the MFR attains eruptive motion, standard flare reconnection sets in beneath the erupting MFR, and this scenario is common to all models of eruptive flares (e.g., see Vršnak et al. 2004; Veronig et al. 2006, 2018; Liu et al. 2008; Joshi et al. 2013, 2016; Vršnak 2016; Mitra & Joshi 2019; Sahu et al. 2020).

While flares and CMEs result in large-scale changes in the magnetic configuration, coronal jets are relatively small-scale solar eruptive phenomena identified as collimated ejection of plasma in the solar atmosphere (see, e.g., Brueckner & Bartoe 1983). Jets are believed to play an important role in transporting mass and energy from the lower to the upper corona, which may have implications for the coronal heating problem (see review by Raouafi et al. 2016). Observations by the Soft X-ray Telescope on board Yohkoh (Tsuneta et al. 1991) initiated extensive investigations of coronal jets, and it was realized that jets are the manifestations of interchange reconnection between a closed and a nearby open magnetic field region (see, e.g., Shibata et al. 1992, 1996; Bhatnagar 1996; Shimojo et al. 1996, 1998). Such magnetic configurations can be formed when a magnetic patch emerges in a coronal hole (CH) of opposite polarity ("anemone"-type AR; see Asai et al. 2008). It should be noted that such collimated eruptions that eject into the corona having their bases magnetically rooted in the photosphere (Moore et al. 2010) are observed in different wavelengths and have been named according to the associated observing wavelength regime, e.g., extreme ultraviolet (EUV) jets, Hα surges, EUV and Hα macrospicules, etc. (see, e.g., Moore et al. 1977; Schmieder et al. 1995; Jiang et al. 2007). Moore et al. (2010) proposed a dichotomy in solar jets: standard and blowout. In the standard jet scenario, reconnection between a preexisting open field and a newly emerging magnetic field of opposite polarity is responsible for guiding the hot plasma along the postreconnection open field, resulting in a narrow, long jet spire. On the other hand, the blowout category of jets involves eruption of the jet's base arch that contains a mini flux rope, resulting in a broader and apparently untwisting jet spire and a CME (see also Archontis & Hood 2013; Joshi et al. 2016, 2017b; Chandra et al. 2017).

During 2017, when the Sun was moving toward the minimum phase of solar cycle 24, a simple α-type AR, NOAA 12673, emerged on the eastern limb of the Sun on 2017 August 28. It gradually became complex with time and turned into a $\beta\gamma\delta$-type sunspot on 2017 September 5. Before disappearing over the western limb of the Sun on 2017 September 10, it produced four X-class and 27 M-class flares, along with numerous C-class flares, making it one of the most powerful ARs of solar cycle 24. Notably, it produced the two biggest flares of solar cycle 24, namely, the X9.3 event on 2017 September 6 and the X8.2 flare on 2017 September 10, which were subject to numerous studies (e.g., Yang et al. 2017; Gary et al. 2018; Guo et al. 2018; Hou et al. 2018; Liu et al. 2018a, 2018c, 2019; Mitra et al. 2018; Romano et al. 2018, 2019; Seaton & Darnel 2018; Verma 2018; Veronig et al. 2018; Duan et al. 2019; Moraitis et al. 2019; Chen et al. 2020). Most of the flaring activity from the AR occurred from the central region, where the sunspot group arranged into a δ-configuration (Künzel 1960). This region was characterized by a sharp polarity inversion line (PIL) and exhibited a high magnetic gradient across it; for example, Mitra et al. (2018) noted a magnetic gradient of 2.4 kG Mm^{-1} in the line-of-sight (LOS) magnetic field across the PIL prior to the X-class flares of 2017 September 6.

In this paper, we present a comprehensive multiwavelength analysis of two impulsive flares of classes M1.4 and M7.3, which occurred on 2017 September 7 in a very localized region situated near the edge of the main sunspot group of AR 12673. Both events were accompanied by highly collimated eruptions, a characteristic of the coronal jet. The jet-flare events initiated from an unusually small coronal sigmoid, which we explore in detail by (E)UV imaging and coronal magnetic field modeling thanks to the high-resolution data from the Solar Dynamics Observatory (SDO; Pesnell et al. 2012). An important aspect of this study lies in the early dynamics of the eruptions during the flares. Section 2 provides a brief account of the observational data and analysis techniques. In Section 3, we derive the observational results on the basis of measurements taken at photospheric, chromospheric, and coronal levels. In Section 4, we compare the chromospheric and coronal observations of different flare-associated features with the modeled coronal magnetic configurations. We discuss and interpret our results in Section 5.

2. Observational Data and Analysis Techniques

For imaging the solar atmosphere, we used observations from the Atmospheric Imaging Assembly (AIA; Lemen et al. 2012) on board SDO. The AIA produces 4096 × 4096 pixel full-disk solar images with a spatial resolution of 1".5 and pixel scale of 0".6 in 10 (E)UV channels originating in different heights of the solar atmosphere. In particular, the 12 s cadence observations in the 94 Å (Fe XVIII; $\log(T) = 6.8$) and 335 Å (Fe XVI; $\log(T) = 6.4$) filters, along with the 193 Å (Fe XII, XXIV; $\log(T) = 6.2, 7.3$) channel, were used for investigation of coronal activities associated with the flares. For imaging of the lower atmospheric layers, we have extensively used 12 s cadence observations in the 304 Å (He II; $\log(T) = 4.7$) and 24 s cadence observations in the 1600 Å (C IV and continuum; $\log(T) = 5$ and 3.4) channels.

RHESSI (Lin et al. 2002) observed the interval between the two homologous flares and the second (M7.3) flare almost completely, while it missed the first (M1.4) event due to the spacecraft's passage through the South Atlantic Anomaly (SAA).[7] RHESSI observed the full Sun with an unprecedented combination of angular (spatial) resolution (as fine as $\approx 2''.3$) and energy resolution (1–5 keV) in the energy range 3 keV–17 MeV. The image reconstruction is done with the CLEAN algorithm (Hurford et al. 2002) using only front detector segments with an integration time of 12 s and a pixel scale of $2''.0$. Out of nine detector segments, segment 2 was excluded for imaging at 6–12, 12–25, 25–50, and 50–100 keV, while segments 2 and 7 were excluded for 3–6 keV imaging.

Photospheric structures associated with the AR NOAA 12673 were observed from full-disk 4096 × 4096 pixel intensity images and LOS magnetograms from the Helioseismic and Magnetic Imager (HMI; Schou et al. 2012) on board SDO at a spatial resolution of $1''.0$, a pixel scale of $0''.5$, and 45 s cadence. To investigate the coronal magnetic structures associated with the AR, we used a global potential field source surface model (PFSS[8]; Wang & Sheeley 1992) and a nonlinear force-free field (NLFFF) model (Wiegelmann & Inhester 2010; Wiegelmann et al. 2012). As the boundary condition for the NLFFF modeling, we used photospheric vector magnetograms of 2017 September 7 09:46 UT from the "hmi.sharp_cea_720s" series of SDO/HMI at a reduced resolution of $0^\circ.06$ and a temporal cadence of 720 s. The NLFFF extrapolations were done in a Cartesian volume of dimensions 344 × 224 × 224 pixels, which corresponds to a physical size of $\approx 250 \times 160 \times 160$ Mm^3 in the solar atmosphere. The NLFFF field lines were visualized using the Visualization and Analysis Platform for Ocean, Atmosphere, and Solar Researchers (Clyne et al. 2007[9]) software, which produces an interactive 3D visualization environment.

We calculated the magnetic decay index in the NLFFF extrapolation volume using the results of potential field extrapolation obtained by solving a Green's function method (Seehafer 1978). The magnetic decay index (n) is given by the equation $n = -\frac{\log(B_{\rm ex}(z))}{\log(z)}$, where $B_{\rm ex}(z)$ is the horizontal component of the external field above the AR and z is the height (Bateman 1978; Kliem & Török 2006).

The CME that originated from the filament eruption was observed by the C2 and C3 instruments of the Large Angle and Spectrometric Coronagraph (LASCO; Brueckner et al. 1995) on board the Solar and Heliospheric Observatory (SOHO; Domingo et al. 1995). The C2 and C3 instruments are white-light coronagraphs that image the solar corona from 1.5 to 6 and 3.7 to 30 $R_\odot$, respectively.

3. Multiwavelength Observations and Analysis

3.1. Event Overview

We present observations of AR NOAA 12673 on 2017 September 7 from 09:45 to 10:30 UT. During this period, the AR produced two GOES M-class flares.[10] The temporal evolution of the M-class flares is represented by the soft X-ray (SXR) flux variation in the 1–8 Å channel of GOES in Figure 1(a) (shown by the red curve). The first M-class flare (M1.4; indicated by an arrow in Figure 1(a)) initiated at ≈09:51 UT. After a brief period of slow rise from ≈09:51 to ≈09:53 UT, which is often observed to precede the impulsive flare phase (see, e.g., Veronig et al. 2002; Mitra & Joshi 2019), the flux in both GOES SXR channels (i.e., 1–8 and 0.5–4 Å) experienced a rapid enhancement until the peak of the flare at ≈09:54 UT. The decay phase of the M1.4 flare is characterized by a subtle rise at ≈09:57 UT in an otherwise steady decay of both GOES SXR fluxes. The M7.3 flare was characterized by a brief impulsive phase when the flux in either GOES channel experienced an abrupt rise at ≈10:14 UT. The flare peaked at ≈10:16 UT and thereafter decayed until the end of our observing period at 10:30 UT, when the SXR fluxes attained the level of the corresponding preflare backgrounds. RHESSI observed the AR on 2017 September 7 from ≈09:59 to ≈10:24 UT, which almost fully covered the M7.3 flare and the interval between the two flares (Figure 1(b)). Depending on the time evolution of the GOES SXR fluxes, combined with the available RHESSI observations, we divided the entire duration (09:45–10:30 UT) into three periods: periods I and III cover the M1.4 and M7.3 flares with the associated eruptions, respectively, whereas period II covers the rather quiet phase in between the two M-class flares (Figure 1(a)).

The AIA (E)UV light curves from the AR during this time (Figure 1(c)) show a general agreement with the GOES SXR flux variation, signifying that the disk-integrated GOES measurement was largely influenced by the coronal activity of the AR NOAA 12673. The intensity variations in all AIA channels suggest the initiation of the M1.4 flare at ≈09:52 UT and the M7.3 flare at ≈10:14 UT. We note similar intensity variations in the light curves of different AIA channels. We have summarized the different phases of the flares in the studied interval in Table 1.

Figure 2 displays the morphology and configuration of the AR at the photosphere and different layers above it prior to the reported events. Comparison between the continuum image and magnetogram of the AR (Figures 2(a) and (b)) suggests that the southwestern sunspot group was primarily of positive polarity, while negative polarity dominated the northern dispersed sunspot group. Our interest lies in the central part of the AR, which displayed a complex bipolar configuration. The coronal images of the AR show a very interesting feature in the northern part of the central sunspot group (see the region marked by a dashed box in Figures 2(a) and (b)) with the shape of a semicircular arc, which is indicated by the black arrow in Figures 2(c)–(e). Careful observation suggests the shape of this bright feature to be similar to an inverted "S." Comparison between coronal and photospheric images of the AR unveils that the structure was lying over the bipolar sunspot region (see the region indicated in the dashed box in Figures 2(a) and (b)). This inverted S-shaped bright structure can be thought of as a minisigmoidal region. In AIA UV images (Figure 2(f)), though, the minisigmoid is not clearly visible, and a few very localized bright dots can be found at the same location (indicated by the black arrows in Figure 2(f)). In the next three subsections (i.e., Sections 3.2–3.4), we focus on the region shown in the boxes in Figures 2(c) and (e), as both of the M-class flares reported in this paper occurred in this region.

[7] https://heasarc.gsfc.nasa.gov/docs/rosat/gallery/misc_saad.html
[8] https://www.lmsal.com/~derosa/pfsspack/
[9] https://www.vapor.ucar.edu/
[10] http://www.lmsal.com/solarsoft/ssw/last_events-2017/last_events_20170908_1158/index.html

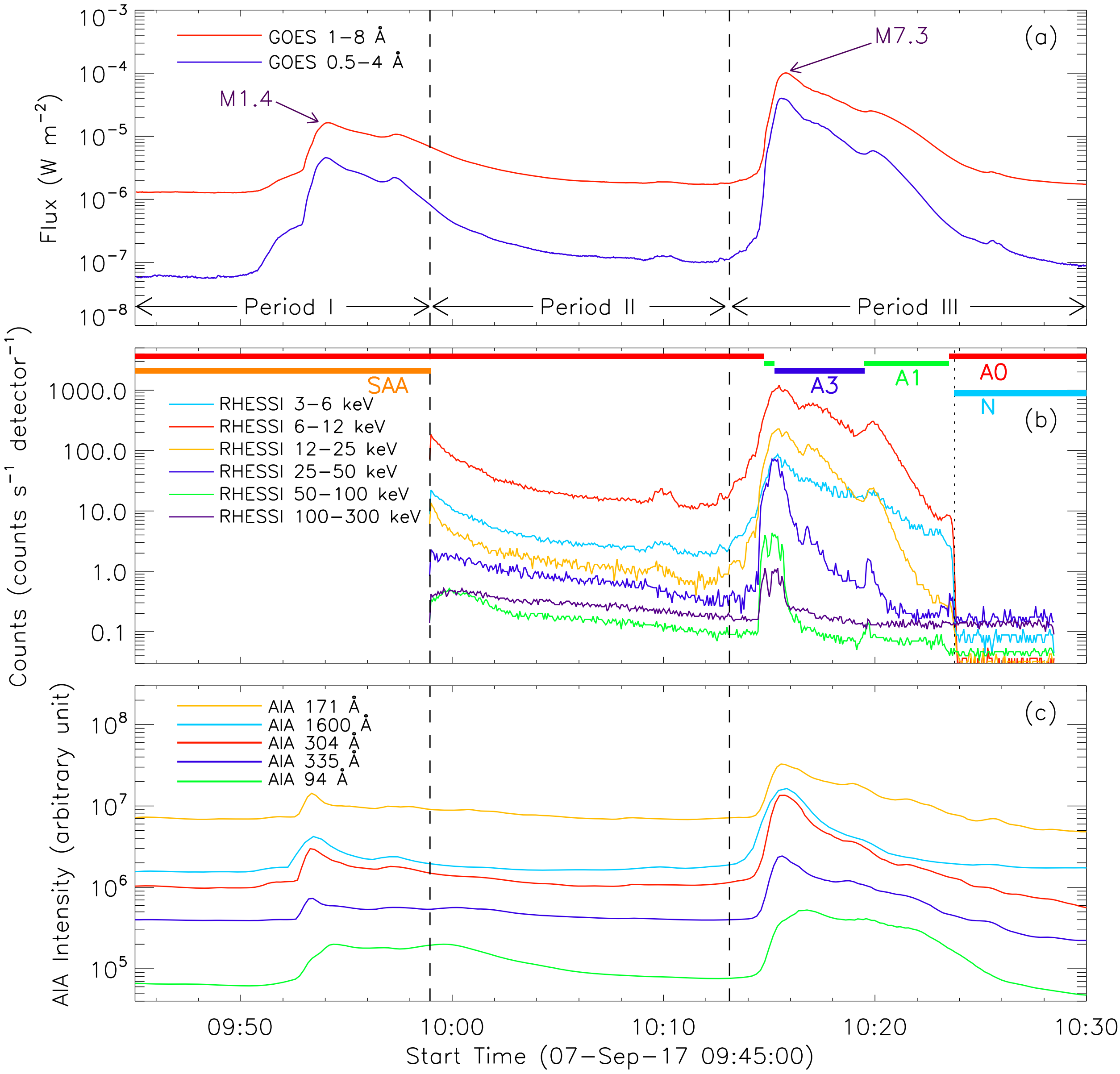

Figure 1. Panel (a): GOES SXR flux in the 1–8 Å (red curve) and 0.5–4 Å (blue curve) bands on 2017 September 7 from 09:45 to 10:30 UT, covering the two M-class flares under study. Panel (b): RHESSI X-ray fluxes normalized by factors of $\frac{1}{10}$, $\frac{1}{30}$, $\frac{1}{100}$, and $\frac{1}{100}$ for the 12–25, 25–50, 50–100, and 100–300 keV energy bands, respectively. The horizontal red, green, and dark blue bars indicate the RHESSI attenuator states (A0, A1, and A3, respectively). The orange and light blue horizontal bars indicate the durations missed by RHESSI due to the SAA and "RHESSI night," respectively. Panel (c): AIA (E)UV light curves. For clear visualization, the AIA light curves in channels 171 and 94 Å are scaled by $\frac{1}{2}$ and $\frac{1}{10}$, respectively. An animation is included with this figure. In addition to panel (a), the animation also shows the sequence of AIA 94 and 304 Å images. The FOV of the AIA images in the animation is indicated by the white boxes in Figures 2(c) and (e). The animation starts on 2017 September 7 at 09:45 UT and ends the same day at 10:30 UT. The duration of the animation is 7 s.

(An animation of this figure is available.)

3.2. Period I: Evolution of the M1.4 Flare

Figure 3 displays a series of AIA 94 (Figures 3(a)–(i)) and 304 (Figures 3(j)–(r)) Å images showing the morphological evolution of the region shown inside the boxes in Figures 2(c) and (e) during the M1.4 flare and the associated jetlike plasma eruption. As discussed in Section 3.1, before the flare onset, the northern part of the AR contained a minisigmoid. In terms of the sharpness of the observed feature and its relative brightness in comparison to the ambient medium, the minisigmoid was apparently more prominent in the hot, coronal AIA 94 Å channel than the relatively cooler AIA 304 Å filter. In Figure 3(a), we outline the minisigmoid with a black dashed line that brightened up after 09:50 UT, marking the onset of the M1.4 flare. After 09:53 UT, we observe a localized kernel-like brightening in the western leg of the minisigmoid (shown by the blue arrow in Figure 3(c)). Further, looking at the spatial extent, as well as the relative intensity, this localized brightening was observed to be more prominent in the 304 Å than the 94 Å observations (see Figures 3(c) and (l)), which suggests that the early energy release during the initiation of the M1.4 flare occurred in lower, i.e., chromospheric, heights (see Figures 3(c) and (l)). At the same time, we observe the ejection of plasma from the middle of the

Table 1
Chronology of Events during the Two M-class Flares that Occurred on 2017 September 7

Sr. No.	Evolutionary Stages	Time	Observing Instrument/ Wavelength	Remarks
1	Preflare phase	09:45 UT	AIA (E)UV and HMI	A very localized inverted "S" structured brightening was observed in AIA 304 and other AIA coronal images in the AR. We call it "minisigmoid."
2	Initiation of the M1.4 flare	09:49 UT	GOES 1–8 Å	
3	Initiation of plasma ejection during the M1.4 flare	09:53 UT	AIA 94 and 304 Å	Collimated ejection of plasma was observed from the core of the minisigmoid toward the east.
4	End of the M1.4 flare	09:58 UT	GOES 1–8 Å	A small filament appeared in the minisigmoid region. The RHESSI observation started at ≈09:59 UT.
5	Initiation of the M7.3 flare	10:11 UT	GOES 1–8 Å	
6	Initiation of the first phase of plasma ejection during the M7.3 flare	10:14 UT	AIA 304 Å	Collimated plasma ejection was observed from the core of the minisigmoid toward the east. RHESSI sources of energies up to ≈100 keV were found from the minisigmoid region.
7	Initiation of the second phase of plasma ejection during the M7.3 flare	10:16 UT	AIA 304 Å	The southern end of the filament erupted, ejecting plasma toward the south.
8	Merging of the plasma ejected in the first phase with plasma ejected in the second phase	10:22 UT	AIA 335 Å	Plasma ejected toward the east during the M7.3 flare strangely changed direction from east to southwest and merged with the plasma ejected in the second phase during the M7.3 flare.
9	End of the M7.3 flare	10:18 UT	GOES 1–8 Å	
10	Detection of CME	10:24 UT	LASCO C2	The CME propagated along the central PA of 254° and angular width of 32° with a linear speed of 470 km s^{-1}.

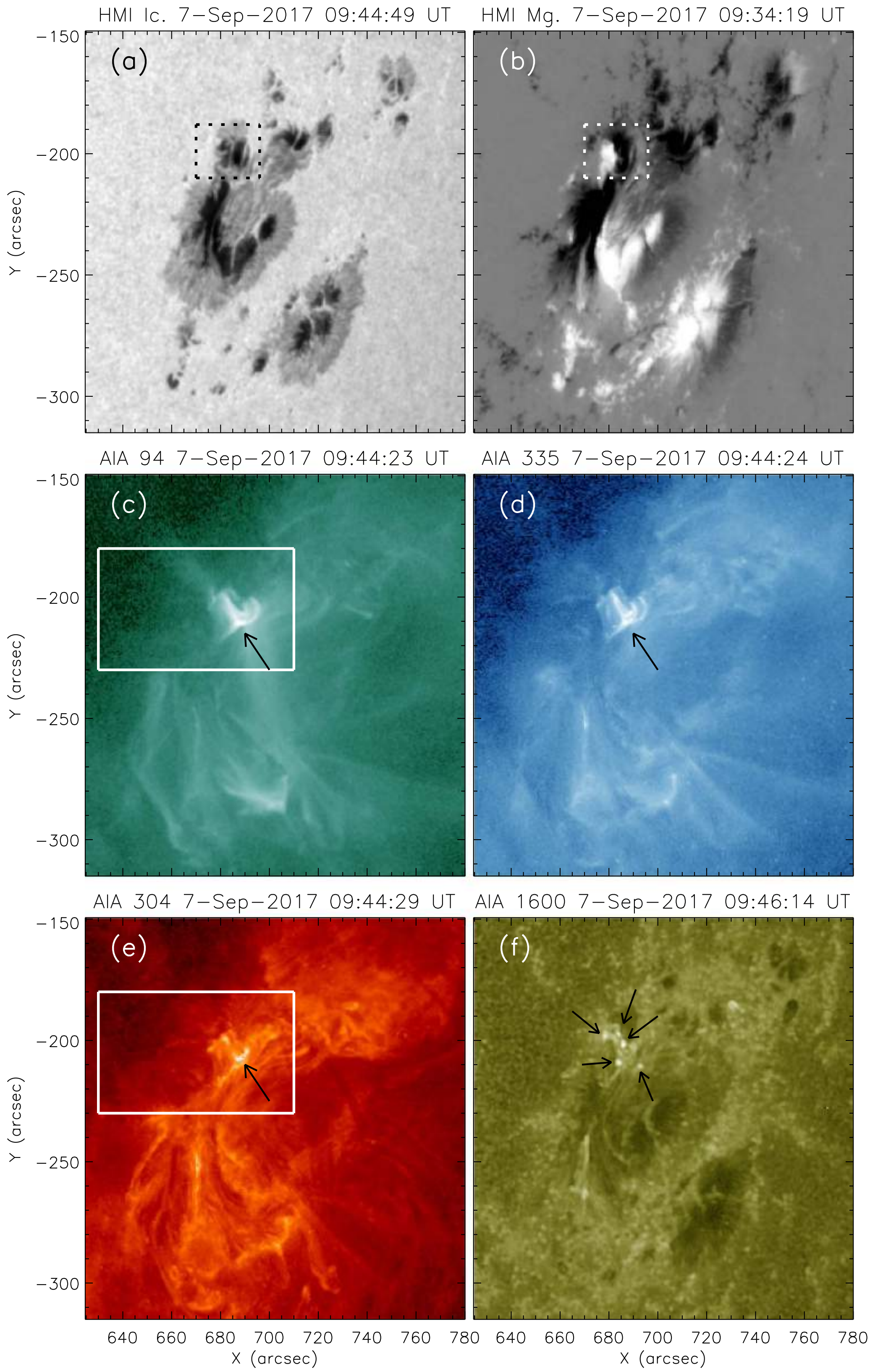

Figure 2. Panel (a): HMI white-light image of AR 12673 on 2017 September 7 09:44 UT. Panel (b): cotemporal HMI magnetogram. Panels (c)–(e): AIA EUV images of the AR in 94, 335, and 304 Å, respectively, showing the morphology of the AR in the corona and chromosphere. Panel (f): AIA UV image of the AR in 1600 Å. The dashed boxes in panels (a) and (b) indicate the photospheric region associated with the two M-class flares. The boxes in panels (c) and (e) indicate the FOV of the AR plotted in Figures 3, 5, and 6. The arrows in panels (c)–(e) indicate the minisigmoid region, whereas the arrows in panel (f) indicate brightenings at the location of the minisigmoid.

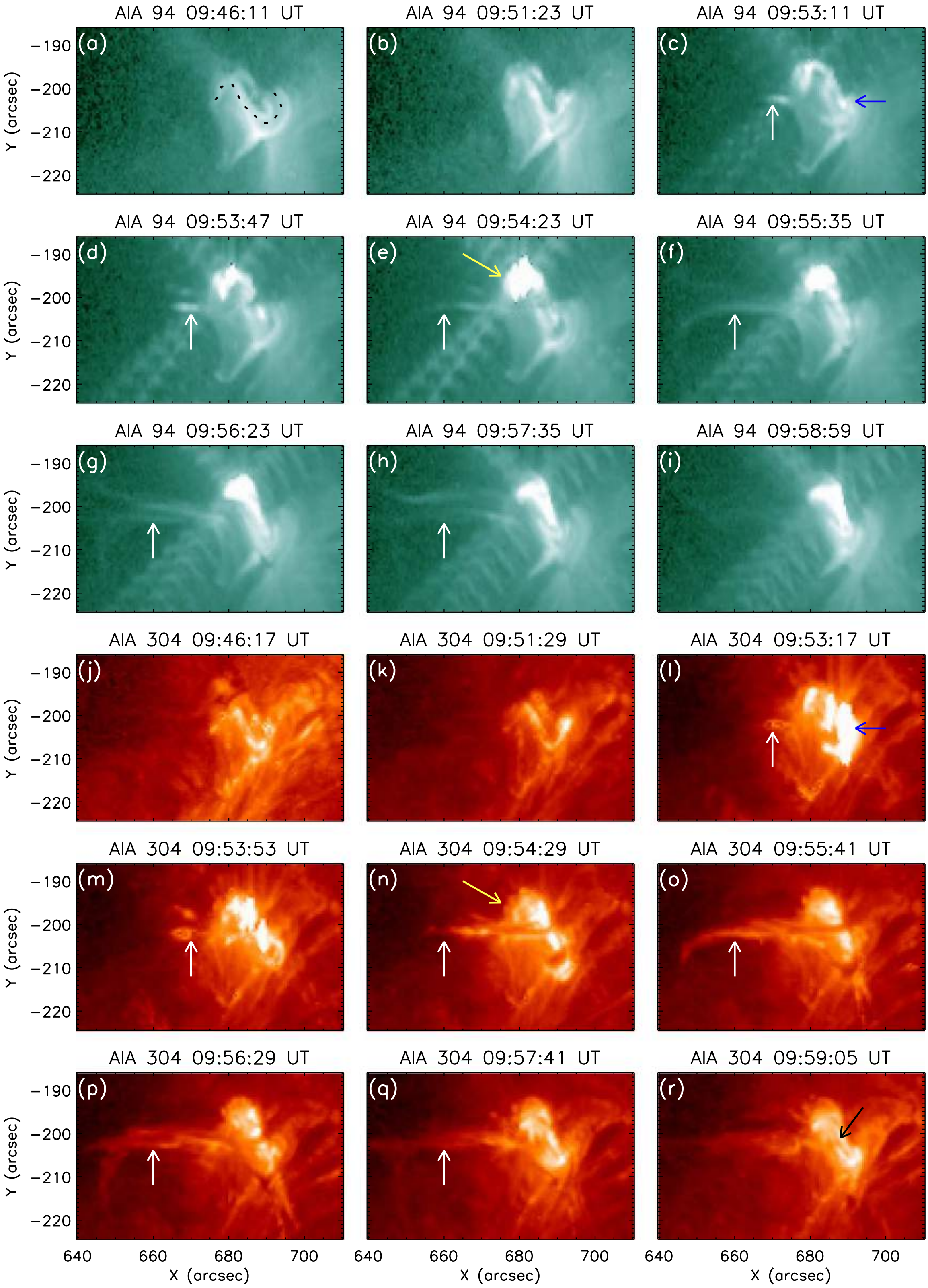

Figure 3. Series of AIA 94 (panels (a)–(i)) and 304 (panels (j)–(r)) Å images showing the time evolution of the M1.4 flare. The minisigmoid structure identified in the preflare phase is outlined by the dashed black dotted curve in panel (a). The white arrows in different panels indicate the ejected jetlike plasma. The blue arrows in panels (c) and (l) indicate a newly emerged brightening in the western end of the minisigmoid that led to the flare onset. The yellow arrows in panels (e) and (n) indicate the brightening in the eastern end of the minisigmoid during the peak phase of the M1.4 flare. The black arrow in panel (r) indicates a newly formed filament structure during the decaying phase of the M1.4 flare.

minisigmoid (shown by the white arrow in Figure 3(c)). The ejected plasma followed a very narrow and collimated path (i.e., a jetlike eruption) toward the east for a distance of ≈40″ and then abruptly changed its direction. The progress of the ejected plasma is indicated by the white arrows in Figures 3(c)–(h) and (l)–(q). Here we note that the ejecting plasma was observed more clearly in AIA 304 Å images than in AIA 94 Å images. This is indicative of cooler plasma being ejected from lower layers in the solar atmosphere (presumably filament material) and partially heated during the ejection process. At the peak phase of the flare, the eastern leg of the minisigmoid became the brightest location in the entire AR, as observed in the AIA 94 Å images (Figure 3(e); shown by the yellow arrow). The decay phase of the M1.4 flare was characterized by the appearance of a small filament structure observed in the AIA 304 Å images (shown by the black arrow in Figure 3(r)).

3.3. Period II: Quiet Phase between the Two M-class Flares

A small filament started to appear during the late phase of the M1.4 flare along the axis of the minisigmoid (Section 3.2). After the M1.4 flare, i.e., in period II of the study (see Figure 1), this filament became prominent. Notably, after missing period I due to the SAA, RHESSI started observing in period II with high sensitivity at low energies (no attenuator in place, state A0). In Figure 4, we show a series of AIA 304 Å images overplotted with the contours of RHESSI X-ray sources in the energy ranges 3–6 (shown by light blue contours) and 6–12 (shown by dark blue contours) keV. We readily find emission in the 6–12 keV range to have a peak intensity along the axis of the minisigmoid (Figure 4(a)). We also note that the X-ray emission in the 3–6 keV energy range at 10:00 UT displayed two distinct sources on either side of the filament. At ≈10:10 UT (Figure 4(e)), when the filament was very prominently visible (shown by the black arrow), we find very localized X-ray emission in the 6–12 keV range. At 10:12 UT, the 6–12 keV emission was characterized by an intense source at the top of the filament and two weaker sources on the either side of the filament (Figure 4(f)).

3.4. Period III: Evolution of the M7.3 Flare and Associated Filament Eruption

The M7.3 flare was initiated at ≈10:14 UT (see Figure 1), when the newly formed filament was distinctly visible in the minisigmoid region in both the coronal and chromospheric images (see Figures 5 and 6, where the filament is indicated by brown and blue arrows, respectively). The flare brightening was first observed at the northern end of the filament and was followed by a jetlike plasma ejection at ≈10:15 UT (indicated by the yellow arrows in Figures 5(d)–(g)). The jetlike plasma ejection was observed slightly earlier in the AIA 335 Å channel than in the AIA 94 Å channel (see Figures 5(c) and 6(c)). However, the eruption was visible in the chromospheric AIA 304 Å images ≈1 minute earlier than in the AIA 94 Å images sampling hot coronal plasma at ∼6 MK (see Figures 1(c) and 5(d), (k), and (l)). It is noteworthy that the motion and direction of the initial phase of plasma ejection were very similar to those during the earlier M1.4 flare. The filament brightened up after ≈10:15 UT, causing the peak phase of the M7.3 flare. Hard X-ray emission up to ≈100 keV was observed from the minisigmoid region by RHESSI during this flare. In Figure 5, we plot the contours of the RHESSI X-ray emission in different energy channels and find the X-ray sources to be cospatial with the EUV brightenings. The AIA 304 Å images of the region displayed an interesting feature during this time. The southern part of the filament kept rising and slowly developed into a cusp-like structure at ≈10:16 UT (the cusp-like structure is indicated by the black arrows in Figure 5(n)). The structure was also visible in the cotemporal AIA 335 Å channel images (Figure 6(f); indicated by the black arrow). A second phase of plasma eruption was initiated at ≈10:16 UT from the cusp-like structure. Simultaneous eruption of collimated plasma during the two phases partially occulted the bright flare emission from the AR thereafter. Observation of the sigmoidal region after 10:16 UT was only possible in those AIA channels that image the lower atmosphere of the Sun (i.e., 1600 Å). We observed two bright ribbon-like structures on either side of the filament in the AIA 1600 Å images until 10:20 UT (indicated by the red arrows in Figures 6(j)–(l)). However, cotemporal AIA 304 Å images of the same location suggest that the bright structures were associated with a postflare arcade viewed from an edge-on angle (outlined by the white boxes in Figures 5(o)–(q)). Therefore, we conclude that the bright structures observed in the AIA 1600 Å images in Figures 6(j)–(l) were a mixture of emissions coming from both the flare ribbons and postflare arcades. After this time, from the AIA 1600 Å images, no significant morphological changes were observed in the AR until the end of our observing period, except for a short-lived brightening found in the western end of the sigmoid region at ≈10:26 UT (shown by the blue arrow in Figure 6(o)). Here we remember that a subtle peak was observed in the decaying SXR fluxes of both GOES channels at the same time (see Figure 1).

3.5. Development of the CME from the Erupting Filament

As discussed in Sections 3.2 and 3.4, both of the M-class flares were associated with plasma ejections. Interestingly, the plasma ejection signatures during the M1.4 flare became too weak to be observed a few minutes after its first appearance within the AIA field of view (FOV). Erupting plasma during the M7.3 flare, however, was distinctly observed to produce a CME by SOHO/LASCO. In this section, we focus on the motion of the ejected plasma during the M7.3 flare (Figure 7) and the corresponding CME (Figure 8). The plasma ejection was initiated in a collimated manner toward the east (shown by the red arrow in Figures 7(b) and (c)) and then dramatically changed its direction toward the southwest. In Figure 7(e), we have approximately outlined the changing direction of the erupting plasma. A second phase of plasma ejection initiated from the western end of the minisigmoid region after ≈10:16 UT (see Section 3.4). Plasma that was ejected in both of these phases (Figures 7(d)–(i)) during the M7.3 flare thereafter proceeded to constitute a CME.

Figure 8 displays a series of running difference images by the LASCO C2 (Figures 8(a) and (b)) and C3 (Figure 8(c)) coronagraphs, where the CME that developed from the plasma ejection during the M-class flares can be observed. According to the LASCO CME catalog[11] (Yashiro et al. 2004), C2 detected the CME at 10:24 UT at ≈2.4 $R_{\odot}$, and it was observed in the FOV of C3 until 16:18 UT, when the leading edge of the CME reached ≈17.0 $R_{\odot}$. The narrow CME (angular width of only 32°) propagated along the position angle 254° with a linear speed of ≈470 km s^{-1}.

[11] https://cdaw.gsfc.nasa.gov/CME_list/UNIVERSAL/2017_09/yht/20170907.102406.w032n.v0470.p244g.yht

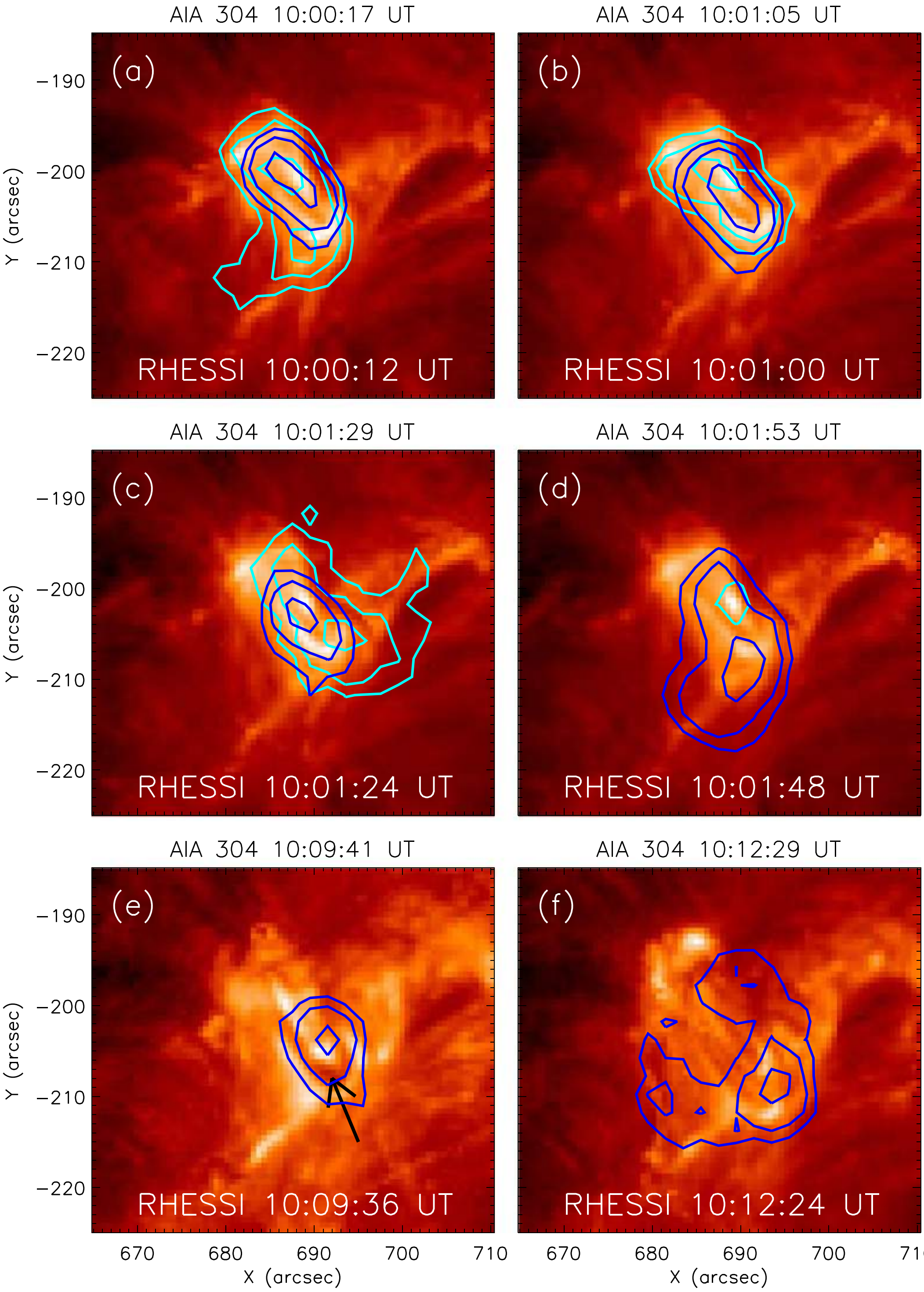

Figure 4. Series of AIA 304 Å images of the flaring region during the relatively quiet period between the two M-class flares. Contours of RHESSI 3–6 (light blue) and 6–12 (dark blue) keV are overplotted on each panel. Contour levels are set as 70%, 80%, and 95% of the corresponding peak flux. The arrow in panel (e) indicates a developing filament from the minisigmoid structure prior to the onset of the M7.3 flare.

3.6. Structure and Evolution of the Magnetic Configuration of AR 12673

The distribution and configuration of the photospheric magnetic flux of AR 12673 (Figure 9(a)) remained without any major changes during our observing period. However, it experienced consistent changes in the magnetic field strength. In Figure 9(b), we plot the photospheric LOS magnetic flux variation associated with the flaring region shown by

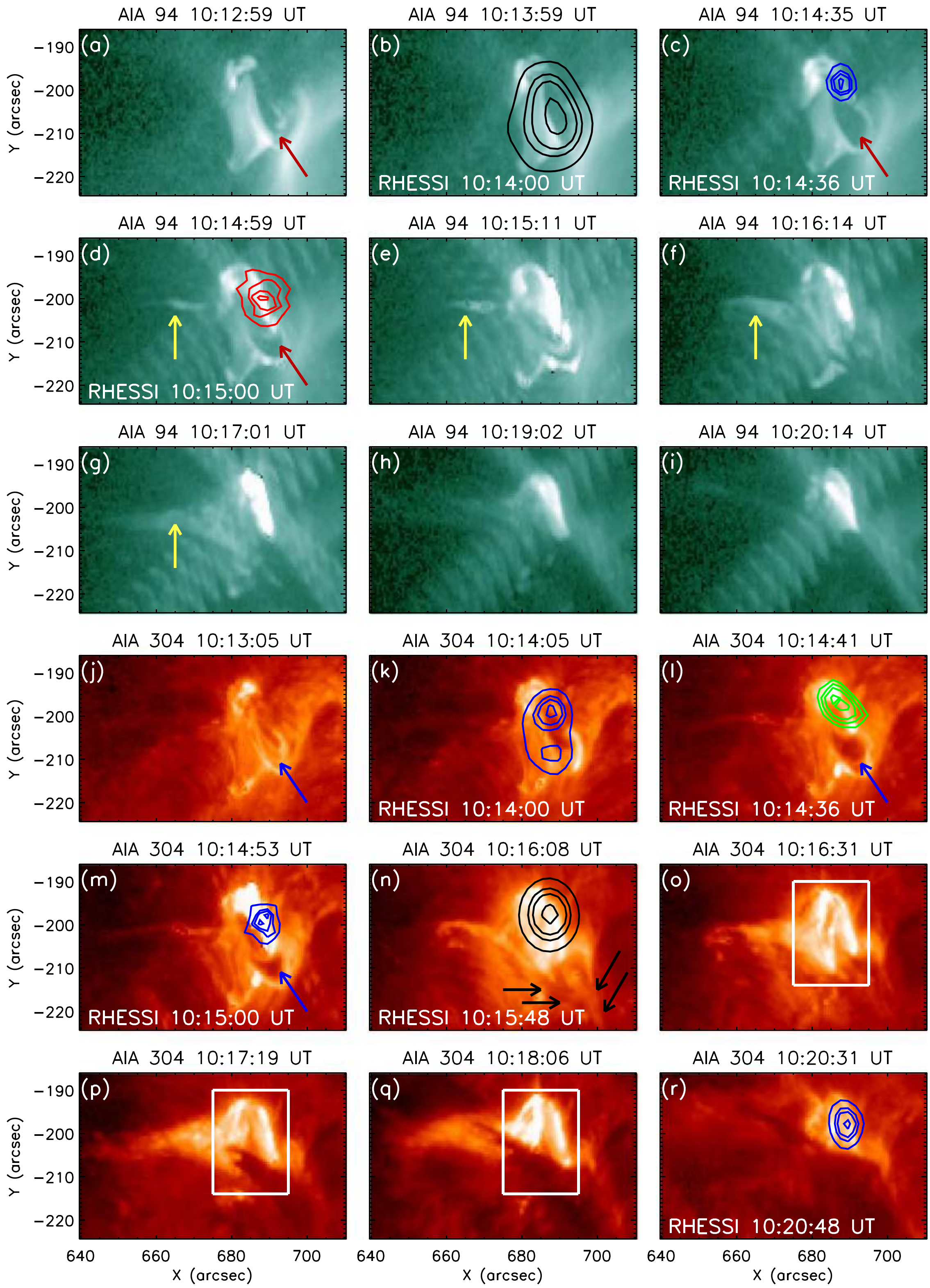

Figure 5. Series of AIA 94 (panels (a)–(i)) and 304 (panels (j)–(r)) Å images showing the time evolution of the M7.3 flare. The brown and blue arrows in different panels indicate the development of the filament. The yellow arrows in panels (d)–(g) indicate the first phase of plasma ejection during the M7.3 flare. The black arrows in panel (n) indicate a second phase of the eruption during the flare. The white boxes in panels (o)–(q) indicate a postflare arcade observed from an edge-on view. Contours of RHESSI 6–12 (blue), 12–25 (black), 25–50 (red), and 50–100 (green) keV are overplotted in different panels. Contour levels are set as 50%, 70%, 80%, and 95% of the corresponding peak flux for the 6–12, 12–25, and 25–50 keV energy bands and 60%, 70%, 80%, and 95% of the corresponding peak flux for the 50–100 keV band.

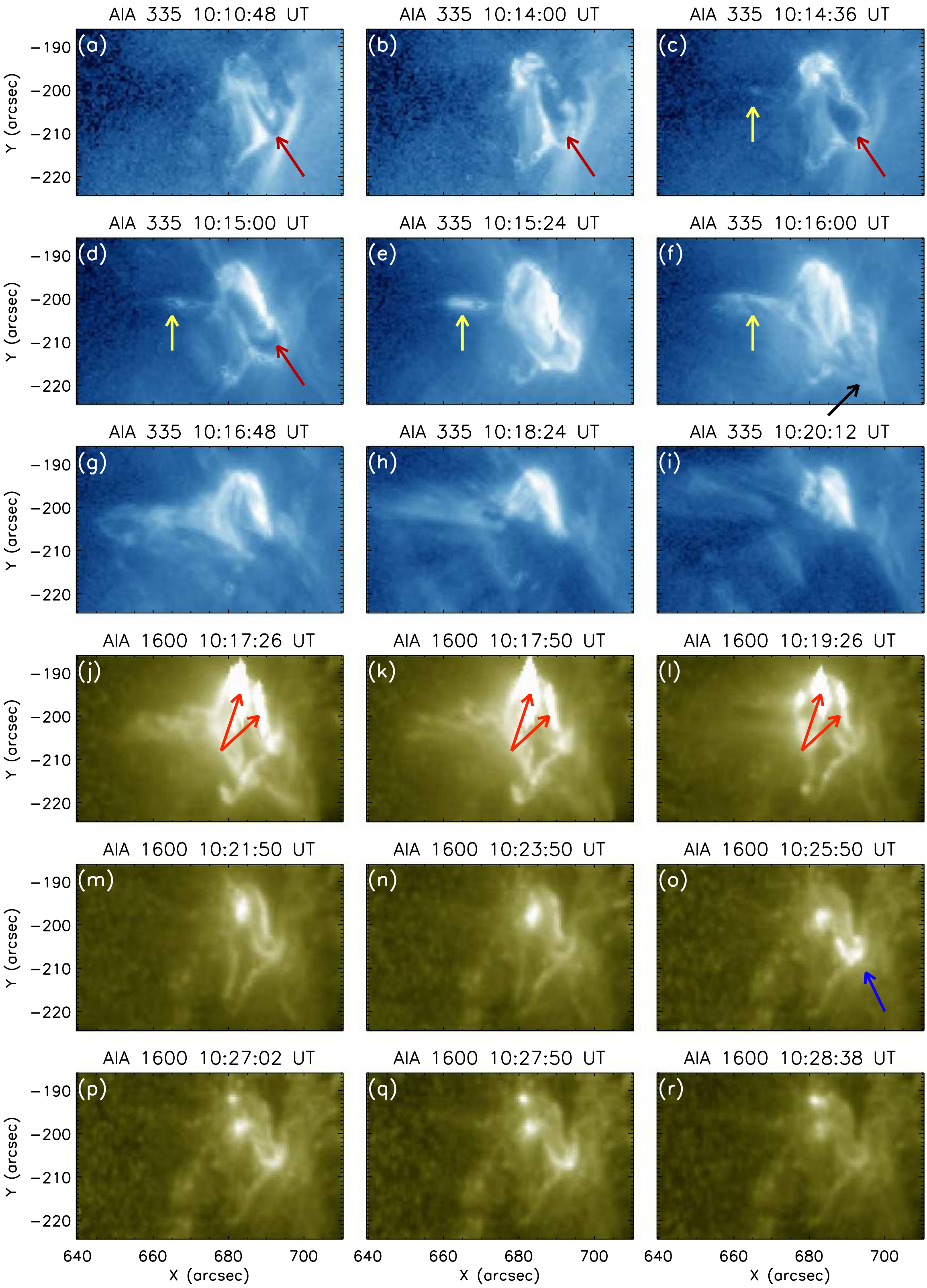

Figure 6. Series of AIA 335 (panels (a)–(i)) and 1600 (panels (j)–(r)) Å images showing the time evolution of the M7.3 flare. Brown arrows in panels (a)–(d) indicate the emergence of a small filament structure in the preflare phase. Yellow arrows in panels (c)–(f) indicate the ejecting plasma. The black arrow in panel (f) indicate the direction of a second stream of ejecting plasma. The red arrows in panels (j)–(l) indicate flare ribbon–like structures formed during the M7.3 flare. The blue arrow in panel (o) indicates a subtle brightening occurring in the decay phase of the flare that was probably responsible for the small enhancement in the GOES SXR light curves (see Figure 1).

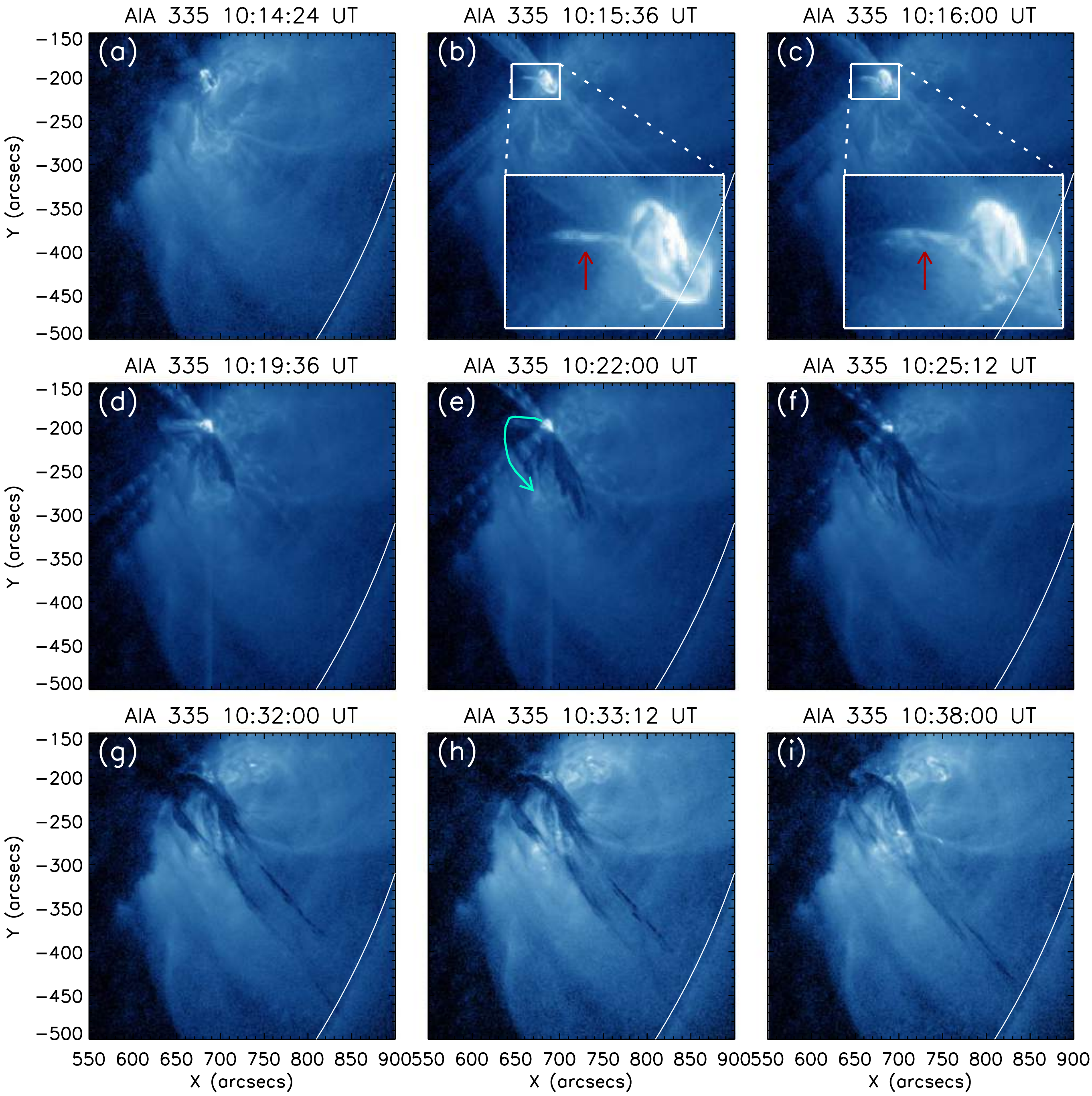

Figure 7. Series of AIA 335 Å images showing large-scale eruption of plasma from AR NOAA 12673 during the M7.3 flare reported in this paper. The red arrows in panels (b) and (c) indicate the initial phases of the ejecting plasma moving toward the east. The curve in panel (e) outlines the unusual turning of the ejecting plasma from east to southwest. The ejected plasma during the M7.3 flare resulted in a CME of medium speed and small angular width. An animation is included with this figure. The video starts on 2017 September 7 at 09:45 UT and ends the same day at 11:30 UT. The video duration is 17 s.

(An animation of this figure is available.)

the dashed box in Figure 9(a) on 2017 September 7 from 08:00 to 10:30 UT. Notably, this region was associated with the formation and eruption of the filament in the minisigmoid. We find that the negative flux underwent a monotonic decrease during the preflare period from ≈08:40 to ≈09:49 UT with a decay rate of ≈2.41×10^{16} Mx s^{-1}. On the other hand, the positive flux underwent a gradual enhancement during the preflare period with two distinguishable phases of flux decrease (≈08:35–08:40 and ≈09:17–09:28 UT). The decrease in magnetic flux can be interpreted as an observational signature of the photospheric flux cancellation. Flux variation during the flaring intervals (indicated by the

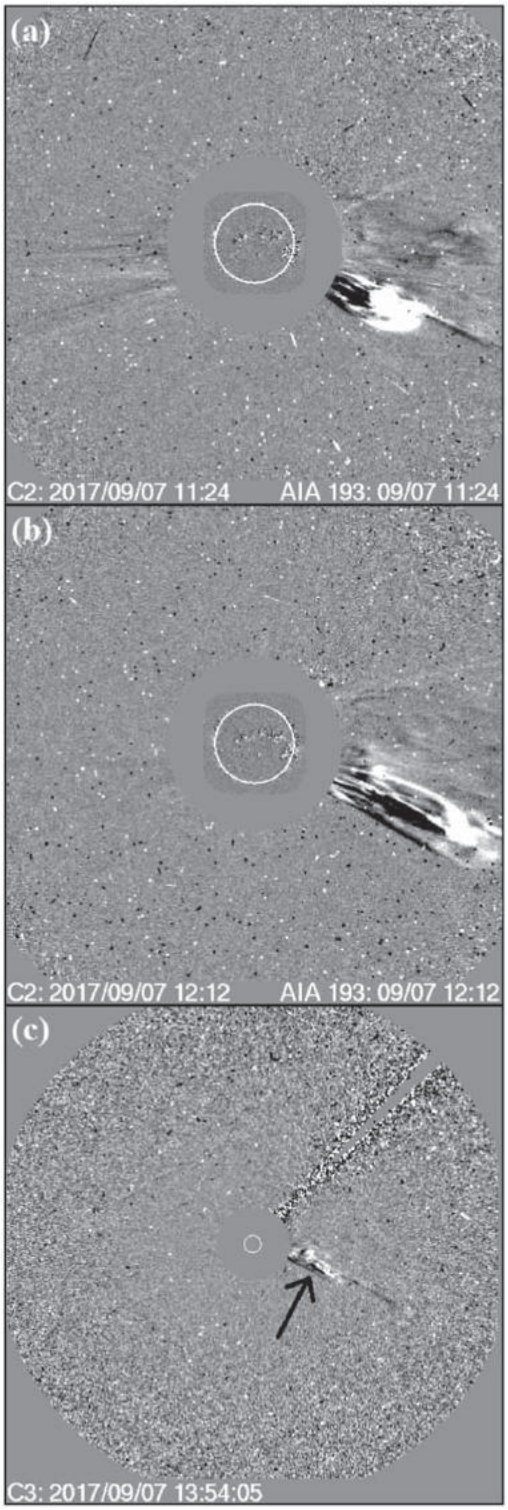

Figure 8. LASCO observations of the CME that developed from the plasma ejection during the M7.3 flare. Panels (a) and (b) present observations from the C2 coronagraph (1.5–6 $R_\odot$), while panel (c) shows observations from the C3 coronagraph (3.7–30 $R_\odot$). The CME is indicated by the black arrow in panel (c). The CME was first observed by LASCO at 10:24 UT and was observed until 16:18 UT.

dashed and dashed–dotted lines) is quite drastic and seems to be driven by the flaring activity. In this context, it is noteworthy that the second flare was a white-light event (WLF), which may produce artifacts in the magnetic field measurements.[12]

4. Magnetic Field Modeling

4.1. Large-scale Magnetic Field Configuration

Large-scale magnetic field configurations, such as open magnetic field lines represented by CHs (Cranmer 2009), may strongly influence the early propagation of CMEs and cause significant deflections of their original direction of motion (Gopalswamy et al. 2009; Heinemann et al. 2019). In order to check if the direction of the CME was influenced by the open field configuration associated with a nearby CH, we extrapolated the global magnetic field using PFSS and looked for observational signatures of CHs in the AIA EUV images (Figures 10). Figure 10(b) shows a global PFSS extrapolation concentrated around the AR NOAA 12673 (the AR is indicated by a black arrow in Figure 10(b)), where open and closed field lines are shown in blue and gray, respectively. From Figure 10(b), we find that open field lines originated to the north of the flaring region close to the negative polarity, as well as to the west, trailing to the south and deflected toward the southwest. Here we recall that the CME associated with the M-class flares propagated along the same direction (see Figure 8). Figures 10(a) and (c) represent AIA 193 Å images close to the peak of the first M1.4 flare on 2017 September 7 and one solar rotation later on 2017 October 4, respectively. There was no unambiguous observational signature of a CH in the EUV images at the time of the events under study. However, one solar rotation later, a small but prominent CH region was observed at the identified location of open field lines (indicated by the white arrow in Figure 10(c)).

4.2. NLFFF Extrapolation

4.2.1. Optimization-based NLFFF Extrapolation Technique

To understand the coronal magnetic field configuration associated with the AR NOAA 12673, we applied an optimization technique (Wheatland et al. 2000; Wiegelmann 2004) to compute the NLFFF equilibrium. Here we used an advanced version of this code, which takes care of measurement errors in the magnetogram (Wiegelmann & Inhester 2010) and has been optimized for use with data from SDO/HMI (Wiegelmann et al. 2012). In the optimization approach, L is minimized (Wiegelmann & Inhester 2010), where

$$L = \int_V \left(\omega_f \frac{|(\nabla \times \boldsymbol{B}) \times \boldsymbol{B}|^2}{B^2} + \omega_d |\nabla \cdot \boldsymbol{B}|^2 \right) dv + \nu \int_S (\boldsymbol{B} - \boldsymbol{B}_{\rm obs}) \cdot \boldsymbol{W} \cdot (\boldsymbol{B} - \boldsymbol{B}_{\rm obs}) d\boldsymbol{S}. \quad (1)$$

Here ω_f, ω_d, and ν are weighting functions, while $\boldsymbol{W}$ is a diagonal error matrix with the elements $w_{\rm los}$, $w_{\rm trans}$, and $w_{\rm trans}$; "los" and "trans" are the LOS and transverse components, respectively. The NLFFF code used in this paper calculates ω_f, ω_d (in the code, ω_f and ω_d are chosen to be identical, i.e., $\omega_f = \omega_d$) and allows ν, $w_{\rm los}$,

[12] During the impulsive phases of WLFs, sudden changes in the LOS photospheric fields were observed by several earlier studies (see, e.g., Maurya & Ambastha 2009; Zhao et al. 2009; Maurya et al. 2012; Kushwaha et al. 2014). The sudden transient changes observed in LOS magnetograms can be interpreted in terms of the theoretical calculations of Ding et al. (2002) that show that the field reversal during strong flares could be an "observational artifact" that is locally induced by bombardment of energetic electron beams at the photosphere.

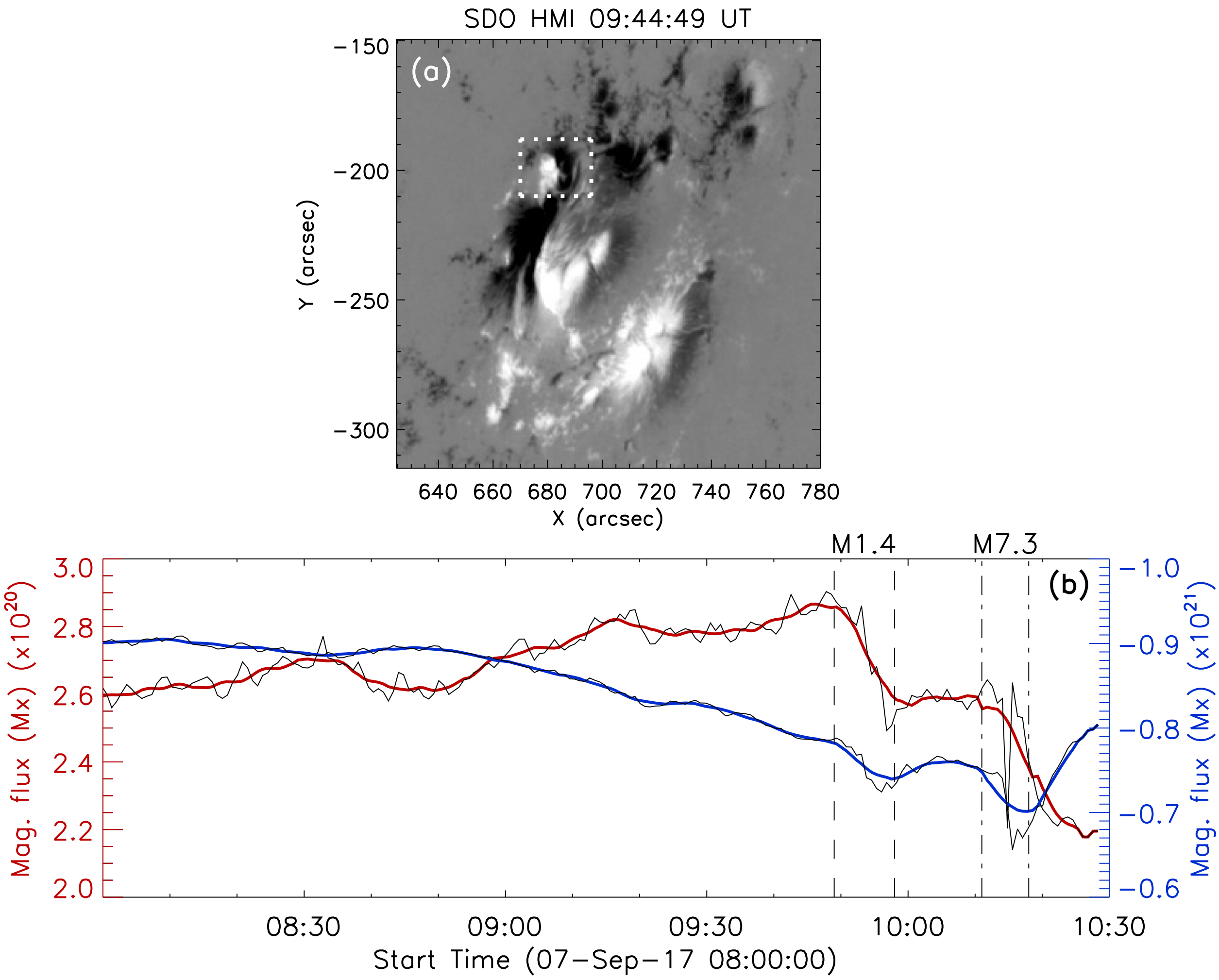

Figure 9. Panel (a): HMI magnetogram of AR 12673 on 2017 September 7 at 09:45 UT. The time evolution of the photospheric magnetic flux of the whole AR and inside the selected region within the dotted box in panel (a) is plotted in panel (b). The dashed lines in panel (b) mark the starting and ending time of the M1.4 flare as observed by GOES, and the dashed–dotted lines mark the starting and ending time of the M7.3 flare as observed by GOES.

and $w_{\rm trans}$ as free parameters (i.e., these parameters can be explicitly defined upon calling of the preprocessing/optimization). Since the photosphere is not force-free, the photospheric magnetograms used as the input boundary conditions need to be preprocessed (Wiegelmann et al. 2006). In Equation (1), $\boldsymbol{B}_{\rm obs}$ denotes the preprocessed magnetic field. For the purpose of preprocessing, a second functional $\mathscr{L}$ is defined as

$$\mathscr{L} = \mu_1\mathscr{L}_1 + \mu_2\mathscr{L}_2 + \mu_3\mathscr{L}_3 + \mu_4\mathscr{L}_4, \tag{2}$$

where

$$\begin{aligned}
\mathscr{L}_1 &= \left(\sum B_x B_z\right)^2 + \left(\sum B_y B_z\right)^2 + \left(\sum B_z^2 - B_x^2 - B_y^2\right)^2\\
\mathscr{L}_2 &= \left(\sum x(B_z^2 - B_x^2 - B_y^2)\right)^2 + \left(\sum y(B_z^2 - B_x^2 - B_y^2)\right)^2\\
&\quad + \left(\sum yB_xB_z - xB_yB_z\right)^2\\
\mathscr{L}_3 &= \sum(B_x - B_{x,\rm obs})^2 + \sum(B_y - B_{y,\rm obs})^2 + \sum(B_z - B_{z,\rm obs})^2\\
\mathscr{L}_4 &= \sum((\Delta B_x)^2 + (\Delta B_y)^2 + (\Delta B_z)^2).
\end{aligned}$$

Here the summations are done over all of the grid nodes of the bottom boundary. The values of μ_1, μ_2, μ_3, and μ_4 are free parameters and therefore user-defined.

Table 2
Values of Different Parameters before and after Preprocessing

Parameter	Before	After
Flux balance	-6.60×10^{-3}	-2.34×10^{-6}
Dimensionless force	0.29	4.18×10^{-4}
Dimensionless torque	0.31	1.05×10^{-3}

In this paper, for preprocessing the input photospheric magnetogram, we used the values of free parameters as follows:

$$\begin{aligned}
&\nu = 0.01;\ \ w_{\rm los} = 1;\ \ w_{\rm trans} = \frac{B_{\rm trans}}{\max(B_{\rm trans})};\\
&\mu_1 = \mu_2 = 1;\ \ \mu_3 = 0.001;\ \ \mu_4 = 0.01.
\end{aligned} \tag{3}$$

In Table 2, we compare the values of dimensionless flux, force, and torque before and after preprocessing, which can be used to assess the degree of force-freeness of the input-processed magnetograms. With the extrapolated magnetic field, the

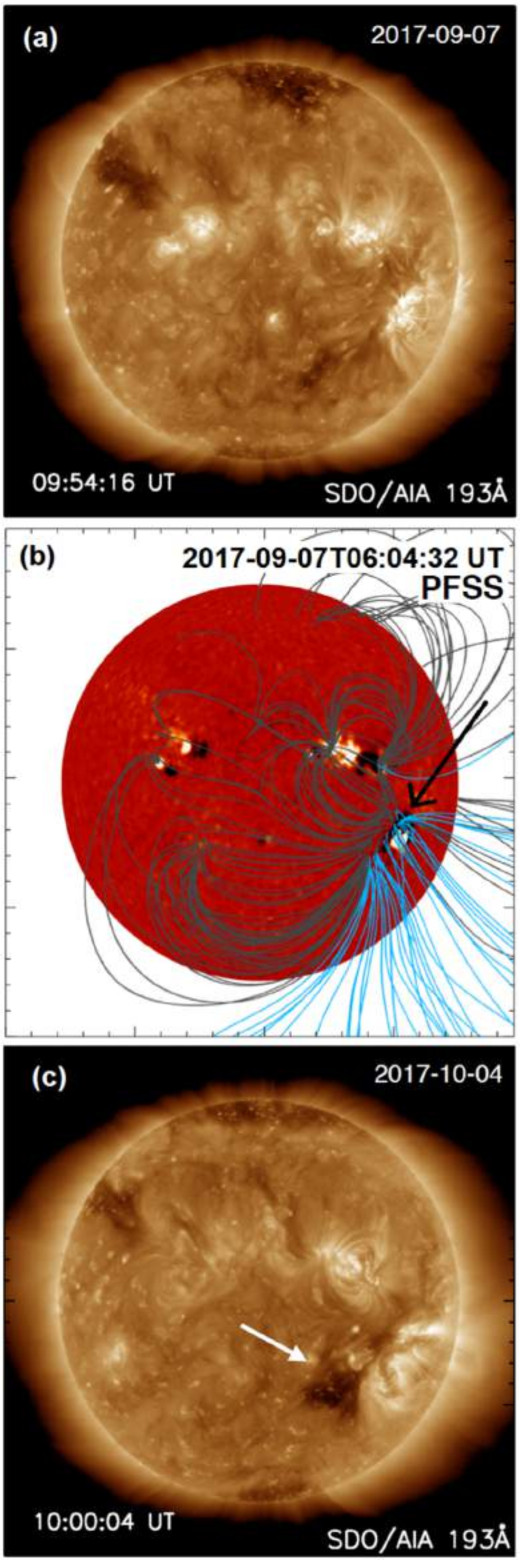

Figure 10. A PFSS extrapolation of the global magnetic field (panel (b)), together with AIA 193 Å images during the events under study (panel (a)) and one solar rotation later on 2017 October 4 (panel (c)). Gray and blue field lines indicate closed and open magnetic field lines, respectively. The open field lines originating to the north and west sides of the flaring AR are observed as the signature of a CH one solar rotation later (indicated by the white arrow).

following parameters were calculated that can be considered as the quantification of force and divergence freeness of the extrapolated magnetic field[13]:

$$\text{Fractional flux ratio } (\langle|f_i|\rangle) = 5.09 \times 10^{-4};\quad |\boldsymbol{J} \times \boldsymbol{B}| = 3.8 \times 10^{-3};\quad \text{weighted angle between } \boldsymbol{J} \text{ and } \boldsymbol{B} = 6\overset{\circ}{.}72. \tag{4}$$

In this context, it is noteworthy that at the time of extrapolation, i.e., 2017 September 7 09:46 UT, the AR NOAA 12673 was centered at the heliographic position ~S07W46.[14] A detailed study by Allen Gary & Hagyard (1990) on the implications of the Sun's curvature on the magnetogram observations suggests that full spherical geometry must be taken into account for off-center regions for angles $>50°$. During the extrapolations, we used cylindrical equal area (CEA; Allen Gary & Hagyard 1990) projected magnetograms, which do not produce results as accurate as those of full spherical geometry, but considering that we were particularly interested in the northeastern area of the AR, which lies well within 50°, CEA projection can be accepted as decently reliable.

4.2.2. Extrapolation Results

In Figure 11(a), we show an LOS magnetogram of the AR during the preflare phase. We specify a small part of the AR (shown inside the blue box in Figure 11(a)) for plotting the NLFFF extrapolated field lines. The region inside the box represents a complex distribution of magnetic polarities in a largely bipolar configuration of major positive and negative fields in the western and eastern parts, respectively. In the northern part of the box, we find a small positive polarity region surrounded by negative polarity regions from three sides (the region inside the green box in Figure 11(a)). On the northwestern side of the AR, we find many dispersed but strong negative polarity patches. For computation of the modeled magnetic field lines, we assume that the region showing flare-associated brightenings (which also includes a filament) contains part of the flux rope that underwent magnetic reconnection (i.e., relevant field lines).

The NLFFF extrapolation results reveal the presence of two small MFRs along the PIL of the minisigmoid region (shown by blue and green lines in Figure 11(b)). The two MFRs were intertwined with each other, forming a "double-decker flux rope system." We plot only the intertwined MFRs in Figure 11(c) for better visualization. Further, NLFFF extrapolation also suggests the presence of relatively large-scale closed magnetic field lines connecting the central positive and northern negative polarity regions (shown by the yellow lines in Figure 11(b)).

4.3. Distribution of Magnetic Decay Index and Twist Number

To explore how the strength of the coronal magnetic field of AR 12673 varied with height, we calculated the magnetic decay index in the whole AR volume (i.e., 344 × 224 × 244 pixels; see Section 2). In Figure 11(d), we show the variation of the magnetic decay index with height in a plane above the flux rope axis. For this purpose, we considered an approximate shape of the axis of the double-decker flux rope system, which

[13] See DeRosa et al. (2015).
[14] https://www.lmsal.com/solarsoft/latest_events_archive/events_summary/2017/09/07/gev_20170907_0949/index.html

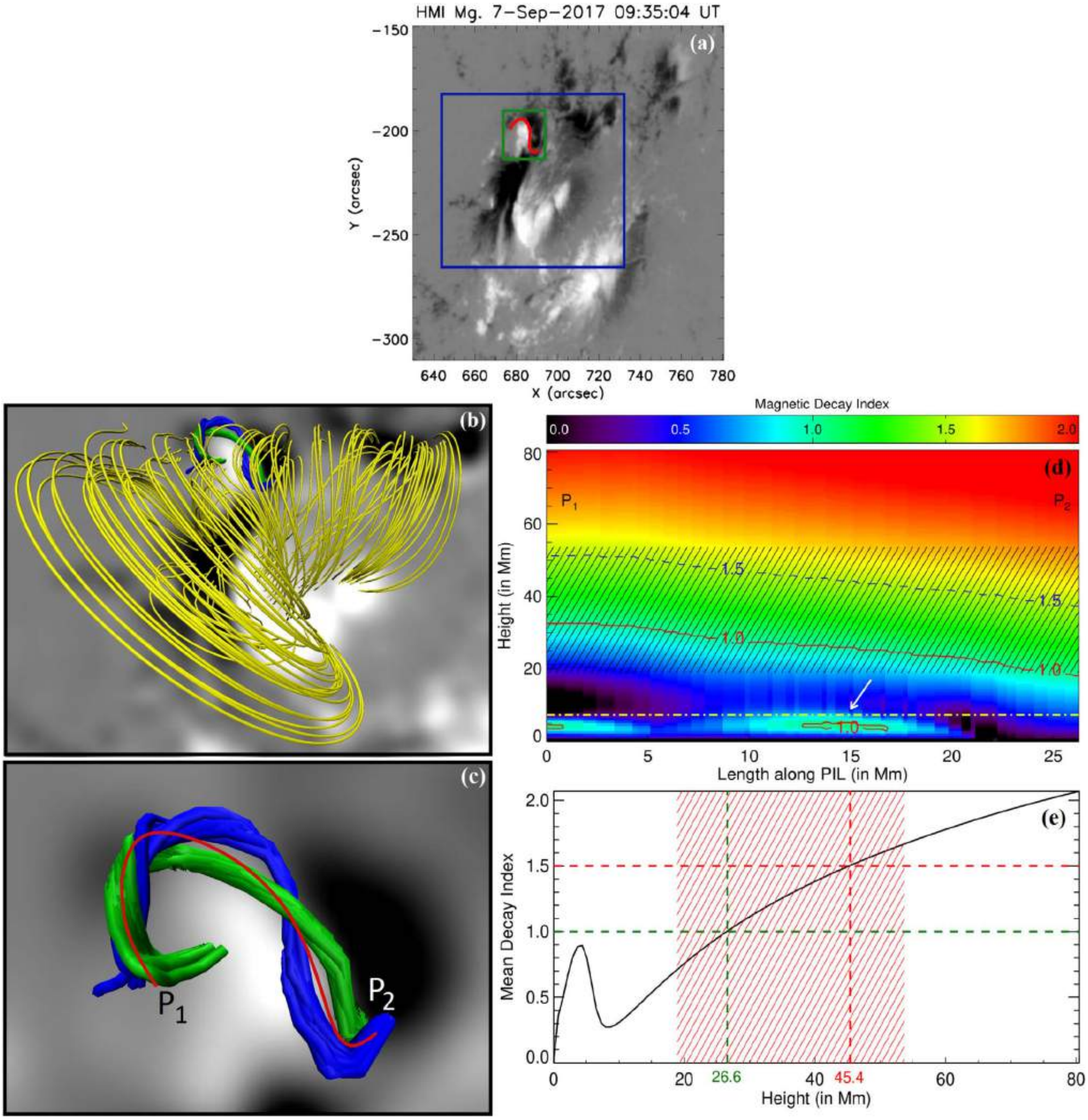

Figure 11. Panel (a): HMI LOS magnetogram showing the photospheric configuration of the AR NOAA 12673 prior to the flaring activity. Panel (b): NLFFF extrapolation results at 2017 September 7 09:45 UT showing coronal connectivities between different parts of the complex AR. Multiple flux ropes were identified in the extrapolation volume and are shown by blue and green lines. The NLFFF extrapolated field lines are drawn over the photospheric region shown inside the blue box in panel (a). In panel (c), we only show the two flux ropes situated in the flaring region within the AR, constituting a double-decker flux rope system. The FOV of panel (c) is approximately indicated in panel (a) by the green box. Panel (d): distribution of magnetic decay index (n) above the PIL, indicated by the red curves in panels (a) and (c). The yellow dashed–dotted line in panel (d) approximately indicates the height of the double-decker flux rope system. The blue dashed and red solid curves in panel (d) refer to contours of $n = 1.0$ and 1.5, respectively. The white arrow in panel (d) indicates a region within the height of the flux ropes characterized by decay index $n \approx 1.0$, which is higher than the surrounding region. Panel (e): variation of mean decay index with height above the PIL. The green and red dashed lines in panel (e) mark the heights corresponding to $n = 1.0$ and 1.5, respectively. The hatched regions in panels (d) and (e) indicate the range of critical decay index height for torus instability as found by Wang et al. (2017).

is shown by the red curves in Figures 11(a) and (c). The approximated PIL was then projected onto the 2D lower boundary, and the decay index was computed in a plane vertically above that approximate path. This process is similar to the technique undertaken by Liu et al. (2015). We plot two contours on the vertical surface with levels $n = 1.0$ and 1.5.

The approximate height of the double-decker system is indicated by the yellow dashed–dotted line in Figure 11(d). We find that a few segments of the double-decker flux rope system were associated with a magnetic decay index as high as ≈1.0. In Figure 11(e), we plot the variation of the decay index averaged over the path of the PIL as a function of height. Our results suggest that initially, the decay index increased and reached a value of ≈0.9 within a height of ≈5 Mm. At larger heights, it experienced a sharp decrease up to the height of ≈9 Mm, where the value of the decay index (n) was ≈0.3. Above this height (≈9 Mm), the average decay index was found to lie within the critical value (1.0–1.5) within the height range of 27–45 Mm.

In order to explore the possibility of kink instability as the triggering mechanism of the eruption of the flux rope, we calculated the twist number (T_w) in the flaring region, defined as (Berger & Prior 2006)

$$T_w = \int_L \frac{(\nabla \times \boldsymbol{B}) \cdot \boldsymbol{B}}{4\pi B^2} dl, \tag{5}$$

where L is the length of the flux rope. Our calculations reveal that the double-decker system was associated with a negative twist. The average value of $|T_w|$ associated with the double-decker system was found to be ≈1.0.

5. Discussion

In this paper, we present a multiwavelength analysis of two M-class flares from the AR NOAA 12673 on 2017 September 7 that resulted in the successive activation of a filament and subsequent narrow CME. As indicated in Figure 1, both M-class flares were very impulsive, with the respective impulsive phases lasting for ≈4 and ≈2 minutes only. The EUV images of the AR revealed that the flaring activity occurred within a very localized region (indicated within the boxes in Figures 2(c) and (e)). The AIA 94 Å images sampling hot coronal plasma clearly revealed an inverted S-shaped structure lying in an east–west orientation at the same location (Figure 3(a)). Such coronal S- (or inverted S-) shaped structures are known as “coronal sigmoids” (see Manoharan et al. 1996; Rust & Kumar 1996). However, while coronal sigmoids are usually observed to have lengths of ∼100–300 Mm (see, e.g., Tripathi et al. 2009; Joshi et al. 2017a; Mitra et al. 2018, 2020), the sigmoidal structure reported in this paper had a characteristic length of only ∼20 Mm (≈30″). In view of the much smaller length scales, we can justifiably term it a “minisigmoid.” During different phases of the two M-class flares, we clearly observed the formation and activation of a small filament from the sigmoidal region and associated jetlike plasma ejection (Figures 3 and 5).

Sigmoids are associated with twisted or helical magnetic structures, i.e., MFRs or filament channels (Gibson et al. 2002). The MFRs are complex structures lying above PILs in the solar atmosphere where a set of magnetic field lines wrap around along its central axis more than once (Gibson & Fan 2006). The results of the NLFFF extrapolation suggest the presence of two MFRs in the AR NOAA 12673 at the site of the M-class flares on 2017 September 7 (Figure 11). Interestingly, the MFRs in the AR seem to wrap around each other, forming a double-decker flux rope system. The double-decker flux rope system was first identified by Liu et al. (2012). While studying an eruptive M1.0 class flare, they observed two vertically well-separated filaments lying above a single PIL that remained stable for a few days before the upper branch erupted in association with an M-class flare. Based on their multipoint and multiwavelength analysis, they concluded that both filament branches emerged from beneath the photosphere with a vertical separation of ≈13 Mm between the two branches. A few hours before the eruptive flare, the filament threads within the lower branch lifted up and merged with the upper branch, triggering its eruption. Cheng et al. (2014) reported another case of double-decker flux ropes associated with an X-class eruptive flare from the sigmoidal AR 11520. They found the primary MFR to be formed ≈40 hr before the flare via tether-cutting reconnection between two J-shaped arcades. The second flux rope became evident in the hot coronal channels just ≈2 hr before the flare, and its eruption developed into a CME. The high temperature of the second flux rope led them to conclude that internal reconnection was responsible for its formation. Notably, the two MFRs reported by Cheng et al. (2014) were intertwined with each other, which is very similar to our case.

The sigmoidal structure reported in this study was sustained after the eruptive flares (Figures 6(m)–(r)), which suggests that only one of the two MFRs from the double-decker system erupted during the M-class flares. The previously reported cases pertaining to the eruption of double-decker flux rope systems exhibited similar situations (Cheng et al. 2014). The specialty of our study lies in the spatial extent of the sigmoid and the MFRs. Whereas signatures of the double-decker flux rope (or filament) system were clearly identified in optical and (E)UV images in the earlier studies, we were not able to resolve two distinct observable features of the MFRs associated with the double-decker configuration in direct images (Figure 3(a)). We attribute this to the circumstance that the flaring region was very localized, making it hard to distinguish between the two flux ropes within the resolution of AIA, besides possible projection effects (see Figures 3 and 5). However, a few of the brightenings observed in AIA 1600 Å images of the preflare phase (see Figure 2(f)) may possibly be the footpoints of the two MFRs of the double-decker configuration. It is worth mentioning that the minisigmoidal structure appeared in the AIA 94 Å channel only ≈1.5 hr before the M1.4 flare, which is a much shorter time compared to the evolution of the sigmoidal structure associated with the double-decker flux rope system reported previously by Cheng et al. (2014), which was ≈40 hr.

Both M-class flares initiated with very localized brightenings at the sigmoid, immediately followed by a collimated plasma ejection (Figures 3 and 5). During the evolution of the flares, we identified the appearance of a small filament, while the localized brightening persisted beneath the filament (Figure 4). The photospheric magnetogram and extrapolated coronal magnetic field configuration clearly revealed the source region of the eruption to be bipolar with high shearing (Figure 11). Further, both the positive and the absolute negative flux decayed prior to the flares from the flaring region (Figure 9(b)). We interpret this evolution as observational signatures of photospheric flux cancellation at the PIL, which is recognized for its association with small-scale magnetic reconnections (van Ballegooijen & Martens 1989) leading to the formation of MFRs; this was well elaborated in subsequent studies (see, e.g., Amari et al. 2010; Xue et al. 2017; Panesar et al. 2018; Mitra et al. 2020). For both flares, localized (E)UV brightenings, underneath the apparent location of the filament body, were observed during their onset. We interpret these findings as evidence for the tether-cutting model of solar eruptions

(Moore & Roumeliotis 1992; Moore et al. 2001). Among the observable signatures of tether-cutting reconnection, compact EUV and hard X-ray brightenings beneath an erupting MFR (or middle of the sigmoid) and collimated plasma outflows may be highlighted (Raftery et al. 2010; Liu et al. 2013; Chen et al. 2014, 2016, 2018). While investigating the onset processes of a solar eruption, Chen et al. (2018) observed clear signatures of flux cancellation from the flaring region, bidirectional jets, and change in the topology of the hot loops during the precursor phase. They argued that bidirectional jetlike flows occurred as a result of the interaction of two coronal loop structures. This led them to conclude that the onset process of the eruption was tether-cutting reconnection. The events reported in this paper evolved with unidirectional jets, which differs from the bidirectional jets reported by Chen et al. (2018). However, EUV images of the flaring region confirm that the locations of the occurrences of the jets were closely associated with the initial brightenings beneath the filaments (Figures 3(e) and (m) and 6(d)), which further supports the tether-cutting reconnection between the two MFRs in the double-decker flux rope system.

It is noteworthy that both M-class flares initiated with highly collimated, unidirectional plasma outflow (Figures 3, 5, and 6) for a relatively short duration (∼5 minutes), a characteristic feature of coronal jets (see Raouafi et al. 2016). In the present observations, the jet structure observed during the first M-class flare (M1.4) was associated with a collimated and narrow spire, while its base was rooted in the highly sheared double-decker flux rope system. Such a configuration of the coronal jet is consistent with the standard jet scenario. On the other hand, the jet occurring during the second M-class flare (M7.3) initiated like a standard jet but gradually moved toward the "blowout" phase. Notably, we found a distinct time gap between the "standard" and "blowout" phases of ∼2 minutes (Figures 5, 6), which is attributed to slow kinematic evolution of the filament constrained by the base arch (see Section 3 in Moore et al. 2010). The intense and impulsive SXR flux, peaking at the M7.3 level, essentially manifests reconnection and the heated field lines as the blowout eruption of the filament proceeds. The jet was eventually associated with the eruption of a filament that resulted in a narrow CME.

The plasma ejection along with the jet's spires during both M-class flares presented some atypical features requiring further investigation. The AIA images clearly displayed that a part of the ejected material, after moving toward the east for a short period, sharply changed direction from east to southwest (Figures 3 and 5). This anomalous dynamics of jet propagation was much more prominent during the second flare. Notably, PFSS extrapolation revealed a set of open field lines that originated near the flaring site and underwent bending toward the southwest direction (Figure 10(b)). Such regions of open field lines have been identified as dark areas in the form of CHs observed in the EUV and SXR images of the Sun (Cranmer 2009). The CH regions are believed to have a strong impact on CMEs when they interact with each other. A statistical study conducted by Gopalswamy et al. (2009) revealed that a significant number of CMEs are deflected away from their initial propagation direction by CHs. Later on, several other studies provided results in support of this finding (see, e.g., Kahler et al. 2012; Mohamed et al. 2012; Wood et al. 2012; Wang et al. 2014; Bilenko 2017; Yang et al. 2018; Heinemann et al. 2019). On 2017 September 7, we did not observe any CHs near the AR NOAA 12673. However, a faint dark region, identified in AIA 193 Å images, situated in the southeastern direction of the AR (Figure 10(a)) developed into a prominent CH after one solar rotation (Figure 10(c)). From its association with the open field lines (Figure 10(b)), we conclude that deflection of the ejected material during the M-class flares reported in this paper was caused by the open field lines originating from the emerging CH region at the trailing part of the AR.

The horizontal magnetic field above the AR experienced a rapid decay with height, and the condition of torus instability was reached within a low atmospheric height (Figure 11(d)). The condition of torus instability has been extensively used to explain the eruptive nature of ARs (see, e.g., Liu 2008; Aulanier et al. 2010; Démoulin & Aulanier 2010; Thalmann et al. 2015, 2016; Chandra et al. 2017; Zuccarello et al. 2017; Liu et al. 2018b; Sarkar & Srivastava 2018). From theoretical calculations, Bateman (1978) proposed that a toroidal current ring becomes unstable for expansion if the surrounding poloidal field radially decreases faster than a critical value ($n = 1.5$). Kliem & Török (2006) generalized this idea and proposed that flux rope structures can attain eruptive motions under the condition of torus instability. Several observational and theoretical studies have revealed the critical value of the magnetic decay index for torus instability to lie within the range [1.0, 1.5] (Liu 2008; Démoulin & Aulanier 2010; Olmedo & Zhang 2010; Zuccarello et al. 2014; Liu et al. 2015). Wang et al. (2017) conducted a statistical survey in order to calculate from the observations the critical height ($h_{\rm crit}$) of torus instability for 60 two-ribbon flares. Their study revealed that, on average, the critical height where the decay index reached a value of $n = 1.5$ was $h_{\rm crit} = 36.3 \pm 17.4$ Mm above the PIL. During the preflare phase of the M-class flares reported in this paper, the condition of torus instability ($n_{\rm crit} = 1.0$–1.5) was achieved at heights of $h_{\rm crit} \approx 27$–45 Mm above the PIL, which is in basic agreement with the statistical results reported in Wang et al. (2017; $h_{\rm crit} = 36.3 \pm 17.4$ Mm) and Baumgartner et al. (2018; $h_{\rm crit} = 21 \pm 10$ Mm).

We further explored the application of kink instability toward the triggering of the flux ropes by computing the twist numbers. Our analysis reveals the average twist associated with the flux ropes to be $|T_w| \approx 1.0$. Extensive statistical work by Duan et al. (2019) concerning the torus and kink instabilities as the triggering mechanisms of flux ropes revealed that the critical value for the onset of kink instability is given by a twist number $|T_w| \approx 2$. In view of this result, we could not establish any conclusive evidence of kink instability as a possible triggering mechanism in our event.

In summary, this paper studies the initiation and evolution of two homologous M-class flares in the AR NOAA 12673, which produced the two largest flares in solar cycle 24. Both flares underwent very impulsive evolution. An interesting feature of these eruptive flares lies in their association with a minisigmoid region, which suggests that sufficient energy storage within even smaller MFRs can also lead to CME initiation, provided the overlying magnetic field configuration is favorable for its further expansion in the corona. Our analysis suggests that the flaring region is associated with a double-decker flux rope configuration, which constitutes a more complex case of energy storage within a compact region. Both M-class flares initiated with jetlike plasma ejections. We find the activation and rise of a filament after the first flare, which then erupted during the second flare. The eruption of the filament at the source region can be justifiably termed "anomalous," as the initial jetlike eruption not only drastically changed its direction but also underwent a large angular expansion as the erupting plasma reached successively higher coronal regions. From multiwavelength EUV imaging and PFSS magnetic field extrapolation, we showed the presence of large-scale open field structures expanding toward the southwest of the AR. Our analysis reveals that the anomalous expansion of the CME at the source region is due to the deflection of erupting material by the large-scale open field lines. In view of the presence of low coronal double-decker flux ropes and compact EUV brightenings beneath a filament, along with the magnetic flux cancellation observed at the PIL, our analysis supports the tether-cutting model of solar eruptions. Further, the distribution of the magnetic decay index above the PIL suggests a rapid decay of the field above the minisigmoid region, implying favorable coronal conditions for the successful eruption of the flux rope initially activated by the tether-cutting process.

We thank the SDO and RHESSI teams for their open data policy. The SDO is NASA's mission under the Living With a Star (LWS) program. RHESSI was NASA's mission under the SMall EXplorer (SMEX) program. We also thank Julia K. Thalmann for help in the NLFFF extrapolation. This work is supported by Indo-Austrian joint research project No. INT/AUSTRIA/BMWF/ P-05/2017 and OeAD project No. IN 03/2017. A.M.V. and K.D. also thank the Austrian Science Fund (FWF): P27292-N20 and I4555-N. We also thank the anonymous referee for constructive comments that helped us improve the overall quality of this paper.

ORCID iDs

Prabir K. Mitra https://orcid.org/0000-0002-0341-7886
Bhuwan Joshi https://orcid.org/0000-0001-5042-2170
Astrid M. Veronig https://orcid.org/0000-0003-2073-002X
Ramesh Chandra https://orcid.org/0000-0002-3518-5856
K. Dissauer https://orcid.org/0000-0001-5661-9759

References

Allen Gary, G., & Hagyard, M. J. 1990, SoPh, 126, 21
Amari, T., Aly, J.-J., Mikic, Z., & Linker, J. 2010, ApJL, 717, L26
Antiochos, S. K., DeVore, C. R., & Klimchuk, J. A. 1999, ApJ, 510, 485
Archontis, V., & Hood, A. W. 2013, ApJL, 769, L21
Asai, A., Shibata, K., Hara, H., & Nitta, N. V. 2008, ApJ, 673, 1188
Aulanier, G. 2014, in IAU Symp. 300, Nature of Prominences and their Role in Space Weather, ed. B. Schmieder, J.-M. Malherbe, & S. T. Wu (Cambridge: Cambridge Univ. Press), 184
Aulanier, G., Démoulin, P., Schrijver, C. J., et al. 2013, A&A, 549, A66
Aulanier, G., Janvier, M., & Schmieder, B. 2012, A&A, 543, A110
Aulanier, G., Török, T., Démoulin, P., & DeLuca, E. E. 2010, ApJ, 708, 314
Bateman, G. 1978, MHD Instabilities (Cambridge, MA: MIT Press)
Baumgartner, C., Thalmann, J. K., & Veronig, A. M. 2018, ApJ, 853, 105
Benz, A. O. 2017, LRSP, 14, 2
Berger, M. A., & Prior, C. 2006, JPhA, 39, 8321
Bhatnagar, A. 1996, Ap&SS, 243, 105
Bilenko, I. A. 2017, Ge&Ae, 57, 952
Brueckner, G. E., & Bartoe, J. D. F. 1983, ApJ, 272, 329
Brueckner, G. E., Howard, R. A., Koomen, M. J., et al. 1995, SoPh, 162, 357
Carmichael, H. 1964, NASSP, 50, 451
Chen, B., Yu, S., Reeves, K. K., & Gary, D. E. 2020, ApJL, 895, L50
Chen, H., Duan, Y., Yang, J., Yang, B., & Dai, J. 2018, ApJ, 869, 78
Chen, H., Zhang, J., Cheng, X., et al. 2014, ApJL, 797, L15
Chen, H., Zhang, J., Li, L., & Ma, S. 2016, ApJL, 818, L27
Cheng, X., Ding, M. D., Zhang, J., et al. 2014, ApJ, 789, 93
Clyne, J., Mininni, P., Norton, A., & Rast, M. 2007, NJPh, 9, 301
Cranmer, S. R. 2009, LRSP, 6, 3
Dalmasse, K., Chandra, R., Schmieder, B., & Aulanier, G. 2015, A&A, 574, A37
Démoulin, P., & Aulanier, G. 2010, ApJ, 718, 1388
DeRosa, M. L., Wheatland, M. S., Leka, K. D., et al. 2015, ApJ, 811, 107
Ding, M. D., Qiu, J., & Wang, H. 2002, ApJL, 576, L83
Domingo, V., Fleck, B., & Poland, A. I. 1995, SoPh, 162, 1
Duan, A., Jiang, C., He, W., et al. 2019, ApJ, 884, 73
Fletcher, L., Dennis, B. R., Hudson, H. S., et al. 2011, SSRv, 159, 19
Gary, D. E., Chen, B., Dennis, B. R., et al. 2018, ApJ, 863, 83
Gibson, S. E., & Fan, Y. 2006, JGRA, 111, A12103
Gibson, S. E., Fletcher, L., Del Zanna, G., et al. 2002, ApJ, 574, 1021
Gopalswamy, N., Mäkelä, P., Xie, H., Akiyama, S., & Yashiro, S. 2009, JGRA, 114, A00A22
Guo, J., Dumbović, M., Wimmer-Schweingruber, R. F., et al. 2018, SpWea, 16, 1156
Gou, T., Veronig, A. M., Dickson, E. C., Hernand ez-Perez, A., & Liu, R. 2017, ApJL, 845, L1
Green, L. M., Török, T., Vršnak, B., Manchester, W., & Veronig, A. 2018, SSRv, 214, 46
Heinemann, S. G., Temmer, M., Farrugia, C. J., et al. 2019, SoPh, 294, 121
Hirayama, T. 1974, SoPh, 34, 323
Hou, Y. J., Zhang, J., Li, T., Yang, S. H., & Li, X. H. 2018, A&A, 619, A100
Hurford, G. J., Schmahl, E. J., Schwartz, R. A., et al. 2002, SoPh, 210, 61
Janvier, M., Aulanier, G., Bommier, V., et al. 2014, ApJ, 788, 60
Janvier, M., Aulanier, G., Pariat, E., & Démoulin, P. 2013, A&A, 555, A77
Jiang, Y. C., Chen, H. D., Li, K. J., Shen, Y. D., & Yang, L. H. 2007, A&A, 469, 331
Joshi, B., Kushwaha, U., Cho, K.-S., & Veronig, A. M. 2013, ApJ, 771, 1
Joshi, B., Kushwaha, U., Veronig, A. M., et al. 2017a, ApJ, 834, 42
Joshi, B., Kushwaha, U., Veronig, A. M., & Cho, K.-S. 2016, ApJ, 832, 130
Joshi, B., Thalmann, J. K., Mitra, P. K., Chandra, R., & Veronig, A. M. 2017b, ApJ, 851, 29
Joshi, B., Veronig, A., Cho, K. S., et al. 2009, ApJ, 706, 1438
Joshi, B., Veronig, A., Manoharan, P. K., & Somov, B. V. 2012, ApSSP, 33, 29
Kahler, S. W., Akiyama, S., & Gopalswamy, N. 2012, ApJ, 754, 100
Karpen, J. T., Antiochos, S. K., & DeVore, C. R. 2012, ApJ, 760, 81
Kliem, B., & Török, T. 2006, PhRvL, 96, 255002
Kopp, R. A., & Pneuman, G. W. 1976, SoPh, 50, 85
Künzel, H. 1960, AN, 285, 271
Kushwaha, U., Joshi, B., Cho, K.-S., et al. 2014, ApJ, 791, 23
Lemen, J. R., Title, A. M., Akin, D. J., et al. 2012, SoPh, 275, 17
Lin, R. P., Dennis, B. R., Hurford, G. J., et al. 2002, SoPh, 210, 3
Liu, C., Deng, N., Lee, J., et al. 2013, ApJL, 778, L36
Liu, C., Deng, N., Liu, R., et al. 2015, ApJL, 812, L19
Liu, L., Cheng, X., Wang, Y., et al. 2018a, ApJL, 867, L5
Liu, L., Cheng, X., Wang, Y., & Zhou, Z. 2019, ApJ, 884, 45
Liu, L., Wang, Y., Zhou, Z., et al. 2018b, ApJ, 858, 121
Liu, R., Kliem, B., Török, T., et al. 2012, ApJ, 756, 59
Liu, W., Jin, M., Downs, C., et al. 2018c, ApJL, 864, L24
Liu, W., Petrosian, V., Dennis, B. R., & Jiang, Y. W. 2008, ApJ, 676, 704
Liu, Y. 2008, ApJL, 679, L151
Manoharan, P. K., van Driel-Gesztelyi, L., Pick, M., & Demoulin, P. 1996, ApJL, 468, L73
Maurya, R. A., & Ambastha, A. 2009, SoPh, 258, 31
Maurya, R. A., Vemareddy, P., & Ambastha, A. 2012, ApJ, 747, 134
Mitra, P. K., & Joshi, B. 2019, ApJ, 884, 46
Mitra, P. K., Joshi, B., & Prasad, A. 2020, SoPh, 295, 29
Mitra, P. K., Joshi, B., Prasad, A., Veronig, A. M., & Bhattacharyya, R. 2018, ApJ, 869, 69
Mohamed, A. A., Gopalswamy, N., Yashiro, S., et al. 2012, JGRA, 117, A01103
Moore, R. L., Cirtain, J. W., Sterling, A. C., & Falconer, D. A. 2010, ApJ, 720, 757
Moore, R. L., & Roumeliotis, G. 1992, IAUCo, 133, 69
Moore, R. L., Sterling, A. C., Hudson, H. S., & Lemen, J. R. 2001, ApJ, 552, 833
Moore, R. L., Tang, F., Bohlin, J. D., & Golub, L. 1977, ApJ, 218, 286
Moraitis, K., Sun, X., Pariat, É., & Linan, L. 2019, A&A, 628, A50
Olmedo, O., & Zhang, J. 2010, ApJ, 718, 433
Panesar, N. K., Sterling, A. C., & Moore, R. L. 2018, ApJ, 853, 189
Pesnell, W. D., Thompson, B. J., & Chamberlin, P. C. 2012, SoPh, 275, 3

Priest, E., & Forbes, T. 2000, Magnetic Reconnection: MHD Theory and Applications (Cambridge: Cambridge Univ. Press)
Priest, E. R., & Forbes, T. G. 2002, A&ARv, 10, 313
Raftery, C. L., Gallagher, P. T., McAteer, R. T. J., Lin, C.-H., & Delahunt, G. 2010, ApJ, 721, 1579
Raouafi, N. E., Patsourakos, S., Pariat, E., et al. 2016, SSRv, 201, 1
Riley, P., Lionello, R., Mikić, Z., & Linker, J. 2008, ApJ, 672, 1221
Chandra, R., Filippov, B., Joshi, R., & Schmieder, B. 2017, SoPh, 292, 81
Romano, P., Elmhamdi, A., Falco, M., et al. 2018, ApJL, 852, L10
Romano, P., Elmhamdi, A., & Kordi, A. S. 2019, SoPh, 294, 4
Rust, D. M., & Kumar, A. 1996, ApJL, 464, L199
Sahu, S., Joshi, B., Mitra, P. K., Veronig, A. M., & Yurchyshyn, V. 2020, ApJ, 897, 157
Sarkar, R., & Srivastava, N. 2018, SoPh, 293, 16
Schmieder, B., Shibata, K., van Driel-Gesztelyi, L., & Freeland, S. 1995, SoPh, 156, 245
Schou, J., Scherrer, P. H., Bush, R. I., et al. 2012, SoPh, 275, 229
Seaton, D. B., & Darnel, J. M. 2018, ApJL, 852, L9
Seehafer, N. 1978, SoPh, 58, 215
Shibata, K., Ishido, Y., Acton, L. W., et al. 1992, PASJ, 44, L173
Shibata, K., & Magara, T. 2011, LRSP, 8, 6
Shibata, K., Yokoyama, T., & Shimojo, M. 1996, JGG, 48, 19
Shimojo, M., Hashimoto, S., Shibata, K., et al. 1996, PASJ, 48, 123
Shimojo, M., Shibata, K., & Harvey, K. L. 1998, SoPh, 178, 379
Sturrock, P. A. 1966, Natur, 211, 695
Thalmann, J. K., Su, Y., Temmer, M., & Veronig, A. M. 2015, ApJL, 801, L23
Thalmann, J. K., Su, Y., Temmer, M., & Veronig, A. M. 2016, in IAU Symp. 320, Solar and Stellar Flares and their Effects on Planets, ed. A. G. Kosovichev, S. L. Hawley, & P. Heinzel (Cambridge: Cambridge Univ. Press), 60
Titov, V. S., Hornig, G., & Démoulin, P. 2002, JGRA, 107, 1164
Török, T., Kliem, B., & Titov, V. S. 2004, A&A, 413, L27
Tripathi, D., Kliem, B., Mason, H. E., Young, P. R., & Green, L. M. 2009, ApJL, 698, L27
Tsuneta, S., Acton, L., Bruner, M., et al. 1991, SoPh, 136, 37
van Ballegooijen, A. A., & Martens, P. C. H. 1989, ApJ, 343, 971
Verma, M. 2018, A&A, 612, A101
Veronig, A., Vršnak, B., Temmer, M., & Hanslmeier, A. 2002, SoPh, 208, 297
Veronig, A. M., Karlický, M., Vršnak, B., et al. 2006, A&A, 446, 675
Veronig, A. M., Podladchikova, T., Dissauer, K., et al. 2018, ApJ, 868, 107
Vršnak, B. 2016, AN, 337, 1002
Vršnak, B., Maričić, D., Stanger, A. L., & Veronig, A. 2004, SoPh, 225, 355
Wang, D., Liu, R., Wang, Y., et al. 2017, ApJL, 843, L9
Wang, Y., Wang, B., Shen, C., Shen, F., & Lugaz, N. 2014, JGRA, 119, 5117
Wang, Y.-M., & Sheeley, N. R., Jr. 1992, ApJ, 392, 310
Wheatland, M. S., Sturrock, P. A., & Roumeliotis, G. 2000, ApJ, 540, 1150
Wiegelmann, T. 2004, SoPh, 219, 87
Wiegelmann, T., & Inhester, B. 2010, A&A, 516, A107
Wiegelmann, T., Inhester, B., & Sakurai, T. 2006, SoPh, 233, 215
Wiegelmann, T., Thalmann, J. K., Inhester, B., et al. 2012, SoPh, 281, 37
Wood, B. E., Wu, C. C., Rouillard, A. P., Howard, R. A., & Socker, D. G. 2012, ApJ, 755, 43
Xue, Z., Yan, X., Yang, L., Wang, J., & Zhao, L. 2017, ApJL, 840, L23
Yang, J., Dai, J., Chen, H., Li, H., & Jiang, Y. 2018, ApJ, 862, 86
Yang, S., Zhang, J., Zhu, X., & Song, Q. 2017, ApJL, 849, L21
Yashiro, S., Gopalswamy, N., Michalek, G., et al. 2004, JGRA, 109, A07105
Zhao, M., Wang, J.-X., Matthews, S., et al. 2009, RAA, 9, 812
Zuccarello, F. P., Chandra, R., Schmieder, B., Aulanier, G., & Joshi, R. 2017, A&A, 601, A26
Zuccarello, F. P., Seaton, D. B., Filippov, B., et al. 2014, ApJ, 795, 175

Monthly Notices of the ROYAL ASTRONOMICAL SOCIETY

MNRAS **503,** 1017–1035 (2021)
Advance Access publication 2021 January 22
doi:10.1093/mnras/stab175

Successive occurrences of quasi-circular ribbon flares in a fan-spine-like configuration involving hyperbolic flux tube

Prabir K. Mitra [1,2]★ and Bhuwan Joshi [1]

[1] *Udaipur Solar Observatory, Physical Research Laboratory, Udaipur 313 001, India*
[2] *Department of Physics, Gujarat University, Ahmedabad 380 009, India*

Accepted 2021 January 19. Received 2021 January 19; in original form 2020 October 8

ABSTRACT

We present a comprehensive analysis of the formation and the evolution of a fan-spine-like configuration that developed over a complex photospheric configuration where dispersed negative polarity regions were surrounded by positive polarity regions. This unique photospheric configuration, analogous to the geological 'atoll' shape, hosted four homologous flares within its boundary. Computation of the degree of squashing factor (Q) maps clearly revealed an elongated region of high Q-values between the inner and outer spine-like lines, implying the presence of an hyperbolic flux tube (HFT). The coronal region associated with the photospheric atoll configuration was distinctly identified in the form of a diffused dome-shaped bright structure directly observed in Extreme Ultraviolet (EUV) images. A filament channel resided near the boundary of the atoll region. The activation and eruption of flux ropes from the filament channel led to the onset of four eruptive homologous quasi-circular ribbon flares within an interval of $\approx$11 h. During the interval of the four flares, we observed continuous decay and cancellation of negative polarity flux within the atoll region. Accordingly, the apparent length of the HFT gradually reduced to a null-point-like configuration before the fourth flare. Prior to each flare, we observed localized brightening beneath the filaments which, together with flux cancellation, provided support for the tether-cutting model of solar eruption. The analysis of magnetic decay index revealed favourable conditions for the eruption, once the pre-activated flux ropes attained the critical heights for torus instability.

Key words: Sun: activity – Sun: filaments, prominences – Sun: flares – Sun: magnetic fields – sunspots.

1 INTRODUCTION

Solar flares are sudden, localized enhancement of brightness in the solar atmosphere during which energy up to $\sim10^{32}$ erg can be released in the entire electromagnetic spectrum (see review articles by Fletcher et al. 2011; Benz 2017). It is well understood that magnetic field remains at the helm of all the catastrophic processes occurring in the solar atmosphere including flares, as the energy released during flares is supplied from the magnetic energy that is stored in the flaring region prior to the flare (see e.g. Shibata & Magara 2011). Therefore, the pre-flare magnetic configuration plays a crucial role in determining the trigger and subsequent evolution of solar flares and associated eruptive phenomena (e.g. Joshi et al. 2015, 2017c; Hernandez-Perez et al. 2019; Mitra, Joshi & Prasad 2020a; Qiu et al. 2020).

Traditionally, solar flares were observed to be associated with a pair of ribbon like brightening identified in chromospheric H α images, which were situated on the opposite sides of a polarity inversion line (PIL). To explain such parallel ribbon flares, a 'standard flare model' was proposed combining the works of Carmichael (1964), Sturrock (1966), Hirayama (1974), and Kopp & Pneuman (1976), which is also known as the 'CSHKP' model (Shibata & Magara 2011). According to this model, magnetic reconnection takes place along a vertical current sheet, formed between the inflowing magnetic fields beneath an erupting prominence. During reconnection, magnetic energy gets transformed into heat and particle accelerations resulting in localized sudden flash in the solar atmosphere and highly accelerated electrons that are projected with almost relativistic speeds towards the lower, denser chromospheric layer of the Sun along the reconnected field lines. The accelerated electrons collide with the dense chromospheric plasma giving rise to hard X-ray (HXR) footpoint sources in association with EUV and optically observable conjugate ribbons termed as chromospheric flare ribbons (Fletcher et al. 2013; Musset, Vilmer & Bommier 2015; Joshi et al. 2017a; Kazachenko et al. 2017). Despite the general success of the CSHKP model towards explaining the commonly observed features of eruptive parallel ribbon flares, i.e. footpoint and looptop HXR sources, post-flare arcade, hot cusp, etc., several studies have reported flaring activities to involve complex structures of flare ribbons and dynamics of overlying coronal loops implying that CSHKP model alone cannot explain all the flares (e.g. Veronig et al. 2006; Joshi et al. 2009; Kushwaha et al. 2015; Mitra et al. 2018).

It is also important to note that the CSHKP model, being a 2D model, cannot explain the 3D aspects of typical solar flares such as, evolution of shear from the pre-flare loops to post-flare arcades; relative positions, shapes, and motions of the flare ribbons, etc. To incorporate these features, the CSHKP model has been extended in 3D with numerical simulations (Aulanier, Janvier & Schmieder 2012; Aulanier et al. 2013). The 3D standard flare model suggests that small-scale current sheets are generated between the highly sheared

★ E-mail: prabir@prl.res.in

pre-flare magnetic field configuration. Reconnection on these current sheets drives the transfer of differential magnetic shear, from the pre- to the post-eruptive configuration. With the evolution of the flare, as the eruption of the flux rope initiates, magnetic loops enveloping it straighten vertically and the current sheet extends along with them. Thus, magnetic reconnection continues beneath the erupting flux rope that is in line with the 2D standard flare model.

Further, the formation of the flux rope and the triggering of its eruption goes beyond the scope of the CSHKP model. Flux ropes are defined by a set of magnetic field lines that are wrapped around each other in a braided fashion or wrapped around a central axis (braided and twisted flux ropes, respectively, see Prior & Yeates 2016). Observationally, a flux rope can be identified in different forms: filament (Zirin 1988; Martin 1998), prominence (Tandberg-Hanssen 1995; Parenti 2014), coronal cavity (Forland et al. 2013; Gibson 2015), hot channel (Zhang, Cheng & Ding 2012; Cheng et al. 2013; Mitra & Joshi 2019; Sahu et al. 2020), coronal sigmoid (Rust & Kumar 1996; Manoharan et al. 1996; Joshi et al. 2017a; Mitra et al. 2018), etc. The processes involved in the triggering of a flux rope from its stable condition and its successive evolution within the source region are rather complex and debatable (see e.g. Chatterjee & Fan 2013; Kumar et al. 2016; Prasad et al. 2020). Different mechanisms have been proposed in this regard, which can be classified in two general groups: ideal instability and resistive instability. Ideal instability models put forward the idea that a flux rope can attain eruptive instability if the values of some parameters go beyond a critical value, e.g. decay index (n; $n = -\frac{\mathrm{d}log(B_\mathrm{h})}{\mathrm{d}log(h)}$; B_h and h being horizontal magnetic field and height, respectively) more than 1.5 for torus instability (Kliem & Török 2006) or the twist of the flux rope more than $\approx 3.5\pi$ for kink instability (Török, Kliem & Titov 2004). On the other hand, resistive instability models recognize the role of initial small-scale reconnection in the active region as the triggering mechanism of a flux rope (or core field), e.g. initial reconnection beneath a flux rope or sheared arcade for the case of tether-cutting model (Moore & Roumeliotis 1992; Moore et al. 2001) or reconnection at a coronal null well above the core field for the case of breakout model (Antiochos, DeVore & Klimchuk 1999). Once the MFR attains eruptive motion, magnetic reconnection initiates beneath the flux rope and two parallel ribbons are observed along with other observable flare signatures explained in the CSHKP model.

Morphologically, a completely different category of flares is circular (or quasi-circular) ribbon flares (Masson et al. 2009) that are usually associated with a fan-spine configuration in a 3D null-point topology (Lau & Finn 1990; Sun et al. 2013). Coronal null-points are locations in the solar corona, where the strengths of all the three components of magnetic field become locally zero (see review by Longcope 2005). Magnetic field beyond the immediate neighbourhood of the null-point is characterized by a spine line and a fan surface. Depending on the sign of the null-point (positive or negative), magnetic field lines approach the null-point along the spine line and move away from it along the fan surface (for positive null; see fig. 4 in Longcope 2005); or approach the null along the fan surface and recede from it along the spine line (negative null). In the context of such 3D null-point configurations generating fan and spine lines, the anemone-type active regions where a compact magnetic region is surrounded by magnetic regions of opposite polarity (see Shibata et al. 1994) are of special significance. The inner compact region is connected with the surrounding opposite polarity region by small-scale closed magnetic loops, while a set of relatively large field lines connect the surrounding polarity to a remote region of polarity similar to that of the inner compact region.

In this way, the two sets of field lines constitute two sets of fan lines (inner and outer fan lines) and two sets of spine lines (inner and outer spine lines). The two sets of fan lines are separated by a dome-shaped surface (i.e. fan separatrix) characterized by high degree of squashing factor (Q; see, Priest & Démoulin 1995; Titov, Hornig & Démoulin 2002), which intersects the spine lines at the null-point (Sun et al. 2013). In general, domains corresponding to drastic changes in the magnetic field connectivity gradient are identified as quasi-separatrix layers (QSLs; see e.g. Janvier et al. 2013). While the values of Q corresponding to QSLs are high ($\gg$2; see, Aulanier, G. et al. 2005), null-points can be characterized by $Q \rightarrow \infty$. The finite values of Q at the QSLs imply that although magnetic fields show drastic change in the connectivity, they are still continuous, which is contrary to the cases of null-points where magnetic field becomes discontinuous. In complex photospheric configurations, e.g. those formed by two bipolar sunspots, a pair of photospheric null-points of opposite signs may exist that are connected by 'separators' (Titov et al. 2002). A separator can be identified by narrow elongated strips of high Q-values, i.e. a QSL, with a pair of null-points at both of its ends. Further, a generalization of the concept of separator lines reveals a special geometrical feature called 'hyperbolic flux tubes' (HFTs; Titov et al. 2002) that can be understood as the intersection of two QSLs. The middle of an HFT is characterized by 'X'-type cross-section comprised of high Q-values. Such structures of high Q-values are preferred sites for the formation of current sheets and initiation of magnetic reconnection (Titov, Galsgaard & Neukirch 2003). Moreover, magnetic field lines can constantly change their connectivities along the QSLs as a consequence of local diffusion in the region, allowing neighbouring field lines to exchange connectivities (Aulanier et al. 2006). This can be observed as an apparent slipping or flipping motion of loop connectivities and are termed as 'slipping reconnction' (see e.g. Priest & Démoulin 1995; Aulanier et al. 2006; Janvier et al. 2013).

With the advancements of observational facilities and numerical techniques, in the recent years a number of studies have reported flaring activities that involved both the circular and parallel ribbons where the parallel ribbons usually reside at the inside edge of the circular ribbon (e.g. Joshi et al. 2015, 2017b; Hernandez-Perez et al. 2017; Li et al. 2017; Xu et al. 2017; Li et al. 2018a,b; Hou et al. 2019; Shen et al. 2019; Devi et al. 2020). Such events usually develop as a small flux rope erupts within a fan-dome that then triggers reconnection at the null-point. The null-point reconnection itself is a complex, multistage mechanism that initially includes slipping reconnection at the quasi-separatrix surface at the fan-dome giving rise to the circular or quasi-circular ribbon and during the subsequent stage, interchange reconnection takes place between the inner close fan lines and the outer open spine lines causing the remote brightening (see, Masson et al. 2009). In response to the interchange reconnection at the coronal null-point, collimated ejection of plasma, i.e. coronal jets or H α surges have been identified in several studies (Pariat, Antiochos & DeVore 2009a, 2010). These findings point towards the fact that magnetic configurations on the Sun could be very complex, and more studies are extremely essential towards reaching at a general understanding of the complex sunspot configurations and associated flaring activities.

In this article, we report four homologous quasi-circular ribbon flares from the active region NOAA 11977, which were triggered by erupting filaments from the circular ribbon region. With the help of high resolution images of atmospheric imaging assembly (AIA; Lemen et al. 2012) and helioseismic and magnetic imager (HMI; Schou et al. 2012) on board the *Solar Dynamics Observatory* (SDO; Pesnell, Thompson & Chamberlin 2012), we study the evolution of

Table 1. Summary of the flares occurred on 2014 February 16 from the magnetic atoll region of NOAA 11977.

Flare Id.	Location	Flare timing (UT) Start/ Peak/ End	GOES class	Remarks
F_1	S10E00	09:20/ 09:26/ 09:29	M1.1	Observation of quasi-circular ribbon
F_2	S10W01	13:48/ 14:00/ 14:05	C3.4	Observation of shortened quasi-circular ribbon
F_3	S10W03	17:35/ 17:38/ 17:40	C1.2	Observation of arc-shaped ribbon
F_4	S10W04	19:20/ 19:23/ 19:28	C1.7	Observation of arc-shaped ribbon

the active region and the complex flares in detail. Magnetic field modelling based on a 'non-linear force-free field' (NLFFF) method has revealed a fan-spine-like configuration associated with the flaring region. The most important finding of this study is the absence of coronal null-point in the fan-spine-like configuration. Instead, the calculation of Q revealed the presence of an HFT between the inner and outer spine-like lines. In Section 2, we provide a brief description of the observational data sources and the image analysis techniques along with the numerical methods used in this article. We discuss the morphology and evolution of the active region as well as give a brief account of all the flares produced by it in Section 3. Results obtained from imaging analysis of the two circular ribbon flares and NLFFF extrapolation are presented in Sections 4 and 5. We discuss and interpret the results in Section 6.

2 OBSERVATIONAL DATA AND ANALYSIS TECHNIQUES

For EUV imaging, we have utilized the 12 s cadence, 4096 × 4096 pixel full disc observations from the AIA on board the *SDO* with pixel resolution of 0″.6. For the chromospheric imaging of the Sun, we have used the 2048 × 2048 pixel full disc images in the Hα passband with a pixel resolution of ≈1″.0, obtained from the archive global oscillation network group (GONG; Harvey et al. 1996, 2011). We have studied the photospheric structures associated with the active region NOAA 11977 using the 45 s cadence, 4096 × 4096 pixel full disc continuum and line-of-sight (LOS) magnetogram observations with spatial sampling resolution of 0″.5 pixel^{-1} by HMI on board the *SDO*. The HMI LOS intensity and magnetogram images were further processed with the IDL-based algorithm '*hmi_prep*' to co-align them with AIA pixel resolution. Coronal magnetic fields were extrapolated by employing the optimisation based NLFFF extrapolation method developed by Wiegelmann & Inhester (2010) and Wiegelmann et al. (2012). For the purpose, we have used the vector magnetogram data from the '*hmi.sharp_cea_720s*' series of HMI at a reduced spatial resolution of 1″.0 pixel^{-1} as the input boundary condition. Extrapolations were done within a volume of dimensions 453 × 270 × 240 pixels that corresponds to the physical dimension of ≈328 × 196 ×174 Mm^3. Based on the NLFFF extrapolation results, we calculated the degree of squashing factor (Q) and twist number (T_w) in the extrapolation volume using the IDL-based code developed by Liu et al. (2016). In order to locate 3D null-points within the extrapolation volume, we used the trilinear method as suggested by Haynes & Parnell (2007). For the purpose, the whole active region volume was divided into grid cells of dimension 2 × 2 × 2 pixels. The first step of the trilinear method is to quickly scan through every grid cell by examining the signs of each component of magnetic field at all the eight corners of the grid cells. If any of the three components have same sign at all the eight corners, a null-point cannot reside within the grid cell and therefore, the corresponding cell is excluded from further analysis. Each of the remaining other cells is then further divided into 100 × 100 × 100 subgrid cells and the threshold $\Delta x \leq 2$ subgrid cell width was used for locating null-points. For visualizing the modelled field lines and the distribution of Q in the active region volume, we have used the Visualization and Analysis Platform for Ocean, Atmosphere, and Solar Researchers[1] (Clyne et al. 2007) software.

3 STRUCTURE AND EVOLUTION OF THE ACTIVE REGION NOAA 11977

The active region NOAA 11977 appeared on the eastern limb of the Sun on 2014 February 11 as a simple α-type active region. It quickly transformed into a relatively more complex β-type on the very next day. The active region gradually developed into $\beta\gamma$-type on 2014 February 14 and remained so for the next 4 d. Notably, the active region started to decay in its area since 2014 February 15. On 2014 February 16, an intriguing configuration of magnetic fields, involving complex distribution and topology, developed in the westernmost part of the active region that we study comprehensively in Section 3.2. Notably, one M and three C-class flares originated from this region within an interval of ≈11 h on February 16 (see Table 1). The magnetic complexity of the active region reduced to β-type on 2014 February 19. The active region disappeared from the western limb of the Sun on 2014 February 23 as an α-type sunspot.

3.1 Morphology of the active region NOAA 11977

In Fig. 1, we show a comparison of the photospheric structure of the active region with its coronal configuration, prior to the M-class flare on 2014 February 16. We find that, the active region was comprised of a few prominent sunspots and many pores. We consider two subregions of the active region: the leading sunspot group and the trailing sunspot group (shown by the dashed and dotted boxes in Fig. 1a, respectively). Comparison of a co-temporal LOS magnetogram (Fig. 1b) of the active region with the intensity image reveals that the leading sunspot group was consisted of mostly positive polarity, while the trailing part of the active region was dominated by negative polarity magnetic field. However, the most interesting aspect of the active region, in the context of our analysis, is the magnetic configuration that developed in the extreme western part of it where magnetic patches of positive and negative polarities formed a configuration similar to an 'atoll' (within the white box in Fig. 1b). AIA images suggest that the active region, on the whole, consisted of different sets of coronal loops of varying spatial extents and projected heights. In Figs 1(c) and (d), we recognize some of these loops by the arrows of different colours (white, green, and red).

We note striking coronal structures over the photospheric atoll region that can be easily distinguished by its peculiar morphology. The region is outlined by the white boxes in Figs 1(c) and (d). The

[1] https://www.vapor.ucar.edu/

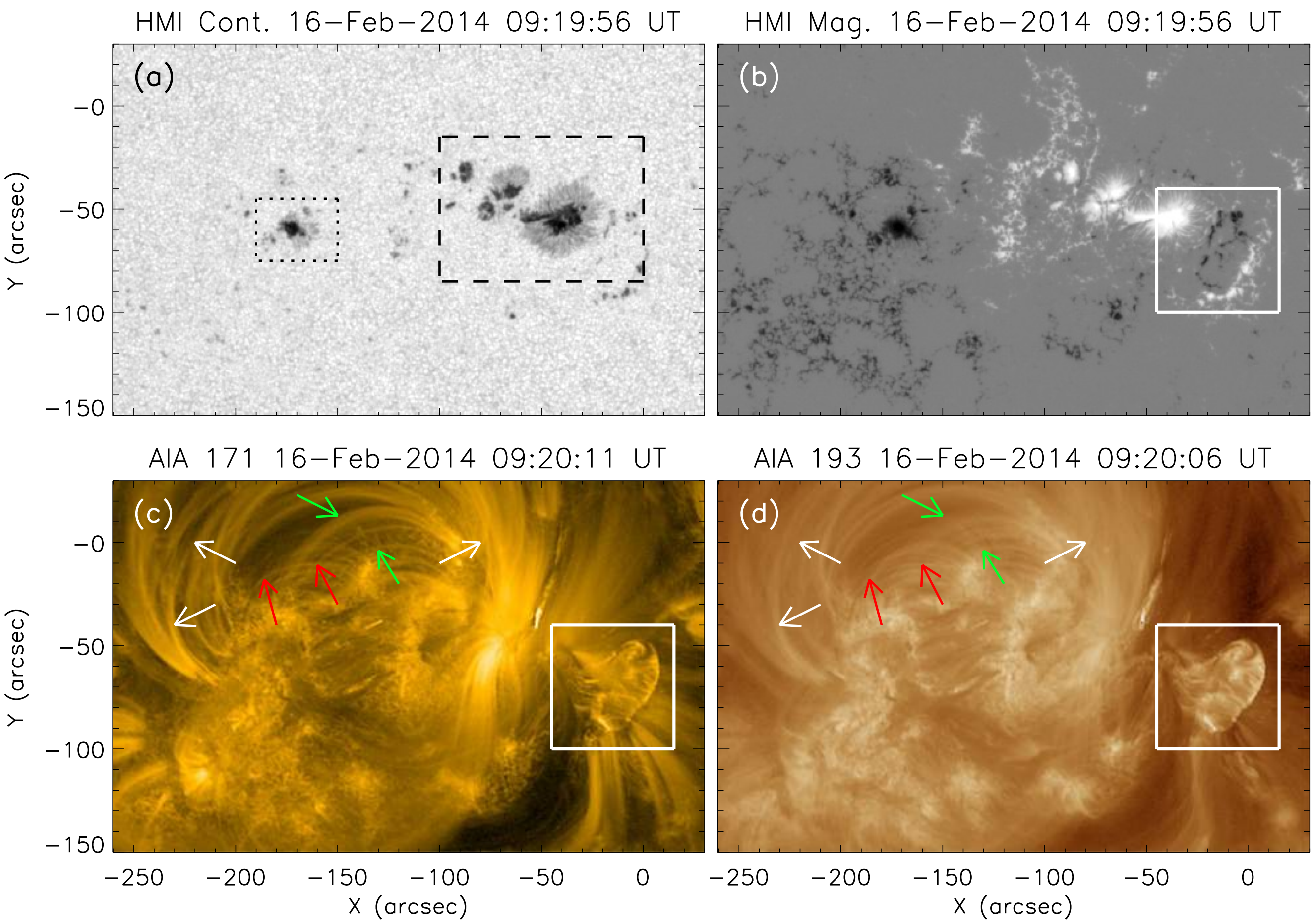

Figure 1. The morphology of the active region NOAA 11977 on the photosphere (panels a and b) and different coronal temperatures (panels c and d). The flaring activity occurred from the region shown within the white box in panels (b)–(d).

EUV images of the coronal region, over the atoll-shaped magnetic structure in the photosphere, clearly reveal enhanced structured brightening within a sharp boundary that forms an oval-shaped feature. All the four events of 2014 February 16 occurred within this region.

3.2 Formation of the 'magnetic atoll' region

In order to understand the formation and development of the magnetic atoll region, in Figs 2(a)–(f), we present a series of LOS magnetograms corresponding to the photospheric region (shown within the white box in Fig. 1b). Since, the diffused brightening region was intrinsically related with the magnetic atoll region, we have also plotted co-temporal AIA 304 Å images of the same region in Figs 2(g)–(l). Our observations reveal that the atoll region started to develop from 2014 February 15 with the emergence a of few small negative polarity flux regions. In Fig. 2(a), we indicate these emerging negative polarity regions by the yellow arrows. With time, negative polarity magnetic flux kept emerging in this region and by the first hour of 2014 February 16, a relatively large magnetic patch of negative polarity was developed (indicated by the blue arrow in Fig. 2c). Co-temporal AIA 304 Å images suggest that the distinct oval-shaped region displaying enhanced-diffused brightening started to build-up from around this time onwards [cf. Figs 2(i) and (c)]. Gradually, this diffused brightening region became more prominent and extended spatially [cf. Figs 2(i)–(l)]. In the same duration, positive flux also emerged in this region that surrounded the negative polarity patches in the south-west (SW) direction (cf. the regions indicated by the pink arrows in Figs 2c and f). In general, the atoll region can be characterized by newly emerged and spatially dispersed prominent patches of negative magnetic flux surrounded by positive polarity regions from two sides, i.e. north-east (NE; by the positive polarity sunspot) and SW (by the dispersed positive polarity patches). Further, from HMI LOS magnetograms during the early hours of 2014 February 16, we could identify several instances of flux emergence and cancellation in the magnetic atoll region. We have identified a few events of flux changes by the blue, red, and green arrows in Figs 2(c)–(f). During the same interval, we also observed formation of a filament channel in the diffused brightening region along the PIL between the positive polarity sunspot and adjacent negative polarity patches. We have indicated it by a green arrow in Fig. 2(j).

4 FOUR SUCCESSIVE FLARES FROM THE MAGNETIC ATOLL REGION

The magnetic atoll region produced four successive flares on 2014 February 16. In Fig. 3(a), we plot SXR flux in the GOES 1–8 Å channel along with EUV intensities of AIA 94 and 304 Å channels from 2014 February 16 00:00 UT–20:00 UT that displays the onset and

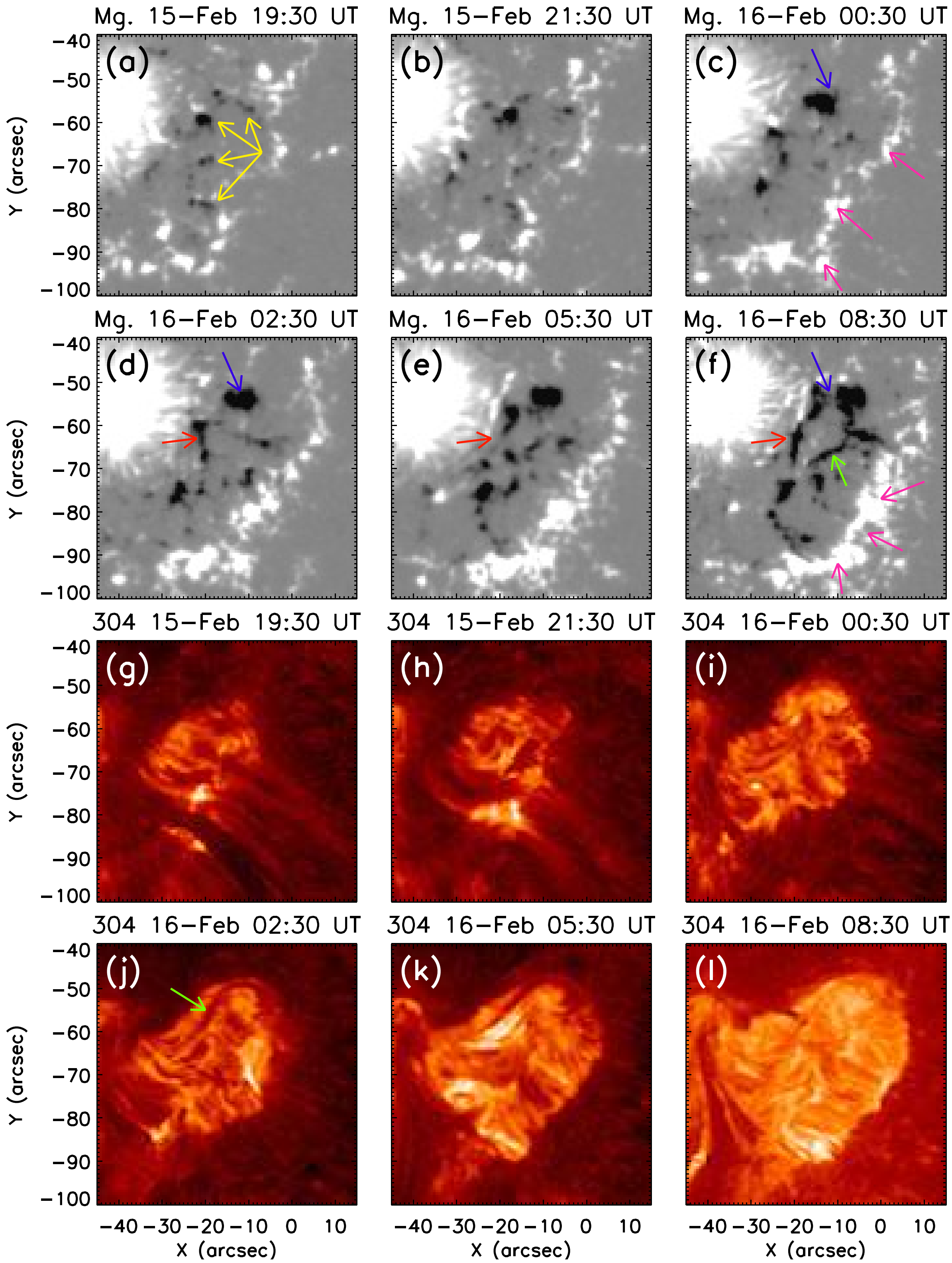

Figure 2. Series of HMI LOS magnetograms showing the development of the magnetic 'atoll' region (panels a–f). The arrows of different colour indicate few prominent locations of negative magnetic flux emergence. Panels (g)–(l) are AIA 304 Å images associated with the magnetic atoll region displaying the formation of the diffused circular brightening region. All the images are derotated to 2014 February 16 09:20 UT.

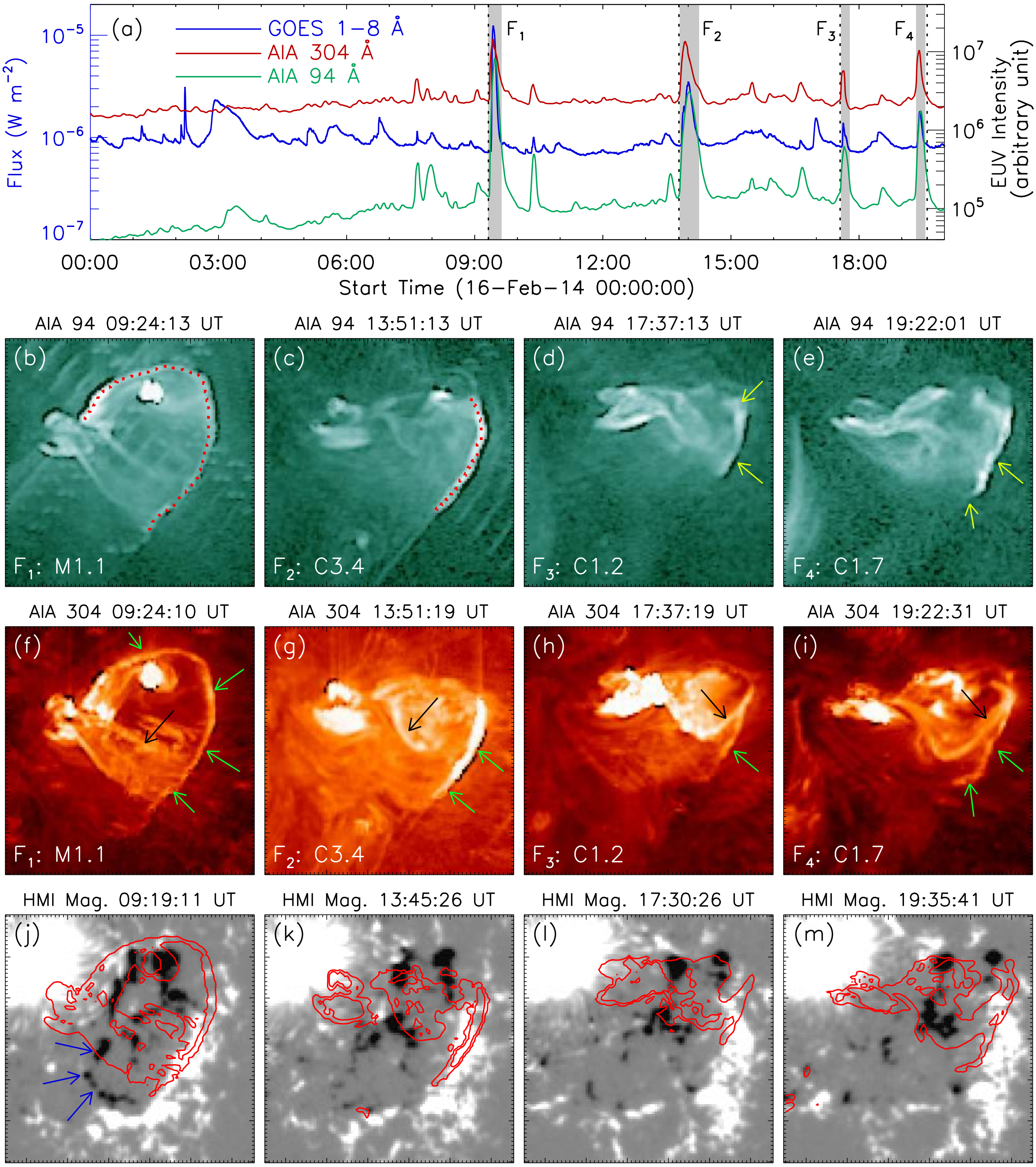

Figure 3. Panel (a): GOES 1–8 Å flux (the blue curve), AIA 304 Å (the red curve), and AIA 94 Å (the green curve) intensities showing the onset and evolution of four flares from the diffused brightening region. The duration of the flares is indicated by four shaded regions. The individual fares are named as 'F_1', 'F_2', 'F_3', and 'F_4'. Panels (b)–(e): AIA 94 Å images of the diffused brightening region during the peak phases of the four flares. The red-dotted curves in panels (b) and (c) indicate the quasi-circular ribbon observed during F_1 and F_2, while the yellow arrows in panels (d)–(e) indicate arc-shaped ribbons during F_3 and F_4 flares, respectively. Panels (j)–(i): AIA 304 Å images showing the peak phases of the four flares. The green arrows in different panels indicate the quasi-circular (panel f), semicircular (panel g) and arc-shaped (panels h and i) ribbons observed during the flares. The black arrows indicate the erupting filament. Panels (j)–(m): HMI LOS magnetograms of the 'magnetic atoll' region prior to the onset of the F_1–F_3 flares (panels j–l) and after the F_4 flare (panel m). The blue arrows in panel (j) indicate few negative flux region that disappeared with time. Contours of co-temporal EUV intensities in AIA 304 Å are overplotted on the bottom row. Contour levels are [4, 80] per cent, [12, 60] per cent, [11, 60] per cent, and [9, 40] per cent of the corresponding peak intensities in panels (j), (k), (l), and (m), respectively. An animation associated with this figure is attached in the online supplementary materials.

temporal evolutions of the four flares (see summary of events in Table 1). These multiwavelength lightcurves suggest that the first flare of GOES class M1.1 initiated at ≈09:20 UT. This short-lived flare reached to its peak at ≈09:26 UT. The second flare (GOES class C3.4) initiated at ≈13:48 UT and after a relatively extended rise phase of ≈12 min, reached its peak intensity. Interestingly, the subsequent two flares originating from this region were rather impulsive and short-lived. According to the GOES 1–8 Å flux profile, these C class flares originated at ≈17:35 UT and 19:20 UT, while their impulsive phases lasted for only ≈3 min each. In Fig. 3(a), we indicate the durations of the four flares by the grey-shaded intervals and assign the notations 'F_1', 'F_2', 'F_3', and 'F_4' to the flares in the chronological order.

In Figs 3(b)–(e) and (f)–(i), we show AIA 94 and AIA 304 Å images, respectively, of the diffused brightening region during the peak phases of the circular ribbon flares. From these images it becomes evident that, all the four flares were associated with some degree of ribbon-like brightening along the circumference of the diffused brightening region. We observed quite prominent signatures of an extended quasi-circular ribbon brightening during F_1, which is delineated by the red-dotted curve in Fig. 3(b) and the green arrows in Fig. 3(f). The quasi-circular ribbon shortened significantly during F_2, which we have indicated by the red-dotted curve in Fig. 3(c) and the green arrows in Fig. 3(g). During F_3 and F_4 the flare ribbons along with only a small portion of the boundary of the diffused brightening region displayed enhanced emission. This arc-shaped flare brightening is indicated by the yellow arrows in Figs 3(d)–(e) and the green arrows in Figs 3(h)–(i).

In Figs 3(j)–(m), we plot preflare HMI LOS magnetograms corresponding to all the four flares, respectively. We find that the negative polarity flux regions from the magnetic atoll region continuously decayed with the evolution of each flares. This cancellation of negative flux was much more prominent in the southern part of the atoll region than the northern part [cf. the negative flux regions indicated by blue arrows in Figs 3(j) and (m)]. For a better understanding of the relation between the photospheric flux regions and the flare emission, we plotted contours of EUV intensities in AIA 304 Å channel over the LOS magnetograms in Figs 3(j)–(m). From the overplotted contours, it becomes clear that the quasi-circular ribbon brightening during the peak phases of the flares were co-spatial with the positive polarity flux regions situated at the boundary of the photospheric atoll region.

In Fig. 4, we plot chromospheric images of the diffused brightening region in the H α passband during the pre-flare phases of each flares. From these images, we clearly identified impressions of the filaments, implying recursive development of filaments at the filament channel situated along the PIL between the positive polarity sunspot and the parasitic negative polarity patches (Fig. 2 and Section 3.2). It is worth mentioning that the evolution of the quasi-circular ribbon flares in the H α-passband (not shown here) was broadly similar to that observed in EUV channels.

In order to have a comprehensive understanding towards the influence of photospheric flux on the evolution of the diffused brightening region as well as on the homologous flares originated from it, in Fig. 5, we examine the evolution of photospheric flux over a prolonged period that also covers the time span of the four flares. For the purpose, we emphasize on the small-scale flux changes within the atoll region [in Figs 5(b_1)–(b_8)] and the temporal evolution of flux from it (Fig. 5c) by analysing HMI LOS magnetograms. The atoll region is enclosed in Fig. 5(a) by the black box. We clearly identified several instances of small-scale flux cancellation; a few of them are indicated by different colours of ovals and arrows in Figs 5(b_1)–(b_8). During the pre-flare phase of F_1 [Figs 5(b_1)–(b_2)]

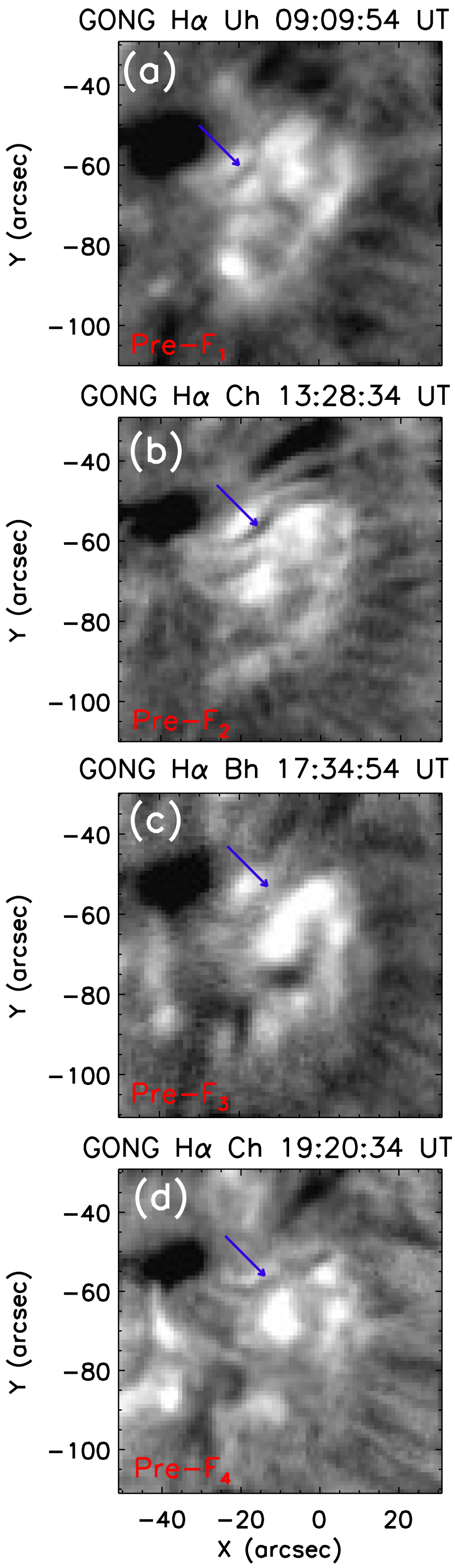

Figure 4. Selective of H α images of the diffused brightening region during the pre-flare phases of the quasi-circular ribbon flares, recorded by different stations of the GONG network. The corresponding GONG stations are indicated in the titles in each panel as Uh (Udaipur Solar Observatory, India), Ch (Cerro Tololo Inter-American Observatory, Chile), and Bh (Big Bear Solar Observatory, USA). The blue arrows indicate the presence of small filaments prior to the flares.

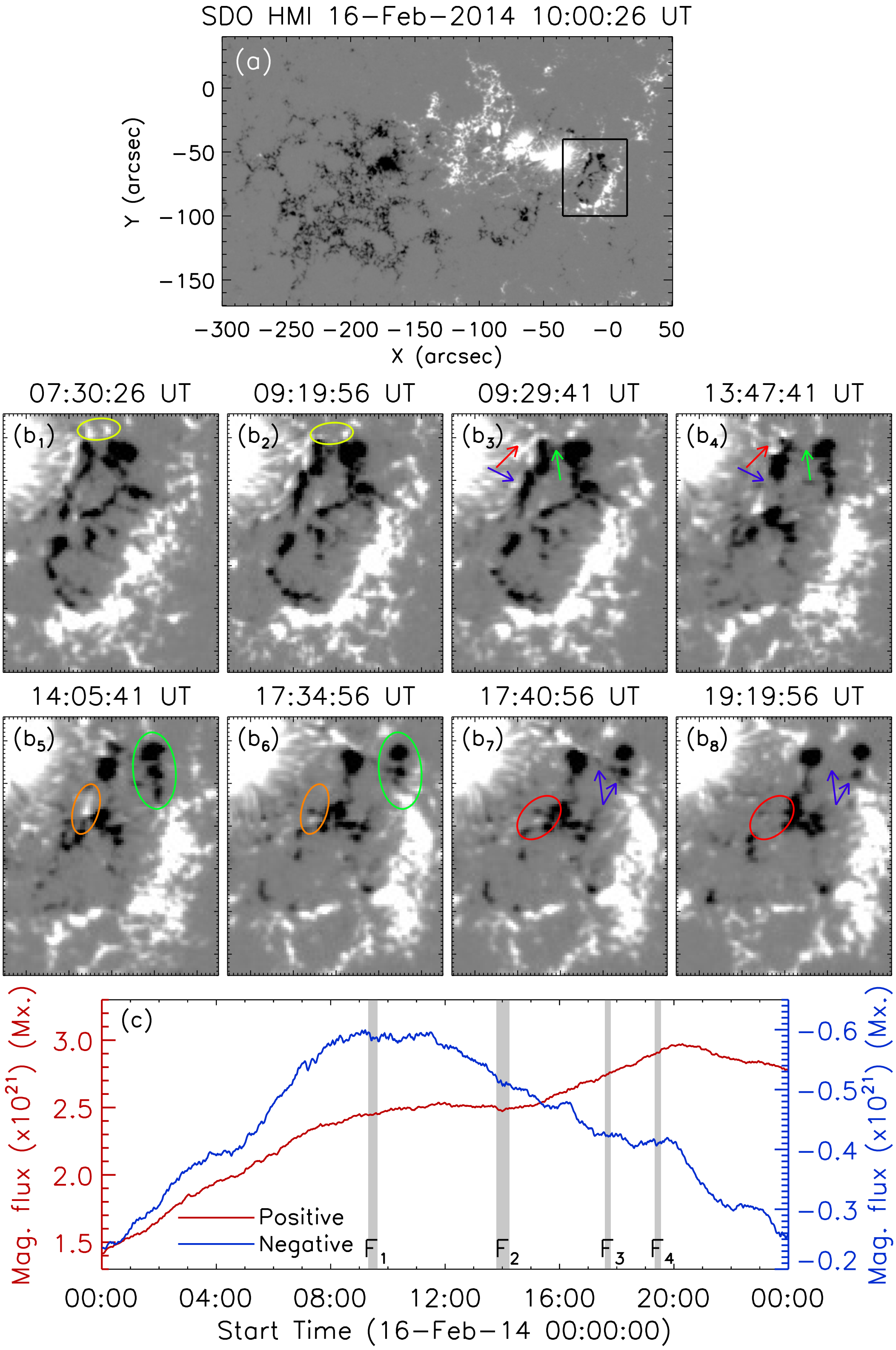

Figure 5. Panel (a): LOS magnetogram of the active region NOAA 11977 where the magnetic atoll region is enclosed within the black box. Panels (b_1)–(b_8): Selective LOS magnetograms of the atoll region displaying several instances of flux cancellation. We have indicated few of such flux cancellation by the arrows and the ovals of different colours in different panels. Panel (c): Evolution of magnetic flux in the magnetic atoll region indicated in panel (a). The shaded intervals in panel (c) indicate the durations of flares occurred from the magnetic atoll region.

we observed cancellation of positive flux at the region of the PIL of the filament, which is indicated by the yellow ovals. During the interval between F_1 and F_2, we could identify multiple instances of flux cancellation of both polarities at the PIL region situated at the northern part of the atoll region [cf. the arrow heads of the red, blue, and green arrows in Figs 5(b_3)–(b_4)]. Between F_3 and F_4, a major part of a relatively prominent negative flux region got decayed [cf. the region enclosed by the green ovals in Figs 5(b_5)–(b_6)]. We further observed cancellation of positive flux in the atoll region that we have highlighted within the orange ovals in Figs 5(b_5)–(b_6). This region was observed with flux cancellation between F_3 and F_4 also that is indicated by the red arrows in Figs 5(b_7)–(b_8). We also observed cancellation of small negative fluxes from the atoll region in this duration that are indicated by the blue arrows in Figs 5(b_7)–(b_8).

In general, the atoll region experienced a significant decrease of negative flux [Figs 3(j)–(m) and 5(b_1)–(b_8)] that is readily recognized by the temporal evolution of negative flux [the blue curve in Fig. 5c]. The flux profiles suggest that in the first part of 2014 February 16, the flaring region (enclosed by the black box in Fig. 5a), underwent a rapid increase of negative flux beside relatively moderate positive flux enhancement (see 00:00 UT – 08:00 UT in Fig. 5c). Notably, this period can be characterized by the formation of the atoll and associated diffused brightening region (Section 3.2 and Fig. 2). The first flare (F_1) initiated when negative flux reached to its peak; afterwards negative flux from the region remained relatively unchanged for ≈3 h and then continuously decayed till ≈19:30 UT. After this time, negative flux maintained an approximately constant level for ≈1.5 h when the last flare from this region (F_4) took place. From ≈20:00 UT, negative flux primarily decayed characterizing the decay of the overall diffused brightening region. On the other hand, positive flux in this region displayed stepwise enhancement till ≈20:00 UT after which decayed slowly till the end of the period of our calculation.

4.1 Morphological evolution of quasi-circular ribbon flares

All the four flares originating from the oval-shaped diffused brightening region initiated with the activation and eruption of the filaments situated along the PIL between the positive polarity sunspot the negative flux regions. We recall that the coronal region showing oval-shaped diffused brightening was lying over the peculiar magnetic atoll region at the photosphere (see Section 3.2 and Fig. 2). Further, during all the four flares, we observed flare ribbons along the boundary of the diffused brightening region that form quasi-circular ribbons (Fig. 3). The quasi-circular ribbon was the most prominent and extended during F_1 of GOES class M1.1. The subsequent three flares were very similar in their onset and evolution. However, as explained in Section 4 (Fig. 3), the length of quasi-circular ribbon decreased progressively during the subsequent flares (i.e. F_2–F_4). More importantly, during F_2–F_4, the filament evolved with a complete blow-out-type eruption from the diffused brightening region while such catastrophic eruption of the filament was not observed during F_1. In this section, we focus on the detailed morphological evolution of F_1 and F_2 flares.

4.1.1 Filament eruption and quasi-circular ribbon during F_1

In Fig. 6, we plot a series of AIA 304 Å images of the diffused brightening region to investigate the evolution and eruption of the filament in association with F_1, i.e. the GOES M1.1 flare. Our observations suggest that the impression of the filament at the northern boundary of the diffused brightening region was first identified at around ≈02:30 UT (Section 3.2 and Fig. 2). In Fig. 6(b), we indicate the initial filament by the blue arrows, and we will refer this filament as FL_1 henceforth. A comparison of the location of FL_1 with the LOS magnetograms in Fig. 6(a) immediately reveals that the filament was situated along the PIL between the positive polarity sunspot and the dispersed negative magnetic field regions. The filament was associated with a series of localized small-scale brightenings (indicated by the green arrows in Figs 6c and d) during an extended period prior to the onset of the GOES M-class flare (i.e F_1). The filament was observed most prominently at ≈09:20 UT, which is indicated by the blue-dotted curve in Fig. 6(e). After ≈09:21 UT, a subtle enhancement in the brightness at the northern leg of the filament was observed that was immediately followed by eruption of the filament from its northern end. In Fig. 6(f), we indicate the erupting part of the filament by a blue arrow and the localized brightening by a white arrow. The enhanced brightening advanced southwards [cf. the white arrowheads in Figs 6(d) and (c)] as the erupting front of the filament induced upward erupting motion in the southern part of the filament also. The southward-induced eruption of the filament is further outlined by the blue-dotted curve in Fig. 6(g) and indicated by the blue arrows in Figs 6(h) and (i). Two localized ribbon-like bright structures formed at both sides of the filament (indicated by the black arrows in Fig. 6i) at around 09:24 UT, which resembles with 'standard flare ribbons'. At the same time, a circular ribbon brightening was prominently observed at the boundary of the diffused brightening region. After ≈09:25 UT, the filamentary structure (FL_1) appeared as a straight, long structure with one end still attached to its initial location (outlined by the blue-dotted curve in Fig. 6j). Interestingly, during this time, it was observed as a bright structure suggesting strong heating of the filamentary materials during the flaring process. The open end of the filamentary structure was associated with plasma eruption after ≈09:25 UT. The direction of the erupting plasma is indicated by the arrows in Fig. 6(j). Notably, both the parallel and circular ribbon brightening increased up to ≈09:27 UT (the circular ribbon brightening is outlined by the black-dotted curve in Fig. 6g) after which, flare brightenings from the active region slowly decreased while eruption continued. In Figs 6(k), we indicate the erupting plasma by the white arrows. Formation of post-flare arcade was observed after ≈09:32 UT that sustained till ≈09:42 UT. We have indicated the post-flare arcade by the black arrows in Fig. 6(l).

4.1.2 Filament eruption and shortened quasi-circular ribbon during F_2

Although the filament situated along the northern edge of the diffused brightening region (FL_1), partially erupted during F_1, the corresponding PIL showed the presence of a filament channel throughout the lifetime of the diffused brightening region. Before the onset of F_2, another filament was observed quite prominently at the same location (i.e. FL_1), which is highlighted by a blue-dotted line in Fig. 7(a). Importantly, we noticed impressions of a second filament near FL_1 that we mark as 'FL_2' (indicated by the green arrow in Figs 7a). Similar to the pre-flare phase prior to F_1, the localized region associated with the filaments, underwent small-scale brightenings during the pre-flare phase of F_2 also. We have indicated few such episodes of brightenings by the yellow arrows in Figs 7(a) and (b). With time, FL_1 became more prominent, which is indicated by the blue arrow in Fig. 7(b). Few minutes prior to the onset of F_2, the filament FL_2 also became very prominent, making a

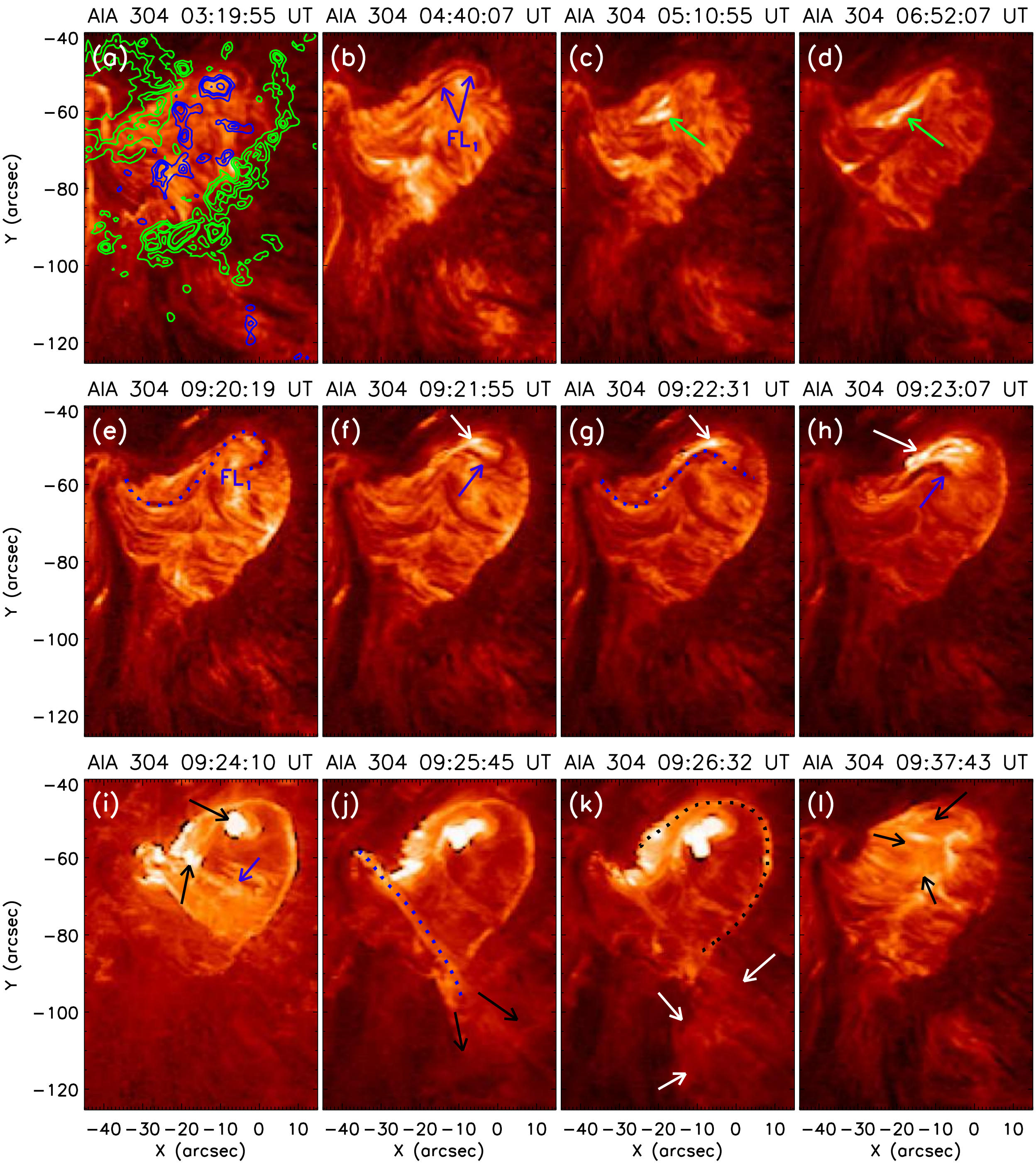

Figure 6. Representative AIA 304 Å images depicting filament eruption and associated M1.1 flare. The two blue arrows indicate a filament that is referred to as 'FL_1'. The green arrows in panels (c) and (d) indicate small-scale brightenings observed at the location of the filament. In panel (e), we outline the 'S'-shaped filament by the dotted curve. The filament during its initial eruption phase is shown by the blue arrows in panels (f) and (h) and the blue-dotted line in panel (g). The white arrows in panels (c)–(h) indicate initial flare brightening beneath the northern end of the erupting filament. The final stage of filament eruption from the active region is outlined by the blue arrow in panel 9(i) and the blue-dotted curve in panel (j). The black arrows in panel (e) indicate parallel flare brightening during the impulsive phase of the flare. The black arrows in panel (j) and the white arrows in panel (k) indicate erupting plasma. The black-dotted curve in panel (k) indicate the quasi-circular ribbon. Co-temporal LOS HMI magnetogram contours at levels ±[300, 500, 1000] G are plotted in panel(a). The green and blue contours refer to positive and negative polarity, respectively. An animation associated with this figure is attached in the online supplementary materials.

double decker flux rope system in association with FL_1. In Fig. 7(c), we indicate the two filaments of the double-decker system by the blue- and green-dotted lines. Notably, this double-decker system is confirmed by the presence of two intertwined flux ropes (Section 5.2). Interestingly, the north-western end of the FL_2 was associated with narrow collimated plasma eruption even before the flare was initiated (indicated by the yellow arrow in Fig. 7c). Our observations suggest that the flare onset took place as the filament FL_1 went through a

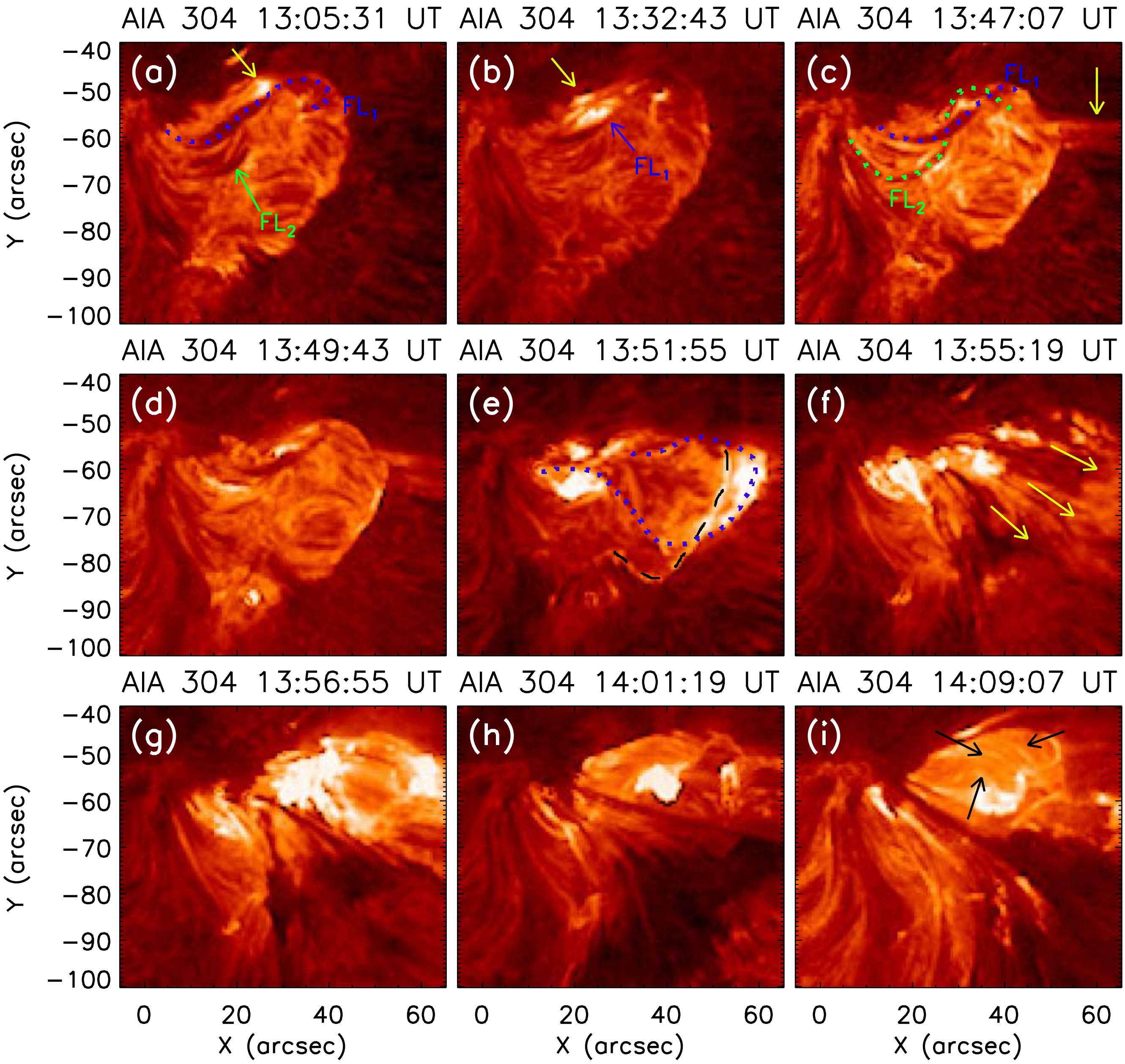

Figure 7. Representative AIA 304 Å images depicting the eruption of the filament. The filament FL_1 is indicated by the blue-dotted curve in panel (a) and the blue arrow in panel (b). A second filament (FL_2) is indicated by the green arrow in panel (a). The yellow arrows in panels (a) and (b) indicate small-scale brightenings at the location of the filaments during the pre-flare phase. The blue- and green-dotted lines in panel (c) indicate the double-decker flux rope configuration formed by FL_1 and FL_2. The yellow arrow in panel (c) indicate jet-like plasma ejection prior to the onset of the flare. The blue-dotted curve in panel (e) indicates erupting filament, while the black-dashed curve in the same panel indicates a quasi-circular ribbon during the F_2 flare. The yellow arrows in panel (f) indicate the direction of the erupting plasma during the flare. The black arrows in panel (i) indicate post-flare arcade. An animation associated with this figure is attached in the online supplementary materials.

complete eruption at ≈13:51 UT. In Fig. 7(e), we have outlined the erupting FL_1 by a blue-dotted line. At the same time, a part of the western boundary of the diffused brightening region became very bright implying the formation of a circular ribbon, which we have highlighted by the black-dashed curve in Fig. 7(e). Soon after the onset of the eruption, the active region was partially masked by the cool erupting plasma (the direction of erupting plasma is indicated by the yellow arrows in Fig. 7f). During the gradual phase, we observed a dense post flare arcade (indicated by the black arrows in Fig. 7i) that is expected.

5 CORONAL MAGNETIC FIELD MODELLING

5.1 Extrapolation set-up

In order to investigate the coronal magnetic configurations prior to the onset of the quasi-circular ribbon flares, we employed an NLFFF extrapolation method with a particular focus to the magnetic atoll (i.e. flaring) region, using the vector magnetograms from the '*hmi.sharp_cea_720s*' series at four times: 09:22 UT (prior to F_1; Fig. 8), 13:46 UT (prior to F_2; Fig. 9), 17:34 UT [prior to F_3; Fig. 10(a)–

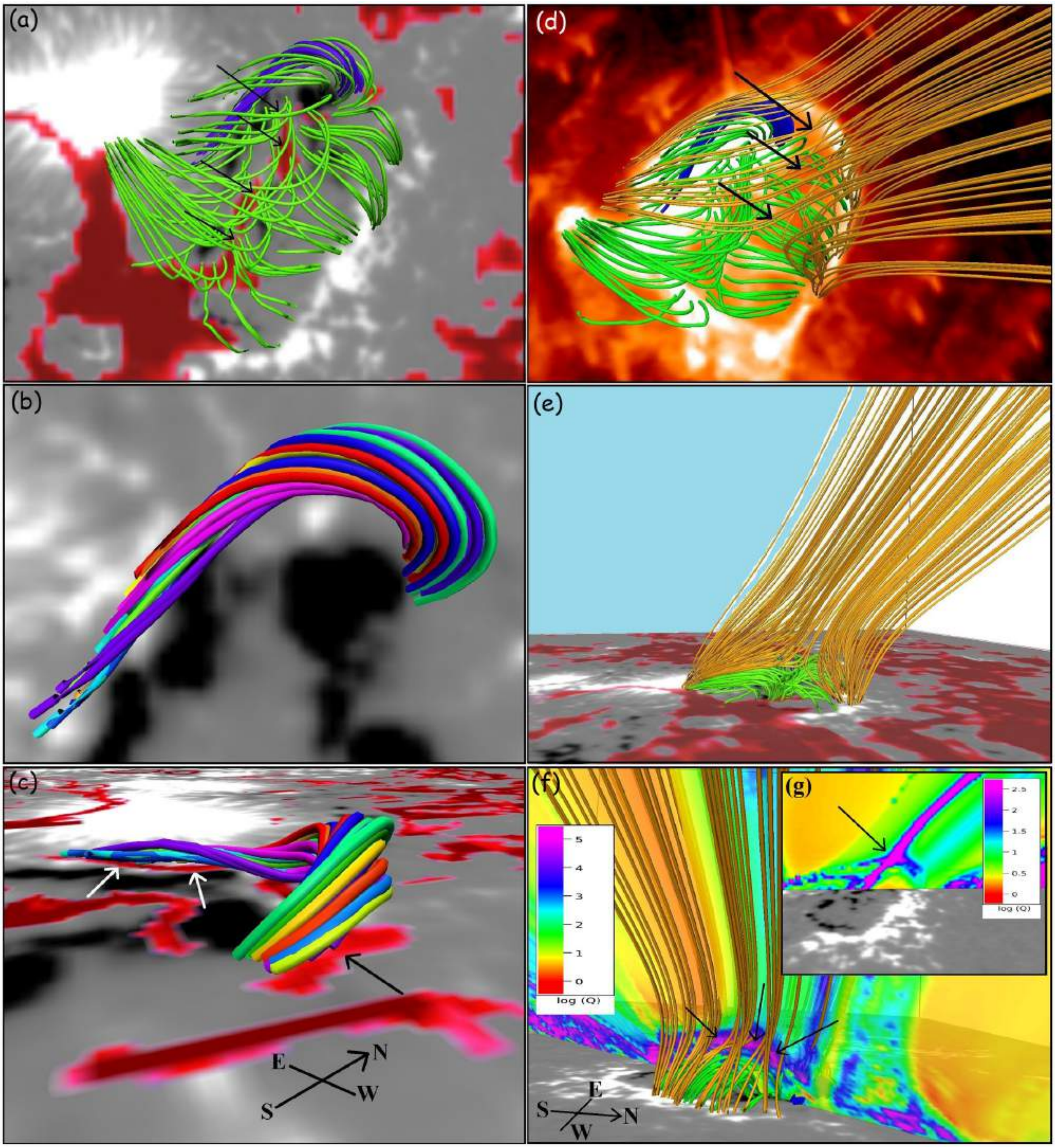

Figure 8. Non-linear force-free field extrapolation results of the magnetic atoll region prior to the flare F_1 (at 09:22 UT) showing the presence of a flux rope and closed magnetic loops within the region (the green lines) besides large open field lines originating from the outer magnetic patches of the atoll region (the yellow lines). To understand the structures of the flux ropes clearly, we provide zoomed views of the flux rope with multiple colours in panels (b; top view) and (c; side view). The red patches over the background HMI magnetogram in panels (a), (c), and (e) represent regions with high Q-value [$\log(Q) > 2$]. The arrows in panel (c) highlight the close association between the legs of the flux rope and photospheric regions with high Q-value. The Y–Z tilted vertical surface in panel (f) drawn along the yellow lines represents the distribution of Q-values. In panel (g), the distribution of Q is shown along a plane passing across the magnetic atoll region, i.e. along X–Z plane. The arrow in panel (g) indicates an 'X'-shape formed by the regions of high Q. For reference, we have included the colour-table showing the distribution of $\log(Q)$ values in the box in panels (f) and (g). Top boundary in panels (a), (b), (d) as well as the sky-coloured boundary in panel (e) represent north. We have plotted a compass for representing the direction in panels (c) and (f). An AIA 304 Å image of 09:26 UT has been plotted in the background in panel (d).

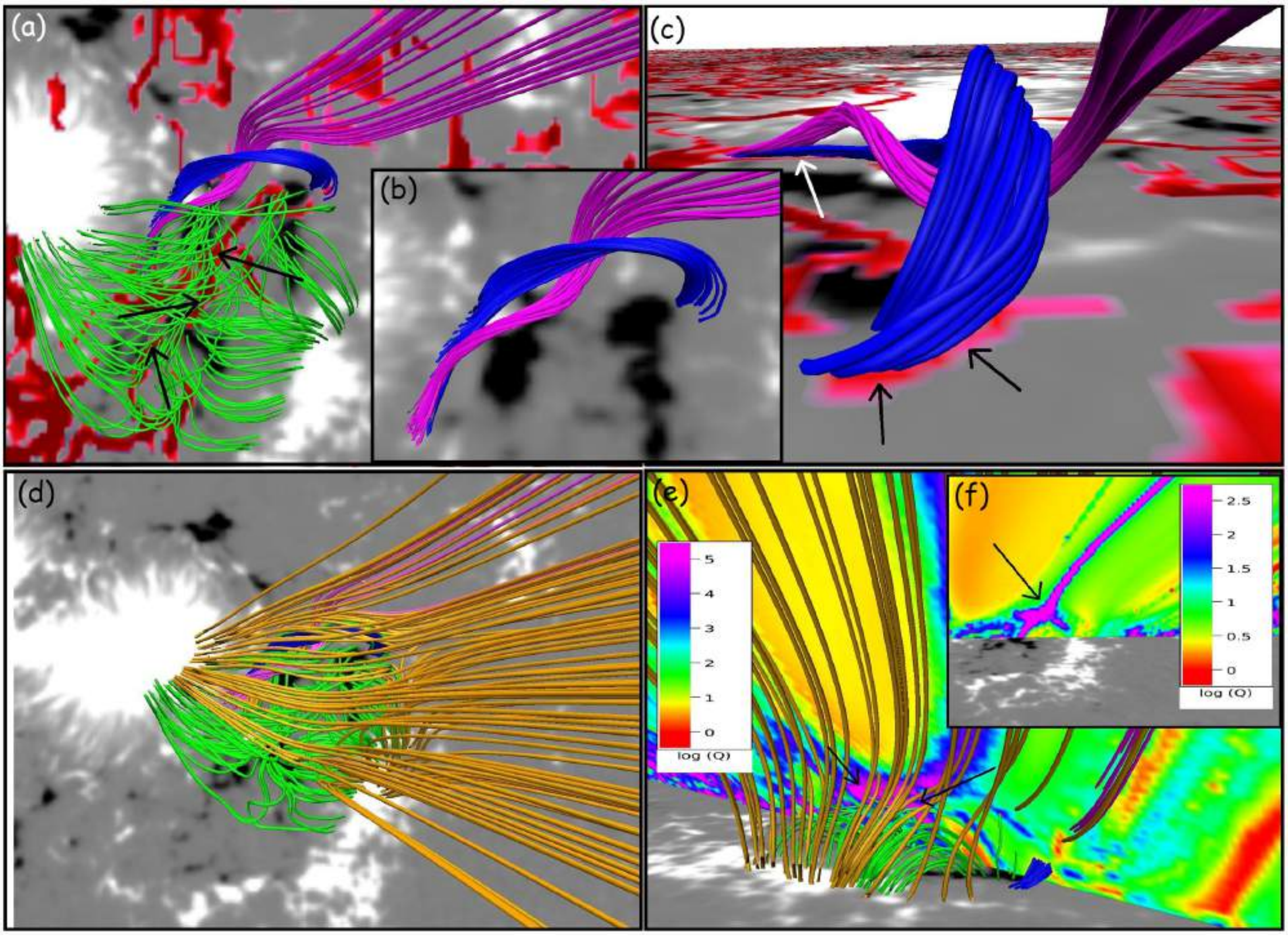

Figure 9. Non-linear force-free field extrapolation results on the magnetic atoll region prior to the F$_2$ flare (at 13:46 UT) showing the presence of a flux rope (the blue lines) and closed magnetic loops within the region (the green lines) as well as large open field lines originating from magnetic patches of the atoll region (the yellow lines). A set of twisted field lines having origin in the south-western end of the polarity inversion line and extending north-westwards as a part of open field lines, i.e. 'open flux rope' are shown in pink colour. In panels (b) and (c), only the two flux ropes are shown from top and side views, respectively. The red patches over the background HMI magnetogram in panels (a) and (c) represent regions with high Q-value [log(Q) > 2]. The arrows in panel (c) highlight the close association between the legs of the flux ropes and photospheric regions with high Q. Panels (e) and (f) are same as Figs 8(f) and (g), respectively. Top boundary in panels (a), (b), and (d) represent north. Top boundary in panel (c) represents east.

(d1)], and 18:58 UT [prior to F$_4$; Fig. 10(e)–(h1)] on 2014 February 16 as the input boundary conditions. Since the photosphere is not force free, the photospheric magnetograms used as the input boundary conditions were pre-processed, as explained in Wiegelmann, Inhester & Sakurai (2006). The optimization-based NLFFF code, including the part of pre-processing of input magnetic field, allows a number of 'free parameters' for the user's consideration, which are ν, $w_{\rm los}$, $w_{\rm trans}$, μ_1, μ_2, μ_3, and μ_4 (for a quick summary, see Mitra et al. 2020b). In all the four instances of coronal magnetic field extrapolation conducted in this work, we used the following values of the free parameters: $\nu = 0.01$; $w_{los} = 1$; $w_{trans} = \frac{B_{trans}}{max(B_{trans})}$; $\mu_1 = \mu_2 = 1$; $\mu_3 = 0.001$; $\mu_4 = 0.01$. Theoretically, in the NLFFF model, the angle between current ($\vec{J}$) and magnetic field ($\vec{B}$) should be 0. However, since the NLFFF-code uses real measurements of magnetic field, small but non-zero values of $|\vec{J} \times \vec{B}|$ is expected from the reconstructed magnetic field. Therefore, to assess the quality of the coronal magnetic field reconstruction, the average value of fractional flux ratio ($<|f_i|> = <|(\vec{\nabla} \cdot \vec{B})_i|/(6|\vec{B}|_i/\triangle x)>$), weighted angle ($\theta_J$) between $\vec{J}$ and $\vec{B}$ can be considered (see DeRosa et al. 2015). In general, NLFFF solutions returning the values $|\vec{J} \times \vec{B}| \lesssim 10^{-2}$, $<|f_i|> \lesssim 2 \times 10^{-3}$, $\theta_J \lesssim 10^\circ$ are considered as good solutions (see e.g. DeRosa et al. 2015; Thalmann et al. 2019). In Table 2, we have listed the values of these parameters corresponding to all the four extrapolations used in this paper. Here, it should be noted that, the extrapolations were conducted over the entire active region (Fig. 5a), however, in this section and in Figs 8–10, we have only shown and discussed the modelled coronal configuration associated with the atoll region.

5.2 Preflare coronal magnetic connectivities

NLFFF extrapolation results at 09:22 UT readily indicate the presence of a flux rope in the apparent location of FL$_1$, which are drawn by the blue lines in Figs 8(a) and (d). For a better understanding of the structure of the flux rope, we have shown only the field lines constituting the flux rope from top and side views in Figs 8(b) and (c), respectively, where different field lines are plotted in different colours. The flux rope is enveloped by a set of highly sheared overlying closed loops (shown by the green lines in Fig. 8). Notably, these field lines connect the outer positive polarity regions to the

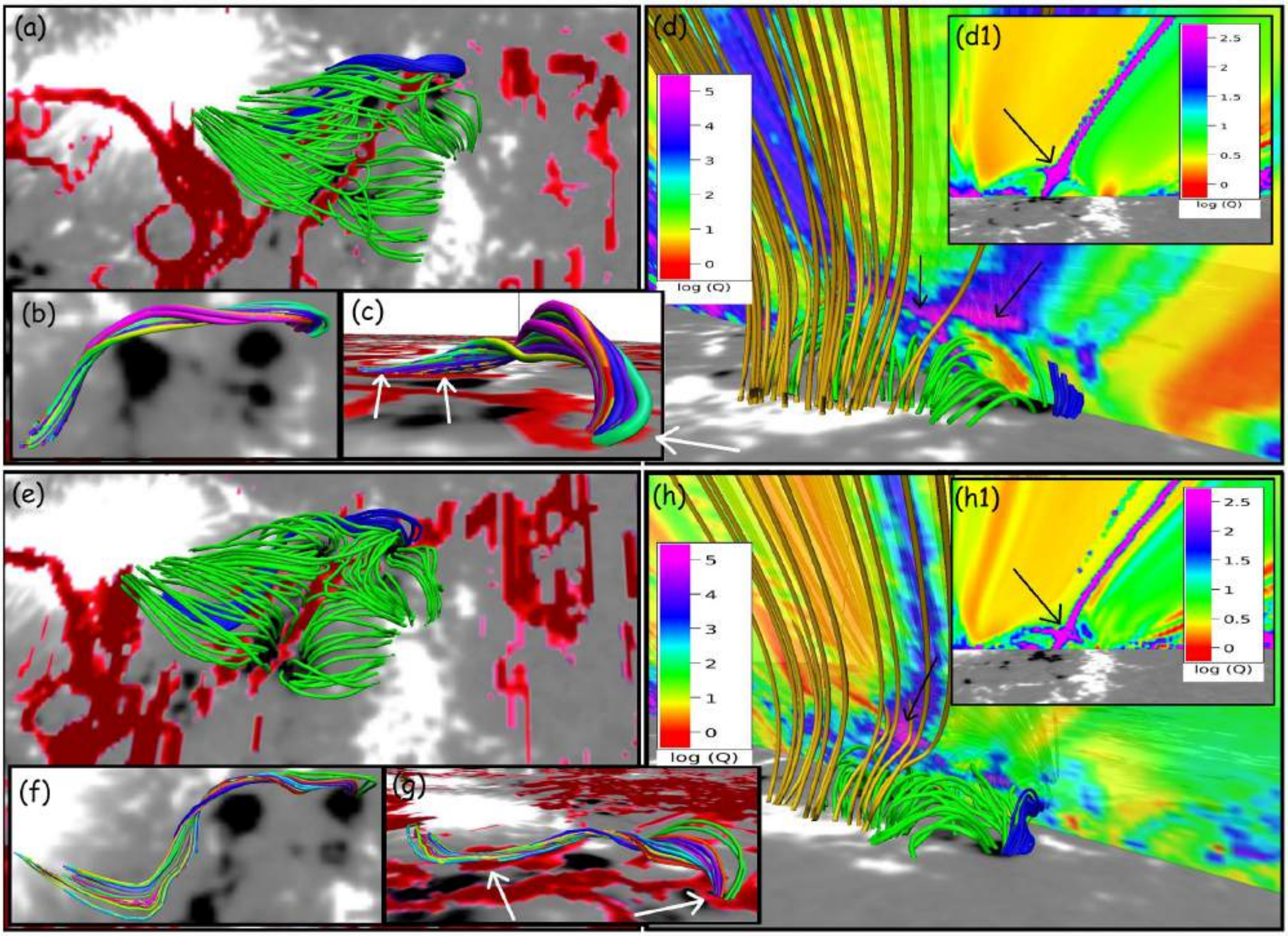

Figure 10. NLFFF extrapolation results showing the coronal configurations prior to the F_3 [at 17:34 UT; panels (a)–(d1)] and F_4 flare [at 18:58 UT; panels (e)–(h1)]. Panels (a) and (e) show the flux ropes (in blue colour) and the inner fan-like lines (in green colour) from top view. The flux ropes prior to the F_3 and F_4 flares are exclusively shown in multiple colours from the top view in panels (b) and (f), respectively, and from side views in panels (c) and (g), respectively. Panels (d)–(d1) and (h)–(h1) are same as Figs 8(f)–(g), respectively. The arrows in panels (c) and (g) highlight the close association between the legs of the flux ropes and photospheric regions with high Q.

Table 2. Summary of the parameters for assessing the quality of NLFFF extrapolation.

Time of extrapolation	$<\|\vec{J} \times \vec{B}\|>$	$<\|f_i\|>$	θ_J
09:22 UT	4.16×10^{-3}	6.79×10^{-4}	8.35°
13:46 UT	4.82×10^{-3}	7.26×10^{-4}	8.24°
17:34 UT	3.89×10^{-3}	6.93×10^{-4}	7.88°
18:58 UT	5.67×10^{-3}	6.58×10^{-4}	7.59°

central dispersed negative polarity regions. The green lines are surrounded by a set of open field lines [shown by the yellow colour in Figs 8(d)–(f)] that originate from the outer positive polarity regions. Interestingly, the boundary of the diffused, nearly circular flare brightening apparently delineates the footpoints of the open field lines (cf. the modelled yellow lines and the background AIA 304 Å image in Fig. 8d). In this way, the entire structure made of the green and yellow lines resembles a spine-fan-like configuration. However, although few low-lying null-points were located close to the bottom boundary of the extrapolation volume, we could not find presence of any null-point near or within our region of interest, suggesting that the coronal configuration associated with the flaring activities reported in this article, differed from the 3D spine-fan configuration. Further, the laterally extended nature of the spine-like lines (indicated by the black arrows in Figs 8a and d) is also uncharacteristic of the spine-fan configuration. In Fig. 8(e), we show the whole configuration from a different angle for an overall visualization. This atypical, spine-fan-like configuration is also recognized prior to the onset of F_2, which is indicated by the black arrows in Figs 9(d)–(e). Our extrapolation results reveal that this spine-fan-like configuration decays significantly in spatial extent afterwards [Figs 10(a) and (e)] vis-à-vis changes in the corresponding photospheric magnetic field structure of the magnetic atoll region [Figs 3(j)–(m)].

The model field structure during the pre-flare phase of F_2 reveals two sets of twisted field lines intertwined with each other in a double-decker flux rope configuration [shown by the blue and pink colours in Figs 9(a)–(c)]. While the twisted field lines shown in blue are similar to the flux rope identified during the pre-flare phase of F_1 (i.e. FL_1), the apparent twist associated with it is found to be more than the previous flux rope (see Table 3). The other set of twisted field lines shown in pink colour is rather interesting. One leg of these lines is situated in the PIL region where one leg of the blue flux rope is also located. Further, we note that, the location of the pink lines is same as the apparent location of FL_2 [cf. Figs 9(b) and 7(c)]. However,

Table 3. Summary of the twist number $|T_w|$ and critical height ($h_{\rm crit}$) for magnetic decay index n = 1.0 and 1.5, prior to the four flares from the magnetic atoll region.

Flare Id.	$\lvert T_w \rvert$	$h_{crit}(n = 1.0)$ (Mm)	$h_{crit}(n = 1.5)$ (Mm)	Maximum height of the flux rope (Mm)
F_1	$\approx$0.93 ± 0.11	$\approx$15	$\approx$25	$\approx$ 4
F_2	$\approx$1.12 ± 0.18	$\approx$19	$\approx$30	$\approx$ 4
F_3	$\approx$1.20 ± 0.20	$\approx$17	$\approx$28	$\approx$ 5
F_4	$\approx$1.22 ± 0.20	$\approx$17	$\approx$27	$\approx$ 4

while the blue flux rope is anchored to the photosphere at both the ends, the field lines constituting the pink flux rope is anchored only at its southern end. At the northern end, the field lines of the flux rope become a part of the open lines instead of terminating on the photosphere [cf. the open end of the pink lines in Figs 9(a) and the open yellow lines in Fig. 9(d)]. In Figs 9(b) and (c), we show only the double-decker flux rope configuration from top and side views for a better understanding of their structures. In Fig. 10, we show the modelled magnetic configuration above the magnetic atoll region prior to the onset of the F_3 [Figs 10(a)–(d1)] and F_4 [Figs 10(e)–(h1)] flares. We find that, similar to F_1, prior to the F_3 and F_4 flares also, single flux rope structures are identified from the modelled coronal magnetic field that are shown from top views in Figs 10(a) and (b) and 10(e) and (f), respectively, and side views in Figs 10(c) and (g), respectively.

5.3 Distribution of squashing factor (Q)

NLFFF modelling reveals a complex coronal magnetic configuration prior to the successive four flares. While the overall coronal structures resemble a fan-spine-like configuration, they lack a coronal null-point. To further investigate the fan-spine-like configuration, we calculated the squashing factor (Q) in the active region using the NLFFF extrapolated magnetic fields in the extrapolation volume. The relevant panels in Figs 8–10 display the photospheric regions associated with high Q [$\log(Q) > 2$] values by the red-coloured patches. From Figs 8(a), 9(a), 10(a), and (e), we readily observe that along the elongated footpoint locations of the green lines over the negative polarity magnetic field region [indicated by the black arrows in Figs 8(a) and 9(a)], the Q-values are higher than 10^2 that provides substantial evidence for the laterally extended nature of the spine-like lines. Notably, the footpoint regions of the flux ropes are also found to be associated with high Q-values that can be inferred from the red-coloured patches indicated by the arrows in Figs 8(c), 9(c), 10(c), and (g).

To understand the variation of Q-values along the laterally extended spine-like lines, we draw tilted vertical planes passing through the outer spine-like lines [i.e. the yellow lines shown in Figs 8(d)–(e), 9(d)]; distribution of Q along which are shown in Fig. 8(f), 9(e), and 10(d) and (h). We find that immediately over the inner fan-like lines (shown by the green colour), the Q-values approached maximum values [$\log(Q) \gtrsim 5$] signifying drastic change in the magnetic connectivity between the green and the yellow lines. The extended arc-shaped high Q region [shown in the purple colour and the arrows in Figs 8(f), 9(e) 10(d) and (h)] in the absence of coronal nulls, suggests the presence of an HFT between the green and yellow lines. In Fig. 8(g), we plot Q-values along a plane that crosses perpendicularly the tilted plane of Fig. 8(f), i.e. it shows the variation of Q across the spine-fan-like configuration. From this panel, we readily observe the 'X'-shape formed by high Q-values (indicated by the black arrow) that further confirms the presence of the HFT in the coronal magnetic configuration above the atoll region. Notably, similar configurations are also found prior to the onset of the subsequent flares [indicated by the arrow in Figs 9(f), 10(d1) and (h1)]; however, with the decay of the magnetic atoll region, the extended coronal region of high Q-values over the inner fan-like lines [indicated by the arrows in Figs 8(f), 9(e) and 10(d)], gradually reduced and concentrated to a point-like structure prior to the onset of the F_4 flare (indicated by the black arrow in Fig. 10h).

5.4 Calculation of twist number and magnetic decay index

Both GONG H α and AIA 304 Å images suggest the filaments going through eruptive evolution during the flares (Figs 4, 6, and 7). The presence of the filaments isonfirmed by the presence of the flux ropes identified in the NLFFF-modelled coronal configuration (Figs 8, 9, and 10). For a quantitative assessment of the twists of the flux ropes, we compare distribution of twist number (T_w; see, Berger & Prior 2006) associated with the location of the flux ropes within the extrapolation volume, defined as

$$T_w = \frac{1}{4\pi}\int_L \frac{(\nabla \times \vec{B})\cdot \vec{B}}{B^2}\mathrm{d}l, \tag{1}$$

where L is the length of the flux rope. In Table 3, we present average twist number (T_w) associated with the flux ropes corresponding to consecutive flares prior to their onset (F_1–F_4). We find that T_w increased successively from F_1 to F_4. While T_w prior to F_1 was only $\lesssim$0.93, it increased to $\approx$1.22 prior to the onset of F_4.

To understand how the horizontal magnetic field changed with height over the flux ropes, we calculate magnetic decay index (n). For this purpose, we have considered the PILs over which the flux ropes were situated and computed average decay index along vertical surfaces above it. In Fig. 11, we plot the variation of magnetic decay index averaged over the PILs, with height; where we have indicated the critical heights at which the value of decay index reached n = 1.0 [$h_{\rm crit}(n = 1.0)$] and n = 1.5 [$h_{\rm crit}(n = 1.5)$] prior to all the four flares, by the dotted and dashed vertical lines. In Table 3, we have summarized the values of $h_{\rm crit}$ and approximate maximum heights of the flux ropes before the onset of all the four flares. Our calculations suggest that prior to the F_1 flare, $h_{\rm crit}$ was $\approx$25 Mm, while it slightly increased to $\approx$27–30 Mm prior to the subsequent flares. However, the maximum heights of the flux ropes prior to the onset of the flares were found to be only $\approx$4–5 Mm (Table 3), which are much less compared to the critical heights.

6 DISCUSSION

In this article, we present a detailed analysis of four successive flares (F_1, F_2, F_3, F_4; in the order of their occurrence) associated with quasi-circular ribbons. These flares were originated from the active region NOAA 11977 on a single day within a period of $\approx$11 h (see Table 1). The flaring region possessed a fan-spine-like

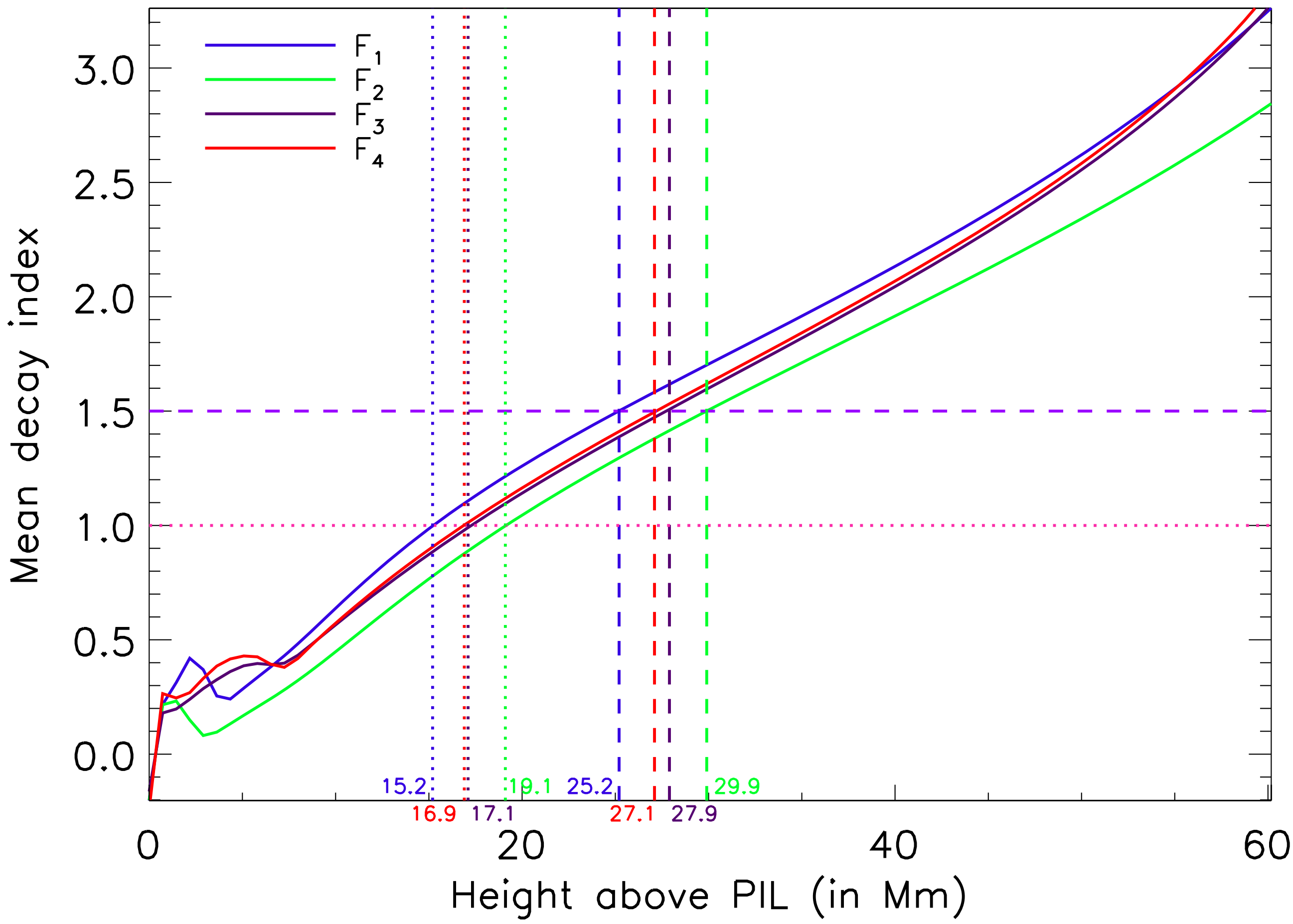

Figure 11. Plot of decay index (n) above the PIL as a function of height, prior to the four events. The values of decay index $n = 1.0$ and 1.5 are indicated by the pink-dotted and purple-dashed horizontal lines. The critical heights corresponding to the values $n = 1.0$ and 1.5 prior to the flares are represented by the dotted and dashed vertical lines, respectively, and noted at the bottom of the plot. Colours of these vertical lines and the values of critical heights corresponding to the events are synchronized with the colours of the decay index plots.

configuration that involved an HFT. Observationally, the fan-spine-like configuration was identified in the form of a region with diffused EUV brightening that spread within a circular base prior to F_1. The fan-spine-like structure decayed following each flare and, as a consequence, the prominent quasi-circular brightening identified prior to F_1 also decomposed and simplified during the succeeding flares.

Our observations revealed that the development of the interesting coronal configuration prior to F_1, facilitating the origin of the subsequent morphologically similar flaring events, was eventually connected with the emergence of negative polarity patches on the photosphere that formed a magnetic atoll region (Fig. 2). Further, the location over which negative polarity patches emerged can be characterized by a geometric stadium shape[2] with the longitudinal dimension lying along north-west–south-east (NW–SE) direction (Fig. 2f). These negative polarity regions were surrounded by positive polarity regions on NE and SW sides. Thus, the photospheric structure of the flaring region consisted of a longitudinally stretched magnetic patch bounded by regions of opposite polarity on both sides. NLFFF extrapolation results suggested a complex configuration in which open field lines originating from the positive polarity regions enclosed an extended fan-like structure (Figs 8–10) such that the overall coronal magnetic configuration resembled the topology of pseudo-streamers (Wang, Sheeley & Rich 2007; Titov et al. 2011, 2012; Masson et al. 2014) albeit in a much smaller spatial scale. Notably, since pseudo-streamers connect coronal holes of the same polarity, involving even number of PILs, 2D depiction of the cross-section of pseudo-streamers indicate the presence of X-shaped high Q-structures (Titov et al. 2012), which may represent true 3D null-points or topological structures such as separators connecting multiple null-points, HFTs, etc. (Gibson et al. 2017). In the absence of any null-point, the coronal magnetic configuration, derived from our analysis, can be physically well interpreted by considering a small-scale pseudo-streamer involving an HFT.

The presence of the HFT in the flaring region was further confirmed by their cross-sectional X-shaped high Q-regions (Figs 8g, 9f, 10d1, and h1). The high Q values of these regions imply high gradient of magnetic field (i.e. QSLs) within the diffused brightening region. Intense current sheets are formed naturally around QSLs as gradient in magnetic field contributes towards the generation of current (Lau & Finn 1990; Priest & Titov 1996; Aulanier, G. et al. 2005; Démoulin 2007). Using MHD simulations, the formation of electric current has also been demonstrated in magnetic flux ropes, coronal sigmoids, beneath an erupting flux rope, etc. (see e.g. Aulanier et al. 2009; Pariat, Masson & Aulanier 2009b; Wilmot-Smith, Hornig & Pontin

[2]http://mathworld.wolfram.com/Stadium.html

2009). Joule heating due to dissipation of these currents associated with the QSL formed by the inner fan-like lines was most likely responsible for the diffused EUV brightness confined within a quasi-circular border and was most prominent during the pre-flare phase of F_1 (see Fig. 2i). Evidently, the dome-shaped active pre-flare coronal structure, observed in EUV, was co-spatial with the photospheric magnetic atoll region.

EUV images clearly revealed the formation of distinct quasi-circular flare ribbons along the boundary of dome-shaped pre-flare structure as the filament eruption proceeded (Figs 4, 6, and 7). Notably, prior to the flares, the filament resided within the EUV-dome, i.e. modelled fan-spine-like configuration (Figs 8–10). This is definitive signature that the quasi-circular ribbon flares were triggered as the erupting flux rope interacted with the fan-like separatrix surface. Using MHD simulations, it has been established that stressed QSL regions can give rise to slipping reconnections even without the presence of a coronal null-point and for sufficiently thin QSLs and high resistivities, the field line footpoints can slip-run at super-Alfvénic speeds along the intersection of the QSLs (slip running reconnection; Aulanier et al. 2006). While studying a circular ribbon in association with a coronal null-point topology, Masson et al. (2009) observed that slip-running reconnection and null-point reconnection can occur sequentially. They also found that Q is a highly effective parameter that determines which mode of reconnection will occur in a null-point topology: cut-paste-type null-point reconnetion occurs when the value of Q reaches infinity and slipping (or slip-running) reconnection occurs for lesser values of Q. As observational signature of slipping/slip-running reconnection, circular ribbon and remote brightening can be highlighted (Masson et al. 2009), while the null-point reconnection usually gives rise to collimated eruptions, i.e. coronal jets or H α surges (Pariat et al. 2009a, 2010).

Notably, we observed collimated eruption of plasma prior to the onset of the C3.4 flare (Fig. 7c). AIA 304 Å images clearly revealed two adjacent filaments at the flaring location that apparently crossed each other (Fig. 7c). NLFFF extrapolation clearly identified two braided flux ropes within the atoll region (Fig. 9). Such arrangement of intertwining flux ropes is called ‘double-decker flux rope systems’ (see e.g. Liu et al. 2012; Cheng et al. 2014; Mitra et al. 2020b). Jet-like plasma ejections resulting from the interaction between the flux ropes within a double-decker system has been reported in Mitra et al. (2020b). Further, the double-decker region reported in Mitra et al. (2020b) was associated with a set of open field lines that guided the eruption of collimated jets. NLFFF model magnetic field structure prior to the onset of F_2 revealed that one end of one flux rope within the double-decker system was directly connected to the open spine-like-lines (i.e. open flux rope; shown in the pink colour in Fig. 9). These findings led us to conclude that the jet-like eruption was triggered as a result of the interaction between the two flux ropes of the double-decker flux ropes system, while the open field lines was responsible for guiding eruption in a collimated manner. We also clarify that, in our case, the collimated eruption observed prior to the C3.4 flare should not be related with magnetic reconnection at the HFT. Here, it is worth mentioning that magnetic structures similar to the open flux rope shown in Fig. 9, where magnetic field lines constituting the flux rope, becomes open at one end, has been previously noted by Lugaz et al. (2011) and Janvier et al. (2016). While numerically investigating evolution of eruptive flares from complex photospheric configurations of the active regions NOAA 10798 and 11283, respectively, both the studies found that opening of the field lines of flux rope structures can lead to and guide solar eruptions resulting in the formation of CMEs.

We would like to highlight the association of flux ropes with QSL which we noted in all the four cases [Figs 8(c), 9(c), 10(c) and (g)]. Our analysis readily revealed that the photospheric regions associated with the legs of the flux ropes were characterized by high Q-values. High Q-values at the boundaries of flux ropes essentially associated with two different sets of magnetic field lines: one set forming the flux rope and the other set forming the relatively potential, ambient magnetic field (see e.g. Savcheva et al. 2012; Janvier et al. 2016; Zhao et al. 2016; Guo et al. 2019).

The atoll region produced four homologous flares on 2014 February 16 (Table 1). All the flares triggered as a filament lying over the PIL between the positive polarity sunspot and negative polarity regions, got destabilized. The erupting filament interacted with the fan-spine configuration that led to some degree of circular ribbon brightening during all the flares (Fig. 3). Prior to the onset of each flare, we could identify instances of flux cancellation from the PIL region (Fig. 5) as well as localized brightenings beneath the filaments (Fig. 6 and 7). These observational findings support the tether-cutting model of solar eruptions (Moore & Roumeliotis 1992; Moore et al. 2001). We also explored the possibility of torus and kink instabilities as the triggering mechanism, by computing the decay index and twist numbers. Our analysis suggests that the critical decay height for $n = 1.5$ above the PIL of the flux rope prior to all the four flares remained consistent within the heights of ≈25–30 Mm (Table 3). Statistical surveys concerning the torus instability as the triggering mechanism for eruptive flares by Wang et al. (2017) and Baumgartner, Thalmann & Veronig (2018) revealed the ciritical decay height to lie within the ranges of ≈36 ± 17 Mm and 21 ± 10 Mm. Our results of decay height calculations are in well agreement with these statistically established values, suggesting a favourable role played by torus instability. However, considering the average decay index over the PIL, as followed in the present analysis, is rather a simplistic approach. Detailed studies devoted to the analysis of decay index (see e.g. Zuccarello et al. 2014, 2017; Myshyakov & Tsvetkov 2020) have shown that a flux rope eruption can take place even when the critical height (h_{crit}) becomes sufficiently low in a few discrete locations over the flux rope. Further, theoretical studies have shown that the critical height strongly depend on the magnetic topology (Kliem et al. 2014). In this context we note that, the coronal magnetic configuration associated with all the four flares reported in this paper was much complex compared to the general cases without spine-fan configurations. Rapid decay of magnetic field within the fan-surface is expected which in turns results in high values of magnetic decay index. Average twist number associated with the flux ropes increased successively from ≈0.93 prior to F_1 to ≈1.22 prior to F_4 (Table 3). Although the increase in twist suggest higher storage of magnetic free energy in the flux ropes, the critical value of twist number for resulting in the destabilisation of the flux ropes was statistically established to be $|T_w| \approx 2$ (Duan et al. 2019). Therefore, we could not find any conclusive evidence for kink instability as the triggering mechanism for the homologous flares reported in this paper.

It is also noteworthy that, although a clear circular ribbon appeared during the M-class flare (F_1), no observable signature of null-point-like reconnection (i.e. jet/surge, breakout-type eruption, etc.) was observed during it. AIA 304 Å images during the flare clearly suggested that the erupting filament experienced an apparent sliding motion from the northern end to the southern end within the diffused brightening region. Plasma eruption from one end of the filament was observed only when the sliding filament eventually reached the southern boundary of the diffused brightening region. These observational features suggest the occurrence of predominantly QSL-reconnection during the M1.1 flare, rather than the reconnection between the inner and outer fan-like lines. On the other hand, all the subsequent C-class flares (F_2–F_4) evolved with complete eruption of the filaments from the diffused brightening region, clearly implying reconnection at the HFT. Here, we remember that twist number associated with the flux ropes successively increased from F_1 to F_4. Additionally, negative flux within the magnetic atoll region decreased almost monotonically following the onset of F_1 flare signifying less constraining energy stored in the fan-spine configuration during the subsequent flares compared to F_1. Therefore, we speculate that excess energy stored in the flux rope (in the form of higher twist number) and less energy stored in the constraining magnetic field resulted in the complete destruction of the fan-spine-like configuration during the subsequent C-class flares, while during the M1.1 flare, less twisted flux rope did not have enough energy to trigger exchange type reconnection at the HFT.

In summary, all the eruptive flares initiated from a diffused brightening region that formed over a complex magnetic configuration where dispersed negative polarity regions were surrounded by positive polarity regions (magnetic atoll region). The coronal configuration associated with the magnetic atoll region was a fan-spine-like configuration that involved an HFT situated in the corona above the elongated parasitic negative polarity regions; a configuration similar to those of pseudo-streamers, in a much smaller spatial scale. All the four flares were initiated as a flux rope was activated and erupted within the fan dome. Prior to all the flares, we observed localized brightenings associated with the filaments as well as small-scale flux cancellation from the PIL region that supports the tether-cutting model of solar eruption. The magnetic decay index reached to the value of 1.5 within low coronal heights prior to all the four flares signifying favourable coronal conditions for driving successful eruption of the flux ropes. Interaction between the erupting flux rope and the fan-like-separatrix surface gave rise to circular ribbon brightening during the flares. During the first flare, the erupting flux rope with relatively less twist, could not trigger reconnection in the HFT, while during the subsequent flares, the flux ropes having relatively higher twist, could blow out the already decaying fan-spine-like configuration leading to the complete eruption of the core fields. We further emphasize that, occurrence of successive quasi-circular ribbon flares from complex fan-spine-like configurations including HFTs, have been rarely reported in the literature and subsequent studies involving theoretical and observational analyses of similar events are essential to reach to a general understanding of the complex coronal configurations in the solar atmosphere.

SUPPLEMENTARY MATERIAL

Videos are attached with Figs 3, 6, and 7, which are available in the online article.

ACKNOWLEDGEMENTS

We would like to thank the *SDO* team for their open data policy. *SDO* is NASA's mission under the Living With a Star (LWS) program. This work utilizes GONG data from NSO, which is operated by AURA under a cooperative agreement with NSF and with additional financial support from NOAA, NASA, and USAF. We are thankful to Dr. Thomas Wiegelmann for providing the NLFFF code. We are also thankful to the anonymous referee for his/her important comments and suggestions that enhanced the scientific content and overall presentation of the article.

DATA AVAILABILITY

Observational data from AIA and HMI on board *SDO* utilized in this article are available at http://jsoc.stanford.edu/ajax/lookdata.html. GONG H α data used in this article are available at GONG data archive (https://gong2.nso.edu/archive/patch.pl?menutype = a). The NLFFF code employed in this article for coronal magnetic field modelling is provided by Dr. Thomas Wiegelmann. Different aspects of the code are explained and discussed in https://doi.org/10.1023/B:SOLA.0000021799.39465.36, https://doi.org/10.1007/s11207-006-2092-z, https://doi.org/10.1051/0004-6361/201014391, and https://doi.org/10.1007/s11207-012-9966-z. The IDL-based code used for the computation of Q and T_w is available at http://staff.ustc.edu.cn/~rliu/qfactor.html.

REFERENCES

Antiochos S. K., DeVore C. R., Klimchuk J. A., 1999, ApJ, 510, 485
Aulanier G., Pariat E. Démoulin P., 2005, A&A, 444, 961
Aulanier G., Pariat E., Démoulin P., Devore C. R., 2006, Sol. Phys., 238, 347
Aulanier G., Török T., Démoulin P., DeLuca E. E., 2009, ApJ, 708, 314
Aulanier G., Janvier M., Schmieder B., 2012, A&A, 543, A110
Aulanier G., Démoulin P., Schrijver C. J., Janvier M., Pariat E., Schmieder B., 2013, A&A, 549, A66
Baumgartner C., Thalmann J. K., Veronig A. M., 2018, ApJ, 853, 105
Benz A. O., 2017, Living Rev. Sol. Phys., 14, 2
Berger M. A., Prior C., 2006, J. Phys. A Math. Gen., 39, 8321
Carmichael H., 1964, NASA Spec. Publ., 50, 451
Chatterjee P., Fan Y., 2013, ApJ, 778, L8
Cheng X., Zhang J., Ding M. D., Liu Y., Poomvises W., 2013, ApJ, 763, 43
Cheng X., Ding M. D., Zhang J., Sun X. D., Guo Y., Wang Y. M., Kliem B., Deng Y. Y., 2014, ApJ, 789, 93
Clyne J., Mininni P., Norton A., Rast M., 2007, New J. Phys., 9, 301
Démoulin P., 2007, Adv. Space Res., 39, 1367
DeRosa M. L. et al., 2015, ApJ, 811, 107
Devi P., Joshi B., Chandra R., Mitra P. K., Veronig A. M., Joshi R., 2020, Sol. Phys., 295, 75
Duan A., Jiang C., He W., Feng X., Zou P., Cui J., 2019, ApJ, 884, 73
Fletcher L. et al., 2011, Space Sci. Rev., 159, 19
Fletcher L., Hannah I. G., Hudson H. S., Innes D. E., 2013, ApJ, 771, 104
Forland B. C., Gibson S. E., Dove J. B., Rachmeler L. A., Fan Y., 2013, Sol. Phys., 288, 603
Gibson S., 2015, Coronal Cavities: Observations and Implications for the Magnetic Environment of Prominences, Springer, Switzerland, p. 323
Gibson S. E., Dalmasse K., Rachmeler L. A., De Rosa M. L., Tomczyk S., de Toma G., Burkepile J., Galloy M., 2017, ApJ, 840, L13
Guo Y., Xu Y., Ding M. D., Chen P. F., Xia C., Keppens R., 2019, ApJ, 884, L1
Harvey J. W. et al., 1996, Science, 272, 1284
Harvey J. W. et al., 2011, AAS/Solar Physics Division Abstracts #42. AAS/Solar Physics Division Meeting, Vol. 43, Bulletin of the American Astronomical Society, p. 17.45
Haynes A. L., Parnell C. E., 2007, Phys. Plasmas, 14, 082107
Hernandez-Perez A., Thalmann J. K., Veronig A. M., Su Y., Gömöry P., Dickson E. C., 2017, ApJ, 847, 124
Hernandez-Perez A., Su Y., Thalmann J., Veronig A. M., Dickson E. C., Dissauer K., Joshi B., Chandra R., 2019, ApJ, 887, L28
Hirayama T., 1974, Sol. Phys., 34, 323
Hou Y., Li T., Yang S., Zhang J., 2019, ApJ, 871, 4
Janvier M. et al., 2016, A&A, 591, A141
Janvier M., Aulanier G., Pariat E., Démoulin P., 2013, A&A, 555, A77
Joshi B. et al., 2009, ApJ, 706, 1438
Joshi B., Kushwaha U., Veronig A. M., Dhara S. K., Shanmugaraju A., Moon Y.-J., 2017a, ApJ, 834, 42
Joshi B., Thalmann J. K., Mitra P. K., Chand ra R., Veronig A. M., 2017c, ApJ, 851, 29

Joshi N. C., Liu C., Sun X., Wang H., Magara T., Moon Y. J., 2015, ApJ, 812, 50
Joshi N. C., Sterling A. C., Moore R. L., Magara T., Moon Y.-J., 2017b, ApJ, 845, 26
Kazachenko M. D., Lynch B. J., Welsch B. T., Sun X., 2017, ApJ, 845, 49
Kliem B., Török T., 2006, Phys. Rev. Lett., 96, 255002
Kliem B., Lin J., Forbes T. G., Priest E. R., Török T., 2014, ApJ, 789, 46
Kopp R. A., Pneuman G. W., 1976, Sol. Phys., 50, 85
Kumar S., Bhattacharyya R., Joshi B., Smolarkiewicz P. K., 2016, ApJ, 830, 80
Kushwaha U., Joshi B., Veronig A. M., Moon Y.-J., 2015, ApJ, 807, 101
Lau Y.-T., Finn J. M., 1990, ApJ, 350, 672
Lemen J. R. et al., 2012, Sol. Phys., 275, 17
Li H., Jiang Y., Yang J., Yang B., Xu Z., Hong J., Bi Y., 2017, ApJ, 836, 235
Li H., Yang J., Jiang Y., Bi Y., Qu Z., Chen H., 2018a, Ap&SS, 363, 26
Li T., Yang S., Zhang Q., Hou Y., Zhang J., 2018b, ApJ, 859, 122
Liu R. et al., 2016, ApJ, 818, 148
Liu R., Kliem B., Török T., Liu C., Titov V. S., Lionello R., Linker J. A., Wang H., 2012, ApJ, 756, 59
Longcope D. W., 2005, Living Rev. Sol. Phys., 2, 7
Lugaz N., Downs C., Shibata K., Roussev I. I., Asai A., Gombosi T. I., 2011, ApJ, 738, 127
Manoharan P. K., van Driel-Gesztelyi L., Pick M., Démoulin P., 1996, ApJ, 468, L73
Martin S. F., 1998, Sol. Phys., 182, 107
Masson S., Pariat E., Aulanier G., Schrijver C. J., 2009, ApJ, 700, 559
Masson S., McCauley P., Golub L., Reeves K. K., DeLuca E. E., 2014, ApJ, 787, 145
Mitra P. K., Joshi B., 2019, ApJ, 884, 46
Mitra P. K., Joshi B., Prasad A., Veronig A. M., Bhattacharyya R., 2018, ApJ, 869, 69
Mitra P. K., Joshi B., Prasad A., 2020a, Sol. Phys., 295, 29
Mitra P. K., Joshi B., Veronig A. M., Chand ra R., Dissauer K., Wiegelmann T., 2020b, ApJ, 900, 23
Moore R. L., Roumeliotis G., 1992, in Svestka Z., Jackson B. V., Machado M. E., eds, Lecture Notes in Physics, Vol. 399, IAU Colloq. 133: Eruptive Solar Flares. Springer Verlag, Berlin, p. 69
Moore R. L., Sterling A. C., Hudson H. S., Lemen J. R., 2001, ApJ, 552, 833
Musset S., Vilmer N., Bommier V., 2015, A&A, 580, A106
Myshyakov I., Tsvetkov T., 2020, ApJ, 889, 28
Parenti S., 2014, Living Rev. Sol. Phys., 11, 1
Pariat E., Antiochos S. K., DeVore C. R., 2009a, ApJ, 691, 61
Pariat E., Masson S., Aulanier G., 2009b, ApJ, 701, 1911
Pariat E., Antiochos S. K., DeVore C. R., 2010, ApJ, 714, 1762
Pesnell W. D., Thompson B. J., Chamberlin P. C., 2012, Sol. Phys., 275, 3
Prasad A., Dissauer K., Hu Q., Bhattacharyya R., Veronig A. M., Kumar S., Joshi B., 2020, ApJ, 903, 129
Priest E. R., Démoulin P., 1995, J. Geophys. Res., 100, 23443
Priest E. R., Titov V. S., 1996, Phil. Trans. R. Soc. A, 354, 2951
Prior C., Yeates A. R., 2016, A&A, 591, A16
Qiu Y., Guo Y., Ding M., Zhong Z., 2020, ApJ, 901, 13
Rust D. M., Kumar A., 1996, ApJ, 464, L199
Sahu S., Joshi B., Mitra P. K., Veronig A. M., Yurchyshyn V., 2020, ApJ, 897, 157
Savcheva A., Pariat E., van Ballegooijen A., Aulanier G., DeLuca E., 2012, ApJ, 750, 15
Schou J. et al., 2012, Sol. Phys., 275, 229
Shen Y., Qu Z., Zhou C., Duan Y., Tang Z., Yuan D., 2019, ApJ, 885, L11
Shibata K., Magara T., 2011, Living Rev. Sol. Phys., 8, 6
Shibata K., Nitta N., Strong K. T., Matsumoto R., Yokoyama T., Hirayama T., Hudson H., Ogawara Y., 1994, ApJ, 431, L51
Sturrock P. A., 1966, Nature, 211, 695
Sun X., Hoeksema J. T., Liu Y., Aulanier G., Su Y., Hannah I. G., Hock R. A., 2013, ApJ, 778, 139
Tandberg-Hanssen E., 1995, Physical Parameters of the Prominence Plasma. Springer Netherlands, Dordrecht, p. 81
Thalmann J. K., Moraitis K., Linan L., Pariat E., Valori G., Dalmasse K., 2019, ApJ, 887, 64
Titov V. S., Hornig G., Démoulin P., 2002, J. Geophys. Res., 107, 1164
Titov V. S., Galsgaard K., Neukirch T., 2003, ApJ, 582, 1172
Titov V. S., Mikić Z., Linker J. A., Lionello R., Antiochos S. K., 2011, ApJ, 731, 111
Titov V. S., Mikic Z., Török T., Linker J. A., Panasenco O., 2012, ApJ, 759, 70
Török T., Kliem B., Titov V. S., 2004, A&A, 413, L27
Veronig A. M., Karlický M., Vršnak B., Temmer M., Magdalenić J., Dennis B. R., Otruba W., Pötzi W., 2006, A&A, 446, 675
Wang D., Liu R., Wang Y., Liu K., Chen J., Liu J., Zhou Z., Zhang M., 2017, ApJ, 843, L9
Wang Y. M., Sheeley N. R. J., Rich N. B., 2007, ApJ, 658, 1340
Wiegelmann T., Inhester B., 2010, A&A, 516, A107
Wiegelmann T., Inhester B., Sakurai T., 2006, Sol. Phys., 233, 215
Wiegelmann T., Thalmann J. K., Inhester B., Tadesse T., Sun X., Hoeksema J. T., 2012, Sol. Phys., 281, 37
Wilmot-Smith A. L., Hornig G., Pontin D. I., 2009, ApJ, 704, 1288
Xu Z., Yang K., Guo Y., Zhao J., Zhao Z. J., Kashapova L., 2017, ApJ, 851, 30
Zhang J., Cheng X., Ding M.-D., 2012, Nat. Commun., 3, 747
Zhao J., Gilchrist S. A., Aulanier G., Schmieder B., Pariat E., Li H., 2016, ApJ, 823, 62
Zirin H., 1988, Astrophysics of the Sun, Cambridge Univ. Press, Cambridge
Zuccarello F. P., Seaton D. B., Mierla M., Poedts S., Rachmeler L. A., Romano P., Zuccarello F., 2014, ApJ, 785, 88
Zuccarello F. P., Chandra R., Schmieder B., Aulanier G., Joshi R., 2017, A&A, 601, A26

SUPPORTING INFORMATION

Supplementary data are available at *MNRAS* online.

Figure_3.mp4
Figure_6.mp4
Figure_7.mp4

Please note: Oxford University Press is not responsible for the content or functionality of any supporting materials supplied by the authors. Any queries (other than missing material) should be directed to the corresponding author for the article.

This paper has been typeset from a TEX/LATEX file prepared by the author.

The Astrophysical Journal, 926:143 (17pp), 2022 February 20 https://doi.org/10.3847/1538-4357/ac4756

Multiwavelength Signatures of Episodic Nullpoint Reconnection in a Quadrupolar Magnetic Configuration and the Cause of Failed Flux Rope Eruption

Prabir K. Mitra[1,2,3], Bhuwan Joshi[1], Astrid M. Veronig[3,4], and Thomas Wiegelmann[5]
[1] Udaipur Solar Observatory, Physical Research Laboratory, Udaipur 313 001, India; prabir@prl.res.in
[2] Department of Physics, Gujarat University, Ahmedabad 380 009, India
[3] Institute of Physics, University of Graz, Universitätsplatz 5, A-8010 Graz, Austria
[4] Kanzelhöhe Observatory for Solar and Environmental Research, University of Graz, Kanzelhöhe 19, A-9521 Treffen, Austria
[5] Max-Planck-Institut für Sonnensystemforschung, Justus-von-Liebig-Weg 3, D-37077 Göttingen, Germany
Received 2021 February 26; revised 2021 December 23; accepted 2021 December 28; published 2022 February 21

Abstract

In this paper, we present multiwavelength observations of the triggering of a failed-eruptive M-class flare from active region NOAA 11302 and investigate the possible reasons for the associated failed eruption. Photospheric observations and nonlinear force-free field extrapolated coronal magnetic field revealed that the flaring region had a complex quadrupolar configuration with a preexisting coronal nullpoint situated above the core field. Prior to the onset of the M-class flare, we observed multiple periods of small-scale flux enhancements in GOES and RHESSI soft X-ray observations from the location of the nullpoint. The preflare configuration and evolution reported here are similar to the configurations presented in the breakout model, but at much lower coronal heights. The core of the flaring region was characterized by the presence of two flux ropes in a double-decker configuration. During the impulsive phase of the flare, one of the two flux ropes initially started erupting, but resulted in a failed eruption. Calculation of the magnetic decay index revealed a saddle-like profile where the decay index initially increased to the torus-unstable limits within the heights of the flux ropes, but then decreased rapidly and reached negative values, which was most likely responsible for the failed eruption of the initially torus-unstable flux rope.

Unified Astronomy Thesaurus concepts: Active sun (18); Solar activity (1475); Solar active region filaments (1977); Solar flares (1496); Active solar corona (1988)

Supporting material: animation

1. Introduction

Solar eruptive phenomena are violent activities occurring in the solar atmosphere that include catastrophic energy releases within a short time in a localized region, i.e., flares (Priest & Forbes 2002; Fletcher et al. 2011; Benz 2017), along with the expulsion of plasma and magnetic field into the interplanetary space, i.e., coronal mass ejections (CMEs; Chen 2011; Green et al. 2018). Earth-directed CMEs inflict hazardous effects in the near-Earth environment that include damage to satellites, disruption of the telecommunication system, and damage of the electrical power grids on Earth (space weather; see, Moldwin 2008; Koskinen et al. 2017; Lanzerotti 2017). While most of the major flares are associated with CMEs (i.e., eruptive flares), a significant number of flares does not lead to CMEs (i.e., confined flares; see, e.g., Yashiro et al. 2005; Baumgartner et al. 2018; Li et al. 2020). Observationally, a particular variant of confined flares also involves so-called failed flux rope eruptions, where a flux rope is initially activated from the source region, but subsequently fails to escape from the overlying layers of the solar corona, and the material eventually falls back (Gilbert et al. 2007, see also Ji et al. 2003; Alexander et al. 2006; Liu et al. 2009; Kushwaha et al. 2015). With an ever-increasing urge to understand the factors leading to CME eruptions and develop methods to predict space weather, the observational and theoretical studies of failed eruptions have recently gained much attention and have become an important research topic in contemporary solar physics (see, e.g., Cheng et al. 2011; Amari et al. 2018; Sarkar & Srivastava 2018).

Eruptive flares are usually characterized by the formation of two parallel, ribbon-like brightenings followed by the development of a coronal flare arcade connecting the two ribbons (Švestka & Cliver 1992). To explain these two-ribbon flares, the standard flare model, also known as the CSHKP model, was developed. It includes the pioneering works of Carmichael (1964), Sturrock (1966), Hirayama (1974), and Kopp & Pneuman (1976). In recent years, this model has been extended to three dimensions (Aulanier et al. 2012, 2013; Janvier et al. 2013). According to this model, when a preexisting magnetic flux rope (MFR) is triggered for upward eruption, inflow of magnetic field occurs beneath the MFR, where a current sheet is eventually generated. Magnetic reconnection at these current sheets rapidly converts previously stored magnetic energy into plasma heating and kinetic energy of accelerated particles, and also adds magnetic flux to the erupting flux rope, prolonging the driving Lorentz force (Vršnak 2016; Veronig et al. 2018). The CSHKP model is quite successful in explaining commonly observed large-scale features of eruptive flares, e.g., footpoint and looptop hard X-ray (HXR) sources; the expansion of flare ribbons in opposite polarities observed in optical, extreme-UV (EUV), and soft X-ray (SXR) wavelengths; the formation of highly structured loop arcades observed in optical, EUV, and SXR wavelengths that connect the flare ribbons; and the formation of hot cusp-like structures (see, e.g., Tsuneta et al. 1992; Masuda et al. 1994; Sui et al. 2006; Veronig et al. 2006; Miklenic et al. 2007; Joshi et al. 2017; Gou et al. 2019; Mitra & Joshi 2019). However, some important aspects related to solar eruptions remain beyond the scope of the standard flare model, e.g., the processes of flux rope formation; onset or triggering of eruptions; and the initial dynamical evolution of the CME or flux rope (Green et al. 2018, see also Joshi et al. 2019).

Theoretically, an MFR is defined as a set of magnetic field lines that are wrapped around a central axis (Gibson & Fan 2006). Observationally, MFRs can be identified in the form of filaments or prominences, coronal cavities, coronal sigmoids, hot coronal channels, etc. (see the review by Patsourakos et al. 2020). Filaments are dark, thread-like structures observed in chromospheric images of the Sun (Martin 1998). When filaments are observed above the limb of the Sun, they appear as bright structures, and therefore, they are called prominences (see the review by Gibson 2018). Although the exact structure of filaments is still debated (see, e.g., Antiochos et al. 1994), it is now believed that MFRs form the basic structures of active region filaments. Coronal cavities represent the transverse cross-sectional view of MFRs, where the accumulation of plasma can be observed at the bottom of the dark cavity, providing important insights into the relation between MFRs and filaments (Gibson 2015). Coronal sigmoids are S (or reverse-S) shaped structures observed in SXR (Manoharan et al. 1996; Rust & Kumar 1996) and EUV wavelengths (Joshi et al. 2017; Mitra et al. 2018), and they are interpreted as manifestations of highly twisted MFRs (Green et al. 2018). Hot channels are coherent structures observed in the high-temperature passband EUV images of the solar corona, which indicate activated, quasi-stable MFRs (Zhang et al. 2012; Cheng et al. 2013; Nindos et al. 2015; Joshi et al. 2018; Hernandez-Perez et al. 2019; Mitra & Joshi 2019; Sahu et al. 2020; Kharayat et al. 2021). Two possible scenarios of flux rope formation have been proposed: emergence of MFRs from the convection zone of the Sun into the solar atmosphere by magnetic buoyancy (Archontis & Hood 2008; Chatterjee & Fan 2013), and the formation of MFRs from sheared arcades in response to small-scale magnetic reconnection in the corona (Aulanier et al. 2010; Inoue et al. 2018; Mitra et al. 2020a).

Successful eruptions of MFRs are essential for the generation of CMEs. In order to explain the triggering of MFRs toward an eruption, different models have been proposed that can be largely classified into two groups: models relying on ideal magnetohydrodynamics (MHD) instability (kink and torus instability), and models relying on magnetic reconnection (tether-cutting model, breakout model, etc.). According to the torus instability (Kliem & Török 2006), a toroidal current ring may be triggered to erupt if the ambient poloidal magnetic field decreases with height faster than a critical rate. The magnetic decay index (n), defined as $n = -\frac{d\log(B_p)}{d\log(z)}$; where B_p and z are the external poloidal magnetic field and height, respectively, is used as the quantification of the decay of the magnetic field with height above the relevant polarity inversion line. Theoretically, it was found that an MFR is subject to torus instability when it reaches a region characterized by $n > 1.5$ (Bateman 1978). However, a number of observational studies revealed that the threshold value of n for the torus instability lies within the range [1.1–1.75] (e.g., Liu 2008; Kliem et al. 2013; Zuccarello et al. 2015). Kink instability suggests that an MFR may be destabilized if its twist increases beyond $\approx 3.5\pi$ (Török et al. 2004). The tether-cutting model explains the triggering of solar eruptions from a highly sheared bipolar magnetic configuration in which the initial magnetic reconnection takes place deep within the sheared core field (Moore & Roumeliotis 1992). Here, the flux rope is developed from the sheared arcades in response to these preflare magnetic reconnections, and the successful eruption of the flux rope depends on the flux content of the sheared core field relative to the overlying envelope field (Moore et al. 2001). In contrast to the tether-cutting model, the breakout model involves complex multipolar topology with one or more nullpoints situated well above the core field (Antiochos et al. 1999). As the photospheric magnetic field evolves (in the form of flux emergence, shearing motion, etc.), the core field extends outward, stretching the nullpoint, which leads to the formation of breakout current sheets (Karpen et al. 2012). The initial reconnection (breakout reconnection) takes place on these breakout current sheets, which reduces the downward strapping force of the enveloping field and allows the core field to erupt successfully. Notably, once the triggered flux rope attains upward eruptive motion, standard flare reconnection (as explained in the CSHKP model) sets in beneath the flux rope, a process that is common to all the triggering mechanisms.

The presence of the coronal nullpoint in the preflare configuration is an essential requirement in the breakout model as the breakout current sheet is formed by stretching the nullpoint. Theoretically, magnetic nullpoints are defined as locations where all the three components of magnetic field become zero and increase linearly with distance from it (Chapter 6 in Priest 2014). Thus, nullpoints create discontinuities in the coronal magnetic field and separate different domains of flux regions. In general, regions of strong gradients in continuous magnetic fields are identified as quasi-separatrix layers (QSLs; Priest & Démoulin 1995). The gradient of magnetic connectivity can be quantified by computing the degree of squashing factor (Q) by calculating the norm (N) of the field line mapping of magnetic domains (Demoulin et al. 1996; Pariat & Démoulin 2012). Theoretically, Titov et al. (2002) showed that in all physical scenarios, $Q = 2$ is the lowest possible value of Q, and QSLs are therefore characterized by $Q \gg 2$ (Aulanier et al. 2005), while $Q \to \infty$ is representative of nullpoints. Due to local diffusion, magnetic fields in QSLs can constantly change their connectivities (Aulanier et al. 2006), which can observationally be identified as apparent slipping motion of flare kernels in imagery of the lower solar atmosphere, which is called "slipping" or "slip-running" reconnection (see, e.g., Janvier et al. 2013).

In this paper, we report an M4.0 flare from active region NOAA 11302 on 2011 September 26, which was associated with the failed eruption of a filament. Different multiwavelength aspects of this event with the main focus on the nonthermal energy evolution were studied by Kushwaha et al. (2014). Their observations suggest that the impulsive phase of the flare was characterized by two short-lived microwave (MW) peaks in 17 and 34 GHz observed by the Nobeyama Radioheliograph (NoRH; Nakajima et al. 1994; Takano et al. 1997). Interestingly, while the first MW burst occurred cotemporal with a sudden peak in hard X-ray (HXR) wavelengths observed by the Reuven Ramaty High Energy Solar Spectroscopic Imager (RHESSI; Lin et al. 2002) with energies up to ≈200 keV following a power law with a hard photon spectral index (γ) ~3, the second nonthermal burst observed in MW was much less pronounced in HXRs. Importantly, the onset of the X-ray emission during the flare occurred immediately after the emergence of a pair of small-scale magnetic transients of opposite polarities in the inner core region, which led them to conclude that small-scale changes in the magnetic structure may play a crucial role in triggering the flare process by disturbing the preflare magnetic configurations. In view of the rapid temporal evolution of the HXR and MW flux during the early impulsive phase of the flare, they concluded that an abrupt energy release via spontaneous magnetic reconnection was responsible for the occurrence of the flare. In order to investigate whether this apparent spontaneous magnetic reconnection was influenced by topological features, e.g., flux ropes or nullpoints, we revisited the event considering a longer period of observation and analysis. Our study readily revealed that the flare was preceded by a number of subtle SXR flux enhancements, suggesting that a possible influence of external factors is responsible for triggering the flare. By employing a nonlinear force-free ield (NLFFF) extrapolation model, complemented by EUV observations of the Atmospheric Imaging Assembly (AIA; Lemen et al. 2012) on board the Solar Dynamics Observatory (SDO; Pesnell et al. 2012), we investigate the causal connection between the activities during the extended preflare phase and the main flare, and we investigate the factors responsible for the failed filament eruption. The structure of the paper is as follows: Section 2 provides a brief description of the observational data sets and different analysis techniques used in this work. We discuss the temporal evolution of X-ray and EUV emission from the flaring active region in Section 3. Section 4 gives a detailed overview of the photospheric magnetic configuration of the active region and discusses the coronal magnetic configuration of the flaring region. Section 5 presents the observational results on the basis of a coronal and chromospheric imaging analysis. The results obtained by modeling coronal magnetic field are explained in Section 6. We discuss and interpret the results in Section 7.

2. Observational Data and Analysis Techniques

2.1. Data

In this work, we have combined multiwavelength observational data from different sources. For EUV imaging of the Sun, we used observations provided by the AIA on board SDO. In particular, we extensively used the full disk 4096×4096 pixel solar images in 304 Å ($\log(T) = 4.7$), 171 Å ($\log(T) = 5.8$), 94 Å ($\log(T) = 6.8$), and 131 Å ($\log(T) = 5.6, 7.0$) channels at a pixel scale of 0.″6 and a cadence of 12 s. In order to enhance the fine structures, all the AIA images have been filtered with the unsharp_mask image processing algorithm. Chromospheric observations of the Sun in the Hα passband were obtained from the Global Oscillation Network Group (GONG; Harvey et al. 1996). GONG provides 2096×2096 pixel full-disk Hα images[6] of the Sun with a pixel scale of ≈1.″0 (Harvey et al. 2011). To study the evolution of photospheric magnetic structures, we used data from the Helioseismic and Magnetic Imager (HMI; Schou et al. 2012) on board SDO. Among the different products of HMI, we have used the 4096×4096 pixel full-disk intensity images and line-of-sight (LOS) magnetograms at a pixel scale of 0.″5 and cadence of 45 s. We used X-ray observations of the RHESSI (Lin et al. 2002), which has a spatial resolution (as fine as ∼2.″3) and energy resolution (1–5 keV) over the energy range 3 keV–17 MeV. To construct RHESSI X-ray images, we used the PIXON algorithm (Metcalf et al. 1996) with the natural weighting scheme for front detector segments 2–9 (excluding 7).

2.2. Numerical Analysis Techniques

In order to investigate the coronal magnetic configuration of the active region with the aim to understand the cause of the failed eruption associated with the event, we carried out coronal magnetic field modeling using the optimization-based NLFFF extrapolation technique developed by Wiegelmann & Inhester (2010) and Wiegelmann et al. (2012). As the boundary condition for the extrapolation, we used the vector magnetogram of 2011 September 26 04:58 UT from the hmi_sharp_cea_720s series of HMI/SDO with a reduced resolution of 1.″0 pixel^{-1}. The extrapolation was made in a Cartesian volume of $616 \times 288 \times 256$ pixels, which corresponds to physical dimensions of $\approx 447 \times 209 \times 186$ Mm^3. According to the theory of the NLFFF model, the angle between current ($\boldsymbol{J}$) and magnetic field ($\boldsymbol{B}$) should be 0 as the total value of the Lorentz force, i.e., $|\boldsymbol{J} \times \boldsymbol{B}|$, is 0. However, because the extrapolation approach is based on numerical techniques, the NLFFF-reconstructed magnetic field is expected to return nonzero values of $|\boldsymbol{J} \times \boldsymbol{B}|$. Therefore, to assess the quality of the coronal magnetic field reconstruction, the average value of the fractional flux ratio ($|f_i| = |(\vec{\nabla} \cdot \boldsymbol{B})_i| / (6|\boldsymbol{B}|_i / \triangle x)$), weighted angle ($\theta_J$) between $\boldsymbol{J}$ and $\boldsymbol{B}$ can be considered (see DeRosa et al. 2015). In this study, we obtained the values of the residual errors by averaging these parameters over the entire computation domain, i.e., $616 \times 288 \times 256$ pixels, with pixel dimensions physically translating into ≈0.725 Mm. The residual errors were found to be

$$<|f_i|> \approx 4.06 \times 10^{-4};\ \frac{|\boldsymbol{J} \times \boldsymbol{B}|}{|\boldsymbol{J} \cdot \boldsymbol{B}|} \approx 0.14;\ \theta_J \approx 6^{\circ}.76. \quad (1)$$

In general, NLFFF solutions are considered good solutions if they return the values $<|f_i|> \lesssim 2 \times 10^{-3}$ and $\theta_J \lesssim 10°$ (see, e.g., DeRosa et al. 2015).

Using the NLFFF extrapolation results, we calculated the degree of squashing factor (Q) and the twist number (T_w) within the extrapolation volume by employing the code developed by Liu et al. (2016). In order to locate 3D nullpoints within the extrapolation volume, we used the trilinear method (Haynes & Parnell 2007) by dividing the whole active region volume into grid cells of dimension $2 \times 2 \times 2$ pixels. If any of the three components of the magnetic field vector have same sign at all the eight corners of the grids, it is considered that the corresponding grid cell cannot contain any nullpoint within it, and therefore, the corresponding cell is excluded from further analysis. Each of the remaining other cells is then further divided into $100 \times 100 \times 100$ subgrid cells and the nullpoint is located by using the Newton–Raphson method[7] for finding roots of equations. This iterative method was continued until the uncertainty in the solution reached to $\lesssim 2$ subgrid cell width. To visualize the results obtained from the NLFFF extrapolation, we used the software called Visualization and Analysis Platform for Ocean, Atmosphere, and Solar Researchers (VAPOR; Clyne et al. 2007).

[6] See http://halpha.nso.edu.

[7] http://fourier.eng.hmc.edu/e176/lectures/NM/node21.html

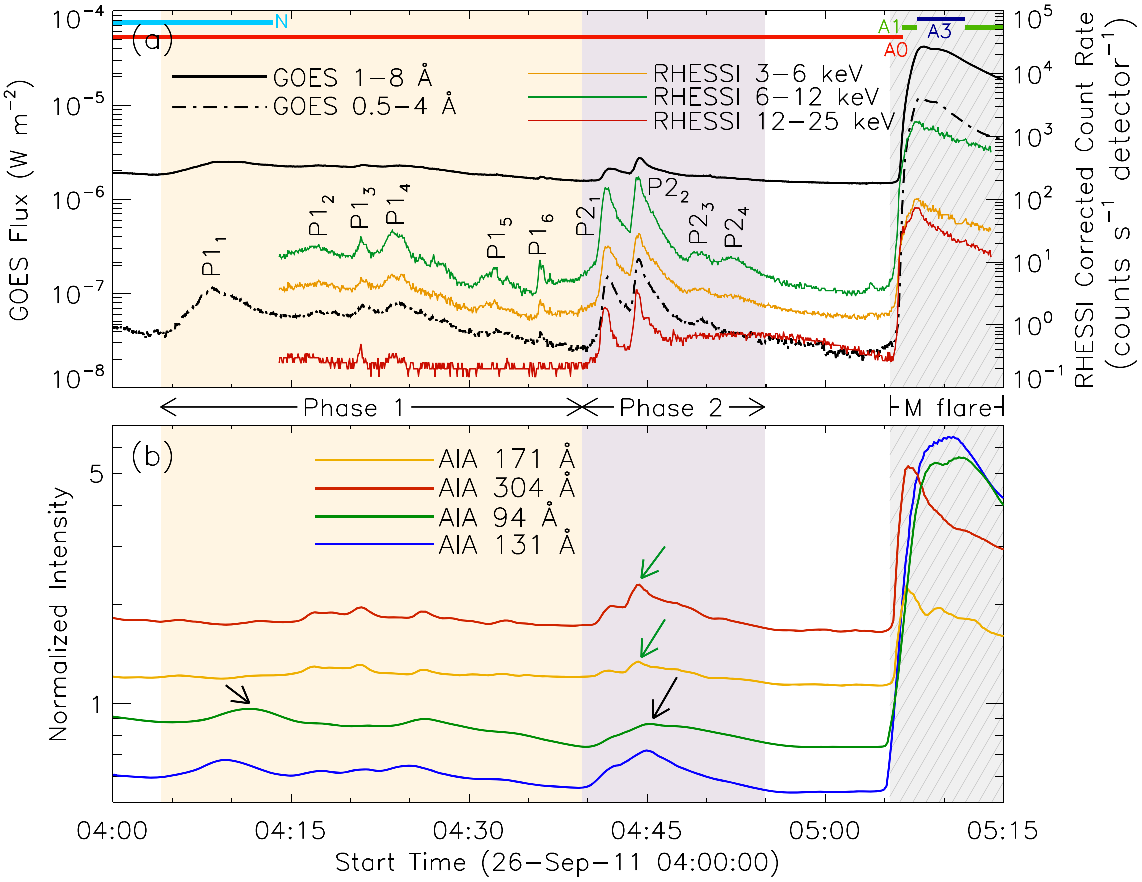

Figure 1. Panel (a): Evolution of X-ray flux in different GOES and RHESSI channels showing the extended preflare phase along with the evolution of the M4.0 flare. For better visualization, RHESSI fluxes are normalized by $\frac{1}{2}$ and $\frac{1}{20}$ for 3–6 keV and 12–25 keV channels. The horizontal bars at the top represent the status of RHESSI observation and attenuator states. Panel (b): Normalized AIA EUV intensity variations for the same duration as in panel (a). For better visualization, AIA 171, 304, 94, and 131 Å channels are scaled by factors of 1.2, 1.8, 0.9, and 0.6, respectively. The light yellow and light purple shaded intervals represent the durations of the two preflare periods of SXR flux enhancements, which are further identified as Phase 1 and Phase 2, respectively. Individual SXR peaks during Phase 1 and Phase 2 are identified as $P1_1$–$P1_6$ and $P2_1$–$P2_4$, respectively. The hatched light gray shaded interval represents the impulsive and early gradual phase of the M2.4 flare. The two green arrows in panel (b) indicate the intensity enhancement in AIA 171 and 304 Å channels during $P2_2$, while the two black arrows indicate mild enhancement in the intensities in AIA 94 and 131 Å channels during $P1_1$ and $P2_2$.

3. Temporal Evolution of X-Ray and EUV Emission

In Figure 1 we compare the temporal evolution of the X-ray fluxes in the 1–8 Å and 0.5–4 Å channels of GOES and multiple energy channels of RHESSI covering the energy range 3–25 keV (Figure 1(a)) and EUV fluxes derived from different AIA channels (Figure 1(b)) during 2011 September 26 04:00 UT—05:15 UT, which included an extended phase prior to the onset of the M4.0 flare as well as the impulsive and a part of the gradual phase of it. GOES did not observe the Sun during 05:15 UT—06:25 UT, which covered most of the declining phase of the flare.[8] RHESSI missed the initial phase of our observing period (until ∼04:13 UT) due to RHESSI night. From Figure 1(a), we find a number of episodes of small emission enhancements prior to the M-class flare during ≈04:04 UT—04:53 UT, which were most prominent in GOES 0.5–4 Å and RHESSI channels up to 12 keV. Multiwavelength EUV and X-ray imaging (discussed in detail in Sections 5.1) suggested that a localized region undergoes compact brightening during these flux-enhancing periods. Based on the intensity and compactness of the EUV and X-ray sources, we divided the whole period into two phases: Phase 1 from 04:04 UT—04:39 UT (highlighted by light yellow background in Figure 1), and Phase 2 from 04:39 UT—04:53 UT (highlighted by light purple background in Figure 1), and we identify the flux peaks by $P1_1$–$P1_6$ and $P2_1$–$P2_4$, respectively. The onset of the flare occurred at ≈05:06 UT, which was followed by an impulsive rise in flare emission. The flare reached its peak at ≈05:08 UT after undergoing a brief impulsive phase lasting for only ≈2 minutes. AIA EUV intensities displayed a general agreement with the X-ray flux variation, although the small-scale enhancements observed in the GOES 0.5–4 Å and RHESSI light curves up to energies ≈12 keV during Phase 1 were much less pronounced in EUV light curves. Notably, the AIA 171 and 304 Å intensities showed a significant enhancement during the $P2_2$ peak (indicated by the green arrows in Figure 1(b)), while they remained completely unchanged during $P1_1$. Intensities in the AIA 94 and 131 Å channels showed mild enhancements during both the aforementioned X-ray peaks (indicated by the black arrows in Figure 1(b)).

It is worth mentioning that the soft and hard X-ray light curves obtained from GOES and RHESSI (Figure 1(a)) are disk integrated, i.e., they include emission originating from the full solar disk. On the other hand, the EUV light curves from

[8] See https://www.swpc.noaa.gov/products/goes-x-ray-flux.

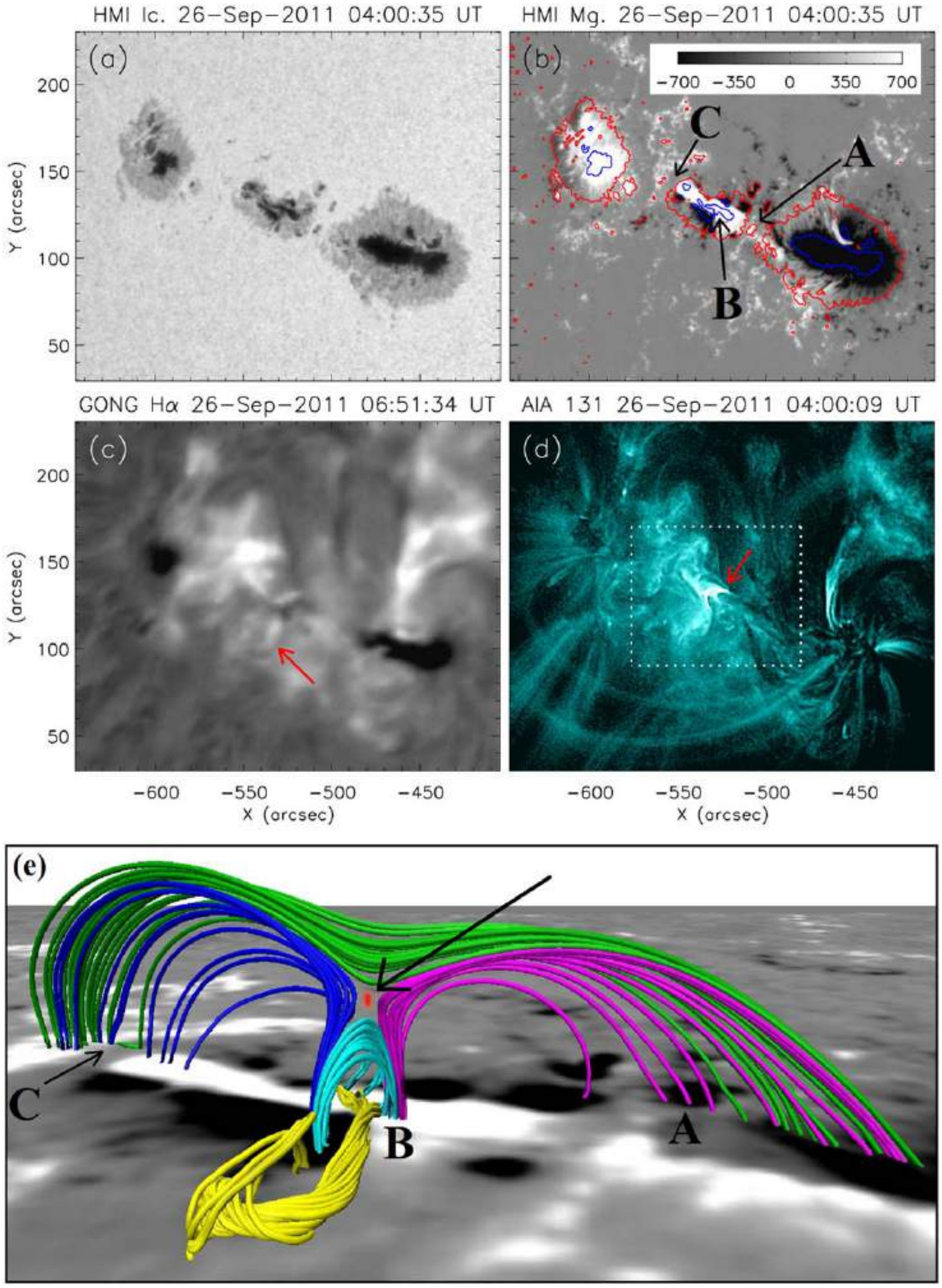

Figure 2. Panel (a): HMI white-light image of active region 11302 on 2011 September 26 04:00 UT. Panel (b): Cotemporal HMI LOS magnetogram. Magnetic flux density in Gauss is color-coded as the color bar shown in the inset. The blue and red contours in panel (b) indicate the spatial extent of the umbrae and penumbrae of the sunspot groups as observed in white light. The contour levels are 35% and 75% of the maximum white-light emission, respectively. Panel (c): GONG Learmonth Hα image of the active region showing the presence of multiple filaments. The red arrow indicates a faint filament that was involved in the M-class flare under study. Panel (d): AIA 131 Å image of the active region showing a set of significantly bright, small coronal loops during the preflare phase (indicated by the red arrow). The dotted white boxes in panel (d) indicate the FOV of Figures 3(b)–(m). Panel (e): NLFFF extrapolation results of the flaring region showing a flux rope (displayed by the yellow lines) and four sets of coronal loops connecting different photospheric flux regions associated with the quadrupolar configuration of the central sunspot group. The red patch (indicated by the black arrow) represents a coronal nullpoint obtained by the trilinear method, which was situated in the quadrupolar configuration. The red patch is further characterized by the Q value of $\log(Q) = 8.5$. Stamps A, B, and C in panels (b) and (e) are for comparison between the FOVs of the corresponding panels.

SDO/AIA displayed in Figure 1(b) were derived by integrating the counts within the flaring region of with a field of view (FOV) of [(−405.″0:−645.″0), (30.″0:230.″0)], shown in Figure 2(d). Despite the difference in the regions used to construct the light curves in Figures 1(a) and (b), their general agreement suggests that the overall activity of the Sun was primarily dominated by the flaring activities occurring within active region NOAA 11302. This is expected because the intensities in the EUV, SXR, and HXR domains from flaring active regions increase by orders of magnitude during flares and thus become the dominant contribution to the changes in the full-Sun light curves.

4. NOAA 11302: δ-sunspot Region and Quadrupolar Configuration

During the M-class flare under study, active region NOAA 11302 was centered at the heliographic location ≈N15E35. The white-light image of the active region (Figure 2(a)) shows that the active region was comprised of three separate sunspot groups that were distributed along the northeast–southwest (NE–SW) direction. In addition to the three prominent sunspots, the active region also contained a few small pores. Comparison of a cotemporal magnetogram of the active region (Figure 2(b)) with the white-light image suggests that the easternmost sunspot group was of predominantly positive polarity, while the westernmost sunspot group was mostly composed of negative flux, although a few dispersed positive flux regions were distributed around it. The middle sunspot group is particularly interesting as it had bipolar magnetic structures. The intensity contours over the magnetogram in Figure 2(b) show that this sunspot group had fragmented umbrae of opposite polarities within a single penumbra, which suggests that the active region is a δ-type AR. Notably, the M-class flare and associated failed eruption reported in this paper originated from this sunspot group. The chromospheric Hα image shows a very small, faint filament with one leg attached to the middle sunspot group (indicated by the red arrow in Figure 2(c)). Coronal images of the active region, particularly in the hot AIA EUV channels, e.g., 94 Å and 131 Å, revealed an interesting structure at the northern end of the filament (indicated by the red arrow in Figure 2(d)), which was composed of multiple small coronal loops connecting different polarity regions of the middle sunspot group.

The NLFFF extrapolation results readily validated the observed coronal structures at large and small scales. In Figure 2(e) we show the modeled coronal configuration associated with the central sunspot group. Notably, the coronal loops shown in blue, green, pink, and teal constituted a well-defined quadrupolar coronal configuration. Importantly, our analysis further confirms the presence of a coronal nullpoint in the quadrupolar configuration above the central sunspot group (shown by the red patch in Figure 2(e) and indicated by the black arrow). The NLFFF extrapolation also demonstrated the presence of a flux rope associated with the central sunspot region (shown by the yellow lines in Figure 2(e)).

5. Multiwavelength Imaging of Coronal Energy Release: Onset and Consequences

In Figure 3 we present an overview of the prominent episodes of energy release in multiple EUV channels of AIA (171, 131, and 304 Å) with respect to the X-ray flux evolution obtained from the GOES 0.5–4 Å channel and RHESSI 6-12 keV energy band. AIA images during the $P1_1$ peak (see Figure 1) suggest a localized brightening (indicated by the red arrow in Figure 3(c)) situated at the northern end of the filament (indicated by the white arrows in Figures 3(b)–(d)). Notably, this brightening was most prominent in the high-temperature AIA 131 Å channel compared to the AIA filters that sample plasma at lower temperatures, e.g., 171 and 304 Å. Emission from this localized region significantly increased in all the AIA EUV channels during the $P2_1$ and $P2_2$ peaks (indicated by the red arrows in Figures 3(e)–(f) and the teal arrow in Figure 3(g)). This localized region was identified as a coronal nullpoint configuration in the NLFFF extrapolation results (Figure 2), suggesting nullpoint reconnection to be responsible for the repetitive flux enhancements during the extended periods of Phase 1 and Phase 2. During this time, we observed signatures of a second filament (indicated by the green arrows in Figures 3(e) and (g)) close to the filament previously observed (indicated by white arrows in Figures 3(e) and (g) and also in Figures 3(b)–(d)). The onset of the impulsive phase of the M4.0 flare was characterized by the activation of the first filament, which resulted in intensified emission (the filament appearance changed from absorption to emission, indicated by the white arrows in Figures 3(h) and (j)). During the impulsive phase, the filament initially displayed eruptive motion and extended spatially along its length. However, the eruption of the filament ceased to continue within ≈2 minutes, after which we observed a complex structure in which the two activated filaments became intertwined with each other during the peak phase of the flare. In Figures 3(k) and (m) we indicate the two activated intertwined filaments by the white and green arrows. Notably, during this time, we observed quite intense emission from a second location as well, which was situated remotely to the north of the filaments (indicated by the teal arrows in Figures 3(k) and (m)). A summary of the different evolutionary phases under study is provided in Table 1.

5.1. Episodic Energy Release at Nullpoint Topology

Comparison of Figures 1(a) and (b) readily suggests that the small-scale flux enhancements observed in X-ray channels were more in agreement with hot AIA channel intensity variations (i.e., 94 and 131 Å) compared to the low-temperature channels (i.e., 304 and 171 Å). Therefore, in order to have a thorough understanding of the activities during Phase 1 and Phase 2, we examine the AIA 131 Å images of the flaring region in Figures 4 and 5, respectively. Hot AIA EUV imaging clearly revealed that repetitive X-ray/EUV peaks during Phases 1 and 2 were essentially linked with an episodic, impulsive brightening of the compact loop structure. Notably, as discussed in Section 4 (see also Figure 2), the region of these compact bright loops has been identified with the location of the coronal nullpoint topology.

In Figure 4(a) we show AIA 131 Å image of the region, in which we outline the bright loops by dashed red curves. From the overplotted line-of-sight (LOS) magnetogram contours (Figure 4(a)), it becomes evident that the bright loops were connecting different opposite-polarity regions of the central sunspot group (see also Figures 2(b), d)). During the subsequent emission peaks of Phase 1, i.e., $P1_2$–$P1_6$, we observed clear X-ray sources up to 25 keV that originated from the location of the compact loop system associated with the nullpoint. Despite continued X-ray emission and enhanced loop brightening in the EUV, there was no significant change in the morphology of the compact loop system. This brightness of the compact EUV loop system increased during Phase 2 (Figure 5), which is also evident from the EUV light curves (Figure 1(b)). Notably, RHESSI sources were identified to be more compact during Phase 2 than in Phase 1. Furthermore, during Phase 2, we found continued X-ray emission at higher energy (12–25 keV). Thus, the morphology and intensity of X-ray and EUV sources during Phase 2 suggest that the reconnection activities at the nullpoint are more energetic. Moreover, we observed eruptions of small loop-like structures from the location of the nullpoint during the peaks $P2_1$ and $P2_2$ (indicated by the yellow arrows in Figures 5(b) and (c)), which point toward the

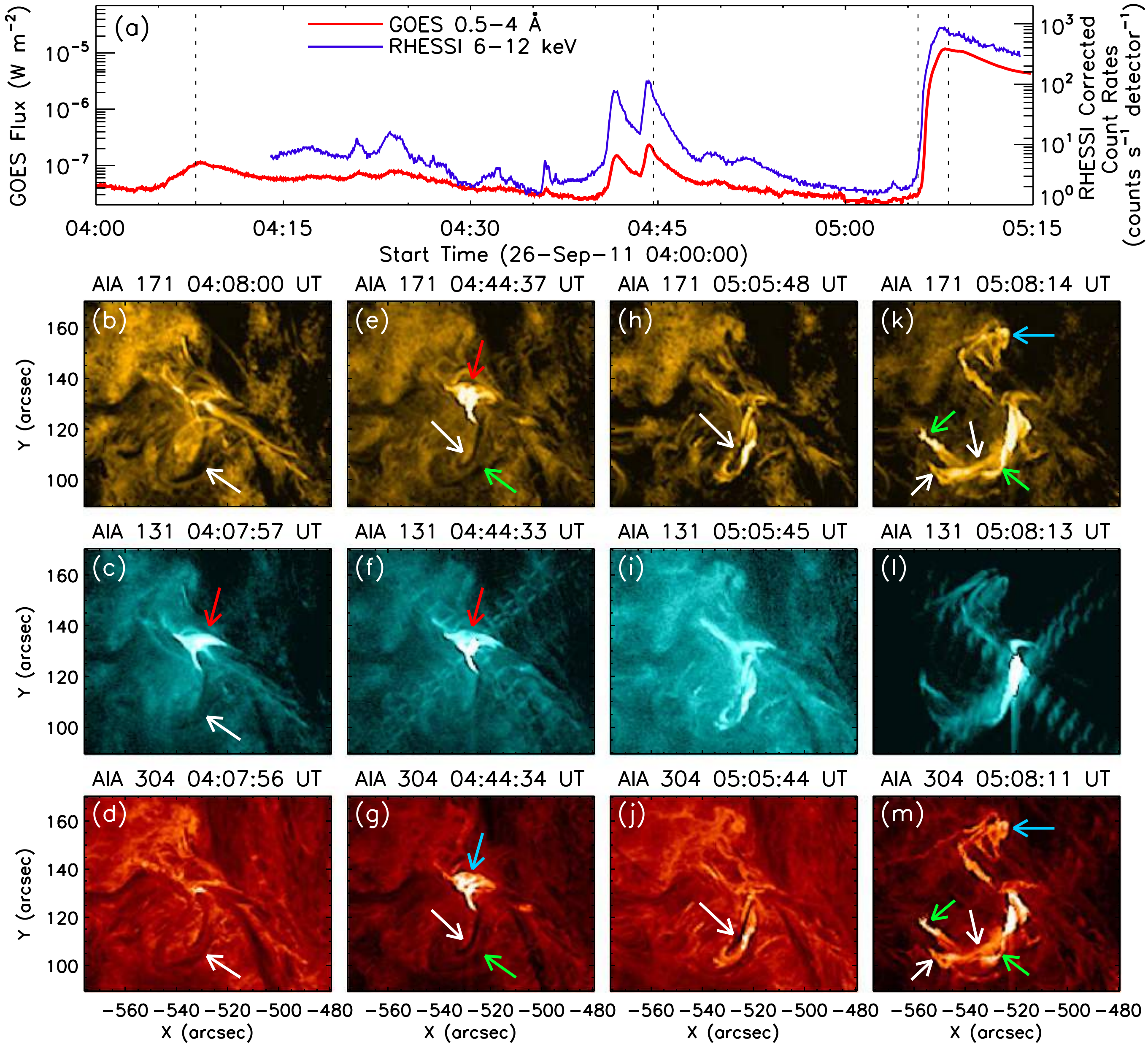

Figure 3. Panel (a): SXR flux in the GOES 0.5–4 Å (red curve) and RHESSI 6–12 keV (blue curve) channels. Panels (b)–(m): Multiwavelength evolution of the core active region in AIA 171 Å (panels (b), (e), (h), and (k)), 131 Å (panels (c), (f), (i), and (l)), and 304 Å (panels (d), (g), (j), and (m)). For comparison, four dashed lines are drawn in panel (a) corresponding to the time informations of the images of the four columns. The white and green arrows in different panels indicate filaments during different phases within the studied interval. The red arrows in different panels and the teal arrow in panel (g) indicate the location of preflare brightening. The teal arrows in panels (k) and (m) indicate a remote brightening observed during the peak phases of the flare. The FOVs of these panels are shown by the dotted boxes in Figures 2(d). An animation of the figure is available. The animation has a duration of 23 s and displays the temporal evolution of the active region in AIA 171, 131, and 304 Å wavelengths with 12 s cadence between 04:00 UT and 05:15 UT on 2011 September 26.

(An animation of this figure is available.)

restructuring of the magnetic configuration in the vicinity of the nullpoint as a result of nullpoint reconnection.

5.2. Failed Eruption of the Filament and Associated M4.0 Flare

After a prolonged period of repetitive events of small-scale coronal energy release, the main M4.0 flare was initiated at ≈05:06 UT. In Figure 6 we show a series of AIA 94 Å images of the core region displaying different phases of the main flare. The preflare filament was not prominently visible (indicated by the red arrow in Figure 6(a)) in the AIA 94 Å channel images. It samples high-temperature coronal plasma (≈6 MK), but during the onset of the highly impulsive rise phase of the flare, we observe narrow, stretched bright emission beneath the filament along its entire length (indicated by the black arrow in Figure 6(b)). During the impulsive phase, the activated filament went through an eruptive motion toward the projected eastern direction (see arrows in Figures 6(b)–(e)). We observed strong X-ray sources up to energy ≈50 keV from the location of the

Table 1
Summary of the Pre- to Postflare Evolution of active region NOAA 11302 on 2011 September 26

Sr. No.	Phase	Flux Peaks	Time (UT)	Remarks
1	Phase1 (04: 04UT—04: 39UT)	$P1_1$ $P1_2$ $P1_3$ $P1_4$ $P1_5$ $P1_6$	≈04: 08 ≈04: 17 ≈04: 21 ≈04: 24 ≈04: 32 ≈04: 36	Brightening in compact loop system associated with coronal nullpoint topology. RHESSI missed observation of $P1_1$ due to RHESSI night. Localized RHESSI sources within the energy range 3–25 keV from the location during subsequent SXR peaks.
2	Phase2 (04: 39UT—04: 53UT)	$P2_1$ $P2_2$ $P2_3$ $P2_4$	≈04: 41 ≈04: 44 ≈04: 49 ≈04: 52	Highly compact X-ray sources up to ≈25 keV energy from the location of the nullpoint. Eruption of small loop-like structures from the nullpoint configuration during $P2_1$ and $P2_2$.
3	Impulsive (05: 06UT—05: 08UT)			Activation and failed eruption of one filament. Development of intertwined double-decker flux rope system. X-ray sources up to energy ≈50 keV from the location of the activated filaments.
4	Gradual (05: 08UT—05: 13UT)			Brightening of a highly structured loop system. Intense EUV emission from flare ribbons and post-reconnection loop arcade. Multiple ribbon-like brightening from regions situated north of the core flaring location.

activated filament. Notably, the X-ray sources seem to coincide well with the initial location of the spatially elongated filament, which was most likely generated from the newly formed post-reconnection arcade (Figure 6(d)). During the gradual phase, the erupting filament interacted with a set of closed low-coronal loops lying above the core region, which most likely caused the eruption of the filament to cease, leading to a classification of the flare in the "failed eruptive" category. The gradual phase of the flare was characterized by intense emission from these closed low-coronal loops (indicated by the blue arrow in Figure 6(f)) as well as from the postflare arcade following the erupting filament (indicated by the black arrow in Figure 6(f)). A comparison of the AIA 94 Å image with the overplotted contours of the cotemporal HMI LOS magnetogram (Figure 6(f)) reveals that the overlying coronal loops connected the negative polarity regions of the central sunspot region to the dispersed positive-polarity region situated north of the central sunspot group.

In order to investigate the evolution in the low atmospheric layers of the Sun, we look at AIA 304 Å images (Figure 7), where we readily observe signatures of two quite prominent filaments that appeared to be separated spatially prior to the onset of the flare (indicated by the yellow arrows in Figure 7(a)). During the impulsive phase, as the filament displayed a brief period of eruption, we observed intense emission from the core of the active region (Figures 7(b)–(c)). During the peak phase of the flare, the two filaments appeared to become intertwined with each other, resembling a double-decker flux rope system. The two hot filaments of the double-decker system are indicated by the green and teal arrows in Figure 7(d). The double-decker structure shrank during the early gradual phase of the flare (indicated by the yellow arrows in Figure 7(e)), which was further followed by the formation of flare ribbons and postflare arcades (within the dashed green box in Figure 7(f)).

Interestingly, during the peak phase of the M4.0 flare (≈05:08 UT), we observed multiple ribbon-like brightening from regions situated north of the location of the filaments (indicated by the white arrows in Figure 7(d)). During the gradual phase, emission from the ribbon-like structures significantly intensified (see Figures 7(d), (e), (f)). Topological analysis was carried out to explore the physical connections of these remote brightenings with the flaring processes (Section 6.1).

6. Coronal Magnetic Field Modeling

6.1. Preflare Coronal Configuration and Postflare Arcade

In Figure 8 we plot NLFFF-extrapolated coronal field lines in the active region prior to the onset of the M4.0 flare and compare them with the coronal loops observed in EUV images. For convenience, we plot cotemporal LOS magnetogram and AIA 171 Å image of the active region in Figures 8(a) and (b), respectively. From the contours of the HMI LOS magnetogram plotted on top of the AIA 171 Å image (Figure 8(b)), it becomes clear that in addition to the flaring region, the active region was characterized by a set of large coronal loops that extended up to high coronal heights, which is indicated by the teal arrows. We further note the presence of a different filament within the active region that was not involved in the reported flaring activity. In Figure 8(b) we indicate the filament by a black arrow.

In Figure 8(c) we display a few sets of modeled coronal field lines in the overall AR. We find that the teal field lines correlate well with the coronal loops indicated by the teal arrows in Figure 8(b). In Figures 8(d)–(f) we focus on the NLFFF-extrapolated field lines within the flaring region alone, where we readily identify three flux ropes that are shown in bright yellow, pink, and light yellow. Interestingly, the flux rope shown in light yellow is precisely cospatial with the filament indicated by the black arrow in Figure 8(b), which is further demonstrated by the AIA 304 Å image in the background of Figure 8(d). Furthermore, the two flux ropes shown in bright yellow and pink constitute a double-decker flux rope configuration that is exactly cospatial with the two filaments that were involved in the M4.0 flare (Figures 3, 7).

Here we recall that, during the gradual phase of the flare, multiple ribbon-like brightenings situated north of the core region became very bright (indicated by the white arrow in Figure 7(f); Section 5.2). NLFFF-extrapolation results suggest that a set of field lines connect this region to the northern leg of the double-decker flux rope system; they are shown in green

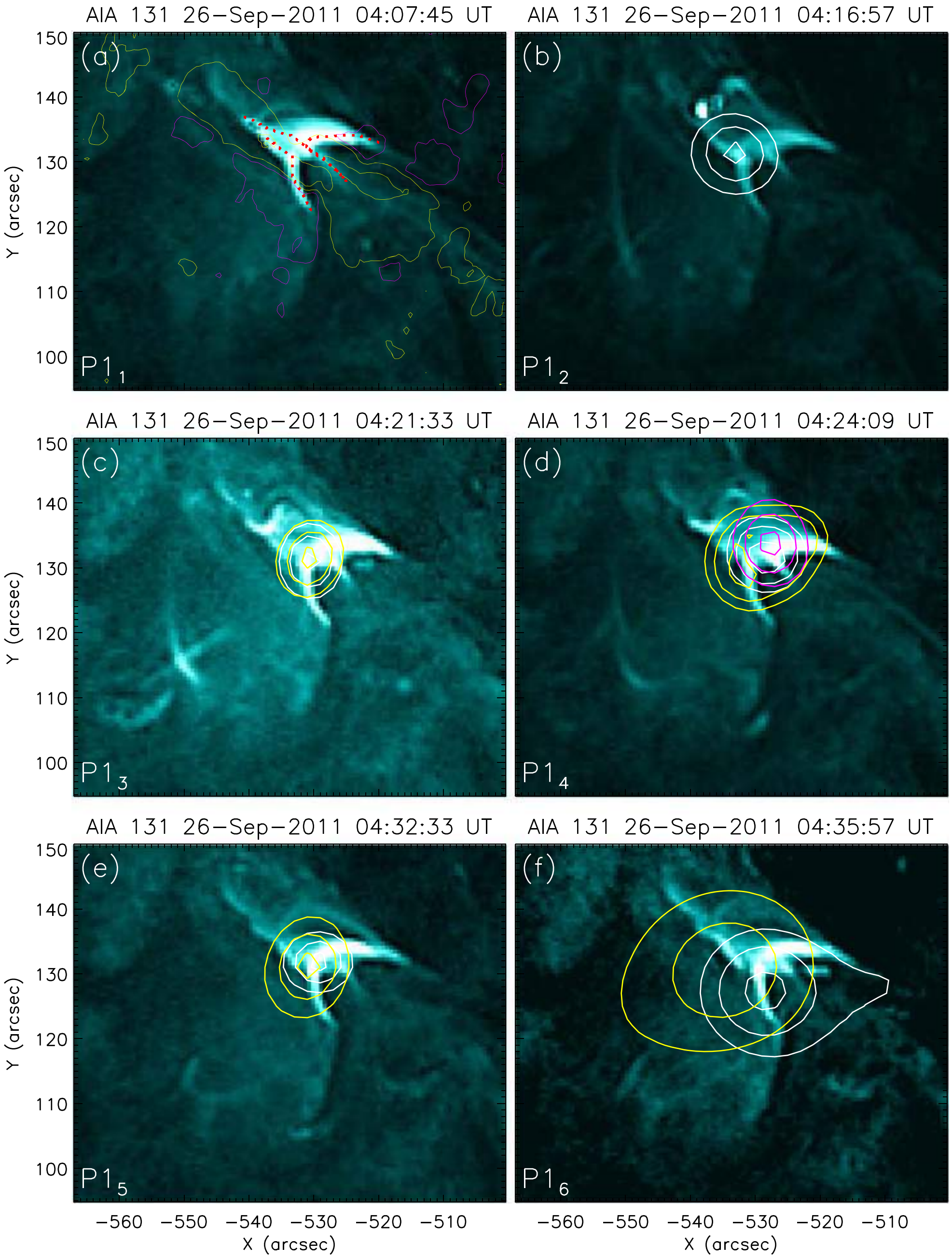

Figure 4. Evolution of Phase 1 in the AIA 131 Å channel. The dotted red curves in panel (a) indicate the coronal loops involved in the nullpoint topology during the different flux peaks of Phase 1 (i.e., $P1_1$–$P1_6$). Contours of a cotemporal HMI LOS Magnetograms are overplotted in panel (a). Contour levels are ±[400, 1400] G. Yellow and purple contours refer to positive and negative field, respectively. Cotemporal RHESSI contours of 3–6 keV (white), 6–12 keV (yellow), and 12–25 keV (pink) energy bands are plotted over panels (b)–(f). Contour levels are 55%, 75%, and 95% of the corresponding peak flux.

(Figures 8(d)–(f)). Notably, a few of the green lines, exactly above the northern leg of the flux rope shown in bright yellow, were characterized by high values of the squashing factor ($\log(Q) = 3$), which is represented by the teal patch in Figures 8(d)–(f). Furthermore, the footpoints of the green model coronal loops were characterized by high Q-values, which is evident from the background red patches representing $\log(Q) = 2$ in Figures 8(e)–(f). Notably, the coronal loops involved in the quadrupolar configuration are shown by the blue lines in Figures 8(c)–(e).

In Figure 9 we show the association of the double-decker flux ropes and the quadrupolar coronal configuration from different viewing angles. From the top and side views of the whole configuration, we readily understand that the quadrupolar configuration including the nullpoint (indicated by the green, orange, and black arrows in Figures 9(a)–(c), respectively) was only lying over the yellow flux rope. NLFFF-modeled field lines, complemented by AIA observations, clearly demonstrate that the nullpoint is situated above the central part of the yellow flux rope (see the green and red arrows indicating the nullpoint and the northern leg of the yellow flux rope, respectively, in Figure 9(a)). Furthermore, we could identify a different set of model field lines (shown in teal in Figure 9(d)) that manifest a structure similar to the dense

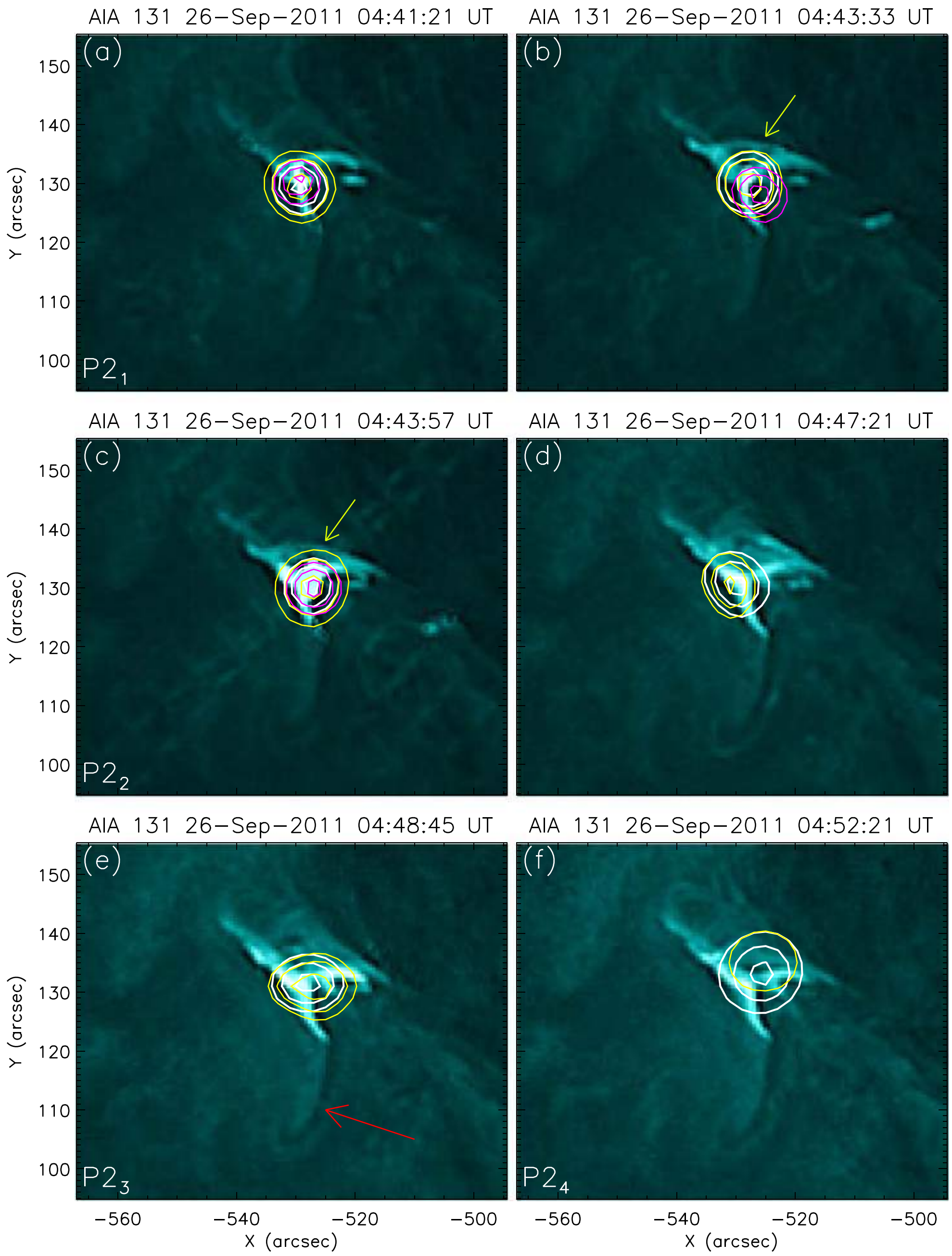

Figure 5. Evolution of Phase 2 in the AIA 131 Å channel. Panels (a), (c), (e), and (f) are during $P2_1$–$P2_4$ peaks, respectively. Contours of cotemporal RHESSI sources in 3–6 keV (white), 6–12 keV (yellow), and 12–25 keV (pink) energy bands are plotted in selected panels. Contour levels are 55%, 75%, and 95% of the corresponding peak flux. Yellow arrows in panels (b) and (c) indicate small- loop-like erupting structures. The red arrow in panel (e) indicates the filament that underwent activation during the M-class flare.

coronal arcade (indicated by the blue arrow in Figure 6(f)) that developed during the gradual phase of the flare. During the impulsive phase of the flare, the flux rope (shown in bright yellow) might have undergone eruptive motion toward the east, interacted with the teal lines, giving rise to the enhanced emission from the highly structured teal lines.

6.2. Decay Index and Twist Number

EUV observations revealed that the eruption of the filament was constrained within a short while after initiation, leading to a failed eruption. In order to investigate the coronal conditions responsible for the failed eruption, we calculated the magnetic decay index (n) within the extrapolation volume.

Theoretically, if a current ring of major radius R is embedded in an external magnetic field, then the ring experiences a radially outward hoop force because of its curvature. In stable conditions, this hoop force is balanced by the inwardly directed Lorentz force. If the Lorentz force due to the external field decreases faster with R than the hoop force, the system becomes unstable due to the torus instability (Bateman 1978). The decay rate of the external magnetic field is quantified by the magnetic decay index (n). Considering the fact that the

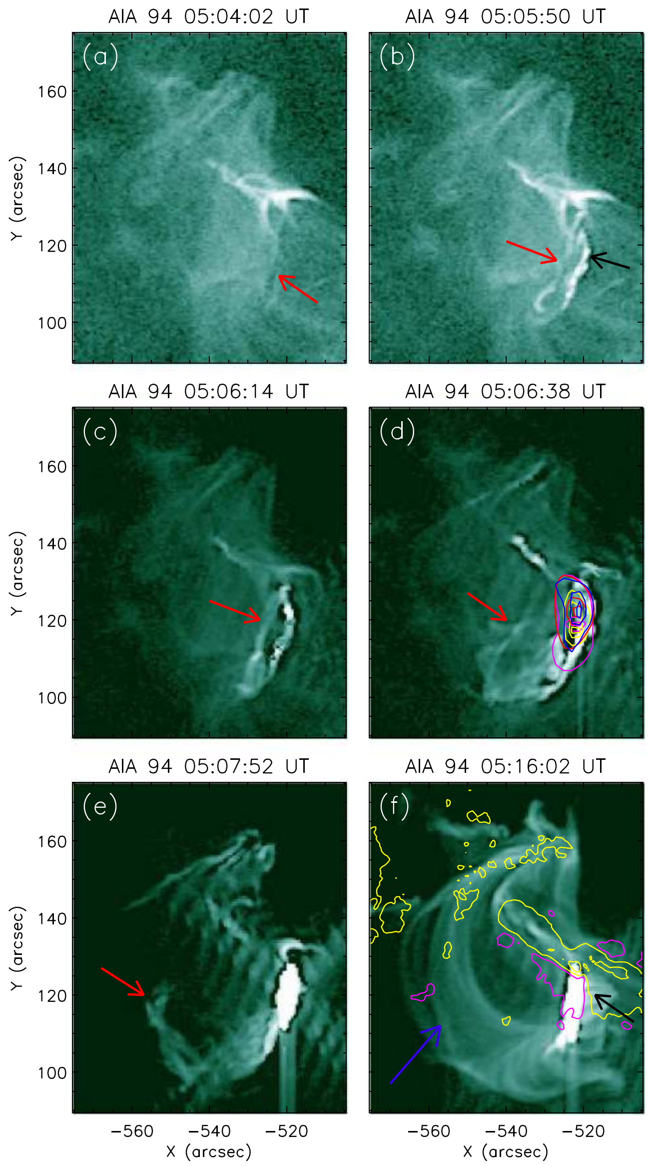

Figure 6. Series of AIA 94 Å images depicting the evolution of the M-class flare. The black arrow in panel (b) indicates the localized brightening that suggests the onset of the flare. The red arrows in panels (a)–(e) indicate the filament during different phases of its failed eruption. The black arrow in panel (f) indicates emission from the flare arcade. The blue arrow in panel (f) indicates highly structured coronal loops overlying the post-reconnection arcade. Contours of the HMI LOS magnetogram are overplotted in panel (f). Contour levels are ±(500, 1500) G. Yellow and pink contours refer to positive and negative flux, respectively. Contours of cotemporal RHESSI sources in 3–6 keV (pink), 6–12 keV (yellow), 12–25 keV (red), and 25–50 keV (blue) energy bands are plotted in selected panels. Contour levels are 50%, 80%, and 95% of the corresponding peak flux.

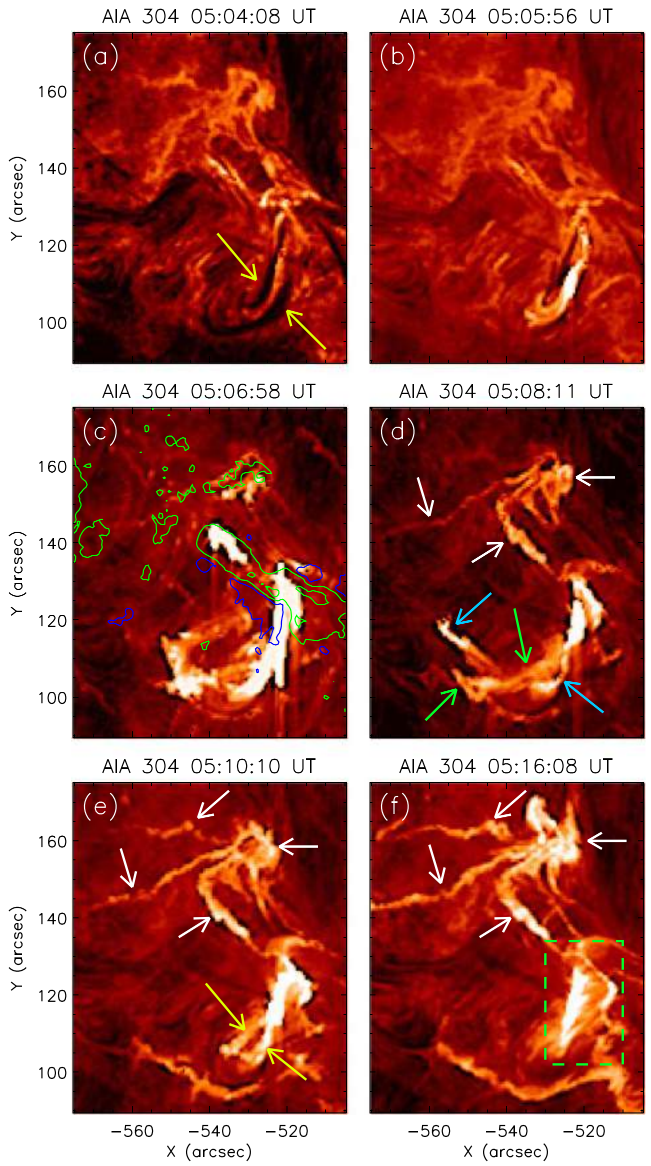

Figure 7. Series of AIA 304 Å images depicting the evolution of the M-class flare. The yellow arrows in panel (a) indicate the two filaments prior to the onset of the flare. The teal and green arrows in panel (d) indicate the two filaments during the peak phase of the flare. The yellow arrows in panel (e) indicate the two filaments after the failed eruption. The dashed green box in panel (f) outlines the core region during the gradual phase of the flare where intense emission from the flare ribbons and post-reconnection arcade can be identified. The white arrows in panels (d)–(f) indicate ribbon-like brightenings observed during the gradual phase of the flare. Contours of the HMI LOS magnetogram are overplotted in panel (c). Contour levels are ±(500, 1500) G. Green and blue contours refer to positive and negative flux, respectively.

toroidal component (directed along the axis of the flux rope) of the external magnetic field does not contribute to the strapping force (a nice visual depiction is provided in "Extended Data Figure 2" in Myers et al. 2015), in the ideal current-wire approach, the magnetic decay index is calculated as

$$n = -\frac{d\,\log(B_p)}{d\,\log(h)} \tag{2}$$

,where B_p is the external poloidal field (along the transverse direction of the flux rope axis), and h is the height.

However, in reality, flux ropes are observed to significantly differ from the simplified shape of a semicircular current wire (see, e.g., Démoulin & Aulanier 2010; Fan 2010; Olmedo & Zhang 2010). Therefore, in order to calculate the magnetic decay index, we manually determined the approximate 2D projection of the flux rope axis on the photosphere (shown by the red curve in Figure 8(a)). The 3D magnetic field vectors at each pixel on the vertical surface above the axis were then decomposed into two components: along the direction of the axis, i.e., the toroidal component, and perpendicular to the axis, i.e., the poloidal component. This perpendicular

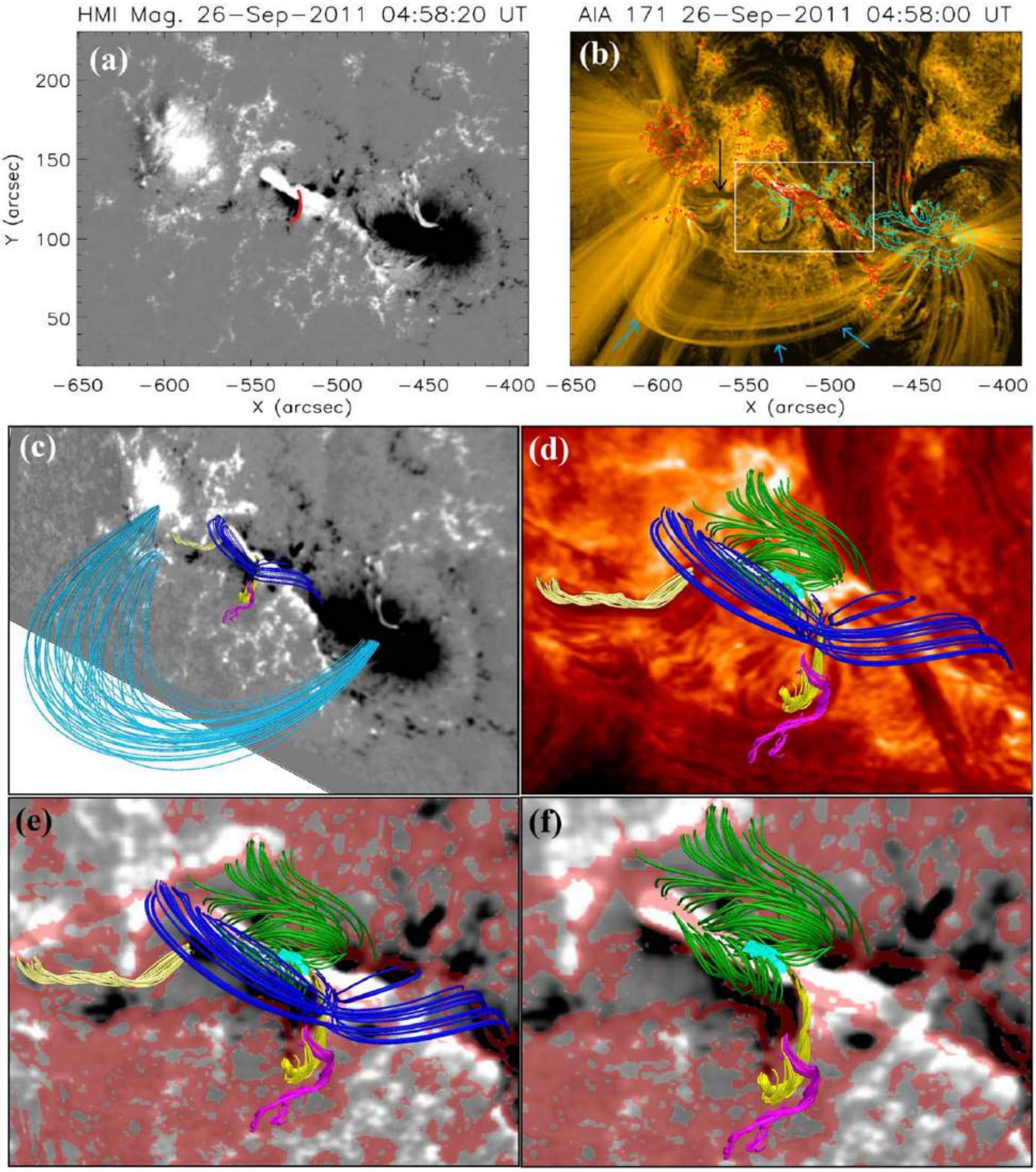

Figure 8. Panel (a): HMI LOS magnetogram of active region NOAA 11302. Panel (b): Cotemporal AIA 171 Å image. The flaring region is outlined by the white box. The teal arrows indicate a set of large, high-lying coronal loops above the flaring region. Contours of the LOS magnetograms are plotted over the AIA 171 Å image at levels of ±[500, 1000, 1500] G. Red and cyan contours refer to positive and negative polarities, respectively. Panel (c): NLFFF-extrapolated magnetic field lines showing the important coronal connectivities in the overall active region. In panels (d)–(f), we show only the model field lines in the flaring region. The bright yellow and pink lines represent two flux ropes. The northern part of the flux rope shown in bright yellow was enveloped by the blue lines. A set of field lines (shown in green) situated north of the flux rope shown in bright yellow was associated with a high squashing factor. The teal patch in panels (d)–(f) within the region of green lines is characterized by $\log(Q) = 3$. The light yellow lines in panels (d) and (e) represent another flux rope that was present in the active region, but did not take part in the flaring activity. In panel (f), we show the same model coronal loops except for the blue and light yellow lines to better visualize the green lines. The color template used in the background magnetograms is same as in Figure 2(b). The background of panel (d) is the AIA 304 Å image. The reddish patches over the background in panels (e)–(f) are characterized by $\log(Q) = 2$. The red curve in panel (a) approximately denotes the axis of the bright yellow flux rope, which is used for the magnetic decay index analysis shown in Figure 10.

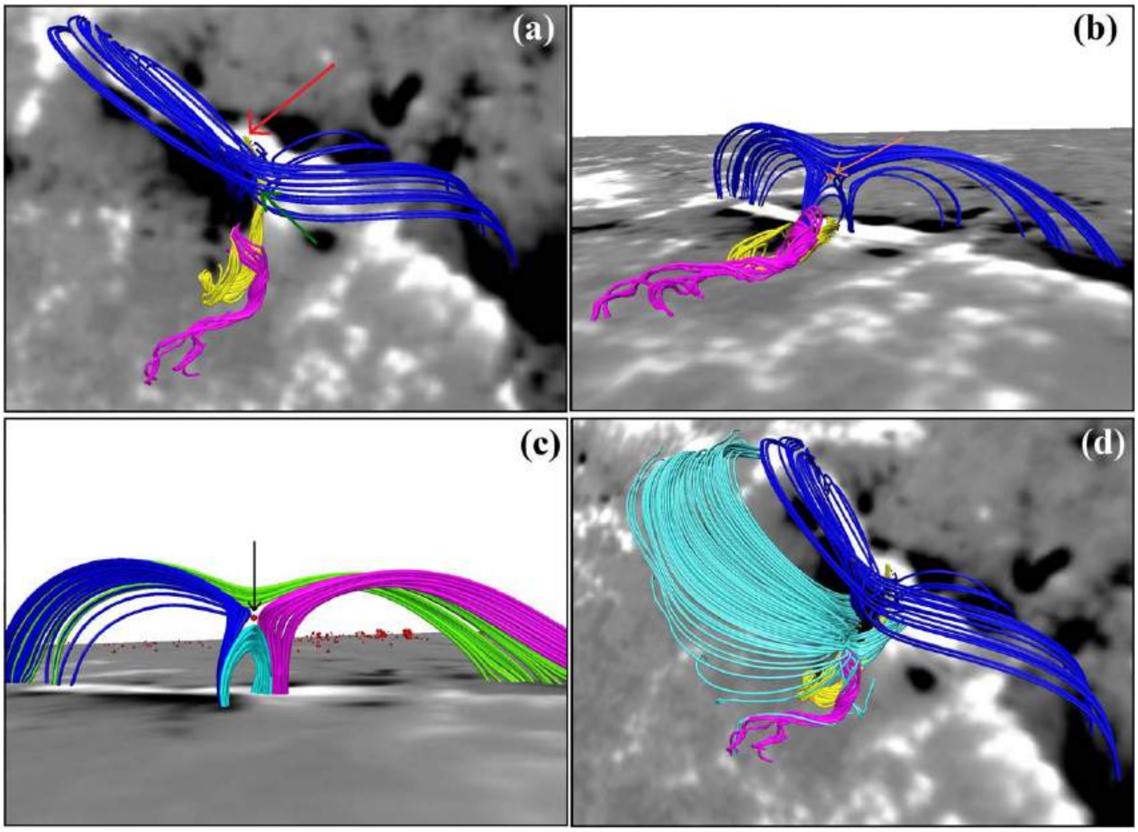

Figure 9. Modeled coronal configuration involved in the preflare activities and the M-class flare including the two flux ropes (shown in bright yellow and pink color) and the low-coronal closed loops connecting the multipolar photospheric configuration (shown in blue color). The northern leg of the yellow-colored flux rope is indicated by the red arrows in panels (a). The red-colored patch within the blue lines (also indicated by the orange arrow in panel (b)) is characterized by $\log(Q) = 8.5$ which represents a coronal nullpoint. The green arrow in panel (a) indicate the approximate location of the nullpoint. In panel (c), only the representative magnetic lines involved in the nullpoint configuration are shown. For a better representation, the four domains of magnetic field lines are shown in different colors. The black arrow indicates the nullpoint. The sky-colored lines in panel (d) represent the set of coronal loops that intensified during the gradual phase of the flare (indicated by the blue arrow in Figure 6(f)). The color template used in the background magnetograms is same as in Figure 2(b).

component was used in Equation (2) to compute the magnetic decay index.

From the distribution of the magnetic decay index above the flux rope axis (Figure 10), we find that within a very low height above the flux rope, we found an extended region of high magnetic decay index (depicted by the red patch in Figure 10(a)). This region was immediately enveloped by another region in which the decay index was as low as ≈ -3 (the region shown in blue in Figure 10(a)). Above this region, the value of the decay index slowly increased and again reached 1.5 at a quite high coronal layer (indicated by the yellow curve in the top portion of Figure 10(a)). In Figure 10(b) we plot the variation in decay index averaged over the axis of the double-decker filament with height, where we find that the average value of decay index in the high corona reached values of 1.0 and 1.5 at heights of $\approx$43 Mm and $\approx$64 Mm, respectively.

In order to investigate the applicability of the kink instability as the triggering mechanism of the flux ropes, we calculated the twist number within the extrapolation volume using the IDL-based code developed by Liu et al. (2016). The twist number (T_w; Berger & Prior 2006) associated with a flux rope is defined as

$$\tau_w = \int_L \frac{(\nabla \times \boldsymbol{B}) \cdot \boldsymbol{B}}{4\pi B^2} dl, \tag{3}$$

where L denotes the length of the flux rope. Our calculations suggest that the two flux ropes in the double-decker flux rope system were associated with a positive twist. The average value of the twist number associated with the flux rope shown in bright yellow was found to be $\approx$1.5, while the twist number associated with the flux rope shown in pink was found to be $\approx$1.7. A statistical survey conducted by Duan et al. (2019) revealed the critical value of $|\tau_w|$ for kink instability to be 2, which suggests that the kink instability was not responsible for the activation of the filament during the onset of the M4.0 flares.

7. Discussion

In this paper, we have investigated the triggering and subsequent failed eruption of a small filament from active region NOAA 11302. The morphology of the active region was highly interesting as three prominent and distinct sunspot groups in this active region were distributed in an almost linear manner. While the central sunspot group was the smallest of the three, it was the only bipolar sunspot group containing δ spots. Notably, the reported flare occurred from the central sunspot group.

While one filament underwent a failed eruption, EUV images of the flaring region prior to the onset of the M4.0 flare

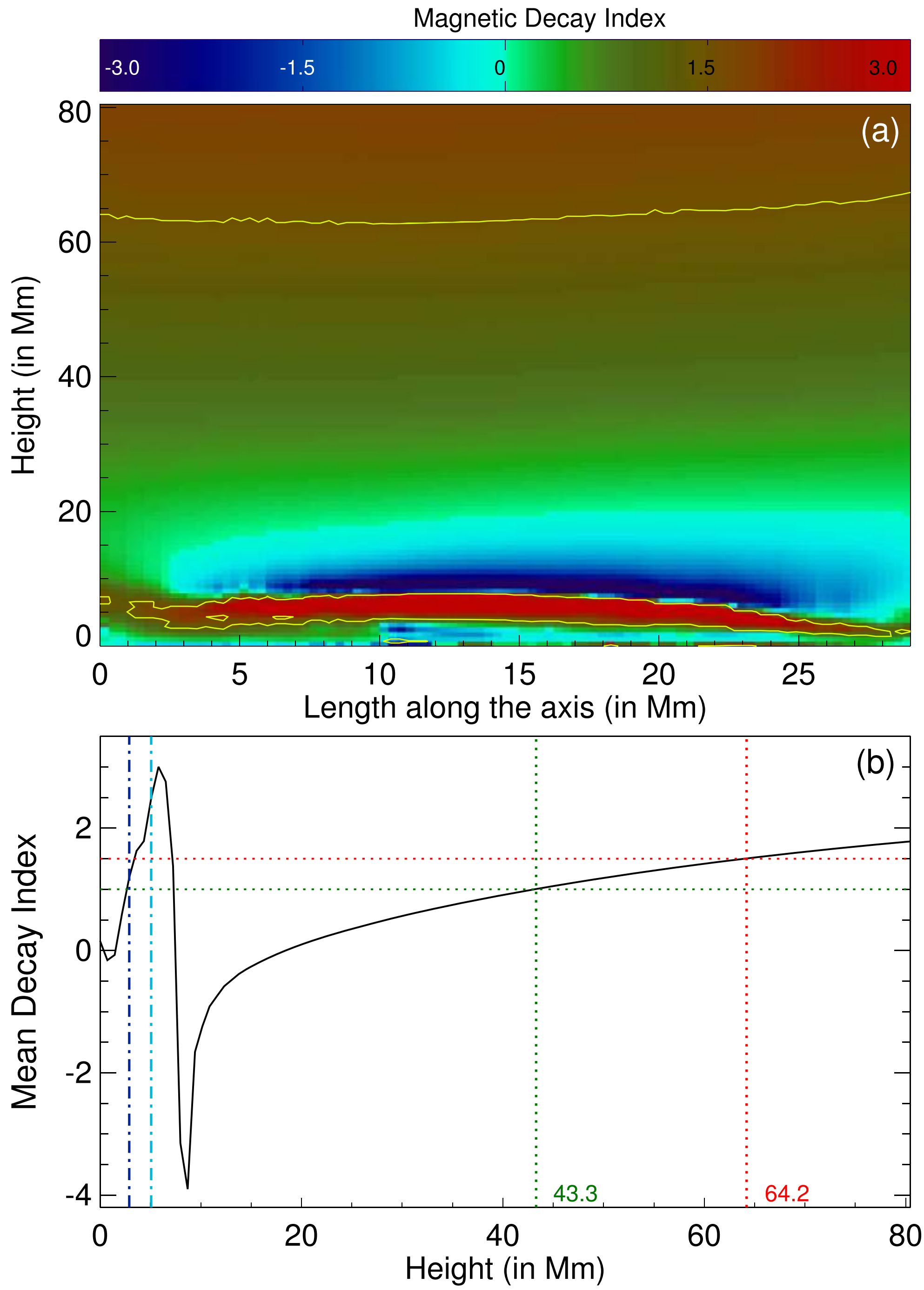

Figure 10. Panel (a): Distribution of magnetic decay index with height along the vertical surface above the axis of the yellow flux rope (indicated by the red curve in Figure 8(a)). The yellow curves refer to $n = 1.5$. The variation in decay index with height, averaged over the flux rope axis, is shown in panel (b). The dotted green and red lines indicate the critical heights corresponding to $n = 1.0$ and $n = 1.5$, respectively. The dash-dotted blue and teal lines indicate the maximum heights of the yellow and pink flux ropes, respectively (see Figure 9).

clearly revealed signatures of two distinct filaments (Figures 3, 7(a)). During the impulsive phase of the flare, both filaments were activated, extended spatially, and developed into a complex structure in which both filaments were intertwined with each other (Figures 3(k)–(m), 7(d)). NLFFF extrapolation results suggest the presence of two flux ropes in the flaring region in a double-decker flux rope configuration. The contemporary concept of the double-decker flux rope system was first reported by Liu et al. (2012), and only a handful of articles have reported such complex structures since then (e.g., Cheng et al. 2014; Kliem et al. 2014; Dhakal et al. 2018; Tian et al. 2018; Wang et al. 2018; Awasthi et al. 2019; Zheng et al. 2019; Mitra et al. 2020b; Mitra & Joshi 2021). Despite the small number of reportings, double-decker flux rope systems can be mostly divided into two categories. While most of the reported double-decker flux rope systems were identified as two vertically well separated filaments, one of them undergoing eruption (e.g., Liu et al. 2012; Dhakal et al. 2018; Tian et al. 2018; Awasthi et al. 2019; Zheng et al. 2019), the second category comprises complex preflare sigmoidal structures involving intertwined flux ropes (Cheng et al. 2014; Mitra et al. 2020b; Mitra & Joshi 2021). In the first category, triggering and eruption of flux ropes are generally caused by photospheric activity, i.e., shearing and/or rotating motion. However, in this case, the activation of one flux rope in the double-decker system may or may not influence the stability of the other flux rope (see, e.g., Liu et al. 2012). On the other hand, in the case of intertwined flux ropes, interaction between the two flux ropes mostly causes an activation and eruption of the system. The two filaments reported in this article were spatially well separated during the preflare phase. During the impulsive phase, they extended longitudinally and became intertwined with each other. Furthermore, the onset of the flare in this case followed clear preflare activities that occurred at a separate location from the filaments, which was identified both in the SXR flux evolution and in the AIA EUV images. In view of this, the double-decker system reported in this study seems to have characteristics of both the categories of double-decker systems discussed above. This complex and intriguing behavior of magnetic flux ropes challenges our general understanding of solar magnetic fields and their evolution during transient activities.

The SXR flux evolution prior to the onset of the M-class flare revealed multiple episodes of flux enhancements (Figure 1). Comparison of SXR light curves with EUV images of the active region suggested that these preflare flux enhancements are associated with a localized brightening that originated above the northern end of the filaments. The photospheric magnetic field of the region manifested a complex distribution of magnetic polarities involving δ spots (i.e., the central sunspot group; see Figure 2). The NLFFF extrapolation revealed a multiflux topology in the flaring region that forms a quadrupolar configuration with a coronal nullpoint (Figures 2(e), 9). This preflare coronal configuration is in agreement with the scenario prescribed in the breakout model of solar eruptions (Antiochos et al. 1999; Karpen et al. 2012). According to this model, the small-scale preflare reconnections at the nullpoint will remove the overlying (constraining) magnetic flux by transferring it to the side-lobe field lines (see Figure 1 in Karpen et al. 2012). In view of this, the observed preflare episodic brightening of the coronal loops associated with the nullpoint is well consistent with the initiation process of the eruptive flux ropes invoked in the breakout model. We note intense and structured emission during the preflare phase (see Figure 5) that continued until the earliest development of the M-class flare (Figure 6(a)). This structured emission can be readily perceived as the brightening of multiple low-lying loops of the quadrupolar configuration in and around the coronal nullpoint, providing credence to our proposed scenario of preflare energy release by nullpoint reconnection.

Notably, the location of the nullpoint above the filament by identifying the region of highest value of the degree of squashing factor (Q) within the extrapolation volume. Nullpoints are essentially singular points in the corona in which all the components of the magnetic field vanish (Aschwanden 2005). Theoretically, a nullpoint can be characterized by $Q \to \infty$ as it works as a separator between different topological domains of the magnetic field (see, e.g., Longcope & Klapper 2002). However, numerical techniques used to calculate Q-values will always return finite values, thus we can expect a coronal nullpoint to be associated with high-degree Q-values (Pariat & Démoulin 2012). In a number of studies concerning coronal nullpoints and their evolution, the coronal nullpoints were found to be associated with a wide range of Q-values ($\sim 10^4$–10^{12}; see Yang et al. 2015; Liu et al. 2020; Qiu et al. 2020; Prasad et al. 2020). In the present study, we observed the nullpoint to be associated with a value of $Q \approx 10^{8.5}$. Regions with smaller Q are identified as quasi-separatrix layers (QSL; Aulanier et al. 2006). Here we recall that during the gradual phase of the M4.0 flare, multiple ribbon-like brightenings were observed from locations north of the flaring region (Figures 7(d)–(f)). The NLFFF extrapolation results revealed the presence of a set of coronal loops that connect the remote region with the region situated at the northern footpoint of the flux rope (shown by the green lines in Figures 8(d)–(f)). Calculation of Q has further revealed that the green lines are associated with strong Q-values (Figures 8(d)–(f)). These findings demonstrate that the remote brightening during the peak phase of the main flare is an observational manifestation of slip-running reconnection influenced by the QSLs.

The most important aspect of this study is the investigation of the failed eruption of the flux ropes. Analysis of the magnetic decay index (n) suggests the presence of an extended region just above the flux ropes characterized by $n > 1.5$ (Figure 10), which suggests that the flux ropes were subject to torus instability. The topological configuration of the active region corona in our event presented a special scenario in which a coronal nullpoint existed in the core region and the region of torus instability resided immediately below the nullpoint (Figure 9(c)). High decay of magnetic field is expected below a nullpoint, which in turn increases the value of the decay index. However, the coronal region within the height range $\approx$7–20 Mm above the flux ropes (Figure 10(c)) is of particular interest in view of the negative magnetic decay index within this height range. Notably, the variation of average decay index with height presents a so-called saddle-like profile where a local maximum of n in lower height is followed by a local minimum of n at relatively larger height (Wang et al. 2017). Such a saddle-like profile of the decay index produces a favorable condition for a failed eruption of flux ropes because the toroidal strapping force (responsible for constraining the erupting magnetic structure) increases in height after an initial decrease (see, e.g., Wang et al. 2017; Filippov 2020b). However, a number of studies have reported successful eruption of flux ropes even though the coronal decay index profile was saddle-like (e.g., Cheng et al. 2011; Wang et al. 2017; Filippov 2020a), suggesting the involvement of other factors toward the successful eruption. Among the number of parameters such as the Lorentz force and the nonpotentiality of the source region, the value of decay index at the saddle bottom is believed to be important in determining the eruption profile of flux ropes (Liu et al. 2018). Inoue et al. (2018) investigated a successful flux rope eruption through a saddle-like decay index profile by numerical simulation and found that the feedback relation between the eruption of the flux rope and reconnection rate beneath it enabled the flux rope to pass through the torus-stable zone. The event reported here is a good example of a failed eruption due to a saddle-like decay index profile of the corona above the flux rope. This event is special through the negative decay index region above the torus-unstable zone within a low height ($\lesssim$20 Mm; Figures 10(c), (e)), which is rarely observed (see Filippov 2020a). The negative value of the magnetic decay index not only decelerated the eruption of the flux rope, but also repelled it downward.

In the present study, we analyze and interpret an intriguing case of the failed eruption of a torus-unstable, complex double-decker flux rope system. We show that the continuation of a flux rope eruption against the overlying coronal fields is essentially controlled by the extended decay index profile characterizing the strength of the strapping field through the larger coronal heights above the flux rope axis. Investigations of the failed eruptions of torus-unstable flux ropes have emerged as one of the most crucial topics in the contemporary solar physics because of their importance in the space-weather prediction. In this context, in addition to the classical torus instability, some additional factors have been assessed to understand the cause of the failed eruption, which are worth discussing (Myers et al. 2015; Zhong et al. 2021). Based on the results of laboratory experiments, Myers et al. (2015) found that the failed eruption can also occur when the guide magnetic field, i.e., the toroidal field (the ambient field that runs along the flux rope) is strong enough to prevent the flux rope from kinking. Under these conditions, the guide field interacts with electric currents in the flux rope to produce a dynamic toroidal field tension force that halts the eruption. The study by Zhong et al. (2021) presents a data-driven MHD simulation for a confined eruption. They showed a Lorentz force component, resulting from the radial magnetic field or the nonaxisymmetry of the flux rope, which can essentially constrain the eruption. In the light of the above studies and our work, we understand that the ultimate fate of solar eruptions is determined by a complex interplay of coronal magnetic fields involving the magnetic flux rope and the core and envelope fields. To this end, we plan to carry out a series of subsequent studies of failed eruptions of torus-unstable flux ropes in order to reach further understanding of the mechanism(s) of successful or failed solar eruptions.

We would like to thank the SDO and RHESSI teams for their open-data policy. SDO is NASA's mission under the Living With a Star (LWS) program. RHESSI was the sixth mission in the SMall EXplorer (SMEX) program of NASA. This work uses GONG data from NSO, which is operated by AURA under a cooperative agreement with NSF and with additional financial support from NOAA, NASA, and USAF. A.M.V. and P.K.M. acknowledge the Austrian Science Fund (FWF) project no. I4555. T.W. acknowledges the DLR grant 50 OC 2101 and DFG grant WI 3211/5-1. We are thankful to the referee for providing important comments that helped us improve the overall content of the paper.

Appendix
Calculation of the Twist Number

For a smooth, non-self-intersecting curve $\boldsymbol{x}(s)$ parameterized by arclength s and a second such curve $\boldsymbol{y}(s)$ surrounding $\boldsymbol{x}$, jointly defining a ribbon, the twist number τ_g is given by (Equation (12) in Berger & Prior 2006)

$$\tau_g = \frac{1}{2\pi}\int_{\boldsymbol{x}} \hat{\boldsymbol{T}}(s)\cdot\hat{\boldsymbol{V}}(s)\times\frac{d\hat{\boldsymbol{V}}(s)}{ds}ds\,, \tag{A1}$$

where $\hat{\boldsymbol{T}}(s)$ represent the unit tangent vector to $\boldsymbol{x}(s)$ and $\hat{\boldsymbol{V}}(s)$ denotes the unit vector normal to $\boldsymbol{x}(s)$. Here, any point on $\boldsymbol{y}(s)$ is related to $\boldsymbol{x}(s)$ by

$$\boldsymbol{y}(t) = \boldsymbol{x}(t) + \epsilon\boldsymbol{V}(t)\,. \tag{A2}$$

In the context of the present analysis, $\hat{\boldsymbol{T}} = \hat{\boldsymbol{B}} = \frac{\boldsymbol{B}}{|\boldsymbol{B}|}$, and $\boldsymbol{J} = \frac{1}{\mu_0}\vec{\nabla}\times\boldsymbol{B}$. A detailed calculation conducted by Liu et al. (2016) reveals

$$\frac{d\tau_g}{ds} \simeq \frac{\mu_0 J_{||}}{4\pi|\boldsymbol{B}|} + \frac{c}{2\pi|\boldsymbol{B}|} \tag{A3}$$

$$\Rightarrow \tau_g = \int_x \frac{\mu_0 J_{||}}{4\pi|\boldsymbol{B}|}ds + \int_x \frac{c}{2\pi|\boldsymbol{B}|}ds\,, \tag{A4}$$

where $J_{||} = \frac{\boldsymbol{J}\cdot\boldsymbol{B}}{|\boldsymbol{B}|}$, and c is a constant dependent on $\hat{\boldsymbol{V}}$ and on the spatial variation of $\boldsymbol{B}$. The first term in the right-hand side approaches τ_w close to the axis of the flux rope, i.e.,

$$\lim_{\epsilon\to 0}\tau_w(\epsilon) = \tau_g - \int_x \frac{c}{2\pi|\boldsymbol{B}|}ds\,. \tag{A5}$$

From Equation (A5), it becomes clear that τ_w provides an underestimation of the true twist number of flux ropes. However, calculation of τ_g requires including the exact geometry of the flux rope. Finding the exact geometry of a flux rope from the extrapolated magnetic field is practically not possible. Considering the flux rope to have approximated uniform twist, i.e., a uniform α-flux rope (Lundquist 1950), $c \approx 0$, i.e., $\tau_w \approx \tau_g$ (Liu et al. 2016).

ORCID iDs

Prabir K. Mitra https://orcid.org/0000-0002-0341-7886
Bhuwan Joshi https://orcid.org/0000-0001-5042-2170
Astrid M. Veronig https://orcid.org/0000-0003-2073-002X
Thomas Wiegelmann https://orcid.org/0000-0001-6238-0721

References

Alexander, D., Liu, R., & Gilbert, H. R. 2006, ApJ, 653, 719
Amari, T., Canou, A., Aly, J.-J., Delyon, F., & Alauzet, F. 2018, Natur, 554, 211
Antiochos, S. K., Dahlburg, R. B., & Klimchuk, J. A. 1994, ApJL, 420, L41
Antiochos, S. K., DeVore, C. R., & Klimchuk, J. A. 1999, ApJ, 510, 485
Archontis, V., & Hood, A. W. 2008, ApJL, 674, L113
Aschwanden, M. J. 2005, Physics of the Solar Corona. An Introduction with Problems and Solutions (2nd edn.; Berlin: Springer)
Aulanier, G., Démoulin, P., Schrijver, C. J., et al. 2013, A&A, 549, A66
Aulanier, G., Janvier, M., & Schmieder, B. 2012, A&A, 543, A110
Aulanier, G., Pariat, E., & Démoulin, P. 2005, A&A, 444, 961
Aulanier, G., Pariat, E., Démoulin, P., & DeVore, C. R. 2006, SoPh, 238, 347
Aulanier, G., Török, T., Démoulin, P., & DeLuca, E. E. 2010, ApJ, 708, 314
Awasthi, A. K., Liu, R., & Wang, Y. 2019, ApJ, 872, 109
Bateman, G. 1978, MHD Instabilities (Cambridge, MA: MIT Press)
Baumgartner, C., Thalmann, J. K., & Veronig, A. M. 2018, ApJ, 853, 105
Benz, A. O. 2017, LRSP, 14, 2
Berger, M. A., & Prior, C. 2006, JPhA, 39, 8321
Carmichael, H. 1964, NASSP, 50, 451
Chatterjee, P., & Fan, Y. 2013, ApJL, 778, L8
Chen, P. F. 2011, LRSP, 8, 1
Cheng, X., Ding, M. D., Zhang, J., et al. 2014, ApJ, 789, 93
Cheng, X., Zhang, J., Ding, M. D., Guo, Y., & Su, J. T. 2011, ApJ, 732, 87
Cheng, X., Zhang, J., Ding, M. D., Liu, Y., & Poomvises, W. 2013, ApJ, 763, 43
Clyne, J., Mininni, P., Norton, A., & Rast, M. 2007, NJPh, 9, 301
Démoulin, P., & Aulanier, G. 2010, ApJ, 718, 1388
Demoulin, P., Henoux, J. C., Priest, E. R., & Mandrini, C. H. 1996, A&A, 308, 643
DeRosa, M. L., Wheatland, M. S., Leka, K. D., et al. 2015, ApJ, 811, 107
Dhakal, S. K., Chintzoglou, G., & Zhang, J. 2018, ApJ, 860, 35
Duan, A., Jiang, C., He, W., et al. 2019, ApJ, 884, 73
Fan, Y. 2010, ApJ, 719, 728
Filippov, B. 2020a, MNRAS, 494, 2166
Filippov, B. P. 2020b, ARep, 64, 272
Fletcher, L., Dennis, B. R., Hudson, H. S., et al. 2011, SSRv, 159, 19
Gibson, S. 2015, in Solar Prominences, Astrophysics and Space Science Library, ed. J.-C. Vial & O. Engvold, 415 (Cham: Springer), 323
Gibson, S. E. 2018, LRSP, 15, 7
Gibson, S. E., & Fan, Y. 2006, JGRA, 111, A12103

Gilbert, H. R., Alexander, D., & Liu, R. 2007, SoPh, 245, 287
Gou, T., Liu, R., Kliem, B., Wang, Y., & Veronig, A. M. 2019, SciA, 5, 7004
Green, L. M., Török, T., Vršnak, B., Manchester, W., & Veronig, A. 2018, SSRv, 214, 46
Harvey, J. W., Bolding, J., Clark, R., et al. 2011, AAS/Solar Physics Division Abstracts, AAS/Solar Physics Division Meeting, 42, 17.45
Harvey, J. W., Hill, F., Hubbard, R. P., et al. 1996, Sci, 272, 1284
Haynes, A. L., & Parnell, C. E. 2007, PhPl, 14, 082107
Hernandez-Perez, A., Su, Y., Veronig, A. M., et al. 2019, ApJ, 874, 122
Hirayama, T. 1974, SoPh, 34, 323
Inoue, S., Kusano, K., Büchner, J., & Skála, J. 2018, NatCo, 9, 174
Janvier, M., Aulanier, G., Pariat, E., & Démoulin, P. 2013, A&A, 555, A77
Ji, H., Wang, H., Schmahl, E. J., Moon, Y. J., & Jiang, Y. 2003, ApJL, 595, L135
Joshi, B., Ibrahim, M. S., Shanmugaraju, A., & Chakrabarty, D. 2018, SoPh, 293, 107
Joshi, B., Kushwaha, U., Veronig, A. M., et al. 2017, ApJ, 834, 42
Joshi, N. C., Zhu, X., Schmieder, B., et al. 2019, ApJ, 871, 165
Karpen, J. T., Antiochos, S. K., & DeVore, C. R. 2012, ApJ, 760, 81
Kharayat, H., Joshi, B., Mitra, P. K., Manoharan, P. K., & Monstein, C. 2021, SoPh, 296, 99
Kliem, B., Su, Y. N., van Ballegooijen, A. A., & DeLuca, E. E. 2013, ApJ, 779, 129
Kliem, B., & Török, T. 2006, PhRvL, 96, 255002
Kliem, B., Török, T., Titov, V. S., et al. 2014, ApJ, 792, 107
Kopp, R. A., & Pneuman, G. W. 1976, SoPh, 50, 85
Koskinen, H. E. J., Baker, D. N., Balogh, A., et al. 2017, SSRv, 212, 1137
Kushwaha, U., Joshi, B., Cho, K.-S., et al. 2014, ApJ, 791, 23
Kushwaha, U., Joshi, B., Veronig, A. M., & Moon, Y.-J. 2015, ApJ, 807, 101
Lanzerotti, L. J. 2017, SSRv, 212, 1253
Lemen, J. R., Title, A. M., Akin, D. J., et al. 2012, SoPh, 275, 17
Li, T., Hou, Y., Yang, S., et al. 2020, ApJ, 900, 128
Lin, R. P., Dennis, B. R., Hurford, G. J., et al. 2002, SoPh, 210, 3
Liu, C., Prasad, A., Lee, J., & Wang, H. 2020, ApJ, 899, 34
Liu, L., Wang, Y., Zhou, Z., et al. 2018, ApJ, 858, 121
Liu, R., Kliem, B., Titov, V. S., et al. 2016, ApJ, 818, 148
Liu, R., Kliem, B., Török, T., et al. 2012, ApJ, 756, 59
Liu, Y. 2008, ApJL, 679, L151
Liu, Y., Su, J., Xu, Z., et al. 2009, ApJL, 696, L70
Longcope, D. W., & Klapper, I. 2002, ApJ, 579, 468
Lundquist, S. 1950, Arkiv for Fysik, B2, 361, https://ci.nii.ac.jp/naid/10007639617/en/
Manoharan, P. K., van Driel-Gesztelyi, L., Pick, M., & Demoulin, P. 1996, ApJL, 468, L73
Martin, S. F. 1998, SoPh, 182, 107
Masuda, S., Kosugi, T., Hara, H., Tsuneta, S., & Ogawara, Y. 1994, Natur, 371, 495
Metcalf, T. R., Hudson, H. S., Kosugi, T., Puetter, R. C., & Pina, R. K. 1996, ApJ, 466, 585
Miklenic, C. H., Veronig, A. M., Vršnak, B., & Hanslmeier, A. 2007, A&A, 461, 697
Mitra, P. K., & Joshi, B. 2019, ApJ, 884, 46
Mitra, P. K., & Joshi, B. 2021, MNRAS, 503, 1017
Mitra, P. K., Joshi, B., & Prasad, A. 2020a, SoPh, 295, 29
Mitra, P. K., Joshi, B., Prasad, A., Veronig, A. M., & Bhattacharyya, R. 2018, ApJ, 869, 69
Mitra, P. K., Joshi, B., Veronig, A. M., et al. 2020b, ApJ, 900, 23
Moldwin, M. 2008, An Introduction to Space Weather (Cambridge: Cambridge Univ. Press)
Moore, R. L., & Roumeliotis, G. 1992, in in Lecture Notes in Physics, Vol. 399, IAU Colloq. 133: Eruptive Solar Flares, ed. Z. Svestka, B. V. Jackson, & M. E. Machado (Berlin: Springer), 69
Moore, R. L., Sterling, A. C., Hudson, H. S., & Lemen, J. R. 2001, ApJ, 552, 833
Myers, C. E., Yamada, M., Ji, H., et al. 2015, Natur, 528, 526
Nakajima, H., Nishio, M., Enome, S., et al. 1994, IEEE Proc., 82, 705
Nindos, A., Patsourakos, S., Vourlidas, A., & Tagikas, C. 2015, ApJ, 808, 117
Olmedo, O., & Zhang, J. 2010, ApJ, 718, 433
Pariat, E., & Démoulin, P. 2012, A&A, 541, A78
Patsourakos, S., Vourlidas, A., Török, T., et al. 2020, SSRv, 216, 131
Pesnell, W. D., Thompson, B. J., & Chamberlin, P. C. 2012, SoPh, 275, 3
Prasad, A., Dissauer, K., Hu, Q., et al. 2020, ApJ, 903, 129
Priest, E. 2014, Magnetohydrodynamics of the Sun (Cambridge: Cambridge Univ. Press)
Priest, E. R., & Démoulin, P. 1995, JGR, 100, 23443
Priest, E. R., & Forbes, T. G. 2002, A&ARv, 10, 313
Qiu, Y., Guo, Y., Ding, M., & Zhong, Z. 2020, ApJ, 901, 13
Rust, D. M., & Kumar, A. 1996, ApJL, 464, L199
Sahu, S., Joshi, B., Mitra, P. K., Veronig, A. M., & Yurchyshyn, V. 2020, ApJ, 897, 157
Sarkar, R., & Srivastava, N. 2018, SoPh, 293, 16
Schou, J., Scherrer, P. H., Bush, R. I., et al. 2012, SoPh, 275, 229
Sturrock, P. A. 1966, Natur, 211, 695
Sui, L., Holman, G. D., & Dennis, B. R. 2006, ApJ, 646, 605
Švestka, Z., & Cliver, E. W. 1992, in Eruptive Solar Flares, ed. Z. Švestka, B. V. Jackson, & M. E. Machado (Berlin: Springer), 1
Takano, T., Nakajima, H., Enome, S., et al. 1997, in Proc. CESRA Workshop 483, Coronal Physics from Radio and Space Observations, ed. G. Trottet (Cham: Springer), 183
Tian, Z., Shen, Y., & Liu, Y. 2018, NewA, 65, 7
Titov, V. S., Hornig, G., & Démoulin, P. 2002, JGRA, 107, 1164
Török, T., Kliem, B., & Titov, V. S. 2004, A&A, 413, L27
Tsuneta, S., Hara, H., Shimizu, T., et al. 1992, PASJ, 44, L63
Veronig, A. M., Karlický, M., Vršnak, B., et al. 2006, A&A, 446, 675
Veronig, A. M., Podladchikova, T., Dissauer, K., et al. 2018, ApJ, 868, 107
Vršnak, B. 2016, AN, 337, 1002
Wang, D., Liu, R., Wang, Y., et al. 2017, ApJL, 843, L9
Wang, Y., Su, Y., Shen, J., et al. 2018, ApJ, 859, 148
Wiegelmann, T., & Inhester, B. 2010, A&A, 516, A107
Wiegelmann, T., Thalmann, J. K., Inhester, B., et al. 2012, SoPh, 281, 37
Yang, K., Guo, Y., & Ding, M. D. 2015, ApJ, 806, 171
Yashiro, S., Gopalswamy, N., Akiyama, S., Michalek, G., & Howard, R. A. 2005, JGRA, 110, A12S05
Zhang, J., Cheng, X., & Ding, M.-D. 2012, NatCo, 3, 747
Zheng, R., Yang, S., Rao, C., et al. 2019, ApJ, 875, 71
Zhong, Z., Guo, Y., & Ding, M. D. 2021, NatCo, 12, 2734
Zuccarello, F. P., Aulanier, G., & Gilchrist, S. A. 2015, ApJ, 814, 126